

# Turbulence Modeling for CFD

# **Turbulence Modeling for CFD**

by

**David C. Wilcox**

**DCW Industries, Inc.  
La Cañada, California**

*Dedicated to my Wife*

BARBARA

*my Children*

KINLEY and BOB

*and my Dad*

## **Turbulence Modeling for CFD**

Copyright © 1993, 1994 by DCW Industries, Inc. All rights reserved.

First Printing: July, 1993

Second Printing: November, 1994 (with corrections)

No part of this book may be reproduced or transmitted in any form or by any means, electronic or mechanical, including photocopying, recording, or any information storage and retrieval system, without permission in writing from DCW Industries, Inc.

DCW Industries, Inc.  
5354 Palm Drive, La Cañada, California 91011  
818/790-3844 (FAX) 818/952-1272

This book was prepared with  $\text{\LaTeX}$ , and was printed in the United States of America by Griffin Printing, Glendale, California.

## **Library of Congress Cataloging in Publication Data**

Wilcox, David C.

Turbulence Modeling for CFD / David C. Wilcox—1st ed.

Includes bibliography, index and  $3\frac{1}{2}$  inch floppy disk.

1. Turbulence—Mathematical Models.

2. Fluid Dynamics—Mathematical Models.

TA357.5.T87 W542 1993

93-224752

ISBN 0-9636051-0-0

# About the Author

**Dr. David C. Wilcox**, was born in Wilmington, Delaware. He did his undergraduate studies from 1963 to 1966 at the Massachusetts Institute of Technology, graduating with a Bachelor of Science degree in Aeronautics and Astronautics. From 1966 to 1967, he was an Engineer Scientist Specialist at McDonnell Douglas Aircraft Division in Long Beach, California, working for A. M. O. Smith. His experience with McDonnell Douglas was primarily in subsonic and transonic flow calculations. From 1967 to 1970, he attended the California Institute of Technology, graduating with a Ph.D. in Aeronautics. In 1970 he joined TRW Systems, Inc. in Redondo Beach, California, as a Member of the Technical Staff. He performed studies of both high- and low-speed fluid-mechanical and heat-transfer problems, such as turbulent hypersonic flow and thermal radiation from a flame. From 1972 to 1973, he was a staff scientist for Applied Theory, Inc., in Los Angeles, California, responsible for scientific-project management. He participated directly in many research efforts involving numerical computation and analysis of a wide range of fluid flows such as separated turbulent flow, transitional flow and hypersonic plume-body interaction. In 1973, he founded DCW Industries, Inc., a La Cañada, California firm engaged in engineering research, software development and publishing, for which he is currently the President. He has taught several fluid mechanics and applied mathematics courses at the University of Southern California and at the University of California, Los Angeles.

Dr. Wilcox has published many papers and reports on turbulence modeling, computational fluid dynamics, boundary-layer separation, boundary-layer transition, thermal radiation, and rapidly rotating fluids. He is an Associate Fellow of the American Institute of Aeronautics and Astronautics (AIAA) and has served as an Associate Editor for the AIAA Journal.



# Contents

<b>Notation</b>	<b>xi</b>
<b>Preface</b>	<b>xvii</b>
<b>1 Introduction</b>	<b>1</b>
1.1 Definition of an Ideal Turbulence Model . . . . .	1
1.2 How Complex Does a Turbulence Model Have to Be? . . . .	1
1.3 Comments on the Physics of Turbulence . . . . .	2
1.4 A Brief History of Turbulence Modeling . . . . .	5
<b>2 The Closure Problem</b>	<b>11</b>
2.1 Reynolds Averaging . . . . .	11
2.2 Correlations . . . . .	15
2.3 Reynolds-Averaged Equations . . . . .	15
2.4 The Reynolds-Stress Equation . . . . .	17
<b>3 Algebraic Models</b>	<b>23</b>
3.1 Molecular Transport of Momentum . . . . .	24
3.2 The Mixing-Length Hypothesis . . . . .	27
3.3 Application to Free Shear Flows . . . . .	30
3.3.1 The Far Wake . . . . .	32
3.3.2 The Mixing Layer . . . . .	38
3.3.3 The Jet . . . . .	41
3.4 Modern Variants of the Mixing-Length Model . . . . .	44
3.4.1 Cebeci-Smith Model . . . . .	50
3.4.2 Baldwin-Lomax Model . . . . .	52
3.5 Application to Wall-Bounded Flows . . . . .	53
3.5.1 Channel and Pipe Flow . . . . .	53
3.5.2 Boundary Layers . . . . .	59
3.6 Separated Flows . . . . .	61

3.7	The 1/2-Equation Model . . . . .	65
3.8	Range of Applicability . . . . .	67
<b>4</b>	<b>Turbulence Energy Equation Models</b>	<b>73</b>
4.1	The Turbulence Energy Equation . . . . .	74
4.2	One-Equation Models . . . . .	77
4.3	Two-Equation Models . . . . .	83
4.3.1	The $k$ - $\omega$ Model . . . . .	84
4.3.2	The $k$ - $\epsilon$ Model . . . . .	87
4.3.3	Other Two-Equation Models . . . . .	90
4.4	Closure Coefficients . . . . .	92
4.5	Application to Free Shear Flows . . . . .	95
4.6	Perturbation Analysis of the Boundary Layer . . . . .	104
4.6.1	The Log Layer . . . . .	105
4.6.2	The Defect Layer . . . . .	110
4.6.3	The Viscous Sublayer . . . . .	122
4.7	Surface Boundary Conditions . . . . .	126
4.7.1	Wall Functions . . . . .	126
4.7.2	Surface Roughness . . . . .	128
4.7.3	Surface Mass Injection . . . . .	131
4.8	Application to Wall-Bounded Flows . . . . .	131
4.8.1	Channel and Pipe Flow . . . . .	132
4.8.2	Boundary Layers . . . . .	133
4.9	Low-Reynolds-Number Effects . . . . .	138
4.9.1	Asymptotic Consistency . . . . .	138
4.9.2	Transition . . . . .	146
4.10	Separated Flows . . . . .	160
4.11	Range of Applicability . . . . .	163
<b>5</b>	<b>Effects of Compressibility</b>	<b>171</b>
5.1	Physical Considerations . . . . .	171
5.2	Favre Averaging . . . . .	172
5.3	Favre-Averaged Equations . . . . .	174
5.4	Compressible-Flow Closure Approximations . . . . .	180
5.5	Dilatation Dissipation . . . . .	183
5.6	Compressible Law of the Wall . . . . .	189
5.7	Compressible Boundary Layers . . . . .	195
5.8	Shock-Induced Boundary-Layer Separation . . . . .	203

<b>6</b>	<b>Beyond the Boussinesq Approximation</b>	<b>213</b>
6.1	Boussinesq-Approximation Deficiencies . . . . .	213
6.2	Nonlinear Constitutive Relations . . . . .	218
6.3	Second-Order Closure Models . . . . .	223
6.3.1	Closure Approximations . . . . .	224
6.3.2	Launder-Reece-Rodi Model . . . . .	231
6.3.3	Wilcox Multiscale Model . . . . .	232
6.4	Application to Homogeneous Turbulent Flows . . . . .	235
6.5	Application to Free Shear Flows . . . . .	242
6.6	Application to Wall-Bounded Flows . . . . .	243
6.6.1	Surface Boundary Conditions . . . . .	244
6.6.2	Channel and Pipe Flow . . . . .	248
6.6.3	Boundary Layers . . . . .	253
6.7	Application to Separated Flows . . . . .	261
6.8	Range of Applicability . . . . .	266
<b>7</b>	<b>Numerical Considerations</b>	<b>273</b>
7.1	Multiple Time Scales and Stiffness . . . . .	273
7.2	Numerical Accuracy Near Boundaries . . . . .	275
7.2.1	Solid Surfaces . . . . .	275
7.2.2	Turbulent/Nonturbulent Interfaces . . . . .	279
7.3	Parabolic Marching Methods . . . . .	287
7.4	Elementary Time-Marching Methods . . . . .	292
7.5	Block-Implicit Methods . . . . .	297
7.6	Solution Convergence and Grid Sensitivity . . . . .	303
<b>8</b>	<b>New Horizons</b>	<b>313</b>
8.1	Background Information . . . . .	313
8.2	Direct Numerical Simulation . . . . .	316
8.3	Large Eddy Simulation . . . . .	322
8.4	Chaos . . . . .	328
<b>A</b>	<b>Cartesian Tensor Analysis</b>	<b>331</b>
<b>B</b>	<b>Rudiments of Perturbation Methods</b>	<b>337</b>
<b>C</b>	<b>Companion Software</b>	<b>349</b>
C.1	Overview . . . . .	349
C.1.1	Program Structure . . . . .	350
C.1.2	Program Input . . . . .	351
C.1.3	Program Output . . . . .	352
C.2	Free Shear Flows . . . . .	353

C.2.1	Program WAKE: Far Wake . . . . .	355
C.2.2	Program MIXER: Mixing Layer . . . . .	357
C.2.3	Program JET: Plane, Round and Radial Jet . . . . .	359
C.2.4	Program PLOTF: Plotting Utility . . . . .	361
C.3	Channel and Pipe Flow . . . . .	364
C.3.1	Program PIPE: Channel and Pipe Flow . . . . .	365
C.3.2	Program PLOTP: Plotting Utility . . . . .	367
C.4	Boundary-Layer Perturbation Analysis . . . . .	371
C.4.1	Program SUBLAY: Viscous Sublayer . . . . .	373
C.4.2	Program DEFECT: Defect Layer . . . . .	375
C.4.3	Program PLOTS: Sublayer Plotting Utility . . . . .	376
C.4.4	Program PLOTD: Defect-Layer Plotting Utility . . . . .	379
C.5	Miscellaneous Routines . . . . .	382
C.5.1	Function ERF: Error Function . . . . .	383
C.5.2	Subroutine NAMSYS: Fortran Portability . . . . .	384
C.5.3	Subroutine RKGS: Runge-Kutta Integration . . . . .	386
C.5.4	Subroutine RTNI: Newton's Iterations . . . . .	388
C.5.5	Subroutine TRI: Tridiagonal Matrix Inversion . . . . .	389
C.6	Diskette Contents . . . . .	390
<b>D</b>	<b>Program EDDYBL</b>	<b>391</b>
D.1	Overview . . . . .	391
D.1.1	Acknowledgments . . . . .	391
D.1.2	Required Hardware and Software . . . . .	392
D.2	Getting Started Quickly . . . . .	392
D.3	Installing SETEBL . . . . .	397
D.3.1	Boot-Console Installation . . . . .	397
D.3.2	Remote-Terminal Installation . . . . .	398
D.4	Installing EDDYBL . . . . .	398
D.5	Running a General Case . . . . .	399
D.5.1	Preliminary Operations . . . . .	399
D.5.2	Units Selection . . . . .	400
D.5.3	Main Parameters . . . . .	400
D.5.4	Taking a Lunch Break . . . . .	402
D.5.5	Edge/Wall Conditions . . . . .	403
D.5.6	Preparing Edge/Wall Condition Data Files . . . . .	404
D.5.7	Generating Edge/Wall Conditions . . . . .	406
D.5.8	Initial Profiles . . . . .	406
D.5.9	Selecting a Turbulence Model . . . . .	408
D.5.10	Logical Unit Numbers and Plotting Files . . . . .	408
D.5.11	Running the Boundary-Layer Program . . . . .	410
D.5.12	Restart Run . . . . .	410

D.5.13 Gas Properties and Profile Printing . . . . .	411
D.5.14 Selecting Laminar, Transitional or Turbulent Flow . . . . .	412
D.6 Applicability and Limitations . . . . .	412
D.7 EDDYBL Output Parameters . . . . .	413
D.8 Program PLOTEB: Plotting Utility . . . . .	415
D.9 Adapting to Other Compilers/Systems . . . . .	419
D.10 Compile and Link Commands . . . . .	420
D.11 Additional Technical Information . . . . .	423
D.11.1 Mean-Flow Equations . . . . .	423
D.11.2 $k$ - $\omega$ and Multiscale Model Equations . . . . .	424
D.11.3 $k$ - $\epsilon$ Model Equations . . . . .	426
D.11.4 Transformed Equations . . . . .	429
D.12 Software Package Modules . . . . .	432
<b>E Plotting Program Details</b>	<b>433</b>
E.1 Font Files . . . . .	433
E.2 Video Devices . . . . .	433
E.3 Plotting Colors . . . . .	435
E.4 Hardcopy Devices . . . . .	435
<b>Bibliography</b>	<b>437</b>
<b>Index</b>	<b>456</b>

# Notation

This section includes the most commonly used notation in this book. In order to avoid departing too much from conventions normally used in literature on turbulence modeling and general fluid mechanics, a few symbols denote more than one quantity.

## English Symbols

Symbol	Definition
$a$	Speed of sound
$a_{ijkl}$	Rapid pressure-strain tensor
$A_n, B_n, C_n, D_n$	Coefficients in tridiagonal matrix equation
$A_o^+$	Van Driest damping constant
$A_{ij}$	Slow pressure-strain tensor
$b_{ij}$	Dimensionless Reynolds-stress anisotropy tensor
$B$	Additive constant in the law of the wall
$c_{b1}, c_{b2}$	Closure coefficients
$c_f$	Skin friction based on edge velocity, $\tau_w / (\frac{1}{2}\rho U_e^2)$
$c_{f\infty}$	Skin friction based on freestream velocity, $\tau_w / (\frac{1}{2}\rho U_\infty^2)$
$c_{w1}, c_{w2}, c_{w3}$	Closure coefficients
$C_1, C_2$	Closure coefficients
$C_{cp}, C_{wk}$	Closure coefficients
$C_D, C_E$	Closure coefficients
$C_{dif}, C_{Kleb}$	Closure coefficients
$C_K$	Kolmogorov constant
$C_{L1}, C_{L2}$	Closure coefficients
$C_p$	Specific heat at constant pressure; pressure coefficient
$C_s, C_\epsilon$	Closure coefficients
$C_S$	Smagorinsky constant
$C_v$	Specific heat at constant volume
$C_\delta$	Shear-layer spreading rate

$C_{\epsilon 1}, C_{\epsilon 2}, C_{\epsilon 3}$	Closure coefficients
$C_{\tau 1}, C_{\tau 2}$	Closure coefficients
$C_{\mu}$	Closure coefficient
$C_{ij}$	LES cross-term stress tensor
$C_{ijk}$	Turbulent transport tensor
$D$	Drag per unit body width
$D_{ij}$	Production tensor, $\tau_{im}\partial U_m/\partial x_j + \tau_{jm}\partial U_m/\partial x_i$
$e$	Specific internal energy ; small-eddy energy
$E$	Total energy; viscous damping function
$E(\kappa)$	Energy spectral density
$E(\eta)$	Dimensionless self-similar dissipation rate
$E_h$	Discretization error
$f_{\mu}, f_1, f_2, f_s$	Viscous damping functions
$\mathbf{f}, \mathbf{f}_v$	Turbulence flux vectors
$F(\eta)$	Dimensionless self-similar streamfunction
$F_{Kleb}(y; \delta)$	Klebanoff intermittency function
$\mathbf{F}, \mathbf{F}_v$	Mean-flow flux vectors
$G$	Amplitude factor in von Neumann stability analysis
$G(\mathbf{x} - \boldsymbol{\xi})$	LES filter
$h$	Specific enthalpy
$H$	Total enthalpy; channel height; shape factor, $\delta^*/\theta$
$\mathcal{H}(x)$	Heaviside step function
$\mathbf{i}, \mathbf{j}, \mathbf{k}$	Unit vectors in $x, y, z$ directions
$I$	Unit (identity) matrix
$II, III$	Stress tensor invariants
$j$	Two-dimensional ( $j = 0$ ), axisymmetric ( $j = 1$ ) index
$J$	Specific momentum flux (flux per unit mass)
$k$	Kinetic energy of turbulent fluctuations per unit mass
$k_g$	Geometric progression ratio
$k_R$	Surface roughness height
$K$	Distortion parameter
$K(\eta)$	Dimensionless self-similar turbulence kinetic energy
$K_{\epsilon}, K_{\omega}$	Effective Kármán constant for compressible flows
$Kn$	Knudsen number
$\ell$	Turbulence length scale; characteristic eddy size
$\ell_{mfp}$	Mean free path
$\ell_{mix}$	Mixing length
$L$	Characteristic length scale
$L_{ij}$	Leonard stress tensor
$M$	Mach number
$M_{ijkl}$	Rapid pressure-strain tensor
$M_c$	Convective Mach number

$M_t$	Turbulence Mach number, $\sqrt{2k}/a$
$M_{to}$	Closure coefficient
$N(\eta)$	Dimensionless self-similar eddy viscosity
$N_{CFL}$	CFL number
$N_\omega$	Constant in near-wall solution for $\omega$
$\mathcal{N}(u_i)$	Navier-Stokes operator
$p$	Instantaneous static pressure
$p_{ij}$	Instantaneous momentum-flux tensor
$P$	Mean static pressure
$P_{ij}$	Production tensor, $\tau_{im}\partial U_j/\partial x_m + \tau_{jm}\partial U_i/\partial x_m$
$P_k, P_\omega, P_\epsilon$	Net production per unit dissipation of $k, \omega, \epsilon$
$Pr_L, Pr_T$	Laminar, turbulent Prandtl number
$q_j$	Heat-flux vector
$q_w$	Surface heat flux
$q_{Lj}, q_{Tj}$	Laminar, turbulent mean heat-flux vector
$Q_{ij}$	LES stress tensor, $C_{ij} + R_{ij}$
$\mathbf{Q}$	Dependent variable vector
$r, \theta, x$	Cylindrical polar coordinates
$R$	Pipe radius; channel half height; perfect gas constant
$R_{ij}$	SGS Reynolds stress tensor
$R_{ij}(\mathbf{x}, t; \mathbf{r})$	Two-point velocity correlation tensor
$\mathcal{R}$	Radius of curvature
$\mathcal{R}_{ij}(\mathbf{x}, t; t')$	Autocorrelation tensor
$R^+$	Sublayer scaled radius or half height, $u_\tau R/\nu$
$R_\beta, R_k, R_\omega$	Closure coefficients in viscous damping functions
$Re_L$	Reynolds number based on length $L$
$Re_T$	Turbulence Reynolds number, $k^{1/2}\ell/\nu$
$Re_\tau$	Sublayer scaled radius or half height, $R^+$
$Ri_T$	Turbulence Richardson number
$R_y$	Near-wall turbulence Reynolds number, $k^{1/2}y/\nu$
$s_{ij}$	Instantaneous strain-rate tensor
$\mathbf{s}, \mathbf{S}$	Source-term vectors
$S$	Source term — production minus dissipation
$S_{ij}$	Mean strain-rate tensor
$\overset{\circ}{S}_{ij}$	Oldroyd derivative of $S_{ij}$
$S_e, S_k, S_u, S_w$	Source terms in a similarity solution
$S_B$	Dimensionless surface mass injection function
$S_R$	Dimensionless surface roughness function
$t$	Time
$t_{ij}$	Instantaneous viscous stress tensor
$T$	Temperature; characteristic time scale



$T'$	Freestream turbulence intensity
$u, v, w$	Instantaneous velocity components in $x, y, z$ directions
$u_i$	Instantaneous velocity in tensor notation
$\mathbf{u}$	Instantaneous velocity in vector notation
$u', v', w'$	Fluctuating velocity components in $x, y, z$ directions
$u'_i$	Fluctuating velocity in tensor notation
$\mathbf{u}'$	Fluctuating velocity in vector notation
$\tilde{u}, \tilde{v}, \tilde{w}$	Favre-averaged velocity components in $x, y, z$ directions
$\tilde{u}_i$	Favre-averaged velocity in tensor notation
$\tilde{\mathbf{u}}$	Favre-averaged velocity in vector notation
$u'', v'', w''$	Favre fluctuating velocity components in $x, y, z$ directions
$u''_i$	Favre fluctuating velocity in tensor notation
$\mathbf{u}''$	Favre fluctuating velocity; fluctuating molecular velocity
$u_{rms}, v_{rms}$	RMS fluctuating velocity components in $x, y$ directions
$\overline{u'_i u'_j}$	Temporal average of fluctuating velocities
$u_\tau$	Friction velocity, $\sqrt{\tau_w / \rho_w}$
$\hat{\mathbf{u}}$	Velocity perturbation vector
$U, V, W$	Mean velocity components in $x, y, z$ directions
$U_i$	Mean velocity in tensor notation
$\mathbf{U}$	Mean velocity in vector notation
$U^+$	Dimensionless, sublayer-scaled, velocity, $U/u_\tau$
$U_m$	Maximum or centerline velocity
$\mathcal{U}(\eta)$	Dimensionless self-similar streamwise velocity
$v_{mix}$	Mixing velocity
$v_{th}$	Thermal velocity
$v_w$	Surface injection velocity
$\mathcal{V}(\eta)$	Dimensionless self-similar normal velocity
$W(\eta)$	Dimensionless self-similar specific dissipation rate
$x, y, z$	Rectangular Cartesian coordinates
$x_i$	Position vector in tensor notation
$\mathbf{x}$	Position vector in vector notation
$y^+$	Dimensionless, sublayer-scaled, distance, $u_\tau y / \nu$
$y_2^+$	$y^+$ at first grid point above surface
$y_m$	Inner/outer layer matching point

## Greek Symbols

Symbol	Definition
$\alpha, \alpha^*$	Closure coefficients
$\hat{\alpha}, \hat{\beta}, \hat{\gamma}$	Closure coefficients
$\alpha_o, \alpha_o^*$	Closure coefficients in viscous damping functions

$\alpha_T, \sigma_T, \omega_T$	Defect-layer similarity parameters
$\beta, \beta^*$	Closure coefficients
$\beta_T$	Equilibrium parameter, $(\delta^*/\tau_w)dP/dx$
$\gamma$	Specific heat ratio, $C_p/C_v$
$\delta$	Boundary layer or shear layer thickness
$\delta^*$	Displacement thickness, $\int_0^\delta \left(1 - \frac{\rho}{\rho_e} \frac{U}{U_e}\right) dy$
$\delta_v^*$	Velocity thickness, $\int_0^\delta \left(1 - \frac{U}{U_e}\right) dy$
$\delta_x$	Finite-difference matrix operator
$\delta_{ij}$	Kronecker delta
$\Delta$	LES filter width
$\Delta(x)$	Clauser thickness, $U_e \delta^*/u_\tau$
$\Delta \mathbf{Q}, \Delta x, \Delta y$	Incremental change in $\mathbf{Q}, x, y$
$\Delta t$	Timestep
$\epsilon$	Dissipation per unit mass
$\epsilon_d$	Dilatation dissipation
$\epsilon_s$	Solenoidal dissipation
$\epsilon_{ij}$	Dissipation tensor
$\epsilon_{ijk}$	Permutation tensor
$\zeta$	Second viscosity coefficient
$\eta$	Kolmogorov length scale; similarity variable
$\theta$	Momentum thickness, $\int_0^\delta \frac{\rho}{\rho_e} \frac{U}{U_e} \left(1 - \frac{U}{U_e}\right) dy$
$\kappa$	Kármán constant; thermal conductivity; wavenumber
$\kappa_v$	Effective Kármán constant for flows with mass injection
$\lambda$	Taylor microscale
$\lambda_{max}$	Largest eigenvalue
$\mu$	Molecular viscosity
$\mu_T$	Eddy viscosity
$\mu_{T_i}$	Inner-layer eddy viscosity
$\mu_{T_o}$	Outer-layer eddy viscosity
$\nu$	Kinematic molecular viscosity, $\mu/\rho$
$\nu_T$	Kinematic eddy viscosity, $\mu_T/\rho$
$\xi$	Dimensionless streamwise distance
$\xi^*, \hat{\xi}$	Closure coefficients
$\tilde{\pi}$	Coles' wake-strength parameter
$\Pi_{ij}$	Pressure-strain correlation tensor
$\rho$	Mass density
$\sigma, \sigma^*$	Closure coefficients
$\sigma_k, \sigma_\epsilon$	Closure coefficients
$\sigma_{L1}, \sigma_{L2}$	Closure coefficients
$\sigma_\tau, \sigma_{\tau 1}, \sigma_{\tau 2}$	Closure coefficients

$\sigma(x)$	Nonequilibrium parameter
$\sigma_{ij}$	Instantaneous total stress tensor
$\tau$	Kolmogorov time scale; turbulence dissipation time
$\tau_{ij}$	Reynolds stress tensor
$\tau_{turnover}$	Eddy turnover time
$\tau_{xy}$	Reynolds shear stress
$\tau_{xx}, \tau_{yy}, \tau_{zz}$	Normal Reynolds stresses
$\tau_w$	Surface shear stress
$\nu$	Kolmogorov velocity scale; closure coefficient
$\phi$	Dimensionless parameter, $(\nu_w/\rho u_r^3)dP/dx$
$\chi$	Free shear layer closure coefficient
$\psi$	Streamfunction
$\psi_k, \psi_\epsilon, \psi_\omega$	Parabolic marching scheme coefficients
$\omega$	Specific dissipation rate; vorticity vector magnitude

## Other

Symbol	Definition
$\partial \mathbf{f} / \partial \mathbf{q}$	Turbulence flux-Jacobian matrix
$\partial \mathbf{F} / \partial \mathbf{Q}$	Mean-flow flux-Jacobian matrix
$\partial \mathbf{s} / \partial \mathbf{q}$	Source-Jacobian matrix

## Subscripts

Symbol	Definition
<i>DNS</i>	Direct Numerical Simulation
<i>e</i>	Boundary-layer-edge value
<i>eq</i>	Equilibrium value
<i>LES</i>	Large Eddy Simulation
<i>o</i>	Centerline value
<i>v</i>	Viscous
<i>w</i>	Wall (surface) value
$\infty$	Freestream value

## Superscripts

Symbol	Definition
+	Sublayer-scaled value

# Preface

This book has been developed from the author's lecture notes used in presenting a post-graduate course on turbulence modeling at the University of Southern California. While several computational fluid dynamics (CFD) texts include some information about turbulence modeling, very few texts dealing exclusively with turbulence modeling have been written. As a consequence, turbulence modeling is regarded by many CFD researchers as "black magic," lacking in rigor and physical foundation. This book has been written to show that turbulence modeling can be done in a systematic and physically sound manner. This is not to say all turbulence modeling has been done in such a manner, for indeed many ill-conceived and ill-fated turbulence models have appeared in engineering journals. Even this author, early in his career, devised a turbulence model that violated Galilean invariance of the time-averaged Navier-Stokes equations! However, with judicious use of relatively simple mathematical tools, systematic construction of a well-founded turbulence model is not only possible but can be an exciting and challenging research project.

Thus, the primary goal of this book is to provide a systematic approach to developing a set of constitutive equations suitable for computation of turbulent flows. The engineer who feels no existing turbulence model is suitable for his or her needs and wishes to modify an existing model or to devise a new model will benefit from this feature of the text. A methodology is presented in Chapters 3 and 4 for devising and testing such equations. The methodology is illustrated in great detail for two-equation turbulence models. However, it is by no means limited to such models and is used again in Chapter 6 for a full Reynolds-stress model, but with less detail.

A secondary goal of this book is to provide a rational way for deciding how complex a model is needed for a given problem. The engineer who wishes to select an existing model that is sufficient for his or her needs will benefit most from this feature of the text. Chapter 3 begins with the simplest turbulence models and subsequent chapters chart a course leading to some of the most complex models that have been applied to a nontrivial

turbulent flow problem. Two things are done at each level of complexity. First, the range of applicability of the model is estimated. Second, many of the applications are repeated for all of the models to illustrate how accuracy changes with complexity.

The methodology makes extensive use of tensor analysis, similarity solutions, singular perturbation methods, and numerical procedures. The text assumes the user has limited prior knowledge of these mathematical concepts and provides what is needed both in the main text and in the Appendices. For example, Appendix A introduces rudiments of tensor analysis to facilitate manipulation of the Navier-Stokes equation, which is done extensively in Chapter 2. Chapter 3 shows, in detail, the way a similarity solution is generated. Similarity solutions are then obtained for the turbulent mixing layer, jet and far wake. Appendix B presents elements of singular perturbation theory. Chapters 4, 5 and 6 use the methods to dissect model-predicted features of the turbulent boundary layer.

No book on turbulence-model equations is complete without a discussion of numerical solution methods. Anyone who has ever tried to obtain a numerical solution to a set of turbulence transport equations can attest to this. Often, standard numerical procedures just won't work and alternative methods must be found to obtain accurate converged solutions. Chapter 7 focuses on numerical methods and elucidates some of the commonly encountered problems such as stiffness, sharp turbulent-nonturbulent interfaces, and difficulties attending turbulence related time scales.

The concluding chapter presents a brief overview of new horizons including direct numerical simulation (DNS), large-eddy simulation (LES) and the interesting mathematical theory of chaos.

Because turbulence modeling is a key ingredient in CFD work, the text would be incomplete without companion software implementing numerical solutions to standard turbulence model equations. Appendices C and D describe several computer programs that are included on the floppy disk accompanying the book. The programs all have a similar structure and can be easily modified to include new turbulence models.

The material presented in this book is appropriate for a one-semester, first or second year graduate course, or as a reference text for a CFD course. Successful study of this material requires an understanding of viscous-flow and boundary-layer theory. Some degree of proficiency in solving partial differential equations is also needed. A knowledge of computer programming, preferably in FORTRAN, will help the reader gain maximum benefit from the companion software described in the Appendices.

I extend my thanks to Dr. L. G. Redekopp of USC for encouraging and supporting development of the course for which this book is intended. A friend of many years, Dr. P. Bradshaw, reviewed the entire manuscript as I

wrote it, and taught me a lot through numerous discussions, comments and suggestions that greatly improved the final draft. Another long time friend, Dr. D. D. Knight, helped me understand why I had to write this book, reviewed the manuscript from cover to cover and offered a great deal of physical and computational insight in the process. My favorite mathematics teacher, Dr. D. S. Cohen, made sure I omitted the dot over every  $\iota$  and crossed every  $z$  in Appendix B. Drs. F. R. Menter and C. C. Horstman were kind enough to provide results of several of their computations in digital form. Thanks are also due for the support and help of several friends and colleagues, most notably Drs. P. J. Roache, C. G. Speziale and R. M. C. So.

I thank the nine students who were the first to take the course that this book was written for. Their patience was especially noteworthy, particularly in regard to typographical errors in the homework problems! That outstanding group of young engineers is D. Foley, R. T. Holbrook, N. Kale, T.-S. Leu, H. Lin, T. Magee, S. Tadepalli, P. Taniguchi and D. Wallace.

Finally, I owe a lifelong debt to my loving wife Barbara for tolerating the hectic pace first in college and then in the business world. Without her, this book would not have been possible.

*David C. Wilcox*

# Chapter 1

## Introduction

### 1.1 Definition of an Ideal Turbulence Model

Turbulence modeling is one of three key elements in Computational Fluid Dynamics (CFD). Very precise mathematical theories have evolved for the other two key elements, viz., grid generation and algorithm development. By its nature — in creating a mathematical model that approximates the physical behavior of turbulent flows — far less precision has been achieved in turbulence modeling. This is not really a surprising event since our objective has been to approximate an extremely complicated phenomenon.

The field is, to some extent, a throwback to the days of Prandtl, Taylor, von Kármán and all the many other clever engineers who spent a good portion of their time devising engineering approximations and models describing complicated physical flows. Simplicity combined with physical insight seems to have been a common denominator of the work of these great men. Using their work as a gauge, **an ideal model should introduce the minimum amount of complexity while capturing the essence of the relevant physics.** This description of an ideal model serves as the main keystone of this text.

### 1.2 How Complex Does a Turbulence Model Have to Be?

Aside from any physical considerations, turbulence is inherently three dimensional and time dependent. Thus, an enormous amount of information is required to completely describe a turbulent flow. Fortunately, we usually

require something less than a complete time history over all spatial coordinates for every flow property. Thus, for a given turbulent-flow application, we must pose the following question. Given a set of initial and/or boundary conditions, how do we predict the physically meaningful properties of the flow? What properties of a given flow are meaningful is generally dictated by the application. For the simplest applications, we may require only the skin friction and heat-transfer coefficients. More esoteric applications may require detailed knowledge of energy spectra, turbulence fluctuation magnitudes and scales.

Certainly, we should expect the complexity of the mathematics needed for a given application to increase as the amount of required flowfield detail increases. On the one hand, if all we require is skin friction for an attached flow, a simple mixing-length model (Chapter 3) may suffice. Such models are well developed and can be implemented with very little specialized knowledge. On the other hand, if we desire a complete time history of every aspect of a turbulent flow, only a solution to the complete Navier-Stokes equation will suffice. Such a solution requires an extremely accurate numerical solver and may require use of subtle transform techniques, not to mention vast computer resources. Most engineering problems fall somewhere between these two extremes.

**Thus, once the question of how much detail we need is answered, the level of complexity of the model follows, qualitatively speaking.** In the spirit of Prandtl, Taylor and von Kármán, the conscientious engineer will strive to use as conceptually simple an approach as possible to achieve his ends. Overkill is often accompanied by unexpected difficulties that, in CFD applications, almost always manifest themselves as numerical difficulties!

### 1.3 Comments on the Physics of Turbulence

Before plunging into the mathematics of turbulence, it is worthwhile to first discuss physical aspects of the phenomenon. The following discussion is not intended as a complete description of this complex topic. Rather, we focus upon a few features of interest in engineering applications, and in construction of a mathematical model. For a more-complete introduction, refer to a basic text on the physics of turbulence such as those by Tennekes and Lumley (1983) or Landahl and Mollo-Christensen (1992).

In 1937, Taylor and von Kármán [see Goldstein (1938)] proposed the following definition of turbulence: “Turbulence is an irregular motion which in general makes its appearance in fluids, gaseous or liquid, when they flow past solid surfaces or even when neighboring streams of the same fluid flow



past or over one another.” It is characterized by the presence of a large range of excited length and time scales. The irregular nature of turbulence stands in contrast to laminar motion, so called historically, because the fluid was imagined to flow in smooth laminae, or layers. Virtually all flows of practical engineering interest are turbulent. Turbulent flows always occur when the Reynolds number is large. For slightly viscous fluids such as water and air, large Reynolds number corresponds to anything stronger than a small swirl or a puff of wind. Careful analysis of solutions to the Navier-Stokes equation, or more typically to its boundary-layer form, show that turbulence develops as an instability of laminar flow.

To analyze the stability of laminar flows, virtually all methods begin by linearizing the equations of motion. Although some degree of success can be achieved in predicting the onset of instabilities that ultimately lead to turbulence with linear theories, the inherent nonlinearity of the Navier-Stokes equation precludes a complete analytical description of the actual transition process, let alone the fully-turbulent state. For a real (i.e., viscous) fluid, the instabilities result from interaction between the Navier-Stokes equation’s nonlinear inertial terms and viscous terms. The interaction is very complex because it is rotational, fully three dimensional and time dependent.

The strongly rotational nature of turbulence goes hand-in-hand with its three dimensionality. Vigorous stretching of vortex lines is required to maintain the ever-present fluctuating vorticity in a turbulent flow. Vortex stretching is absent in two-dimensional flows so that turbulence must be three dimensional. This inherent three dimensionality means there are no satisfactory two-dimensional approximations and this is one of the reasons turbulence remains the most noteworthy unsolved scientific problem of the twentieth century.

The time-dependent nature of turbulence also contributes to its intractability. The additional complexity goes beyond the introduction of an additional dimension. Turbulence is characterized by random fluctuations thus obviating a deterministic approach to the problem. Rather, we must use statistical methods. On the one hand, this aspect is not really a problem from the engineer’s view. Even if we had a complete time history of a turbulent flow, we would usually integrate the flow properties of interest over time to extract time-averages. On the other hand, time averaging operations lead to statistical correlations in the equations of motion that cannot be determined a priori. This is the classical closure problem, which is the primary focus of this text.

In principle, the time-dependent, three-dimensional Navier-Stokes equation contains all of the physics of a given turbulent flow. That this is true follows from the fact that turbulence is a continuum phenomenon. As noted

by Tennekes and Lumley (1983), “Even the smallest scales occurring in a turbulent flow are ordinarily far larger than any molecular length scale.” Nevertheless, the smallest scales of turbulence are still extremely small. They are generally many orders of magnitude smaller than the largest scales of turbulence, the latter being of the same order of magnitude as the dimension of the object about which the fluid is flowing. Furthermore, the ratio of smallest to largest scales decreases rapidly as the Reynolds number increases. To make an accurate numerical simulation (i.e., a full time-dependent three-dimensional solution) of a turbulent flow, all physically relevant scales must be resolved. While more and more progress is being made with such simulations, computers of the early 1990’s have insufficient memory and speed to solve any turbulent flow problem of practical interest. To underscore the magnitude of the problem, Speziale (1985) notes that a numerical simulation of turbulent pipe flow at a Reynolds number of 500,000 would require a computer 10 million times faster than a Cray Y/MP. However, the results are very useful in developing and testing turbulence models in the limit of low Reynolds number.

Turbulence consists of a continuous spectrum of scales ranging from largest to smallest, as opposed to a discrete set of scales. In order to visualize a turbulent flow with a spectrum of scales we often refer to turbulent eddies. A turbulent eddy can be thought of as a local swirling motion whose characteristic dimension is the local turbulence scale (Figure 1.1). Eddies overlap in space, large ones carrying smaller ones. Turbulence features a cascading process whereby, as the turbulence decays, its kinetic energy transfers from larger eddies to smaller eddies. Ultimately, the smallest eddies dissipate into heat through the action of molecular viscosity. Thus, we observe that turbulent flows are always dissipative.

Perhaps the most important feature of turbulence from an engineering point of view is its enhanced diffusivity. Turbulent diffusion greatly enhances the transfer of mass, momentum and energy. Apparent stresses often develop in turbulent flows that are several orders of magnitude larger than in corresponding laminar flows.

The nonlinearity of the Navier-Stokes equation leads to interactions between fluctuations of differing wavelengths and directions. As discussed above, the wavelengths of the motion usually extend all the way from a maximum comparable to the width of the flow to a minimum fixed by viscous dissipation of energy. The main physical process that spreads the motion over a wide range of wavelengths is vortex stretching. The turbulence gains energy if the vortex elements are primarily oriented in a direction in which the mean velocity gradients can stretch them. Most importantly, wavelengths that are not too small compared to the mean-flow width interact most strongly with the mean flow. Consequently, the larger-scale

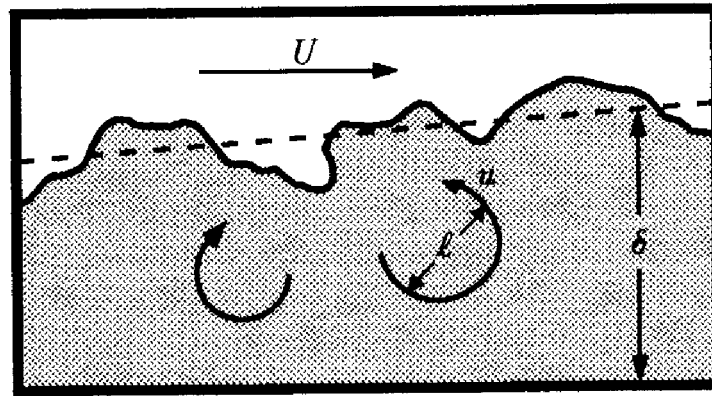


Figure 1.1: Large eddies in a turbulent boundary layer. The flow above the boundary layer has a steady velocity  $U$ ; the eddies move at randomly-fluctuating velocities of the order of a tenth of  $U$ . The largest eddy size ( $\ell$ ) is comparable to the boundary-layer thickness ( $\delta$ ). The interface and the flow above the boundary is quite sharp [Corrsin and Kistler (1954)].

turbulent motion carries most of the energy and is mainly responsible for the enhanced diffusivity and attending stresses. In turn, the larger eddies randomly stretch the vortex elements that comprise the smaller eddies, cascading energy to them.

An especially striking feature of a turbulent shear flow is the way large bodies of fluid migrate across the flow, carrying smaller-scale disturbances with them. The arrival of these large eddies near the interface between the turbulent region and nonturbulent fluid distorts the interface into a highly convoluted shape (Figure 1.1). In addition to migrating across the flow, they have a lifetime so long that they persist for distances as much as 30 times the width of the flow [Bradshaw (1972)]. Hence, the turbulent stresses at a given position depend upon upstream history and cannot be uniquely specified in terms of the local strain-rate tensor as in laminar flow.

As we progress through the following chapters, we will introduce more specific details of turbulence properties for common flows on an as-needed basis.

## 1.4 A Brief History of Turbulence Modeling

The primary emphasis in this book is upon the time-averaged Navier-Stokes equation. The origin of this approach dates back to the end of the nineteenth century when Reynolds (1895) published results of his research on turbulence. His pioneering work proved to have such profound importance

for all future developments that we refer to the standard time-averaging process as one type of Reynolds averaging.

The earliest attempts at developing a mathematical description of turbulent stresses sought to mimic the molecular gradient-diffusion process. In this spirit, Boussinesq (1877) introduced the concept of an eddy viscosity. As with Reynolds, Boussinesq has been immortalized in turbulence literature. The Boussinesq eddy-viscosity approximation is so widely known that few authors find a need to reference his original paper.

Neither Reynolds nor Boussinesq attempted solution of the Reynolds-averaged Navier-Stokes equation in any systematic manner. Much of the physics of viscous flows was a mystery in the nineteenth century, and further progress awaited Prandtl's discovery of the boundary layer in 1904. Focusing upon turbulent flows, Prandtl (1925) introduced the mixing length (an analog of the mean-free path of a gas) and a straightforward prescription for computing the eddy viscosity in terms of the mixing length. The mixing-length hypothesis, closely related to the eddy-viscosity concept, formed the basis of virtually all turbulence-modeling research for the next twenty years. Important early contributions were made by several researchers, most notably by von Kármán (1930). In modern terminology, we refer to a mixing-length model as an **algebraic model** or a **zero-equation model of turbulence**. By definition, an **n-equation model** signifies a model that requires solution of **n** additional differential transport equations in addition to those expressing conservation of mass, momentum and energy.

To improve the ability to predict properties of turbulent flows and to develop a more realistic mathematical description of the turbulent stresses, Prandtl (1945) postulated a model in which the eddy viscosity depends upon the kinetic energy of the turbulent fluctuations,  $k$ . He proposed a modeled differential equation approximating the exact equation for  $k$ . This improvement, on a conceptual level, takes account of the fact that the eddy viscosity is affected by where the flow has been, i.e., upon flow history. Thus was born the concept of the so-called **one-equation model of turbulence**.

While having an eddy viscosity that depends upon flow history provides a more physically realistic model, the need to specify a turbulence length scale remains. Since the length scale can be thought of as a characteristic eddy size and since such scales are different for each flow, turbulence models that do not provide a length scale are **incomplete**. That is, we must know something about the flow, other than initial and boundary conditions, in advance in order to obtain a solution. Such models are not without merit and, in fact, have proven to be of great value in many engineering applications.

To elaborate a bit further, an incomplete model generally defines a

turbulence length in a prescribed manner from the mean flow, e.g. the displacement thickness,  $\delta^*$ , for an attached boundary layer. However, a different length in this example would be needed when the boundary layer separates since  $\delta^*$  may be negative. Yet another length might be needed for free shear flows, etc. In essence, incomplete models usually define quantities that may vary more simply or more slowly than the Reynolds stresses (e.g. eddy viscosity and mixing length). Presumably such quantities are easier to correlate than the actual stresses.

A particularly desirable type of turbulence model would be one that can be applied to a given turbulent flow by prescribing at most the appropriate boundary and/or initial conditions. Ideally, no advance knowledge of any property of the turbulence should be required to obtain a solution. We define such a model as being **complete**. Note that our definition implies nothing regarding the accuracy or universality of the model, only that it can be used to determine a flow with no prior knowledge of any flow details.

Kolmogorov (1942) introduced the first **complete** model of turbulence. In addition to having a modeled equation for  $k$ , he introduced a second parameter  $\omega$  that he referred to as “the rate of dissipation of energy in unit volume and time.” The reciprocal of  $\omega$  serves as a turbulence time scale, while  $k^{1/2}/\omega$  serves as the analog of the mixing length. In this model, known as a  $k$ - $\omega$  model,  $\omega$  satisfies a differential equation similar to the equation for  $k$ . The model is thus termed a **two-equation model of turbulence**. While this model offered great promise, it went with virtually no applications for the next quarter century because of the unavailability of computers to solve its nonlinear differential equations.

Rotta (1951) laid the foundation for turbulence models that obviate use of the Boussinesq approximation. He devised a plausible model for the differential equation governing evolution of the tensor that represents the turbulent stresses, i.e., the Reynolds-stress tensor. This approach is called **second-order or second-moment closure**. The primary conceptual advantage of second-order closure is the natural manner in which nonlocal and history effects are incorporated. Such models automatically accommodate complicating effects such as streamline curvature, rigid-body rotation, and body forces. This stands in contrast to eddy-viscosity models that fail to properly account for these effects. For a three-dimensional flow, a second-order closure model introduces seven equations, one for the turbulence scale and six for the components of the Reynolds-stress tensor. As with Kolmogorov’s  $k$ - $\omega$  model, second-order closure models awaited adequate computer resources.

Thus, by the early 1950’s, four main categories of turbulence models had evolved, viz.,

1. Algebraic (Zero-Equation) Models
2. One-Equation Models
3. Two-Equation Models
4. Second-Order Closure Models

With the coming of the age of computers since the 1960's, further development of all four classes of turbulence models has occurred. The following overview lists a few of the most important modern developments for each of the four classes.

**Algebraic Models.** Van Driest (1956) devised a viscous damping correction for the mixing-length model that is included in virtually all algebraic models in use today. Cebeci and Smith (1974) refined the eddy-viscosity/mixing-length model to a point that it can be used with great confidence for most attached boundary layers. To remove some of the difficulties in defining the turbulence length scale from the shear-layer thickness, Baldwin and Lomax (1978) have proposed an alternative algebraic model that enjoys widespread use.

**One-Equation Models.** Of the four types of turbulence models described above, the one-equation model has enjoyed the least popularity and success. Perhaps the most successful model of this type was formulated by Bradshaw, Ferriss and Atwell (1967). In the 1968 Stanford Conference on Computation of Turbulent Boundary Layers [Coles and Hirst (1969)] the best turbulence models of the day were tested against the best experimental data of the day. In this author's opinion, of all the models used, the Bradshaw-Ferriss-Atwell model most faithfully reproduced measured flow properties. There has been some renewed interest in one-equation models [c.f. Baldwin and Barth (1990), Goldberg (1991) and Spalart and Allmaras (1992)], motivated primarily by the ease with which such model equations can be solved numerically, relative to two-equation models and second-order closure models.

**Two-Equation Models.** While Kolmogorov's  $k$ - $\omega$  model was the first of this type, it remained in obscurity until the coming of the computer. By far, the most extensive work on two-equation models has been done by Launder and Spalding (1972) and a continuing succession of students and colleagues. Launder's  $k$ - $\epsilon$  model, where  $\epsilon$  is proportional to the product of  $k$  and  $\omega$ , is as well known as the mixing-length model and is the most widely used two-equation model. Even the model's demonstrable inadequacy for flows with adverse pressure gradient [c.f. Rodi and Scheuerer (1986) and Wilcox (1988a)] has done little to discourage its widespread use. With no prior knowledge of Kolmogorov's work, Saffman (1970) formulated a  $k$ - $\omega$

model that enjoys advantages over the  $k$ - $\epsilon$  model, especially for integrating through the viscous sublayer and for predicting effects of adverse pressure gradient. Wilcox and Alber (1972), Saffman and Wilcox (1974), Wilcox and Traci (1976), Wilcox and Rubesin (1980), and Wilcox (1988a), for example, have pursued further development and application of  $k$ - $\omega$  models. As pointed out by Lakshminarayana (1986),  $k$ - $\omega$  models are the second most widely used type of two-equation turbulence model.

**Second-Order Closure Models.** By the 1970's, sufficient computer resources became available to permit serious development of this class of model. The most noteworthy efforts were those of Donaldson [Donaldson and Rosenbaum (1968)], Daly and Harlow (1970) and Launder, Reece and Rodi (1975). The latter has become the baseline second-order closure model: more recent contributions by Lumley (1978), Speziale (1985, 1987a) and Reynolds (1987) have added mathematical rigor to the closure process. However, because of the large number of equations and complexity involved in second-order closure models, they have thus far found their way into a relatively small number of applications compared to algebraic and two-equation models.

This book investigates all four classes of turbulence models. The primary emphasis is upon examining the underlying physical foundation and upon developing the mathematical tools for analyzing and testing the models. **The text is not intended to be a catalog of all turbulence models.** Rather, we approach each class of models in a generic sense. Detailed information is provided for models that have stood the test of time; additionally, references are given for most models.

## Chapter 2

# The Closure Problem

Because turbulence consists of random fluctuations of the various flow properties, we use a statistical approach. Our purposes are best served by using the procedure introduced by Reynolds (1895) in which all quantities are expressed as the sum of mean and fluctuating parts. We then form the time average of the continuity and Navier-Stokes equations. As we will see in this chapter, the nonlinearity of the Navier-Stokes equation leads to the appearance of momentum fluxes that act as apparent stresses throughout the flow. These momentum fluxes are unknown a priori. We then derive equations for these stresses and the resulting equations include additional unknown quantities. This illustrates the issue of closure, i.e., establishing a sufficient number of equations for all of the unknowns.

### 2.1 Reynolds Averaging

We begin with the averaging concepts introduced by Reynolds (1895). In general, Reynolds averaging assumes a variety of forms involving either an integral or a summation. The three forms most pertinent in turbulence-model research are the **time average**, the **spatial average** and the **ensemble average**.

**Time averaging** is appropriate for **stationary turbulence**, i.e., a turbulent flow that, on the average, does not vary with time. For such a flow, we express an instantaneous flow variable as  $f(\mathbf{x}, t)$ . Its time average,  $F_T(\mathbf{x})$ , is defined by

$$F_T(\mathbf{x}) = \lim_{T \rightarrow \infty} \frac{1}{T} \int_t^{t+T} f(\mathbf{x}, t) dt \quad (2.1)$$



**Spatial averaging** is appropriate for **homogeneous** turbulence, which is a turbulent flow that, on the average, is uniform in all directions. We average over all spatial coordinates by doing a volume integral. Calling the average  $F_V$ , we have

$$F_V(t) = \lim_{V \rightarrow \infty} \frac{1}{V} \iiint f(\mathbf{x}, t) dV \quad (2.2)$$

**Ensemble averaging** is the most general type of averaging. As an idealized example, in terms of measurements from  $N$  identical experiments where  $f(\mathbf{x}, t) = f_n(\mathbf{x}, t)$  in the  $n^{\text{th}}$  experiment, the average is  $F_E$ , where

$$F_E(\mathbf{x}, t) = \lim_{N \rightarrow \infty} \frac{1}{N} \sum_{n=1}^N f_n(\mathbf{x}, t) \quad (2.3)$$

For turbulence that is both stationary and homogeneous, we may assume that these three averages are all equal. This assumption is known as the **ergodic hypothesis**.

Because virtually all engineering problems involve **inhomogeneous turbulence**, time averaging is the most appropriate form of Reynolds averaging. The time-averaging process is most clearly explained for stationary turbulence. For such a flow, we express the instantaneous velocity,  $u_i(\mathbf{x}, t)$ , as the sum of a mean,  $U_i(\mathbf{x})$ , and a fluctuating part,  $u'_i(\mathbf{x}, t)$ , so that

$$u_i(\mathbf{x}, t) = U_i(\mathbf{x}) + u'_i(\mathbf{x}, t) \quad (2.4)$$

As in Equation (2.1), the quantity  $U_i(\mathbf{x})$  is the time-averaged, or mean, velocity defined by

$$U_i(\mathbf{x}) = \lim_{T \rightarrow \infty} \frac{1}{T} \int_t^{t+T} u_i(\mathbf{x}, t) dt \quad (2.5)$$

The time average of the mean velocity is again the same time-averaged value, i.e.,

$$\overline{U_i(\mathbf{x})} = \lim_{T \rightarrow \infty} \frac{1}{T} \int_t^{t+T} U_i(\mathbf{x}) dt = U_i(\mathbf{x}) \quad (2.6)$$

where an overbar is shorthand for time average. The time average of the fluctuating part of the velocity is zero. That is, using Equation (2.6),

$$\overline{u'_i} = \lim_{T \rightarrow \infty} \frac{1}{T} \int_t^{t+T} [u_i(\mathbf{x}, t) - U_i(\mathbf{x})] dt = U_i(\mathbf{x}) - \overline{U_i(\mathbf{x})} = 0 \quad (2.7)$$

While Equation (2.5) is mathematically well defined, we can never truly realize infinite  $T$  in any physical flow. This is not a serious problem in

practice however. In forming our time average, we just select a time  $T$  that is very long relative to the maximum period of the velocity fluctuations,  $T_1$ . In other words, rather than formally taking the limit  $T \rightarrow \infty$ , we do the indicated integration in Equation (2.5) with  $T \gg T_1$ . As an example, for flow at 10 m/sec in a 5 cm diameter pipe, an integration time of 20 seconds would probably be adequate. In this time the flow moves 4,000 pipe diameters.

There are some flows for which the mean flow contains very slow variations with time that are not turbulent in nature. For instance, we might impose a slowly varying periodic pressure gradient in a duct or we might wish to compute flow over a helicopter blade. Clearly, Equations (2.4) and (2.5) must be modified to accommodate such applications. The simplest, but a bit more arbitrary, method is to replace Equations (2.4) and (2.5) with

$$u_i(\mathbf{x}, t) = U_i(\mathbf{x}, t) + u'_i(\mathbf{x}, t) \quad (2.8)$$

and

$$U_i(\mathbf{x}, t) = \frac{1}{T} \int_t^{t+T} u_i(\mathbf{x}, t) dt, \quad T_1 \ll T \ll T_2 \quad (2.9)$$

where  $T_2$  is the time scale characteristic of the slow variations in the flow that we do not wish to regard as belonging to the turbulence. Figure 2.1 illustrates these concepts.

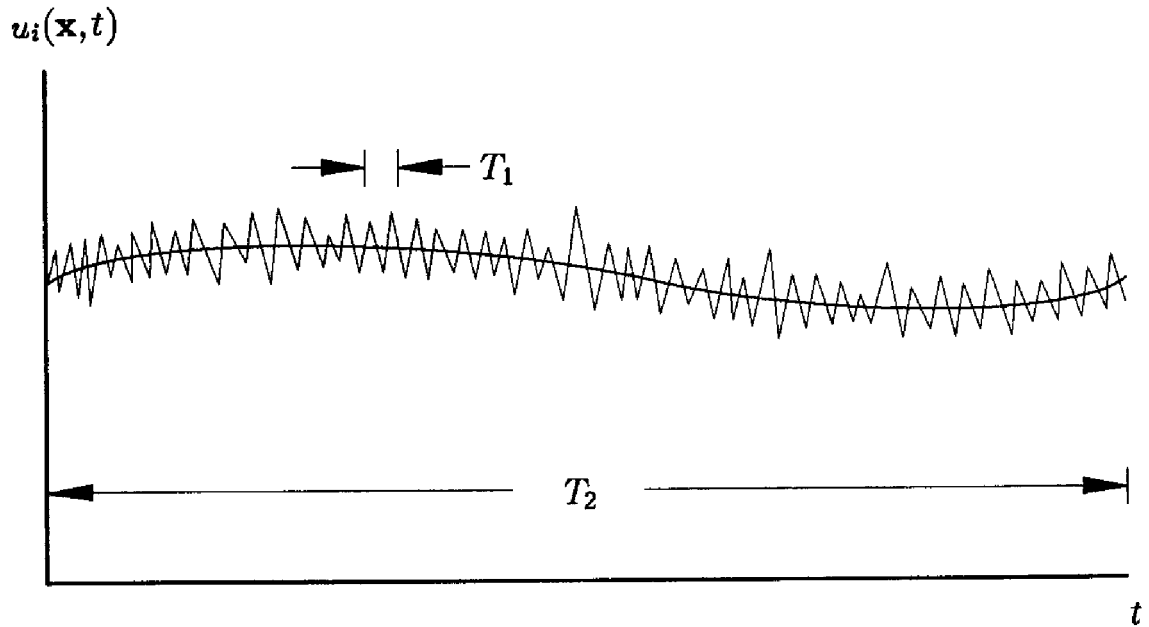


Figure 2.1: Time averaging for nonstationary turbulence.

A word of caution is in order regarding Equation (2.9). We are implicitly assuming that time scales  $T_1$  and  $T_2$  exist that differ by several

orders of magnitude. Very few unsteady flows of engineering interest are guaranteed to satisfy this condition. We cannot use Equations (2.8) and (2.9) for such flows because there is no distinct boundary between our imposed unsteadiness and turbulent fluctuations. For such flows, the mean and fluctuating components are correlated, i.e., the time average of their product is non-vanishing. In meteorology, for example, this is known as the **spectral gap problem**. If the flow is periodic, **Phase Averaging** (see Problems) can be used; otherwise, ensemble averaging is necessary. For a rigorous approach, an alternative method such as Large Eddy Simulation (Chapter 8) will be required.

Clearly our time averaging process, involving integrals over time, commutes with spatial differentiation. Thus, for any scalar  $p$  and vector  $u_i$ ,

$$\overline{p_{,i}} = P_{,i} \quad \text{and} \quad \overline{u_{i,j}} = U_{i,j} \quad (2.10)$$

Because we are dealing with definite integrals, time averaging is a linear operation. Thus if  $c_1$  and  $c_2$  are constants while  $a$  and  $b$  denote any two flow properties, then

$$\overline{c_1 a + c_2 b} = c_1 A + c_2 B \quad (2.11)$$

The time average of an unsteady term like  $\partial u_i / \partial t$  is obviously zero for stationary turbulence. For nonstationary turbulence, we must look a little closer. We know that

$$\frac{1}{T} \int_t^{t+T} \frac{\partial}{\partial t} (U_i + u'_i) dt = \frac{U_i(\mathbf{x}, t+T) - U_i(\mathbf{x}, t)}{T} + \frac{u'_i(\mathbf{x}, t+T) - u'_i(\mathbf{x}, t)}{T} \quad (2.12)$$

The second term on the right-hand side of Equation (2.12) vanishes because  $T$  effectively approaches  $\infty$  on the time scale of the turbulent fluctuations. By contrast,  $T$  is very small relative to the time scale of the mean flow, so that the first term is the value corresponding to the limit  $T \rightarrow 0$ , i.e.,  $\partial U_i / \partial t$ . Hence,

$$\overline{\frac{\partial u_i}{\partial t}} = \frac{\partial U_i}{\partial t} \quad (2.13)$$

Although it may seem a bit unusual to be taking the limit  $T \rightarrow \infty$  and  $T \rightarrow 0$  in the same equation, the process can be fully justified using the two-timing method from perturbation theory [see Kevorkian and Cole (1981)]. The notion is simply that we have a slow time scale and a fast time scale, similar to the case of small damping on a linear oscillator. In a perturbation analysis of such a problem, dependent variables become functions of two independent time variables (essentially  $t/T_1$  and  $t/T_2$ ). In the normal spirit of perturbation theory, the limit  $t/T_1 \rightarrow \infty$  corresponds to the limit  $t/T_2 \rightarrow 0$ .

## 2.2 Correlations

Thus far we have considered time averages of linear quantities. When we time average the product of two properties, say  $\phi$  and  $\psi$ , we have the following:

$$\overline{\phi\psi} = \overline{(\Phi + \phi')(\Psi + \psi')} = \overline{\Phi\Psi + \Phi\psi' + \Psi\phi' + \phi'\psi'} = \Phi\Psi + \overline{\phi'\psi'} \quad (2.14)$$

where we take advantage of the fact that the product of a mean quantity and a fluctuating quantity has zero mean. There is no a priori reason for the time average of the product of two fluctuating quantities to vanish. Thus, Equation (2.14) tells us the mean value of a product,  $\overline{\phi\psi}$ , differs from the product of the mean values,  $\Phi\Psi$ . The quantities  $\phi'$  and  $\psi'$  are said to be **correlated** if  $\overline{\phi'\psi'} \neq 0$ . They are **uncorrelated** if  $\overline{\phi'\psi'} = 0$ .

Similarly, for a triple product, we find

$$\overline{\phi\psi\xi} = \Phi\Psi\Xi + \overline{\phi'\psi'\Xi} + \overline{\psi'\xi'\Phi} + \overline{\phi'\xi'\Psi} + \overline{\phi'\psi'\xi'} \quad (2.15)$$

Again, terms linear in  $\phi'$ ,  $\psi'$  or  $\xi'$  have zero mean. As with terms quadratic in fluctuating quantities, there is no a priori reason for the cubic term,  $\overline{\phi'\psi'\xi'}$ , to vanish.

## 2.3 Reynolds-Averaged Equations

For simplicity we confine our attention to incompressible flow. Effects of compressibility will be addressed in Chapter 5. The equations for conservation of mass and momentum are

$$\frac{\partial u_i}{\partial x_i} = 0 \quad (2.16)$$

$$\rho \frac{\partial u_i}{\partial t} + \rho u_j \frac{\partial u_i}{\partial x_j} = -\frac{\partial p}{\partial x_i} + \frac{\partial t_{ji}}{\partial x_j} \quad (2.17)$$

The vectors  $u_i$  and  $x_i$  are velocity and position,  $t$  is time,  $p$  is pressure,  $\rho$  is density and  $t_{ij}$  is the viscous stress tensor defined by

$$t_{ij} = 2\mu s_{ij} \quad (2.18)$$

where  $\mu$  is molecular viscosity and  $s_{ij}$  is the strain-rate tensor,

$$s_{ij} = \frac{1}{2} \left( \frac{\partial u_i}{\partial x_j} + \frac{\partial u_j}{\partial x_i} \right) \quad (2.19)$$

To simplify the time-averaging process, we rewrite the convective term in conservation form, i.e.,

$$u_j \frac{\partial u_i}{\partial x_j} = \frac{\partial}{\partial x_j}(u_j u_i) - u_i \frac{\partial u_j}{\partial x_j} = \frac{\partial}{\partial x_j}(u_j u_i) \quad (2.20)$$

where we take advantage of Equation (2.16) in order to drop  $u_i \partial u_j / \partial x_j$ . Combining Equations (2.17) through (2.20) yields the Navier-Stokes equation in conservation form.

$$\rho \frac{\partial u_i}{\partial t} + \rho \frac{\partial}{\partial x_j}(u_j u_i) = -\frac{\partial p}{\partial x_i} + \frac{\partial}{\partial x_j}(2\mu s_{ji}) \quad (2.21)$$

Time averaging Equations (2.16) and (2.21) yields the **Reynolds averaged equations of motion in conservation form**, viz.,

$$\frac{\partial U_i}{\partial x_i} = 0 \quad (2.22)$$

$$\rho \frac{\partial U_i}{\partial t} + \rho \frac{\partial}{\partial x_j} \left( U_j U_i + \overline{u'_j u'_i} \right) = -\frac{\partial P}{\partial x_i} + \frac{\partial}{\partial x_j}(2\mu S_{ji}) \quad (2.23)$$

The time-averaged conservation of mass, Equation (2.22), is identical to the instantaneous Equation (2.16) with the mean velocity replacing the instantaneous velocity. Subtracting Equation (2.22) from Equation (2.16) shows that the fluctuating velocity,  $u'_i$ , also has zero divergence. Aside from replacement of instantaneous variables by mean values, the only difference between the time-averaged and instantaneous momentum equations is the appearance of the correlation  $\overline{u'_i u'_j}$ .

**Herein lies the fundamental problem of turbulence for the engineer.** In order to compute all mean-flow properties of the turbulent flow under consideration, we need a prescription for computing  $\overline{u'_i u'_j}$ .

Equation (2.23) can be written in its most recognizable form by using Equation (2.20) in reverse. There follows

$$\rho \frac{\partial U_i}{\partial t} + \rho U_j \frac{\partial U_i}{\partial x_j} = -\frac{\partial P}{\partial x_i} + \frac{\partial}{\partial x_j} \left( 2\mu S_{ji} - \overline{\rho u'_j u'_i} \right) \quad (2.24)$$

Equation (2.24) is usually referred to as the **Reynolds-averaged Navier-Stokes equation**. The quantity  $-\overline{\rho u'_i u'_j}$  is known as the **Reynolds-stress tensor** and we denote it by  $\tau_{ij}$ . Thus,

$$\tau_{ij} = -\overline{\rho u'_i u'_j} \quad (2.25)$$

By inspection,  $\tau_{ij} = \tau_{ji}$  so that this is a symmetric tensor, and thus has six independent components. Hence, we have produced six unknown quantities as a result of Reynolds averaging. Unfortunately, we have gained no

additional equations. So, for general three-dimensional flows, we have four unknown mean-flow properties, viz., pressure and the three velocity components. Along with the six Reynolds-stress components, we thus have ten unknowns. Our equations are mass conservation [Equation (2.22)] and the three components of Equation (2.24) for a grand total of four. This means our system is not yet **closed**. To close the system, we must find enough equations to solve for our unknowns.

## 2.4 The Reynolds-Stress Equation

In quest of additional equations, we can take moments of the Navier-Stokes equation. That is, we multiply the Navier-Stokes equation by a fluctuating property and time average the product. Using this procedure, we can derive a differential equation for the Reynolds-stress tensor. To illustrate the process, we introduce some special notation. Let  $\mathcal{N}(u_i)$  denote the Navier-Stokes operator, viz.,

$$\mathcal{N}(u_i) = \rho \frac{\partial u_i}{\partial t} + \rho u_k \frac{\partial u_i}{\partial x_k} + \frac{\partial p}{\partial x_i} - \mu \frac{\partial^2 u_i}{\partial x_k \partial x_k} \quad (2.26)$$

The viscous term has been simplified by noting from mass conservation (for incompressible flow) that  $s_{ki,k} = u_{i,kk}$ . Thus, the Navier-Stokes equation can be written symbolically as

$$\mathcal{N}(u_i) = 0 \quad (2.27)$$

In order to derive an equation for the Reynolds stress tensor, we form the following time average.

$$\overline{u'_i \mathcal{N}(u_j) + u'_j \mathcal{N}(u_i)} = 0 \quad (2.28)$$

Note that, consistent with the symmetry of the Reynolds stress tensor, the resulting equation is also symmetric in  $i$  and  $j$ . For the sake of clarity, we proceed term by term. Also, for economy of space, we use tensor notation for derivatives throughout the time averaging process. First, we consider the **unsteady term**.

$$\begin{aligned} \overline{u'_i(\rho u_j)_{,t} + u'_j(\rho u_i)_{,t}} &= \overline{\rho u'_i(U_j + u'_j)_{,t}} + \overline{\rho u'_j(U_i + u'_i)_{,t}} \\ &= \overline{\rho u'_i U_{j,t}} + \overline{\rho u'_i u'_{j,t}} + \overline{\rho u'_j U_{i,t}} + \overline{\rho u'_j u'_{i,t}} \\ &= \overline{\rho u'_i u'_{j,t}} + \overline{\rho u'_j u'_{i,t}} \\ &= \overline{(\rho u'_i u'_j)_{,t}} \\ &= -\frac{\partial \tau_{ij}}{\partial t} \end{aligned} \quad (2.29)$$

Turning to the **convective term**, we have

$$\begin{aligned}
\overline{\rho u'_i u_k u_{j,k} + \rho u'_j u_k u_{i,k}} &= \overline{\rho u'_i (U_k + u'_k) (U_j + u'_j)_{,k}} \\
&+ \overline{\rho u'_j (U_k + u'_k) (U_i + u'_i)_{,k}} \\
&= \overline{\rho u'_i U_k u'_{j,k}} + \overline{\rho u'_i u'_k (U_j + u'_j)_{,k}} \\
&+ \overline{\rho u'_j U_k u'_{i,k}} + \overline{\rho u'_j u'_k (U_i + u'_i)_{,k}} \\
&= \overline{U_k (\rho u'_i u'_{j,k})} + \overline{\rho u'_i u'_k U_{j,k}} \\
&+ \overline{\rho u'_j u'_k U_{i,k}} + \overline{\rho u'_k (u'_i u'_j)_{,k}} \\
&= -U_k \frac{\partial \tau_{ij}}{\partial x_k} - \tau_{ik} \frac{\partial U_j}{\partial x_k} - \tau_{jk} \frac{\partial U_i}{\partial x_k} \\
&+ \frac{\partial}{\partial x_k} \overline{(\rho u'_i u'_j u'_k)} \tag{2.30}
\end{aligned}$$

In order to arrive at the final line of Equation (2.30), we use the fact that  $\partial u'_k / \partial x_k = 0$ . The **pressure gradient** term is straightforward.

$$\begin{aligned}
\overline{u'_i p_{,j} + u'_j p_{,i}} &= \overline{u'_i (P + p')_{,j}} + \overline{u'_j (P + p')_{,i}} \\
&= \overline{u'_i p'_{,j} + u'_j p'_{,i}} \\
&= \overline{u'_i \frac{\partial p'}{\partial x_j} + u'_j \frac{\partial p'}{\partial x_i}} \tag{2.31}
\end{aligned}$$

Finally, the **viscous term** yields

$$\begin{aligned}
\overline{\mu (u'_i u_{j,kk} + u'_j u_{i,kk})} &= \overline{\mu u'_i (U_j + u'_j)_{,kk}} + \overline{\mu u'_j (U_i + u'_i)_{,kk}} \\
&= \overline{\mu u'_i u'_{j,kk}} + \overline{\mu u'_j u'_{i,kk}} \\
&= \overline{\mu (u'_i u'_{j,k})_{,k}} + \overline{\mu (u'_j u'_{i,k})_{,k}} - \overline{2\mu u'_{i,k} u'_{j,k}} \\
&= \overline{\mu (u'_i u'_j)_{,kk}} - \overline{2\mu u'_{i,k} u'_{j,k}} \\
&= -\nu \frac{\partial^2 \tau_{ij}}{\partial x_k \partial x_k} - 2\mu \frac{\partial u'_i}{\partial x_k} \frac{\partial u'_j}{\partial x_k} \tag{2.32}
\end{aligned}$$

Collecting terms, we arrive at the equation for the Reynolds stress tensor.

$$\begin{aligned}
\frac{\partial \tau_{ij}}{\partial t} + U_k \frac{\partial \tau_{ij}}{\partial x_k} &= -\tau_{ik} \frac{\partial U_j}{\partial x_k} - \tau_{jk} \frac{\partial U_i}{\partial x_k} + 2\mu \frac{\partial u'_i}{\partial x_k} \frac{\partial u'_j}{\partial x_k} + \overline{u'_i \frac{\partial p'}{\partial x_j} + u'_j \frac{\partial p'}{\partial x_i}} \\
&+ \frac{\partial}{\partial x_k} \left[ \nu \frac{\partial \tau_{ij}}{\partial x_k} + \overline{\rho u'_i u'_j u'_k} \right] \tag{2.33}
\end{aligned}$$

We have gained six new equations, one for each independent component of the Reynolds-stress tensor. However, we have also generated 22 new unknowns! Specifically, accounting for all symmetries, we have the following.

$$\begin{aligned}\overline{\rho u'_i u'_j u'_k} &\rightarrow 10 \text{ unknowns} \\ \overline{2\mu \frac{\partial u'_i}{\partial x_k} \frac{\partial u'_j}{\partial x_k}} &\rightarrow 6 \text{ unknowns} \\ \overline{u'_i \frac{\partial p'}{\partial x_j} + u'_j \frac{\partial p'}{\partial x_i}} &\rightarrow 6 \text{ unknowns}\end{aligned}$$

With a little rearrangement of terms, we can cast the **Reynolds-stress equation** in its most recognizable form, viz.,

$$\frac{\partial \tau_{ij}}{\partial t} + U_k \frac{\partial \tau_{ij}}{\partial x_k} = -\tau_{ik} \frac{\partial U_j}{\partial x_k} - \tau_{jk} \frac{\partial U_i}{\partial x_k} + \epsilon_{ij} - \Pi_{ij} + \frac{\partial}{\partial x_k} \left[ \nu \frac{\partial \tau_{ij}}{\partial x_k} + C_{ijk} \right] \quad (2.34)$$

where

$$\Pi_{ij} = \overline{p' \left( \frac{\partial u'_i}{\partial x_j} + \frac{\partial u'_j}{\partial x_i} \right)} \quad (2.35)$$

$$\epsilon_{ij} = \overline{2\mu \frac{\partial u'_i}{\partial x_k} \frac{\partial u'_j}{\partial x_k}} \quad (2.36)$$

$$C_{ijk} = \overline{\rho u'_i u'_j u'_k} + \overline{p' u'_i \delta_{jk}} + \overline{p' u'_j \delta_{ik}} \quad (2.37)$$

This exercise illustrates the closure problem of turbulence. Because of the nonlinearity of the Navier-Stokes equation, as we take higher and higher moments, we generate additional unknowns at each level. At no point will this procedure balance our unknowns/equations ledger. On physical grounds, this is not a particularly surprising situation. After all, such operations are strictly mathematical in nature, and introduce no additional physical principles. The function of turbulence modeling is to devise approximations for the unknown correlations in terms of flow properties that are known so that a sufficient number of equations exists. In making such approximations, we close the system.



## Problems

**2.1** Suppose we have a velocity field that consists of: (i) a slowly varying component  $U(t) = U_0 e^{-t/\tau}$  where  $U_0$  and  $\tau$  are constants and (ii) a rapidly varying component  $u' = aU_0 \cos(2\pi t/\epsilon^2\tau)$  where  $a$  and  $\epsilon$  are constants with  $\epsilon \ll 1$ . We want to show that by choosing  $T = \epsilon\tau$ , the limiting process in Equation (2.9) makes sense.

- (a) Compute the exact time average of  $u = U + u'$ .
- (b) Replace  $T$  by  $\epsilon\tau$  in the slowly varying part of the time average of  $u$  and let  $t_f = \epsilon^2\tau$  in the fluctuating part of  $u$  to show that

$$\overline{U + u'} = U(t) + O(\epsilon)$$

where  $O(\epsilon)$  denotes a quantity that goes to zero linearly with  $\epsilon$  as  $\epsilon \rightarrow 0$ .

- (c) Repeat Parts (a) and (b) for  $du/dt$ .

**2.2** For an imposed periodic mean flow, a standard way of decomposing flow properties is to write

$$u(\mathbf{x}, t) = U(\mathbf{x}) + \hat{u}(\mathbf{x}, t) + u'(\mathbf{x}, t)$$

where  $U(\mathbf{x})$  is the mean-value,  $\hat{u}(\mathbf{x}, t)$  is the organized response component due to the imposed organized unsteadiness, and  $u'(\mathbf{x}, t)$  is the turbulent fluctuation.  $U(\mathbf{x})$  is defined as in Equation (2.5). We also use the **Phase Average** defined by

$$\langle u(\mathbf{x}, t) \rangle \equiv \lim_{N \rightarrow \infty} \frac{1}{N} \sum_{n=0}^{N-1} u(\mathbf{x}, t + n\tau)$$

where  $\tau$  is the period of the imposed excitation. Then, by definition,

$$\langle u(\mathbf{x}, t) \rangle = U(\mathbf{x}) + \hat{u}(\mathbf{x}, t), \quad \overline{\langle u(\mathbf{x}, t) \rangle} = U(\mathbf{x}), \quad \langle \hat{u}(\mathbf{x}, t) \rangle = \hat{u}(\mathbf{x}, t)$$

Verify the following.

- |                              |  |  |
|------------------------------|--|--|
| (a) $\langle U \rangle = U$  | (d) $\langle u' \rangle = 0$                               | (g) $\langle \hat{u}v' \rangle = 0$            |
| (b) $\overline{\hat{u}} = 0$ | (e) $\overline{\hat{u}v'} = 0$                             | (h) $\langle Uv \rangle = U \langle v \rangle$ |
| (c) $\overline{u'} = 0$      | (f) $\langle \hat{u}v \rangle = \hat{u} \langle v \rangle$ |  |

**2.3** For an incompressible flow, we have an imposed freestream velocity given by

$$u(x, t) = U_0(1 - ax) + U_0ax \sin 2\pi ft$$

where  $a$  is a constant of dimension 1/length,  $U_0$  is a constant reference velocity, and  $f$  is frequency. Integrating over one period, compute the average pressure gradient,  $dP/dx$ , for  $f = 0$  and  $f \neq 0$  in the freestream where the inviscid Euler equation holds, i.e.,

$$\rho \frac{\partial u}{\partial t} + \rho u \frac{\partial u}{\partial x} = -\frac{\partial p}{\partial x}$$

**2.4** Compute the difference between the Reynolds average of a quadruple product  $\phi\psi\xi\upsilon$  and the product of the means,  $\Phi\Psi\Xi\Upsilon$ .

**2.5** Consider the Reynolds stress equation as stated in Equation (2.34).

- (a) Show how Equation (2.34) follows from Equation (2.33).
- (b) Contract Equation (2.34), i.e., set  $i = j$  and perform the indicated summation, to derive a differential equation for the kinetic energy of the turbulence per unit mass defined by  $k \equiv \frac{1}{2}\overline{u'_i u'_i}$ .

## Chapter 3

# Algebraic Models

The simplest of all turbulence models are known as algebraic models. These models use the **Boussinesq eddy-viscosity approximation** to compute the Reynolds stress tensor as the product of an eddy viscosity and the mean strain-rate tensor. For computational simplicity, the eddy viscosity, in turn, is often computed in terms of a mixing length that is analogous to the mean free path in a gas. We will find that, in contrast to the molecular viscosity that is an intrinsic property of the fluid, the eddy viscosity (and hence the mixing length) depends upon the flow. Because the eddy viscosity and mixing length depend upon the particular flow under consideration they must be specified in advance. Thus, algebraic models are, by definition, **incomplete** models of turbulence.

We begin this chapter by first discussing molecular transport of momentum. Next we introduce Prandtl's mixing-length hypothesis and discuss its physical implications and limitations. The mixing-length model is then applied to free shear flows for which self-similar solutions hold. We discuss two modern algebraic turbulence models that are based on the mixing-length hypothesis, including applications to attached and separated wall-bounded flows. The latter applications illustrate the limit to the algebraic model's range of applicability. An interesting separated-flow replacement for algebraic models, known as the **Half-Equation Model**, improves agreement between computed and measured flow properties. The chapter concludes with a discussion of the range of applicability of algebraic models.

### 3.1 Molecular Transport of Momentum

To understand the motivation for the Boussinesq approximation, it is instructive to discuss momentum transport at the molecular level. However, as a word of caution, **molecules and turbulent eddies are fundamentally different**. They are so different that we will ultimately find, in Section 3.2, that the analogy between turbulent and molecular mixing is questionable, to say the least! It is nevertheless fruitful to pursue the analogy to illustrate how important it is to check the premises underlying turbulence closure approximations. At first glance, mimicking the molecular mixing process appears to be a careful exercise in physics. As we will see, the model just cannot stand up under close scrutiny.

We begin by considering a shear flow in which the velocity is given by

$$\mathbf{U} = U(y) \mathbf{i} \quad (3.1)$$

where  $\mathbf{i}$  is a unit vector in the  $x$  direction. Figure 3.1 depicts such a flow. We consider the flux of momentum across the plane  $y = 0$ , noting that molecular motion is random in both magnitude and direction. Molecules migrating across  $y = 0$  are **typical of where they come from**. That is, molecules moving up bring a momentum deficit and vice versa. This gives rise to a shear stress  $t_{xy}$ .

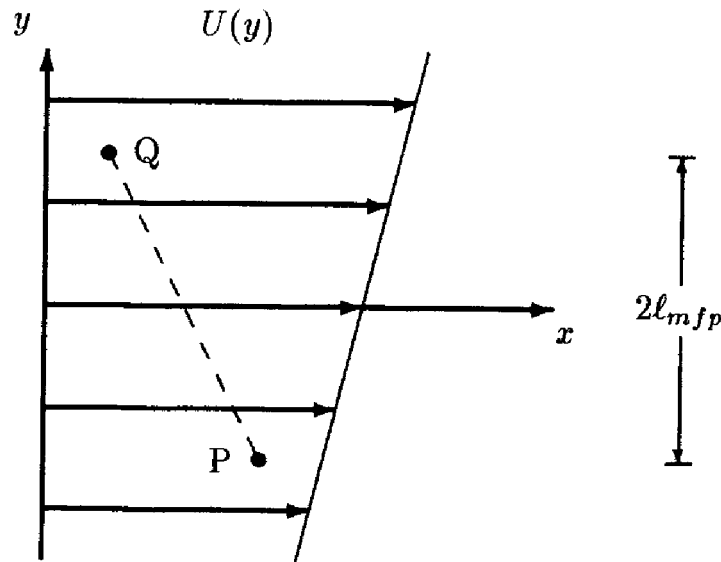


Figure 3.1: Shear flow schematic.

At the molecular level, we decompose the velocity according to

$$\mathbf{u} = \mathbf{U} + \mathbf{u}'' \quad (3.2)$$

where  $U$  is the average velocity defined in Equation (3.1) and  $u''$  represents the random molecular motion. The instantaneous flux of any property across  $y = 0$  is proportional to the velocity normal to the plane which, for this flow, is simply  $v''$ . Thus, the instantaneous flux of  $x$ -directed momentum,  $dp_{xy}$ , across a differential surface area  $dS$  is

$$dp_{xy} = \rho(U + u'')v'' dS \quad (3.3)$$

Performing an ensemble average over all molecules, we find

$$dP_{xy} = \overline{\rho u'' v''} dS \quad (3.4)$$

By definition, the stress acting on  $y = 0$  is given by  $\sigma_{xy} = dP_{xy}/dS$ . It is customary in fluid mechanics to set  $\sigma_{ij} = p\delta_{ij} - t_{ij}$ , where  $t_{ij}$  is the viscous stress tensor. Thus,

$$t_{xy} = -\overline{\rho u'' v''} \quad (3.5)$$

Equation (3.5) bears a strong resemblance to the Reynolds-stress tensor. This is not a coincidence. As pointed out by Tennekes and Lumley (1983), a stress that is generated as a momentum flux can always be written in this form. The only real difference is that, at the macroscopic level, the turbulent fluctuations,  $u'$  and  $v'$ , appear in place of the random molecular fluctuations,  $u''$  and  $v''$ . **This similarity is the basis of the Boussinesq eddy-viscosity approximation.**

Referring again to Figure 3.1, we can appeal to arguments from the kinetic theory of gases [e.g., Jeans (1962)] to determine  $t_{xy}$  in terms of  $U(y)$  and the fluid viscosity,  $\mu$ . First, consider the average number of molecules moving across unit area in the positive  $y$  direction. For a perfect gas, molecular velocities follow the Maxwellian distribution so that all directions are equally probable. The average molecular velocity is the thermal velocity,  $v_{th}$ , which is approximately 4/3 times the speed of sound in air. On average, half of the molecules move in the positive  $y$  direction while the other half move in the negative  $y$  direction. Also, the average vertical component of the velocity is  $v_{th} \cos \phi$  where  $\phi$  is the angle from the vertical. Integrating over a hemispherical shell, the average vertical speed is  $v_{th}/2$ . Thus, the average number of molecules moving across unit area in the positive  $y$  direction is  $nv_{th}/4$ , where  $n$  is the number of molecules per unit volume.

Now consider the transfer of momentum that occurs when molecules starting from point P cross the  $y = 0$  plane. We assume molecules are **typical of where they come from** which, on the molecular scale, is one mean free path away, the mean free path being the average distance a molecule travels between collisions with other molecules. Each molecule starting from

a point P below  $y = 0$  brings a momentum deficit of  $m[U(0) - U(-\ell_{mfp})]$ , where  $m$  is the molecular mass and  $\ell_{mfp}$  is the mean free path. Hence, the momentum flux from below is

$$\Delta P_- = \frac{1}{4}\rho v_{th}[U(0) - U(-\ell_{mfp})] \approx \frac{1}{4}\rho v_{th}\ell_{mfp}\frac{dU}{dy} \quad (3.6)$$

We have replaced  $U(-\ell_{mfp})$  by the first two terms of its Taylor-series expansion in Equation (3.6) and used the fact that  $\rho = mn$ . Similarly, molecules moving from a point Q above  $y = 0$  bring a momentum surplus of  $m[U(\ell_{mfp}) - U(0)]$ , and the momentum flux from above is

$$\Delta P_+ = \frac{1}{4}\rho v_{th}[U(\ell_{mfp}) - U(0)] \approx \frac{1}{4}\rho v_{th}\ell_{mfp}\frac{dU}{dy} \quad (3.7)$$

Consequently, the net shearing stress is the sum of  $\Delta P_-$  and  $\Delta P_+$ , wherefore

$$t_{xy} = \Delta P_- + \Delta P_+ \approx \frac{1}{2}\rho v_{th}\ell_{mfp}\frac{dU}{dy} \quad (3.8)$$

Hence, we conclude that the shear stress resulting from molecular transport of momentum in a perfect gas is given by

$$t_{xy} = \mu \frac{dU}{dy} \quad (3.9)$$

where  $\mu$  is the molecular viscosity defined by

$$\mu = \frac{1}{2}\rho v_{th}\ell_{mfp} \quad (3.10)$$

The arguments leading to Equations (3.9) and (3.10) are approximate and only roughly represent the true statistical nature of molecular motion. Interestingly, Jeans (1962) indicates that a precise analysis yields  $\mu = 0.499v_{th}\ell_{mfp}$ , wherefore our approximate analysis is remarkably accurate! However, we have made two implicit assumptions in our analysis that require justification.

**First**, we have truncated the Taylor series appearing in Equations (3.6) and (3.7) at the linear terms. For this approximation to be valid, we must have  $\ell_{mfp}|d^2U/dy^2| \ll |dU/dy|$ . The length scale  $L$  defined by

$$L \equiv \frac{|dU/dy|}{|d^2U/dy^2|} \quad (3.11)$$

is a length scale characteristic of the mean flow. Thus, the linear relation between stress and strain-rate implied by Equation (3.9) is valid provided the Knudsen number,  $Kn$ , is very small, i.e.,

$$Kn = \ell_{mfp}/L \ll 1 \quad (3.12)$$

For most practical flow conditions, the mean free path is several orders of magnitude smaller than any characteristic length scale of the mean flow. Thus, Equation (3.12) is satisfied for virtually all engineering problems.

**Second**, in computing the rate at which molecules cross  $y = 0$ , we assumed that  $\mathbf{u}''$  remained Maxwellian even in the presence of shear. This will be true if molecules experience many collisions on the time scale of the mean flow. Now, the average time between collisions is  $\ell_{mfp}/v_{th}$ . The characteristic time scale for the mean flow is  $|dU/dy|^{-1}$ . Thus, we also require that

$$\ell_{mfp} \ll \frac{v_{th}}{|dU/dy|} \quad (3.13)$$

Since  $v_{th}$  is of the same order of magnitude as the speed of sound, the right-hand side of Equation (3.13) defines yet another mean-flow length scale. As above, the mean free path is several orders smaller than this length scale for virtually all flows of engineering interest.

## 3.2 The Mixing-Length Hypothesis

Prandtl (1925) put forth the mixing-length hypothesis. He visualized a simplified model for turbulent fluid motion in which fluid particles coalesce into lumps that cling together and move as a unit. He further visualized that in a shear flow such as that depicted in Figure 3.1, the lumps retain their  $x$ -directed momentum for a distance in the  $y$  direction,  $\ell_{mix}$ , that he called the mixing length. In analogy to the molecular momentum transport process with Prandtl's lump of fluid replacing the molecule and  $\ell_{mix}$  replacing  $\ell_{mfp}$ , we can say that similar to Equation (3.8),

$$\tau_{xy} = \frac{1}{2} \rho v_{mix} \ell_{mix} \frac{dU}{dy} \quad (3.14)$$

The formulation is not yet complete because the **mixing velocity**,  $v_{mix}$ , has not been specified. Prandtl further postulated that

$$v_{mix} = \text{constant} \cdot \ell_{mix} \left| \frac{dU}{dy} \right| \quad (3.15)$$

which makes sense on dimensional grounds. Because  $\ell_{mix}$  is not a physical property of the fluid, we can always absorb the constant in Equation (3.15)

and the factor 1/2 in Equation (3.14) in the mixing length. Thus, in analogy to Equations (3.9) and (3.10), Prandtl's mixing-length hypothesis leads to

$$\tau_{xy} = \mu_T \frac{dU}{dy} \quad (3.16)$$

where  $\mu_T$  is the **eddy viscosity** given by

$$\mu_T = \rho \ell_{mix}^2 \left| \frac{dU}{dy} \right| \quad (3.17)$$

Our formulation still remains incomplete since we have replaced Boussinesq's empirical eddy viscosity,  $\mu_T$ , with Prandtl's empirical mixing length,  $\ell_{mix}$ . Prandtl postulated further that for flows near solid boundaries the mixing length is proportional to distance from the surface. This turns out to be a reasonably good approximation over a limited portion of a turbulent boundary layer. As we will see in Section 3.3, for free shear flows such as jets, wakes and mixing layers, the mixing length is proportional to the width of the layer,  $\delta$ . However, each of these flows requires a different coefficient of proportionality between  $\ell_{mix}$  and  $\delta$ . The point is, the mixing length is different for each flow (its ratio to the flow width, for example) and must be known in advance to obtain a solution.

Note that Equation (3.17) can be deduced directly from dimensional analysis. Assuming molecular transport of momentum is unimportant relative to turbulent transport, we expect molecular viscosity has no significance in a dimensional analysis. The only other dimensional parameters available in a shear flow are the fluid density,  $\rho$ , our assumed mixing length,  $\ell_{mix}$ , and the velocity gradient,  $dU/dy$ . (The eddy viscosity cannot depend upon  $U$  since that would violate Galilean invariance.) A straightforward dimensional analysis yields Equation (3.17).

Another interesting observation follows from replacing  $\tau_{xy}$  by its definition so that

$$-\overline{u'v'} = \left| \ell_{mix} \frac{dU}{dy} \right|^2 \quad (3.18)$$

The mixing velocity,  $v_{mix}$ , must be proportional to an appropriate average of  $v'$  such as the RMS value defined by  $v_{rms} = (\overline{v'^2})^{1/2}$ . Also, Townsend (1976) states that in all turbulent shear flows, experimental measurements indicate

$$|-\overline{u'v'}| \approx 0.4 u_{rms} v_{rms} \quad (3.19)$$

Consequently, if  $v_{rms} \sim v_{mix}$ , comparison of Equations (3.15) and (3.18) shows that the mixing-length model implies  $v_{rms}$  and  $u_{rms}$  are of the same order of magnitude. This is generally true although  $u_{rms}$  is usually 25% to 75% larger than  $v_{rms}$ .



At this point, we need to examine the appropriateness of the mixing-length hypothesis in representing turbulent transport of momentum. Because we have made a direct analogy to the molecular transport process, we have implicitly made the same two basic assumptions we made for molecular transport. Specifically, we have assumed that the Boussinesq approximation holds and that the turbulence is unaltered by the mean shear. Unfortunately, neither condition is rigorously satisfied in practice!

**Concerning the Boussinesq approximation**, its applicability depends upon the Knudsen number being small. Close to a solid boundary, for example, the mixing length is approximately linear with distance from the surface,  $y$ . Specifically, measurements indicate that  $\ell_{mix} \approx 0.41y$ . In the same vicinity, the velocity follows the well-known law of the wall [see Schlichting (1979)], and the velocity gradient varies inversely with  $y$ . Thus, the length  $L$  defined in Equation (3.11) is equal to  $y$ . Consequently, the Knudsen number is of order one, i.e.,

$$Kn = \ell_{mix}/L \approx 0.41 \quad (3.20)$$

Hence, the linear stress/strain-rate relation of Equation (3.16) is suspect.

**Concerning the effect of the mean shear on the turbulence**, the assumed lifetime of Prandtl's lumps of fluid is  $\ell_{mix}/v_{mix}$ . Reference to Equation (3.15) shows that this time is proportional to  $|dU/dy|^{-1}$ . Hence, the analog to Equation (3.13) is

$$\ell_{mix} \sim \frac{v_{mix}}{|dU/dy|} \quad (3.21)$$

Equation (3.21) tells us that the lumps of fluid will undergo changes as they travel from points P and Q toward  $y = 0$ . This is indeed consistent with the observed nature of turbulent shear flows. Tennekes and Lumley (1983) describe the situation by saying, "the general conclusion must be that turbulence in a shear flow cannot possibly be in a state of equilibrium which is independent of the flow field involved. The turbulence is continually trying to adjust to its environment, without ever succeeding."

Thus, the theoretical foundation of the mixing-length hypothesis is a bit flimsy to say the least. On the one hand, this is a forewarning that a turbulence model built on this foundation is unlikely to possess a very wide range of applicability. On the other hand, as the entire formulation is empirical in its essence, the usefulness of and justification for any of its approximations ultimately lies in how well the model performs in applications, and we defer to the applications of the following sections as its justification.

As a pleasant surprise, we will see that despite its theoretical shortcomings, the mixing-length model does an excellent job of reproducing experimental measurements. It can be easily calibrated for a specific class of flows,

and the model's predictions are consistent with measurements provided we don't depart too far from the established data base used to calibrate the mixing length. Eddy viscosity models based on the mixing length have been fine tuned for many flows since 1925, most notably by Cebeci and Smith (1974). Strictly speaking, the term **equilibrium** is nonsensical in the context of turbulent shear flows since, as noted above, turbulence is continually attempting to adjust to its environment, without ever succeeding. Nevertheless, most turbulence researchers describe certain flows as **equilibrium turbulent flows**. What they actually mean is a relatively simple flow with slowly varying properties. Most flows of this type can be accurately described by a mixing-length computation. In this spirit, a fitting definition of equilibrium turbulent flow might be a flow that can be accurately described using a mixing-length model!

### 3.3 Application to Free Shear Flows

Our first applications will be to incompressible **free shear flows**. A flow is termed free if it is not bounded by solid surfaces. Figure 3.2 illustrates three different types of free shear flows, viz., the **far wake**, the **mixing layer**, and the **jet**. A wake forms downstream of any object placed in a stream of fluid; we will consider only the two-dimensional wake. A mixing layer occurs between two parallel streams moving at different speeds; for the case shown in the figure, the lower stream is at rest. A jet occurs when fluid is ejected from a nozzle or orifice. We will assume the jet issues into a quiescent fluid, and we will analyze both the (two-dimensional) plane jet and the (axisymmetric) round jet.

All three of these flows approach what is known as **self similarity** far enough downstream that details of the geometry and flow conditions near  $x = 0$  become unimportant. The velocity component  $U(x, y)$ , for example, can be expressed in the form

$$U(x, y) = u_o(x)F(y/\delta(x)) \quad (3.22)$$

This amounts to saying that two velocity profiles located at different  $x$  stations have the same shape when plotted in the scaled form  $U(x, y)/u_o(x)$  versus  $y/\delta(x)$ . Flows with this property are also referred to as **self preserving**.

Free shear flows are interesting building-block cases to test a turbulence model on for several reasons. First, there are no solid boundaries so that we avoid the complications boundaries add to the complexity of a turbulent flow. Second, they are mathematically easy to calculate because similarity solutions exist, where the Reynolds-averaged equations of motion can be

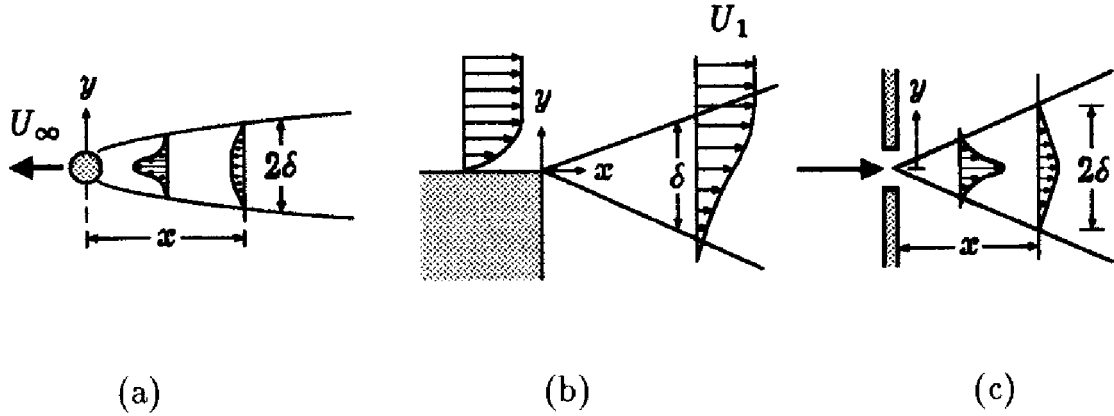


Figure 3.2: Free shear flows: (a) far wake; (b) mixing layer; and, (c) jet.

reduced to ordinary differential equations. This greatly simplifies the task of obtaining a solution. Third, there is a wealth of experimental data available to test model predictions against.

The standard boundary-layer approximations hold for all three of the shear flows considered in this Section. Additionally, molecular transport of momentum is negligible compared to turbulent transport. Since all three flows have constant pressure, the equations of motion are (with  $j = 0$  for two-dimensional flow and  $j = 1$  for axisymmetric flow):

$$\frac{\partial U}{\partial x} + \frac{1}{y^j} \frac{\partial}{\partial y} (y^j V) = 0 \quad (3.23)$$

$$\rho U \frac{\partial U}{\partial x} + \rho V \frac{\partial U}{\partial y} = \frac{1}{y^j} \frac{\partial}{\partial y} (y^j \tau_{xy}) \quad (3.24)$$

Of course, while the equations are the same for all three flows, boundary conditions are different. The appropriate boundary conditions will be stated when we discuss each flow.

As a historical note, in addition to the mixing-length model, Prandtl also proposed a simpler eddy viscosity model specifically for free shear flows. In this model,

$$\mu_T = \chi \rho [U_{max}(x) - U_{min}(x)] \delta(x) \quad (3.25)$$

where  $U_{max}$  and  $U_{min}$  are the maximum and minimum values of mean velocity in the layer,  $\delta$  is the half width of the layer, and  $\chi$  is a dimensionless empirical parameter. This model is very convenient for free shear flows because it is a function only of  $x$  by construction, and excellent results can be obtained if  $\chi$  is assumed to be constant across the layer. Consequently, laminar flow solutions can be generalized for turbulent flow with,

at most, minor notation changes. We leave application of this model to the Problems section. All of the applications in this Section will be done using Equations (3.16) and (3.17).

We begin by analyzing the far wake in Subsection 3.3.1. Complete details of the similarity solution method are given for the benefit of the reader who has not had much experience with the method. The far wake is especially attractive as our first application because a simple closed-form solution can be obtained using the mixing-length model. Then, we proceed to the mixing layer in Subsection 3.3.2. While an analytical solution is possible for the mixing layer, numerical integration of the equations proves to be far simpler. Finally, we study the plane jet and the round jet in Subsection 3.3.3.

### 3.3.1 The Far Wake

Clearly the flow in the wake of the body indicated in Figure 3.2(a) is symmetric about the  $x$  axis. Thus, we solve for  $0 \leq y < \infty$ . The relevant boundary conditions follow from symmetry on the axis and the requirement that the velocity approach its freestream value far from the body. Hence, the boundary conditions are

$$U(x, y) \rightarrow U_\infty \quad \text{as} \quad y \rightarrow \infty \quad (3.26)$$

$$\frac{\partial U}{\partial y} = 0 \quad \text{at} \quad y = 0 \quad (3.27)$$

The classical approach to this problem is to linearize the momentum equation, an approximation that is strictly valid only in the far wake [Schlichting (1979)]. Thus, we say that

$$\mathbf{U}(x, y) = U_\infty \mathbf{i} - \hat{\mathbf{u}} \quad (3.28)$$

where  $|\hat{\mathbf{u}}| \ll U_\infty$ . The linearized momentum equation and boundary conditions become

$$\rho U_\infty \frac{\partial \hat{u}}{\partial x} = -\frac{\partial \tau_{xy}}{\partial y} \quad (3.29)$$

$$\hat{u}(x, y) \rightarrow 0 \quad \text{as} \quad y \rightarrow \infty \quad (3.30)$$

$$\frac{\partial \hat{u}}{\partial y} = 0 \quad \text{at} \quad y = 0 \quad (3.31)$$

There is also an integral constraint that must be satisfied by the solution. If we consider a control volume surrounding the body and extending to infinity, conservation of momentum leads to the following requirement [see Schlichting (1979)],

$$\int_0^\infty \rho U(U_\infty - U) dy = \frac{1}{2} D \quad (3.32)$$

where  $D$  is the drag of the body per unit width.

We use the mixing-length model to specify the Reynolds stress  $\tau_{xy}$ , so that

$$\tau_{xy} = -\rho \ell_{mix}^2 \left| \frac{\partial \hat{u}}{\partial y} \right| \frac{\partial \hat{u}}{\partial y} \quad (3.33)$$

Finally, to close our set of equations, we assume the mixing length is proportional to the half-width of the wake,  $\delta(x)$  [see Figure 3.2(a)]. Thus, we say that

$$\ell_{mix} = \alpha \delta(x) \quad (3.34)$$

where  $\alpha$  is a constant that we refer to as a **closure coefficient**. Our fondest hope would be that the same value of  $\alpha$  works for all free shear flows. Unfortunately, this is not the case so that the mixing-length model must be recalibrated for each type of shear flow.

To obtain the similarity solution to Equations (3.29) through (3.34), we proceed in a series of interrelated steps. The sequence is as follows.

1. Assume the form of the solution.
2. Transform the equations of motion.
3. Transform the boundary conditions and the integral constraint.
4. Determine the conditions required for existence of the similarity solution.
5. Solve the resulting ordinary differential equation subject to the transformed boundary conditions.

In addition to these 5 steps, we will also determine the value of the **closure coefficient**  $\alpha$  in Equation (3.34) by comparison with experimental data.

**Step 1.** We begin by assuming the similarity solution can be written in terms of an as yet unknown velocity scale function,  $u_o(x)$ , and the wake half width,  $\delta(x)$ . Thus, we assume that the velocity can be written as

$$\hat{u}(x, y) = u_o(x) F(\eta) \quad (3.35)$$

where the **similarity variable**,  $\eta$ , is defined by

$$\eta = y/\delta(x) \quad (3.36)$$

**Step 2.** In order to transform Equation (3.29), we have to take account of the fact that we are making a formal change of dependent variables. We are transforming from  $(x, y)$  space to  $(x, \eta)$  space which means that derivatives must be transformed according to the chain rule of calculus. Thus, derivatives transform according to the following rules. Note that a subscript means that differentiation is done holding the subscripted variable constant.

$$\begin{aligned} \left(\frac{\partial}{\partial x}\right)_y &= \left(\frac{\partial x}{\partial x}\right)_y \left(\frac{\partial}{\partial x}\right)_\eta + \left(\frac{\partial \eta}{\partial x}\right)_y \left(\frac{\partial}{\partial \eta}\right)_x \\ &= \left(\frac{\partial}{\partial x}\right)_\eta + \left(\frac{\partial \eta}{\partial x}\right)_y \left(\frac{\partial}{\partial \eta}\right)_x \\ &= \left(\frac{\partial}{\partial x}\right)_\eta - \frac{\delta'(x)}{\delta(x)} \eta \left(\frac{\partial}{\partial \eta}\right)_x \end{aligned} \quad (3.37)$$

$$\begin{aligned} \left(\frac{\partial}{\partial y}\right)_x &= \left(\frac{\partial x}{\partial y}\right)_x \left(\frac{\partial}{\partial x}\right)_\eta + \left(\frac{\partial \eta}{\partial y}\right)_x \left(\frac{\partial}{\partial \eta}\right)_x \\ &= \left(\frac{\partial \eta}{\partial y}\right)_x \left(\frac{\partial}{\partial \eta}\right)_x \\ &= \frac{1}{\delta(x)} \left(\frac{\partial}{\partial \eta}\right)_x \end{aligned} \quad (3.38)$$

A prime denotes ordinary differentiation so that  $\delta'(x) = d\delta/dx$  in Equation (3.37). We now proceed to transform Equation (3.29). For example, the derivatives of  $\hat{u}$  are

$$\frac{\partial \hat{u}}{\partial x} = u'_o F(\eta) - \frac{u_o \delta'}{\delta} \eta \frac{dF}{d\eta} \quad (3.39)$$

$$\frac{\partial \hat{u}}{\partial y} = \frac{u_o}{\delta} \frac{dF}{d\eta} \quad (3.40)$$

Proceeding in this manner for all terms in Equation (3.29) and using the mixing-length prescription for the Reynolds stress leads to the transformed momentum equation.

$$\frac{U_\infty \delta u'_o}{u_o^2} F(\eta) - \frac{U_\infty \delta'}{u_o} \eta \frac{dF}{d\eta} = \alpha^2 \frac{d}{d\eta} \left( \left| \frac{dF}{d\eta} \right| \frac{dF}{d\eta} \right) \quad (3.41)$$

**Step 3.** Clearly,  $y \rightarrow \infty$  corresponds to  $\eta \rightarrow \infty$  and  $y \rightarrow 0$  corresponds to  $\eta \rightarrow 0$ . Thus, the boundary conditions in Equations (3.30) and (3.31) transform to

$$F(\eta) \rightarrow 0 \quad \text{as} \quad \eta \rightarrow \infty \quad (3.42)$$

$$\frac{dF}{d\eta} = 0 \quad \text{at} \quad \eta = 0 \quad (3.43)$$

and the integral constraint becomes

$$\int_0^\infty F(\eta) d\eta = \frac{D}{2\rho U_\infty u_o \delta} \quad (3.44)$$

**Step 4.** In seeking a similarity solution, we are attempting to make a separation of variables. The two terms on the left-hand side of Equation (3.41) have coefficients that in general vary with  $x$ . Also, the right-hand side of Equation (3.44) is a function of  $x$ . **The condition for existence of the similarity solution is that these three coefficients be independent of  $x$ .** Thus, we require the following three conditions.

$$\frac{U_\infty \delta u_o'}{u_o^2} = a_1, \quad \frac{U_\infty \delta'}{u_o} = a_2, \quad \frac{D}{2\rho U_\infty u_o \delta} = 1 \quad (3.45)$$

The quantities  $a_1$  and  $a_2$  must, of course, be constant. Note that we could have introduced a third constant in the integral constraint, but it is unnecessary (we, in effect, absorb the third constant in  $\delta$ ). The solution to these three simultaneous equations is simply

$$\delta(x) = \sqrt{\frac{a_2 D x}{\rho U_\infty^2}} \quad (3.46)$$

$$u_o(x) = \frac{1}{2} \sqrt{\frac{D}{a_2 \rho x}} \quad (3.47)$$

$$a_1 = -a_2 \quad (3.48)$$

**Step 5.** Finally, we expect that  $F(\eta)$  will have its maximum value on the axis, and then fall monotonically to zero approaching the freestream. If this is true, then  $F'(\eta)$  will be negative for all values of  $\eta$  and we can replace its absolute value with  $-F'(\eta)$ . Taking account of Equations (3.45) through (3.48), the momentum equation now simplifies to

$$\alpha^2 \frac{d}{d\eta} [(F')^2] - a_2 (\eta F' + F) = 0 \quad (3.49)$$

The second term is a perfect differential so that Equation (3.49) can be rewritten as

$$\frac{d}{d\eta} [\alpha^2 (F')^2 - a_2 \eta F] = 0 \quad (3.50)$$

Integrating once and imposing the symmetry condition at  $\eta = 0$  [Equation (3.43)] yields

$$\alpha \frac{dF}{d\eta} = -\sqrt{a_2 \eta F} \quad (3.51)$$

where we observe that  $F'(\eta)$  is everywhere less than zero. Integrating once more, we find that the solution for  $F(\eta)$  is

$$F(\eta) = C^2 \left[ 1 - (\eta/\eta_e)^{3/2} \right]^2 \quad (3.52)$$

where  $C$  is a constant of integration and  $\eta_e$  is given by

$$\eta_e = (3\alpha C / \sqrt{a_2})^{2/3} \quad (3.53)$$

This solution has a peak value at  $\eta = 0$  and decreases monotonically to zero as  $\eta \rightarrow \eta_e$ . It then increases without limit for  $\eta > \eta_e$ . The only way we can satisfy the far field boundary condition [Equation (3.42)] is to use Equation (3.52) for  $0 \leq \eta \leq \eta_e$  and to use the trivial solution,  $F(\eta) = 0$ , for values of  $\eta$  in excess of  $\eta_e$ .

With no loss of generality, we can set  $\eta_e = 1$ . To understand this, note that  $\eta/\eta_e = y/[\eta_e \delta(x)]$ . Hence, by setting  $\eta_e = 1$  we simply rescale the  $\eta$  coordinate so that  $\delta(x)$  is the wake half width as originally planned. Therefore,

$$3\alpha C = \sqrt{a_2} \quad (3.54)$$

Finally, imposing the integral constraint, Equation (3.44), yields an equation for the constant  $C$ . Performing the integration, we have

$$\int_0^1 C^2 [1 - \eta^{3/2}]^2 d\eta = \frac{9}{20} C^2 = 1 \quad (3.55)$$

Therefore,

$$C = \sqrt{20}/3 = 1.491 \quad (3.56)$$

and

$$\alpha = \sqrt{a_2/20} \quad (3.57)$$

If the closure coefficient  $\alpha$  were known, our solution would be completely determined at this point with Equation (3.57) specifying  $a_2$ . This



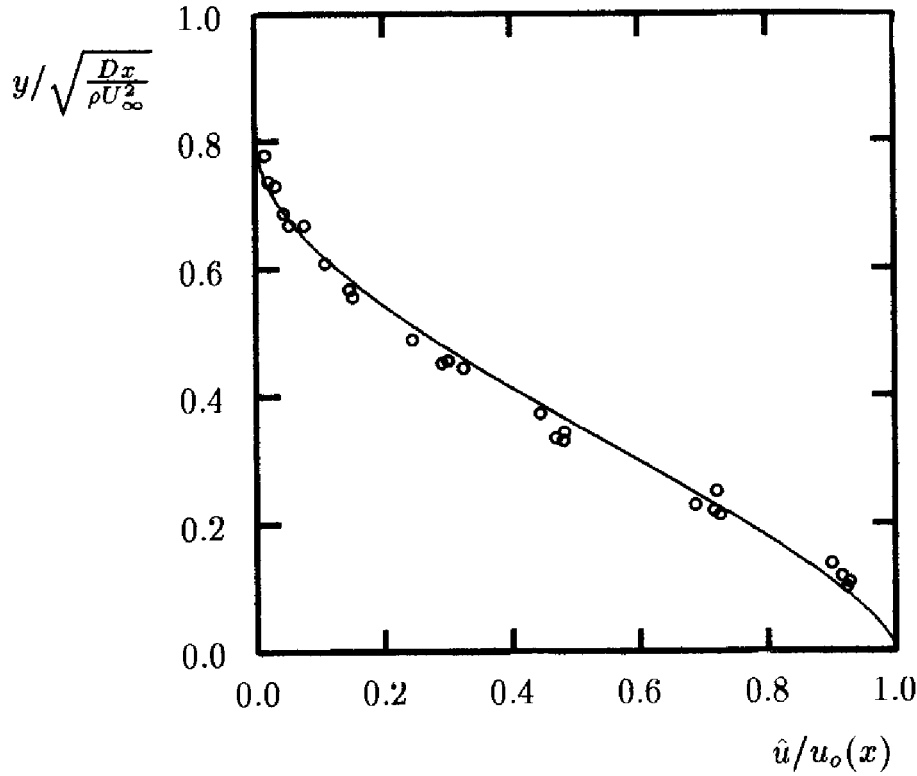


Figure 3.3: Comparison of computed and measured velocity profiles for the far wake; — Mixing length;  $\circ$  Fage and Falkner.

is the nature of an **incomplete** turbulence model. The coefficient  $\alpha$  is unknown because the mixing length [Equation (3.34)] is unknown a priori for this flow. To complete the solution, we appeal to experimental data [c.f. Schlichting (1979)], which show that the wake half width grows according to

$$\delta(x) \approx 0.805 \sqrt{\frac{Dx}{\rho U_\infty^2}} \quad (3.58)$$

Comparison of Equations (3.46) and (3.58) shows that the value of  $a_2$  is

$$a_2 = 0.648 \quad (3.59)$$

The value of the coefficient  $\alpha$  then follows from Equation (3.57), i.e.,

$$\alpha = 0.18 \quad (3.60)$$

Collecting all of this, the final solution for the far wake, according to the mixing-length model is

$$U(x, y) = U_\infty - 1.38 \sqrt{\frac{D}{\rho x}} \left[ 1 - (y/\delta)^{3/2} \right]^2 \quad (3.61)$$

where  $\delta(x)$  is given by Equation (3.58). Figure 3.3 compares the theoretical profile with experimental data of Fage and Falkner (1932). As shown, the mixing-length model, once calibrated, does an excellent job of reproducing measured values. As a final comment, this solution has an interesting feature that we will see in many of our applications. Specifically, we have found a sharp turbulent/nonturbulent interface. This manifests itself in the nonanalytic behavior of the solution at  $y/\delta = 1$ , i.e., all derivatives of  $U$  above  $\partial^2 U/\partial y^2$  are discontinuous at  $y/\delta = 1$ . Measurements confirm existence of such interfaces in all turbulent flows. However, the time-averaged interface is continuous to high order, being subjected to a near-Gaussian jitter. Time averaging would thus smooth out the sharpness of the physical interface. Consistent with this smoothing, we should actually expect analytical behavior approaching the freestream. Hence, the mixing-length model is predicting a nonphysical feature.

### 3.3.2 The Mixing Layer

For the mixing layer, we consider two parallel streams with velocities  $U_1$  and  $U_2$ . By convention, the stream with velocity  $U_1$  lies above  $y = 0$  and  $U_1 > U_2$ . The boundary conditions are thus

$$U(x, y) \rightarrow U_1 \quad \text{as} \quad y \rightarrow +\infty \quad (3.62)$$

$$U(x, y) \rightarrow U_2 \quad \text{as} \quad y \rightarrow -\infty \quad (3.63)$$

The most convenient way to solve this problem is to introduce the streamfunction,  $\psi$ . The velocity components are given in terms of  $\psi$  as follows.

$$U = \frac{\partial \psi}{\partial y} \quad \text{and} \quad V = -\frac{\partial \psi}{\partial x} \quad (3.64)$$

Equation (3.23) is automatically satisfied and the momentum equation becomes

$$\frac{\partial \psi}{\partial y} \frac{\partial^2 \psi}{\partial x \partial y} - \frac{\partial \psi}{\partial x} \frac{\partial^2 \psi}{\partial y^2} = \frac{\partial}{\partial y} \left[ \ell_{mix}^2 \left| \frac{\partial^2 \psi}{\partial y^2} \right| \frac{\partial^2 \psi}{\partial y^2} \right] \quad (3.65)$$

The boundary conditions on  $\psi$  are

$$\frac{\partial \psi}{\partial y} \rightarrow U_1 \quad \text{as} \quad y \rightarrow +\infty \quad (3.66)$$

$$\frac{\partial \psi}{\partial y} \rightarrow U_2 \quad \text{as} \quad y \rightarrow -\infty \quad (3.67)$$

Because the velocity is obtained from the streamfunction by differentiation,  $\psi$  involves a constant of integration. For the sake of uniqueness, we can specify an additional boundary condition on  $\psi$ , although at this point it is unclear where we should impose the extra boundary condition. The choice will become obvious when we set up the similarity solution. As with the far wake, we assume

$$\psi(x, y) = \psi_o(x)F(\eta) \quad (3.68)$$

where the similarity variable,  $\eta$ , is defined by

$$\eta = y/\delta(x) \quad (3.69)$$

As can be verified by substituting Equations (3.68) and (3.69) into Equation (3.65), a similarity solution exists provided we choose

$$\psi_o(x) = AU_1x \quad (3.70)$$

$$\delta(x) = Ax \quad (3.71)$$

where  $A$  is a constant to be determined. Using Equation (3.34) to determine the mixing length, Equation (3.65) transforms to

$$\alpha^2 \frac{d}{d\eta} [(F'')^2] + AF F'' = 0 \quad (3.72)$$

Note that we have removed the absolute value sign in Equation (3.65) by noting that we expect a solution with  $\partial U/\partial y = \partial^2 \psi/\partial y^2 > 0$ . As an immediate consequence, we can simplify Equation (3.72). Specifically, expanding the first term leads to the following **linear** equation for the transformed streamfunction,  $F(\eta)$ .

$$2\alpha^2 \frac{d^3 F}{d\eta^3} + AF = 0 \quad (3.73)$$

To determine the constant of integration in the streamfunction, note that our assumed form for  $\psi$  [Equation (3.68)] is consistent with letting  $F(\eta)$  vanish at  $\eta = 0$ . This is known as the dividing streamline. Thus, our boundary conditions are

$$\frac{dF}{d\eta} \rightarrow 1 \quad \text{as} \quad \eta \rightarrow +\infty \quad (3.74)$$

$$\frac{dF}{d\eta} \rightarrow U_2/U_1 \quad \text{as} \quad \eta \rightarrow -\infty \quad (3.75)$$

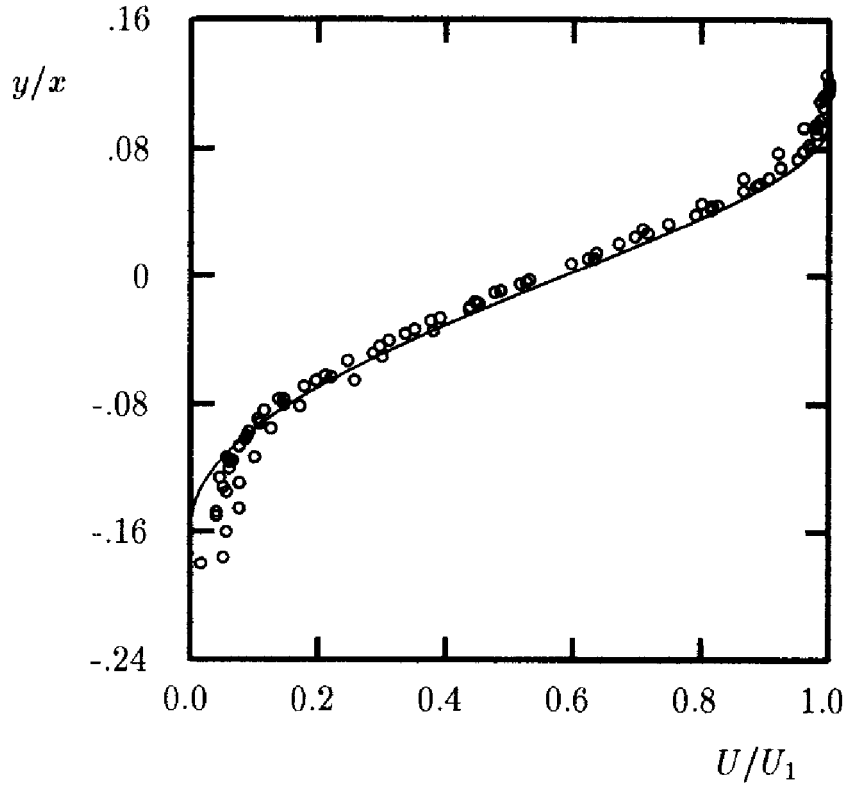


Figure 3.4: Comparison of computed and measured velocity profiles for a mixing layer; — Mixing length;  $\circ$  Liepmann and Laufer.

$$F(0) = 0 \quad (3.76)$$

For simplicity, we consider the limiting case  $U_2 = 0$ . This problem can be solved in closed form using elementary methods. Unfortunately, the solution is a bit complicated. Furthermore, as with the far-wake solution, the mixing-length model predicts a sharp turbulent/nonturbulent interface and it becomes a rather difficult chore to determine a straightforward relationship between the closure coefficient  $\alpha$  and the constant  $A$ . The easier way to proceed is to solve the equation numerically for various values of  $\alpha^2/A$  and compare with experimental measurements to infer the values of  $\alpha$  and  $A$ . Proceeding in this manner (see Program MIXER in Appendix C), optimum agreement between computed and measured [Liepmann and Laufer (1947)] velocity profiles occurs if we choose

$$A = 0.247 \quad \text{and} \quad \alpha = 0.071 \quad (\text{Mixing Layer}) \quad (3.77)$$

This value of  $\alpha$  is nearly identical to the value (0.070) quoted by Launder and Spalding (1972). Figure 3.4 compares computed and measured velocity profiles. The traditional definition of spreading rate,  $C_\delta$ , for the mixing

layer is the difference between the values of  $y/x$  where  $(U - U_2)^2 / (U_1 - U_2)^2$  is 9/10 and 1/10. The values of  $A$  and  $\alpha$  have been selected to match the experimentally measured spreading rate, viz.,

$$C_\delta = 0.115 \quad (3.78)$$

While the computed velocity goes to zero more rapidly than measured on the low speed side of the mixing layer, the overall agreement between theory and experiment is remarkably good.

### 3.3.3 The Jet

We now analyze the two-dimensional, or **plane jet**, and the axisymmetric, or **round jet**. Referring to Figure 3.2(c), we assume the jet issues into a stagnant fluid. The jet entrains fluid from the surrounding fluid and grows in width downstream of the origin. Equations (3.23) and (3.24) govern the motion with  $j = 0$  corresponding to the plane jet and  $j = 1$  corresponding to the round jet. As with the far wake, we take advantage of the symmetry about the  $x$  axis and solve for  $0 \leq y < \infty$ . The boundary conditions for both the plane and the round jet are

$$U(x, y) \rightarrow 0 \quad \text{as} \quad y \rightarrow \infty \quad (3.79)$$

$$\frac{\partial U}{\partial y} = 0 \quad \text{at} \quad y = 0 \quad (3.80)$$

To insure that the momentum in the jet is conserved, our solution must satisfy the following integral constraint:

$$\pi^j \int_0^\infty U^2 y^j dy = \frac{1}{2} J \quad (3.81)$$

where  $J$  is the momentum flux per unit mass, or, **specific momentum flux**.

To solve, we introduce the streamfunction, which can be generalized to account for the axisymmetry of the round jet, i.e.,

$$y^j U = \frac{\partial \psi}{\partial y} \quad \text{and} \quad y^j V = -\frac{\partial \psi}{\partial x} \quad (3.82)$$

The momentum equation thus becomes

$$\begin{aligned} y^{-j} \frac{\partial \psi}{\partial y} \frac{\partial^2 \psi}{\partial x \partial y} & - \frac{\partial \psi}{\partial x} \frac{\partial}{\partial y} \left( y^{-j} \frac{\partial \psi}{\partial y} \right) \\ & = \frac{\partial}{\partial y} \left[ y^j \ell_{mix}^2 \left| \frac{\partial}{\partial y} \left( y^{-j} \frac{\partial \psi}{\partial y} \right) \right| \frac{\partial}{\partial y} \left( y^{-j} \frac{\partial \psi}{\partial y} \right) \right] \end{aligned} \quad (3.83)$$

Assuming a similarity solution of the form given in Equations (3.68) and (3.69), the appropriate forms for  $\psi_o(x)$  and  $\delta(x)$  are

$$\psi_o(x) = \sqrt{\frac{JA^{j+1}x^{j+1}}{2\pi^j}} \quad (3.84)$$

$$\delta(x) = Ax \quad (3.85)$$

where  $A$  is a constant that will be determined by comparison with experimental data. For the jet, we expect to have  $\partial U/\partial y \leq 0$ . Using this fact to replace the absolute value in Equation (3.83) with a minus sign, the following ordinary differential equation for the transformed streamfunction,  $F(\eta)$ , results.

$$\alpha^2 \eta^j \left[ \frac{d}{d\eta} \left( \frac{F'}{\eta^j} \right) \right]^2 = \frac{j+1}{2} A F \left( \frac{F'}{\eta^j} \right) \quad (3.86)$$

This equation must be solved subject to the following conditions.

$$F(0) = 0 \quad (3.87)$$

$$\frac{1}{\eta^j} \frac{dF}{d\eta} \rightarrow 0 \quad \text{as} \quad y \rightarrow \infty \quad (3.88)$$

$$\frac{d}{d\eta} \left[ \frac{1}{\eta^j} \frac{dF}{d\eta} \right] \quad \text{as} \quad y \rightarrow 0 \quad (3.89)$$

$$\int_0^\infty \frac{(F')^2}{\eta^j} d\eta = 1 \quad (3.90)$$

Performing a numerical solution of Equation (3.86) subject to Equations (3.87) through (3.90), and comparing with experiment yields

$$A = 0.246 \quad \text{and} \quad \alpha = 0.098 \quad (\text{Plane Jet}) \quad (3.91)$$

$$A = 0.233 \quad \text{and} \quad \alpha = 0.080 \quad (\text{Round Jet}) \quad (3.92)$$

The values for  $\alpha$  are about 8% larger than corresponding values (0.090 and 0.075) quoted by Launder and Spalding (1972). The Launder-Spalding results were obtained using numerical procedures of the 1960's and are unlikely to be free of numerical error. By contrast, the values quoted in Equations (3.91) and (3.92) have been obtained using an accurate solver (see Program JET in Appendix C). Figures 3.5 and 3.6 compare computed and measured [Wynanski and Fiedler (1968), Bradbury (1965)] velocity profiles for the plane and round jets. Somewhat larger discrepancies between theory and experiment are present for the plane jet than for the round jet.

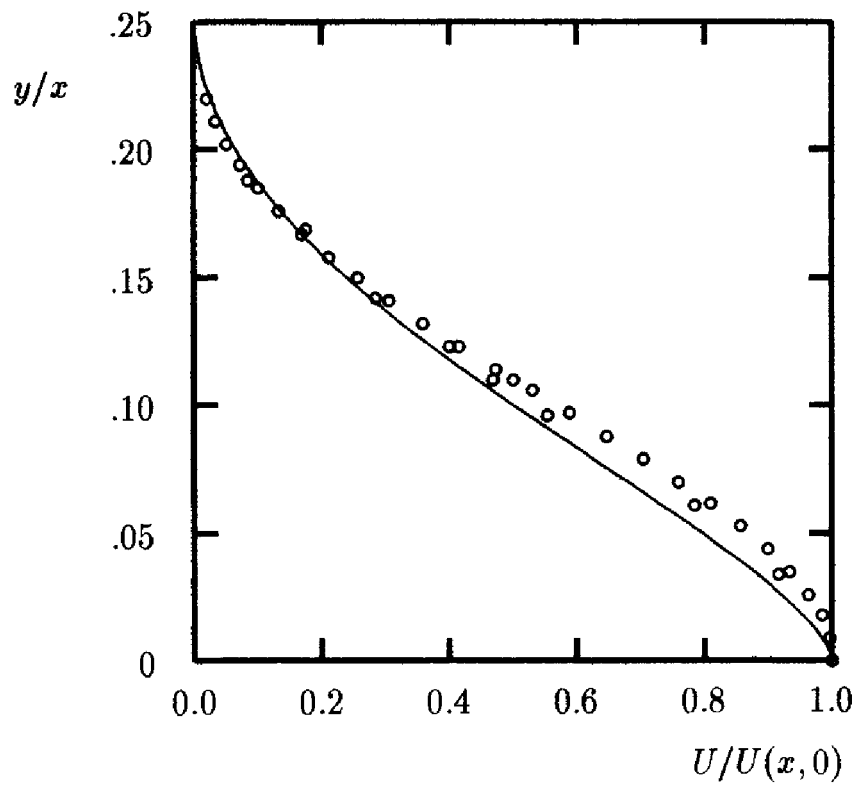


Figure 3.5: Comparison of computed and measured velocity profiles for the plane jet; — Mixing length;  $\circ$  Wygnanski and Fiedler.

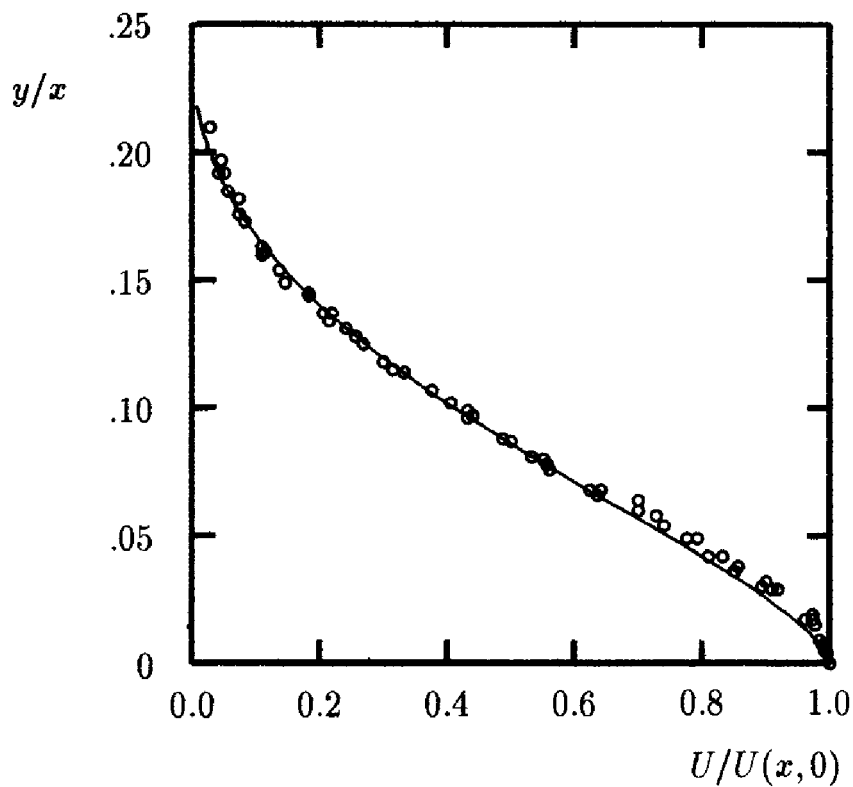


Figure 3.6: Comparison of computed and measured velocity profiles for the round jet; — Mixing length;  $\circ$  Bradbury.

The traditional definition of spreading rate,  $C_\delta$ , for the jet is the value of  $y/x$  where the velocity is half its peak value. Experimental data indicate  $C_\delta$  is between 0.100 and 0.110 for the plane jet and between 0.086 and 0.095 for the round jet. The mixing-length computational results shown in Figures 3.5 and 3.6 correspond to

$$C_\delta = \begin{cases} 0.100 & \text{(Plane Jet)} \\ 0.086 & \text{(Round Jet)} \end{cases} \quad (3.93)$$

This concludes our application of the mixing-length model to free shear flows. A few final comments will help put this model into proper perspective. We postulated in Equation (3.34) that the mixing length is proportional to the width of the shear layer. Our theory thus has a single **closure coefficient**,  $\alpha$ , and we have found that it must be changed for each flow. The following values are optimum for the four cases considered.

Far Wake	$\alpha = 0.180$
Mixing Layer	$\alpha = 0.071$
Plane Jet	$\alpha = 0.098$
Round Jet	$\alpha = 0.080$

While fairly close agreement has been obtained between computed and measured velocity profiles, we have not predicted the all important spreading rate. In fact, we established the value of our closure coefficient by forcing agreement with the measured spreading rate. If we are only interested in far-wake applications or round jets we might use this model with the appropriate closure coefficient for a parametric study in which some flow property might be varied. However, we must proceed with some degree of trepidation knowing that our formulation lacks in universality.

### 3.4 Modern Variants of the Mixing-Length Model

For free shear flows, we have seen that the mixing length is constant across the layer and proportional to the width of the layer. For flow near a solid boundary, turbulence behaves differently and, not too surprisingly, we must use a different prescription for the mixing length. Prandtl originally postulated that for flows near solid boundaries the mixing length is proportional to the distance from the surface. As we will demonstrate shortly, this postulate is consistent with the well-known **law of the wall**, which has been observed for a wide range of wall-bounded flows.



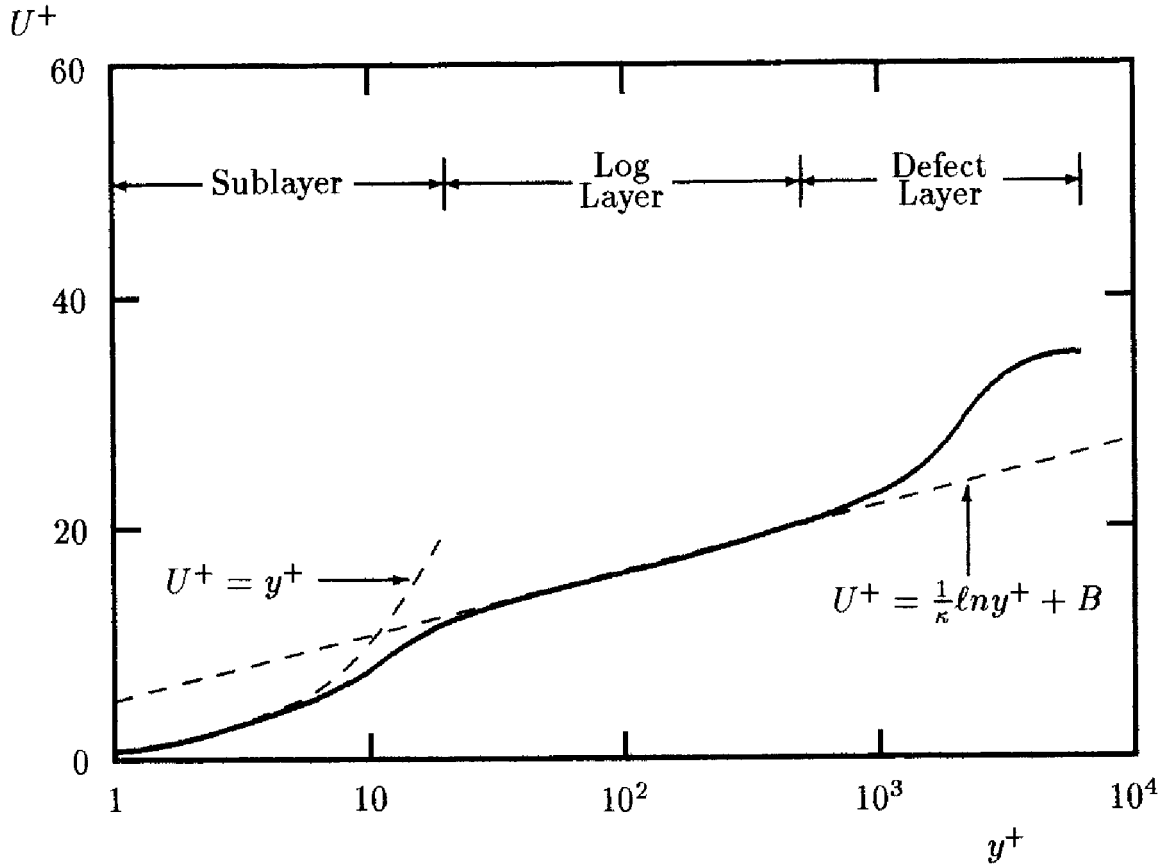


Figure 3.7: Typical velocity profile for a turbulent boundary layer.

Figure 3.7 shows a typical velocity profile for a turbulent boundary layer. The quantity  $y^+$ , which will be defined below [Equation (3.101)], is dimensionless distance from the surface. From an experimenter's point of view, three distinct regions are discernible, viz., the **viscous sublayer**, the **log layer** and the **defect layer**. By definition, the log layer, sometimes referred to as the “fully turbulent wall layer,” is the portion of the boundary layer sufficiently close to the surface that inertial terms can be neglected yet sufficiently distant that the molecular, or viscous, stress is negligible compared to the Reynolds stress. This region typically lies between  $y^+ = 30$  and  $y = 0.1\delta$ , where the upper boundary is dependent upon Reynolds number. Of particular interest to the present discussion, the **law of the wall** holds in the log layer. The viscous sublayer is the region between the surface and the log layer. Close to the surface, the velocity varies approximately linearly with  $y^+$ , and gradually asymptotes to the law of the wall for large values of  $y^+$ . The defect layer lies between the log layer and the edge of the boundary layer. The velocity asymptotes to the law of the wall as  $y/\delta \rightarrow 0$ , and makes a noticeable departure from the law of the

wall approaching the freestream. Chapter 4 discusses these three layers in great detail.

From a mathematician's point of view, there are actually only two layers, viz., the viscous sublayer and the defect layer. In the parlance of singular perturbation theory (Appendix B), the defect layer is the region in which the outer expansion is valid, while the viscous sublayer is the region where the inner expansion holds. In performing the classical matching procedure, we envision the existence of an overlap region, in which both the viscous sublayer and defect-layer solutions are valid. In the present context, we choose to call the overlap region the log layer. Strictly speaking, the log layer is not a distinct layer, but rather the asymptotic limit of the inner and outer layers. Nevertheless, we will find the log layer to be useful because of the simplicity of the equations of motion in the layer.

Consider a constant-pressure boundary layer. The flow is governed by the standard boundary-layer equations.

$$\frac{\partial U}{\partial x} + \frac{\partial V}{\partial y} = 0 \quad (3.94)$$

$$\rho U \frac{\partial U}{\partial x} + \rho V \frac{\partial U}{\partial y} = \frac{\partial}{\partial y} \left[ \mu \frac{\partial U}{\partial y} + \tau_{xy} \right] \quad (3.95)$$

Because the convective terms are negligible in the log layer, the sum of the viscous and Reynolds shear stress must be constant. Hence, we can say

$$\mu \frac{\partial U}{\partial y} + \tau_{xy} \approx \mu \left( \frac{\partial U}{\partial y} \right)_w = \tau_w = \rho u_\tau^2 \quad (3.96)$$

where subscript  $w$  denotes value at the wall and  $u_\tau = \sqrt{\tau_w / \rho}$  is known as the **friction velocity**. As noted above, the Reynolds stress is much larger than the viscous stress in the log layer. Consequently, according to the mixing-length model,

$$\ell_{mix}^2 \left( \frac{\partial U}{\partial y} \right)^2 \approx u_\tau^2 \quad (3.97)$$

If we say that the mixing length is given by

$$\ell_{mix} = \kappa y \quad (3.98)$$

where  $\kappa$  is a constant, Equation (3.97) can be integrated immediately to yield

$$U \approx \frac{u_\tau}{\kappa} \ln y + \text{constant} \quad (3.99)$$

This equation assumes a more familiar form when we introduce the dimensionless velocity and normal distance defined by

$$U^+ = U/u_\tau \quad (3.100)$$

$$y^+ = u_\tau y/\nu \quad (3.101)$$

Introducing Equations (3.100) and (3.101) into Equation (3.99) yields the classical **law of the wall**, viz.,

$$U^+ \approx \frac{1}{\kappa} \ell n y^+ + B \quad (3.102)$$

The coefficient  $\kappa$  is known as the **Kármán constant**, and  $B$  is a dimensionless constant. Coles and Hirst (1969) found from correlation of experimental data for a large number of attached, incompressible boundary layers with and without pressure gradient that

$$\kappa \approx 0.41 \quad (3.103)$$

$$B \approx 5.0 \quad (3.104)$$

Note that this is not intended as a derivation of the law of the wall. Rather, it simply illustrates consistency of Equation (3.98) with the law of the wall.

Using Equation (3.98) all the way from  $y = 0$  to  $y = \delta$ , the mixing-length model fails to provide close agreement with measured skin friction for boundary layers. Of course, not even Prandtl expected that  $\ell_{mix} = \kappa y$  throughout the boundary layer. Since the mixing length was first postulated, considerable effort has been made aimed at finding a suitable prescription for boundary-layer computations. Several key modifications to Equation (3.98) have evolved, three of which deserve our immediate attention. See Schlichting (1979) or Hinze (1975) for a more-complete history of the mixing-length model's evolution.

**The first key modification** was devised by Van Driest (1956) who proposed that the mixing length should be multiplied by a damping function. Specifically, Van Driest proposed, with some theoretical support but mainly as a good fit to data, that the mixing length should behave according to

$$\ell_{mix} = \kappa y \left[ 1 - e^{-y^+/A_o^+} \right] \quad (3.105)$$

where the constant  $A_o^+$  is

$$A_o^+ = 26 \quad (3.106)$$

Aside from the primary need to improve predictive accuracy, the Van Driest modification improves our description of the Reynolds stress in the

limit  $y \rightarrow 0$ . With  $\ell_{mix}$  given by Equation (3.98), the Reynolds shear stress  $\tau_{xy} \sim y^2$  as  $y \rightarrow 0$ . However, the no-slip boundary condition tells us that  $u' = 0$  at  $y = 0$ . Since there is no a priori reason for  $\partial u' / \partial y$  to vanish at the surface, we conclude that  $u' \sim y$  as  $y \rightarrow 0$ . Since the fluctuating velocity satisfies the continuity equation, we also conclude that  $v' \sim y^2$ . Hence, the Reynolds shear stress must go to zero as  $y^3$ . Results of DNS studies (Chapter 8) indicate that indeed  $\tau_{xy} \sim y^3$  as  $y \rightarrow 0$ . However, as noted by Hinze (1975), the coefficient of the  $y^3$  term in a Taylor series expansion for  $\tau_{xy}$  must be very small as measurements are as close to  $\tau_{xy} \sim y^4$  as they are to  $\tau_{xy} \sim y^3$  when  $y \rightarrow 0$ . In the limit of small  $y$  the Van Driest mixing length implies  $\tau_{xy}$  goes to zero as  $y^4$  approaching the surface.

**The second key modification** was made by Clauser (1956) who addressed the proper form of the eddy viscosity in the defect layer. In analogy to Prandtl's special form of the eddy viscosity for wake flows given in Equation (3.25), Clauser specifies that

$$\mu_{T_o} = \alpha \rho U_e \delta^* \quad (3.107)$$

where  $\mu_{T_o}$  is the eddy viscosity in the outer part of the layer,  $\delta^*$  is the displacement thickness,  $U_e$  is the velocity at the edge of the layer, and  $\alpha$  is a closure coefficient.

In a similar vein, Escudier (1966) found that predictive accuracy is improved by limiting the peak value of the mixing length according to

$$(\ell_{mix})_{max} = 0.09\delta \quad (3.108)$$

where  $\delta$  is boundary-layer thickness. Escudier's modification is the same approximation we used in analyzing free shear flows [Equation (3.34)], although the value 0.09 is half the value we found for the far wake.

Using an eddy viscosity appropriate to wake flow in the outer portion of the boundary layer also improves our physical description of the turbulent boundary layer. Measurements indeed indicate that the turbulent boundary layer exhibits wake-like characteristics in the defect layer. As pointed out by Coles and Hirst (1969), **"a typical boundary layer flow can be viewed as a wake-like structure which is constrained by a wall."** Figure 3.8 illustrates Coles' notion that the defect layer resembles a wake flow while the wall constraint is felt primarily in the sublayer and log layer. Strictly speaking, turbulence structure differs a lot between a boundary layer and a wake. Hence, the terminology "wake component" is conceivably a bit misleading from a conceptual point of view. Nevertheless, the mathematical approximations that yield accurate predictions for a wake and for the outer portion of a turbulent boundary layer are remarkably similar.

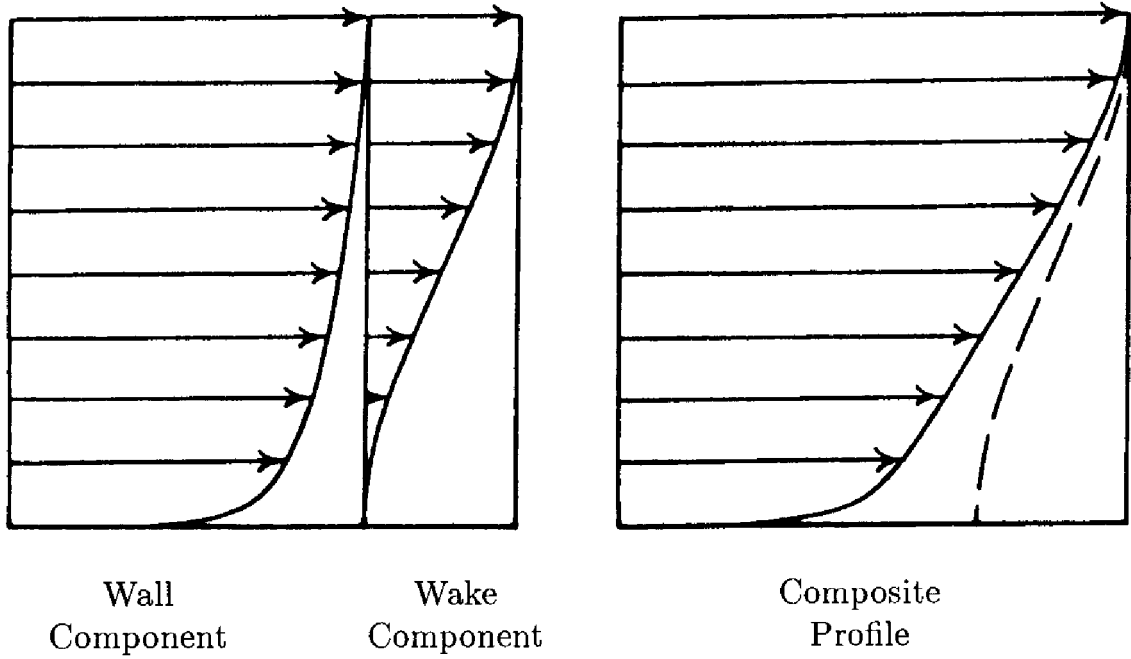


Figure 3.8: Coles' description of the turbulent boundary layer. [From Coles and Hirst (1969) — Used with permission.]

**The third key modification** is due to Corrsin and Kistler (1954) and Klebanoff (1956) as a corollary result of their experimental studies of **intermittency**. They found that approaching the freestream from within the boundary layer, the flow is not always turbulent. Rather, it is sometimes laminar and sometimes turbulent, i.e., it is **intermittent**. Their measurements indicate that for smooth walls, the eddy viscosity should be multiplied by

$$F_{Kleb}(y; \delta) = \left[ 1 + 5.5 \left( \frac{y}{\delta} \right)^6 \right]^{-1} \quad (3.109)$$

where  $\delta$  is the boundary-layer thickness. This provides a measure of the effect of intermittency on the flow.

All of these modifications have evolved as a result of the great increase in power and accuracy of computing equipment and experimental measurement techniques since the 1940's. The next two subsections introduce the two most noteworthy models in use today that are based on the mixing-length concept. Both include variants of the Van Driest, Clauser, and Klebanoff modifications. Although it is not used in these two models, the Escudier modification has also enjoyed great popularity.

As a final comment, we have introduced two new closure coefficients,  $A_o^+$  and  $\alpha$ , and an empirical function,  $F_{Kleb}$ . As we continue in our journey through this book, we will find that the number of such coefficients increases as we attempt to describe more and more features of the turbulence.

### 3.4.1 Cebeci-Smith Model

The Cebeci-Smith model [Smith and Cebeci (1967)] is a two-layer model with  $\mu_T$  given by separate expressions in each layer. The eddy viscosity is

$$\mu_T = \begin{cases} \mu_{T_i}, & y \leq y_m \\ \mu_{T_o}, & y > y_m \end{cases} \quad (3.110)$$

where  $y_m$  is the smallest value of  $y$  for which  $\mu_{T_i} = \mu_{T_o}$ . The values of  $\mu_T$  in the inner layer,  $\mu_{T_i}$ , and the outer layer,  $\mu_{T_o}$ , are computed as follows.

**Inner Layer:**

$$\mu_{T_i} = \rho \ell_{mix}^2 \left[ \left( \frac{\partial U}{\partial y} \right)^2 + \left( \frac{\partial V}{\partial x} \right)^2 \right]^{1/2} \quad (3.111)$$

$$\ell_{mix} = \kappa y \left[ 1 - e^{-y^+/A^+} \right] \quad (3.112)$$

**Outer layer:**

$$\mu_{T_o} = \alpha \rho U_e \delta_v^* F_{Kleb}(y; \delta) \quad (3.113)$$

**Closure Coefficients:**

$$\kappa = 0.40, \quad \alpha = 0.0168, \quad A^+ = 26 \left[ 1 + y \frac{dP/dx}{\rho u_\tau^2} \right]^{-1/2} \quad (3.114)$$

The function  $F_{Kleb}$  is the Klebanoff intermittency function given by Equation (3.109),  $U_e$  is boundary-layer edge velocity, and  $\delta_v^*$  is the **velocity thickness** defined by

$$\delta_v^* = \int_0^\delta (1 - U/U_e) dy \quad (3.115)$$

Note that velocity thickness is identical to displacement thickness for incompressible flow. The coefficient  $A^+$  differs from Van Driest's value to improve predictive accuracy for boundary layers with nonzero pressure gradient. The prescription for  $\mu_{T_i}$  above is appropriate only for two-dimensional flows; for three-dimensional flows, it should be proportional to a quantity such as the magnitude of the vorticity vector. There are many other subtle modifications to this model for specialized applications including surface mass transfer, streamline curvature, surface roughness, low Reynolds number, etc. Cebeci and Smith (1974) give complete details of their model with all its variations.

The Cebeci-Smith model is especially elegant and easy to implement. Most of the computational effort, relative to a laminar case, goes into computing the velocity thickness. This quantity is readily available in boundary-layer computations so that a laminar flow program can usually be converted to a turbulent flow program with just a few extra lines of instructions. Figure 3.9 illustrates a typical eddy viscosity profile constructed by using  $\mu_{T_i}$  between  $y = 0$  and  $y = y_m$ , and  $\mu_{T_o}$  for the rest of the layer. At Reynolds numbers typical of fully-developed turbulence, matching between the inner and outer layers will occur well into the log layer.

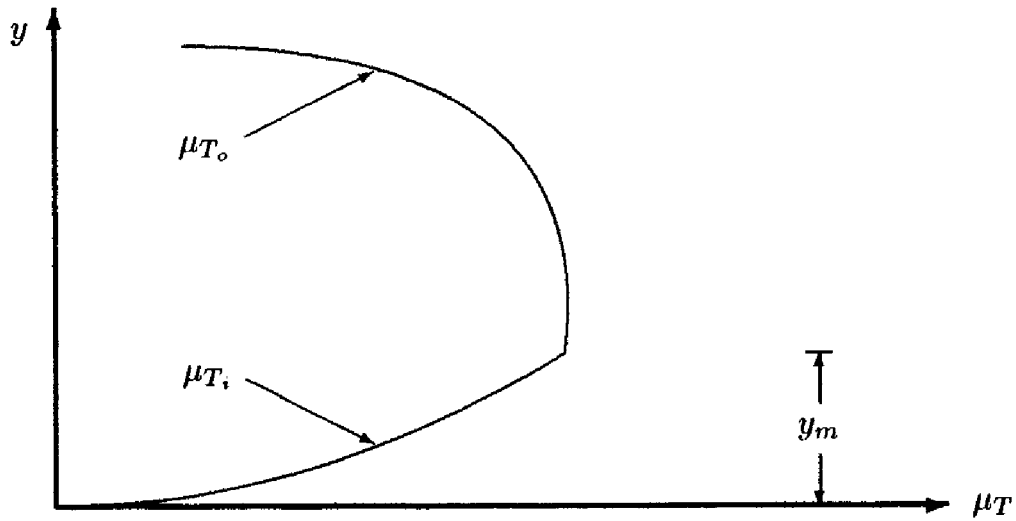


Figure 3.9: Eddy viscosity for the Cebeci-Smith model.

We can estimate the value of  $y_m^+$  as follows. Since we expect the matching point to lie well within the log layer, the exponential term in the Van Driest damping function will be negligible. Also, the law of the wall [Equation (3.99)] tells us  $\partial U / \partial y \approx u_\tau / (\kappa y)$ . Thus,

$$\mu_{T_i} \approx \rho \kappa^2 y^2 \frac{u_\tau}{\kappa y} \approx \rho \kappa u_\tau y = \kappa \mu y^+ \quad (3.116)$$

Since the matching point also lies close enough to the surface that we can say  $y/\delta \ll 1$ , the Klebanoff intermittency function will be close to one so that (with  $\delta_v^* = \delta^*$ ):

$$\mu_{T_o} \approx \alpha \rho U_e \delta^* = \alpha \mu Re_{\delta^*} \quad (3.117)$$

Hence, equating  $\mu_{T_i}$  and  $\mu_{T_o}$ , we find that

$$y_m^+ \approx \frac{\alpha}{\kappa} Re_{\delta^*} \approx 0.04 Re_{\delta^*} \quad (3.118)$$

Assuming a typical turbulent boundary layer for which  $Re_{\delta^*} \sim 10^4$ , the matching point will lie at  $y_m^+ \sim 400$ .

### 3.4.2 Baldwin-Lomax Model

The Baldwin-Lomax model [Baldwin and Lomax (1978)] was formulated for use in computations where boundary-layer properties such as  $\delta$ ,  $\delta_v^*$  and  $U_e$  are difficult to determine. This situation often arises in numerical simulation of separated flows, especially for flows with shock waves. Like the Cebeci-Smith model, this is a two-layer model. The eddy viscosity is given by Equation (3.110), and the inner and outer layer viscosities are as follows:

**Inner Layer:**

$$\mu_{T_i} = \rho \ell_{mix}^2 |\omega| \quad (3.119)$$

$$\ell_{mix} = \kappa y \left[ 1 - e^{-y^+/A_o^+} \right] \quad (3.120)$$

**Outer Layer:**

$$\mu_{T_o} = \rho \alpha C_{cp} F_{wake} F_{Kleb}(y; y_{max}/C_{Kleb}) \quad (3.121)$$

$$F_{wake} = \min \left[ y_{max} F_{max}; C_{wk} y_{max} U_{dif}^2 / F_{max} \right] \quad (3.122)$$

$$F_{max} = \frac{1}{\kappa} \left[ \max_y (\ell_{mix} |\omega|) \right] \quad (3.123)$$

where  $y_{max}$  is the value of  $y$  at which  $\ell_{mix} |\omega|$  achieves its maximum value.

**Closure Coefficients:**

$$\left. \begin{aligned} \kappa &= 0.40, & \alpha &= 0.0168, & A_o^+ &= 26 \\ C_{cp} &= 1.6, & C_{Kleb} &= 0.3, & C_{wk} &= 1 \end{aligned} \right\} \quad (3.124)$$

The function  $F_{Kleb}$  is Klebanoff's intermittency function [Equation (3.109)] with  $\delta$  replaced by  $y_{max}/C_{Kleb}$ , and  $\omega$  is the magnitude of the vorticity vector, i.e.,

$$\omega = \left[ \left( \frac{\partial V}{\partial x} - \frac{\partial U}{\partial y} \right)^2 + \left( \frac{\partial W}{\partial y} - \frac{\partial V}{\partial z} \right)^2 + \left( \frac{\partial U}{\partial z} - \frac{\partial W}{\partial x} \right)^2 \right]^{1/2} \quad (3.125)$$

for fully three-dimensional flows. This simplifies to  $\omega = |\partial V/\partial x - \partial U/\partial y|$  in a two-dimensional flow. If the boundary layer approximations are used in a two-dimensional flow, then  $\omega = |\partial U/\partial y|$ .



$U_{dif}$  is the maximum value of  $U$  for boundary layers. For free shear layers,  $U_{dif}$  is the difference between the maximum velocity in the layer and the value of  $U$  at  $y = y_{max}$ .

The primary difference between the Baldwin-Lomax and Cebeci-Smith models is in the outer layer, where the product  $C_{cp}F_{wake}$  replaces  $U_e\delta_v^*$ . To avoid the need to locate the boundary-layer edge, the Baldwin-Lomax model establishes the outer-layer length scale in terms of the vorticity in the layer. On the one hand, using  $F_{wake} = y_{max}F_{max}$ , we in effect replace  $\delta_v^*$  by  $y_{max}^2\omega/U_e$ . On the other hand, using  $F_{wake} = C_{wk}y_{max}U_{dif}^2/F_{max}$  effectively replaces the shear layer width,  $\delta$ , in Prandtl's eddy-viscosity model [Equation (3.25)] by  $U_{dif}/|\omega|$ .

As a final comment, while Equation (3.124) implies this model has six closure coefficients, there are actually only five. The coefficient  $C_{cp}$  appears only in Equation (3.121) where it is multiplied by  $\alpha$ , so  $\alpha C_{cp}$  can be treated as a single constant.

## 3.5 Application to Wall-Bounded Flows

We turn our attention now to application of the Cebeci-Smith and Baldwin-Lomax models to wall-bounded flows, i.e., to flows with a solid boundary. The no-slip boundary condition must be enforced for wall-bounded flows, and we expect to find a viscous layer similar to that depicted in Figure 3.7. This Section first examines two internal flows, viz., channel flow and pipe flow. Then, we consider external flows, i.e., boundary layers growing in a semi-infinite medium.

### 3.5.1 Channel and Pipe Flow

Like the free shear flow applications of Section 3.3, constant-section channel and pipe flow are excellent building-block cases for testing a turbulence model. Although we have the added complication of a solid boundary, the motion can be described with ordinary differential equations and is therefore easy to analyze mathematically. Also, experimental data are abundant for these flows.

The classical problems of flow in a channel, or duct, and a pipe are the idealized case of an infinitely long channel or pipe (Figure 3.10). This approximation is appropriate provided we are not too close to the inlet of the channel/pipe so that the flow has become **fully-developed**. For turbulent flow in a pipe, flow becomes fully developed approximately 50 pipe diameters downstream of the inlet. Because, by definition, properties no longer vary with distance along the channel/pipe, we conclude immediately that

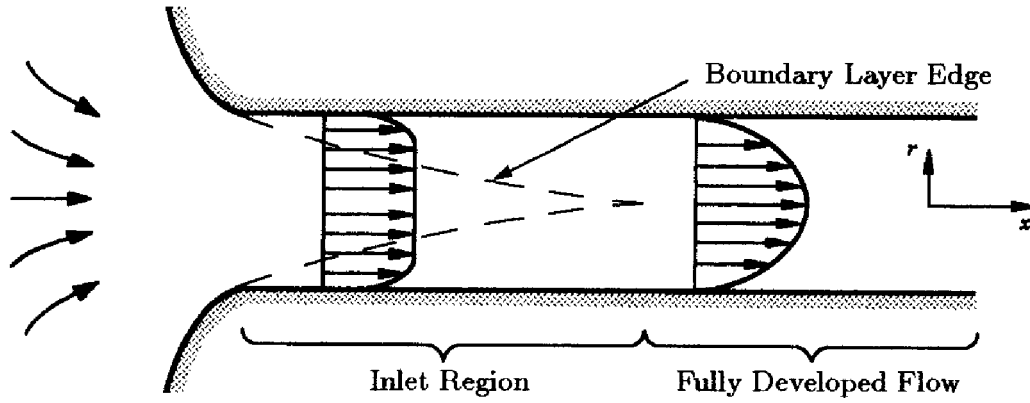


Figure 3.10: Fully-developed flow in a channel or pipe.

$$\frac{\partial U}{\partial x} = 0 \quad (3.126)$$

Denoting distance from the center of the channel or pipe by  $r$ , conservation of mass is

$$\frac{\partial U}{\partial x} + \frac{1}{r^j} \frac{\partial}{\partial r} [r^j V] = 0 \quad (3.127)$$

where  $j = 0$  for channel flow and  $j = 1$  for pipe flow. In light of Equation (3.126), we see that  $V$  does not vary across the channel/pipe. Since  $V$  must vanish at the channel/pipe walls, we conclude that  $V = 0$  throughout the fully-developed region. Hence, for both channel and pipe flow, the inertial terms are exactly zero, so that the momentum equation simplifies to

$$0 = -\frac{dP}{dx} + \frac{1}{r^j} \frac{d}{dr} \left[ r^j \left( \mu \frac{dU}{dr} + \tau_{xr} \right) \right] \quad (3.128)$$

In fully-developed flow pressure gradient must be independent of  $x$  and if  $V = 0$  it is also exactly independent of  $y$ . Hence, we can integrate once to obtain

$$\mu \frac{dU}{dr} + \tau_{xr} = \frac{r}{j+1} \frac{dP}{dx} \quad (3.129)$$

Now, the Reynolds stress vanishes at the channel/pipe walls and this establishes a direct relationship between the pressure gradient and the shear stress at the walls. If we let  $R$  denote the half-height of the channel or the radius of the pipe, applying Equation (3.129) at  $r = R$  tells us that

$$\tau_w = -\frac{R}{j+1} \frac{dP}{dx} \quad (3.130)$$

Hence, introducing the friction velocity,  $u_\tau$ , the momentum equation for channel/pipe flow simplifies to the following first-order, ordinary differential equation.

$$\mu \frac{dU}{dr} + \tau_{xr} = -\rho u_\tau^2 \frac{r}{R} \quad (3.131)$$

Noting that both channel and pipe flow are symmetric about the centerline, we can obtain the complete solution by solving Equation (3.131) with  $r$  varying between 0 and  $R$ . It is more convenient however to define  $y$  as the distance from the wall so that

$$y = R - r \quad (3.132)$$

Hence, representing the Reynolds stress in terms of the eddy viscosity,  $\mu_T$ , we arrive at the following equation for the velocity.

$$(\mu + \mu_T) \frac{dU}{dy} = \rho u_\tau^2 \left(1 - \frac{y}{R}\right) \quad (3.133)$$

Finally, we introduce sublayer coordinates,  $U^+$  and  $y^+$  from Equations (3.100) and (3.101), as well as  $\mu_T^+ = \mu_T/\mu$ . This results in the dimensionless form of the momentum equation for channel flow and pipe flow, viz.,

$$(1 + \mu_T^+) \frac{dU^+}{dy^+} = \left(1 - \frac{y^+}{R^+}\right) \quad (3.134)$$

where

$$R^+ = u_\tau R/\nu \quad (3.135)$$

Equation (3.134) must be solved subject to the no-slip boundary condition at the channel/pipe wall. Thus, we require

$$U^+(0) = 0 \quad (3.136)$$

At first glance, this appears to be a standard initial value problem that can, in principle, be solved using an integration scheme such as the Runge-Kutta method. However, the problem is a bit more difficult, and we find that for both the Cebeci-Smith and Baldwin-Lomax models, the problem must be solved iteratively. That is, for the Cebeci-Smith model, we don't know  $U_e$  and  $\delta_v^*$  a priori. Similarly, with the Baldwin-Lomax model we don't know the values of  $U_{dif}$  and  $y_{max}$  until we have determined the entire velocity profile. This is not a serious complication however, and the solution can be obtained after just a few iterations.

The equations for channel and pipe flow can be conveniently solved using a standard over-relaxation iterative procedure. Appendix C describes a

program called PIPE that yields a numerical solution for several turbulence models, including the Cebeci-Smith and Baldwin-Lomax models.

Figure 3.11 compares computed two-dimensional channel-flow profiles with direct numerical simulation (DNS) results of Mansour, Kim and Moin (1988) for Reynolds number based on channel height and average velocity of 13,750. As shown, the Cebeci-Smith and Baldwin-Lomax velocity profiles are within 8% and 5%, respectively, of the DNS profiles. Computed Reynolds shear stress profiles for both models differ from the DNS profiles by no more than 2%. Computed skin friction for both models differs by less than 2% from Halleen and Johnston's (1967) correlation of experimental data, viz.,

$$c_f = 0.0706 Re_H^{-1/4} \quad (3.137)$$

where the skin friction and Reynolds number are based on the average velocity across the channel and the channel height  $H$ , i.e.,  $c_f = \tau_w / (\frac{1}{2} \rho U_{avg}^2)$  and  $Re_H = U_{avg} H / \nu$ .

Figure 3.12 compares model predicted pipe-flow properties with the experimental data of Laufer (1952) for a Reynolds number based on pipe diameter and average velocity of 40,000. Baldwin-Lomax velocity and Reynolds shear stress differ from measured values by no more than 3%. As with channel flow, the Cebeci-Smith velocity shows greater differences (8%) from the data. Computed skin friction is within 7% and 1% for the Cebeci-Smith and Baldwin-Lomax models, respectively, of Prandtl's universal law of friction for smooth pipes [see Schlichting (1979)] given by

$$\frac{1}{\sqrt{c_f}} = 4 \log_{10} (2 Re_D \sqrt{c_f}) - 1.6 \quad (3.138)$$

where  $c_f$  and  $Re_D$  are based on average velocity across the pipe and pipe diameter,  $D$ .

These computations illustrate that subtle differences in the Reynolds shear stress can lead to much larger differences in velocity for pipe and channel flow. This means we must determine the Reynolds shear stress very accurately in order to obtain accurate velocity profiles. To some extent this seems odd. The Reynolds stress is a higher-order correlation while velocity is a simple time average. Our natural expectation is for the mean velocity to be determined with great precision while higher-order quantities such as Reynolds stress are determined with a bit less precision. The dilemma appears to stem from the fact that we need the same precision in  $\tau_{xy}$  as in  $\partial U / \partial y$ . As we advance to more complicated turbulence models, we will see this accuracy dilemma repeated, although generally with less severity. As applications go, channel and pipe flow are not very forgiving.

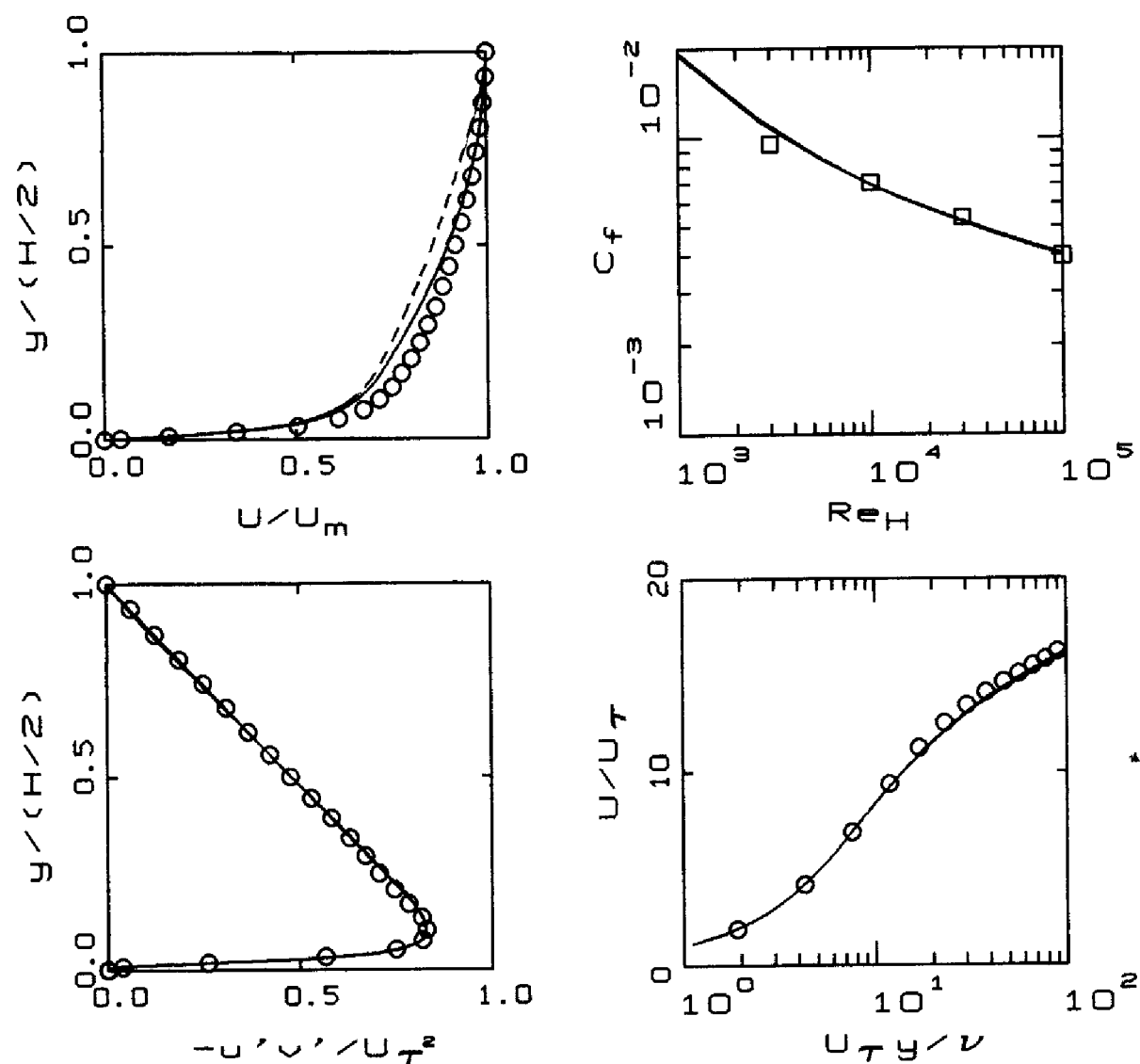


Figure 3.11: Comparison of computed and measured channel-flow properties,  $Re_H = 13,750$ . — Baldwin-Lomax; - - - Cebeci-Smith; o Mansour et al. (DNS); □ Halleen-Johnston correlation.

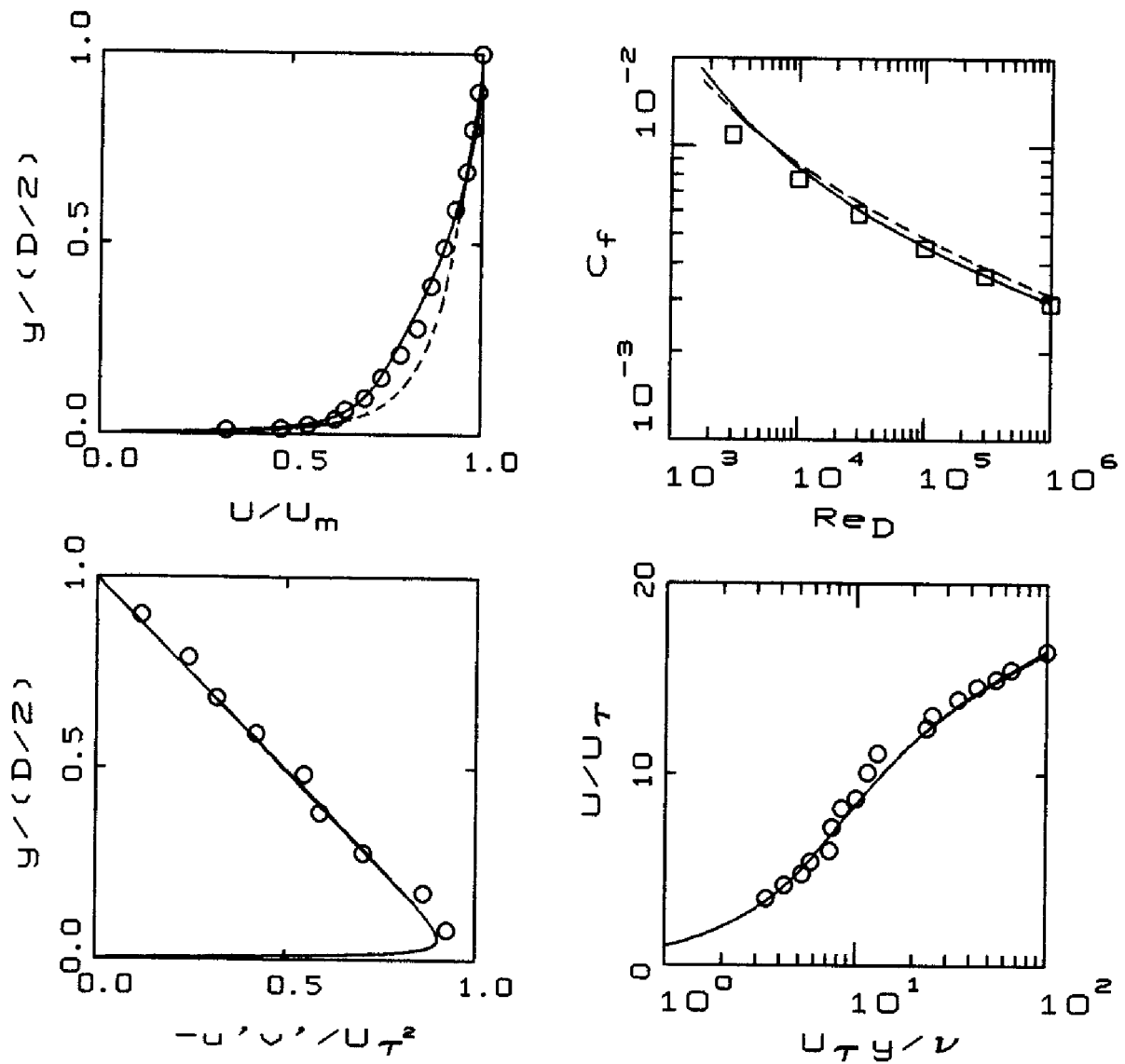


Figure 3.12: Comparison of computed and measured pipe-flow properties,  $Re_D = 40,000$ . — Baldwin-Lomax; - - - Cebeci-Smith; o Laufer; □ Prandtl correlation.

Interestingly, for the higher Reynolds number pipe flow, more acceleration is predicted with the Cebeci-Smith model than with the Baldwin-Lomax model. The opposite is true for the lower Reynolds number channel-flow case. Cebeci and Smith (1974) have devised low-Reynolds-number corrections for their model which, presumably, would reduce the differences from the DNS channel-flow results.

### 3.5.2 Boundary Layers

In general, for a typical boundary layer, we must account for pressure gradient. Ignoring effects of normal Reynolds stresses and introducing the eddy viscosity to determine the Reynolds shear stress, the two-dimensional ( $j = 0$ ) and axisymmetric ( $j = 1$ ) boundary-layer equations are as follows.

$$\frac{\partial U}{\partial x} + \frac{1}{y^j} \frac{\partial}{\partial y} (y^j V) = 0 \quad (3.139)$$

$$\rho U \frac{\partial U}{\partial x} + \rho V \frac{\partial U}{\partial y} = -\frac{dP}{dx} + \frac{1}{y^j} \frac{\partial}{\partial y} \left[ y^j (\mu + \mu_T) \frac{\partial U}{\partial y} \right] \quad (3.140)$$

The appropriate boundary conditions follow from the no slip condition at the surface and from insisting that  $U \rightarrow U_e$  as we approach the boundary-layer edge. Consequently, we must solve Equations (3.139) and (3.140) subject to

$$\left. \begin{aligned} U(x, 0) &= 0 \\ V(x, 0) &= 0 \\ U(x, y) &\rightarrow U_e(x) \quad \text{as } y \rightarrow \delta(x) \end{aligned} \right\} \quad (3.141)$$

where  $\delta(x)$  is the boundary-layer thickness.

The Cebeci-Smith model has been applied to a wide range of boundary-layer flows and has enjoyed a great deal of success. Figure 3.13, for example, compares computed skin friction,  $c_f$ , and shape factor,  $H$ , for a constant-pressure (flat-plate) boundary layer with Coles' [Coles and Hirst (1969)] correlation of experimental data. Results are expressed as functions of Reynolds number based on momentum thickness,  $Re_\theta$ . As shown, model predictions virtually duplicate correlated values.

The model remains reasonably accurate for favorable pressure gradient and for mild adverse pressure gradient. Because the model has been fine tuned for boundary-layer flows, differences between computed and measured velocity profiles generally are small. However, integral parameters such as momentum thickness and shape factor often show 10% differences from measured values.

Figure 3.14 compares computed and measured boundary layer properties for two of the flows considered in the 1968 AFOSR-IFP-Stanford

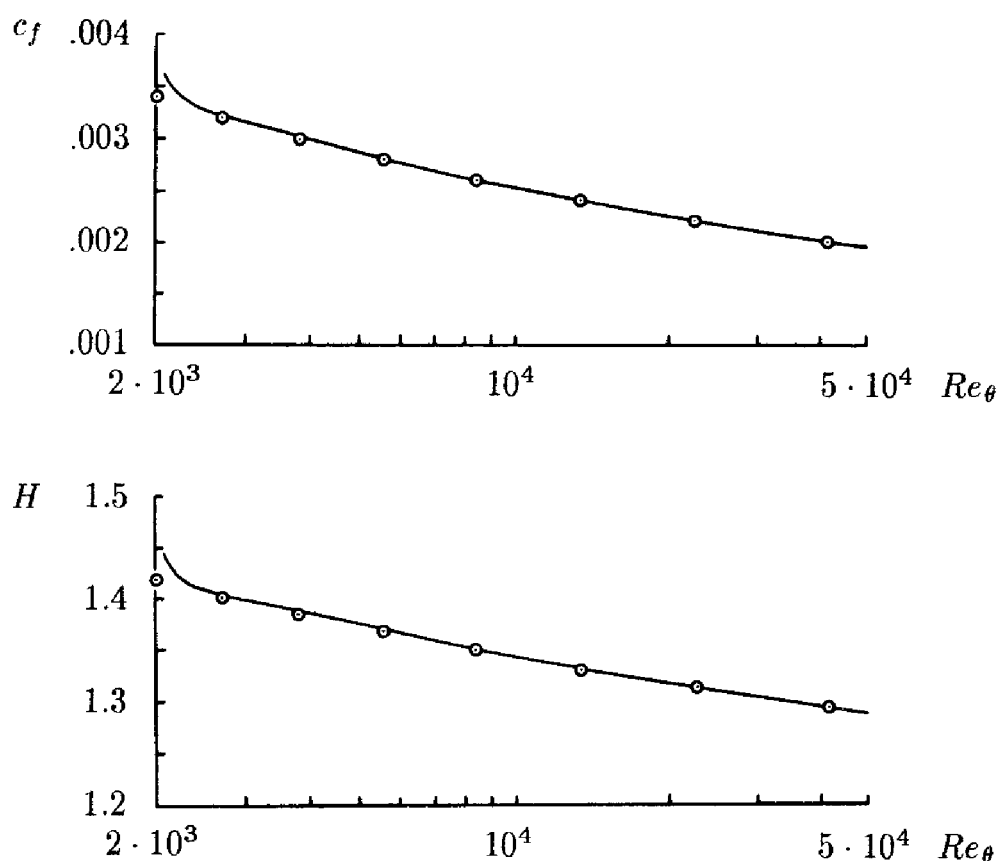


Figure 3.13: Comparison of computed and correlated shape factor and skin friction for flat-plate boundary layer flow;  $\circ$  Coles; — Cebeci-Smith model. [From Kline et al. (1969) — Used with permission.]

Conference on the Computation of Turbulent Boundary Layers (this conference is often referred to colloquially as Stanford Olympics I). For both cases, computed and measured velocity profiles are nearly identical. Flow 3100 is two dimensional with a mild favorable pressure gradient. Despite the close agreement in velocity profiles overall, differences in shape factor are between 8% and 10%. Flow 3600 is axisymmetric with an adverse pressure gradient. For this flow, shape factors differ by less than 5%.

The Baldwin-Lomax model also closely reproduces correlated values of flat-plate boundary-layer properties. It performs reasonably well even for adverse pressure gradient as evidenced in Figure 3.15. The flow considered is an incompressible boundary layer in an increasingly adverse pressure gradient which has been studied experimentally by Samuel and Joubert [see Kline et al. (1981)]. The close agreement between theory and experiment for this flow is actually remarkable. This boundary layer was presumed to be a “simple” flow for the 1980-81 AFOSR-HTTM-Stanford Conference on Complex Turbulent Flows (known colloquially as Stanford Olympics II).



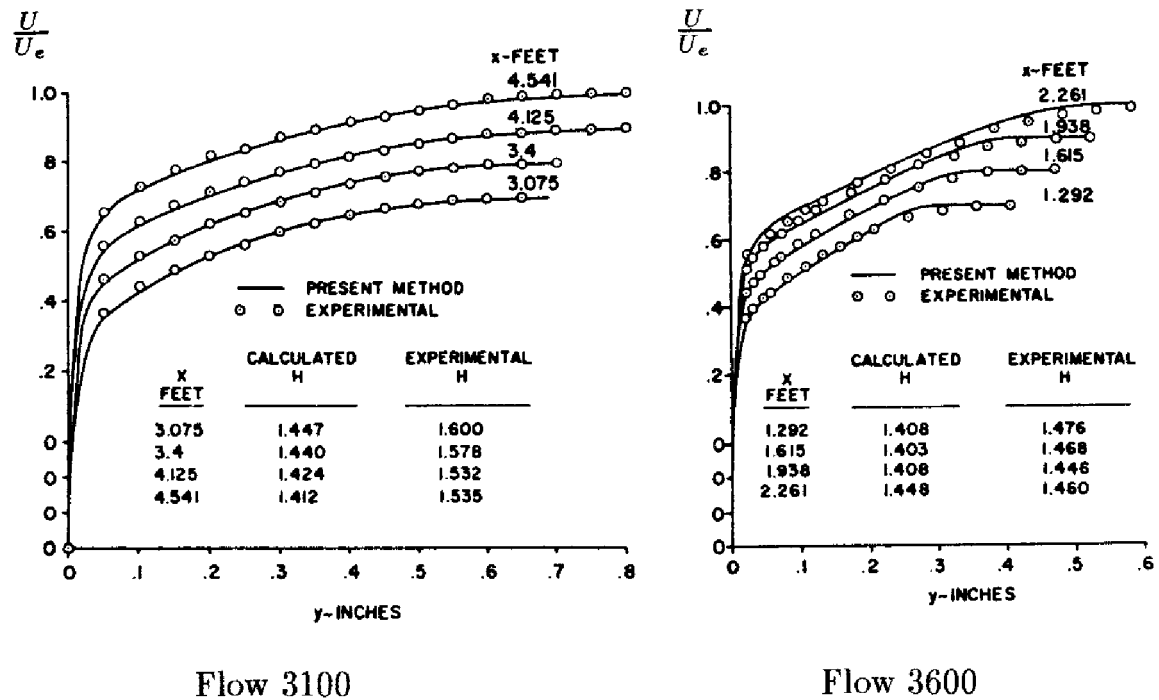


Figure 3.14: Comparison of computed and measured boundary layer velocity profiles and shape factor for flows with nonzero pressure gradient; Cebeci-Smith model. [From Kline et al. (1969) — Used with permission.]

However, as we will discuss further in Chapter 4, it proved to be the Achilles heel of the best turbulence models of the day.

Figure 3.16 compares computed and measured skin friction for Flow 3300 of the 1968 AFOSR-IFP-Stanford Conference on the Computation of Turbulent Boundary Layers. This flow, also known as Bradshaw Flow C, has a strongly adverse pressure gradient that is gradually relaxed and corresponds to an experiment performed by Bradshaw (1969). It was generally regarded as one of the most difficult to predict of all flows considered in the Conference. As shown, both models predict skin friction significantly higher than measured. The Cebeci-Smith value for  $c_f$  at the final station ( $x = 7$  ft.) is 22% higher than the measured value. The Baldwin-Lomax value exceeds the measured value at  $x = 7$  ft. by 36%.

## 3.6 Separated Flows

All of the applications in the preceding section are for attached boundary layers. We turn now to flows having an adverse pressure gradient of sufficient strength to cause the boundary layer to separate. Separation occurs

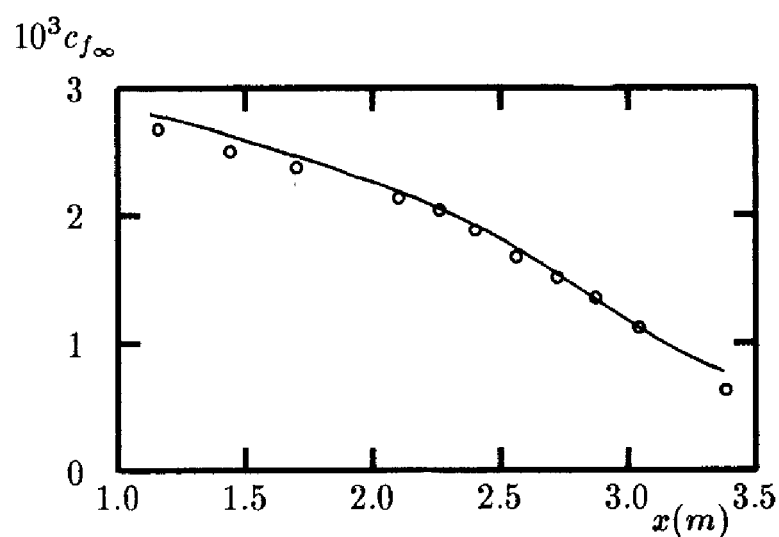


Figure 3.15: Computed and measured skin friction for Samuel-Joubert's adverse pressure gradient flow; — Baldwin-Lomax model;  $\circ$  Samuel-Joubert.

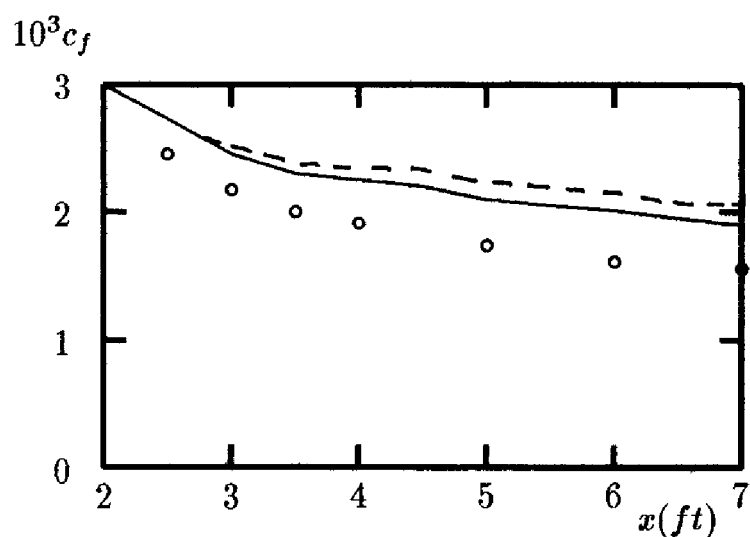


Figure 3.16: Comparison of computed and measured skin friction for Bradshaw Flow C; — Cebeci-Smith; - - - Baldwin-Lomax;  $\circ$  Bradshaw.

in many practical applications including stalled airfoils, flow near the stern of a ship, flow through a diffuser, etc. Engineering design would be greatly enhanced if our turbulence model were a reliable analytical tool for predicting separation and its effect on surface pressure, skin friction and heat transfer. Unfortunately, algebraic models are quite unreliable for separated flows.

When a boundary layer separates, the streamlines are no longer nearly parallel to the surface as they are for attached boundary layers. We must solve the full Reynolds-averaged Navier-Stokes equation [Equation (2.24)], which includes all components of the Reynolds-stress tensor. In analogy to Stokes hypothesis for laminar flow, we set

$$\tau_{ij} = 2\mu_T S_{ij} \quad (3.142)$$

where  $S_{ij}$  is the mean strain-rate tensor defined by

$$S_{ij} = \frac{1}{2}[U_{i,j} + U_{j,i}] \quad (3.143)$$

Figure 3.17 is typical of separated flow results for an algebraic model. Menter (1992b) applied the Baldwin-Lomax model to an axisymmetric flow with a strong adverse pressure gradient. The experiment was conducted by Driver (1991). Inspection of the skin friction shows that the Baldwin-Lomax model yields a separation bubble nearly twice as long as the experimentally observed bubble. The corresponding rise in pressure over the separation region is 15% to 20% higher than measured. As pointed out by Menter, the Cebeci-Smith model yields similar results.

It is not surprising that a turbulence model devoid of any information about flow history will perform poorly for separated flows. On the one hand, the mean strain-rate tensor undergoes rapid changes in a separated flow associated with the curved streamlines over and within the separation bubble. On the other hand, the turbulence adjusts to changes in the flow on a time scale unrelated to the mean rate of strain. Rotta (1962), for example, concludes from analysis of experimental data that when a turbulent boundary layer is perturbed from its equilibrium state, a new equilibrium state is not attained for at least 10 boundary-layer thicknesses downstream of the perturbation. In other words, separated flows are very much out of “equilibrium.” The Boussinesq approximation, along with all the “equilibrium” approximations implicit in an algebraic model, can hardly be expected to provide an accurate description for separated flows.

Attempts have been made to remedy the problem of poor separated flow predictions with the Cebeci-Smith model. Shang and Hankey (1975) introduced the notion of a relaxation length,  $L$ , to account for upstream

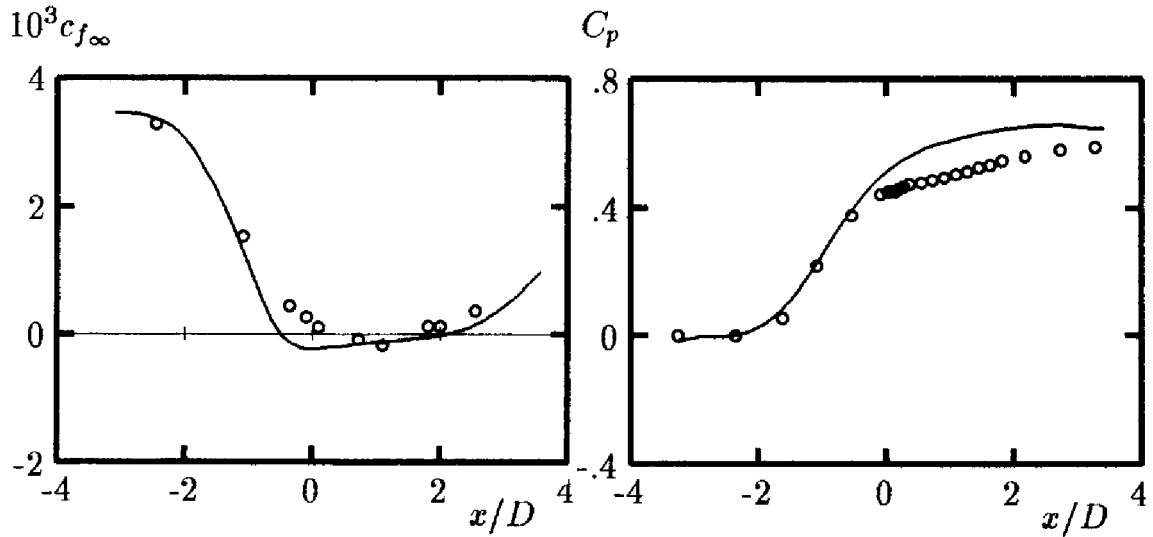


Figure 3.17: Computed and measured flow properties for Driver's separated flow; — Baldwin-Lomax; o Driver.

turbulence history effects. They introduced what they called a **relaxation eddy viscosity model** and determined the eddy viscosity as follows.

$$\mu_T = \mu_{T_{eq}} - (\mu_{T_{eq}} - \mu_{T_1})e^{-(x-x_1)/L} \quad (3.144)$$

The quantity  $\mu_{T_{eq}}$  denotes the equilibrium eddy viscosity given by Equations (3.110) through (3.113), while  $\mu_{T_1}$  is the value of the eddy viscosity at a reference point,  $x = x_1$ , upstream of the separation region. Typically, the relaxation length is about  $5\delta_1$ , where  $\delta_1$  is the boundary-layer thickness at  $x = x_1$ . The principal effect of Equation (3.144) is to reduce the Reynolds stress from the “equilibrium” value predicted by the Cebeci-Smith model. This mimics the experimental observation that the Reynolds stress remains nearly frozen at its initial value while it is being convected along streamlines in the separation region, and approaches a new equilibrium state exponentially.

In a similar vein, Hung (1976) proposed a differential form of Equation (3.144), viz.,

$$\frac{d\mu_T}{dx} = \frac{\mu_{T_{eq}} - \mu_T}{L} \quad (3.145)$$

Hung (1976) exercised these relaxation models in several supersonic shock-separated flows. He was able to force close agreement between computed and measured locations of the separation point and the surface pressure distribution. However, he found that these improvements came at the expense of increased discrepancies between computed and measured skin friction, heat transfer and reattachment-point location.

### 3.7 The 1/2-Equation Model

Johnson and King (1985) [see also Johnson (1987) and Johnson and Coakley (1990)] have devised a “non-equilibrium” version of the algebraic model. Their starting point is a so-called “equilibrium” algebraic model in which the eddy viscosity is

$$\mu_T = \mu_{T_o} \tanh(\mu_{T_i}/\mu_{T_o}) \quad (3.146)$$

#### Inner Layer:

The inner layer viscosity,  $\mu_{T_i}$ , is similar to the form used in the Cebeci-Smith and Baldwin-Lomax models. However, the dependence on velocity gradient has been replaced by explicit dependence on distance from the surface,  $y$ , and two primary velocity scales,  $u_\tau$  and  $u_m$ , as follows:

$$\mu_{T_i} = \rho \left[ 1 - \exp \left( -\frac{u_D y / \nu}{A^+} \right) \right]^2 \kappa u_s y \quad (3.147)$$

$$u_s = \sqrt{\rho_w / \rho} u_\tau (1 - \gamma_2) + \sqrt{\rho_m / \rho} u_m \gamma_2 \quad (3.148)$$

$$\gamma_2 = \tanh(y/L_c) \quad (3.149)$$

$$L_c = \frac{\sqrt{\rho_w} u_\tau}{\sqrt{\rho_w} u_\tau + \sqrt{\rho_m} u_m} L_m \quad (3.150)$$

$$L_m = \begin{cases} \kappa y_m, & y_m/\delta \leq C_1/\kappa \\ C_1 \delta, & y_m/\delta > C_1/\kappa \end{cases} \quad (3.151)$$

$$u_m = \sqrt{\tau_m / \rho_m} \quad (3.152)$$

$$u_D = \max[u_m, u_\tau] \quad (3.153)$$

where subscript  $m$  denotes the value at the point,  $y = y_m$ , at which the Reynolds shear stress,  $\tau_{xy}$ , assumes its maximum value denoted by  $\tau_m = (\tau_{xy})_{max}$ . Additionally  $u_\tau$  is the conventional friction velocity and  $\rho_w$  is the density at the surface,  $y = 0$ . In its original form, this model used only the velocity scale  $u_m$  in Equation (3.147). This scale proved to provide better predictions of velocity profile shape for separated flows than the velocity-gradient prescription of Prandtl [Equation (3.15)]. Later, the secondary velocity scales  $u_s$  and  $u_D$  were added to improve predictions for reattaching flows and for flows with nontrivial effects of compressibility.

#### Outer Layer:

The “non-equilibrium” feature of the model comes in through the appearance of a “nonequilibrium parameter,”  $\sigma(x)$ , so that:

$$\mu_{T_o} = \alpha \rho U_e \delta_v^* F_{Kleb}(y; \delta) \sigma(x) \quad (3.154)$$

Comparison of this equation with Equation (3.113) shows that the outer layer viscosity,  $\mu_{T_o}$ , is equal to the prescription used in the Cebeci-Smith model multiplied by  $\sigma(x)$ . The Johnson-King model solves the following **ordinary differential equation** for the maximum value of the Reynolds shear stress:

$$U_m \frac{d}{dx} \left( \frac{\tau_m}{\rho_m} \right) = a_1 \frac{[(u_m)_{eq} - u_m]}{L_m} \left( \frac{\tau_m}{\rho_m} \right) - C_{dif} \frac{(\tau_m/\rho_m)^{3/2}}{[C_2\delta - y_m]} |1 - \sigma^{1/2}(x)| \quad (3.155)$$

where  $(u_m)_{eq}$  is the value of  $u_m$  according to the “equilibrium” algebraic model [ $\sigma(x) = 1$ ]. The first term on the right-hand side of Equation (3.155) is reminiscent of Hung’s relaxation model [Equation (3.145)]. The second term is an estimate of the effect of turbulent diffusion on the Reynolds shear stress. Equation (3.155) is solved along with the Reynolds-averaged equations to determine  $\tau_m$ . As the solution proceeds, the coefficient  $\sigma(x)$  is determined so that the maximum Reynolds shear stress is given by

$$\tau_m = (\mu_T)_m \left( \frac{\partial U}{\partial y} + \frac{\partial V}{\partial x} \right)_m \quad (3.156)$$

That is, the  $\mu_T$  distribution is adjusted to agree with  $\tau_m$ . In using this model, computations must be done iteratively since  $\sigma(x)$  is unknown a priori, wherefore the value from a previous iteration or an extrapolated value must be used in solving Equation (3.155) for  $\tau_m$ .

#### Closure Coefficients:

$$\left. \begin{array}{lll} \kappa = 0.40, & \alpha = 0.0168, & A^+ = 17 \\ a_1 = 0.25, & C_1 = 0.09, & C_2 = 0.70 \\ C_{dif} = 0.50 & \text{for } \sigma(x) \geq 1; & 0 \text{ otherwise} \end{array} \right\} \quad (3.157)$$

The general idea of this model is that the Reynolds shear stress adjusts to departures from “equilibrium” at a rate different from that predicted by the algebraic model. The ordinary differential equation for  $\tau_m$  is used to account for the difference in rates. Because this equation is an **ordinary**, as opposed to a **partial**, differential equation, the turbulence community has chosen the curious terminology **1/2-Equation Model** to describe this model. It is unclear whether this means it has half the number of dimensions (but then, it would have to be a 1/3-Equation Model for three-dimensional applications) or if partial differential equations are twice as hard to solve as ordinary differential equations.

Menter (1992b) has applied the Johnson-King model to the attached boundary-layer flow of Samuel and Joubert [see Kline et al. (1981)] and

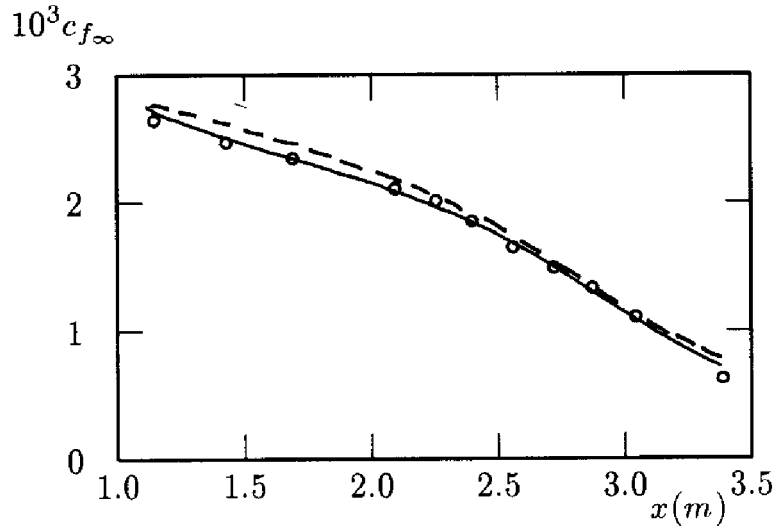


Figure 3.18: Computed and measured skin friction for Samuel-Joubert's adverse pressure gradient flow; — Johnson-King; - - - Baldwin-Lomax;  $\circ$  Samuel-Joubert.

to Driver's (1991) separated flow. Figures 3.18 and 3.19 compare computed and measured values; results for the Baldwin-Lomax model are also included. As shown, the Johnson-King model predictions are somewhat closer to measured values for the Samuel-Joubert flow. For the separated case, Johnson-King predictions are much closer to measurements, most notably in the size of the separation region.

### 3.8 Range of Applicability

Algebraic models are the simplest and easiest to implement of all turbulence models. They are conceptually very simple and rarely cause unexpected numerical difficulties. Because algebraic models are so easy to use, they should be replaced only where demonstrably superior alternatives are available.

The user must always be aware of the issue of **incompleteness**. These models will work well only for the flows for which they have been fine tuned. There is very little hope of extrapolating beyond the established data base for which an algebraic model is calibrated. We need only recall that for the four free shear flows considered in Section 3.3, four different values for the mixing length are needed—and none of these lengths is appropriate for wall-bounded flows!

On balance, both the Cebeci-Smith and Baldwin-Lomax models faithfully reproduce skin friction and velocity profiles for incompressible turbulent boundary layers provided the pressure gradient is not too strong.

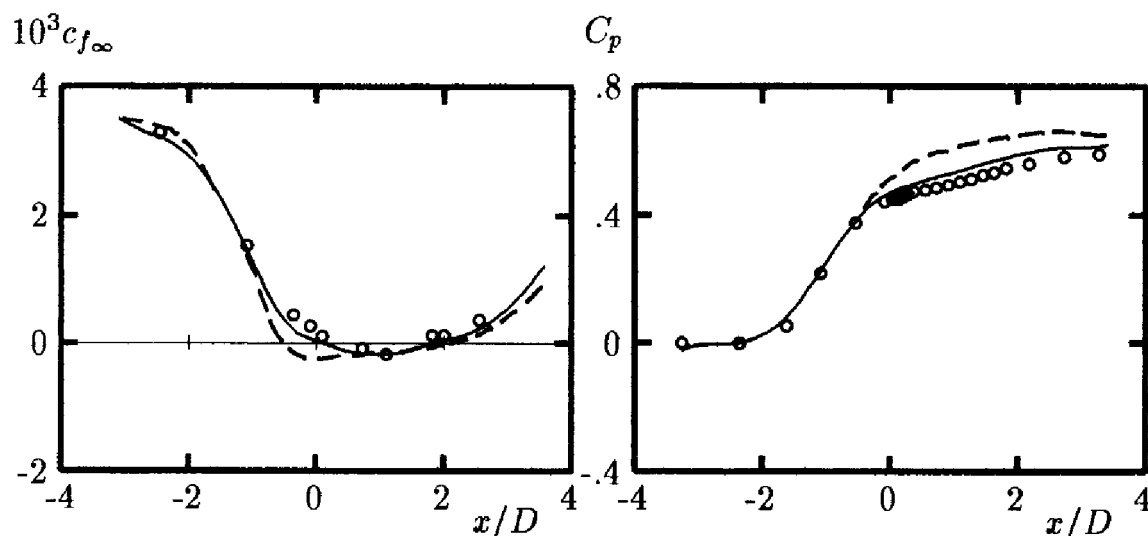


Figure 3.19: Computed and measured flow properties for Driver's separated flow; — Johnson-King; - - - Baldwin-Lomax; o Driver.

Neither model is clearly superior to the other: the accuracy level is about the same for both models. The chief virtue of the Baldwin-Lomax model over the Cebeci-Smith model is its independence from properties such as  $\delta_v^*$  that can be difficult to compute accurately in complex flows. Its other differences from the Cebeci-Smith model are probably accidental. However, neither model is reliable for separated flows. Despite this well-known limitation, many incautious researchers have applied these models to extraordinarily complex flows where their only virtue is that they don't cause the computations to blow up.

The Johnson-King model offers a promising modification that removes much of the inadequacy of algebraic models for separated flows. However, like algebraic models, the Johnson-King model provides no information about the turbulence length scale and is thus **incomplete**. Consequently, it shares many of the shortcomings of the underlying algebraic model. **On the negative side**, the improved agreement between theory and experiment has been gained at the expense of the elegance and simplicity of the Cebeci-Smith model. The number of ad hoc closure coefficients has increased from three to seven, and the model inherently requires an iterative solution procedure. The model is also formulated specifically for wall-bounded flows and is thus restricted to such flows, i.e., the model is highly geometry dependent. **On the positive side**, the Johnson-King model has been applied to many transonic flows that tend to be particularly difficult to predict with modern turbulence models. The model's track record has been quite good with such flows. On balance, this model appears to be a useful engineering design tool, within its verified range of applicability.



## Problems

**3.1** For the far wake, verify that the solution to Equations (3.45) is given by Equations (3.46) - (3.48).

**3.2** For the mixing layer, beginning with Equation (3.65), introduce Equations (3.68) - (3.71) and derive Equation (3.73).

**3.3** For the jet, begin with Equation (3.83) and derive Equation (3.86).

**3.4** Using Equation (3.25) to represent the eddy viscosity, generate a similarity solution for the far wake. Obtain the exact closed-form solution, and determine the value of  $\chi$  by forcing agreement with the corresponding  $u_o(x)$  and  $\delta(x)$  derived in this chapter. The following integral will be useful when you apply the integral constraint.

$$\int_0^\infty e^{-\xi^2} d\xi = \frac{\sqrt{\pi}}{2}$$

**3.5** Using Equation (3.25) to represent the eddy viscosity, generate a similarity solution for the plane jet. Obtain the exact closed-form solution, and determine the value of  $\chi$  by forcing agreement with the corresponding  $u_o(x)$  and  $\delta(x)$  derived in this chapter. The following integrals will be useful in deriving the solution.

$$\int \frac{dx}{c^2 - x^2} = \frac{1}{c} \tanh^{-1} \left( \frac{x}{c} \right) + \text{constant}$$

$$\int_0^\infty [1 - \tanh^2 \xi]^2 d\xi = \frac{2}{3}$$

**3.6** Show that using Equation (3.98) for the mixing length in the viscous sublayer yields a velocity that behaves according to:

$$U^+ \approx y^+ - \frac{\kappa^2}{3}(y^+)^3 + \dots \quad \text{as} \quad y^+ \rightarrow 0$$

**3.7** Using a standard numerical integration scheme such as the Runge-Kutta method, determine the constant,  $B$ , in the law of the wall implied by the mixing-length model. That is, solve the following equation for  $U^+$ .

$$(1 + \mu_T^+) \frac{dU^+}{dy^+} = 1$$

Integrate from  $y^+ = 0$  to  $y^+ = 500$  and calculate the limiting value of  $B$  as  $y^+ \rightarrow \infty$  from examination of

$$B = U^+ - \frac{1}{\kappa} \ell n y^+ \quad \text{at} \quad y^+ = 200, 300, 400 \text{ and } 500$$

Do the computation with the mixing length given by:

(a) Equation (3.98)

(b) Equation (3.105)

**NOTE:** To avoid truncation error, verify the following limiting form of the equation for  $dU^+/dy^+$ .

$$\frac{dU^+}{dy^+} \approx 1 - (\ell_{mix}^+)^2 + 2(\ell_{mix}^+)^4 + \dots \quad \text{as} \quad \ell_{mix}^+ \rightarrow 0$$

Use this asymptotic form very close to  $y^+ = 0$ .

**3.8** For a constant-pressure turbulent boundary layer, the skin friction and displacement thickness are approximately

$$c_f \approx 0.045 Re_\delta^{-1/4} \quad \text{and} \quad \delta^* \approx \frac{1}{8} \delta$$

where  $Re_\delta = U_e \delta / \nu$  is Reynolds number based on  $\delta$ . Note also that, by definition,  $c_f = 2u_\tau^2 / U_e^2$ . Assuming the matching point always occurs in the log layer so that  $\partial U / \partial y = u_\tau / (\kappa y)$ , make a graph of  $y_m / \delta$  and  $y_m^+$  versus  $Re_\delta$  for the Cebeci-Smith model. Let  $Re_\delta$  vary between  $10^4$  and  $10^6$ . You should first rewrite the equations for  $\mu_{T_i}$  and  $\mu_{T_o}$  in terms of  $y/\delta$  and  $Re_\delta$ . Then, solve the resulting equation for  $y_m / \delta$  with an iterative procedure such as Newton's method. Compare your numerical results with Equation (3.118).

**3.9** Assume the velocity in a boundary layer for  $y^+ \gg 1$  is given by

$$U^+ \approx \frac{1}{\kappa} \ell n y^+ + 5.0 + \frac{1}{\kappa} \sin^2 \left( \frac{\pi y}{2\delta} \right)$$

Also, assume that  $y_{max} \gg 26\nu / u_\tau$  for the Baldwin-Lomax model. Compute the quantities  $y_{max} F_{max}$  and  $C_{wk} y_{max} U_{dif}^2 / F_{max}$  for this boundary layer. Then, noting that  $c_f = 2u_\tau^2 / U_e^2$ , determine the largest value of  $c_f$  for which  $F_{wake} = y_{max} F_{max}$ .

**3.10** For a turbulent boundary layer with surface mass transfer, the momentum equation in the sublayer and log layer simplifies to:

$$v_w \frac{dU}{dy} = \frac{d}{dy} \left[ (\nu + \nu_T) \frac{dU}{dy} \right]$$

where  $v_w$  is the (constant) vertical velocity at the surface.

- (a) Integrate once using the appropriate surface boundary conditions. Introduce the friction velocity,  $u_\tau$ , in stating your integrated equation.
- (b) Focusing now upon the log layer where  $\nu_T \gg \nu$ , what is the approximate form of the equation derived in Part (a) if we use the Cebeci-Smith model?
- (c) Verify that the solution to the simplified equation of Part (b) is

$$2 \frac{u_\tau}{v_w} \sqrt{1 + v_w U / u_\tau^2} = \frac{1}{\kappa} \ln y + \text{constant}$$

**3.11** Generate a solution for channel and pipe flow using a mixing-length model with the mixing length in the inner and outer layers given by

$$\ell_{mix} = \begin{cases} \kappa y \left[ 1 - e^{-y^+/26} \right] & , \text{ Inner Layer} \\ .09R & , \text{ Outer Layer} \end{cases}$$

where  $R$  is channel half-height or pipe radius. Use a numerical integration scheme such as the Runge-Kutta method, or modify Program PIPE (Appendix C). Compare computed skin friction with Equations (3.137) and (3.138). **See NOTE below.**

**3.12** Generate a solution for pipe flow using a mixing-length model with the mixing length given by Nikuradse's formula, i.e.,

$$\ell_{mix}/R = 0.14 - 0.08(1 - y/R)^2 - 0.06(1 - y/R)^4$$

where  $R$  is pipe radius. Use a numerical integration scheme such as the Runge-Kutta method, or modify Program PIPE (Appendix C). Compare computed skin friction with Equation (3.138). **See NOTE below.**

**NOTE:** To assist in presenting your results, verify that  $c_f = 2/(U_{avg}^+)^2$  and  $Re_D = 2U_{avg}^+ R^+$  where  $R^+ = u_\tau R/\nu$  and  $U_{avg}$  is the average velocity

across the channel/pipe. Also, to avoid truncation error, verify the following limiting form of the equation for  $dU^+/dy^+$  in the limit  $\ell_{mix}^+ \rightarrow 0$ .

$$\frac{dU^+}{dy^+} \approx \left(1 - \frac{y^+}{R^+}\right) \left[1 - \left(1 - \frac{y^+}{R^+}\right) (\ell_{mix}^+)^2 + 2 \left(1 - \frac{y^+}{R^+}\right)^2 (\ell_{mix}^+)^4\right]$$

Use this asymptotic form very close to  $y^+ = 0$ .

## Chapter 4

# Turbulence Energy Equation Models

As computers have increased in power since the 1960's, turbulence models based upon the equation for the turbulence kinetic energy have become the cornerstone of modern turbulence modeling research. This chapter discusses two types of turbulence energy equation models, viz., **One-Equation Models** and **Two-Equation Models**, with most of the emphasis on the latter. These models both retain the Boussinesq eddy-viscosity approximation, but differ in one important respect. One-equation models are **incomplete** as they relate the turbulence length scale to some typical flow dimension. By contrast, two-equation models provide an equation for the turbulence length scale or its equivalent and are thus **complete**.

The chapter begins with a derivation and discussion of the turbulence energy equation. We proceed to a general discussion of one-equation models including examples of how such models fare for several flows. Next, we introduce two-equation models with specific details of the two most commonly used models. Our first applications are to the same free shear flows considered in Chapter 3. Then, our attention focuses upon a very powerful tool, singular perturbation theory, that we use to analyze model-predicted features of the turbulent boundary layer. We apply the two-equation model to attached wall-bounded flows and compare to corresponding algebraic-model predictions. We discuss the issue of asymptotic consistency approaching a solid boundary, and the ability of two-equation models to predict transition from laminar to turbulent flow. Our final applications are to separated flows. The concluding section discusses the range of applicability of one- and two-equation models.

## 4.1 The Turbulence Energy Equation

Turbulence energy equation models have been developed to incorporate nonlocal and flow history effects in the eddy viscosity. Prandtl (1945) postulated computing a characteristic velocity scale for the turbulence,  $v_{mix}$ , thus obviating the need for assuming that  $v_{mix} \sim \ell_{mix} |\partial U / \partial y|$  [c.f. Equation (3.15)]. He chose the kinetic energy (per unit mass) of the turbulent fluctuations,  $k$ , as the basis of his velocity scale, i.e.,

$$k = \frac{1}{2} \overline{u'_i u'_i} = \frac{1}{2} (\overline{u'^2} + \overline{v'^2} + \overline{w'^2}) \quad (4.1)$$

Thus, in terms of the density,  $\rho$ , a turbulence length scale,  $\ell$ , and  $k$ , dimensional arguments dictate that the eddy viscosity is given by

$$\mu_T = \text{constant} \cdot \rho k^{1/2} \ell \quad (4.2)$$

Note that we drop subscript “mix” in this chapter for convenience, and to avoid confusion with the mixing length used in algebraic models.

The question now arises as to how we determine  $k$ . The answer is provided by taking the trace of the Reynolds stress tensor, which yields the following.

$$\tau_{ii} = -\rho \overline{u'_i u'_i} = -2\rho k \quad (4.3)$$

Thus, the trace of the Reynolds stress tensor is proportional to the kinetic energy per unit volume of the turbulent fluctuations. The quantity  $k$  should strictly be referred to as **specific turbulence kinetic energy** (“specific” meaning “per unit mass”), but is often just called **turbulence kinetic energy**.

In Chapter 2 we derived a differential equation describing the behavior of the Reynolds stress tensor,  $\tau_{ij}$ , i.e., Equation (2.34). We can derive a corresponding equation for  $k$  by taking the trace of the Reynolds stress equation. Noting that the trace of the tensor  $\Pi_{ij}$  vanishes for incompressible flow, contracting Equation (2.34) leads to the following **transport equation** for the turbulence kinetic energy.

$$\rho \frac{\partial k}{\partial t} + \rho U_j \frac{\partial k}{\partial x_j} = \tau_{ij} \frac{\partial U_i}{\partial x_j} - \rho \epsilon + \frac{\partial}{\partial x_j} \left[ \mu \frac{\partial k}{\partial x_j} - \frac{1}{2} \rho \overline{u'_i u'_i u'_j} - \overline{p' u'_j} \right] \quad (4.4)$$

The quantity  $\epsilon$  is the **dissipation per unit mass** and is defined by the following correlation.

$$\epsilon = \nu \overline{\frac{\partial u'_i}{\partial x_k} \frac{\partial u'_i}{\partial x_k}} \quad (4.5)$$

The various terms appearing in Equation (4.4) represent physical processes occurring as the turbulence moves about in a given flow. The sum

of the two terms on the left-hand side, i.e., the **unsteady term** and the **convection**, is the familiar Eulerian derivative of  $k$  that gives the rate of change of  $k$  following a fluid particle. The first term on the right-hand side is known as **Production**, and represents the rate at which kinetic energy is transferred from the mean flow to the turbulence. Rewritten as  $\tau_{ij}S_{ij}$ , this term is seen to be the rate at which work is done by the mean strain rate against the turbulent stresses. **Dissipation** is the rate at which turbulence kinetic energy is converted into thermal internal energy, equal to the mean rate at which work is done by the fluctuating part of the strain rate against the fluctuating viscous stresses. The term involving  $\mu\partial k/\partial x_j$  is called **Molecular Diffusion**, and represents the diffusion of turbulence energy caused by the fluid's natural molecular transport process. We refer to the triple velocity correlation term as **Turbulent Transport**, and regard it as the rate at which turbulence energy is transported through the fluid by turbulent fluctuations. The last term on the right-hand side of the equation is called **Pressure Diffusion**, another form of turbulent transport resulting from correlation of pressure and velocity fluctuations.

The unsteady term, convection and molecular diffusion are exact while production, dissipation, turbulent transport and pressure diffusion involve unknown correlations. To close this equation, we must specify  $\tau_{ij}$ , dissipation, turbulent transport and pressure diffusion.

The conventional approach to closure of the  $k$  equation was initiated by Prandtl (1945) who established arguments for each term in the equation. This term-by-term modeling approach amounts to performing **drastic surgery** on the exact equation, replacing unknown correlations with closure approximations. This process is by no means rigorous. The closure approximations are no better than the turbulence data upon which they are based. Our hope is that we can find universally valid closure approximations that make accurate solutions possible. We will discuss this point in greater detail when we introduce two-equation models.

**Reynolds-Stress Tensor:** For the class of turbulence models considered in this chapter, we assume the Boussinesq approximation is valid. Thus, we say that the Reynolds stress tensor is given by

$$\tau_{ij} = 2\mu_T S_{ij} - \frac{2}{3}\rho k \delta_{ij} \quad (4.6)$$

where  $S_{ij}$  is the mean strain-rate tensor. Note that the second term on the right-hand side of Equation (4.6) is needed to obtain the proper trace of  $\tau_{ij}$ . That is, since  $S_{ii} = 0$  for incompressible flow, contracting Equation (4.6) yields  $\tau_{ii} = -2\rho k$  in accord with Equation (4.3).

**Turbulent Transport and Pressure Diffusion:** The standard approximation made to represent turbulent transport of scalar quantities in a turbulent flow is that of gradient-diffusion. In analogy to molecular transport processes, we say that  $-\overline{u'_j \phi'} \sim \mu_T \partial \Phi / \partial x_j$ . Unfortunately, there is no corresponding straightforward analog for the pressure diffusion term. For want of definitive experimental data, the pressure diffusion term has generally been grouped with the turbulent transport, and the sum assumed to behave as a gradient-transport process. Fortunately, recent DNS results [e.g., Mansour, Kim and Moin (1988)] indicate that the term is quite small for simple flows. Thus, we assume that

$$\frac{1}{2} \overline{\rho u'_i u'_i u'_j} + \overline{p' u'_j} = -\frac{\mu_T}{\sigma_k} \frac{\partial k}{\partial x_j} \quad (4.7)$$

where  $\sigma_k$  is a closure coefficient. Note that Equation (4.7) simply defines  $\sigma_k$ . As stressed by Bradshaw (1992), this statement applies to all turbulence closure coefficients. At this point, no approximation has entered although, of course, we hope the model is realistic enough that  $\sigma_k$  can be chosen to be constant.

**Dissipation:** The manner in which we determine the dissipation is not unique amongst turbulence energy equation models. It suffices at this point to note that we still have two unknown parameters, which are the turbulence length scale,  $\ell$ , and the dissipation,  $\epsilon$ . If both properties are assumed to be strictly functions of the turbulence independent of natural fluid properties such as molecular viscosity, purely dimensional arguments [Taylor (1935)] show that

$$\epsilon \sim k^{3/2} / \ell \quad (4.8)$$

Hence, we still need a prescription for the length scale of the turbulence in order to close our system of equations. In the following sections, we will explore the various methods that have been devised to determine the length scale.

Combining Equations (4.4) and (4.7), we can write the modeled version of the turbulence kinetic energy equation that is used in virtually all turbulence energy equation models. The equation assumes the following form,

$$\rho \frac{\partial k}{\partial t} + \rho U_j \frac{\partial k}{\partial x_j} = \tau_{ij} \frac{\partial U_i}{\partial x_j} - \rho \epsilon + \frac{\partial}{\partial x_j} \left[ (\mu + \mu_T / \sigma_k) \frac{\partial k}{\partial x_j} \right] \quad (4.9)$$

where  $\tau_{ij}$  is given by Equation (4.6).



## 4.2 One-Equation Models

To complete closure of the turbulence kinetic energy equation, Prandtl postulated that the dissipation assumes the form quoted in Equation (4.8). Introducing a closure coefficient that we will call  $C_D$ , the dissipation is

$$\epsilon = C_D k^{3/2} / \ell \quad (4.10)$$

and the turbulence length scale remains the only unspecified part of the model. Given twenty years of experience with the mixing-length model, Prandtl had sufficient confidence that he could generalize established prescriptions for the turbulence length scale  $\ell$ . Of course,  $\ell \propto \ell_{mix}$  only if the ratio of production to dissipation is constant. To see this, note that in a thin shear layer, production balancing dissipation means we have  $\partial U / \partial y = (-\overline{u'v'})^{1/2} / \ell_{mix}$ . Hence, we obtain  $(-\overline{u'v'})^{3/2} / \ell_{mix} = C_D k^{3/2} / \ell$  so that  $\ell \propto \ell_{mix}$  if  $-\overline{u'v'} / k = \text{constant}$ . Thus, the first **One-Equation Model** appears as follows:

$$\rho \frac{\partial k}{\partial t} + \rho U_j \frac{\partial k}{\partial x_j} = \tau_{ij} \frac{\partial U_i}{\partial x_j} - C_D \rho \frac{k^{3/2}}{\ell} + \frac{\partial}{\partial x_j} \left[ (\mu + \mu_T / \sigma_k) \frac{\partial k}{\partial x_j} \right] \quad (4.11)$$

where  $\tau_{ij}$  is given by Equation (4.6) and the eddy viscosity is

$$\mu_T = \rho k^{1/2} \ell \quad (4.12)$$

Note that at this point we make an implicit assumption regarding the “constant” in Equation (4.2), which has been set equal to one. That is, there is no a priori reason why  $\mu_T$  should depend only upon  $k$  and  $\ell$ , i.e., no reason why “constant” should really be constant. In reality,  $\mu_T$  is the ratio of a turbulence quantity (e.g.,  $-\rho \overline{u'v'}$ ) to a mean flow quantity (e.g.,  $\partial U / \partial y + \partial V / \partial x$ ). Consequently,  $\mu_T$  will not, in general, precisely follow mean-flow scales such as  $U_e$  and  $\delta^*$  or turbulence scales such as  $k$  and  $\ell$ . Only in **equilibrium flows** for which production and dissipation balance are mean-flow and turbulence scales proportional — and then either can be used for  $\mu_T$ . Otherwise, an unknown mix of scales is needed.

Emmons (1954) proposed essentially the same model in an independent research effort. Before the model can be used in applications, the length scale,  $\ell$ , and the closure coefficients  $\sigma_k$  and  $C_D$  must be specified. Emmons (1954) and Glushko (1965) applied this model to several flows with some degree of success using  $\sigma_k = 1$  and  $C_D$  ranging between 0.07 and 0.09. Their length scale distributions were similar to those used for the mixing-length model. Wolfshtein (1967) found that by introducing damping factors in the dissipation and eddy viscosity similar to the Van Driest

factor [Equation (3.105)], more satisfactory results can be obtained with this model for low-Reynolds-number flows. More recently, Goldberg (1991) has refined the model even further.

Although more complex than an algebraic model, the Prandtl-Emmons-Glushko one-equation model is certainly straightforward and elegant. As originally postulated it involves two closure coefficients and one closure function (the length scale). Even with Wolfshtein's low-Reynolds-number corrections, the number of closure coefficients increases by only two so that the model actually has fewer closure coefficients than the Baldwin-Lomax and Johnson-King models. For attached flows, the Goldberg model has five closure coefficients, two damping functions, and a closure function for the length scale. Goldberg's number of closure coefficients and empirical functions more than doubles for separated flows.

Bradshaw, Ferriss and Atwell (1967) formulated a one-equation model that avoids introducing a gradient-diffusion approximation. Rather than introduce the Boussinesq approximation, they argue that for a wide range of flows, the ratio of the Reynolds shear stress,  $\tau_{xy}$ , to the turbulence kinetic energy,  $k$ , is constant. Measurements [Townsend (1976)] indicate that for boundary layers, wakes and mixing layers the ratio is very nearly the same and given by

$$\tau_{xy} \approx 0.3\rho k \quad (4.13)$$

Building upon this presumably universal result, Bradshaw, Ferriss and Atwell formulated a one-equation model based on the turbulence kinetic energy. A novel feature of their formulation is that the equations are hyperbolic for boundary layers rather than parabolic. This is a direct consequence of introducing Equation (4.13) in modeling the  $k$  equation's turbulent transport term rather than a gradient-diffusion approximation. The resulting equations are thus solved using the method of characteristics. Figure 4.1 compares computed and measured skin friction for Flow 3300 of the 1968 AFOSR-IFP-Stanford Conference on the Computation of Turbulent Boundary Layers. As shown, the differences between theory and experiment are much less than those obtained using the Cebeci-Smith and Baldwin-Lomax models [see Figure 3.16]. Overall, the Bradshaw-Ferriss-Atwell model's skin friction for boundary layers in adverse pressure gradient was closest of the various models tested in the 1968 Conference to measured values.

One-equation models have been formulated that are based on something other than the turbulence energy equation. Nee and Kovasznay (1968), for example, postulated a phenomenological transport equation for the kinematic eddy viscosity,  $\nu_T = \mu_T/\rho$ . The equation involves terms similar to those appearing in Equation (4.11). The model has four closure coefficients

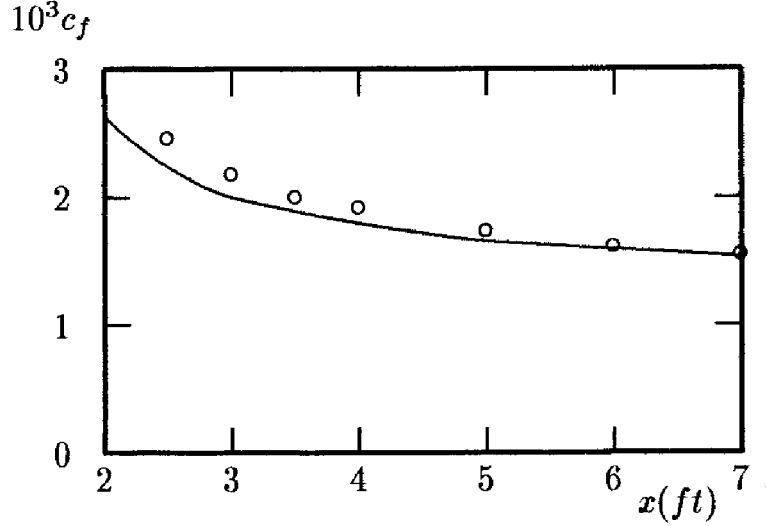


Figure 4.1: Comparison of computed and measured skin friction for Bradshaw Flow C; — Bradshaw-Ferriss-Atwell; o Bradshaw.

and requires prescription of the turbulence length scale.

More recently, Baldwin and Barth (1990) and Spalart and Allmaras (1992) have devised even more elaborate model equations for the eddy viscosity. The Baldwin-Barth model, for example, includes seven closure coefficients, two empirical damping functions and a function describing the turbulence length scale. The Baldwin-Barth model is as follows.

#### Kinematic Eddy Viscosity

$$\nu_T = C_\mu \nu \tilde{R}_T D_1 D_2 \quad (4.14)$$

#### Turbulence Reynolds Number

$$\begin{aligned} \frac{\partial}{\partial t} (\nu \tilde{R}_T) + U_j \frac{\partial}{\partial x_j} (\nu \tilde{R}_T) &= (C_{\epsilon 2} f_2 - C_{\epsilon 1}) \sqrt{\nu \tilde{R}_T P} \\ &+ (\nu + \nu_T / \sigma_\epsilon) \frac{\partial^2 (\nu \tilde{R}_T)}{\partial x_k \partial x_k} - \frac{1}{\sigma_\epsilon} \frac{\partial \nu_T}{\partial x_k} \frac{\partial (\nu \tilde{R}_T)}{\partial x_k} \end{aligned} \quad (4.15)$$

#### Closure Coefficients

$$C_{\epsilon 1} = 1.2, \quad C_{\epsilon 2} = 2.0, \quad C_\mu = 0.09, \quad A_o^+ = 26, \quad A_2^+ = 10 \quad (4.16)$$

$$\frac{1}{\sigma_\epsilon} = (C_{\epsilon 2} - C_{\epsilon 1}) \sqrt{C_\mu} / \kappa^2, \quad \kappa = 0.41 \quad (4.17)$$

#### Auxiliary Relations

$$P = \nu_T \left[ \left( \frac{\partial U_i}{\partial x_j} + \frac{\partial U_j}{\partial x_i} \right) \frac{\partial U_i}{\partial x_j} - \frac{2}{3} \frac{\partial U_k}{\partial x_k} \frac{\partial U_k}{\partial x_k} \right] \quad (4.18)$$

$$D_1 = 1 - e^{-y^+/A_o^+} \quad \text{and} \quad D_2 = 1 - e^{-y^+/A_2^+} \quad (4.19)$$

$$f_2 = \frac{C_{\epsilon 1}}{C_{\epsilon 2}} + \left(1 - \frac{C_{\epsilon 1}}{C_{\epsilon 2}}\right) \left(\frac{1}{\kappa y^+} + D_1 D_2\right) \cdot \left[ \sqrt{D_1 D_2} + \frac{y^+}{\sqrt{D_1 D_2}} \left( \frac{D_2}{A_o^+} e^{-y^+/A_o^+} + \frac{D_1}{A_2^+} e^{-y^+/A_2^+} \right) \right] \quad (4.20)$$

The Spalart-Allmaras model is also written in terms of the eddy viscosity. The model includes eight closure coefficients and three damping functions. Its defining equations are as follows.

### Kinematic Eddy Viscosity

$$\nu_T = \tilde{\nu} f_{v1} \quad (4.21)$$

### Eddy Viscosity Equation

$$\begin{aligned} \frac{\partial \tilde{\nu}}{\partial t} + U_j \frac{\partial \tilde{\nu}}{\partial x_j} &= c_{b1} \tilde{S} \tilde{\nu} - c_{w1} f_w \left( \frac{\tilde{\nu}}{d} \right)^2 \\ &+ \frac{1}{\sigma} \frac{\partial}{\partial x_k} \left[ (\nu + \tilde{\nu}) \frac{\partial \tilde{\nu}}{\partial x_k} \right] + \frac{c_{b2}}{\sigma} \frac{\partial \tilde{\nu}}{\partial x_k} \frac{\partial \tilde{\nu}}{\partial x_k} \end{aligned} \quad (4.22)$$

### Closure Coefficients

$$c_{b1} = 0.1355, \quad c_{b2} = 0.622, \quad c_{v1} = 7.1, \quad \sigma = 2/3 \quad (4.23)$$

$$c_{w1} = \frac{c_{b1}}{\kappa^2} + \frac{(1 + c_{b2})}{\sigma}, \quad c_{w2} = 0.3, \quad c_{w3} = 2, \quad \kappa = 0.41 \quad (4.24)$$

### Auxiliary Relations

$$f_{v1} = \frac{\chi^3}{\chi^3 + c_{v1}^3}, \quad f_{v2} = 1 - \frac{\chi}{1 + \chi f_{v1}}, \quad f_w = g \left[ \frac{1 + c_{w3}^6}{g^6 + c_{w3}^6} \right]^{1/6} \quad (4.25)$$

$$\chi = \frac{\tilde{\nu}}{\nu}, \quad g = r + c_{w2}(r^6 - r), \quad r = \frac{\tilde{\nu}}{\tilde{S} \kappa^2 d^2} \quad (4.26)$$

$$\tilde{S} = S + \frac{\tilde{\nu}}{\kappa^2 d^2} f_{v2}, \quad S = \sqrt{2 \Omega_{ij} \Omega_{ij}} \quad (4.27)$$

The tensor  $\Omega_{ij} = \frac{1}{2}(\partial U_i / \partial x_j - \partial U_j / \partial x_i)$  is the rotation tensor and  $d$  is distance from the closest surface. Although not listed here, the model even includes a transition correction that introduces four additional closure coefficients and two more empirical functions.

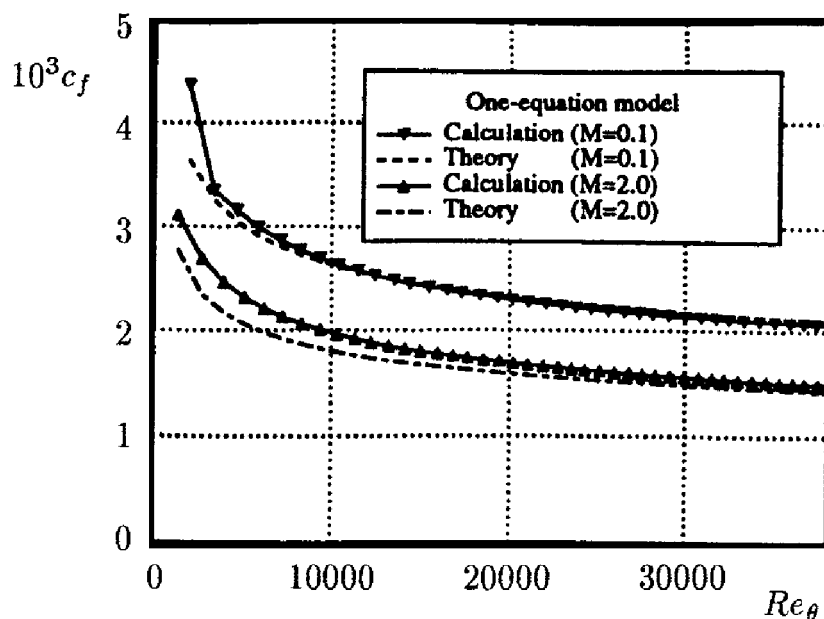


Figure 4.2: Comparison of computed and measured flat-plate boundary layer skin friction at Mach 0.1 and Mach 2.0; Baldwin-Barth model. [From Baldwin and Barth (1990).]

Figure 4.2 illustrates how well the Baldwin-Barth model reproduces correlations of measured skin friction [see Hopkins and Inouye (1971)] for constant-pressure boundary layers.

Figures 4.3 and 4.4 show how the Baldwin-Barth model fares for the two key flows considered by Menter (1992b). For both flows, the Baldwin-Barth model skin friction deviates from measured values even more than the Baldwin-Lomax model (see Figures 3.15 and 3.17). Although not shown, the Spalart-Allmaras model yields  $c_f$  for the Samuel-Joubert case that lies about as far above the measurements as the Baldwin-Barth  $c_f$  lies below [see Spalart and Allmaras (1992)].

In summary, only a modest advantage is gained in using a one-equation model rather than a mixing-length model. While the recent developments by Goldberg, Baldwin and Barth and Spalart and Allmaras show improved predictive capability (relative to early one-equation models) for some flows, their track record remains spotty. On the one hand, the Goldberg, Baldwin-Barth and Spalart-Allmaras models have achieved closer agreement with measurements for a limited number of separated flows than is possible with algebraic models. On the other hand, the Baldwin-Lomax model appears to be superior to the Baldwin-Barth model for the relatively simple Samuel-Joubert flow and for Driver's separated flow. While these newer models appear promising for separated flows, more research and testing is needed.

Given all of these facts, we clearly have not yet arrived at anything

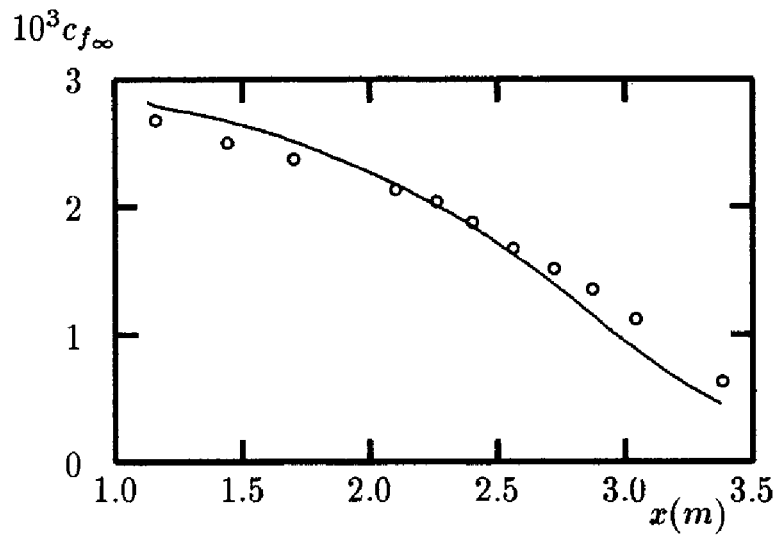


Figure 4.3: Computed and measured skin friction for Samuel-Joubert's adverse pressure gradient flow; — Baldwin-Barth;  $\circ$  Samuel-Joubert.

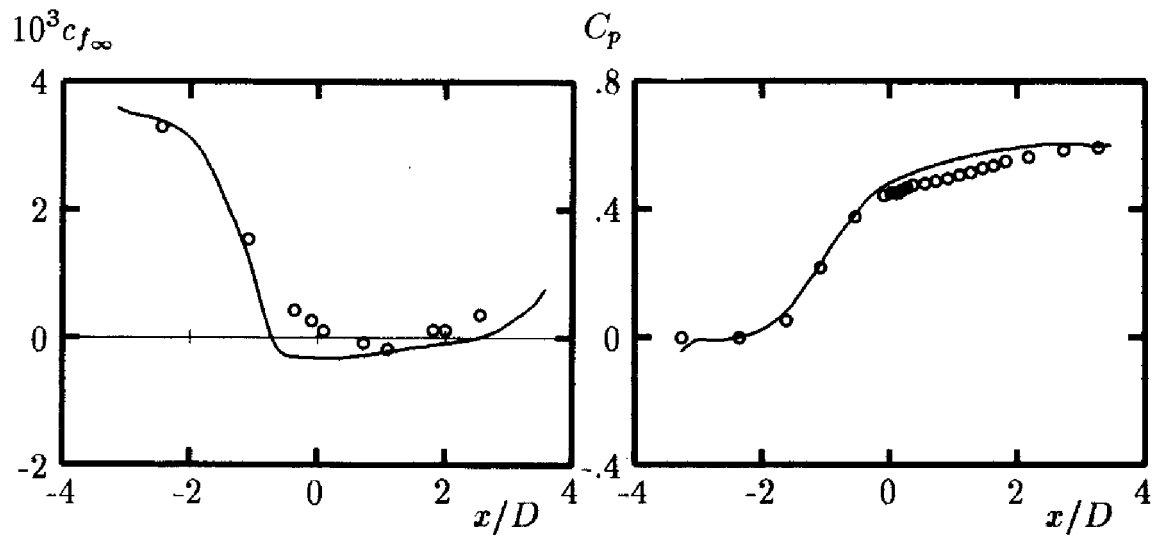


Figure 4.4: Computed and measured flow properties for Driver's separated flow; — Baldwin-Barth;  $\circ$  Driver.

resembling a universal turbulence model. While there is a smaller need for adjustment from flow to flow than with the mixing-length model, abrupt changes from wall-bounded to free shear flows (e.g., flow at a trailing edge of an airfoil) cannot be easily accommodated. In general, one-equation models share a few of the failures as well as most of the successes of the mixing-length model. To reach a more-nearly universal model, especially for separated flows, we must seek a model in which transport effects on the turbulence length scale are also accounted for. The rest of this chapter is devoted to investigating models that indeed include transport effects on the turbulence length scale.

## 4.3 Two-Equation Models

**Two-Equation Models** of turbulence have served as the foundation for much of the turbulence model research during the past two decades. For example, almost all of the computations done for the 1980-81 AFOSR-HTTM-Stanford Conference on Complex Turbulent Flows used two-equation turbulence models. These models provide not only for computation of  $k$ , but also for the turbulence length scale or equivalent. Consequently, two-equation models are **complete**, i.e., can be used to predict properties of a given turbulent flow with no prior knowledge of the turbulence structure. They are, in fact, the simplest complete model of turbulence.

The starting point for virtually all two-equation models is the Boussinesq approximation, Equation (4.6), and the turbulence kinetic energy equation in the form of Equation (4.9). As pointed out at the end of Section 4.1, there is a non-uniqueness in the way we determine the dissipation,  $\epsilon$ , or equivalently, the turbulence length scale,  $\ell$ .

Kolmogorov (1942), for example, pointed out that a second transport equation is needed to compute the so-called **specific dissipation rate**,  $\omega$ . This quantity has dimensions of  $(\text{time})^{-1}$ . On dimensional grounds, the eddy viscosity, turbulence length scale and dissipation can be determined from

$$\mu_T \sim \rho k / \omega, \quad \ell \sim k^{1/2} / \omega, \quad \epsilon \sim \omega k \quad (4.28)$$

Chou (1945) proposed modeling the exact equation for  $\epsilon$ . In terms of this formulation, the eddy viscosity and turbulence length scale are

$$\mu_T \sim \rho k^2 / \epsilon, \quad \ell \sim k^{3/2} / \epsilon \quad (4.29)$$

Rotta (1951) first suggested a transport equation for the turbulence length scale and later (1968) proposed an equation for the product of  $k$  and  $\ell$ . In either case,

$$\mu_T \sim \rho k^{1/2} \ell, \quad \epsilon \sim k^{3/2} / \ell \quad (4.30)$$

More recently, Zeierman and Wolfshtein (1986) introduced a transport equation for the product of  $k$  and a **turbulence dissipation time**,  $\tau$ , which is essentially the reciprocal of Kolmogorov's  $\omega$ . Also, Speziale, Abid and Anderson (1990) have postulated an equation for  $\tau$ . For these models,

$$\mu_T \sim \rho k \tau, \quad \ell \sim k^{1/2} \tau, \quad \epsilon \sim k / \tau \quad (4.31)$$

Regardless of the choice of the second variable in our two-equation model, we see a recurring theme. Specifically, the dissipation, eddy viscosity and length scale are all related on the basis of dimensional arguments. Historically, dimensional analysis has been one of the most powerful tools available for deducing and correlating properties of turbulent flows. However, we should always be aware that while dimensional analysis is extremely useful, it unveils nothing about the physics underlying its implied scaling relationships. The physics is in the choice of variables.

One of the key conclusions of the 1980-81 AFOSR-HTTM-Stanford Conference on Complex Turbulent Flows was that the greatest amount of uncertainty about two-equation models lies in the transport equation complementing the equation for  $k$ . Further, it was even unclear about what the most appropriate choice of the second dependent variable is. In the decade following the Conference, interesting developments have occurred, most notably with the  $k$ - $\omega$  model that help clear up some, but not all, of the uncertainty.

Before proceeding to details of two-equation models, it is worthwhile to pause and note the following. As with one-equation models, there is no fundamental reason that  $\mu_T$  should depend only upon turbulence parameters such as  $k$ ,  $\ell$ ,  $\epsilon$  or  $\omega$ . In general, the ratio of individual Reynolds stresses to mean strain rate components depends upon both mean-flow and turbulence scales. Thus, two-equation turbulence models are no more likely than one-equation models to apply universally to turbulent flows, and can be expected to be inaccurate for many non-equilibrium turbulent flows.

### 4.3.1 The $k$ - $\omega$ Model

As noted above, Kolmogorov (1942) proposed the first two-equation model of turbulence. Kolmogorov chose the kinetic energy of the turbulence as one of his turbulence parameters and, like Prandtl (1945), modeled the differential equation governing its behavior. His second parameter was the dissipation per unit turbulence kinetic energy,  $\omega$ . In his  $k$ - $\omega$  model,  $\omega$  satisfies a differential equation similar to the equation for  $k$ . With no prior knowledge of Kolmogorov's work, Saffman (1970) formulated a  $k$ - $\omega$  model that would prove superior to the Kolmogorov model. As part of the Imperial



College efforts on two-equation models, Spalding [see Launder and Spalding (1972)] offered an improved version of the Kolmogorov model that removed some of its flaws. Shortly after formulation of Saffman's model and continuing to the present time, Wilcox et al. [Wilcox and Alber (1972), Saffman and Wilcox (1974), Wilcox and Traci (1976), Wilcox and Rubesin (1980), and Wilcox (1988a)] have pursued further development and application of  $k$ - $\omega$  turbulence models in earnest. Coakley (1983) has developed a  $k^{1/2}$ - $\omega$  model. In their critical review of two-equation turbulence models, Speziale, Abid and Anderson (1990) also propose a  $k$ - $\omega$  model.

In formulating his model, Kolmogorov referred to  $\omega$  as "the rate of dissipation of energy in unit volume and time." To underscore its physical relation to the "external scale" of turbulence,  $\ell$ , he also called it "some mean 'frequency' determined by  $\omega = ck^{1/2}/\ell$ , where  $c$  is a constant." On the one hand, the reciprocal of  $\omega$  is the time scale on which dissipation of turbulence energy occurs. While the actual process of dissipation takes place in the smallest eddies, the rate of dissipation is the rate of transfer of turbulence kinetic energy to the smallest eddies. Hence, this rate is set by the properties of the large eddies, and thus scales with  $k$  and  $\ell$ , wherefore  $\omega$  is indirectly associated with dissipative processes. On the other hand, in analogy to molecular viscosity, we expect the eddy viscosity to be proportional to the product of length and velocity scales characteristic of turbulent fluctuations, which is consistent with Kolmogorov's argument that  $\omega \sim k^{1/2}/\ell$ . Of course, we should keep in mind that analogies between molecular and turbulent processes are not trustworthy, and Kolmogorov's argument is essentially an exercise in dimensional analysis, not fundamental physics.

The development of the Kolmogorov model (1942) is quite brief and doesn't even establish values for all of the closure coefficients. Since little formal development of the equations is given, we can only speculate about how this great turbulence researcher may have arrived at his model equations. Since he makes no specific reference to any exact equations, it seems unlikely that he attempted to close the  $k$  equation or other moments of the Navier Stokes equation term by term. Rather, as the great believer in the power of dimensional analysis that he was, it is easy to imagine that Kolmogorov's original reasoning may have gone something like this (note that for the sake of clarity the arguments below are in terms of kinematic eddy viscosity,  $\nu_T = \mu_T/\rho$ ).

- Since  $k$  already appears in the postulated constitutive relation [Equation (4.6)], it is plausible that  $\nu_T \propto k$ .
- The dimensions of  $\nu_T$  are (length)<sup>2</sup>/(time) while the dimensions of  $k$  are (length)<sup>2</sup>/(time)<sup>2</sup>.

- Consequently  $\nu_T/k$  has dimensions (time).
- Turbulence dissipation  $\epsilon$  has dimensions  $(\text{length})^2/(\text{time})^3$ .
- Consequently  $\epsilon/k$  has dimensions  $1/(\text{time})$ .
- We can close Equations (4.6) and (4.9) by introducing a variable with dimensions (time) or  $1/(\text{time})$ .

The next step is to postulate an equation for  $\omega$ . In doing so, the avenue that Kolmogorov took was to recognize that there are a fairly small number of physical processes commonly observed in the motion of a fluid. The most common processes are unsteadiness, convection (often referred to as advection), diffusion, dissipation, dispersion and production. Combining physical reasoning with dimensional analysis, Kolmogorov postulated the following equation for  $\omega$ .

$$\rho \frac{\partial \omega}{\partial t} + \rho U_j \frac{\partial \omega}{\partial x_j} = -\beta \rho \omega^2 + \frac{\partial}{\partial x_j} \left[ \sigma \mu_T \frac{\partial \omega}{\partial x_j} \right] \quad (4.32)$$

We have taken some notational liberties in writing Equation (4.32), and  $\beta$  and  $\sigma$  are two new closure coefficients. This equation has three particularly noteworthy features. **First**, there is no analog to the  $k$ -equation's turbulence production term. The absence of a production term is consistent with Kolmogorov's notion that  $\omega$  is associated with the smallest scales of the turbulence, and thus has no direct interaction with the mean motion. Note that his logic is flawed on this issue as the large-scale, energy-bearing eddies are primarily responsible for determining the appropriate time scale of the turbulence, and the rate of dissipation itself. **Second**, the equation is written in terms of  $\omega$  rather than  $\omega^2$ . As will be shown when we analyze the defect layer in Subsection 4.6.2, Kolmogorov's decision to write his equation in terms of  $\omega$  was a somewhat prophetic choice. **Third**, there is no molecular diffusion term so that this equation applies strictly to high-Reynolds-number flows and cannot be integrated through the viscous sublayer as it stands.

In subsequent development efforts, the interpretation of  $\omega$  has behaved a bit like the turbulent fluctuations it is intended to describe. Saffman (1970) described  $\omega$  as "a frequency characteristic of the turbulence decay process under its self-interaction." He stated further, "The rough idea is that  $\omega^2$  is the mean square vorticity of the 'energy containing eddies' and  $[k]$  is the kinetic energy of the motion induced by this vorticity." Spalding [Launder and Spalding (1972)] and Wilcox and Alber (1972) identify  $\omega$  as the RMS fluctuating vorticity, which is also known as **enstrophy**. Wilcox and Rubesin (1980), Wilcox (1988a) and Speziale et al. (1990) regard  $\omega$  as

the ratio of  $\epsilon$  to  $k$ , i.e., the rate of dissipation per unit turbulence kinetic energy.

The form of the equation for  $\omega$  has changed as the  $k$ - $\omega$  model has evolved over the past five decades. A production term has been added by all model developers subsequent to Kolmogorov. Like Kolmogorov, Wilcox (1988a) and Speziale et al. (1990) write the equation for  $\omega$  in terms of  $\omega$ . By contrast, most other  $k$ - $\omega$  models known to this author use an equation for  $\omega^2$ . Because it has been tested more extensively than any other  $k$ - $\omega$  model, we present the Wilcox (1988a) model as the state-of-the-art formulation.

### Eddy Viscosity

$$\mu_T = \rho k / \omega \quad (4.33)$$

### Turbulence Kinetic Energy

$$\rho \frac{\partial k}{\partial t} + \rho U_j \frac{\partial k}{\partial x_j} = \tau_{ij} \frac{\partial U_i}{\partial x_j} - \beta^* \rho k \omega + \frac{\partial}{\partial x_j} \left[ (\mu + \sigma^* \mu_T) \frac{\partial k}{\partial x_j} \right] \quad (4.34)$$

### Specific Dissipation Rate

$$\rho \frac{\partial \omega}{\partial t} + \rho U_j \frac{\partial \omega}{\partial x_j} = \alpha \frac{\omega}{k} \tau_{ij} \frac{\partial U_i}{\partial x_j} - \beta \rho \omega^2 + \frac{\partial}{\partial x_j} \left[ (\mu + \sigma \mu_T) \frac{\partial \omega}{\partial x_j} \right] \quad (4.35)$$

### Closure Coefficients

$$\alpha = 5/9, \quad \beta = 3/40, \quad \beta^* = 9/100, \quad \sigma = 1/2, \quad \sigma^* = 1/2 \quad (4.36)$$

### Auxiliary Relations

$$\epsilon = \beta^* \omega k \quad \text{and} \quad \ell = k^{1/2} / \omega \quad (4.37)$$

## 4.3.2 The $k$ - $\epsilon$ Model

By far, the most popular two-equation model is the  $k$ - $\epsilon$  model. The earliest development efforts based on this model were those of Chou (1945), Davidov (1961) and Harlow and Nakayama (1968). The central paper however, is that by Jones and Launder (1972) that, in the turbulence modeling community, has nearly reached the status of the Boussinesq and Reynolds papers. That is, the model is so well known that it is often referred to as the **Standard  $k$ - $\epsilon$  model** and reference to the Jones-Launder paper is often omitted. Actually, Launder and Sharma (1974) “retuned” the model’s closure coefficients and most researchers use the form of the model presented in the 1974 paper.

Again, we begin with Equations (4.6) and (4.9). In formulating the  $k$ - $\epsilon$  model, the idea is to derive the exact equation for  $\epsilon$  and to find suitable closure approximations for the exact equation governing its behavior. Recall that  $\epsilon$  is defined by Equation (4.5). The exact equation for  $\epsilon$  is derived by taking the following moment of the Navier-Stokes equation.

$$\overline{2\nu \frac{\partial u'_i}{\partial x_j} \frac{\partial}{\partial x_j} [\mathcal{N}(u_i)]} = 0 \quad (4.38)$$

where  $\mathcal{N}(u_i)$  is the Navier-Stokes operator defined in Equation (2.26). After a considerable amount of algebra, the following equation for  $\epsilon$  results.

$$\begin{aligned} \rho \frac{\partial \epsilon}{\partial t} + \rho U_j \frac{\partial \epsilon}{\partial x_j} = & -2\mu \left[ \overline{u'_{i,k} u'_{j,k}} + \overline{u'_{k,i} u'_{k,j}} \right] \frac{\partial U_i}{\partial x_j} - 2\mu \overline{u'_k u'_{i,j}} \frac{\partial^2 U_i}{\partial x_k \partial x_j} \\ & - 2\mu \overline{u'_{i,k} u'_{i,m} u'_{k,m}} - 2\mu \nu \overline{u'_{i,km} u'_{i,km}} \\ & + \frac{\partial}{\partial x_j} \left[ \mu \frac{\partial \epsilon}{\partial x_j} - \mu \overline{u'_j u'_{i,m} u'_{i,m}} - 2\nu \overline{p'_{,m} u'_{j,m}} \right] \end{aligned} \quad (4.39)$$

This equation is far more complicated than the turbulence kinetic energy equation and involves several new unknown double and triple correlations of fluctuating velocity, pressure and velocity gradients. The terms on the three lines of the right-hand side of Equation (4.39) are generally regarded as **Production of Dissipation**, **Dissipation of Dissipation**, and the sum of **Molecular Diffusion of Dissipation** and **Turbulent Transport of Dissipation**, respectively. These correlations are essentially impossible to measure with any degree of accuracy so that there is presently little hope of finding reliable guidance from experimentalists regarding suitable closure approximations. Recent DNS studies such as the work of Mansour, Kim and Moin (1988) have helped gain some insight on the exact  $\epsilon$  transport equation for low-Reynolds-number flows. However, the database for establishing closure approximations similar to those used for the  $k$  equation remains very sparse.

Many researchers have proceeded undaunted by the lack of a rational basis for establishing closure approximations with a feeling of security that using Equation (4.39) as their foundation adds rigor to their approach. The strongest claim that can actually be made is that the conventional closure approximations used for Equation (4.39) are dimensionally correct. But this is not very different from the Kolmogorov (1942) and Saffman (1970) approaches that are guided almost exclusively by physical reasoning and dimensional analysis. An important point we should keep in mind is to **avoid modeling the differential equations rather than the physics of turbulence**. That is not to say we should avoid any reference to the

differential equations, for then we might formulate a model that violates a fundamental physical feature of the Navier-Stokes equation. Rather, we should avoid deluding ourselves into thinking that the **drastic surgery** approach to something as complex as Equation (4.39) is any more rigorous than dimensional-analysis arguments.

As a final comment, even if we had demonstrably accurate closure approximations for the exact  $\epsilon$  transport equation, there is a serious question of their relevance to our basic closure problem. That is, the length or time scale required is that of the energy-containing, Reynolds-stress-bearing eddies rather than the dissipating eddies represented by the exact  $\epsilon$  equation. So, we must ask whether the modeled  $\epsilon$  equation represents the dissipation as such [as Equation (4.39) does], or whether it is actually an empirical equation for the rate of energy transfer from the large eddies (equal, of course, to the rate of dissipation in the small eddies). The answer seems clear since the closure approximations normally used parametrize the various terms in the modeled  $\epsilon$  equation as functions of large-eddy scales (our use of dimensional analysis does this implicitly). As a consequence, the relation between the modeled equation for  $\epsilon$  and the exact equation is so tenuous as to not need serious consideration.

The **Standard  $k$ - $\epsilon$  model** is as follows.

#### Eddy Viscosity

$$\mu_T = \rho C_\mu k^2 / \epsilon \quad (4.40)$$

#### Turbulence Kinetic Energy

$$\rho \frac{\partial k}{\partial t} + \rho U_j \frac{\partial k}{\partial x_j} = \tau_{ij} \frac{\partial U_i}{\partial x_j} - \rho \epsilon + \frac{\partial}{\partial x_j} \left[ (\mu + \mu_T / \sigma_k) \frac{\partial k}{\partial x_j} \right] \quad (4.41)$$

#### Dissipation Rate

$$\rho \frac{\partial \epsilon}{\partial t} + \rho U_j \frac{\partial \epsilon}{\partial x_j} = C_{\epsilon 1} \frac{\epsilon}{k} \tau_{ij} \frac{\partial U_i}{\partial x_j} - C_{\epsilon 2} \rho \frac{\epsilon^2}{k} + \frac{\partial}{\partial x_j} \left[ (\mu + \mu_T / \sigma_\epsilon) \frac{\partial \epsilon}{\partial x_j} \right] \quad (4.42)$$

#### Closure Coefficients

$$C_{\epsilon 1} = 1.44, \quad C_{\epsilon 2} = 1.92, \quad C_\mu = 0.09, \quad \sigma_k = 1.0, \quad \sigma_\epsilon = 1.3 \quad (4.43)$$

#### Auxiliary Relations

$$\omega = \epsilon / (C_\mu k) \quad \text{and} \quad \ell = C_\mu k^{3/2} / \epsilon \quad (4.44)$$

### 4.3.3 Other Two-Equation Models

Two-equation models based on the turbulence length scale,  $\ell$ , and the turbulence time scale,  $\tau$ , have received less attention than the  $k$ - $\omega$  and  $k$ - $\epsilon$  models. Generally speaking, the level of agreement between measurements and predictions made with other models is comparable to  $k$ - $\omega$  and  $k$ - $\epsilon$  predictions for simple constant-pressure flows, but these models have not been pursued to any great extent. This subsection presents a brief overview of some of the length-scale and time-scale models. More details can be found in the various papers referenced in the discussion.

The proposed foundation for Rotta's (1968)  $k$ - $k\ell$  model is the **two-point velocity correlation tensor**. The correlation functions we have dealt with thus far are known as **single-point correlations** and involve products of fluctuating properties at a single point in the flow,  $\mathbf{x}$ . In a two-point correlation, we consider two points in the flow, say  $\mathbf{x}$  and  $\mathbf{x}+\mathbf{r}$ , and do our time average. The two-point velocity correlation tensor is defined as

$$R_{ij}(\mathbf{x}, t; \mathbf{r}) = \overline{u'_i(\mathbf{x}, t) u'_j(\mathbf{x} + \mathbf{r}, t)} \quad (4.45)$$

The turbulence kinetic energy is simply one half the trace of  $R_{ij}$  with a displacement  $\mathbf{r} = \mathbf{0}$ . Rotta's second variable is the product of  $k$  and the **integral scale**,  $\ell$ , which is the integral of  $R_{ii}$  over all displacements,  $r = |\mathbf{r}|$ . Thus Rotta's variables are given by

$$k = \frac{1}{2} R_{ii}(\mathbf{x}, t; \mathbf{0}) \quad (4.46)$$

$$k\ell = \frac{3}{16} \int_{-\infty}^{\infty} R_{ii}(\mathbf{x}, t; r) dr \quad (4.47)$$

As with attempts to model the exact dissipation equation, no particular advantage has been gained by introducing the double velocity correlation tensor. While an exact equation for  $k\ell$  can indeed be derived, Rotta (1968) still must perform drastic surgery on the exact equation. For example, using standard closure approximations based largely on the strength of dimensional analysis, the following modeled version of the exact  $k\ell$  equation results.

$$\begin{aligned} \rho \frac{\partial}{\partial t}(k\ell) + \rho U_j \frac{\partial}{\partial x_j}(k\ell) &= C_{L1} \rho \ell \tau_{ij} \frac{\partial U_i}{\partial x_j} - C_{L2} \rho k^{3/2} \\ &+ \frac{\partial}{\partial x_j} \left[ \mu \frac{\partial}{\partial x_j}(k\ell) + (\mu_T / \sigma_{L1}) \ell \frac{\partial k}{\partial x_j} + (\mu_T / \sigma_{L2}) k \frac{\partial \ell}{\partial x_j} \right] \end{aligned} \quad (4.48)$$

For this model,  $k$  and  $\mu_T$  are given by Equations (4.11) and (4.12). Rodi and Spalding (1970) and Ng and Spalding (1972) developed this model further. More recently, Smith (1990) has pursued development of the  $k$ - $k\ell$  model. Ng and Spalding found that for wall-bounded flows, the closure coefficient  $C_{L2}$  must vary with distance from the surface. They propose the following set of closure coefficients.

$$C_{L1} = 0.98, \quad C_{L2} = 0.059 + 702(\ell/y)^6, \quad C_D = 0.09, \quad \sigma_k = \sigma_{L1} = \sigma_{L2} = 1 \quad (4.49)$$

On a similar tack, Zeierman and Wolfshtein (1986) base their model upon the **autocorrelation tensor** that involves the time average of fluctuating quantities at the same point in space but at different times. Thus, they work with the tensor

$$\mathcal{R}_{ij}(\mathbf{x}, t; t') = \overline{u'_i(\mathbf{x}, t) u'_j(\mathbf{x}, t + t')} \quad (4.50)$$

The turbulence kinetic energy is half the trace of  $\mathcal{R}_{ij}$  with  $t' = 0$ , while the **integral time scale** is proportional to the integral of  $\mathcal{R}_{ii}$  over all possible values of  $t'$ . Thus,

$$k = \frac{1}{2} \mathcal{R}_{ii}(\mathbf{x}, t; 0) \quad (4.51)$$

$$k\tau = \frac{1}{4} \int_{-\infty}^{\infty} \mathcal{R}_{ii}(\mathbf{x}, t; t') dt' \quad (4.52)$$

The Zeierman-Wolfshtein  $k$ - $k\tau$  model is as follows.

#### Eddy Viscosity

$$\mu_T = \rho C_\mu k\tau \quad (4.53)$$

#### Turbulence Kinetic Energy

$$\rho \frac{\partial k}{\partial t} + \rho U_j \frac{\partial k}{\partial x_j} = \tau_{ij} \frac{\partial U_i}{\partial x_j} - \rho \frac{k}{\tau} + \frac{\partial}{\partial x_j} \left[ (\mu + \mu_T / \sigma_k) \frac{\partial k}{\partial x_j} \right] \quad (4.54)$$

#### Integral Time Scale

$$\begin{aligned} \rho \frac{\partial}{\partial t}(k\tau) + \rho U_j \frac{\partial}{\partial x_j}(k\tau) &= C_{\tau 1} \tau \tau_{ij} \frac{\partial U_i}{\partial x_j} - C_{\tau 2} \rho k \\ &\quad + \frac{\partial}{\partial x_j} \left[ (\mu + \mu_T / \sigma_\tau) \frac{\partial}{\partial x_j}(k\tau) \right] \end{aligned} \quad (4.55)$$

#### Closure Coefficients

$$C_{\tau 1} = 0.173, \quad C_{\tau 2} = 0.225, \quad C_\mu = 0.09, \quad \sigma_k = 1.46, \quad \sigma_\tau = 10.8 \quad (4.56)$$

**Auxiliary Relations**

$$\omega = 1/(C_\mu \tau), \quad \epsilon = k/\tau \quad \text{and} \quad \ell = C_\mu k^{1/2} \tau \quad (4.57)$$

Note that because the eddy viscosity is proportional to  $k\tau$ , Equation (4.55) can also be regarded as an equation for  $\mu_T$ .

Speziale, Abid and Anderson (1990) have taken a different approach in devising a  $k$ - $\tau$  model. Specifically, they introduce the formal change of dependent variables  $\epsilon = k/\tau$  and transform the Standard  $k$ - $\epsilon$  model. The resulting equation for  $\tau$  is as follows.

$$\begin{aligned} \rho \frac{\partial \tau}{\partial t} + \rho U_j \frac{\partial \tau}{\partial x_j} = & (1 - C_{\epsilon 1}) \frac{\tau}{k} \tau_{ij} \frac{\partial U_i}{\partial x_j} + (C_{\epsilon 2} - 1) \rho \\ & + \frac{\partial}{\partial x_j} \left[ (\mu + \mu_T / \sigma_{\tau 2}) \frac{\partial \tau}{\partial x_j} \right] \\ & + \frac{2}{k} (\mu + \mu_T / \sigma_{\tau 1}) \frac{\partial k}{\partial x_k} \frac{\partial \tau}{\partial x_k} - \frac{2}{\tau} (\mu + \mu_T / \sigma_{\tau 2}) \frac{\partial \tau}{\partial x_k} \frac{\partial \tau}{\partial x_k} \end{aligned} \quad (4.58)$$

Speziale, Abid and Anderson use the following revised set of closure coefficient values for their  $k$ - $\tau$  model that make it a bit different from the Standard  $k$ - $\epsilon$  model.

$$C_{\epsilon 1} = 1.44, \quad C_{\epsilon 2} = 1.83, \quad C_\mu = 0.09, \quad \sigma_k = \sigma_{\tau 1} = \sigma_{\tau 2} = 1.36 \quad (4.59)$$

In summary, the models listed above are representative of the various two-equation models that have been devised since Kolmogorov's (1942)  $k$ - $\omega$  model. While other models have been created, the intent of this text is to study models in a generic sense, as opposed to creating an encyclopedia of turbulence models. In the following sections we investigate several aspects of two-equation models including: (a) details on how the closure-coefficient values are chosen; (b) surface boundary conditions for wall-bounded flows; and, (c) applications to a variety of flows.

**4.4 Closure Coefficients**

All of the two-equation models have closure coefficients that have been introduced in replacing unknown double and triple correlations with algebraic expressions involving known turbulence and mean-flow properties. The Wilcox  $k$ - $\omega$  model, for example, has five, viz.,  $\alpha$ ,  $\beta$ ,  $\beta^*$ ,  $\sigma$  and  $\sigma^*$ . If our theory were exact, we could set the values of these coefficients from first principles much as we use the kinetic theory of gases to determine the viscosity coefficient in Stokes' approximation for laminar flows. Unfortunately, the theory is not exact, but rather a model developed mainly on the



strength of dimensional analysis. Consequently, the best we can do is to set the values of the closure coefficients to assure agreement with observed properties of turbulence.

This section describes the manner in which the closure coefficients have been determined for the Wilcox  $k$ - $\omega$  model. There is no loss of generality in doing this however, since **these same general arguments have been used in establishing the values of the closure coefficients in most two-equation models.** The Problems section at the end of the chapter examines some of the (relatively minor) differences among the various models.

We can establish the ratio of  $\beta^*$  to  $\beta$  by applying the model to decaying homogeneous, isotropic turbulence. In this kind of turbulence, there are no spatial gradients of any mean-flow properties wherefore Equations (4.34) and (4.35) simplify to

$$\frac{dk}{dt} = -\beta^* \omega k \quad \text{and} \quad \frac{d\omega}{dt} = -\beta \omega^2 \quad (4.60)$$

from which the asymptotic solution for  $k$  is readily found to be

$$k \sim t^{-\beta^*/\beta} \quad (4.61)$$

Experimental observations [Townsend (1976)] indicate that  $k \sim t^{-n}$  where  $n = 1.25 \pm 0.06$  for decaying homogeneous, isotropic turbulence. Choosing  $\beta^*/\beta = 6/5$  sets the ratio at the lower end of the range of accepted values.

Values for the coefficients  $\alpha$  and  $\beta^*$  can be established by examining the **log layer**. Recall from Section 3.4 that the log layer is defined as the portion of the boundary layer sufficiently distant from the surface that molecular viscosity is negligible relative to eddy viscosity, yet close enough for convective effects to be negligible. In the limiting case of an incompressible constant-pressure boundary layer, defining  $\nu_T = \mu_T/\rho$ , the mean-momentum equation and the equations for  $k$  and  $\omega$  simplify to

$$\left. \begin{aligned} 0 &= \frac{\partial}{\partial y} \left[ \nu_T \frac{\partial U}{\partial y} \right] \\ 0 &= \nu_T \left( \frac{\partial U}{\partial y} \right)^2 - \beta^* \omega k + \sigma^* \frac{\partial}{\partial y} \left[ \nu_T \frac{\partial k}{\partial y} \right] \\ 0 &= \alpha \left( \frac{\partial U}{\partial y} \right)^2 - \beta \omega^2 + \sigma \frac{\partial}{\partial y} \left[ \nu_T \frac{\partial \omega}{\partial y} \right] \end{aligned} \right\} \quad (4.62)$$

We will justify the limiting form of these equations when we use perturbation methods to analyze the log layer in Subsection 4.6.1. We seek the

conditions under which these simplified equations yield a solution consistent with the law of the wall. As can be easily verified, Equations (4.62) possess such a solution, viz.,

$$U = \frac{u_\tau}{\kappa} \ln y + \text{constant}, \quad k = \frac{u_\tau^2}{\sqrt{\beta^*}}, \quad \omega = \frac{u_\tau}{\sqrt{\beta^*} \kappa y} \quad (4.63)$$

where  $u_\tau$  is the conventional friction velocity and  $\kappa$  is Kármán's constant. There is one constraint imposed in the solution to Equations (4.62), namely, a unique relation exists between the implied value of Kármán's constant and the various closure coefficients. Specifically, the following equation must hold.

$$\alpha = \beta/\beta^* - \sigma\kappa^2/\sqrt{\beta^*} \quad (4.64)$$

Additionally, according to our solution the Reynolds shear stress,  $\tau_{xy}$ , is constant and equal to  $\rho u_\tau^2$ . Inspection of Equations (4.63) shows that this implies  $\tau_{xy} = \sqrt{\beta^*} \rho k$  in the log layer. A variety of measurements [Townsend (1976)] indicate the ratio of  $\tau_{xy}$  to  $\rho k$  is about 3/10 in the log layer. This is the same ratio Bradshaw, Ferriss and Atwell (1967) used in formulating their one-equation model [c.f. Equation (4.13)]. Thus, the predicted log-layer solution is consistent with experimental observations provided we select  $\beta^* = 9/100$ .

We must work a bit harder to determine the values of  $\sigma$  and  $\sigma^*$ . As we will see in Subsections 4.6.2 and 4.6.3, detailed analysis of the defect layer and the sublayer indicates that the optimum choice is  $\sigma = \sigma^* = 1/2$ . Finally, Equation (4.64) shows that selecting  $\alpha = 5/9$  is consistent with Coles' value for the Kármán constant of 0.41.

Other arguments have been used to determine closure coefficients prior to any applications or computer optimization. Saffman (1970), for example, uses estimates based on vortex-stretching processes in simple shear and pure extension to effectively establish bounds on a coefficient similar to  $\alpha$ . He also requires that the length scale,  $\ell$ , be discontinuous at a turbulent-nonturbulent interface and finds that his model requires  $\sigma = \sigma^* = 1/2$  to guarantee such behavior.

Zeierman and Wolfshtein (1986) use the fact that very close to separation, measurements [Townsend (1976)] indicate the law of the wall is replaced by

$$U \rightarrow \frac{1}{0.24} \sqrt{\frac{y}{\rho} \frac{dp}{dx}} \quad \text{as} \quad y \rightarrow 0 \quad (4.65)$$

They also observe from measurements of Laufer (1950) and Clark (1968) that, for flow near the center of a channel, the turbulence kinetic energy

and velocity are closely approximated by

$$\left. \begin{aligned} k/k_o &\approx 1 + 6.67(y/R)^2 \\ U/U_o &\approx 1 - 0.242(y/R)^2 \\ u_\tau^2 &\approx 0.048U_o k_o^{1/2} \end{aligned} \right\} \quad \text{as } y \rightarrow R \quad (4.66)$$

In conclusion, the specific arguments selected for determination of the closure coefficients are a free choice of the developer. For example, using arguments based on homogeneous turbulence **and** boundary layers assumes we have a degree of universality that may be grossly optimistic. That is, we are implicitly assuming our model is valid for grid turbulence, boundary layers, and many flows in between. Dropping this argument in favor of another boundary-layer argument may yield a model optimized for boundary layers but restricted to such flows. Ideally, we would find arguments that isolate each closure coefficient. Often, more than one is involved [e.g., Equation (4.64)]. In any event, for the sake of clarity, the arguments should be as simple as possible.

## 4.5 Application to Free Shear Flows

Our first applications will be for free shear flows. As with the mixing-length model, we seek similarity solutions to determine far-field behavior for the plane wake, mixing layer, plane jet and round jet. There are two noteworthy changes in our approach to obtaining a solution for free shear flows. **First**, for the mixing layer and the jets we can choose our similarity variable to be  $\eta = y/x$ . That is, with no loss of generality, we can set all scaling constants such as  $A$  in Equations (3.70) and (3.71) equal to one. We had to carry such scaling coefficients for the mixing-length model because, by hypothesis, the mixing length is proportional to the width of the layer, which is proportional to the coefficient  $A$ . With two-equation models, the turbulence length scale is determined as part of the solution so that the way in which we scale the similarity variable  $\eta$  is of no consequence. **Second**, while the rest of the methodology is the same, the addition of two extra differential equations complicates the problem somewhat. Because they are the most widely used two-equation models, we confine our attention to the  $k$ - $\omega$  and  $k$ - $\epsilon$  models. With the standard boundary-layer/shear-layer approximations, the equations of motion become:

$$\frac{\partial U}{\partial x} + \frac{1}{y^j} \frac{\partial}{\partial y} [y^j V] = 0 \quad (4.67)$$

$$\rho U \frac{\partial U}{\partial x} + \rho V \frac{\partial U}{\partial y} = \frac{1}{y^j} \frac{\partial}{\partial y} [y^j \tau_{xy}] \quad (4.68)$$

$$\tau_{xy} = \mu_T \frac{\partial U}{\partial y} \quad (4.69)$$

**k- $\omega$  Model:**

$$\left. \begin{aligned} \rho U \frac{\partial k}{\partial x} + \rho V \frac{\partial k}{\partial y} &= \tau_{xy} \frac{\partial U}{\partial y} - \beta^* \rho \omega k + \frac{1}{y^j} \frac{\partial}{\partial y} \left[ y^j \sigma^* \mu_T \frac{\partial k}{\partial y} \right] \\ \rho U \frac{\partial \omega}{\partial x} + \rho V \frac{\partial \omega}{\partial y} &= \alpha \frac{\omega}{k} \tau_{xy} \frac{\partial U}{\partial y} - \beta \rho \omega^2 + \frac{1}{y^j} \frac{\partial}{\partial y} \left[ y^j \sigma \mu_T \frac{\partial \omega}{\partial y} \right] \\ \mu_T &= \rho k / \omega \end{aligned} \right\} \quad (4.70)$$

**k- $\epsilon$  Model:**

$$\left. \begin{aligned} \rho U \frac{\partial k}{\partial x} + \rho V \frac{\partial k}{\partial y} &= \tau_{xy} \frac{\partial U}{\partial y} - \rho \epsilon + \frac{1}{y^j} \frac{\partial}{\partial y} \left[ y^j \frac{\mu_T}{\sigma_k} \frac{\partial k}{\partial y} \right] \\ \rho U \frac{\partial \epsilon}{\partial x} + \rho V \frac{\partial \epsilon}{\partial y} &= C_{\epsilon 1} \frac{\epsilon}{k} \tau_{xy} \frac{\partial U}{\partial y} - C_{\epsilon 2} \rho \frac{\epsilon^2}{k} + \frac{1}{y^j} \frac{\partial}{\partial y} \left[ y^j \frac{\mu_T}{\sigma_\epsilon} \frac{\partial \epsilon}{\partial y} \right] \\ \mu_T &= C_\mu \rho k^2 / \epsilon \end{aligned} \right\} \quad (4.71)$$

The similarity solution for the various free shear flows can be written in the following compact form.

**Far Wake:**

$$\left. \begin{aligned} U(x, y) &= U_\infty - \sqrt{\frac{D}{\rho x}} \mathcal{U}(\eta), \quad k(x, y) = \frac{D}{\rho x} K(\eta) \\ \omega(x, y) &= \frac{U_\infty}{x} W(\eta), \quad \epsilon(x, y) = \frac{D U_\infty}{\rho x^2} E(\eta) \\ \eta &= y \sqrt{\frac{\rho U_\infty^2}{D x}} \end{aligned} \right\} \quad (4.72)$$

**Mixing Layer:**

$$\left. \begin{aligned} U(x, y) &= U_1 \mathcal{U}(\eta), \quad k(x, y) = U_1^2 K(\eta) \\ \omega(x, y) &= \frac{U_1}{x} W(\eta), \quad \epsilon(x, y) = \frac{U_1^3}{x} E(\eta) \\ \eta &= \frac{y}{x} \end{aligned} \right\} \quad (4.73)$$

**Jet:**

$$\left. \begin{aligned} U(x, y) &= \frac{J^{1/2}}{x^{(j+1)/2}} \mathcal{U}(\eta), \quad k(x, y) = \frac{J}{x^{(j+1)}} K(\eta) \\ \omega(x, y) &= \frac{J^{1/2}}{x^{(j+3)/2}} W(\eta), \quad \epsilon(x, y) = \frac{J^{3/2}}{x^{(3j+5)/2}} E(\eta) \\ \eta &= \frac{y}{x} \end{aligned} \right\} \quad (4.74)$$

Substituting these self-similar representations into the mean momentum equation yields the following transformed equation.

$$\mathcal{V} \frac{d\mathcal{U}}{d\eta} - \frac{1}{\eta^j} \frac{d}{d\eta} \left[ \eta^j N \frac{d\mathcal{U}}{d\eta} \right] = S_u \mathcal{U} \quad (4.75)$$

where the function  $N(\eta)$  is the transformed eddy viscosity,  $j = 1$  for the round jet, and  $j = 0$  for the other three cases. The two terms on the left-hand side of Equation (4.75) are essentially vertical convection and diffusion. The term on the right-hand side is a source term that originates from the streamwise convection of momentum; Table 4.1 lists the coefficient  $S_u$  and the normal velocity-like function,  $\mathcal{V}(\eta)$ , for each of the free shear flows considered. The transformed  $k$ ,  $\omega$  and  $\epsilon$  equations are:

**$k$ - $\omega$  Model:**

$$\left. \begin{aligned} \mathcal{V} \frac{dK}{d\eta} - \frac{1}{\eta^j} \frac{d}{d\eta} \left[ \eta^j \sigma^* N \frac{dK}{d\eta} \right] &= S_k K + N \left( \frac{d\mathcal{U}}{d\eta} \right)^2 - \beta^* W K \\ \mathcal{V} \frac{dW}{d\eta} - \frac{1}{\eta^j} \frac{d}{d\eta} \left[ \eta^j \sigma N \frac{dW}{d\eta} \right] &= S_w W + \alpha \frac{W}{K} N \left( \frac{d\mathcal{U}}{d\eta} \right)^2 - \beta W^2 \\ N &= \frac{K}{W} \end{aligned} \right\} \quad (4.76)$$

**$k$ - $\epsilon$  Model:**

$$\left. \begin{aligned} \mathcal{V} \frac{dK}{d\eta} - \frac{1}{\eta^j} \frac{d}{d\eta} \left[ \eta^j \frac{N}{\sigma_k} \frac{dK}{d\eta} \right] &= S_k K + N \left( \frac{d\mathcal{U}}{d\eta} \right)^2 - E \\ \mathcal{V} \frac{dE}{d\eta} - \frac{1}{\eta^j} \frac{d}{d\eta} \left[ \eta^j \frac{N}{\sigma_\epsilon} \frac{dE}{d\eta} \right] &= S_e E + C_{\epsilon 1} \frac{E}{K} N \left( \frac{d\mathcal{U}}{d\eta} \right)^2 - C_{\epsilon 2} \frac{E^2}{K} \\ N &= C_\mu \frac{K^2}{E} \end{aligned} \right\} \quad (4.77)$$

Table 4.1: Free Shear Flow Parameters

Flow	$S_u$	$S_k$	$S_w$	$S_e$	$j$	$\mathcal{V}(\eta)$
Far Wake	$\frac{1}{2}$	1	1	2	0	$-\frac{1}{2}\eta$
Mixing Layer	0	0	$\mathcal{U}$	$\mathcal{U}$	0	$-\int_0^\eta \mathcal{U}(\eta') d\eta'$
Plane Jet	$\frac{1}{2}\mathcal{U}$	$\mathcal{U}$	$\frac{3}{2}\mathcal{U}$	$\frac{5}{2}\mathcal{U}$	0	$-\frac{1}{2}\int_0^\eta \mathcal{U}(\eta') d\eta'$
Round Jet	$\mathcal{U}$	$2\mathcal{U}$	$2\mathcal{U}$	$4\mathcal{U}$	1	$-\frac{1}{\eta}\int_0^\eta \mathcal{U}(\eta')\eta' d\eta'$

The  $k$ ,  $\omega$  and  $\epsilon$  equations contain convective terms, diffusion terms, and additional source terms corresponding to streamwise convection, production and dissipation. Table 4.1 lists the convective source term coefficients,  $S_k$ ,  $S_w$  and  $S_e$ .

Boundary conditions on the velocity are the same as in Chapter 3. We must also specify boundary conditions for  $K$ ,  $W$  and  $E$ . Solutions to all two-equation model equations feature sharp turbulent-nonturbulent interfaces for free shear flows, i.e., interfaces at which derivatives of flow properties are discontinuous. Consequently, the most sensible boundary conditions in the freestream are those corresponding to non-turbulent flow, i.e.,  $K(\eta)$ ,  $W(\eta)$  and  $E(\eta)$  all vanish approaching the edge of the shear layer. As it turns out,  $k$ - $\epsilon$  model solutions are unaffected by finite values of  $K$  and  $E$  in the freestream while  $k$ - $\omega$  model solutions are very sensitive to the freestream value of  $W$ . Subsection 7.2.2 gives complete details on the nature of two-equation model behavior near turbulent/nonturbulent interfaces. The boundary conditions that appear most appropriate for  $K$ ,  $W$  and  $E$  are as follows.

**Wake and Jet:**

$$K'(0) = W'(0) = E'(0) = 0 \quad (4.78)$$

**Wake, Jet and Mixing Layer:**

$$K(\eta) \rightarrow 0, \quad W(\eta) \rightarrow W_\infty, \quad \text{and} \quad E(\eta) \rightarrow 0 \quad \text{as} \quad |\eta| \rightarrow \infty \quad (4.79)$$

Table 4.2: Free Shear Flow Spreading Rate

Flow	$k-\omega$ Model	$k-\epsilon$ Model	Measured
Far Wake	.301-.500	.256	.365
Mixing Layer	.103-.141	.098	.115
Plane Jet	.090-.136	.109	.100-.110
Round Jet	.073-.371	.120	.086-.095

The conventional definition of **spreading rate for the wake** is the value of  $\eta$  given in Equation (4.72) where the velocity defect is half its maximum value. Similarly **for the plane and round jet, the spreading rate** is the value of  $y/x$  where the velocity is half its centerline value. **For the mixing layer, the spreading rate** is usually defined as the difference between the values of  $y/x$  where  $(U - U_2)^2/(U_1 - U_2)^2$  is 9/10 and 1/10. Table 4.2 compares computed and measured spreading rates for the  $k-\omega$  and  $k-\epsilon$  models. A range of values is quoted for the  $k-\omega$  model corresponding to values of  $W_\infty$  ranging from 0 to 1 for the far wake and mixing layer, 0 to 10 for the plane jet, and 0 to 100 for the round jet. Using larger values of  $W_\infty$  for these flows causes numerical difficulties, so these values appear to cover the permissible values for  $W_\infty$ . The largest spreading rate corresponds to  $W_\infty = 0$ .

These results show that having a **complete** model guarantees nothing regarding accuracy. Overall, the  $k-\epsilon$  model behaves best from a computational point of view because of its insensitivity to freestream boundary conditions. However, its predicted spreading rate is 30% lower than measured for the far wake, 15% lower than measured for the mixing layer, and between 25% to 40% higher than measured for the round jet. Only for the plane jet does its predicted spreading rate fall within the range of measured values.

Using  $W_\infty = 0$ , the  $k-\omega$  model consistently predicts spreading rates larger than measured. Specifically, computed spreading rates exceed corresponding measurements by 37%, 23%, 24% and 291% for the far wake, mixing layer, plane jet and round jet, respectively. There are values of  $W_\infty$  that yield spreading rates much closer to the measured values. Specifically, using  $W_\infty = 0.4$  for the far wake,  $W_\infty = 0.5$  for the mixing layer,  $W_\infty = 5$  for the plane jet, and  $W_\infty = 50$  for the round jet yields spreading rates of .358, .115, .101 and .095, respectively. Figures 4.5 through 4.8 compare computed and measured velocity profiles obtained using these values for  $W_\infty$ . However, since there is no obvious reason for the choice of  $W_\infty$ , this

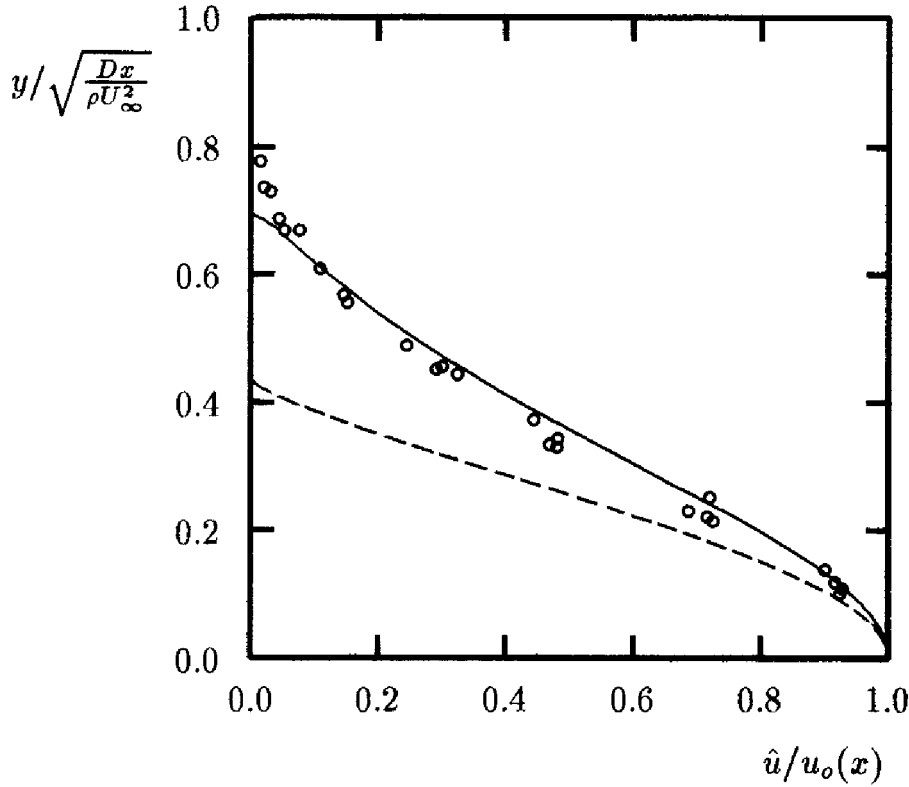


Figure 4.5: Comparison of computed and measured velocity profiles for the far wake; —  $k\text{-}\omega$  model; - - -  $k\text{-}\epsilon$  model; o Fage and Falkner.

amounts to having an adjustable parameter in the model. Clearly, this is not much of an improvement over the mixing-length model predictions of Chapter 3. As a final comment, we can reasonably expect that the optimum values of  $W_\infty$  used with the  $k\text{-}\omega$  model for the self-preserving cases should give good results for non-self-preserving cases.

Menter (1992c) has developed a  $k\text{-}\omega$  model that has no sensitivity to the freestream value of  $\omega$ . He accomplishes this by including a **cross-diffusion** term in the  $\omega$  equation. That is, Menter writes the  $\omega$  equation as follows.

$$\rho \frac{\partial \omega}{\partial t} + \rho U_j \frac{\partial \omega}{\partial x_j} = \alpha \frac{\omega}{k} \tau_{ij} \frac{\partial U_i}{\partial x_j} - \beta \rho \omega^2 + \frac{\partial}{\partial x_j} \left[ (\mu + \sigma \mu_T) \frac{\partial \omega}{\partial x_j} \right] + \sigma_d \frac{\rho}{\omega} \frac{\partial k}{\partial x_j} \frac{\partial \omega}{\partial x_j} \quad (4.80)$$

The term proportional to  $\sigma_d$  in Equation (4.80) is Menter's cross-diffusion term. The effect of this term is to replace the entrainment velocity,  $v$ , in the  $\omega$  equation by  $(v - \sigma_d \omega^{-1} \partial k / \partial y)$ . Since  $k$  decreases approaching the shear layer edge (assuming  $\sigma_d > 0$ ), the net effect is to make the effective entrainment velocity positive (or at least less negative). As a result,  $\omega$  diffuses from the turbulent region into the nonturbulent region, which is



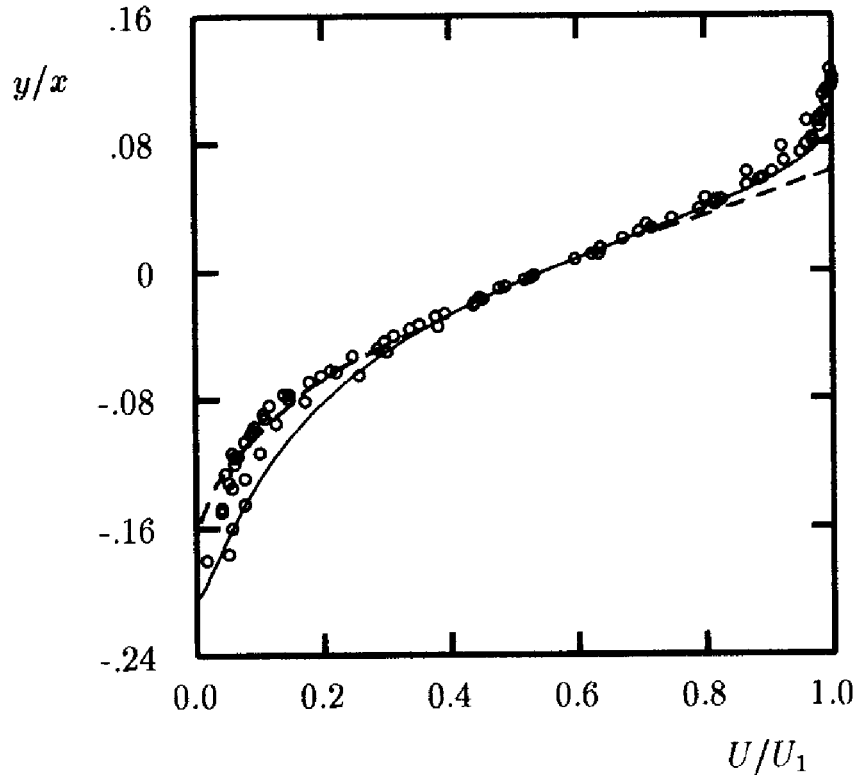


Figure 4.6: Comparison of computed and measured velocity profiles for the mixing layer; —  $k\text{-}\omega$  model; - - -  $k\text{-}\epsilon$  model;  $\circ$  Liepmann and Laufer.

the opposite of what happens with the  $k\text{-}\omega$  model. Thus, the freestream value of  $\omega$  has no effect on the solution.

Menter also introduces a “blending function” that makes  $\sigma_d = 0$  close to solid boundaries, while  $\sigma_d \rightarrow 2\sigma$  away from such boundaries. Additionally, his blending function causes all of the model’s closure coefficients to assume the values in Equation (4.36) near solid boundaries, and to asymptotically approach values similar to those used with the  $k\text{-}\epsilon$  model otherwise. The net result is a model that behaves very much like the Wilcox (1988a)  $k\text{-}\omega$  model for wall-bounded flows, and that is nearly identical to the  $k\text{-}\epsilon$  model for free shear flows.

The author has research in progress at the time of this writing that indicates it may be sufficient to let:

$$\sigma_d = \begin{cases} 0, & \frac{\partial k}{\partial x_j} \frac{\partial \omega}{\partial x_j} \leq 0 \\ \sigma, & \frac{\partial k}{\partial x_j} \frac{\partial \omega}{\partial x_j} > 0 \end{cases} \quad (4.81)$$

Additionally, the value of  $\sigma^*$  must assume a value larger than 0.5. As we will see in Subsection 4.6.2, it is important to suppress this cross-diffusion

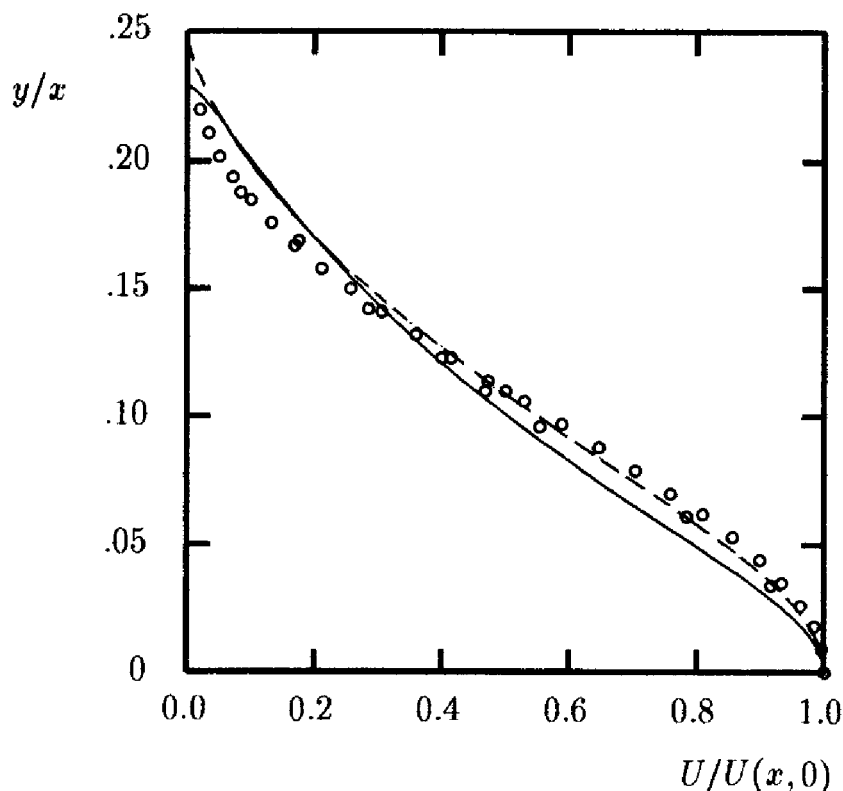


Figure 4.7: Comparison of computed and measured velocity profiles for the plane jet; —  $k\text{-}\omega$  model; - - -  $k\text{-}\epsilon$  model;  $\circ$  Wygnanski and Fiedler.

term close to solid boundaries for wall-bounded flows. Just as Menter's blending function causes  $\sigma_d$  to approach 0 near a solid boundary, so does Equation (4.81) since  $k$  increases and  $\omega$  decreases in the viscous sublayer. As with Menter's approach, this modification to the  $\omega$  equation eliminates the model's sensitivity to the freestream value of  $\omega$ . However, while simpler than Menter's blending function approach, this straightforward modification yields shear layer spreading rates that are a bit farther from measurements than those predicted by the  $k\text{-}\epsilon$  model. Other values of the  $k\text{-}\omega$  model's closure coefficients exist that yield closer agreement with measured spreading rates, but that also compromise the model's accuracy for wall-bounded flows. Consequently, research continues in quest of an optimum formulation.

Pope (1978) has proposed a modification to the  $\epsilon$  equation that resolves the so-called **round-jet/plane-jet anomaly**. That is, while experimental measurements indicate the spreading rate for the round jet is less than that of the plane jet, two-equation turbulence models predict the opposite. In Pope's modification, the **Dissipation of Dissipation** term in the  $\epsilon$

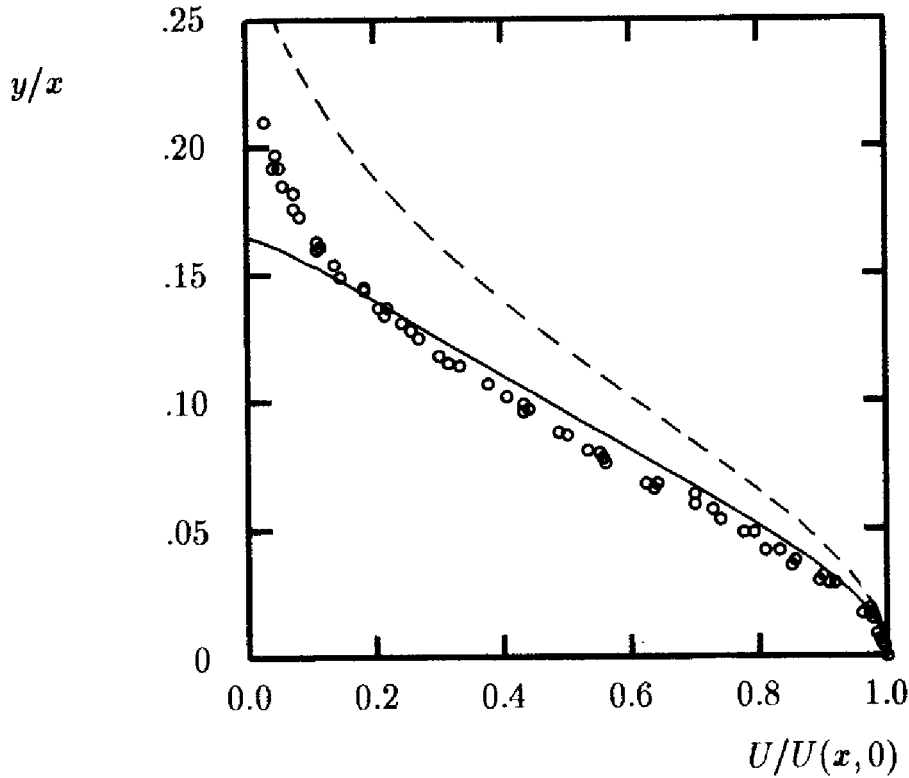


Figure 4.8: Comparison of computed and measured velocity profiles for the round jet; —  $k\text{-}\omega$  model; - - -  $k\text{-}\epsilon$  model; o Bradbury.

equation is replaced by

$$C_{\epsilon 2} \frac{\epsilon^2}{k} \rightarrow [C_{\epsilon 2} - C_{\epsilon 3} \chi] \frac{\epsilon^2}{k} \quad (4.82)$$

where  $\chi$  is a “nondimensional measure of vortex stretching” given by

$$\left. \begin{aligned} \chi &= \tilde{\omega}_{ij} \tilde{\omega}_{jk} \tilde{s}_{ki} \\ \tilde{s}_{ij} &= \frac{1}{2} \frac{k}{\epsilon} (U_{i,j} + U_{j,i}) \\ \tilde{\omega}_{ij} &= \frac{1}{2} \frac{k}{\epsilon} (U_{i,j} - U_{j,i}) \end{aligned} \right\} \quad (4.83)$$

Using  $C_{\epsilon 3} = 0.79$  reduces the  $k\text{-}\epsilon$  model’s predicted spreading rate to 0.86, consistent with measurements. However, as pointed out by Rubel (1985), the Pope correction has an adverse effect on model predictions for the so-called **radial jet**, which we have not discussed here. This is the case of two jets of equal strength colliding and spreading radially. Without the Pope correction, the  $k\text{-}\epsilon$  model predicts a radial-jet spreading rate of 0.095 which is close to the measured range of 0.096 to 0.110 [see Tanaka

and Tanaka (1976) and Witze and Dwyer (1976)]. Using the Pope correction for the radial jet reduces the  $k$ - $\epsilon$  model-predicted spreading rate to 0.040. Hence, as noted by Rubel, “the round jet/plane jet anomaly has been exchanged for a round jet/radial jet anomaly.”

This concludes our analysis of free shear flows. In the following sections we turn our attention to wall-bounded flows. To demonstrate how two-equation models fare for such flows, we are going to use a powerful mathematical tool to analyze fine details of model-predicted structure of the turbulent boundary layer. In particular, we will use **perturbation methods** to analyze the various regions in the turbulent boundary layer.

## 4.6 Perturbation Analysis of the Boundary Layer

The differential equations for all but the simplest turbulence models are sufficiently complicated for most flows that closed-form solutions do not exist. This is especially true for boundary layers because of nonlinearity of the convection terms and the turbulent diffusion terms attending introduction of the eddy viscosity. Our inability to obtain closed-form solutions is unfortunate because such solutions are invaluable in design studies and for determining trends with a parameter such as Reynolds number, or more generally, for establishing laws of similitude. Furthermore, without analytical solutions, our ability to check the accuracy of numerical solutions is limited.

There is a powerful mathematical tool available to us to generate approximate solutions that are valid in special limiting cases, viz., **perturbation analysis**. The idea of perturbation analysis is to develop a solution in the form of an **asymptotic expansion** in terms of a parameter, the error being small for sufficiently small values of the parameter. Our desire in developing such an expansion is for the first few terms of the expansion to illustrate all the essential physics of the problem and to provide a close approximation to the exact solution. Fortunately, this is usually the case in fluid mechanics.

This section shows how perturbation analysis can be used to dissect model-predicted structure of the turbulent boundary layer. Appendix B introduces basic concepts of perturbation theory for the reader with no prior background in the field.

### 4.6.1 The Log Layer

We direct our focus to the turbulent boundary layer. Experimental observations provide a strong argument for using perturbation analysis. Specifically, Coles' description of the turbulent boundary layer as a "wake-like structure constrained by a wall" (see Figure 3.8) suggests that different scales and physical processes are dominant in the inner (near-wall) and outer (main body) of the layer. These are clearly concepts upon which perturbation analysis is based. Coles [see Coles and Hirst (1969)] makes an explicit connection with perturbation theory when he remarks:

*"The idea that there are two distinct scales in a turbulent boundary layer is an old one, although quantitative expressions of this idea have evolved very slowly. . . . To the extent that the outer velocity boundary condition for the inner (wall) profile is the same as the inner velocity boundary condition for the outer (wake) profile, the turbulent boundary layer is a singular perturbation problem of classical type. In fact, we can claim to have discovered the first two terms in a composite expansion, complete with logarithmic behavior."*

Often perturbation solutions are guided by dimensional considerations and a knowledge of physical aspects of the problem. For the turbulent boundary layer, we can draw from empirically established laws to aid us in developing our perturbation solution. We observe that close to a solid boundary, the **law of the wall** holds. We can write this symbolically as

$$U(x, y) = u_\tau(x)f(u_\tau y/\nu); \quad u_\tau = \sqrt{\tau_w/\rho} \quad (4.84)$$

Similarly, the main body of the turbulent boundary layer behaves according to Clauser's (1956) well-known **defect law**, viz.,

$$U(x, y) = U_e(x) - u_\tau(x)F[y/\Delta(x)]; \quad \Delta(x) = U_e\delta^*/u_\tau \quad (4.85)$$

The reader should keep in mind that Equation (4.85) only applies to a special class of boundary layers, i.e., boundary layers that are self preserving. Thus, we seek solutions where  $F(y/\Delta)$  is independent of  $x$ . As we will see, the model equations predict existence of such solutions under precisely the same conditions Clauser discovered experimentally.

We develop the leading terms in a perturbation solution for the turbulent boundary layer in the following subsections. There are two small parameters in our problem, the first being the reciprocal of the Reynolds number. This is consistent with the standard boundary-layer approximations. The second small parameter is  $u_\tau/U_e$ . Clauser's defect law suggests

this parameter since the velocity is expressed as a (presumably) small deviation from the freestream velocity that is proportional to  $u_\tau$ . The analysis will lead to a relation between these two parameters.

The analysis in this section, which is patterned after the work of Bush and Fendell (1972) and Fendell (1972), shows in Subsection 4.6.3 that the inner expansion is of the form quoted in Equation (4.84) and is valid in the **viscous sublayer** (see Figure 3.7). We also show in Subsection 4.6.2 that the outer expansion is identical in form to Equation (4.85) and holds in the **defect layer**. Formal matching of the sublayer and defect-layer solutions occurs in an overlap region that is often described as the **log layer**. In fact, the common part of the inner and outer expansions is precisely the law of the wall. Thus, although it is not formally a separate layer, establishing flow properties in the log layer permits independent analysis of the sublayer and defect layer. It also forms the basis of surface boundary conditions for many two-equation turbulence models. We discuss the log layer in this subsection.

Before performing any analysis, we anticipate that we will be solving a **singular perturbation problem**. We expect this, but not because of a reduction in order of the differential equations. Rather, we have no hope of satisfying the no-slip condition with our outer solution because of the assumed form in the defect layer, i.e., velocity being a small perturbation from the freestream value. Likewise, the sublayer solution, if it is consistent with measurements, predicts velocity increasing logarithmically with distance from the surface as  $y \rightarrow \infty$  so that we cannot satisfy the freestream boundary condition with our inner solution. This is the irregular behavior near boundaries alluded to in Appendix B where we define a singular perturbation problem.

We begin our analysis with the incompressible boundary layer equations. Conservation of mass and momentum are sufficient for establishing the form of the expansions, so that we have no need to introduce the model equations now. For two-dimensional flow, we have

$$\frac{\partial U}{\partial x} + \frac{\partial V}{\partial y} = 0 \quad (4.86)$$

$$U \frac{\partial U}{\partial x} + V \frac{\partial U}{\partial y} = -\frac{1}{\rho} \frac{dP}{dx} + \frac{\partial}{\partial y} \left[ (\nu + \nu_T) \frac{\partial U}{\partial y} \right] \quad (4.87)$$

The easiest way to arrive at the **log-layer** equations is to derive the **sublayer** equations and then to determine the limiting form of the sublayer equations for  $y^+ \rightarrow \infty$ . Consistent with the normal boundary-layer concept that variations in the streamwise ( $x$ ) direction are much less rapid than those in the normal ( $y$ ) direction, we scale  $x$  and  $y$  differently. Letting  $L$

denote a dimension characteristic of distances over which flow properties change in the  $x$  direction, we scale  $x$  and  $y$  according to

$$\xi = x/L \quad \text{and} \quad y^+ = u_\tau y/\nu \quad (4.88)$$

The appropriate expansion for the streamfunction and kinematic eddy viscosity are

$$\psi_{inner}(x, y) \sim \nu[f_0(\xi, y^+) + \phi_1 f_1(\xi, y^+) + o(\phi_1)] \quad (4.89)$$

$$\nu_{T_{inner}}(x, y) \sim \nu[N_0(\xi, y^+) + \phi_1 N_1(\xi, y^+) + o(\phi_1)] \quad (4.90)$$

where the asymptotic sequence  $\{1, \phi_1, \phi_2, \dots\}$  is to be determined. Consequently, the streamwise velocity becomes

$$U(x, y) \sim u_\tau[\hat{u}_0(\xi, y^+) + \phi_1 \hat{u}_1(\xi, y^+) + o(\phi_1)]; \quad \hat{u}_n \equiv \frac{\partial f_n}{\partial y^+} \quad (4.91)$$

Substituting into the momentum equation, we obtain

$$\frac{\partial}{\partial y^+} \left[ (1 + N_0) \frac{\partial \hat{u}_0}{\partial y^+} \right] + O(\phi_1) = \frac{1}{Re_{\delta^*}} \left[ \beta_T + O\left(\frac{\delta^*}{L}\right) \right] \quad (4.92)$$

where  $Re_{\delta^*}$  is Reynolds number based on displacement thickness, and the quantity  $\beta_T$  is the so-called **equilibrium parameter** [see Coles and Hirst (1969)] defined by

$$\beta_T \equiv \frac{\delta^*}{\tau_w} \frac{dP}{dx} \quad (4.93)$$

In general, we regard  $\beta_T$  as being of order one. In fact, when we analyze the defect layer this will be the key parameter quantifying the effect of pressure gradient on our solution. Additionally,  $Re_{\delta^*} \gg 1$  and  $\delta^* \ll L$ . Hence, we conclude that

$$\phi_1 = 1/Re_{\delta^*} \quad (4.94)$$

and

$$\frac{\partial}{\partial y^+} \left[ (1 + N_0) \frac{\partial \hat{u}_0}{\partial y^+} \right] = 0 \quad (4.95)$$

To enhance physical understanding of what we have just proven, it is worthwhile to return to dimensional variables. We have shown that, to leading order, the convective terms and the pressure gradient are small compared to the other terms in the sublayer so that the momentum equation simplifies to

$$\frac{\partial}{\partial y} \left[ (\nu + \nu_T) \frac{\partial U}{\partial y} \right] = 0 \quad (4.96)$$

Integrating once tells us that the sum of the molecular and Reynolds shear stress is constant in the sublayer, i.e.,

$$(\mu + \mu_T) \frac{\partial U}{\partial y} = \tau_w \quad (4.97)$$

Equation (4.96) or (4.97) is the equation for the leading order term in the inner expansion for a turbulent boundary layer. As we will demonstrate in greater detail in Subsection 4.6.3, we can satisfy the no-slip condition ( $U = 0$ ) at  $y = 0$  while the solution as  $y^+ \rightarrow \infty$  asymptotes to the law of the wall, i.e., velocity increasing logarithmically with distance from the surface. Another feature of the solution is that the eddy viscosity increases linearly with  $y^+$  as  $y^+ \rightarrow \infty$  so that the eddy viscosity becomes very large compared to the molecular viscosity. Consistent with this behavior, the molecular viscosity can be neglected in Equation (4.96) or (4.97) for the limiting case  $y^+ \rightarrow \infty$ . As noted above, we refer to the form of the differential equations in this limit as the **log-layer equations**. Thus, we conclude that in the log layer we can neglect convection, pressure gradient and molecular diffusion. The momentum equation thus simplifies to the following equation.

$$0 = \frac{\partial}{\partial y} \left[ \nu_T \frac{\partial U}{\partial y} \right] \quad (4.98)$$

To the same degree of approximation, in the log layer, the  $k$ - $\omega$  model equations simplify to:

**$k$ - $\omega$  Model:**

$$\left. \begin{aligned} 0 &= \nu_T \left( \frac{\partial U}{\partial y} \right)^2 - \beta^* \omega k + \sigma^* \frac{\partial}{\partial y} \left[ \nu_T \frac{\partial k}{\partial y} \right] \\ 0 &= \alpha \left( \frac{\partial U}{\partial y} \right)^2 - \beta \omega^2 + \sigma \frac{\partial}{\partial y} \left[ \nu_T \frac{\partial \omega}{\partial y} \right] \\ \nu_T &= k / \omega \end{aligned} \right\} \quad (4.99)$$

As can be shown by direct substitution, the solution to Equations (4.98) and (4.99) is

$$U = \frac{u_\tau}{\kappa} \ln y + \text{constant}, \quad k = \frac{u_\tau^2}{\sqrt{\beta^*}}, \quad \omega = \frac{u_\tau}{\sqrt{\beta^*} \kappa y} \quad (4.100)$$

where the implied value of the Kármán constant,  $\kappa$ , is given by

$$\kappa^2 = \sqrt{\beta^*} (\beta / \beta^* - \alpha) / \sigma \quad (4.101)$$



Note that the term proportional to  $\sigma^*$  disappears because  $\partial k / \partial y = 0$ . For the closure coefficient values specified by Wilcox [Equation (4.36)], we find  $\kappa = 0.408$ . We discussed the log-layer solution in Section 4.4 to illustrate how values for some of the closure coefficients have been selected. There are additional features of the solution worthy of mention. For example, the eddy viscosity varies linearly with distance from the surface and is given by

$$\nu_T = \kappa u_\tau y \quad (4.102)$$

This variation is equivalent to the mixing-length variation,  $\ell_{mix} = \kappa y$ . Also, the ratio of the Reynolds shear stress to the turbulence energy is constant, i.e.,

$$\tau_{xy} = \sqrt{\beta^*} \rho k \quad (4.103)$$

In a similar way, the  $k$ - $\epsilon$  model equations simplify to the following:

**$k$ - $\epsilon$  Model:**

$$\left. \begin{aligned} 0 &= \nu_T \left( \frac{\partial U}{\partial y} \right)^2 - \epsilon + \frac{\partial}{\partial y} \left[ \frac{\nu_T}{\sigma_k} \frac{\partial k}{\partial y} \right] \\ 0 &= C_{\epsilon 1} C_\mu k \left( \frac{\partial U}{\partial y} \right)^2 - C_{\epsilon 2} \frac{\epsilon^2}{k} + \frac{\partial}{\partial y} \left[ \frac{\nu_T}{\sigma_\epsilon} \frac{\partial \epsilon}{\partial y} \right] \\ \nu_T &= C_\mu k^2 / \epsilon \end{aligned} \right\} \quad (4.104)$$

The solution to Equations (4.98) and (4.104) is

$$U = \frac{u_\tau}{\kappa} \ln y + \text{constant}, \quad k = \frac{u_\tau^2}{\sqrt{C_\mu}}, \quad \epsilon = \frac{u_\tau^3}{\kappa y} \quad (4.105)$$

where we again find an implied value for the Kármán constant,  $\kappa$ , viz.,

$$\kappa^2 = \sqrt{C_\mu} (C_{\epsilon 2} - C_{\epsilon 1}) \sigma_\epsilon \quad (4.106)$$

Using the closure coefficient values for the Standard  $k$ - $\epsilon$  model [Equation (4.43)], the value of  $\kappa$  is 0.433.

Keep in mind that the turbulent boundary layer consists of the sublayer and the defect layer. The sublayer is a thin near-wall region, while the defect layer constitutes most of the boundary layer. In the spirit of matched asymptotic expansions, the log layer is the overlap region which, in practice, often appears to be much thicker than the sublayer (see Figure 3.7). Part of our reason for focusing on this region of the boundary layer is of historical origin. Aside from the  $k$ - $\omega$  model, most two-equation

models fail to agree satisfactorily with experiment in the viscous sublayer unless the coefficients are made empirical functions of an appropriate turbulence Reynolds number. Consequently, the log-layer solution has often been used as a replacement for the no-slip boundary condition. Most  $k$ - $\epsilon$  model solutions, for example, are generated by enforcing the asymptotic behavior given in Equation (4.105). We must postpone further discussion of surface boundary conditions pending detailed analysis of the sublayer. Analysis of the log layer can also prove useful in determining leading-order effects of complicating factors such as surface curvature, coordinate-system rotation, and compressibility. As our most immediate goal, we have, in effect, done our matching in advance. Thus, we are now in a position to analyze the defect layer and the sublayer independent of one another. We turn first to the defect layer.

### 4.6.2 The Defect Layer

In this subsection we use singular perturbation methods to analyze model-predicted structure of the classical defect layer, including effects of pressure gradient. Our analysis includes three turbulence models, viz.: the Wilcox  $k$ - $\omega$  model; the Standard  $k$ - $\epsilon$  model; and the Wilcox-Rubesin (1980)  $k$ - $\omega^2$  model. First, we generate the perturbation solution. Next, we compare solutions for the three models in the absence of pressure gradient. Then, effects of pressure gradient are studied for the three models. Finally, as promised in Section 4.4, we justify the values chosen for  $\sigma$  and  $\sigma^*$  in the  $k$ - $\omega$  model.

To study the defect layer, we continue to confine our analysis to incompressible flow so that we begin with Equations (4.86) and (4.87). The perturbation expansion for the defect layer proceeds in terms of the ratio of friction velocity to the boundary-layer-edge velocity,  $u_\tau/U_e$ , and the dimensionless coordinates,  $\xi$  and  $\eta$ , defined by

$$\xi = x/L \quad \text{and} \quad \eta = y/\Delta(x); \quad \Delta = U_e \delta^*/u_\tau \quad (4.107)$$

where  $\delta^*$  is displacement thickness and  $L$  is a characteristic streamwise length scale that is presumed to be very large compared to  $\delta^*$ . As in our approach to the log layer, we first establish the general form of the solution for the mean momentum equation. We expand the streamfunction and kinematic eddy viscosity as follows.

$$\psi_{outer}(x, y) \sim U_e \Delta \left[ \eta - \frac{u_\tau}{U_e} F_1(\xi, \eta) + o\left(\frac{u_\tau}{U_e}\right) \right] \quad (4.108)$$

$$\nu_{T_{outer}}(x, y) \sim U_e \delta^* [N_0(\xi, \eta) + o(1)] \quad (4.109)$$

Observe that, as is so often the case in perturbation analysis, we needn't continue the expansions beyond the first one or two terms to capture most of the important features of the solution. For the specified streamfunction, the velocity becomes:

$$U(x, y) \sim U_e \left[ 1 - \frac{u_\tau}{U_e} U_1(\xi, \eta) + o\left(\frac{u_\tau}{U_e}\right) \right]; \quad U_1 = \frac{\partial F_1}{\partial \eta} \quad (4.110)$$

Substituting Equations (4.107) - (4.110) into the mean conservation equations [Equations (4.86) and (4.87)] yields the transformed momentum equation, viz.,

$$2\sigma_T \xi \frac{\partial U_1}{\partial \xi} = (\alpha_T - 2\beta_T - 2\omega_T) \eta \frac{\partial U_1}{\partial \eta} + (\beta_T - 2\omega_T) U_1 + \frac{\partial}{\partial \eta} \left[ N_0 \frac{\partial U_1}{\partial \eta} \right] \quad (4.111)$$

where the parameters  $\alpha_T$ ,  $\beta_T$ ,  $\sigma_T$  and  $\omega_T$  are defined in terms of  $\delta^*$ ,  $u_\tau$  and skin friction,  $c_f = 2(u_\tau/U_e)^2$ , i.e.,

$$\alpha_T \equiv \frac{2}{c_f} \frac{d\delta^*}{dx}, \quad \beta_T \equiv \frac{\delta^*}{\tau_w} \frac{dP}{dx}, \quad \sigma_T \equiv \frac{\delta^*}{c_f x}, \quad \omega_T \equiv \frac{\delta^*}{c_f u_\tau} \frac{du_\tau}{dx} \quad (4.112)$$

Equation (4.111) must be solved subject to two boundary conditions. First, to satisfy the requirement that  $U \rightarrow U_e$  as  $y \rightarrow \infty$ , necessarily

$$U_1 \rightarrow 0 \quad \text{as} \quad \eta \rightarrow \infty \quad (4.113)$$

Also, we must asymptote to the log-layer solution as  $\eta \rightarrow 0$ . One way to insure this is to insist that

$$\frac{\partial U_1}{\partial \eta} \rightarrow -\frac{1}{\kappa \eta} \quad \text{as} \quad \eta \rightarrow 0 \quad (4.114)$$

At this point, we have not greatly simplified our problem. Equation (4.111), like the original momentum equation, is a partial differential equation. The only simplification thus far is that molecular viscosity is negligible relative to the eddy viscosity. However, even this is not necessarily advantageous since the no-slip velocity boundary condition has been replaced by singular behavior approaching the surface. And, of course, we are now working in a transformed coordinate system  $(\xi, \eta)$  rather than the familiar Cartesian coordinate system  $(x, y)$ . So why go to all this trouble? The answer is, we have only just begun.

Reexamination of the steps we have taken thus far should reveal a familiar tack; specifically, we appear to be developing a similarity solution. Indeed this is intentional, and inspection of Clauser's defect law [Equation (4.85)] shows that there has been method in our madness. Comparison

of Equation (4.85) with the assumed form of our perturbation expansion for  $U$  given in Equation (4.110) shows that  $U_1$  must be a function only of  $\eta$ . Thus, we now pose the question as to what conditions must be satisfied in order for a similarity solution to exist.

Clearly, the coefficients  $\alpha_T$ ,  $\beta_T$  and  $\omega_T$  must be independent of  $x$ , for then the coefficients of all terms on the right-hand side of Equation (4.111) will be independent of  $x$ . The coefficient  $\sigma_T$  is of no consequence since, if  $U_1$  is independent of  $x$ , the left-hand side of Equation (4.111) vanishes regardless of the value of  $\sigma_T$ . The coefficient  $\omega_T$  is also unimportant because, to leading order, it is zero. This becomes obvious if we now perform the formal matching of the defect-layer and sublayer solutions. As shown in the preceding section,

$$U_{inner}(\xi, y^+) \sim u_\tau \left[ \frac{1}{\kappa} \ell n y^+ + B \right] \quad \text{as} \quad y^+ \rightarrow \infty \quad (4.115)$$

Assuming that a similarity solution exists so that  $U_1$  depends only upon  $\eta$ , straightforward substitution into Equation (4.111) with a vanishing left-hand side shows that

$$U_1 \sim \frac{1}{\kappa} [-\ell n \eta + u_0 - u_1 \eta \ell n \eta + \dots] \quad \text{as} \quad \eta \rightarrow 0 \quad (4.116)$$

where the constants  $u_0, u_1, \dots$  depend upon the complete solution which, in turn, depends upon what turbulence model is used. We now do a formal matching of the inner and outer expansions noting that  $y^+ = \eta Re_{\delta^*}$  and  $U_{outer}(\xi, \eta) \sim [U_e - u_\tau U_1(\eta) + \dots]$ . To match through first order, we require the following:

$$\left[ \frac{1}{\kappa} \ell n y^+ + B \right] - \left[ \frac{U_e}{u_\tau} + \frac{1}{\kappa} \ell n \eta - \frac{u_0}{\kappa} \right] \rightarrow 0 \quad \text{as} \quad y^+ \rightarrow \infty, \quad \eta \rightarrow 0 \quad (4.117)$$

Hence, we conclude from matching that:

$$\frac{U_e}{u_\tau} = \left( B + \frac{u_0}{\kappa} \right) + \frac{1}{\kappa} \ell n Re_{\delta^*} \quad (4.118)$$

This is a useful result that enables us to compute the skin friction from our defect-layer solution, a point we will return to later. For our present purpose, Equation (4.118) provides us with an estimate of the orders of magnitude of  $u_\tau$  and  $c_f$ , i.e.,

$$u_\tau \sim \frac{U_e}{\ell n Re_{\delta^*}} \quad \text{and} \quad c_f \sim \frac{1}{\ell n^2 Re_{\delta^*}} \quad \text{as} \quad Re_{\delta^*} \rightarrow \infty \quad (4.119)$$

As a consequence, estimating that  $d\delta^*/dx \sim \delta^*/x$ , we expect to have

$$\frac{du_\tau}{dx} \sim \frac{U_e}{Re_{\delta^*} \ell n^2 Re_{\delta^*}} \frac{\delta^*}{x} \sim \frac{U_e}{x \ell n^2 Re_{\delta^*}} \quad (4.120)$$

Substituting Equations (4.119) and (4.120) into the definition of  $\omega_T$  [see Equation (4.112)], we arrive at the important result

$$\omega_T \sim \frac{\delta^*}{x} \ell n Re_{\delta^*} \sim o(1) \quad \text{as} \quad x \rightarrow \infty \quad (4.121)$$

The validity of the final estimate follows from the fact that  $\ell n Re_{\delta^*}$  is transcendently small compared to any power of  $Re_{\delta^*}$ , and  $\delta^* \ll x$  as  $x \rightarrow \infty$ .

Thus, we can ignore the parameter  $\omega_T$  in solving for  $U_1$ , although it will appear in the equation at some higher order. This leaves us with the reduced requirement for existence of a similarity solution that only  $\alpha_T$  and  $\beta_T$  are independent of  $x$ . However, we can also show that  $\alpha_T$  and  $\beta_T$  are uniquely related to leading order. To see this, we examine the classical momentum-integral equation that follows from integrating the mean-momentum equation across the boundary layer [c.f., Schlichting (1979)], viz.,

$$\frac{c_f}{2} = \frac{d\theta}{dx} - (2 + H) \frac{\theta}{\rho U_e^2} \frac{dP}{dx} \quad (4.122)$$

where  $\theta$  is momentum thickness and  $H = \delta^*/\theta$  is the shape factor. In terms of  $\alpha_T$  and  $\beta_T$ , the momentum-integral equation can be rewritten as

$$\alpha_T \frac{d\theta}{dx} = \left[ 1 + \frac{(2 + H)}{H} \beta_T \right] \frac{d\delta^*}{dx} \quad (4.123)$$

If we evaluate the displacement and momentum thickness using our perturbation expansion for the velocity profile we find two important facts. First, evaluating the displacement thickness integral yields an integral constraint on our solution for  $U_1$ ,  $U_2$ , etc. Second, we find to leading order that  $\delta^*$  and  $\theta$  are equal, i.e., the shape factor approaches 1 as  $Re_{\delta^*} \rightarrow \infty$  and/or  $u_\tau/U_e \rightarrow 0$ . The proof of these facts is straightforward and thus left for the Problems section; the results are:

$$\int_0^\infty U_1(\eta) d\eta = 1 \quad (4.124)$$

$$\int_0^\infty U_n(\eta) d\eta = 0, \quad n \geq 2 \quad (4.125)$$

and

$$H \sim 1 + O\left(\frac{u_\tau}{U_e}\right) \quad \text{as} \quad Re_{\delta^*} \rightarrow \infty, \quad \frac{u_\tau}{U_e} \rightarrow 0 \quad (4.126)$$

Note that the perturbation solution for  $U_1(\eta)$  provides sufficient information to determine the  $O(u_\tau/U_e)$  term (see Problems section). Hence, Equation (4.123) yields the following relationship between  $\alpha_T$  and  $\beta_T$ .

$$\alpha_T = 1 + 3\beta_T \quad (4.127)$$

Thus, the requirement for existence of a similarity solution to Equation (4.111) for large Reynolds number is simply that the **equilibrium parameter**,  $\beta_T$ , be constant. This is a very satisfactory state of affairs because it is consistent with experimental observations at finite (laboratory-scale) Reynolds numbers. That is, Clauser found that, above the viscous sublayer, turbulent boundary layers assume a self-similar form when the equilibrium parameter is constant. The problem we must solve to determine  $U_1(\eta)$  is:

$$\frac{d}{d\eta} \left[ N_0 \frac{dU_1}{d\eta} \right] + (1 + \beta_T) \eta \frac{dU_1}{d\eta} + \beta_T U_1 = 0 \quad (4.128)$$

$$\frac{dU_1}{d\eta} \rightarrow -\frac{1}{\kappa\eta} \quad \text{as} \quad \eta \rightarrow 0 \quad \text{and} \quad U_1(\eta) \rightarrow 0 \quad \text{as} \quad \eta \rightarrow \infty \quad (4.129)$$

The integral constraint, Equation (4.124), must also be enforced. The dimensionless eddy viscosity,  $N_0(\eta)$ , depends upon the turbulence model selected. For our purposes, we will consider three different turbulence models, viz.: the Wilcox  $k$ - $\omega$  model [Equations (4.33)-(4.36)]; the Standard  $k$ - $\epsilon$  model [Equations (4.40)-(4.43)]; and the Wilcox-Rubesin (1980)  $k$ - $\omega^2$  model whose equations are as follows.

### Eddy Viscosity

$$\mu_T = \rho k / \omega \quad (4.130)$$

### Turbulence Kinetic Energy

$$\rho \frac{\partial k}{\partial t} + \rho U_j \frac{\partial k}{\partial x_j} = \tau_{ij} \frac{\partial U_i}{\partial x_j} - \beta^* \rho k \omega + \frac{\partial}{\partial x_j} \left[ (\mu + \sigma^* \mu_T) \frac{\partial k}{\partial x_j} \right] \quad (4.131)$$

### Specific Dissipation Rate

$$\rho \frac{\partial \omega^2}{\partial t} + \rho U_j \frac{\partial \omega^2}{\partial x_j} = \alpha \frac{\omega^2}{k} \tau_{ij} \frac{\partial U_i}{\partial x_j} - \left[ \beta + 2\sigma \frac{\partial \ell}{\partial x_j} \frac{\partial \ell}{\partial x_j} \right] \rho \omega^3 \quad (4.132)$$

$$+ \frac{\partial}{\partial x_j} \left[ (\mu + \sigma \mu_T) \frac{\partial \omega^2}{\partial x_j} \right] \quad (4.133)$$

### Closure Coefficients

$$\alpha = 10/9, \quad \beta = 3/20, \quad \beta^* = 9/100, \quad \sigma = 1/2, \quad \sigma^* = 1/2 \quad (4.134)$$

**Auxiliary Relations**

$$\epsilon = \beta^* \omega k \quad \text{and} \quad \ell = k^{1/2} / \omega \quad (4.135)$$

Making standard boundary-layer approximations for the model equations, we seek a perturbation solution for  $k$ ,  $\omega$  and  $\epsilon$  of the following form.

$$\left. \begin{aligned} k &\sim \frac{u_\tau^2}{\sqrt{\beta^*}} [K_0(\eta) + o(1)] \\ \omega &\sim \frac{u_\tau}{\sqrt{\beta^*} \Delta} [W_0(\eta) + o(1)] \\ \epsilon &\sim \frac{u_\tau^3}{\Delta} [E_0(\eta) + o(1)] \end{aligned} \right\} \quad (4.136)$$

Note that for the  $k$ - $\epsilon$  model,  $\beta^* = C_\mu$ . For all three turbulence models, the transformed equation for  $k$  can be written as

**All Models:**

$$\sigma^* \frac{d}{d\eta} \left[ N_0 \frac{dK_0}{d\eta} \right] + (1 + \beta_T) \eta \frac{dK_0}{d\eta} + \sqrt{\beta^*} \left[ N_0 \left( \frac{dU_1}{d\eta} \right)^2 - E_0 \right] = 0 \quad (4.137)$$

where, for the  $k$ - $\epsilon$  model, we note that  $\sigma^* = 1/\sigma_k$ . The second equation and auxiliary equations are specific to each model. The transformed equations are:

 **$k$ - $\omega$  Model:**

$$\left. \begin{aligned} &\sigma \frac{d}{d\eta} \left[ N_0 \frac{dW_0}{d\eta} \right] + (1 + \beta_T) \eta \frac{dW_0}{d\eta} + (1 + 2\beta_T) W_0 \\ &+ \sqrt{\beta^*} \left[ \alpha \left( \frac{dU_1}{d\eta} \right)^2 - \frac{\beta}{\beta^*} W_0^2 \right] = 0 \\ &N_0 = K_0/W_0 \quad \text{and} \quad E_0 = K_0 W_0 \end{aligned} \right\} \quad (4.138)$$

 **$k$ - $\omega^2$  Model:**

$$\left. \begin{aligned} &\sigma \frac{d}{d\eta} \left[ N_0 \frac{dW_0^2}{d\eta} \right] + (1 + \beta_T) \eta \frac{dW_0^2}{d\eta} + 2(1 + 2\beta_T) W_0^2 \\ &+ \sqrt{\beta^*} \left[ \alpha W_0 \left( \frac{dU_1}{d\eta} \right)^2 - \left\{ \frac{\beta}{\beta^*} + 2\sigma \left( \frac{dL_0}{d\eta} \right)^2 \right\} W_0^3 \right] = 0 \\ &N_0 = K_0/W_0, \quad E_0 = K_0 W_0, \quad \text{and} \quad L_0 = K_0^{1/2} / W_0 \end{aligned} \right\} \quad (4.139)$$

**$k$ - $\epsilon$  Model:**

$$\left. \begin{aligned} &\sigma_\epsilon^{-1} \frac{d}{d\eta} \left[ N_0 \frac{dE_0}{d\eta} \right] + (1 + \beta_T) \eta \frac{dE_0}{d\eta} + (1 + 2\beta_T) E_0 \\ &+ \sqrt{C_\mu} \left[ C_{\epsilon 1} K_0 \left( \frac{dU_1}{d\eta} \right)^2 - C_{\epsilon 2} \frac{E_0^2}{K_0} \right] = 0 \\ &N_0 = K_0^2 / E_0 \quad \text{and} \quad E_0 = K_0 W_0 \end{aligned} \right\} \quad (4.140)$$

We must specify boundary conditions on  $K_0$ ,  $W_0$  and  $E_0$  both in the freestream and approaching the surface. For non-turbulent flow in the freestream, we require that the turbulence parameters all vanish as  $\eta \rightarrow \infty$ . However, we also stipulate that these quantities approach zero in such a way that  $N_0$  vanishes. Thus, the freestream boundary conditions are:

$$K_0(\eta) \rightarrow 0, \quad W_0(\eta) \rightarrow 0, \quad E_0(\eta) \rightarrow 0, \quad U_1(\eta) \rightarrow 0 \quad \text{as } \eta \rightarrow \infty \quad (4.141)$$

As it turns out, we can also specify  $W_0 = \sqrt{\beta^*}(1 + 2\beta_T)/\beta$  for the  $k$ - $\omega$  model and  $W_0 = 2\sqrt{\beta^*}(1 + 2\beta_T)/\beta$  for the  $k$ - $\omega^2$  model. Regardless of the choice of  $W_0$ , neither model displays the excessive sensitivity to freestream values observed for the  $k$ - $\omega$  model in free shear flows.

Approaching the surface, we must formally match to the law of the wall. Matching is a bit different for each model but is nevertheless straightforward; details of the algebra will thus be omitted in the interest of brevity. The limiting forms used for  $\eta \rightarrow 0$  follow.

$$\left. \begin{aligned} K_0(\eta) &\sim [1 + k_1 \eta \ell n \eta + \dots] \\ E_0(\eta) &\sim \frac{1}{\kappa \eta} [1 + e_1 \eta \ell n \eta + \dots] \\ W_0(\eta) &\sim \frac{1}{\kappa \eta} [1 + w_1 \eta \ell n \eta + \dots] \\ U_1(\eta) &\sim \frac{1}{\kappa} [-\ell n \eta + u_0 - u_1 \eta \ell n \eta + \dots] \end{aligned} \right\} \quad (4.142)$$

The coefficients  $k_1$ ,  $u_1$ ,  $w_1$  and  $e_1$  are as follows, where for notational consistency, we define

$$\alpha^* \equiv \sqrt{\beta^*} = \sqrt{C_\mu} \quad (4.143)$$

Also, we again write some of the results in terms of  $\sigma^*$  with the understanding that  $\sigma^* = 1/\sigma_k$  for the  $k$ - $\epsilon$  model.



**All Models:**

$$k_1 = \frac{\beta_T/\kappa}{\sigma^*\kappa^2/(2\alpha^*) - 1} \quad (4.144)$$

**$k$ - $\omega$  Model:**

$$\left. \begin{aligned} u_1 &= \frac{[\beta/(\alpha\beta^*)][\sigma^*\kappa^2/(2\alpha^*)]}{1 - \beta/(\alpha\beta^*)} k_1 \\ w_1 &= \frac{\sigma^*\kappa^2/(2\alpha^*)}{1 - \beta/(\alpha\beta^*)} k_1 \end{aligned} \right\} \quad (4.145)$$

**$k$ - $\omega^2$  Model:**

$$\left. \begin{aligned} u_1 &= \frac{[\beta/\alpha^*][\sigma^*\kappa^2/(2\alpha^*)] + \sigma\kappa^2}{2\alpha\alpha^*[1 - \beta/(\alpha\beta^*)] + 2\sigma\kappa^2} k_1 \\ w_1 &= \frac{\alpha\alpha^*[\sigma^*\kappa^2/(2\alpha^*)] + \sigma\kappa^2}{2\alpha\alpha^*[1 - \beta/(\alpha\beta^*)] + 2\sigma\kappa^2} k_1 \end{aligned} \right\} \quad (4.146)$$

**$k$ - $\epsilon$  Model:**

$$\left. \begin{aligned} u_1 &= \frac{(1 + \sigma^*\kappa^2/\alpha^*)C_{\epsilon 2} - C_{\epsilon 1}}{2(C_{\epsilon 1} - C_{\epsilon 2})} k_1 \\ e_1 &= \frac{(1 + \sigma^*\kappa^2/\alpha^*)C_{\epsilon 1} - C_{\epsilon 2}}{2(C_{\epsilon 1} - C_{\epsilon 2})} k_1 \end{aligned} \right\} \quad (4.147)$$

Additionally, the coefficient  $u_0$  is determined from the integral constraint for mass conservation, which is guaranteed by the integral constraint in Equation (4.124). Table 4.3 summarizes the equations for the leading-order terms in the defect-layer solution.

Before proceeding to discussion of the defect-layer similarity solution, there are two quantities of interest that follow from the leading order solution, viz., the skin friction,  $c_f$ , and Coles' **wake-strength parameter**,  $\tilde{\pi}$ . Recall that from matching defect-layer and sublayer velocity profiles, we deduced Equation (4.118). Noting that  $c_f = 2(u_\tau/U_e)^2$ , we conclude that

$$\sqrt{\frac{2}{c_f}} = (B + \frac{u_0}{\kappa}) + \frac{1}{\kappa} \ln Re_{\delta^*} \quad (4.148)$$

The **composite law of the wall, law of the wake** profile according to Coles' meticulous correlation of experimental data [see Coles and Hirst (1969)] is given by

$$U^+ = \frac{1}{\kappa} \ln y^+ + B + \frac{2\tilde{\pi}}{\kappa} \sin^2 \left( \frac{\pi y}{2\delta} \right) \quad (4.149)$$

Table 4.3: Summary of the Defect-Layer Equations

Mass (Integral Constraint)	Equation (4.124)
Momentum	Equation (4.128)
Turbulence Kinetic Energy	Equation (4.137)
Specific Dissipation ( $k$ - $\omega$ Model)	Equation (4.138)
Specific Dissipation ( $k$ - $\omega^2$ Model)	Equation (4.139)
Dissipation ( $k$ - $\epsilon$ Model)	Equation (4.140)
Boundary Conditions for $\eta \rightarrow \infty$	Equation (4.141)
Boundary Conditions for $\eta \rightarrow 0$	Equation (4.142)

The  $\sin^2$  function is purely a curve fit: several other functions have been suggested, including forms that yield  $\partial U/\partial y = 0$  at  $y = \delta$  [which is not the case for Equation (4.149)]. Defect-layer solutions include sharp turbulent-nonturbulent interfaces so that the edge of the defect-layer lies at a finite value  $\eta = \eta_e$ . Thus, combining Equations (4.118) and (4.149) leads to the following expression for the wake-strength parameter.

$$\tilde{\pi} = \frac{1}{2}(u_0 - \ell n \eta_e) \quad (4.150)$$

Figure 4.9(a) compares the defect-layer solution for the three models with corresponding experimental data of Wiegardt as tabulated by Coles and Hirst (1969). The experimental data presented are those at the highest Reynolds number for which data are reported. This is consistent with the defect-layer solution that is formally valid for very large Reynolds number. As shown, all three models predict velocity profiles that differ from measured values by no more than about three percent of scale. Interestingly, the  $k$ - $\omega$  model shows the smallest differences from the Wiegardt data. Corresponding computed and measured skin friction values are summarized in the insert on Figure 4.9(a); the largest difference is less than three percent. Thus, based on analysis of the constant-pressure defect layer, there is little difference amongst the three models.

Turning now to the effect of pressure gradient, we consider defect-layer solutions for the equilibrium parameter,  $\beta_T$ , ranging from -0.5 to +9.0, where positive  $\beta_T$  corresponds to an adverse pressure gradient. The choice of this range of  $\beta_T$  has been dictated by the requirement of the perturbation solution that  $\beta_T$  be constant. This appears to be the maximum range over which experimental data have been taken with  $\beta_T$  more-or-less constant.

Figure 4.9(b) compares computed velocity profiles with experimental data of Clauser [see Coles and Hirst (1969)] for  $\beta_T = 8.7$ . As with the

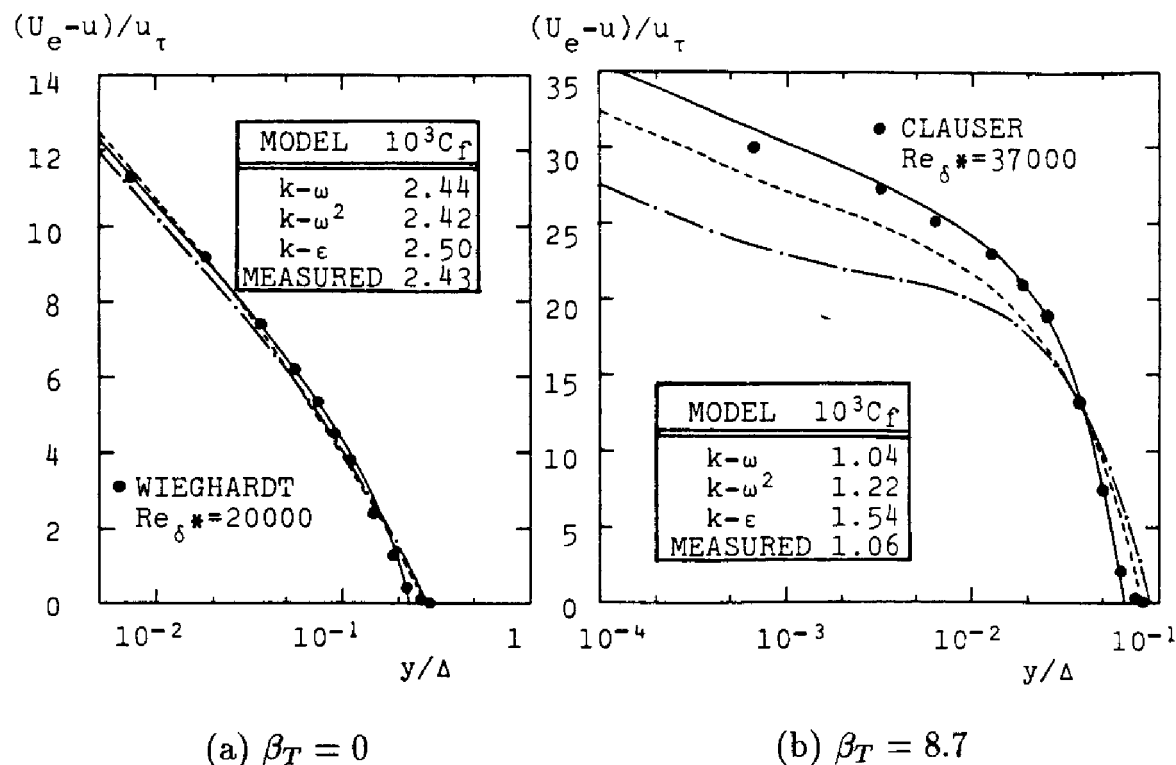


Figure 4.9: Computed and measured defect-layer velocity profiles; —  $k-\omega$  model; ---  $k-\omega^2$  model; - · -  $k-\epsilon$  model. [From Wilcox (1988a) — Copyright © AIAA 1988 — Used with permission.]

constant pressure case, computed and measured skin friction are included in the insert. As shown, the  $k-\omega$  model yields a velocity profile and skin friction closest to measurements while the  $k-\epsilon$  model shows the greatest differences. The  $k-\omega^2$  profile and skin friction lie about midway between those of the other two models.

Figure 4.10 compares computed wake strength,  $\tilde{\pi}$ , with values inferred by Coles and Hirst (1969) from experimental data. Inspection of Figure 4.10 reveals provocative differences amongst the three models. Most notably, the  $k-\omega$  model yields wake strengths closest to values inferred from data over the complete range considered. Consistent with the velocity profile discrepancies shown in Figure 4.9(b), the  $k-\epsilon$  model exhibits the largest differences, with predicted wake strength 50%-100% lower than inferred values when  $\beta_T$  is as small as two!

The explanation of the  $k-\epsilon$  model's poor performance for adverse pressure gradient can be developed from inspection of the asymptotic behavior

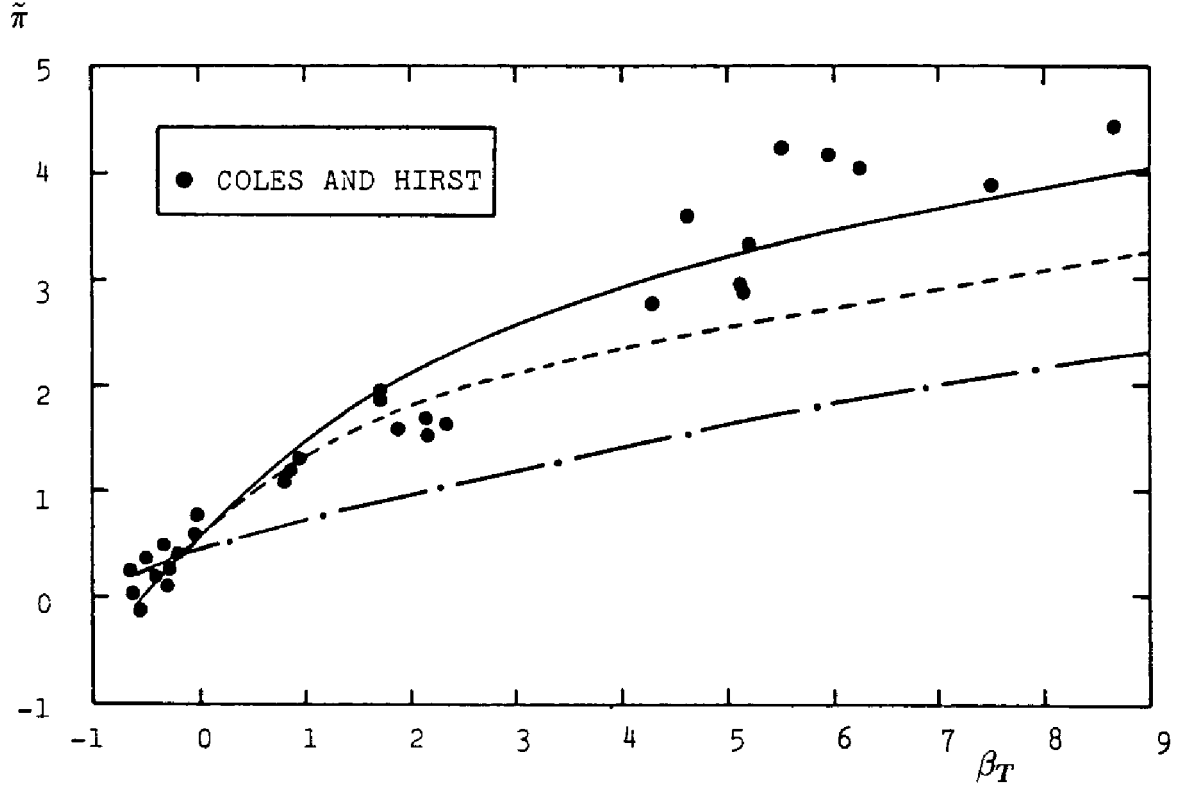


Figure 4.10: Computed and measured wake-strength parameter; —  $k-\omega$  model; ---  $k-\omega^2$  model; - · -  $k-\epsilon$  model. [From Wilcox (1988a) — Copyright © AIAA 1988 — Used with permission.]

of solutions as  $\eta \rightarrow 0$ . For the models analyzed, the velocity behaves as

$$\frac{U_e - U}{u_\tau} \sim -\frac{1}{\kappa} \ell n \eta + A - \beta_T C \eta \ell n \eta + \dots \quad \text{as } \eta \rightarrow 0 \quad (4.151)$$

where Table 4.4 summarizes the constants  $A$  and  $C$ . Note that, while the coefficient  $A = u_0/\kappa$  is determined as part of the solution (from the integral constraint that mass be conserved), the coefficient  $C = u_1/(\beta_T \kappa)$  follows directly from the limiting form of the solution as  $\eta \rightarrow 0$ . As seen from Table 4.4,  $C$  is largest for the  $k-\epsilon$  model and is smallest for the  $k-\omega$  model. The presence of the  $\eta \ell n \eta$  term gives rise to an inflection in the velocity profile as  $\eta \rightarrow 0$  that is most pronounced for the  $k-\epsilon$  model. In terms of turbulence properties, the turbulence length scale,  $\ell$ , behaves according to

$$\ell \sim (\beta^*)^{1/4} \kappa \eta [1 + \beta_T L \eta \ell n \eta + \dots] \quad \text{as } \eta \rightarrow 0 \quad (4.152)$$

Table 4.4 also includes the coefficient  $L$  for each model. Again, we see that the contribution of the  $\eta \ell n \eta$  term is largest for the  $k-\epsilon$  model and smallest for the  $k-\omega$  model. Thus, in the presence of adverse pressure gradient,

Table 4.4: Coefficients  $A$ ,  $C$  and  $L$  for  $\beta_T = 9$ 

Model	$A$	$C$	$L$
$k$ - $\omega$	13.1	2.90	-2.20
$k$ - $\omega^2$	9.8	6.39	-3.62
$k$ - $\epsilon$	5.4	13.57	-6.50

the  $k$ - $\epsilon$  model's turbulence length scale tends to be too large in the near-wall region. Note, of course, that this shortcoming is not evident in the constant-pressure case, which has  $\beta_T = 0$ .

The manner in which the  $k$ - $\omega$  model achieves smaller values of  $\ell$  than does the  $k$ - $\epsilon$  model can be seen by changing dependent variables. That is, starting with the  $k$ - $\omega$  formulation and defining  $\epsilon = \beta^* \omega k$ , we can deduce the following incompressible equation for  $\epsilon$  implied by the  $k$ - $\omega$  model.

$$\begin{aligned}
 U \frac{\partial \epsilon}{\partial x} + V \frac{\partial \epsilon}{\partial y} = (1 + \alpha) k \left( \frac{\partial U}{\partial y} \right)^2 & - (1 + \beta/\beta^*) \frac{\epsilon^2}{k} + \frac{\partial}{\partial y} \left[ \sigma \nu_T \frac{\partial \epsilon}{\partial y} \right] \\
 & - 2\sigma \nu_T \frac{\partial k}{\partial y} \frac{\partial(\epsilon/k)}{\partial y} \quad (4.153)
 \end{aligned}$$

All terms except the last on the right-hand side of Equation (4.153) are identical in form to those of the Standard  $k$ - $\epsilon$  model [see Equation (4.42)]. This so-called **cross-diffusion term** is negligibly small as  $\eta \rightarrow 0$  for constant-pressure boundary layers because  $k \rightarrow \text{constant}$  as  $\eta \rightarrow 0$ . However,  $\partial k / \partial y$  is nonvanishing when  $\beta_T \neq 0$  and  $\partial(\epsilon/k) / \partial y$  generally is quite large as  $\eta \rightarrow 0$ . The net effect of this additional term is to suppress the rate of increase of  $\ell$  close to the surface.

Unlike the three closure coefficients discussed in Section 4.4, simple arguments have not been found to establish the values of  $\sigma$  and  $\sigma^*$  for the  $k$ - $\omega$  model. In Subsection 4.6.3, we will find that using  $\sigma = 1/2$  yields an excellent solution in the viscous sublayer, almost independent of the value of  $\sigma^*$ . Equation (4.145) shows that the coefficient  $C$  is proportional to  $\sigma^*$ , so that smaller values of  $\sigma^*$  should improve the model's predictions for boundary layers with variable pressure. The computed variation of  $\tilde{\pi}$  with  $\beta_T$  (Figure 4.10) closely matches experimental results when  $\sigma^* = 1/2$ , and this is the value that has been chosen for the  $k$ - $\omega$  model.

### 4.6.3 The Viscous Sublayer

In order to facilitate integration of the model equations through the viscous sublayer, we must, at a minimum, have molecular diffusion terms in the equations of motion. Potentially, we might also have to allow the various closure coefficients to be functions of viscosity (i.e., turbulence Reynolds number) as well. This should come as no surprise since even the mixing-length model requires the Van Driest damping factor and one-equation models need similar viscous damping [Wolfshtein (1967)]. In this section, we use perturbation methods to analyze viscous sublayer structure predicted by several two-equation models. As we will see, with the exception of some  $k$ - $\omega$  models, virtually all two-equation models require Reynolds number dependent corrections in order to yield a realistic sublayer solution.

We have already derived the sublayer solution in Subsection 4.6.1 when we discussed the **log layer**. Recapping the highlights of the expansion procedure, the velocity is given by an expansion of the form

$$U(x, y) \sim u_\tau [\hat{u}_0(y^+) + Re_{\delta^*}^{-1} \hat{u}_1(\xi, y^+) + o(Re_{\delta^*}^{-1})] \quad (4.154)$$

To leading order, the convective terms and pressure gradient are negligible. Thus, for example, the leading order equations for the  $k$ - $\omega$  model expressed in terms of dimensional quantities are given by

$$\left. \begin{aligned} (\nu + \nu_T) \frac{dU}{dy} &= u_\tau^2 \\ \frac{d}{dy} \left[ (\nu + \sigma^* \nu_T) \frac{dk}{dy} \right] + \nu_T \left( \frac{dU}{dy} \right)^2 - \beta^* \omega k &= 0 \\ \frac{d}{dy} \left[ (\nu + \sigma \nu_T) \frac{d\omega}{dy} \right] + \alpha \left( \frac{dU}{dy} \right)^2 - \beta \omega^2 &= 0 \\ \nu_T &= \frac{k}{\omega} \end{aligned} \right\} \quad (4.155)$$

Because the Reynolds shear stress is constant, the viscous sublayer is often referred to as the **constant-stress layer**. Five boundary conditions are needed for this fifth-order system, two of which follow from matching to the law of the wall as  $y^+ \rightarrow \infty$ , viz.,

$$k \rightarrow \frac{u_\tau^2}{\sqrt{\beta^*}} \quad \text{and} \quad \omega \rightarrow \frac{u_\tau}{\sqrt{\beta^* \kappa y}} \quad \text{as} \quad y^+ \rightarrow \infty \quad (4.156)$$

where  $y^+ \equiv u_\tau y / \nu$ . Two more boundary conditions follow from **no slip** at

the surface, which implies that  $U$  and  $k$  vanish at  $y = 0$ . Thus,

$$U = k = 0 \quad \text{at} \quad y^+ = 0 \quad (4.157)$$

The final condition follows from examination of the differential equations for  $k$  and  $\omega$  approaching the surface. The  $k$ - $\omega$  model possesses two kinds of solutions. The first type of solution has a finite value of  $\omega$  at the surface. This fact was first observed by Saffman (1970) who speculated that the constant in the law of the wall,  $B$ , would vary with the surface value of  $\omega$ . This feature is unique to  $k$ - $\omega$  and  $k$ - $\omega^2$  models and will be explored in detail in Section 4.7. The second type of solution is common to all two-equation models and this is the one we will focus on now. Examination of the differential equations approaching  $y = 0$  shows that for all two-equation models,

$$k \sim y^n \quad \text{and} \quad \beta^* y^2 \omega / \nu \sim \text{constant} \quad \text{as} \quad y \rightarrow 0 \quad (4.158)$$

Table 4.5 lists the values of  $n$  and the constant for several models. As shown, none of the models predicts the exact theoretical value of 2 for both  $n$  and  $\beta^* y^2 \omega / \nu$ . This can only be accomplished with additional modification of the model equations.

Table 4.5: Sublayer Behavior Without Viscous Damping

Model	Type	$B$	$n$	$\beta^* y^2 \omega / \nu$
Wilcox-Rubesin (1980)	$k$ - $\omega^2$	7.1	4.00	12.00
Saffman (1970)	$k$ - $\omega^2$	6.0	3.7-4.0	12.00
Launder-Spalding (1972)	$k$ - $\omega^2$	5.7	3.79	12.00
Wilcox (1988a)	$k$ - $\omega$	5.1	3.23	7.20
Kolmogorov (1942)	$k$ - $\omega$	3.1	3.62	7.20
Launder-Sharma (1974)	$k$ - $\epsilon$	-2.2	1.39	0.53
Speziale (1990)	$k$ - $\tau$	-2.2	1.39	0.53
Exact/Measured		5.0	2.00	2.00

The exact values follow from expanding the fluctuating velocity in Taylor series near a solid boundary. That is, we know that the fluctuating velocity satisfies the no-slip boundary condition and also satisfies conservation of mass (see Section 2.3). Consequently, the three velocity components must behave as follows.

$$\left. \begin{aligned} u' &\sim A(x, z, t)y + O(y^2) \\ v' &\sim B(x, z, t)y^2 + O(y^3) \\ w' &\sim C(x, z, t)y + O(y^2) \end{aligned} \right\} \quad \text{as} \quad y \rightarrow 0 \quad (4.159)$$

Hence, the turbulence energy and dissipation are given by

$$k \sim \frac{1}{2} (\overline{A^2 + C^2}) y^2 + O(y^3) \quad \text{and} \quad \epsilon \sim \nu (\overline{A^2 + C^2}) + O(y) \quad (4.160)$$

Assuming that  $\epsilon = \beta^* \omega k$ , Equation (4.160) tells us that

$$k \sim y^2 \quad \text{and} \quad \beta^* y^2 \omega / \nu \sim 2 \quad \text{as} \quad y \rightarrow 0 \quad (4.161)$$

Hence, using the asymptotic behavior of  $\omega$  for  $y \rightarrow 0$  appropriate to each model as the fifth boundary condition, we can solve the sublayer equations (see Subsection 7.2.1 for an explanation of how to handle the singular behavior of  $\omega$  numerically). One of the most interesting features of the solution is the constant in the law of the wall,  $B$ , that is evaluated from the following limit.

$$B = \lim_{y^+ \rightarrow \infty} \left[ U^+ - \frac{1}{\kappa} \ln y^+ \right] \quad (4.162)$$

Table 4.5 also lists the computed value of  $B$  for the various two-equation models. As shown, the Spalding  $k-\omega^2$  and Wilcox  $k-\omega$  models are sufficiently close to the standard value of 5.0 to be used with no additional viscous modifications. The Standard  $k-\epsilon$  model and the Speziale et al.  $k-\tau$  model are farthest from the generally accepted value for  $B$ .

Figure 4.11(a) compares  $k-\omega$  model velocity profiles with corresponding measurements of Laufer (1952), Anderson, Kays and Moffat (1972), and Wieghardt [as tabulated by Coles and Hirst (1969)]. As shown, computed velocities generally fall within experimental data scatter. In Figure 4.11(b), we compare computed turbulence production and dissipation terms with Laufer's (1952) near-wall pipe-flow measurements. Again, predictions fall well within experimental error bounds.

This concludes our perturbation analysis of the turbulent boundary layer. As we have seen, using perturbation analysis, we have been able to dissect model-predicted structure of the defect layer, log layer and sublayer, never having to solve more than an ordinary differential equation. This is a great advantage in testing a turbulence model in light of the ease and accuracy with which ordinary differential equations can be solved. The equations are not trivial to solve however since we are dealing with two-point boundary-value problems, and the resulting systems of equations are of sixth order for the defect layer and fifth order for the sublayer. However, this is far easier to handle than the partial differential equations we started with, and parametric studies (e.g., varying the equilibrium parameter,  $\beta_T$ ) are much simpler in the context of the perturbation solution. As a final comment, results obtained in this section should make the following statement obvious.



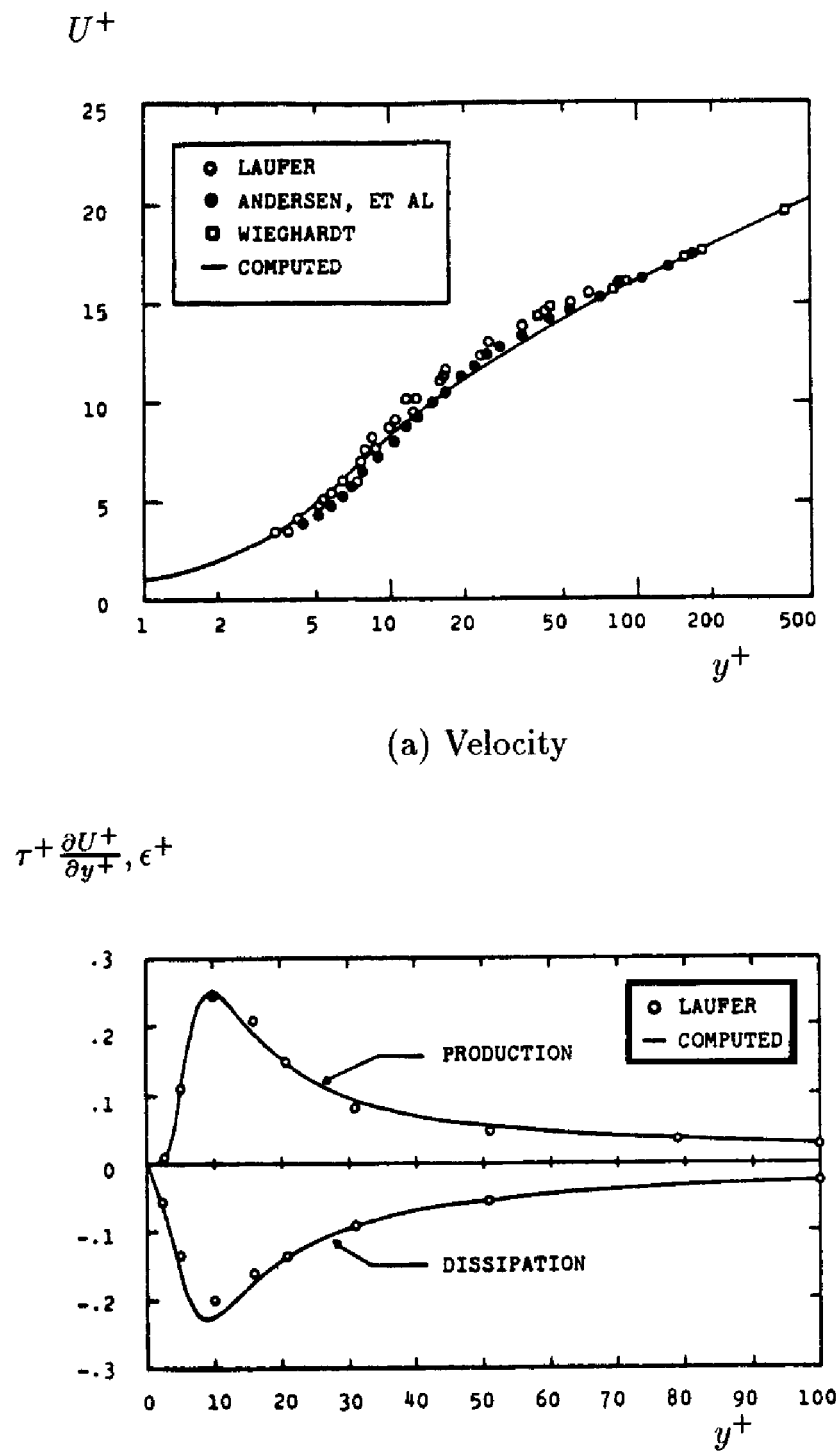


Figure 4.11: Computed and measured sublayer properties;  $k-\omega$  model. [From Wilcox (1988a) — Copyright © AIAA 1988 — Used with permission.]

Given the demonstrated power and utility of perturbation analysis in analyzing the turbulent boundary layer, this type of analysis can, and should, be used in developing all turbulence models.

## 4.7 Surface Boundary Conditions

In order to apply a two-equation turbulence model to wall-bounded flows, we must specify boundary conditions appropriate to a solid boundary for the velocity and the two turbulence parameters. As shown in the preceding section, most two-equation models fail to predict a satisfactory value of the constant  $B$  in the law of the wall (see Table 4.5). Consequently, for most two-equation turbulence models, applying the no-slip boundary condition and integrating through the viscous sublayer yields unsatisfactory results. One approach we can take to remove this deficiency is to introduce viscous damping factors analogous to the Van Driest correction for the mixing-length model. Since introduction of damping factors accomplishes much more than allowing integration through the sublayer, we defer detailed discussion of such modifications to Section 4.9. An alternative approach is to circumvent the inability to predict a satisfactory log-layer solution by simply matching to the law of the wall using a suitable value for  $B$ . This is what we did in analyzing the defect layer, and the procedure is equally valid for general wall-bounded flows.

### 4.7.1 Wall Functions

Historically, researchers implementing this matching procedure have referred to the functional forms used in the limit  $y \rightarrow 0$  as **wall functions**. This procedure uses the law of the wall as the constitutive relation between velocity and surface shear stress. That is, in terms of the velocity at the mesh point closest to the surface, we can regard the law of the wall, viz.,

$$U = u_\tau \left[ \frac{1}{\kappa} \ln \left( \frac{u_\tau y}{\nu} \right) + B \right] \quad (4.163)$$

as a transcendental equation for the friction velocity and, hence, the shear stress. Once the friction velocity is known, we use Equations (4.100) for the  $k$ - $\omega$  model or Equations (4.105) for the  $k$ - $\epsilon$  model to define the values of  $k$  and  $\omega$  or  $\epsilon$  at the grid points closest to the surface. Because  $\omega$  and  $\epsilon$  are odd functions of  $u_\tau$  and both quantities are positive definite, care must be taken for separated flows. We can either use the absolute value of  $u_\tau$  or

combine the equations for  $k$  and  $\omega$  or  $k$  and  $\epsilon$  so that the **wall functions** for  $k$ ,  $\omega$  and  $\epsilon$  become:

$$k = \frac{u_\tau^2}{\sqrt{\beta^*}}, \quad \omega = \frac{k^{1/2}}{(\beta^*)^{1/4} \kappa y}, \quad \epsilon = (\beta^*)^{3/4} \frac{k^{3/2}}{\kappa y} \quad (4.164)$$

The wall-function approach is not entirely satisfactory for several reasons. Most importantly, numerical solutions generally are sensitive to the point above the surface where the wall functions are used, i.e., the point where the matching occurs (see Subsection 7.2.1 for an in-depth discussion of this problem). Furthermore, the law of the wall doesn't always hold for flow near solid boundaries, most notably for separated flows.

There is a more subtle danger attending the use of wall functions. Specifically, when poor results are obtained with a two-equation model, researchers sometimes mistakenly blame their difficulties on the use of non-optimum wall functions. This assessment is too often made when the wall functions are not the real cause of the problem. For example, the  $k$ - $\epsilon$  model just doesn't perform well for boundary layers with adverse pressure gradient. Many articles have appeared claiming that discrepancies between  $k$ - $\epsilon$  model predicted skin friction and corresponding measurements for such flows are caused by the wall functions. This incorrectly assumes that the surface shear is a localized force that depends only upon sublayer structure. As shown in the defect-layer solution of the preceding section, no viscous modification is likely to remove the curious inflection in the  $k$ - $\epsilon$  model's velocity profile unless viscous effects (unrealistically) penetrate far above the viscous sublayer. We mustn't lose sight of the fact that the momentum flux through a boundary layer affects the surface shear and vice versa [see Equation (4.122)]. Hence, inaccurate skin friction predictions go hand in hand with inaccuracies in the velocity profile throughout the layer.

As a final comment on wall functions, Wilcox (1989) demonstrates that pressure gradient must be included in order to achieve grid-independent solutions for flows with pressure gradient. Retaining pressure gradient in the log-layer equations (i.e., retaining  $\beta_T/Re_{\delta^*}$ ), then the asymptotic behavior for the  $k$ - $\omega$  model approaching the surface is given by the following equations:

$$\left. \begin{aligned} U &= u_\tau \left[ \frac{1}{\kappa} \ln \left( \frac{u_\tau y}{\nu} \right) + B - 0.48 \frac{u_\tau y}{\nu} \phi + O(\phi^2) \right] \\ k &= \frac{u_\tau^2}{\sqrt{\beta^*}} \left[ 1 + 1.16 \frac{u_\tau y}{\nu} \phi + O(\phi^2) \right] \\ \omega &= \frac{u_\tau}{\sqrt{\beta^*} \kappa y} \left[ 1 - 0.32 \frac{u_\tau y}{\nu} \phi + O(\phi^2) \right] \end{aligned} \right\} \quad (4.165)$$

where  $\phi$  is the dimensionless pressure gradient parameter defined by

$$\phi = \frac{\nu}{\rho u_\tau^3} \frac{dP}{dx} \quad (4.166)$$

The expansions in Equation (4.165) have been derived assuming  $\phi$  is a small parameter.

### 4.7.2 Surface Roughness

As noted in the preceding section, a key advantage of the  $k$ - $\omega^2$  and  $k$ - $\omega$  formulations over the  $k$ - $\epsilon$  formulation is the fact that  $\omega$ -oriented equations possess solutions in which the value of  $\omega$  may be arbitrarily specified at the surface. This is an advantage because it provides a natural way to incorporate effects of surface roughness through surface boundary conditions. This feature of the equations was originally recognized by Saffman (1970). If we write the surface boundary condition on  $\omega$  as

$$\omega = \frac{u_\tau^2}{\nu} S_R \quad \text{at} \quad y = 0 \quad (4.167)$$

we can generate sublayer solutions for arbitrary  $S_R$ , including the limiting cases  $S_R \rightarrow 0$  and  $S_R \rightarrow \infty$ . Figure 4.12 shows the computed value of  $B$  for a wide range of values of  $S_R$ . As shown, in the limit  $S_R \rightarrow \infty$ ,  $B$  tends to 5.1. In the limit  $S_R \rightarrow 0$ , an excellent correlation of the numerical predictions is given by

$$B \rightarrow 8.4 + \frac{1}{\kappa} \ln(S_R/100) \quad \text{as} \quad S_R \rightarrow 0 \quad (4.168)$$

By experimental means, Nikuradse [see Schlichting (1979)] found that for flow over very rough surfaces,

$$B \rightarrow 8.5 + \frac{1}{\kappa} \ln(1/k_R^+); \quad k_R^+ = u_\tau k_R / \nu \quad (4.169)$$

where  $k_R$  is the average height of sand-grain roughness elements. (Note that the computations use  $\kappa = 0.41$  while Nikuradse used  $\kappa = 0.40$ .) Thus, if we make the correlation

$$S_R = 100/k_R^+; \quad k_R^+ \gg 1 \quad (4.170)$$

then Equations (4.168) and (4.169) are nearly identical. Figure 4.13 compares computed velocity profiles with the analytical fit obtained by using Equations (4.168) and (4.169) in the law of the wall, viz.,

$$U^+ = \frac{1}{\kappa} \ln(y/k_R) + 8.4 \quad (4.171)$$

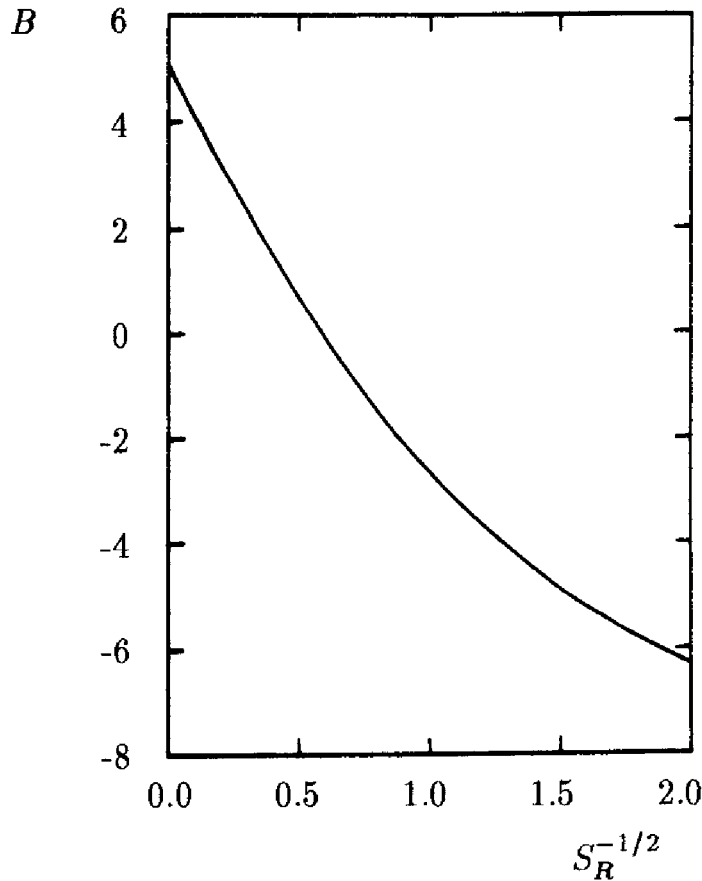


Figure 4.12: Variation of the constant in the law of the wall,  $B$ , with the surface value of the specific dissipation rate. [From Wilcox (1988a) — Copyright © AIAA 1988 — Used with permission.]

for three values of  $k_R^+$ . The correlation is nearly exact. The most remarkable fact about this correlation is that Equation (4.171) is the form the law of the wall assumes for flow over “completely-rough” surfaces, including the value of the additive constant (8.4 and 8.5 differ by one percent).

By making a qualitative argument based on flow over a wavy wall, Wilcox and Chambers (1975) [see Problems section] show that for small roughness heights, we should expect to have

$$S_R \sim (1/k_R^+)^2 \quad \text{as} \quad k_R^+ \rightarrow 0 \quad (4.172)$$

Comparison with Nikuradse’s data shows that the following correlation between  $S_R$  and  $k_R^+$  reproduces measured effects of sand-grain roughness for values of  $k_R^+$  up to about 400.

$$S_R = \begin{cases} (50/k_R^+)^2, & k_R^+ < 25 \\ 100/k_R^+, & k_R^+ \geq 25 \end{cases} \quad (4.173)$$

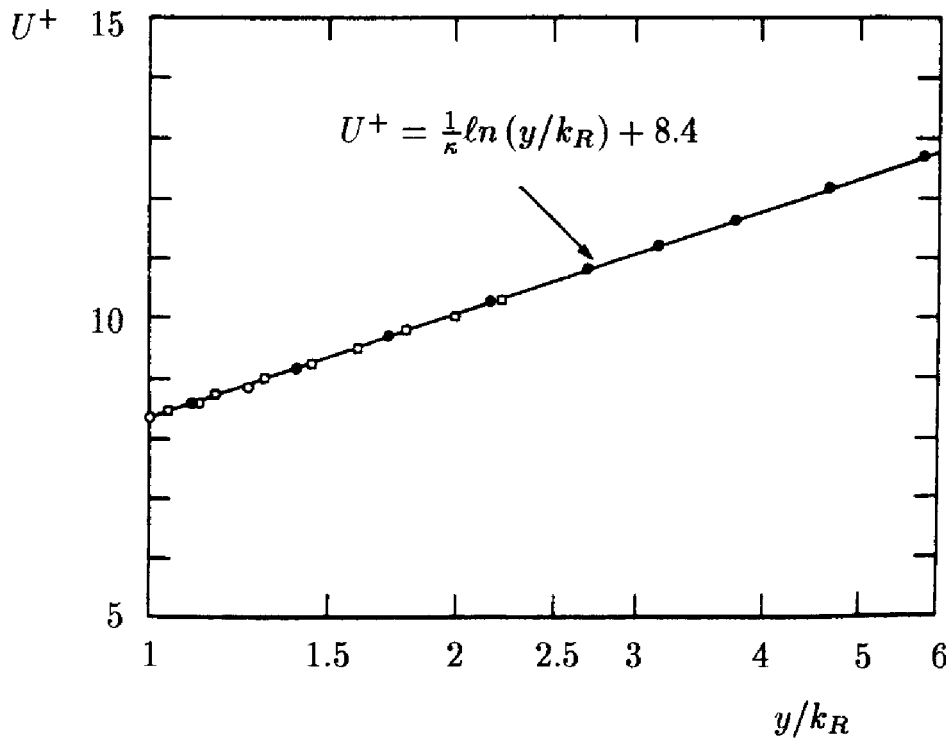


Figure 4.13: Sublayer velocity profiles for “completely rough” surfaces;  $\circ$  Computed,  $k_R^+ = 400$ ;  $\square$  Computed,  $k_R^+ = 225$ ;  $\bullet$  Computed,  $k_R^+ = 50$ . [From Wilcox (1988a) — Copyright © AIAA 1988 — Used with permission.]

As a final comment, the solution for  $k_R^+ \rightarrow 0$  is identical to the sublayer solution discussed in Subsection 4.6.3 [see Equation (4.158)]. The analysis of this section shows that the singular case corresponds to the perfectly-smooth surface. In practice, Equation (4.173) should be used rather than Equation (4.158) even if a perfectly-smooth surface is desired. The advantage in using Equation (4.173) is obvious for several reasons.

- Local geometry (e.g., distance normal to the surface) does not appear so it can be applied even in three-dimensional geometries.
- $k_R$  need only be small enough to have a hydraulically smooth surface, i.e.,  $u_\tau k_R / \nu < 5$ . Resulting surface values of  $\omega$  are rarely ever large enough to cause numerical error provided a sensible finite-difference grid is used (see Subsection 7.2.1).
- Experience has shown Equation (4.173) works well for separated flows.

### 4.7.3 Surface Mass Injection

For boundary layers with surface mass injection, the introduction of an additional velocity scale ( $v_w$  = normal flow velocity at the surface) suggests that the scaling for  $\omega$  at the surface may differ from Equation (4.167). Andersen, Kays and Moffat (1972) provide further evidence that the specific-dissipation-rate boundary condition must be revised when mass injection is present by showing, from correlation of their experimental data, that both  $\kappa$  and  $B$  are functions of  $v_w^+ = v_w/u_\tau$ . Because rough-surface computations show that the value of  $B$  is strongly affected by the surface value of the specific dissipation rate, this suggests that the surface value of  $\omega$  will depend in some manner upon  $v_w$ . Examination of the limiting form of the model equations for  $y^+ \rightarrow \infty$  (i.e., in the log layer) shows immediately that the effective Kármán “constant”,  $\kappa_v$ , varies with  $v_w^+$  according to

$$\kappa_v = \frac{\kappa}{1 + \Xi v_w^+} \quad (4.174)$$

where  $\Xi$  is given by

$$\Xi = 3.11 + 0.61 \ell n y^+ \quad (4.175)$$

The variation of  $\kappa_v$  predicted in Equations (4.174) and (4.175) is consistent with the Andersen et al. data. Including appropriate convective terms in Equations (4.155), Wilcox (1988a) performed sublayer computations for the cases experimentally documented by Andersen et al. In each case, the surface value of  $\omega$  is given by

$$\omega = \frac{u_\tau^2}{\nu} S_B \quad \text{at} \quad y = 0 \quad (4.176)$$

Wilcox varied the value of  $S_B$  to achieve optimum agreement between measured and computed velocities. The correlation between  $S_B$  and  $v_w^+$  is given in analytical form as

$$S_B = \frac{20}{v_w^+(1 + 5v_w^+)} \quad (4.177)$$

Figure 4.14 compares measured velocities with values computed using Equations (4.176) and (4.177).

## 4.8 Application to Wall-Bounded Flows

Using the surface boundary conditions devised in Section 4.7, we can now turn to application of two-equation turbulence models to wall-bounded flows. Because of their relative simplicity, we consider pipe and channel

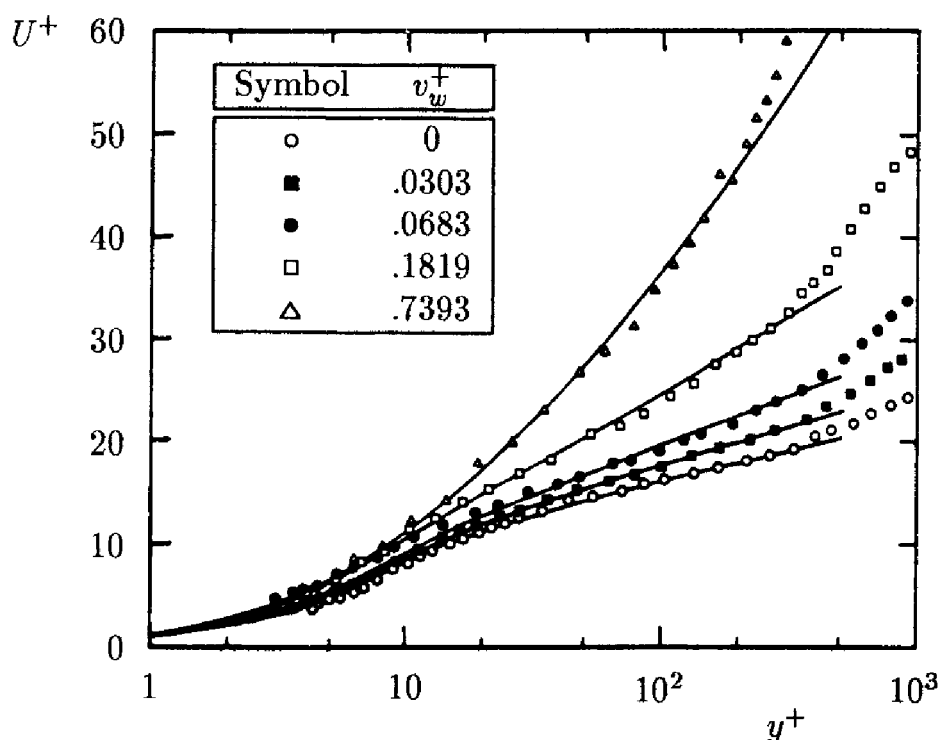


Figure 4.14: Sublayer velocity profiles for boundary layers with surface mass injection; —  $k-\omega$  model; ○ ■ ● □ △ Andersen, et al. [From Wilcox (1988a) — Copyright © AIAA 1988 — Used with permission.]

flow first using the  $k-\omega$  model. Then, we will consider several incompressible boundary-layer applications. In these applications we exercise the  $k-\omega$  model and the  $k-\epsilon$  model.

### 4.8.1 Channel and Pipe Flow

Figures 4.15 and 4.16 compare computed and measured channel and pipe flow properties, respectively. Six different comparisons are shown in each figure, including mean velocity, skin friction, Reynolds shear stress, turbulence kinetic energy, turbulence energy production and dissipation rate.

Figure 4.15 compares  $k-\omega$  model channel flow predictions with the Direct Numerical Simulation (DNS) computations performed by Mansour, Kim and Moin (1988). Reynolds number based on channel height and average velocity is 13,750. Velocity profiles and Reynolds shear stress profiles differ by less than 3%. Computed skin friction differs from Halleen and Johnston's (1967) correlation [Equation (3.137)] by less than about 2% except at the lowest Reynolds number shown. Although the model fails to predict the peak value of  $k$  near the channel wall, the computed  $k$  profile differs from the DNS profile by less than 5% over 80% of the channel. Despite



the fact that the model is not asymptotically consistent (Subsection 4.9.1) approaching the surface, even the turbulence-energy production,  $\tau_{xy}\partial U/\partial y$ , and dissipation,  $\epsilon$ , nearly duplicate the DNS results except very close to the surface. On balance, the  $k$ - $\omega$  results are a bit closer to the DNS results than either the Cebeci-Smith or Baldwin-Lomax models (Subsection 3.5.1).

Figure 4.16 compares  $k$ - $\omega$  model pipe flow results with Laufer's (1952) measurements at a Reynolds number based on pipe diameter and average velocity of 40,000. As shown, computed and measured velocity and Reynolds shear stress profiles differ by less than 6%. As with channel flow, computed and measured turbulence kinetic energy differ by about 4% except close to the surface where the sharp peak occurs. Although computed turbulence energy production and dissipation differ from measured values by less than 5%, it is unclear whether this is a desirable result. That is, some controversy exists about the accuracy of Laufer's dissipation measurements, and the model may be reproducing erroneous results. Finally, computed skin friction is within 4% of Prandtl's universal law of friction [Equation (3.138)]. Overall, predictions are as close to measurements as those obtained with the Cebeci-Smith and Baldwin-Lomax models.

It is interesting, and perhaps illuminating, that the most important flow properties are accurately predicted even though the sharp peak in turbulence energy is underestimated by 40% and 25%, respectively, for channel and pipe flow. That is, for engineering applications, the most important quantity is the skin friction. The next most important quantity typically is the velocity profile. Only for specialized applications is a subtle feature such as the peak value of  $k$  important. Thus, we see that even though the  $k$ - $\omega$  model fails to predict this subtle feature, it is apparently of little consequence for most engineering applications.

### 4.8.2 Boundary Layers

We turn now to application of the  $k$ - $\omega$  and  $k$ - $\epsilon$  model equations to four incompressible boundary layers. All of the  $k$ - $\omega$  model results use the surface boundary conditions described in Subsections 4.7.2 and 4.7.3. By contrast, the  $k$ - $\epsilon$  model computations were done using wall functions.

The first application is for the constant-pressure incompressible boundary layer. The computation begins at a plate-length Reynolds number,  $Re_x = 1 \cdot 10^6$  and continues to  $Re_x = 10.9 \cdot 10^6$ . Figures 4.17(a) and (b) compare computed and measured [Coles and Hirst (1969)] skin friction and velocity profiles. As shown, for the  $k$ - $\omega$  model, computed  $c_f$  virtually duplicates measurements for the entire range of Reynolds numbers considered. Differences between computed and measured  $k$ - $\omega$  velocity profiles are no more than 3% of scale for the three Reynolds numbers indicated.

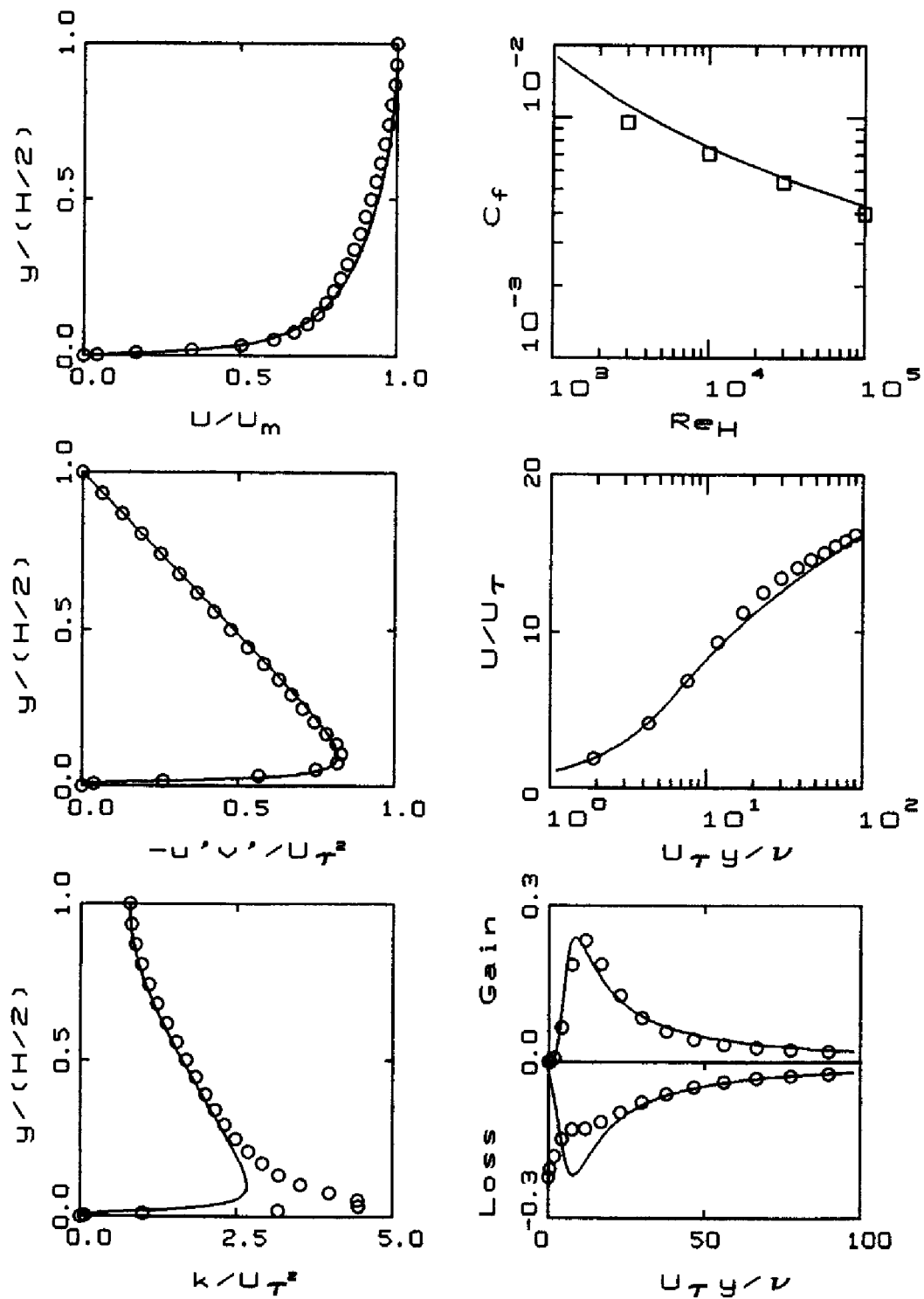


Figure 4.15: Comparison of computed and measured channel-flow properties,  $Re_H = 13,750$ . —  $k-\omega$  model;  $\circ$  Mansour et al. (DNS);  $\square$  Halleen-Johnston correlation.

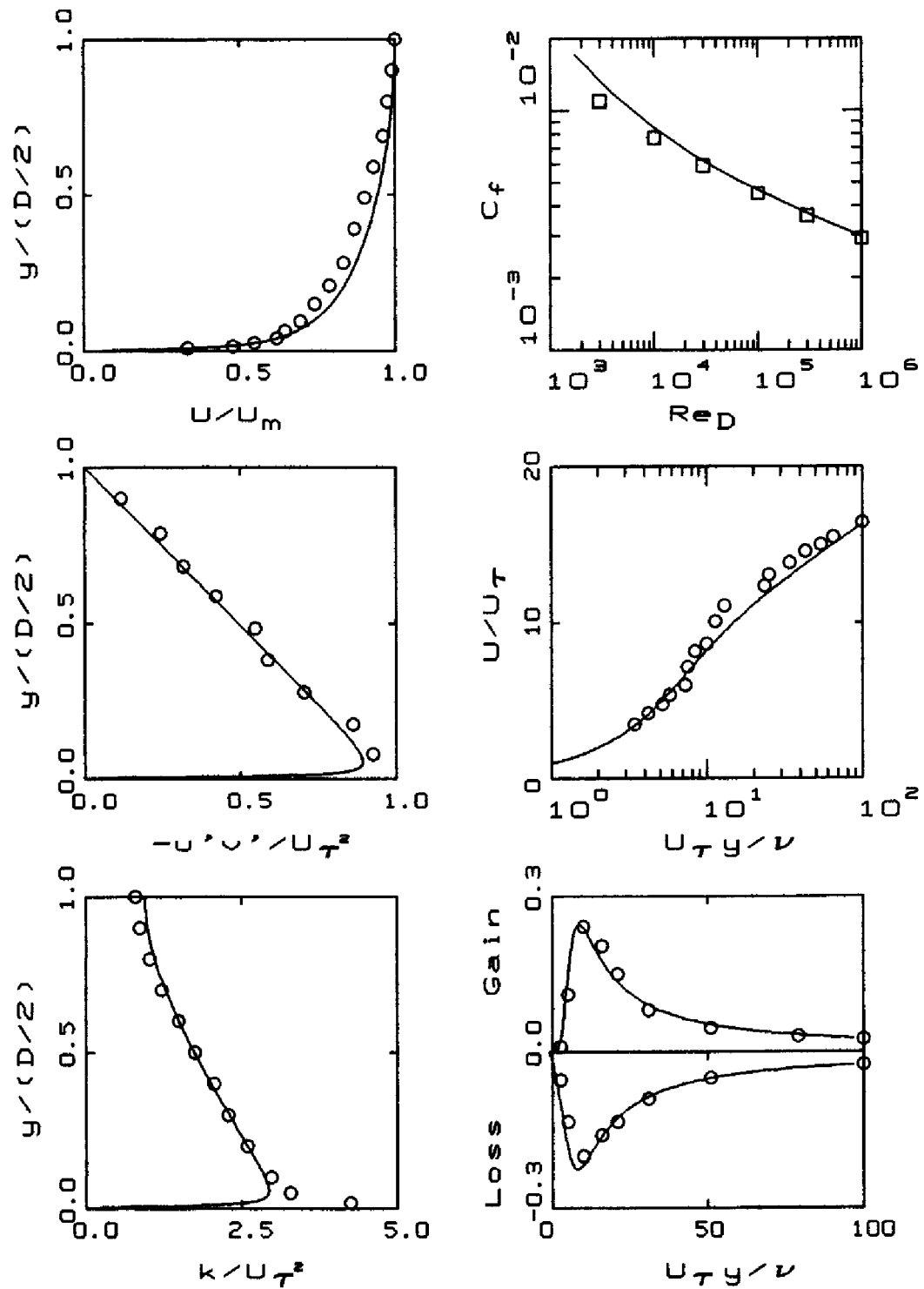


Figure 4.16: Comparison of computed and measured pipe-flow properties,  $Re_D = 40,000$ . —  $k-\omega$  model;  $\circ$  Laufer;  $\square$  Prandtl correlation.

Thus, as no great surprise, the  $k-\omega$  model is quite accurate for the flat-plate boundary layer. Skin friction results [Chambers and Wilcox (1977)] for the  $k-\epsilon$  model are included in Figure 4.17(a). Note that, as predicted in the defect-layer analysis of Subsection 4.6.2, computed  $c_f$  is about 3% higher than measured.

The next two applications are for boundary layers with adverse pressure gradient. The first case is for moderate adverse pressure gradient, the experimental data being those of Bradshaw (1969). The second case has increasingly adverse pressure gradient, the experimental data being those of Samuel and Joubert [see Kline et al. (1981) - Flow 0141].

For the Bradshaw case, streamwise distance extends from  $x = 2.5$  ft to  $x = 7.0$  ft, corresponding to  $Re_x$  increasing from about  $2 \cdot 10^6$  to about  $4 \cdot 10^6$ . Figures 4.17(c) and (d) compare computed and measured skin friction and a velocity profile. Inspection of both graphs shows that differences between  $k-\omega$  model predictions and experiment nowhere exceed 5% for this flow. The figure includes  $k-\epsilon$  results obtained by Chambers and Wilcox (1977); computed  $c_f$  exceeds measured values by as much as 20%. Because the equilibrium parameter  $\beta_T \approx 2$  for this flow, the poor results for the  $k-\epsilon$  model are unsurprising. Note also that the  $k-\omega$  model's skin friction is much closer to measured values than either the Cebeci-Smith or Baldwin-Lomax models (see Figure 3.16).

In the Samuel-Joubert case, we integrate from  $x = 1$  m to  $x = 3.40$  m, corresponding to an  $Re_x$  range of about  $2 \cdot 10^6$  to  $4 \cdot 10^6$ . Figures 4.17(e) and (f) compare computed and measured skin friction and two velocity profiles for this flow. For the  $k-\omega$  model, computed and measured skin friction differ by less than 5% of scale. Also, velocity profiles at  $x = 2.87$  m are within 5% percent while those at  $x = 3.40$  m differ by no more than 9%. The figure also shows skin friction for the  $k-\epsilon$  model obtained by Rodi and Scheuerer (1986). Since  $\beta_T$  exceeds 9 toward the end of the computation, the poor performance of the  $k-\epsilon$  model (computed  $c_f$  exceeds measured values by as much as 35%) is again consistent with the defect-layer analysis of Subsection 4.6.3.

As the final application of the models, we consider a boundary layer with surface mass injection. The case considered was included in the 1980-81 AFOSR-HTTM-Stanford Conference on Complex Turbulent Flows (Flow 0241) and data for the flow were taken by Andersen et al. (1972). Surface mass injection rate,  $v_w$ , is  $.00375U_e$ , where  $U_e$  is the constant boundary-layer-edge velocity, i.e., the flow has constant pressure. Figures 4.17(g) and (h) compare computed and measured skin friction and velocity profiles. As shown, for the  $k-\omega$  model computed and measured skin friction differ by less than 4% of scale while computed and measured velocity profiles are within 3% of each other. Although this flow has zero pressure gradient,

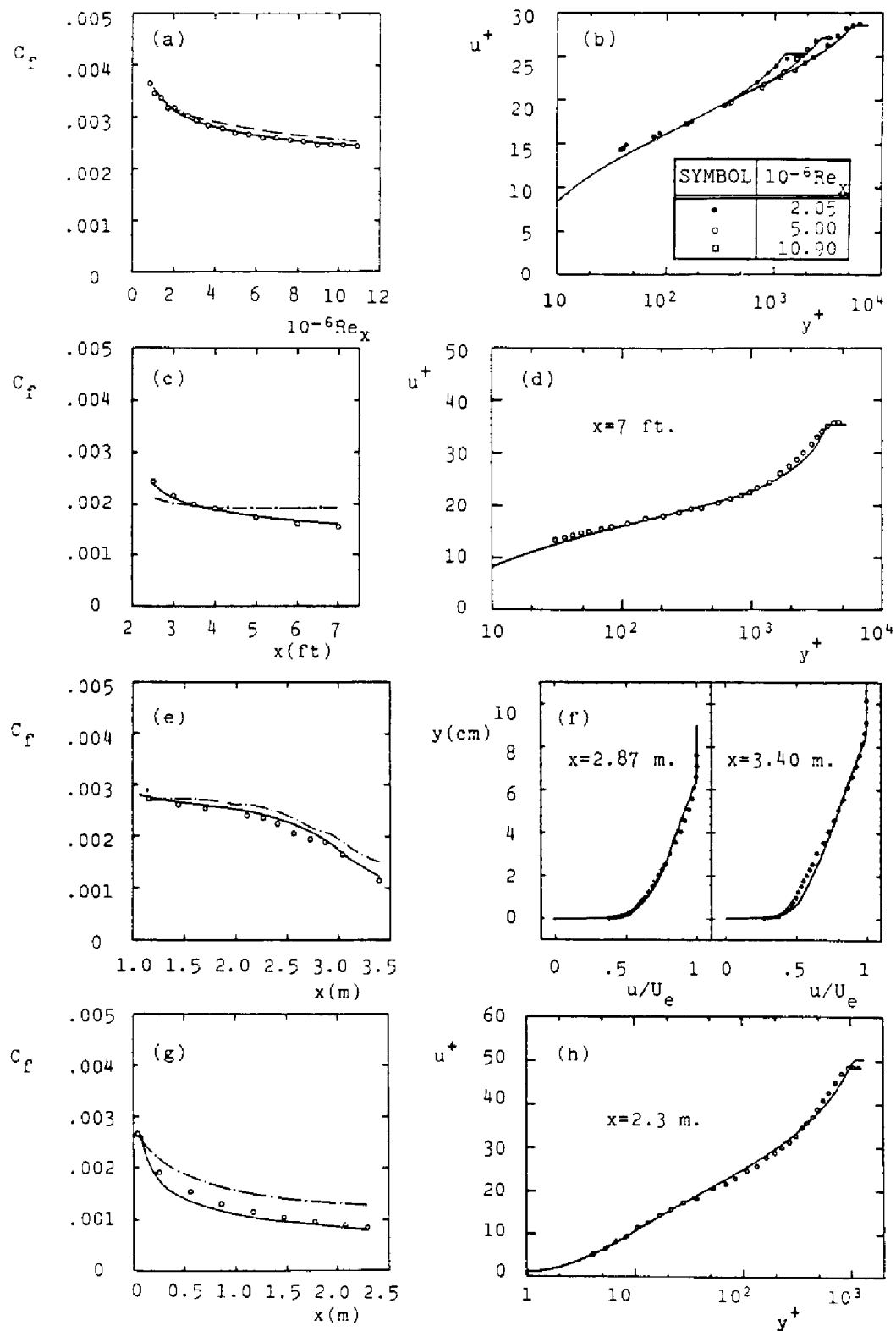


Figure 4.17: Computed and measured skin-friction and velocity profiles for incompressible boundary layers; —  $k-\omega$  model; - · -  $k-\epsilon$  model; o ● measured. [From Wilcox (1988a) — Copyright © AIAA 1988 — Used with permission.]

corresponding skin friction predicted by the  $k$ - $\epsilon$  model [see Kline et al. (1981)] is as much as 50% higher than measured.

## 4.9 Low-Reynolds-Number Effects

Thus far, the turbulence models we have considered are restricted to high-Reynolds number applications. Even in the case of the  $k$ - $\omega$  model, while we have been able to integrate through the viscous sublayer, we have paid no attention to low-Reynolds-number effects. For example, the model fails to predict the sharp peak in turbulence kinetic energy close to the surface for pipe and channel flow (see Figures 4.15 and 4.16). Most importantly, most two-equation models fail to predict a realistic value of the additive constant,  $B$ , in the law of the wall. All such models require viscous damping in order to achieve a realistic value for  $B$ . Finally, there are applications for which viscous effects must be accurately represented, and this section will discuss commonly used low-Reynolds-number corrections.

### 4.9.1 Asymptotic Consistency

In formulating viscous corrections for two-equation models, we can obtain some guidance from looking at the limiting behavior of the fluctuating velocities approaching a solid boundary. That is, we assume standard Taylor series expansions for each of the fluctuating velocities and substitute into the exact equations of motion, viz., the instantaneous continuity and Navier-Stokes equations. We did this in Subsection 4.6.3 when we were formulating surface boundary conditions for the viscous sublayer perturbation solution. Thus, we again begin by assuming

$$\left. \begin{aligned} u' &\sim A(x, z, t)y + O(y^2) \\ v' &\sim B(x, z, t)y^2 + O(y^3) \\ w' &\sim C(x, z, t)y + O(y^2) \end{aligned} \right\} \quad \text{as } y \rightarrow 0 \quad (4.178)$$

where  $A(x, z, t)$ ,  $B(x, z, t)$  and  $C(x, z, t)$  must have zero time average and satisfy the equations of motion. Note that the no-slip surface boundary condition dictates the fact that  $\mathbf{u}'$  must go to zero as  $y \rightarrow 0$ . Since we expect Navier-Stokes solutions to be analytic everywhere, we conclude that the fluctuating velocity components  $u'$  and  $w'$  vary linearly with  $y$ . Also, substituting Equations (4.178) into the continuity equation shows that  $v'$  varies quadratically with  $y$ . While we don't know the precise values of  $A$ ,  $B$  and  $C$  without solving the complete Navier-Stokes equation, we can still use the exact asymptotic variations of  $u'$ ,  $v'$  and  $w'$  with  $y$  to deduce the

limiting behavior of time-averaged properties approaching the surface. For example, the turbulence kinetic energy and dissipation are

$$k \sim \frac{1}{2}(\overline{A^2 + C^2})y^2 + O(y^3) \quad \text{and} \quad \epsilon \sim \nu (\overline{A^2 + C^2}) + O(y) \quad (4.179)$$

Also, the Reynolds shear stress is given by

$$\tau_{xy} \sim -\overline{AB}y^3 + O(y^4) \quad (4.180)$$

A model that duplicates the exact limiting forms of  $k$ ,  $\epsilon$  and  $\tau_{xy}$  given in Equations (4.179) and (4.180) is said to be **asymptotically consistent** with the near-wall behavior of the exact equations of motion.

Many researchers have attempted to devise viscous corrections for the  $k$ - $\epsilon$  model to permit its integration through the viscous sublayer. All have achieved some degree of **asymptotic consistency**. Jones and Launder (1972) were the first to propose viscous modifications for the  $k$ - $\epsilon$  model. Other proposals have been made by Launder and Sharma (1974), Hoffmann (1975), Reynolds (1976), Hassid and Poreh (1978), Lam and Bremhorst (1981), Dutoya and Michard (1981), Chien (1982), Myong and Kasagi (1990), Speziale, Abid and Anderson (1990), Shih and Hsu (1991), Zhang, So, Speziale and Lai (1992), Yang and Shih (1993), and Fan, Lakshminarayana and Barnett (1993). For steady, incompressible boundary layers, all of these models can be written compactly as follows:

$$U \frac{\partial k}{\partial x} + V \frac{\partial k}{\partial y} = \nu_T \left( \frac{\partial U}{\partial y} \right)^2 - \epsilon + \frac{\partial}{\partial y} \left[ (\nu + \nu_T / \sigma_k) \frac{\partial k}{\partial y} \right] \quad (4.181)$$

$$U \frac{\partial \tilde{\epsilon}}{\partial x} + V \frac{\partial \tilde{\epsilon}}{\partial y} = C_{\epsilon 1} f_1 \frac{\tilde{\epsilon}}{k} \nu_T \left( \frac{\partial U}{\partial y} \right)^2 - C_{\epsilon 2} f_2 \frac{\tilde{\epsilon}^2}{k} + E + \frac{\partial}{\partial y} \left[ (\nu + \nu_T / \sigma_\epsilon) \frac{\partial \tilde{\epsilon}}{\partial y} \right] \quad (4.182)$$

where the dissipation,  $\epsilon$ , is related to the quantity  $\tilde{\epsilon}$  by

$$\epsilon = \epsilon_o + \tilde{\epsilon} \quad (4.183)$$

The quantity  $\epsilon_o$  is the value of  $\epsilon$  at  $y = 0$ , and is defined differently for each model. The eddy viscosity is defined as

$$\nu_T = C_\mu f_\mu k^2 / \tilde{\epsilon} \quad (4.184)$$

Equations (4.181) - (4.184) contain five empirical **damping functions**,  $f_1$ ,  $f_2$ ,  $f_\mu$ ,  $\epsilon_o$  and  $E$ . These functions depend upon one or more of the following three dimensionless parameters.

$$Re_T = \frac{k^2}{\tilde{\epsilon} \nu}, \quad R_y = \frac{k^{1/2} y}{\nu}, \quad y^+ = \frac{u_\tau y}{\nu} \quad (4.185)$$

The models devised by Jones and Launder (1972), Launder and Sharma (1974), Lam and Bremhorst (1981), and Chien (1982) exemplify most of the features incorporated in  $k$ - $\epsilon$  model viscous damping functions. The damping functions and closure coefficients for these four models are as follows.

#### Jones-Launder Model

$$\left. \begin{aligned} f_\mu &= e^{-2.5/(1+Re_T/50)} \\ f_1 &= 1 \\ f_2 &= 1 - 0.3e^{-Re_T^2} \\ \epsilon_o &= 2\nu \left( \frac{\partial \sqrt{k}}{\partial y} \right)^2 \\ E &= 2\nu\nu_T \left( \frac{\partial^2 U}{\partial y^2} \right)^2 \\ C_{\epsilon 1} &= 1.45, \quad C_{\epsilon 2} = 2.00, \quad C_\mu = 0.09, \quad \sigma_k = 1.0, \quad \sigma_\epsilon = 1.3 \end{aligned} \right\} \quad (4.186)$$

#### Launder-Sharma Model

$$\left. \begin{aligned} f_\mu &= e^{-3.4/(1+Re_T/50)^2} \\ f_1 &= 1 \\ f_2 &= 1 - 0.3e^{-Re_T^2} \\ \epsilon_o &= 2\nu \left( \frac{\partial \sqrt{k}}{\partial y} \right)^2 \\ E &= 2\nu\nu_T \left( \frac{\partial^2 U}{\partial y^2} \right)^2 \\ C_{\epsilon 1} &= 1.44, \quad C_{\epsilon 2} = 1.92, \quad C_\mu = 0.09, \quad \sigma_k = 1.0, \quad \sigma_\epsilon = 1.3 \end{aligned} \right\} \quad (4.187)$$

#### Lam-Bremhorst Model

$$\left. \begin{aligned} f_\mu &= (1 - e^{-0.0165Re_y})^2 (1 + 20.5/Re_T) \\ f_1 &= 1 + (0.05/f_\mu)^3 \\ f_2 &= 1 - e^{-Re_T^2} \\ \epsilon_o &= 0 \\ E &= 0 \\ C_{\epsilon 1} &= 1.44, \quad C_{\epsilon 2} = 1.92, \quad C_\mu = 0.09, \quad \sigma_k = 1.0, \quad \sigma_\epsilon = 1.3 \end{aligned} \right\} \quad (4.188)$$



**Chien Model**

$$\left. \begin{aligned} f_\mu &= 1 - e^{-0.0115y^+} \\ f_1 &= 1 \\ f_2 &= 1 - 0.22e^{-(Re_T/6)^2} \\ \epsilon_o &= 2\nu \frac{k}{y^2} \\ E &= -2\nu \frac{\tilde{\epsilon}}{y^2} e^{-y^+/2} \\ C_{\epsilon 1} &= 1.35, \quad C_{\epsilon 2} = 1.80, \quad C_\mu = 0.09, \quad \sigma_k = 1.0, \quad \sigma_\epsilon = 1.3 \end{aligned} \right\} \quad (4.189)$$

By examining the limiting behavior of each of these models close to a solid boundary where  $y = 0$ , it is easy to demonstrate that, consistent with Equation (4.179), all four models guarantee

$$k \sim y^2 \quad \text{and} \quad \epsilon/k \rightarrow 2\nu/y^2 \quad \text{as} \quad y \rightarrow 0 \quad (4.190)$$

Additionally, the Lam-Bremhorst model predicts  $\tau_{xy} \sim y^4$  while the other three models predict  $\tau_{xy} \sim y^3$ . Thus, all except the Lam-Bremhorst model are consistent with Equation (4.180) as well.

Surface boundary conditions for low-Reynolds-number  $k$ - $\epsilon$  models are not entirely straightforward. On the one hand, the no-slip boundary condition tells us that  $k$  must vanish at a solid boundary. On the other hand, the strongest thing we can say about the surface value of  $\epsilon$  is the second of Equations (4.190). That is, we invariably must tie the surface value of  $\epsilon$  to the second derivative of  $k$  at the surface. The Jones-Launder, Launder-Sharma and Chien models build in the proper asymptotic behavior through introduction of the function  $\epsilon_o$ . Consequently, the boundary conditions appropriate at the surface are

$$k = \tilde{\epsilon} = 0 \quad \text{at} \quad y = 0 \quad (4.191)$$

By contrast, Lam and Bremhorst deal directly with  $\epsilon$  and specify the surface boundary condition on  $\epsilon$  by requiring

$$\epsilon = \nu \frac{\partial^2 k}{\partial y^2} \quad \text{at} \quad y = 0 \quad (4.192)$$

As an alternative, Lam and Bremhorst also propose using

$$\frac{\partial \epsilon}{\partial y} = 0 \quad \text{at} \quad y = 0 \quad (4.193)$$

While Equation (4.193) is easier to implement than Equation (4.192), there is no a priori reason to expect that the next term in the Taylor series expansion for  $\epsilon$  should vanish.

In a review article, Patel, Rodi and Scheuerer (1985) compare seven low-Reynolds-number variants of the  $k$ - $\epsilon$  model and the Wilcox-Rubesin (1980)  $k$ - $\omega^2$  model. Figure 4.18 compares computed and measured velocity and  $k^+ = k/u_\tau^2$  profiles for the flat-plate boundary layer. As shown, the Dutoya-Michard, Hassid-Poreh and Hoffmann models fail to provide accurate solutions for the incompressible flat-plate boundary layer. Figure 4.19(a) shows that for adverse pressure gradient, the Wilcox-Rubesin model (which was not designed with low-Reynolds-number applications in mind) most faithfully matches measured [Anderson et al. (1972)] skin friction. Figure 4.19(b) shows that none of the models reproduces the measured skin friction for the low-Reynolds-number, favorable pressure gradient flow of Simpson and Wallace (1975). This further demonstrates that the only thing low-Reynolds-number modifications do is fix the  $k$ - $\epsilon$  model's problems in predicting the constant  $B$  in the law of the wall.

There is a popular misconception that low-Reynolds-number modifications to the  $k$ - $\epsilon$  model can remove its deficiencies for adverse pressure gradient flows. This mistaken notion overlooks the volumes of data on and physical understanding of turbulent boundary layers established during the twentieth century, most notably by Clauser and Coles. Recall from Subsection 4.6.1 that Coles describes the turbulent boundary layer as a “wake-like structure constrained by a wall” and notes that different scales and physical processes are dominant in the sublayer and defect layer. Since perturbation analysis shows that the  $k$ - $\epsilon$  model is inconsistent with observed defect-layer structure, we cannot reasonably expect viscous corrections (which are negligible in the physical defect layer) to correct the inconsistency.

Figure 4.20 clearly illustrates this point. The figure compares computed and measured skin friction for twelve incompressible boundary layers with adverse pressure gradient. Results are presented for the Jones-Launder, Launder-Sharma, Lam-Bremhorst, Chien, and Wilcox (1988a)  $k$ - $\omega$  models. Eleven of the cases are from the 1968 AFOSR-IFP-Stanford Conference, and the flow numbers from the conference are included for each case. Flow 0141 is the Samuel-Joubert case from the 1980-81 AFOSR-HTTM-Stanford Conference on Complex Turbulent Flows.

As shown, for Bradshaw Flow C (Flow 3300) and the Samuel-Joubert case (Flow 0141), skin friction is similar to results obtained with wall functions [see Figure 4.17(e)]. As categorized by Coles and Hirst (1969), Flows 1100, 2100, 2500 and 4800 have “mild” adverse pressure gradient, Flows 2400, 2600, 3300 and 4500 have “moderate” adverse pressure gradient, and Flows 0141, 1200, 4400 and 5300 have “strong” adverse pressure gradient. Discrepancies between computed and measured  $c_f$  increase dramatically for all four  $k$ - $\epsilon$  models as the strength of the pressure gradient increases. By contrast,  $k$ - $\omega$  results are remarkably close to measured values for all twelve

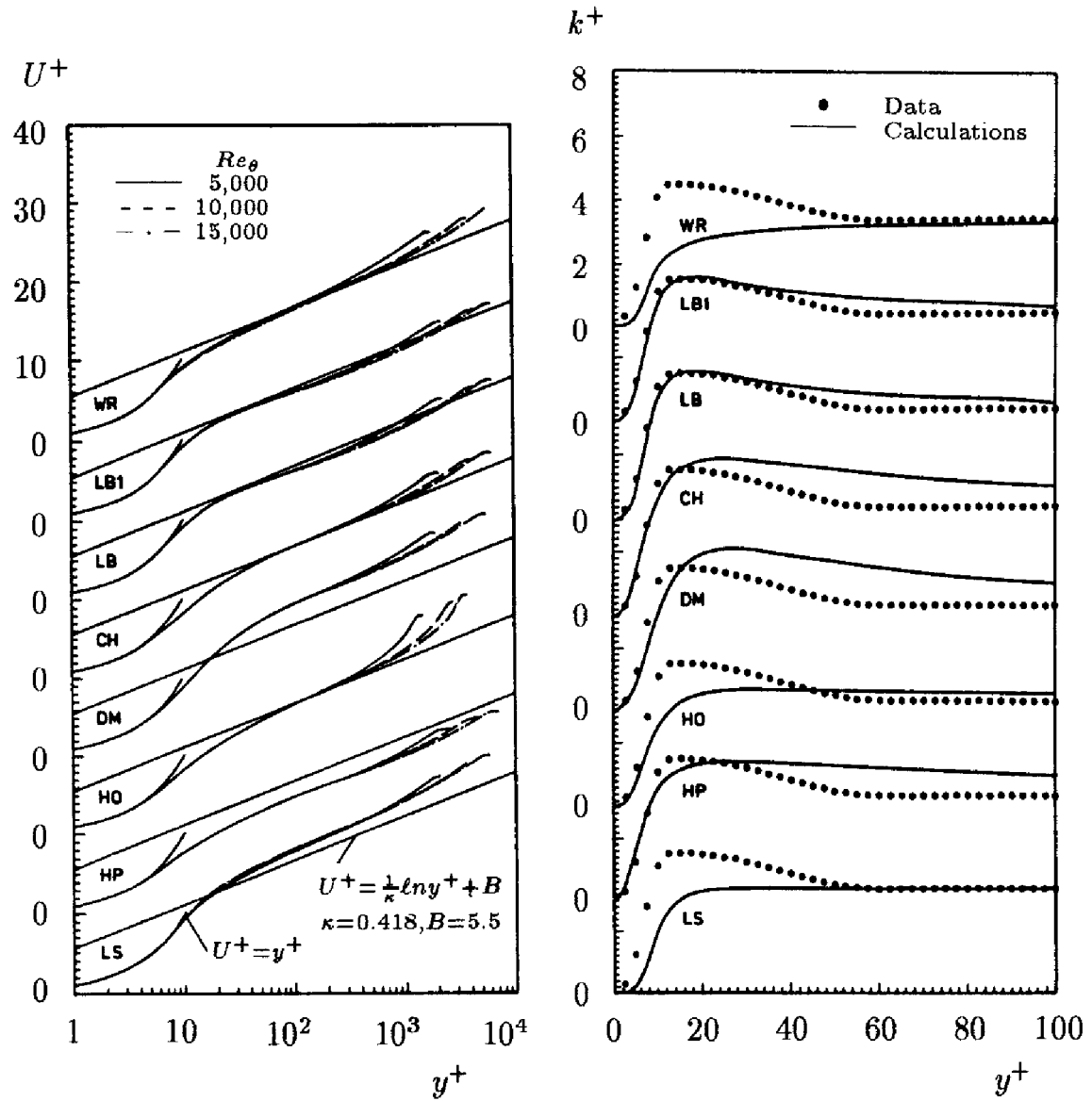


Figure 4.18: Flat-plate boundary layer properties. CH = Chien; DM = Dutoya-Michard; HO = Hoffman; HP = Hassid-Poreh; LB = Lam-Bremhorst with  $\epsilon = \nu \partial^2 k / \partial y^2$ ; LB1 = Lam-Bremhorst with  $\partial \epsilon / \partial y = 0$ ; LS = Launder-Sharma; WR = Wilcox-Rubesin. [From Patel, Rodi and Scheuerer (1985) — Copyright © AIAA 1985 — Used with permission.]

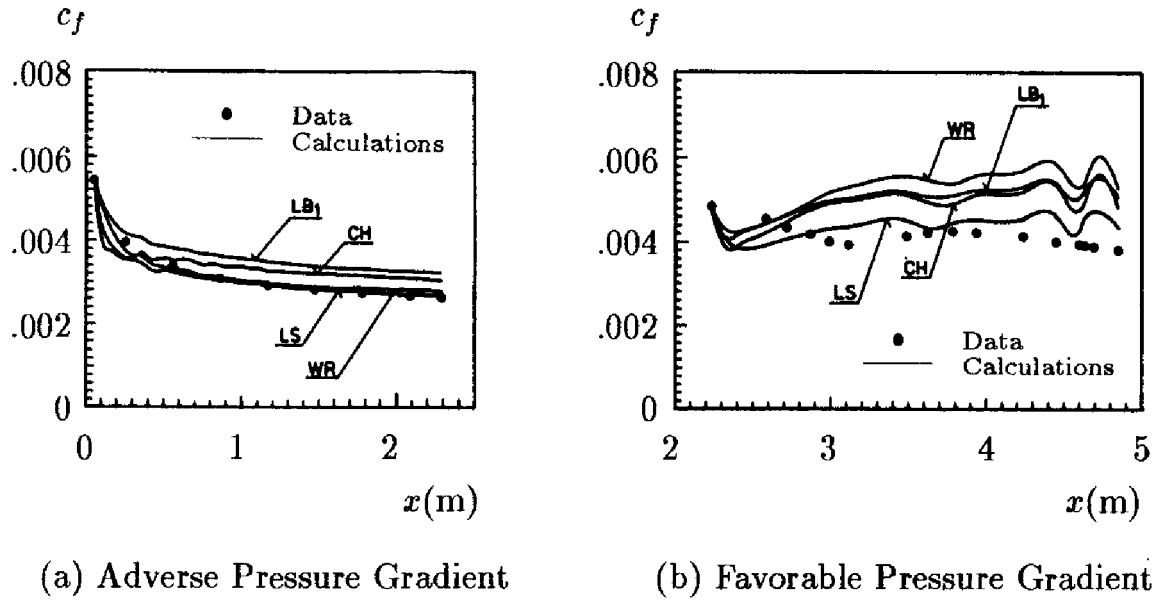


Figure 4.19: Comparison of computed and measured skin friction for low-Reynolds-number flows with pressure gradient. CH = Chien; LB1 = Lam-Bremhorst with  $\partial\epsilon/\partial y = 0$ ; LS = Launder-Sharma; WR = Wilcox-Rubesin. [From Patel, Rodi and Scheuerer (1985) — Copyright © AIAA 1985 — Used with permission.]

cases, including the nearly separated Flow 5300 (the Chien model predicts separation for this case). In terms of the final values of  $c_f$ , the average difference between computation and measurement is 7% for the  $k-\omega$  model, 46% for the Launder-Sharma model, 46% for the Chien model, 58% for the Lam-Bremhorst model, and 74% for the Jones-Launder model.

These results confirm the defect-layer perturbation solution presented in Subsection 4.6.2, which shows that [see Equation (4.151)]:

$$\frac{U_e - U}{u_\tau} \sim -\frac{1}{\kappa} \ln \eta + A - \beta_T C \eta \ln \eta + O(\eta^2 \ln \eta) \quad \text{as } \eta \rightarrow 0 \quad (4.194)$$

where the coefficient  $C$  is given in Table 4.4. Combining Equation (4.194) with Equation (4.148), the effective law of the wall predicted by the  $k-\epsilon$  model is

$$U^+ \sim \frac{1}{\kappa} \ln y^+ + B + \beta_T C \eta \ln \eta \quad \text{as } y^+ \rightarrow \infty \quad (4.195)$$

Figure 4.21 compares the computed Launder-Sharma model near-wall velocity profile with experimental data, the standard law of the wall and Equation (4.195). Examination of the numerical solution shows that the implied constant in the law of the wall,  $B$ , is 5.5. As shown, the asymptotic

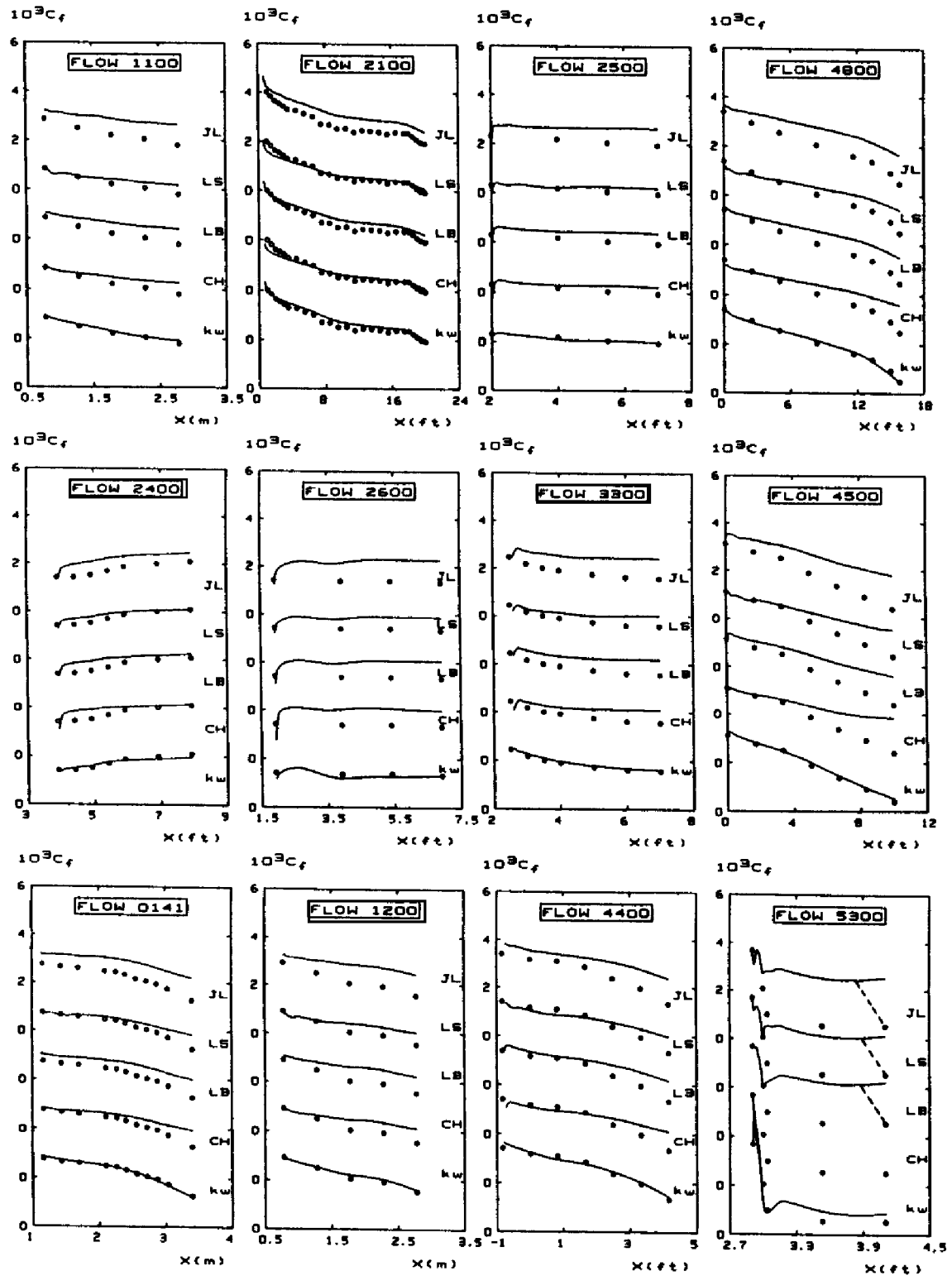


Figure 4.20: Computed and measured skin friction for boundary layers with adverse pressure gradient; CH = Chien; JL = Jones-Launder; LB = Lam-Bremhorst; LS = Launder-Sharma; kw =  $k-\omega$ .

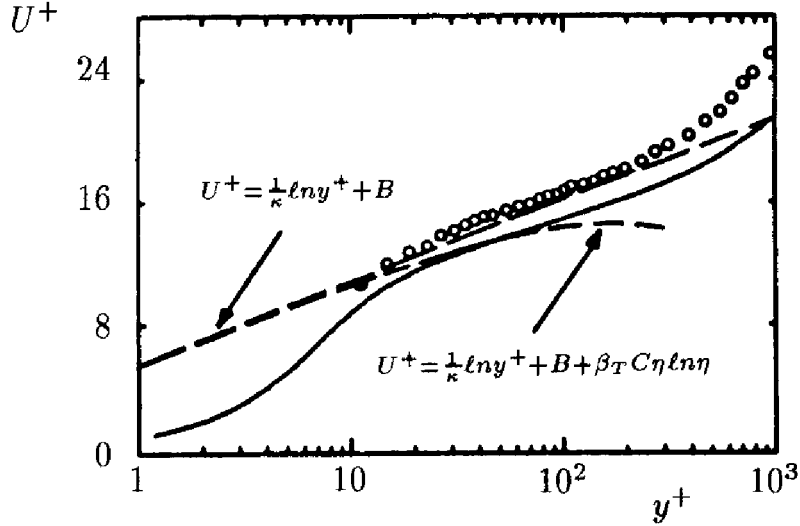


Figure 4.21: Computed and measured near-wall velocity profiles for Samuel and Joubert's adverse pressure gradient flow,  $x = 3.40$  m.; — Launder-Sharma model with  $\kappa = .43$  and  $B = 5.5$ ; o Samuel-Joubert.

formula provides an excellent approximation to the numerical results in the region between  $y^+ = 20$  and 100. If we included the  $O(\eta^2 \ell n \eta)$  term or used the exact defect-layer solution, the match would extend even farther above the sublayer. The important point to note is the impact of the term in Equation (4.195) proportional to the equilibrium parameter,  $\beta_T$ . Its effect is to distort the velocity profile throughout the defect layer, including its asymptotic form approaching the sublayer from above.

As a final comment on low-Reynolds-number corrections for the  $k-\epsilon$  model, using the dimensionless parameters  $R_y$  and  $y^+$  [Equation (4.185)] is ill advised. Both depend upon distance normal to the surface, which can cause difficulty in complex geometries such as a wing-fuselage junction. Also, it is ironic that several additional closure coefficients and functions are needed for the  $k-\epsilon$  model to behave properly in the near-wall region of a turbulent boundary layer. Dissipation is, after all, a phenomenon that occurs in the smallest eddies, and that is all we find in the near-wall region. This further underscores the fact that there is virtually no connection between the exact equation for  $\epsilon$  and its modeled counterpart.

### 4.9.2 Transition

Turbulence model equations can be used to predict transition from laminar to turbulent flow, although most models predict transition to turbulence at Reynolds numbers that are at least an order of magnitude too low. To understand why and how the  $k-\omega$  model predicts transition, consider the

flat-plate boundary layer. For the  $k$ - $\omega$  model, the incompressible, two-dimensional boundary-layer form of the equations for  $k$  and  $\omega$  is as follows.

$$\rho U \frac{\partial U}{\partial x} + \rho V \frac{\partial U}{\partial y} = \frac{\partial}{\partial y} \left[ (\nu + \nu_T) \frac{\partial U}{\partial y} \right] \quad (4.196)$$

$$U \frac{\partial k}{\partial x} + V \frac{\partial k}{\partial y} = \nu_T \left( \frac{\partial U}{\partial y} \right)^2 - \beta^* \omega k + \frac{\partial}{\partial y} \left[ (\nu + \sigma^* \nu_T) \frac{\partial k}{\partial y} \right] \quad (4.197)$$

$$U \frac{\partial \omega}{\partial x} + V \frac{\partial \omega}{\partial y} = \alpha \frac{\omega}{k} \nu_T \left( \frac{\partial U}{\partial y} \right)^2 - \beta \omega^2 + \frac{\partial}{\partial y} \left[ (\nu + \sigma \mu_T) \frac{\partial \omega}{\partial y} \right] \quad (4.198)$$

$$\nu_T = \alpha^* k / \omega \quad (4.199)$$

With one exception, all notation and closure coefficients are as defined in Equations (4.33) to (4.37). The only difference is the appearance of an additional closure coefficient  $\alpha^*$  in Equation (4.199). This coefficient is equal to one for the standard high-Reynolds-number version of the  $k$ - $\omega$  model. We can most clearly illustrate how the model equations predict transition by rearranging terms in Equations (4.197) and (4.198) as follows.

$$U \frac{\partial k}{\partial x} + V \frac{\partial k}{\partial y} = P_k \beta^* \omega k + \frac{\partial}{\partial y} \left[ (\nu + \sigma^* \nu_T) \frac{\partial k}{\partial y} \right] \quad (4.200)$$

$$U \frac{\partial \omega}{\partial x} + V \frac{\partial \omega}{\partial y} = P_\omega \beta \omega^2 + \frac{\partial}{\partial y} \left[ (\nu + \sigma \mu_T) \frac{\partial \omega}{\partial y} \right] \quad (4.201)$$

The **net production per unit dissipation** for the two equations,  $P_k$  and  $P_\omega$ , are defined by:

$$P_k = \frac{\alpha^*}{\beta^*} \left( \frac{\partial U / \partial y}{\omega} \right)^2 - 1 \quad (4.202)$$

$$P_\omega = \frac{\alpha \alpha^*}{\beta} \left( \frac{\partial U / \partial y}{\omega} \right)^2 - 1 \quad (4.203)$$

There are two important observations worthy of mention at this point. **First**, if the turbulence energy is zero, Equation (4.201) has a well-behaved solution. That is, when  $k = 0$ , the eddy viscosity vanishes and the  $\omega$  equation uncouples from the  $k$  equation. Consequently, the  $k$ - $\omega$  model has a nontrivial laminar-flow solution for  $\omega$ . **Second**, the signs of  $P_k$  and  $P_\omega$  determine whether  $k$  and  $\omega$  are amplified or reduced in magnitude. However, it is not obvious by inspection of Equations (4.202) and (4.203)

how the signs of these terms vary with Reynolds number as we move from the plate leading edge to points downstream. We can make the variation obvious by rewriting Equations (4.202) and (4.203) in terms of the Blasius transformation.

Before we introduce the Blasius transformation, we must determine the appropriate scaling for  $\omega$ . To do this, we note that close to the surface of a flat-plate boundary layer, the specific dissipation rate behaves according to [see Equation (4.158) and Table 4.5]:

$$\omega \rightarrow \frac{6\nu}{\beta y^2} \quad \text{as} \quad y \rightarrow 0 \quad (4.204)$$

In terms of the Blasius similarity variable,  $\eta$ , defined by

$$\eta = \frac{y}{\sqrt{\nu x/U_\infty}} \quad (4.205)$$

where  $U_\infty$  is freestream velocity, the asymptotic behavior of  $\omega$  approaching the surface is

$$\omega \rightarrow \frac{U_\infty}{x} \frac{6}{\beta \eta^2} \quad \text{as} \quad \eta \rightarrow 0 \quad (4.206)$$

Consequently, we conclude that the appropriate scaling for  $\omega$  in the Blasius boundary layer is given by

$$\omega = \frac{U_\infty}{x} W(x, \eta) \quad (4.207)$$

where  $W(x, \eta)$  is a dimensionless function to be determined as part of the solution. Hence, if we write the velocity in terms of dimensionless velocity,  $\mathcal{U}(x, \eta)$ , i.e.,

$$u = U_\infty \mathcal{U}(x, \eta) \quad (4.208)$$

the **net production per unit dissipation** terms become

$$P_k = \frac{\alpha^*}{\beta^*} Re_x \left( \frac{\partial \mathcal{U}/\partial \eta}{W} \right)^2 - 1 \quad (4.209)$$

$$P_\omega = \frac{\alpha \alpha^*}{\beta} Re_x \left( \frac{\partial \mathcal{U}/\partial \eta}{W} \right)^2 - 1 \quad (4.210)$$

Thus, both  $P_k$  and  $P_\omega$  increase linearly with Reynolds number,  $Re_x$ . From the exact laminar solution for  $\mathcal{U}(\eta)$  and  $W(\eta)$  [the  $x$  dependence vanishes for the Blasius boundary layer], the maximum value of the ratio of  $\partial \mathcal{U}/\partial \eta$  to  $W$  is given by

$$\left( \frac{\partial \mathcal{U}/\partial \eta}{W} \right)_{max} \approx \frac{1}{300} \quad (4.211)$$



The precise value of this ratio is actually a weak function of the freestream value of  $\omega$ , ranging between 0.0025 and 0.0040. The maximum occurs about midway through the boundary layer ( $y/\delta = 0.56$ ), a point above which the exact near-wall behavior of  $\omega$  [Equation (4.206)] does not hold. Hence, a complete boundary-layer solution is needed to determine the maximum ratio of  $\partial\mathcal{U}/\partial\eta$  to  $W$ .

As long as the eddy viscosity remains small compared to the molecular viscosity, we can specify the precise points where  $P_k$  and  $P_\omega$  change sign. Using Equation (4.211), we conclude that the sign changes occur at the following Reynolds numbers.

$$(Re_x)_k = 9 \cdot 10^4 \frac{\beta^*}{\alpha^*} \quad (4.212)$$

$$(Re_x)_\omega = 9 \cdot 10^4 \frac{\beta}{\alpha\alpha^*} \quad (4.213)$$

With no viscous modifications, the closure coefficients  $\alpha$ ,  $\alpha^*$ ,  $\beta$  and  $\beta^*$  are 5/9, 1, 3/40 and 9/100, respectively. Using these **fully turbulent** values, we find  $(Re_x)_k = 8,100$  and  $(Re_x)_\omega = 12,150$ . Thus, starting from laminar flow at the leading edge of a flat plate (see Figure 4.22), the following sequence of events occurs.

1. The computation starts in a laminar region with  $k = 0$  in the boundary layer and a small freestream value of  $k$ .
2. Initially, because  $P_k < 0$  and  $P_\omega < 0$ , dissipation of both  $k$  and  $\omega$  exceeds production. Turbulence energy is entrained from the freestream and spreads through the boundary layer by molecular diffusion. Neither  $k$  nor  $\omega$  is amplified and the boundary layer remains laminar.
3. At the **critical Reynolds number**,  $Re_{x_c} = 8,100$ , production overtakes dissipation in the  $k$  equation. Downstream of  $x_c$ , production exceeds dissipation in the  $k$  equation and turbulence energy is amplified. At some point in this process, the eddy viscosity grows rapidly and this corresponds to the transition point.
4.  $k$  continues to be amplified and, beyond  $Re_x = 12,150$  production overtakes dissipation in the  $\omega$  equation.  $\omega$  is now amplified and continues growing until a balance between production and dissipation is achieved in the  $k$  equation. When this balance is achieved, transition from laminar to turbulent flow is complete.

Consistent with experimental measurements, the entire process is very sensitive to the freestream value of  $k$ . There is also a sensitivity to the freestream value of  $\omega$ , although the sensitivity is more difficult to quantify.

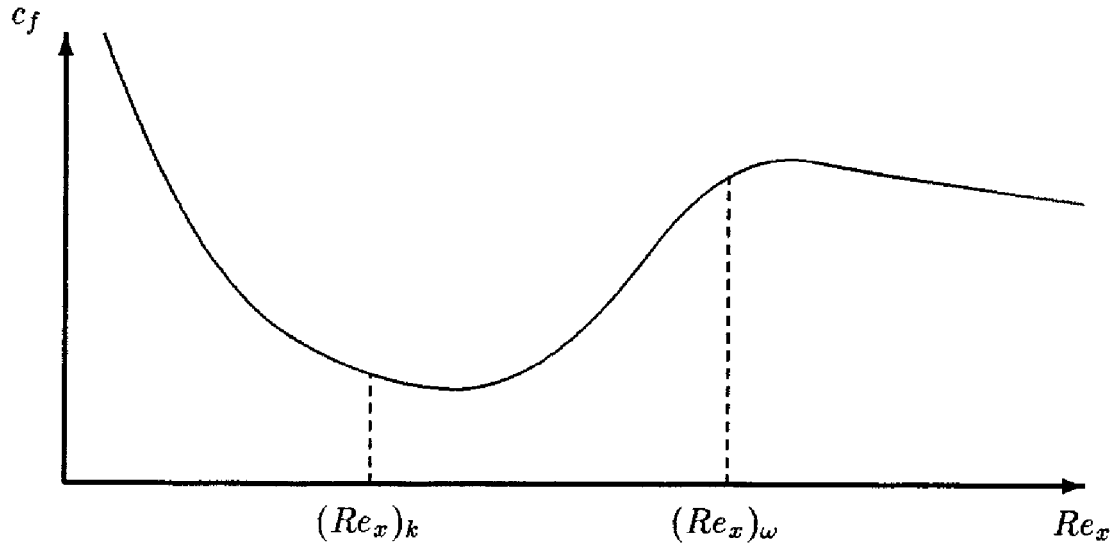


Figure 4.22: Skin friction variation for a boundary layer undergoing transition from laminar to turbulent flow.

Three key points are immediately obvious. **First**,  $k$  begins growing at a Reynolds number of 8,100. By contrast, linear-stability theory tells us that Tollmien-Schlichting waves begin forming in the Blasius boundary layer at a Reynolds number of 90,000. This is known as the **minimum critical Reynolds number**. Correspondingly, we find that the model predicts transition at much too low a Reynolds number. **Second**, inspection of Equations (4.212) and (4.213) shows that the width of the transition region is controlled by the ratio of  $\beta$  to  $\alpha\alpha^*$ . **Third**, transition will never occur if  $P_\omega$  reaches zero earlier than  $P_k$ . Thus, occurrence of transition requires

$$\alpha\alpha^* < \alpha^*\beta/\beta^* \quad \text{as} \quad Re_T \rightarrow 0 \quad (4.214)$$

This fact must be preserved in any viscous modification to the model. Our goal is to devise viscous modifications that depend only upon  $Re_T$ . As noted in the preceding subsection, this quantity is independent of flow geometry and thus preserves the universal nature of the model. We also proceed with two key objectives in mind. The most important objective is to match the **minimum critical Reynolds number**. Reference to Equation (4.212) shows that we must require

$$\beta^*/\alpha^* \rightarrow 1 \quad \text{as} \quad Re_T \rightarrow 0 \quad (4.215)$$

Our secondary objective is to achieve **asymptotic consistency** with the exact behavior of  $k$  and dissipation,  $\epsilon = \beta^*k\omega$ , approaching a solid boundary. That is, we would like to have  $k/y^2 \rightarrow \text{constant}$  and  $\epsilon/k \rightarrow 2\nu/y^2$

as  $y \rightarrow 0$ . Close to a solid boundary, the dissipation and molecular diffusion terms balance in both the  $k$  and  $\omega$  equations. The very-near-wall solution for  $\omega$  is given by Equation (4.204). The solution for  $k$  is of the form

$$k/y^n \rightarrow \text{constant} \quad \text{as} \quad y \rightarrow 0 \quad (4.216)$$

where  $n$  is given by

$$n = \frac{1}{2} \left[ 1 + \sqrt{1 + 24 \frac{\beta^*}{\beta}} \right] \quad (4.217)$$

Noting that dissipation is related to  $k$  and  $\omega$  by

$$\epsilon = \beta^* k \omega \quad (4.218)$$

we can achieve the desired asymptotic behavior of  $k$  provided

$$\beta^*/\beta \rightarrow 1/3 \quad \text{as} \quad Re_T \rightarrow 0 \quad (4.219)$$

Requiring this limiting behavior as  $Re_T \rightarrow 0$  is sufficient to achieve the desired asymptotic behavior as  $y \rightarrow 0$  since the eddy viscosity, and hence,  $Re_T$  vanishes at a solid boundary.

If we choose to have  $\beta$  constant for all values of  $Re_T$ , Equations (4.214), (4.215) and (4.219) are sufficient to determine the limiting values of  $\alpha^*$  and  $\beta^*$  and an upper bound for  $\alpha\alpha^*$  as turbulence Reynolds number becomes vanishingly small. Specifically, we find

$$\left. \begin{array}{l} \alpha\alpha^* < \beta \\ \alpha^* \rightarrow \beta/3 \\ \beta^* \rightarrow \beta/3 \end{array} \right\} \quad \text{as} \quad Re_T \rightarrow 0 \quad (4.220)$$

Wilcox and Rubesin (1980) make the equivalent of  $\alpha\alpha^*$  and  $\alpha^*$  in their  $k$ - $\omega^2$  model approach the same limiting value and obtain excellent agreement with measured transition width for incompressible boundary layers. Numerical experimentation with the  $k$ - $\omega$  model indicates the optimum choice for incompressible boundary layers is  $\alpha\alpha^* \rightarrow 0.74\beta$ , or

$$\alpha\alpha^* \rightarrow 1/18 \quad \text{as} \quad Re_T \rightarrow 0 \quad (4.221)$$

Wilcox (1992a) postulates the following functional dependencies upon  $Re_T$  that guarantee the limiting values in Equations (4.220) and (4.221), as well as the original fully turbulent values for  $Re_T \rightarrow \infty$ .

$$\alpha^* = \frac{\alpha_o^* + Re_T/R_k}{1 + Re_T/R_k} \quad (4.222)$$

$$\alpha = \frac{5}{9} \cdot \frac{\alpha_o + Re_T/R_\omega}{1 + Re_T/R_\omega} \cdot (\alpha^*)^{-1} \quad (4.223)$$

$$\beta^* = \frac{9}{100} \cdot \frac{5/18 + (Re_T/R_\beta)^4}{1 + (Re_T/R_\beta)^4} \quad (4.224)$$

$$\beta = 3/40, \quad \sigma^* = \sigma = 1/2, \quad \alpha_o^* = \beta/3, \quad \alpha_o = 1/10 \quad (4.225)$$

$$R_\beta = 8, \quad R_k = 6, \quad R_\omega = 27/10 \quad (4.226)$$

The quantity  $Re_T$  is turbulence Reynolds number defined by

$$Re_T = \frac{k}{\omega \nu} \quad (4.227)$$

The three coefficients  $R_\beta$ ,  $R_k$  and  $R_\omega$  control the rate at which the closure coefficients approach their fully-turbulent values. We can determine their values by using perturbation methods to analyze the viscous sublayer. Using the procedure discussed in Subsection 4.6.3, we can solve for the constant in the law of the wall,  $B$ . For given values of  $R_\beta$  and  $R_k$ , there is a unique value of  $R_\omega$  that yields a constant in the law of the wall of 5.0. For small values of  $R_\beta$  the peak value of  $k$  near the surface is close to the value achieved without viscous corrections, viz.,  $u_\tau^2/\sqrt{\beta^*}$ . As  $R_\beta$  increases, the maximum value of  $k$  near the surface increases. Comparison of computed sublayer structure with Direct Numerical Simulation (DNS) results of Mansour, Kim and Moin (1988) indicates the optimum choice for these three coefficients is as indicated in Equation (4.226).

The only flaw in the model's asymptotic consistency occurs in the Reynolds shear stress,  $\tau_{xy}$ . While the exact asymptotic behavior is  $\tau_{xy} \sim y^3$ , the model as formulated predicts  $\tau_{xy} \sim y^4$ . This discrepancy could easily be removed with another viscous modification. However, as will be shown later in this subsection, this is of no significant consequence. It has no obvious bearing on either the model's ability to predict transition or properties of interest in turbulent boundary layers. The additional complexity and uncertainty involved in achieving this subtle feature of the very-near-wall behavior of  $\tau_{xy}$  does not appear to be justified.

Given the information developed above, it is a simple matter to explain why little progress has been made in predicting transition with the  $k$ - $\epsilon$  model. The primary difficulties can be easily demonstrated by focusing upon incompressible boundary layers. If we use the standard form of the  $k$ - $\epsilon$  model, Equations (4.197) - (4.199) are replaced by

$$U \frac{\partial k}{\partial x} + V \frac{\partial k}{\partial y} = \nu_T \left( \frac{\partial U}{\partial y} \right)^2 - \epsilon + \frac{\partial}{\partial y} \left[ (\nu + \nu_T / \sigma_k) \frac{\partial k}{\partial y} \right] \quad (4.228)$$

$$U \frac{\partial \epsilon}{\partial x} + V \frac{\partial \epsilon}{\partial y} = C_{\epsilon 1} \frac{\epsilon}{k} \nu_T \left( \frac{\partial U}{\partial y} \right)^2 - C_{\epsilon 2} \frac{\epsilon^2}{k} + \frac{\partial}{\partial y} \left[ (\nu + \mu_T / \sigma_\epsilon) \frac{\partial \epsilon}{\partial y} \right] \quad (4.229)$$

$$\nu_T = C_\mu k^2 / \epsilon \quad (4.230)$$

One critical difference from the  $k$ - $\omega$  model is obvious by inspection of Equations (4.228) - (4.230). Specifically, if the turbulence energy is zero,  $\epsilon$  must also be zero. We cannot simply drop the eddy viscosity in the  $\epsilon$  equation because of the presence of  $k$  in the denominator of the  $\epsilon$  equation's dissipation term. The model does possess a laminar-flow solution for the ratio of  $\epsilon$  to  $k$ . That is, if we make the formal change of variables

$$\epsilon = C_\mu k \omega \quad (4.231)$$

and assume  $\nu_T \ll \nu$ , the following laminar-flow equation for  $\omega$  results.

$$U \frac{\partial \omega}{\partial x} + V \frac{\partial \omega}{\partial y} = (C_{\epsilon 1} - 1) f_\mu \left( \frac{\partial U}{\partial y} \right)^2 - (C_{\epsilon 2} - 1) C_\mu \omega^2 + \nu \frac{\partial^2 \omega}{\partial y^2} + \frac{2\nu}{k} \frac{\partial k}{\partial y} \frac{\partial \omega}{\partial y} \quad (4.232)$$

Equation (4.232) is nearly identical to the limiting form of Equation (4.198) for  $\nu_T / \nu \rightarrow 0$ . The only significant difference is the last term on the right-hand side of Equation (4.232). Except close to the surface where  $k$  must be exactly zero, this term is unlikely to have a significant effect on the solution for small nonzero values of  $k$ . However, in a numerical solution, products of dependent-variable gradients are generally destabilizing, and the problem can only be aggravated by having a coefficient inversely proportional to  $k$ . This is not an insurmountable problem. However, establishing starting conditions is clearly more difficult with the  $k$ - $\epsilon$  model than with the  $k$ - $\omega$  model.

Given the diverse nature of viscous modifications that have been proposed for the  $k$ - $\epsilon$  model, it is impossible to make any universal statements about why a specific model fails to predict realistic transition Reynolds numbers. Perhaps the strongest statement that can be made is, **no one has approached the problem from the transition point of view.** Most researchers have sought only to achieve asymptotic consistency (Subsection 4.9.1) and attempted transition predictions only as an afterthought.

We can gain some insight by examining the net production per unit dissipation terms for the  $k$  and  $\epsilon$  equations that are analogous to Equations (4.209) and (4.210), viz.,

$$P_k = \frac{f_\mu}{C_\mu} Re_x \left( \frac{\partial U / \partial \eta}{W} \right)^2 - 1 \quad (4.233)$$

$$P_\epsilon = \frac{C_{\epsilon 1} f_\mu}{C_{\epsilon 2} C_\mu} Re_x \left( \frac{\partial U / \partial \eta}{W} \right)^2 - 1 \quad (4.234)$$

**On the one hand**, without viscous damping, if we assume Equation (4.211) is valid, we find  $(Re_x)_k = 8,100$  and  $(Re_x)_\epsilon = 10,800$ . Consequently, as with the high-Reynolds-number version of the  $k$ - $\omega$  model, transition will occur at too low a Reynolds number. **On the other hand**, because  $C_\mu$ ,  $C_{\epsilon 2}$  and sometimes  $C_{\epsilon 1}$  are multiplied by functions of distance from the surface and/or functions of  $Re_T$  (c.f.  $f_\mu$ ,  $f_1$  and  $f_2$  in Subsection 4.9.1) in low-Reynolds-number  $k$ - $\epsilon$  models, we cannot simply use Equation (4.211). Furthermore, as discussed in the preceding subsection, some modelers add terms to the  $k$  and  $\epsilon$  equations in addition to damping the closure coefficients. Each set of values for the closure coefficients and additional terms must be used in solving Equation (4.232) to determine the laminar-flow solution for  $\epsilon/k$ . While it is clearly impossible to make a quantitative evaluation of all variants of the  $k$ - $\epsilon$  model, we can nevertheless make some general observations.

From the analysis of the  $k$ - $\omega$  model, it is obvious that having  $f_\mu < 1$  will tend to delay transition. Virtually all modelers implement an  $f_\mu$  that will accomplish this end. However, the modifications of Jones and Launder (1972), Chien (1982), and Lam and Bremhorst (1981), for example, damp  $C_{\epsilon 2}$  to the extent that  $(Re_x)_\epsilon$  is smaller than  $(Re_x)_k$ . This is the opposite of what is needed and will have an undesirable effect on both the onset of and the extent of the transition region.

This discussion is not intended as an exhaustive survey of the numerous low-Reynolds-number versions of the  $k$ - $\epsilon$  model. Rather, it is intended to illustrate how difficult it is to apply the model to the transition problem. Given enough additional closure coefficients and damping functions, the  $k$ - $\epsilon$  model can probably be modified to permit satisfactory transition predictions. However, even if this is done, establishing starting conditions will ultimately require a solution to Equation (4.232). That is, to initialize the computation, we must effectively transform to the  $k$ - $\omega$  model. Since this is the natural starting point, it seems illogical to perform subsequent computations in terms of  $k$  and  $\epsilon$ .

Figure 4.23 compares computed channel-flow skin friction,  $c_f$ , with the Halleen and Johnston (1967) correlation [see Equation (3.137)] for Reynolds

number based on channel height,  $H$ , and average velocity ranging from  $10^3$  to  $10^5$  using the  $k$ - $\omega$  model. As shown, computed  $c_f$  differs from the correlation by less than 3% except at the lowest Reynolds number shown where the correlation probably is inaccurate. Velocity, Reynolds shear stress, and turbulence kinetic energy profiles differ by less than 7%. Most notably, the model predicts the peak value of  $k$  near the channel wall to within 4% of the DNS value. The low-Reynolds-number modifications have been designed to capture this feature. Additionally, approaching the surface, the turbulence-energy production,  $\tau_{xy}\partial U/\partial y$ , and dissipation,  $\epsilon$ , are within 10% of the DNS results except very close to the surface.

Figure 4.24 compares computed pipe flow  $c_f$  with Prandtl's universal law of friction [see Equation (3.138)]. Reynolds number based on pipe diameter,  $D$ , and average velocity varies from  $10^3$  to  $10^6$ . As with channel flow, computed  $c_f$  falls within 5% of the correlation except at the lowest Reynolds number shown where the correlation is likely to be in error.

Computed and measured velocity and Reynolds shear stress profiles differ by less than 8%. As with channel flow, computed and measured turbulence kinetic energy differ by about 5% including close to the surface where the sharp peak occurs. Note that, at this high a Reynolds number, the  $k$  profile has a sharp spike near  $y = 0$  and this feature is captured in the computations. Except very close to the surface, computed turbulence energy production and dissipation differ from measured values by less than 10%. This may actually be a desirable result. That is, some controversy exists about the accuracy of Laufer's dissipation measurements close to the surface.

Turning now to transition, Figure 4.25 compares computed and measured transition Reynolds number,  $Re_{\theta_t}$ , for an incompressible flat-plate boundary layer. We define the transition Reynolds number as the point where the skin friction achieves its minimum value. Results are displayed as a function of freestream turbulence intensity,  $T'$ , defined by

$$T' = 100 \sqrt{\frac{2}{3} \frac{k_e}{U_e^2}} \quad (4.235)$$

where subscript  $e$  denotes the value at the boundary-layer edge. As shown, consistent with the data compiled by Dryden (1959),  $Re_{\theta_t}$  increases as the freestream intensity decreases. Because  $\omega$  can be thought of as an averaged frequency of the freestream turbulence, it is reasonable to expect the predictions to be sensitive to the freestream value of  $\omega$ . To assess the effect, the freestream value of the turbulence length scale  $\ell = k^{1/2}/\omega$  has been varied from  $.001\delta$  to  $.100\delta$  where  $\delta$  is boundary-layer thickness. As shown, computed  $Re_{\theta_t}$  values bracket virtually all of the data. Unlike the situation for

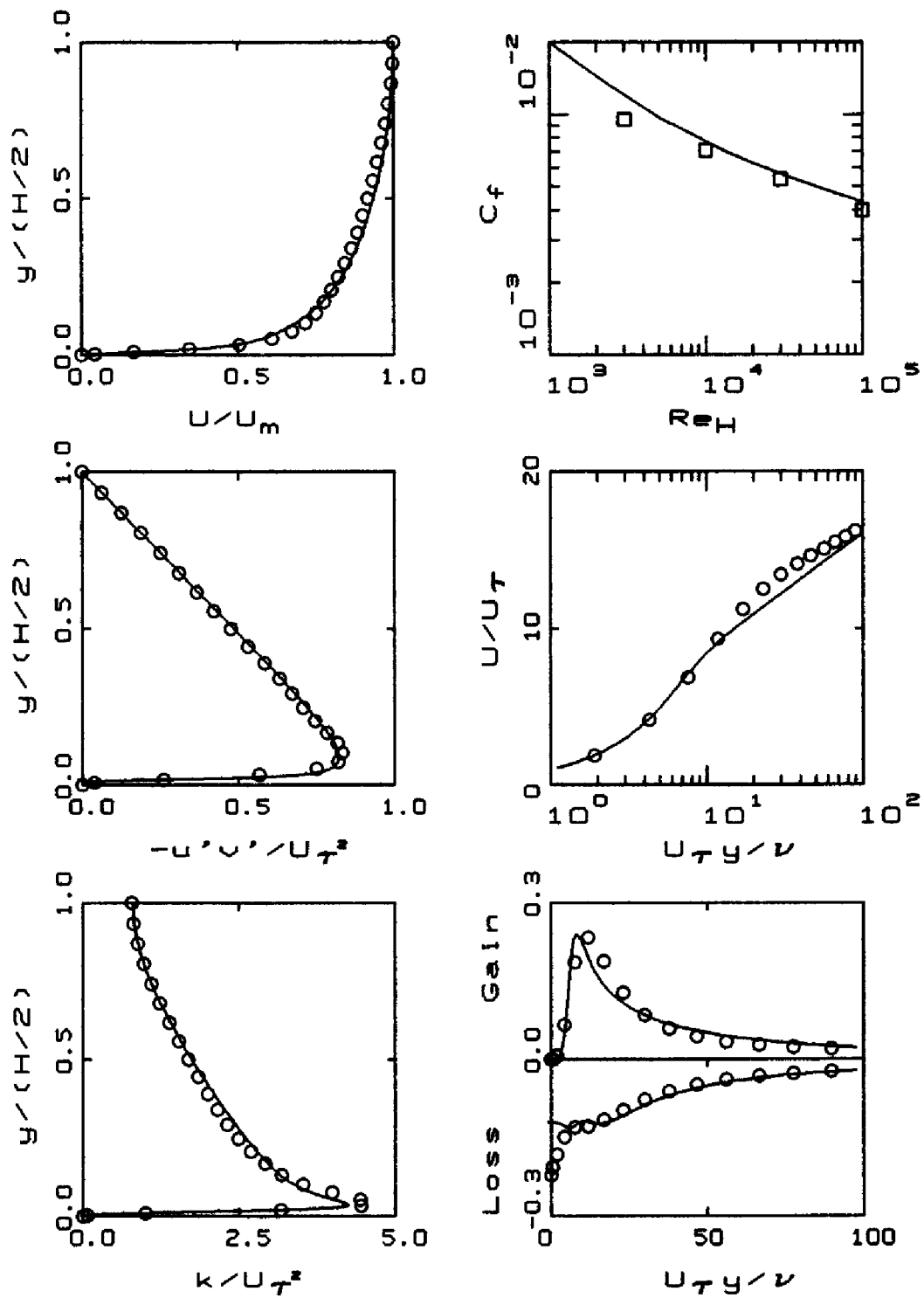


Figure 4.23: Comparison of computed and measured channel-flow properties,  $Re_H = 13,750$ . — Low-Reynolds-number  $k-\omega$  model;  $\circ$  Mansour et al. (DNS);  $\square$  Halleen-Johnston correlation.



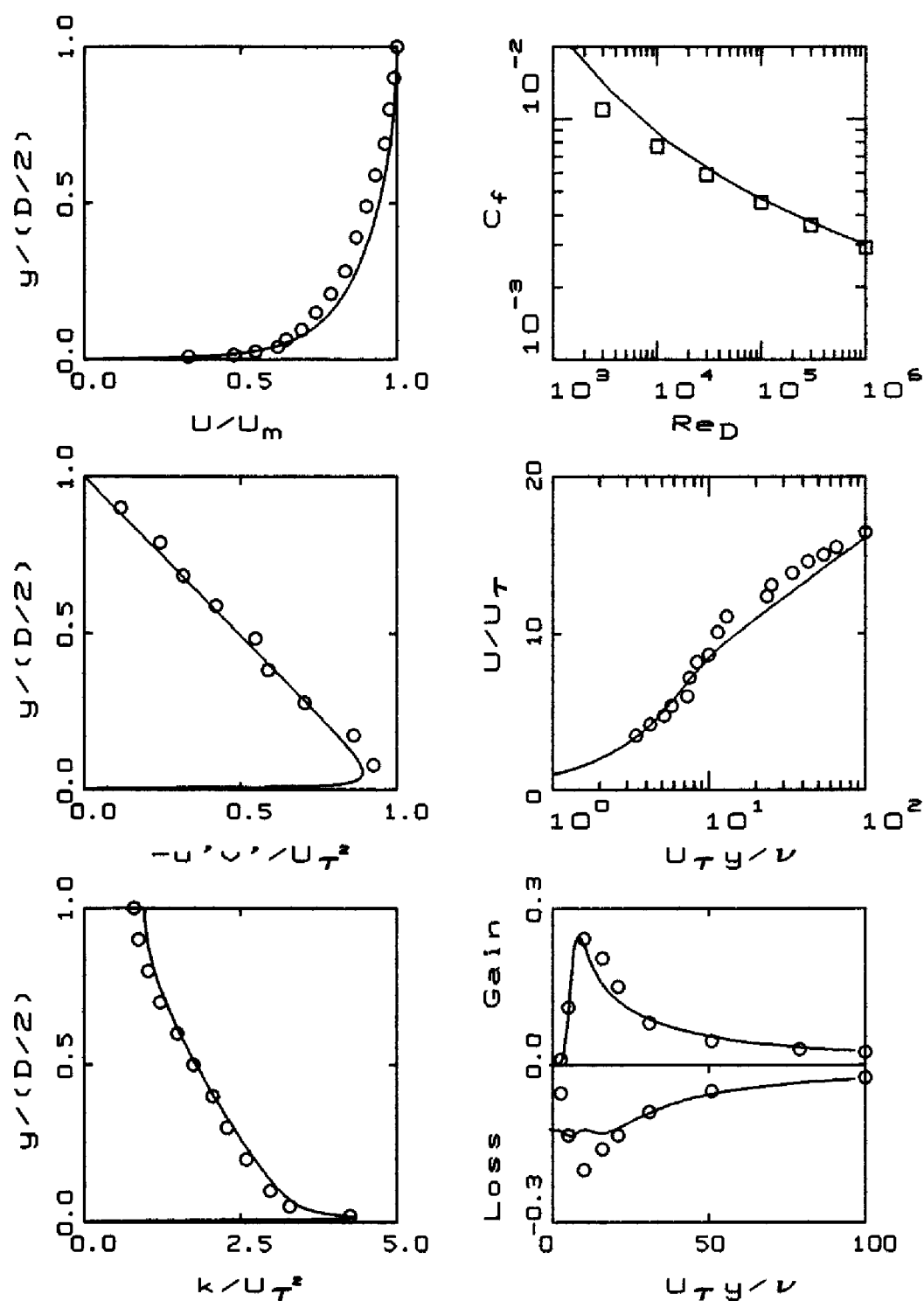


Figure 4.24: Comparison of computed and measured pipe-flow properties,  $Re_D = 40,000$ . — Low-Reynolds-number  $k-\omega$  model;  $\circ$  Laufer;  $\square$  Prandtl correlation.

free shear flows, the  $k$ - $\omega$  model's sensitivity to the freestream value of  $\omega$  is a **desirable** feature for transition applications. Physical transition location is not simply a function of  $T'$ , but rather is frequency dependent. While it is unclear how the freestream value of  $\omega$  should be specified, consistent with measurements, the model is not confined to a single transition location for a given  $T'$  regardless of the frequency of the disturbance.

Figure 4.26 compares computed width of the transition region with measurements of Dhawan and Narasimha (1958), Schubauer and Skramstad (1948), and Fisher and Dougherty (1982). We define transition width,  $\Delta x_t$ , as the distance between minimum and maximum skin-friction points. The computed width,  $Re_{\Delta x_t}$ , falls within experimental data scatter for  $10^4 < Re_{x_t} < 10^7$ .  $\Delta x_t$  is unaffected by the freestream value of  $\omega$ .

While these transition results are interesting, keep in mind that transition is a complicated phenomenon. Transition is triggered by a disturbance in a boundary layer only if the frequency of the disturbance falls in a specific band. Reynolds averaging has masked all spectral effects, and all the model can represent with  $k$  and  $\omega$  is the intensity of the disturbance and an average frequency. Hence, it is possible for the turbulence model to predict transition when it shouldn't occur. The model equations thus are sensible in the transition context only if the triggering disturbance is broad band, i.e., contains all frequencies.

Additionally, we have only guaranteed that the point where  $k$  is first amplified matches the minimum critical Reynolds number for the incompressible, flat-plate boundary layer. To simulate transition with complicating effects such as pressure gradient, surface heat transfer, surface roughness, compressibility, etc., the values of  $\alpha_o^*$  and  $\alpha_o$  must change [see Wilcox (1977)]. Their values can be deduced from linear-stability theory results, or perhaps from a correlation based on stability theory. Nevertheless, some information must be provided regarding the minimum critical Reynolds number for each new application.

Perhaps the most practical way to use the model for transitional flows is in describing the transitional region. Of course, the question of sensitivity to spectral effects in the transition region must be raised. Using linear-stability computations, Wilcox (1981a) shows that after the initial disturbance has grown to a factor of  $e^4$  times its initial value, the turbulence model closure coefficients lose all memory of spectral effects. Thus, we can conclude that not far downstream of the minimum critical Reynolds number, Reynolds averaging is sensible.

As a final comment regarding low-Reynolds-number corrections for two-equation turbulence models, note that the complexity of the model increases significantly. The Standard  $k$ - $\omega$  model has just 5 closure coefficients. The low-Reynolds-number version described in this subsection has 10 closure

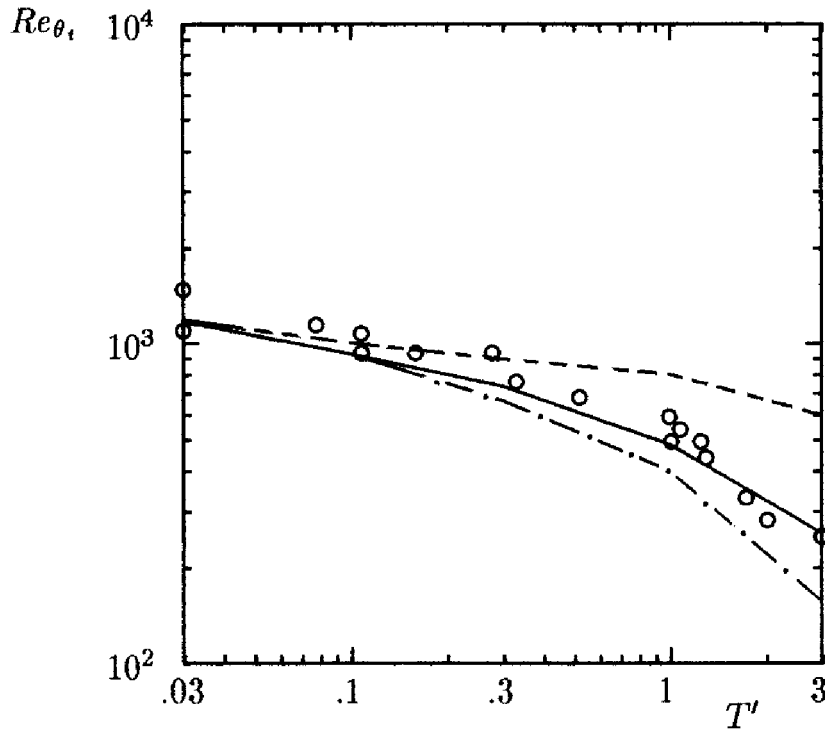


Figure 4.25: Transition location for an incompressible flat-plate boundary layer; - - -  $\ell/\delta = .001$ ; —  $\ell/\delta = .010$ ; - · -  $\ell/\delta = .100$ ;  $\circ$  Dryden.

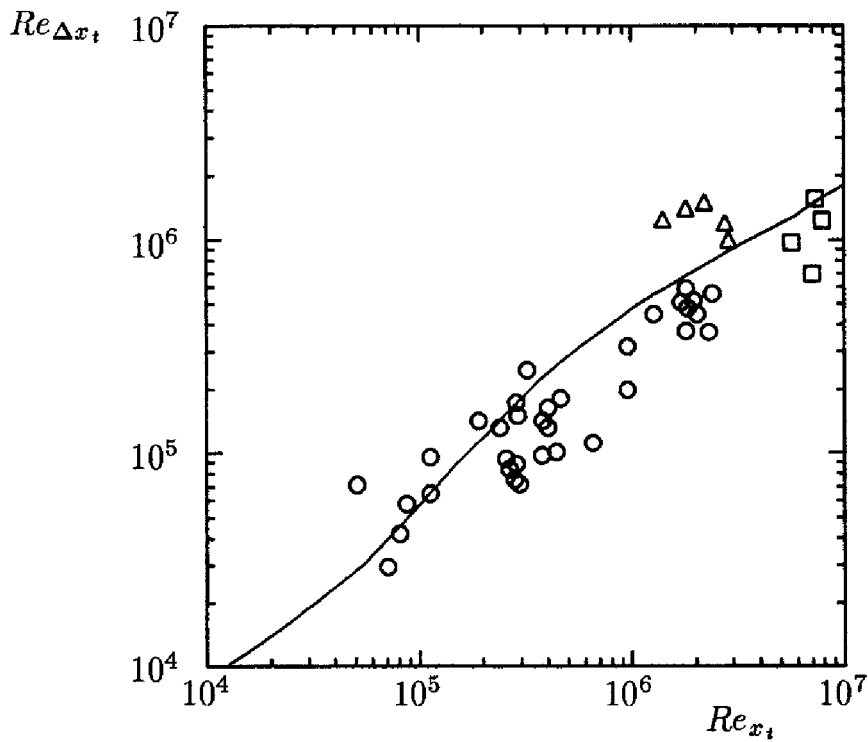


Figure 4.26: Transition width for an incompressible flat-plate boundary layer; —  $k-\omega$  model;  $\circ$  Dhawan-Narasimha;  $\Delta$  Schubauer-Skramstad;  $\square$  Fisher-Dougherty.

coefficients and 3 empirical damping functions. The various low-Reynolds-number models discussed in Subsection 4.9.1 involve a similar increase in the number of closure coefficients and damping functions. If viscous effects are insignificant for a given application, it is advisable to use the simpler high-Reynolds-number version of the model. In the case of the  $k-\epsilon$  model, if you need to integrate through the viscous sublayer, you have no choice but to use one of the low-Reynolds-number models, preferably one that yields a satisfactory solution for simple flows such as the incompressible flat-plate boundary layer. In the case of the  $k-\omega$  model, integration through the sublayer can be done without introducing the viscous corrections, and there is virtually no difference in model-predicted skin friction and velocity profiles with and without viscous corrections for boundary layers.

## 4.10 Separated Flows

Turning to separated flows, we first consider the axisymmetric flow with strong adverse pressure gradient that has been experimentally investigated by Driver (1991). Figure 4.27 compares Menter's (1992b) computed and measured skin friction and surface pressure for the  $k-\omega$  model. As shown, the  $k-\omega$  model yields results almost as close to measurements as those obtained with the Johnson-King model [see Figure 3.19], although pressure downstream of reattachment is somewhat higher than measured. Results are clearly much closer to measurements than those obtained with the Baldwin-Lomax and Baldwin-Barth models.

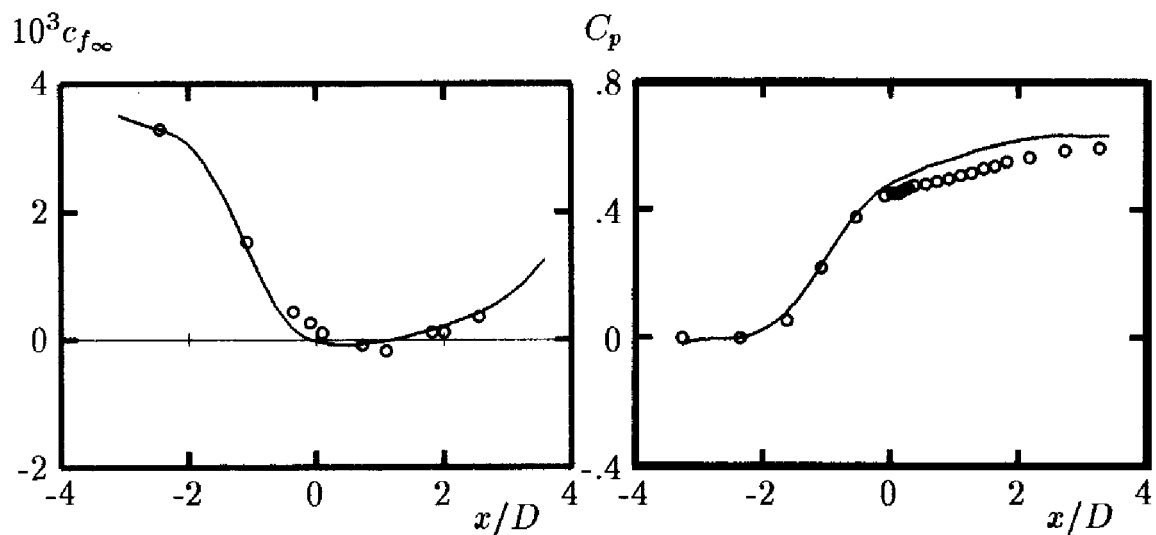
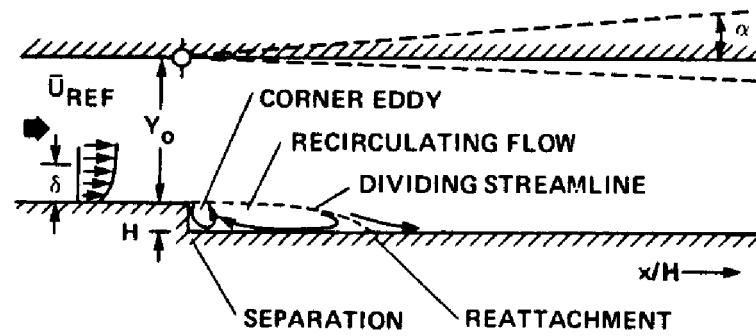


Figure 4.27: Computed and measured flow properties for Driver's separated flow; —  $k-\omega$  model;  $\circ$  Driver.



TUNNEL GEOMETRY:  $H = 1.27 \text{ cm}$ ,  $y_0 = 8H$

TUNNEL SPAN:  $12H$

TOP-WALL ANGLES:  $-2^\circ \leq \alpha \leq 10^\circ$

INLET CONDITIONS:  $U_{\text{REF}} = 44.2 \text{ m/sec}$ ,  $M_{\text{REF}} = 0.128$

$\delta_{\text{BL}} = 1.9 \text{ cm}$ ,  $Re_\theta = 5000$

Figure 4.28: Backward-facing step flow geometry and inlet conditions for the Driver-Seegmiller (1985) experiments. [From Driver and Seegmiller (1985) — Copyright © AIAA 1985 — Used with permission.]

The backward-facing step (Figure 4.28) is a popular test case for turbulence models because the geometry is simple. Additionally, separation occurs at the sharp corner so the flow is easier to predict than a flow for which the separation point is unknown a priori. Figure 4.29 compares computed and measured [Driver and Seegmiller (1985)] skin friction for backstep flow with the upper channel wall inclined to the lower wall at  $0^\circ$  and  $6^\circ$ . Computed results are shown for the Standard  $k-\omega$  model and for the Standard  $k-\epsilon$  model with wall functions; neither model includes viscous corrections. As summarized in Table 4.6, the  $k-\epsilon$  model predicts reattachment well upstream of the measured point for both cases, while the  $k-\omega$  model is within 3% of the measured location for both cases.

Table 4.6: Backstep Reattachment Length

Model	Reference	$\alpha = 0^\circ$	$\alpha = 6^\circ$
$k-\epsilon$	Launder-Sharma (1974)	5.20	5.50
$k-\omega$	Wilcox (1988a)	6.40	8.45
Measured	Driver-Seegmiller (1985)	6.20	8.10

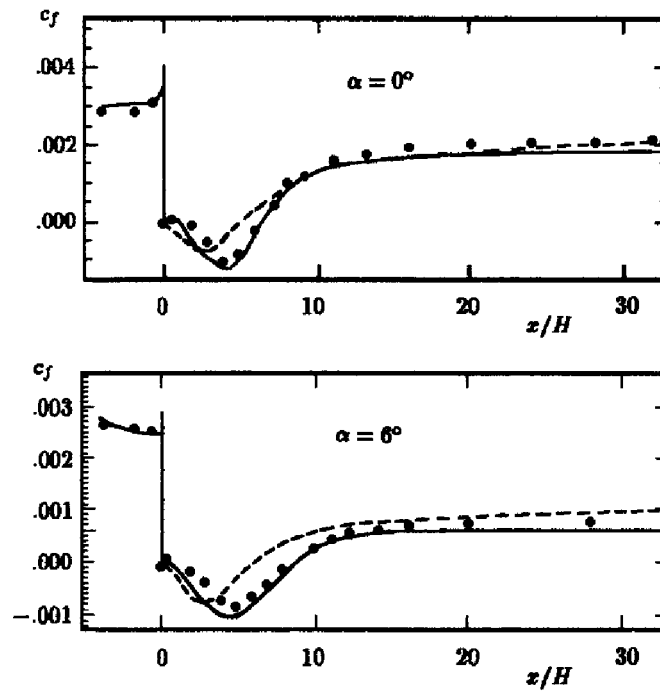


Figure 4.29: Computed and measured skin friction for flow past a backward-facing step; —  $k\text{-}\omega$  model; - -  $k\text{-}\epsilon$  model; • Driver-Seegmiller data. [Partially taken with permission from Menter (1992c).]

Many researchers have proposed modifications to the  $k\text{-}\epsilon$  model aimed at improving its predictions for this flow. Driver and Seegmiller (1985), for example, compare four different versions of the model with their experimental data. We will discuss some of the proposed fixes for the  $k\text{-}\epsilon$  model in Chapter 6. By contrast, the  $k\text{-}\omega$  model's solution for flow past the backward-facing step is satisfactory with no special modifications.

Han (1989) has applied the  $k\text{-}\epsilon$  model with wall functions to flow past a simplified three-dimensional bluff body with a ground plane. The object considered is known as Ahmed's body [Ahmed et al. (1984)] and serves as a simplified automobile-like geometry. In his computations, Han considers a series of afterbody slant angles. Figure 4.30(a) illustrates the shape of Ahmed's body with a  $30^\circ$  slant angle afterbody. Figure 4.30(b) compares computed and measured surface pressure contours on the rear-end surface for a  $12.5^\circ$  slant angle. As shown, computed pressure contours are similar on the slanted surface, but quite different on the vertical base. For slant angles up to  $20^\circ$ , the computed base pressures are significantly lower than measured. Consequently, the computed drag coefficient is about 30% higher than measured. Considering how poorly the  $k\text{-}\epsilon$  model performs for

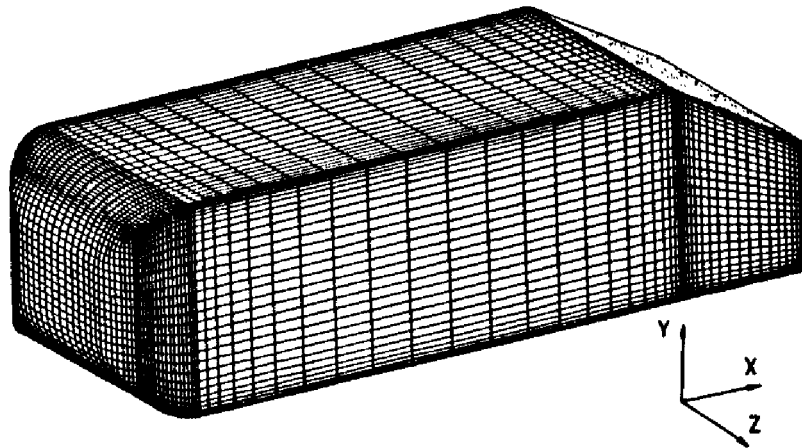
boundary layers in adverse pressure gradient and for the two-dimensional backward-facing step, it is not surprising that the model would predict such a large difference from the measured drag in this extremely complicated three-dimensional, massively-separated flow.

This is a quintessential example of how important turbulence modeling is to Computational Fluid Dynamics. Recall that there are three key elements to CFD, viz., the numerical algorithm, the grid and the turbulence model. Han uses an efficient numerical procedure and demonstrates grid convergence of his solutions. Han's computational tools also include state-of-the-art grid-generation procedures. Han's research efforts on this problem are exemplary on both counts. However, using the  $k$ - $\epsilon$  model undermines the entire computation for the following reasons. Because the model fails to respond in a physically realistic manner to the adverse pressure gradient on the rear-end surface, the predicted skin friction is too high. This means the vorticity at the surface is too large, so that too much vorticity diffuses from the surface. This vorticity is swept into the main flow and too strong a vortex forms when the flow separates. This, of course, reduces the base pressure. Thus, the  $k$ - $\epsilon$  model's inability to accurately respond to adverse pressure gradient distorts the entire flowfield.

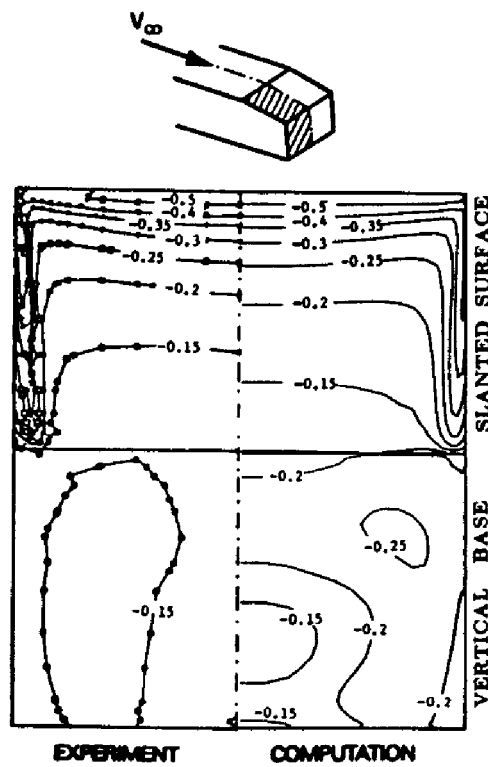
## 4.11 Range of Applicability

Turbulence-energy equation models include both **incomplete** one-equation models and **complete** two-equation models. As discussed in Section 4.2, only a modest advantage is gained in using a one-equation model rather than an algebraic model. The primary difficulty is the need to specify the length scale for each new application. There is no natural way to accommodate an abrupt change from a wall-bounded flow to a free shear flow such as near an airfoil trailing edge or beyond the trunk lid of an automobile. The only real advantage of using a one-equation model rather than a two-equation model stems from the relative difficulty often encountered in solving the model equations numerically. One-equation models tend to be nearly as well behaved as algebraic models. By contrast, two-equation models, especially the  $k$ - $\epsilon$  model, are often very difficult to solve. However, the user must establish his or her priorities on a key issue. Specifically, the user must decide if it is more desirable to have an easy-to-implement, inaccurate model, or a more-difficult-to-implement, accurate model. Those preferring the latter should probably select a two-equation model.

Certainly the  $k$ - $\epsilon$  model is the most widely used two-equation model. It has been applied to many flows with varying degrees of success. Unfortunately, it is inaccurate for flows with adverse pressure gradient and



(a) Body geometry and surface grid



(b) Static-pressure contours

Figure 4.30: Flow past Ahmed's body. [From Han (1989) — Copyright © AIAA 1989 — Used with permission.]



that poses a serious limitation to its general utility. The model is also extremely difficult to integrate through the viscous sublayer and requires viscous corrections to simply reproduce the law of the wall for an incompressible flat-plate boundary layer. No consensus has been achieved on the optimum form of the viscous corrections as evidenced by the number of researchers who have created low-Reynolds-number versions of the model (see Subsection 4.9.1). While the model can be fine tuned for a given application, it is not clear that this represents an improvement over algebraic models. The primary shortcoming of algebraic models is their need of fine tuning for each new application. While saying the  $k$ - $\epsilon$  model always needs such fine tuning would be a bit exaggerated, it still remains that such tuning is too often needed.

The  $k$ - $\omega$  model, although not as popular as the  $k$ - $\epsilon$  model, enjoys several advantages. Most importantly, the model is very accurate for two-dimensional boundary layers with variable pressure gradient (both adverse and favorable). Also, without any special viscous corrections, the model can be easily integrated through the viscous sublayer. Finally, for the limited cases tried to date, the model appears to match measured properties of recirculating flows with no changes to the basic model and its closure coefficients. With viscous corrections included, the  $k$ - $\omega$  model accurately reproduces subtle features of turbulence kinetic energy behavior close to a solid boundary and even describes boundary-layer transition reasonably well. The only weakness of the  $k$ - $\omega$  model appears to be its sensitivity to freestream boundary conditions for free shear flows. While the  $k$ - $\epsilon$  model does not share this sensitivity, its predicted spreading rate matches measurements only for the plane jet.

Other two-equation models have been created, but they have had even less use than the  $k$ - $\omega$  model. Before such models can be taken seriously, they should be tested for simple incompressible boundary layers with adverse pressure gradient. How many interesting flows are there, after all, with constant pressure?

While two-equation models, especially the  $k$ - $\omega$  model, are far more general than less complex models, they nevertheless fail in some applications. In Chapter 5, we will see that these models are unreliable for boundary-layer separation induced by interaction with a shock wave. In Chapter 6, we will see that two-equation models are inaccurate for flows over curved surfaces. Also, two-equation models as presented in this chapter cannot predict secondary motions in noncircular duct flow. In all three of these examples, the difficulty can be traced to the Boussinesq eddy-viscosity approximation.

## Problems

**4.1** Verify that the exact equation for the dissipation,  $\epsilon$ , is given by Equation (4.39). That is, derive the equation that follows from taking the following moment of the Navier-Stokes equation.

$$\overline{2\nu \frac{\partial u'_i}{\partial x_j} \frac{\partial}{\partial x_j} [\mathcal{N}(u_i)]} = 0$$

where  $\mathcal{N}(u_i)$  is the Navier-Stokes operator defined in Equation (2.26).

**4.2** Starting with Equations (4.4) and (4.39), define  $\epsilon = \beta^* \omega k$  and derive an “exact”  $\omega$  equation.

**4.3** Derive the exact equation for the **enstrophy**,  $\omega^2$ , defined by

$$\omega^2 \equiv \frac{1}{2} \overline{\omega'_i \omega'_i} \quad \text{where} \quad \omega'_i = \epsilon_{ijk} \partial u'_k / \partial x_j$$

That is,  $\omega'_i$  is the fluctuating vorticity. **HINT:** First derive the equation for the vorticity, multiply by  $\omega'_i$ , and time average.

**4.4** We wish to create a new two-equation turbulence model. Our first variable is turbulence kinetic energy,  $k$ , while our second variable is the “eddy acceleration,”  $a$ . Assuming  $a$  has dimensions (length)/(time)<sup>2</sup>, use dimensional arguments to deduce plausible algebraic dependencies of eddy viscosity,  $\nu_T$ , turbulence energy dissipation rate,  $\epsilon$ , and turbulence length scale,  $\ell$ , upon  $k$  and  $a$ .

**4.5** Beginning with the  $k$ - $\omega$  model and with  $\sigma = \sigma^*$ , make the formal change of variables  $\epsilon = \beta^* \omega k$  and derive the implied  $k$ - $\epsilon$  model. Express your final results in standard  $k$ - $\epsilon$  model notation and determine the implied values for  $C_\mu$ ,  $C_{\epsilon 1}$ ,  $C_{\epsilon 2}$ ,  $\sigma_k$  and  $\sigma_\epsilon$  in terms of  $\alpha$ ,  $\beta$ ,  $\beta^*$ ,  $\sigma$  and  $\sigma^*$ .

**4.6** Beginning with the  $k$ - $\epsilon$  model, make the formal change of variables  $\epsilon = C_\mu \omega k$  and derive the implied  $k$ - $\omega$  model. Express your final results in standard  $k$ - $\omega$  model notation and determine the implied values for  $\alpha$ ,  $\beta$ ,  $\beta^*$ ,  $\sigma$  and  $\sigma^*$  in terms of  $C_\mu$ ,  $C_{\epsilon 1}$ ,  $C_{\epsilon 2}$ ,  $\sigma_k$  and  $\sigma_\epsilon$ .

**4.7** Simplify the  $k$ - $\epsilon$ ,  $k$ - $k\ell$ ,  $k$ - $k\tau$  and  $k$ - $\tau$  models for homogeneous, isotropic turbulence. Determine the asymptotic decay rate for  $k$  as a function of the closure coefficient values quoted in Equations (4.43), (4.49), (4.56) and (4.59). Make a table of your results and include the decay rate of  $t^{-1.20}$  for the  $k$ - $\omega$  model. (**NOTE:** You can ignore the  $(\ell/y)^6$  contribution to  $C_{L2}$  for the  $k$ - $k\ell$  model.)

**4.8** Simplify the  $k$ - $\epsilon$ ,  $k$ - $k\ell$ ,  $k$ - $k\tau$  and  $k$ - $\tau$  models for the log layer. Determine the value of Kármán's constant,  $\kappa$ , implied by the closure coefficient values quoted in Equations (4.43), (4.49), (4.56) and (4.59). Make a table of your results and include the value 0.41 for the  $k$ - $\omega$  model. **NOTE:** For all models, assume a solution of the form  $dU/dy = u_\tau/(\kappa y)$ ,  $k = u_\tau^2/\sqrt{C_\mu}$  and  $\nu_T = \kappa u_\tau y$ . Also,  $C_\mu = C_D$  for the  $k$ - $k\ell$  model.

**4.9** Beginning with Equations (4.73), derive the self-similar form of the  $k$ - $\omega$  model equations for the mixing layer between a fast stream moving with velocity  $U_1$  and a slow stream with velocity  $U_2$ .

- (a) Assuming a streamfunction of the form  $\psi(x, y) = U_1 x F(\eta)$ , transform the momentum equation, and verify that  $\mathcal{V}$  is as given in Table 4.1.
- (b) Transform the equations for  $k$  and  $\omega$ .
- (c) State the boundary conditions on  $\mathcal{U}$  and  $K$  for  $|\eta| \rightarrow \infty$  and for  $\mathcal{V}(0)$ . Assume  $k \rightarrow 0$  as  $|y| \rightarrow \infty$ .
- (d) Verify that if  $\omega \neq 0$  in the freestream, the only boundary conditions consistent with the similarity solution are:

$$W(\eta) \rightarrow \begin{cases} \frac{1}{\beta}, & \eta \rightarrow +\infty \\ \frac{U_1/U_2}{\beta}, & \eta \rightarrow -\infty \end{cases}$$

**4.10** Exercise Programs WAKE, MIXER and JET (Appendix C) and verify the results quoted in Table 4.2. Cover the following ranges of values for WTIN:

Far Wake	$10^{-6} \leq \text{WTIN} \leq 1$
Mixing Layer	$10^{-6} \leq \text{WTIN} \leq 1$
Plane Jet	$10^{-6} \leq \text{WTIN} \leq 10$
Round Jet	$10^{-6} \leq \text{WTIN} \leq 100$

**4.11** Derive Equation (4.118).

**4.12** Demonstrate the integral constraint on the defect-layer solution, Equation (4.124).

**4.13** Determine the shape factor to  $O(u_\tau/U_e)$  according to the defect-layer solution. Express your answer in terms of an integral involving  $U_1(\eta)$ .

**4.14** For the  $k$ - $\omega$  model, very close to the surface and deep within the viscous sublayer, dissipation balances molecular diffusion in the  $\omega$  equation. Assuming a solution of the form  $\omega = \omega_w / (1 + Ay)^2$ , solve this equation for  $\omega = \omega_w$  at  $y = 0$ . Determine the limiting form of the solution as  $\omega_w \rightarrow \infty$ .

**4.15** Consider a flow with freestream velocity  $U_\infty$  past a wavy wall whose shape is

$$y = \frac{1}{2}k_R \sin\left(\frac{2\pi x}{Nk_R}\right)$$

where  $k_R$  is the peak to valley amplitude and  $Nk_R$  is wavelength. The linearized incompressible solution valid for  $N \gg 1$  is  $U = U_\infty + u'$ ,  $V = v'$  where

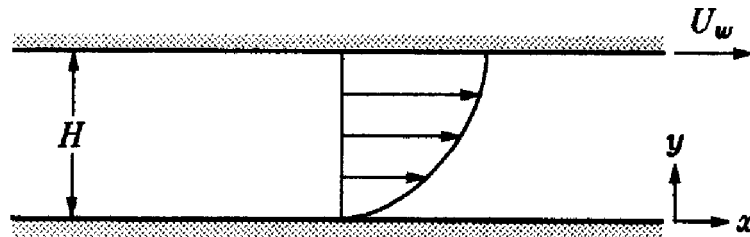
$$u' = \frac{\pi U}{N} \exp\left(-\frac{2\pi y}{Nk_R}\right) \sin\left(\frac{2\pi y}{Nk_R}\right)$$

$$v' = \frac{\pi U}{N} \exp\left(-\frac{2\pi y}{Nk_R}\right) \cos\left(\frac{2\pi y}{Nk_R}\right)$$

Making an analogy between this linearized solution and the fluctuating velocity field in a turbulent flow, compute the specific dissipation rate,  $\omega = \epsilon / (\beta^* k)$ . Ignore contributions from the other fluctuating velocity component,  $w'$ .

**4.16** Using Program SUBLAY (Appendix C), determine the variation of the constant  $B$  in the law of the wall for the  $k$ - $\omega$  model with the surface value of  $\omega$ . Do your computations with ( $nvisc = 0$ ) and without ( $nvisc = 1$ ) viscous modifications. Let  $\omega_w^+$  assume the values 1, 3, 10, 30, 100, 300, 1000 and  $\infty$ . Be sure to use the appropriate value for input parameter  $iruff$ . Present your results in tabular form.

**4.17** Consider incompressible Couette flow with constant pressure, i.e., flow between two parallel plates separated by a distance  $H$ , the lower at rest and the upper moving with constant velocity  $U_w$ .



- (a) Assuming the plates are infinite in extent, simplify the conservation of mass and momentum equations and verify that

$$(\nu + \nu_T) \frac{dU}{dy} = u_\tau^2$$

- (b) Now ignore molecular viscosity. What boundary condition on  $U$  is appropriate at the lower plate?
- (c) Introducing the mixing length given by

$$\ell_{mix} = \kappa y(1 - y/H)$$

solve for the velocity across the channel. **HINT: Using partial fractions:**

$$\frac{1}{y(1 - y/H)} = \frac{1}{y} + \frac{1}{(H - y)}$$

**Don't forget to use the boundary condition stated in Part (b).**

- (d) Develop a relation between friction velocity,  $u_\tau$ , and the average velocity,

$$U_{avg} = \frac{1}{H} \int_0^H U(y) dy$$

- (e) Using the  $k$ - $\omega$  model, simplify the equations for  $k$  and  $\omega$  with the same assumptions made in Parts (a) and (b).
- (f) Deduce the equations for  $k$  and  $\omega$  that follow from changing independent variables from  $y$  to  $U$  so that

$$\nu_T \frac{d}{dy} = u_\tau^2 \frac{d}{dU}$$

- (g) Assuming  $k = u_\tau^2 / \sqrt{\beta^*}$ , simplify the equation for  $\omega$ . **NOTE:** You might want to use the fact that  $(\beta - \alpha\beta^*) = \sigma\sqrt{\beta^*}\kappa^2$ .

**4.18** For incompressible, laminar Couette flow, we know that the velocity is given by

$$U = U_w \frac{y}{H}$$

where  $U_w$  is the velocity of the moving wall,  $y$  is distance from the stationary wall, and  $H$  is the distance between the walls.

- (a) What is the maximum Reynolds number,

$$Re_{H_c} = U_w H / \nu$$

at which the flow remains laminar according to the high-Reynolds-number version of the  $k$ - $\omega$  model? To arrive at your answer, you may assume that

$$\omega = \begin{cases} \frac{6\nu}{\beta y^2}, & 0 \leq y \leq H/2 \\ \frac{6\nu}{\beta(H-y)^2}, & H/2 \leq y \leq H \end{cases}$$

- (b) Above what Reynolds number is  $\omega$  amplified?

**4.19** This problem studies the effect of viscous-modification closure coefficients for the  $k$ - $\omega$  model using Program SUBLAY (Appendix C).

- (a) Modify Subroutine START to permit inputting the values of  $R_k$  and  $R_\omega$  (program variables  $rk$  and  $rw$ ). Determine the value of  $R_\omega$  that yields a smooth-wall constant in the law of the wall,  $B$ , of 5.0 for  $R_k = 4, 6, 8, 10$  and 20.
- (b) Now make provision for inputting the value of  $R_\beta$  (program variable  $rb$ ). For  $R_k = 6$ , determine the value of  $R_\omega$  that yields  $B = 5.0$  when  $R_\beta = 0, 4, 8$ , and 12. Also, determine the maximum value of  $k^+$  for each case.

## Chapter 5

# Effects of Compressibility

For flows in which compressibility effects are important, we must introduce an equation for conservation of energy and an equation of state. Just as Reynolds averaging gives rise to the Reynolds-stress tensor, so we expect that similar averaging will lead to a turbulent heat-flux vector. We should also expect that new compressibility related correlations will appear throughout the equations of motion. These are important issues that must be addressed in constructing a turbulence model suitable for application to compressible flows. This chapter focuses upon these issues.

We begin with a brief discussion of common observations pertaining to compressible turbulence. Then, we introduce the Favre mass-averaging procedure and derive the mass-averaged equations of motion. Next, we demonstrate an elegant development in turbulence modeling for the compressible mixing layer. We follow this analysis with an application of perturbation methods to the compressible log layer. We then apply several models to attached compressible boundary layers, including effects of pressure gradient, surface cooling and surface roughness. The chapter concludes with application of various turbulence models to shock-separated flows.

### 5.1 Physical Considerations

By definition, a compressible flow is one in which significant density changes occur, even when pressure changes are small. Generally speaking, compressibility has a relatively small effect on turbulent eddies in wall-bounded flows. This appears to be true for Mach numbers up to about 5 (and perhaps as high as 8), provided the flow doesn't experience large pressure changes over a short distance such as we might have across a shock wave. At subsonic

speeds, compressibility effects on eddies are usually unimportant for boundary layers provided  $T_w/T_e < 6$ . Based on these observations, Morkovin (1962) hypothesized that the effect of density fluctuations on the turbulence are small provided they remain small relative to the mean density. This is a major simplification for the turbulence modeler because it means that, in practice, he need only account for the nonuniform mean density in computing compressible, shock-free, non-hypersonic turbulent flows.

There are limitations to the applicability of **Morkovin's hypothesis** even at non-hypersonic Mach numbers. For example, because  $\rho'/\bar{\rho}$  is typically not small, it applies neither to flows with significant heat transfer nor to flows with combustion. Also, because density fluctuations generally are much larger in free shear flows, models based on Morkovin's hypothesis fail to predict the measured reduction in spreading rate with increasing freestream Mach number for the compressible mixing layer [Papamoschou and Roshko (1988)]. As we will see in Section 5.5, the level of  $\rho'/\bar{\rho}$  for a boundary layer at Mach 5 is comparable to the level found in a mixing layer at Mach 1. For Mach numbers in excess of 1, the spreading rate for a mixing layer decreases. This is consistent with Mach 5 representing the hypersonic limit for the boundary layer.

As a final observation, note that the difficulty in predicting properties of the compressible mixing layer is reminiscent of our experience with free shear flows in Chapters 3 and 4. That is, we find again that the seemingly simple free shear flow case is more difficult to model than the wall-bounded case.

## 5.2 Favre Averaging

In addition to velocity and pressure fluctuations, we must also account for density and temperature fluctuations when the medium is a compressible fluid. If we use the standard time-averaging procedure introduced in Chapter 2, the mean conservation equations contain additional terms that have no analogs in the laminar equations. To illustrate this, consider conservation of mass. We write the instantaneous density  $\rho$  as the sum of mean,  $\bar{\rho}$ , and fluctuating,  $\rho'$ , parts, i.e.,

$$\rho = \bar{\rho} + \rho' \quad (5.1)$$

Expressing the instantaneous velocity in the usual way [Equation (2.4)], substituting into the continuity equation yields

$$\frac{\partial}{\partial t}(\bar{\rho} + \rho') + \frac{\partial}{\partial x_i}(\bar{\rho}U_i + \rho'U_i + \bar{\rho}u'_i + \rho'u'_i) = 0 \quad (5.2)$$



After time averaging Equation (5.2), we arrive at the Reynolds-averaged continuity equation for compressible flow, viz.,

$$\frac{\partial \bar{\rho}}{\partial t} + \frac{\partial}{\partial x_i} \left( \bar{\rho} U_i + \overline{\rho' u'_i} \right) = 0 \quad (5.3)$$

Some authors refer to this as the **primitive-variable form** of the continuity equation. Note that in order to achieve closure, an approximation for the correlation between  $\rho'$  and  $u'_i$  is needed. The problem is even more complicated for the momentum equation where the Reynolds-stress tensor originates from time averaging the product  $\rho u_i u_j$  that appears in the convective acceleration. Clearly, a triple correlation involving  $\rho'$ ,  $u'_i$ , and  $u'_j$  appears, thus increasing the complexity of establishing suitable closure approximations. The problem of establishing the appropriate form of the time-averaged equations can be simplified dramatically by using the density-weighted averaging procedure suggested by Favre (1965). That is, we introduce the **mass-averaged** velocity,  $\tilde{u}_i$ , defined by

$$\tilde{u}_i = \frac{1}{\bar{\rho}} \lim_{T \rightarrow \infty} \int_t^{t+T} \rho(\mathbf{x}, \tau) u_i(\mathbf{x}, \tau) d\tau \quad (5.4)$$

where  $\bar{\rho}$  is the conventional Reynolds-averaged density. Thus, in terms of conventional Reynolds averaging, we can say that

$$\bar{\rho} \tilde{u}_i = \overline{\rho u_i} \quad (5.5)$$

where an overbar denotes conventional Reynolds average. The value of this averaging process, known as **Favre averaging**, becomes obvious when we expand the right-hand side of Equation (5.5). Performing the indicated Reynolds-averaging process, there follows

$$\bar{\rho} \tilde{u}_i = \bar{\rho} U_i + \overline{\rho' u'_i} \quad (5.6)$$

Inspection of Equation (5.3) shows that conservation of mass can be rewritten as

$$\frac{\partial \bar{\rho}}{\partial t} + \frac{\partial}{\partial x_i} (\bar{\rho} \tilde{u}_i) = 0 \quad (5.7)$$

This is a remarkable simplification as Equation (5.7) looks just like the laminar mass-conservation equation. What we have done is treat the momentum per unit volume,  $\rho u_i$ , as the dependent variable rather than the velocity. This is a sensible thing to do from a physical point of view, especially when we focus upon the momentum equation in the next section. That is, the rate of change of momentum per unit volume, not velocity, is equal to the sum of the imposed forces per unit volume in a flow.

When we use Favre averaging, it is customary to decompose the instantaneous velocity into the mass-averaged part,  $\tilde{u}_i$ , and a fluctuating part,  $u_i''$ , wherefore

$$u_i = \tilde{u}_i + u_i'' \quad (5.8)$$

Now, to form the Favre average, we simply multiply through by  $\rho$  and do a time average in the manner established in Chapter 2. Hence, from Equation (5.8) we find

$$\overline{\rho u_i} = \bar{\rho} \tilde{u}_i + \overline{\rho u_i''} \quad (5.9)$$

But, from the definition of the Favre average given in Equation (5.5), we see immediately that, as expected, the Favre average of the fluctuating velocity,  $u_i''$ , vanishes, i.e.,

$$\overline{\rho u_i''} = 0 \quad (5.10)$$

By contrast, the conventional Reynolds average of  $u_i''$  is not zero. To see this, note that

$$u_i'' = u_i - \tilde{u}_i \quad (5.11)$$

Hence, using Equation (5.6) to eliminate  $\tilde{u}_i$ ,

$$u_i'' = u_i - U_i - \frac{\overline{\rho' u_i'}}{\bar{\rho}} \quad (5.12)$$

Therefore, performing the conventional Reynolds average, we find

$$\overline{u_i''} = -\frac{\overline{\rho' u_i'}}{\bar{\rho}} \neq 0 \quad (5.13)$$

As a final comment, do not lose sight of the fact that while Favre averaging eliminates density fluctuations from the averaged equations, it does not remove the effect the density fluctuations have on the turbulence. Consequently, **Favre averaging is a mathematical simplification, not a physical one.**

### 5.3 Favre-Averaged Equations

For motion in a compressible medium, we must solve the equations governing conservation of mass, momentum and energy. The instantaneous equations are as follows:

$$\frac{\partial \rho}{\partial t} + \frac{\partial}{\partial x_i}(\rho u_i) = 0 \quad (5.14)$$

$$\frac{\partial}{\partial t}(\rho u_i) + \frac{\partial}{\partial x_j}(\rho u_j u_i) = -\frac{\partial p}{\partial x_i} + \frac{\partial t_{ji}}{\partial x_j} \quad (5.15)$$

$$\frac{\partial}{\partial t} \left[ \rho \left( e + \frac{1}{2} u_i u_i \right) \right] + \frac{\partial}{\partial x_j} \left[ \rho u_j \left( h + \frac{1}{2} u_i u_i \right) \right] = \frac{\partial}{\partial x_j} (u_i t_{ij}) - \frac{\partial q_j}{\partial x_j} \quad (5.16)$$

where  $e$  is specific internal energy and  $h = e + p/\rho$  is specific enthalpy. For compressible flow, the viscous stress tensor,  $t_{ij}$ , involves the second viscosity,  $\zeta$ , as well as the conventional molecular viscosity,  $\mu$ . Although it is not necessary for our immediate purposes, we eventually must specify an equation of state. For gases, we use the perfect gas law so that pressure, density and temperature are related by

$$p = \rho R T \quad (5.17)$$

where  $R$  is the perfect gas constant. The constitutive relation between stress and strain rate for a Newtonian fluid is

$$t_{ij} = 2\mu s_{ij} + \zeta \frac{\partial u_k}{\partial x_k} \delta_{ij} \quad (5.18)$$

where  $s_{ij}$  is the instantaneous strain-rate tensor [Equation (2.19)] and  $\delta_{ij}$  is the Kronecker delta. The heat-flux vector,  $q_j$ , is usually obtained from Fourier's law so that

$$q_j = -\kappa \frac{\partial T}{\partial x_j} \quad (5.19)$$

where  $\kappa$  is thermal conductivity. We can simplify our analysis somewhat by introducing two commonly used assumptions. First, we relate second viscosity to  $\mu$  by assuming

$$\zeta = -\frac{2}{3}\mu \quad (5.20)$$

This assumption is correct for a monatomic gas, and is generally used for all gases in standard CFD applications. Assuming Equation (5.20) holds in general guarantees  $t_{ii} = 0$  so that viscous stresses do not contribute to the pressure, even when  $s_{ii} = \partial u_i / \partial x_i \neq 0$ . This is tidy, even if not necessarily true. Second, we assume the fluid is calorically perfect so that its specific heat coefficients are constant, and thus

$$e = C_v T \quad \text{and} \quad h = C_p T \quad (5.21)$$

where  $C_v$  and  $C_p$  are the specific heat coefficients for constant volume and pressure processes, respectively. Then, we can say that

$$q_j = -\kappa \frac{\partial T}{\partial x_j} = -\frac{\mu}{Pr_L} \frac{\partial h}{\partial x_j} \quad (5.22)$$

where  $Pr_L$  is the **laminar Prandtl number** defined by

$$Pr_L = \frac{C_p \mu}{\kappa} \quad (5.23)$$

In order to mass average the conservation equations, we now decompose the various flow properties as follows.

$$\left. \begin{aligned} u_i &= \tilde{u}_i + u_i'' \\ \rho &= \bar{\rho} + \rho' \\ p &= P + p' \\ h &= \tilde{h} + h'' \\ e &= \tilde{e} + e'' \\ T &= \tilde{T} + T'' \\ q_j &= q_{Lj} + q_j' \end{aligned} \right\} \quad (5.24)$$

Note that we decompose  $p$ ,  $\rho$  and  $q_j$  in terms of conventional mean and fluctuating parts. Substituting Equations (5.24) into Equations (5.14) - (5.17) and performing the mass-averaging operations, we arrive at what are generally referred to as the **Favre (mass) averaged mean conservation equations**.

$$\frac{\partial \bar{\rho}}{\partial t} + \frac{\partial}{\partial x_i} (\bar{\rho} \tilde{u}_i) = 0 \quad (5.25)$$

$$\frac{\partial}{\partial t} (\bar{\rho} \tilde{u}_i) + \frac{\partial}{\partial x_j} (\bar{\rho} \tilde{u}_j \tilde{u}_i) = -\frac{\partial P}{\partial x_i} + \frac{\partial}{\partial x_j} [\bar{t}_{ji} - \overline{\rho u_j'' u_i''}] \quad (5.26)$$

$$\begin{aligned} \frac{\partial}{\partial t} \left[ \bar{\rho} \left( \tilde{e} + \frac{\tilde{u}_i \tilde{u}_i}{2} \right) + \frac{\overline{\rho u_i'' u_i''}}{2} \right] + \frac{\partial}{\partial x_j} \left[ \bar{\rho} \tilde{u}_j \left( \tilde{h} + \frac{\tilde{u}_i \tilde{u}_i}{2} \right) + \tilde{u}_j \frac{\overline{\rho u_i'' u_i''}}{2} \right] \\ = \frac{\partial}{\partial x_j} \left[ -q_{Lj} - \overline{\rho u_j'' h''} + \bar{t}_{ji} u_i'' - \overline{\rho u_j'' \frac{1}{2} u_i'' u_i''} \right] \\ + \frac{\partial}{\partial x_j} \left[ \tilde{u}_i \left( \bar{t}_{ij} - \overline{\rho u_i'' u_j''} \right) \right] \end{aligned} \quad (5.27)$$

$$P = \bar{\rho} R \tilde{T} \quad (5.28)$$

Equations (5.25), (5.26) and (5.28) differ from their laminar counterparts only by the appearance of the Favre-averaged Reynolds-stress tensor, viz.,

$$\tau_{ij} = -\overline{\rho u_i'' u_j''} \quad (5.29)$$

As in the incompressible case, the Favre-averaged  $\tau_{ij}$  is a symmetric tensor.

The Favre-averaged mean energy equation for total energy, i.e., the sum of internal energy, mean-flow kinetic energy and turbulence kinetic energy has numerous additional terms, each of which represents an identifiable physical process or property. Consider first the double correlation between

$u_i''$  and itself that appears in each of the two terms on the left-hand side of Equation (5.27). This is the kinetic energy per unit volume of the turbulent fluctuations, so that it makes sense to define

$$\bar{\rho}k = \frac{1}{2}\overline{\rho u_i'' u_i''} \quad (5.30)$$

Next, the correlation between  $u_j''$  and  $h''$  is the turbulent transport of heat. In analogy to the notation selected for the molecular transport of heat, we define

$$qT_j = \overline{\rho u_j'' h''} \quad (5.31)$$

The two terms  $\overline{t_{ji} u_i''}$  and  $\overline{\rho u_j'' \frac{1}{2} u_i'' u_i''}$  on the right-hand side of Equation (5.27) correspond to molecular diffusion and turbulent transport of turbulence kinetic energy, respectively. These terms arise because the mass-averaged total enthalpy appearing in the convective term of Equation (5.27) is the sum of mass-averaged enthalpy, mean kinetic energy and turbulence kinetic energy. They represent transfers between mean energy and turbulence kinetic energy, that naturally arise when we derive the Favre-averaged turbulence kinetic energy equation. The simplest way to derive the equation for  $k$  is to multiply the primitive-variable form of the instantaneous momentum equation by  $u_i''$  and time average.

$$\overline{\rho u_i'' \frac{\partial u_i}{\partial t}} + \overline{\rho u_i'' u_j \frac{\partial u_i}{\partial x_j}} = -\overline{u_i'' \frac{\partial p}{\partial x_i}} + \overline{u_i'' \frac{\partial t_{ji}}{\partial x_j}} \quad (5.32)$$

As in Chapter 2, the most illuminating way to carry out the indicated time-averaging operations is to proceed term by term, and to use tensor notation for all derivatives. Proceeding from left to right, we first consider the **unsteady term**.

$$\begin{aligned} \overline{\rho u_i'' u_{i,t}} &= \overline{\rho u_i'' (\tilde{u}_i + u_i'')_{,t}} \\ &= \overline{\rho u_i'' \tilde{u}_{i,t}} + \overline{\rho u_i'' u_{i,t}''} \\ &= \overline{\rho \left( \frac{1}{2} u_i'' u_i'' \right)_{,t}} \\ &= \frac{\partial}{\partial t} (\bar{\rho}k) - \frac{1}{2} \overline{u_i'' u_i'' \frac{\partial \rho}{\partial t}} \end{aligned} \quad (5.33)$$

Turning now to the **convective term**, we have the following.

$$\begin{aligned}
 \overline{\rho u_i'' u_j u_{i,j}} &= \overline{\rho u_i'' [(\tilde{u}_j + u_j'') \tilde{u}_{i,j} + u_j u_{i,j}'']} \\
 &= \overline{\rho u_i'' \tilde{u}_j \tilde{u}_{i,j}} + \overline{\rho u_i'' u_j' \tilde{u}_{i,j}} + \overline{\rho u_j u_i'' u_{i,j}''} \\
 &= -\tau_{ij} \tilde{u}_{i,j} + \overline{\rho u_j (\frac{1}{2} u_i'' u_i'')_{,j}} \\
 &= -\tau_{ij} \tilde{u}_{i,j} + \overline{(\rho u_j \frac{1}{2} u_i'' u_i'')_{,j}} - \overline{\frac{1}{2} u_i'' u_i'' (\rho u_j)_{,j}} \\
 &= -\tau_{ij} \tilde{u}_{i,j} + \overline{(\rho \tilde{u}_j \frac{1}{2} u_i'' u_i'' + \rho u_j' \frac{1}{2} u_i'' u_i'')_{,j}} - \overline{\frac{1}{2} u_i'' u_i'' (\rho u_j)_{,j}} \\
 &= -\tau_{ij} \frac{\partial \tilde{u}_i}{\partial x_j} + \frac{\partial}{\partial x_j} \left( \overline{\rho \tilde{u}_j k} + \overline{\rho u_j' \frac{1}{2} u_i'' u_i''} \right) - \overline{\frac{1}{2} u_i'' u_i'' \frac{\partial}{\partial x_j} (\rho u_j)}
 \end{aligned} \tag{5.34}$$

The **pressure gradient term** simplifies immediately as follows.

$$\overline{u_i'' p_{,i}} = \overline{u_i''} P_{,i} + \overline{u_i'' p'_{,i}} = \overline{u_i''} \frac{\partial P}{\partial x_i} + \frac{\partial}{\partial x_i} \left( \overline{p' u_i''} \right) - \overline{p' \frac{\partial u_i''}{\partial x_i}} \tag{5.35}$$

Finally, the **viscous term** is simply rewritten as

$$\overline{u_i'' t_{ji,j}} = \frac{\partial}{\partial x_j} \left( \overline{t_{ji} u_i''} \right) - \overline{t_{ji} \frac{\partial u_i''}{\partial x_j}} \tag{5.36}$$

Thus, substituting Equations (5.33) through (5.36) into Equation (5.32), we arrive at the **Favre-averaged turbulence kinetic energy equation**. In arriving at the final result, we make use of the fact that the sum of the last terms on the right-hand sides of Equations (5.33) and (5.34) vanish since their sum is proportional to the two terms appearing in the instantaneous continuity equation. Additionally, to facilitate comparison with the incompressible turbulence kinetic energy equation [Equation (4.4)], we use the Favre-averaged continuity equation to rewrite the unsteady and convective terms in non-conservation form. The exact equation is as follows.

$$\begin{aligned}
 \bar{\rho} \frac{\partial k}{\partial t} + \bar{\rho} \tilde{u}_j \frac{\partial k}{\partial x_j} &= \tau_{ij} \frac{\partial \tilde{u}_i}{\partial x_j} - \overline{t_{ji} \frac{\partial u_i''}{\partial x_j}} + \frac{\partial}{\partial x_j} \left[ \overline{t_{ji} u_i''} - \overline{\rho u_j' \frac{1}{2} u_i'' u_i''} - \overline{p' u_j''} \right] \\
 &\quad - \underbrace{\overline{u_i'' \frac{\partial P}{\partial x_i}}}_{\text{Pressure Work}} + \underbrace{\overline{p' \frac{\partial u_i''}{\partial x_i}}}_{\text{Pressure Dilatation}}
 \end{aligned} \tag{5.37}$$

Comparing the mean energy Equation (5.27) with the turbulence kinetic energy Equation (5.37), we see that indeed the two terms  $\overline{t_{ji} u_i''}$  and

$\overline{\rho u_j'' \frac{1}{2} u_i'' u_i''}$  on the right-hand side of the mean-energy equation are **Molecular Diffusion** and **Turbulent Transport** of turbulence kinetic energy. Inspection of the turbulence kinetic energy equation also indicates that the **Favre-averaged dissipation rate** is given by

$$\bar{\rho}\epsilon = \overline{t_{ji} \frac{\partial u_i''}{\partial x_j}} \quad (5.38)$$

Comparison of Equation (5.37) with the incompressible equation for  $k$  [Equation (4.4)] shows that all except the last two terms, i.e., the **Pressure Work** and **Pressure-Dilatation** terms, have analogs in the incompressible equation. Both of these terms vanish in the limit of incompressible flow with zero density fluctuations. The **Pressure Work** vanishes because the time average of  $u_i''$  is zero when density fluctuations are zero. The **Pressure-Dilatation** term vanishes because the fluctuating field has zero divergence for incompressible flow. Hence, Equation (5.37) simplifies to Equation (4.4) for incompressible flow with zero density fluctuations.

Note that the turbulence kinetic energy production,  $\tau_{ij} \partial \tilde{u}_i / \partial x_j$ , and pressure correlation terms represent a transfer from mean kinetic energy to turbulence kinetic energy. Also, dissipation is a transfer from turbulence kinetic energy to internal energy. Thus, since these transfers simply redistribute energy, they must cancel in the overall energy conservation equation. Consequently, only the two terms involving spatial transport of turbulence kinetic energy appear in Equation (5.27).

Using a similar derivation (we omit the details here for the sake of brevity), the **Favre-averaged Reynolds-stress equation** assumes the following form.

$$\begin{aligned} \frac{\partial \tau_{ij}}{\partial t} + \frac{\partial}{\partial x_k} (\tilde{u}_k \tau_{ij}) &= -\tau_{ik} \frac{\partial \tilde{u}_j}{\partial x_k} - \tau_{jk} \frac{\partial \tilde{u}_i}{\partial x_k} + \epsilon_{ij} - \Pi_{ij} \\ &+ \frac{\partial}{\partial x_k} \left[ -\overline{(t_{kj} u_i'' + t_{ki} u_j'')} + C_{ijk} \right] \\ &+ \overline{u_i''} \frac{\partial P}{\partial x_j} + \overline{u_j''} \frac{\partial P}{\partial x_i} \end{aligned} \quad (5.39)$$

where

$$\Pi_{ij} = \overline{p' \left( \frac{\partial u_i''}{\partial x_j} + \frac{\partial u_j''}{\partial x_i} \right)} \quad (5.40)$$

$$\epsilon_{ij} = \overline{t_{kj} \frac{\partial u_i''}{\partial x_k} + t_{ki} \frac{\partial u_j''}{\partial x_k}} \quad (5.41)$$

$$C_{ijk} = \overline{\rho u_i'' u_j'' u_k''} + \overline{p' u_i''} \delta_{jk} + \overline{p' u_j''} \delta_{ik} \quad (5.42)$$

Taking advantage of the definitions given in Equations (5.29), (5.30), (5.31) and (5.38), we can summarize the Favre-averaged mean equations and turbulence kinetic energy equation in conservation form.

$$\frac{\partial \bar{\rho}}{\partial t} + \frac{\partial}{\partial x_i} (\bar{\rho} \tilde{u}_i) = 0 \quad (5.43)$$

$$\frac{\partial}{\partial t} (\bar{\rho} \tilde{u}_i) + \frac{\partial}{\partial x_j} (\bar{\rho} \tilde{u}_j \tilde{u}_i) = -\frac{\partial P}{\partial x_i} + \frac{\partial}{\partial x_j} [\bar{t}_{ji} + \tau_{ji}] \quad (5.44)$$

$$\begin{aligned} \frac{\partial}{\partial t} (\bar{\rho} E) + \frac{\partial}{\partial x_j} (\bar{\rho} \tilde{u}_j H) &= \frac{\partial}{\partial x_j} \left[ -q_{Lj} - q_{Tj} + \overline{t_{ji} u_i''} - \overline{\rho u_j'' \frac{1}{2} u_i'' u_i''} \right] \\ &+ \frac{\partial}{\partial x_j} [\tilde{u}_i (\bar{t}_{ij} + \tau_{ij})] \end{aligned} \quad (5.45)$$

$$\begin{aligned} \frac{\partial}{\partial t} (\bar{\rho} k) + \frac{\partial}{\partial x_j} (\bar{\rho} \tilde{u}_j k) &= \tau_{ij} \frac{\partial \tilde{u}_i}{\partial x_j} - \bar{\rho} \epsilon + \frac{\partial}{\partial x_j} \left[ \overline{t_{ji} u_i''} - \overline{\rho u_j'' \frac{1}{2} u_i'' u_i''} - \overline{p' u_j''} \right] \\ &- \overline{u_i''} \frac{\partial P}{\partial x_i} + \overline{p' \frac{\partial u_i''}{\partial x_i}} \end{aligned} \quad (5.46)$$

$$P = \bar{\rho} R \tilde{T} \quad (5.47)$$

The quantities  $E$  and  $H$  are the **total energy** and **total enthalpy**, and include the kinetic energy of the fluctuating turbulent field, viz.,

$$E = \tilde{e} + \frac{1}{2} \tilde{u}_i \tilde{u}_i + k \quad \text{and} \quad H = \tilde{h} + \frac{1}{2} \tilde{u}_i \tilde{u}_i + k \quad (5.48)$$

## 5.4 Compressible-Flow Closure Approximations

As discussed in the preceding section, in addition to having variable mean density  $\bar{\rho}$ , Equations (5.39) through (5.48) reflect effects of compressibility through various correlations that are affected by fluctuating density. For all but second-order closure models, closure approximations must be postulated for the mass-averaged Reynolds-stress tensor and heat-flux vector. Depending on the type of turbulence model used, additional closure approximations may be needed to close the system of equations defining the model.



This section briefly reviews some of the most commonly used closure approximations for compressible flows. Because of the paucity of measurements compared to the incompressible case, and the additional complexities attending compressible flows, far less is available to guide development of closure approximations suitable for a wide range of applications. As a result, modeling of compressibility effects is in a continuing state of flux as we approach the end of the twentieth century. The closure approximations discussed in this, and following, sections are those that have stood the test of time.

Before focusing upon specific closure approximations, it is worthwhile to cite important guidelines that should be followed in devising compressible-flow closure approximations. Adhering to the following items will lead to the simplest and most elegant models.

1. All closure approximations should approach the proper limiting value for Mach number and density fluctuations tending to zero.
2. All closure terms should be written in proper tensor form, e.g., not dependent upon a specific geometrical configuration.
3. All closure approximations should be dimensionally consistent and invariant under a Galilean transformation.

It should be obvious that Items 2 and 3 apply for incompressible flows as well. In practice, Galilean invariance seems to be ignored more often than any other item listed, especially for compressible flows. Such models should be rejected as they violate a fundamental feature of the Navier-Stokes equation, and are thus physically unsound.

**Reynolds-stress Tensor:** For zero-, one- and two-equation models, nearly all researchers use the Boussinesq approximation with suitable generalization for compressible flows. Specifically, denoting the eddy viscosity by  $\mu_T$ , the following form is generally assumed.

$$\tau_{ij} \equiv -\overline{\rho u_i'' u_j''} = 2\mu_T \left( S_{ij} - \frac{1}{3} \frac{\partial \tilde{u}_k}{\partial x_k} \delta_{ij} \right) - \frac{2}{3} \bar{\rho} k \delta_{ij} \quad (5.49)$$

The most important consideration in postulating Equation (5.49) is guaranteeing that the trace of  $\tau_{ij}$  is  $-2\bar{\rho}k$ . Note that this means the “second eddy viscosity” must be  $-\frac{2}{3}\mu_T$  [recall Equation (5.20)].

**Turbulent Heat-Flux Vector:** The most commonly used closure approximation for the turbulent heat-flux vector,  $q_{Tj}$ , follows from appealing to the classical analogy [Reynolds (1874)] between momentum and heat

transfer. It is thus assumed to be proportional to the mean temperature gradient, so that

$$q_{Tj} = \overline{\rho u_j'' h''} = -\frac{\mu_T C_p}{Pr_T} \frac{\partial \tilde{T}}{\partial x_j} = -\frac{\mu_T}{Pr_T} \frac{\partial \tilde{h}}{\partial x_j} \quad (5.50)$$

where  $Pr_T$  is the **turbulent Prandtl number**. A constant value for  $Pr_T$  is often used and this is usually satisfactory for shock-free flows up to low supersonic speeds, provided the heat transfer rate is not too high. The most common values assumed for  $Pr_T$  are 0.89 or 0.90, in the case of a boundary layer. Heat-transfer predictions can usually be improved somewhat by letting  $Pr_T$  vary through the boundary layer. For free shear layers, values of the order of 0.5 are more appropriate for  $Pr_T$ .

**Molecular Diffusion and Turbulent Transport:** If a zero-equation model is used, the  $\frac{2}{3}\rho k\delta_{ij}$  contribution in Equation (5.49) is ignored as are the molecular diffusion,  $\overline{t_{ji}u_i''}$ , and turbulent transport,  $\overline{\rho u_j'' \frac{1}{2}u_i''u_i''}$ , terms appearing in the mean-energy equation. Some researchers ignore these terms for higher-order models as well. This is usually a good approximation for flows with Mach numbers up to the supersonic range, which follows from the fact that  $\bar{\rho}k \ll P$  (and hence  $k \ll \tilde{h}$ ) in most flows of engineering interest. However, at hypersonic speeds, it is entirely possible to achieve conditions under which  $\bar{\rho}k$  is a significant fraction of  $P$ . To ensure exact conservation of total energy (which includes turbulence kinetic energy), additional closure approximations are needed. The most straightforward procedure for one-equation, two-equation and second-order closure models is to generalize the low-speed closure approximations for the molecular diffusion and turbulent transport terms. The most commonly used approximation is:

$$\overline{t_{ji}u_i''} - \overline{\rho u_j'' \frac{1}{2}u_i''u_i''} = \left( \mu + \frac{\mu_T}{\sigma_k} \right) \frac{\partial k}{\partial x_j} \quad (5.51)$$

**Pressure Diffusion and Pressure-Dilatation Term:** Section 4.1 discusses the lack of information regarding diffusion by pressure fluctuations in incompressible flows. So little is known that it is simply ignored. Even less is known for compressible flows. However, given the fundamentally different role that pressure plays in a compressible medium relative to its essentially passive role at low speeds, ignoring pressure diffusion and pressure dilatation ultimately must lead to significant error. Purely empirical proposals, especially for the pressure-dilatation mean product, have been made by many authors, but none has received general acceptance. The best prospect for immediate progress at the present time may be to

use Direct Numerical Simulations (DNS). Such work is in progress [e.g., Sarkar et al. (1991) and Zeman (1991)], and preliminary proposals have been made. No generally accepted approximation has emerged at the time of this writing however.

**Pressure Work:** The pressure work term,  $\overline{u_i'' P_{,i}}$  (or  $\overline{u_i'' P_{,j}} + \overline{u_j'' P_{,i}}$  for second-order closure models), arises because the time average of  $\overline{u_i''}$  does not vanish. It is proportional to the density/velocity correlation  $\overline{\rho' u_i'}$ , and illustrates how Favre averaging does not completely eliminate the need to know how these fluctuating properties are correlated. Wilcox and Alber (1972) postulate an empirical model for this term that improves two-equation model predictions for hypersonic base flows. Oh (1974) proposes a closure approximation postulating existence of “eddy shocks” and accurately simulates compressible mixing layers with a one-equation turbulence model. Neither model is entirely satisfactory however as they both involve the mean velocity in a manner that violates Galilean invariance of the Navier-Stokes equation. As with pressure diffusion and pressure dilatation, the best hope for progress in the short term is probably through use of DNS.

## 5.5 Dilatation Dissipation

Using a program such as MIXER (see Appendix C), it is a simple matter to verify that both the  $k$ - $\omega$  model and  $k$ - $\epsilon$  model fail to predict the observed decrease in spreading rate with increasing Mach number for the compressible mixing layer [Kline et al. (1981) and Papamoschou and Roshko (1988)]. Focusing upon the  $k$ - $\epsilon$  model, Sarkar et al. (1989) and Zeman (1990) have devised particularly elegant models for the  $k$  equation that correct the deficiency for the compressible mixing layer. Building upon the Sarkar/Zeman formulations, Wilcox (1992b) has postulated a similar model that enjoys an important advantage for wall-bounded flows. This section shows how a straightforward and elegant modification can dramatically improve a turbulence model’s predictive accuracy.

To understand the Sarkar/Zeman innovation, we must examine the turbulence energy dissipation rate more closely. Recall from Equation (5.38) that

$$\bar{\rho}\epsilon = \overline{t_{ji} \frac{\partial u_i''}{\partial x_j}} \quad (5.52)$$

Hence, in terms of the instantaneous strain-rate tensor,  $s_{ij}$ , we have

$$\bar{\rho}\epsilon = \mu \overline{\left[ 2s_{ji}s_{ij}'' - \frac{2}{3}u_{k,k}u_{i,i}'' \right]} \quad (5.53)$$

Assuming that the correlation between velocity-gradient fluctuations and kinematic viscosity fluctuations is negligible, we can rewrite this equation as

$$\bar{\rho}\epsilon = \bar{\nu} \left[ 2\overline{\rho s''_{ji} s''_{ij}} - \frac{2}{3}\overline{\rho u''_{k,k} u''_{i,i}} \right] \quad (5.54)$$

In terms of the fluctuating vorticity,  $\omega''_i$ , there follows

$$\bar{\rho}\epsilon = \bar{\nu} \left[ \overline{\rho \omega''_i \omega''_i} + 2\overline{\rho u''_{i,j} u''_{j,i}} - \frac{2}{3}\overline{\rho u''_{i,i} u''_{i,i}} \right] \quad (5.55)$$

Finally, we can say  $u''_{i,j} u''_{j,i} \approx (u''_{i,i})^2$ , which is exactly true for homogeneous turbulence, and is a very good approximation for high-Reynolds-number, inhomogeneous turbulence [see, for example, Tennekes and Lumley (1983)]. Hence, we conclude that the dissipation can be written as

$$\bar{\rho}\epsilon = \bar{\rho}\epsilon_s + \bar{\rho}\epsilon_d \quad (5.56)$$

where

$$\bar{\rho}\epsilon_s = \bar{\nu} \overline{\rho \omega''_i \omega''_i} \quad \text{and} \quad \bar{\rho}\epsilon_d = \frac{4}{3}\bar{\nu} \overline{\rho u''_{i,i} u''_{i,i}} \quad (5.57)$$

Thus, we have shown that the compressible turbulence dissipation rate can logically be written in terms of the fluctuating vorticity and the divergence of the fluctuating velocity. Equivalently, we could have written the fluctuating velocity as the sum of a divergence free and a curl free component. At high Reynolds number, these components presumably are uncorrelated (again, an exact result for homogeneous turbulence), and Equation (5.55) would follow directly. The quantity  $\epsilon_s$  is known as the **solenoidal dissipation**, while  $\epsilon_d$  is known as the **dilatation dissipation**. Clearly, the latter contribution is present only for compressible flows.

Sarkar and Zeman postulate that the dilatation dissipation should be a function of turbulence Mach number,  $M_t$ , defined by

$$M_t^2 = 2k/a^2 \quad (5.58)$$

where  $a$  is the speed of sound. They argue that the  $k$  and  $\epsilon$  equations should be replaced by

$$\bar{\rho} \frac{dk}{dt} = -\bar{\rho}(\epsilon_s + \epsilon_d) + \dots \quad (5.59)$$

$$\bar{\rho} \frac{d\epsilon_s}{dt} = -C_{\epsilon 2} \bar{\rho} \epsilon_s^2 / k + \dots \quad (5.60)$$

where  $C_{\epsilon 2}$  is a closure coefficient. Only the dissipation terms are shown explicitly in Equations (5.59) and (5.60) since no changes occur in any

other terms. Particularly noteworthy, both Sarkar and Zeman postulate that the equation for  $\epsilon_s$  is unaffected by compressibility. The dilatation dissipation is further assumed to be proportional to  $\epsilon_s$  so that we say

$$\epsilon_d = \xi^* F(M_t) \epsilon_s \quad (5.61)$$

where  $\xi^*$  is a closure coefficient and  $F(M_t)$  is a prescribed function of  $M_t$ . The Sarkar, Zeman and Wilcox formulations differ in the value of  $\xi^*$  and the functional form of  $F(M_t)$ .

Interestingly, while both Sarkar and Zeman arrive at similar formulations, their basic postulates are fundamentally different. Sarkar et al. postulate that  $\epsilon_d$  “varies on a fast compressibility time scale relative to  $\epsilon_s$ .” As a consequence, they conclude that dilatation dissipation increases with  $M_t$  in a monotone manner. By contrast, Zeman postulates the existence of eddy shocklets that augment only the dilatation dissipation, so that a threshold exists below which dilatation dissipation is zero.

To implement the Sarkar or Zeman modification in the  $k$ - $\omega$  model, we begin by making the formal change of variables given by  $\epsilon_s = \beta^* \omega k$ . This tells us immediately that

$$\bar{\rho} \frac{d\omega}{dt} = \frac{\bar{\rho}}{\beta^* k} \left[ \frac{d\epsilon_s}{dt} - \frac{\epsilon_s}{k} \frac{dk}{dt} \right] \quad (5.62)$$

Consequently, a compressibility term must appear in the  $\omega$  equation as well as in the  $k$  equation. Note that if we identify  $\omega$  as the RMS fluctuating vorticity, a case could be made that the  $\omega$  equation should be unaffected by dilatation dissipation rather than the  $\epsilon$  equation. While this may be true, it would obscure direct comparisons between effects of dilatation dissipation on the two types of models if we depart from the Sarkar/Zeman conventions.

Inspection of Equations (4.34) and (4.35) shows that the Sarkar/Zeman compressibility modifications correspond to letting closure coefficients  $\beta$  and  $\beta^*$  in the  $k$ - $\omega$  model vary with  $M_t$ . In terms of  $\xi^*$  and the compressibility function  $F(M_t)$ ,  $\beta$  and  $\beta^*$  are:

$$\beta^* = \beta_o^* [1 + \xi^* F(M_t)] \quad (5.63)$$

$$\beta = \beta_o - \beta_o^* \xi^* F(M_t) \quad (5.64)$$

where  $\beta_o^*$  and  $\beta_o$  are the corresponding incompressible values of  $\beta^*$  and  $\beta$ . The values of  $\xi^*$  and  $F(M_t)$  for the Sarkar, Zeman and Wilcox models are as follows:

#### Sarkar's Model

$$\xi^* = 1, \quad F(M_t) = M_t^2 \quad (5.65)$$

**Zeman's Model**

$$\xi^* = 3/4, \quad F(M_t) = \left[ 1 - e^{-\frac{1}{2}(\gamma+1)(M_t-M_{t_o})^2/\Lambda^2} \right] \mathcal{H}(M_t - M_{t_o}) \quad (5.66)$$

**Wilcox's Model**

$$\xi^* = 3/2, \quad M_{t_o} = 1/4, \quad F(M_t) = [M_t^2 - M_{t_o}^2] \mathcal{H}(M_t - M_{t_o}) \quad (5.67)$$

where  $\gamma$  is specific heat ratio and  $\mathcal{H}(x)$  is the Heaviside step function. Zeman recommends using  $\Lambda = 0.60$  and  $M_{t_o} = 0.10\sqrt{2/(\gamma+1)}$  for free shear flows. For boundary layers, their values must increase to  $\Lambda = 0.66$  and  $M_{t_o} = 0.25\sqrt{2/(\gamma+1)}$ . Zeman uses a different set of closure coefficients for boundary layers because he postulates that they depend upon the kurtosis,  $\overline{u'^4}/(\overline{u'^2})^2$ . The kurtosis is presumed to be different for free shear flows as compared to boundary layers. While this is most likely true, it is not much help for two-equation or second-order closure models since such models only compute double correlations and make closure approximations for triple correlations. Quadruple correlations such as  $\overline{u'^4}$  are beyond the scope of these models.

To illustrate how well these models perform, we consider mixing of a supersonic stream and a quiescent fluid with constant total temperature. For simplicity, we present results only for the  $k-\omega$  model as  $k-\epsilon$  results are nearly identical. The equations of motion have been transformed to similarity form for the far field and integrated using Program MIXER, which is described in Appendix C. Figure 5.1 compares computed and measured [see Kline et al. (1981)] spreading rate,  $C_\delta$ . As in the incompressible case, spreading rate is defined as the difference between the values of  $y/x$  where  $(U - U_2)^2/(U_1 - U_2)^2$  is 9/10 and 1/10. The quantity  $C_{\delta_o}$  denotes the incompressible spreading rate and  $M_c$  is convective Mach number, viz.,

$$M_c = \frac{U_1 - U_2}{a_1 + a_2} \quad (5.68)$$

Since  $U_2 = 0$ , Equation (5.68) simplifies to

$$M_c = \frac{M_1}{1 + \left[ 1 + \frac{(\gamma-1)}{2} M_1^2 \right]^{1/2}} \quad (5.69)$$

As shown, the unmodified  $k-\omega$  model fails to predict a significant decrease in spreading rate as Mach number increases. By contrast, the Sarkar, Zeman and Wilcox modifications yield much closer agreement between computed and measured spreading rate.

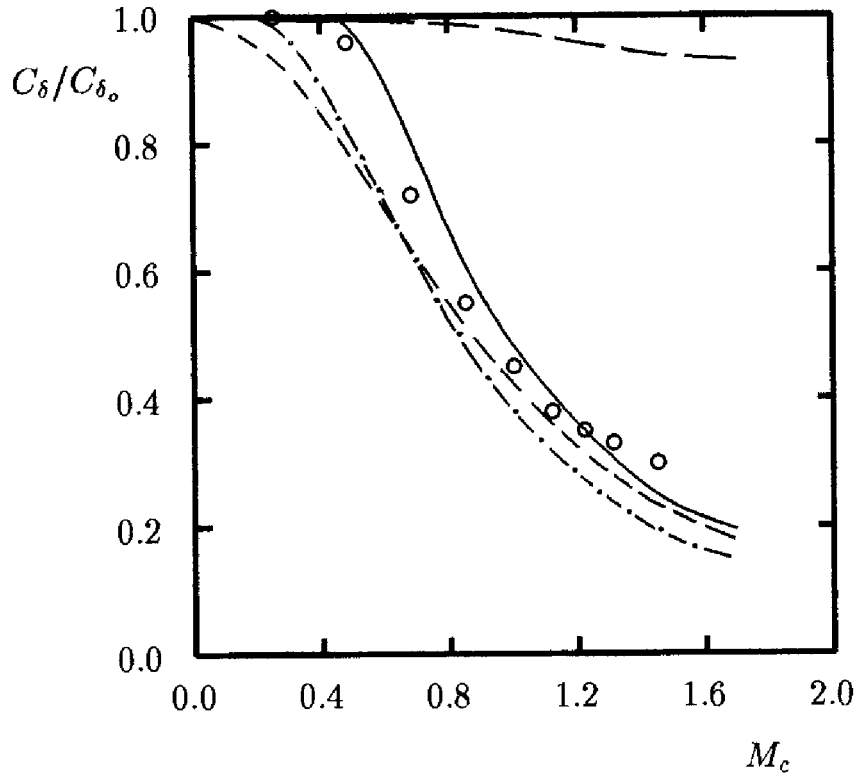


Figure 5.1: Comparison of computed and measured spreading rate for a compressible mixing layer; — — Unmodified  $k$ - $\omega$  model; — Wilcox,  $\xi^* = 3/2$ ; - - - Sarkar,  $\xi^* = 1$ ; - · - Zeman,  $\xi^* = 3/4$ ;  $\circ$  Langley curve [Kline et al. (1981)].

We turn now to the adiabatic-wall flat-plate boundary layer. The equations of motion for the  $k$ - $\omega$  model have been solved with Program EDDYBL (see Appendix D). Figure 5.2 compares computed skin friction,  $c_f$ , with a correlation of measured values for freestream Mach number between 0 and 5. As shown, the unmodified model virtually duplicates measured skin friction. By contrast, the Sarkar compressibility modification yields a value for  $c_f$  at Mach 5 that is 18% lower than the value computed with  $\xi^* = 0$ . Using the Wilcox dilatation-dissipation model yields very little difference in skin friction.

Using  $\Lambda = 0.60$  and  $M_{t_o} = 0.10\sqrt{2/(\gamma+1)}$  in Zeman's model, computed  $c_f$  at Mach 5 is 15% smaller than the value obtained with the unmodified model. Increasing  $\Lambda$  and  $M_{t_o}$  to 0.66 and  $0.25\sqrt{2/(\gamma+1)}$ , respectively, eliminates this discrepancy. However, using this large a value for  $M_{t_o}$  for the mixing layer results in discrepancies in excess of 100% between computed and measured spreading rate for  $M_c$  in excess of 1.

These results make it clear that neither the Sarkar nor the Zeman compressibility term is completely satisfactory for both the mixing layer and

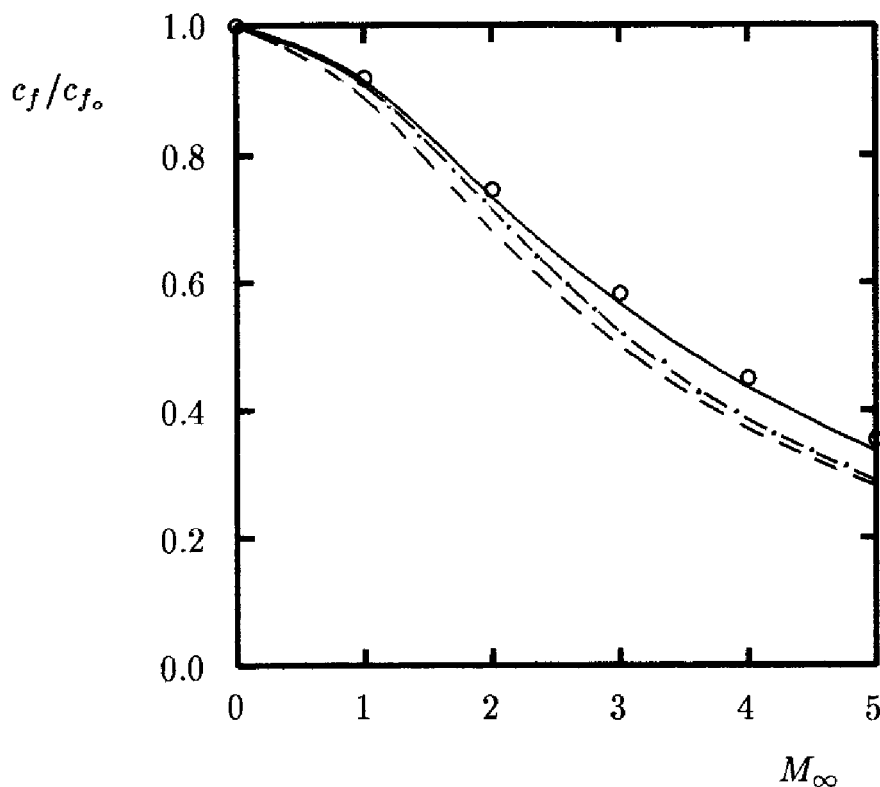


Figure 5.2: Comparison of computed and measured skin friction for a compressible flat-plate boundary layer; —  $k$ - $\omega$  with  $\xi^* = 0$  and  $\xi^* = 3/2$ ; - - - Sarkar,  $\xi^* = 1$ ; - · - Zeman,  $\xi^* = 3/4$ ; o Van Driest correlation.

boundary layers. The Wilcox dilatation-dissipation model was formulated to resolve this dilemma. Decomposing the dissipation into solenoidal and dilatation components is an important innovation, and is not the root cause of the problem. Rather, the postulated form of the function  $F(M_t)$  is the weak link. The Wilcox model provides a satisfactory alternative.

Inspection of the magnitude of turbulence Mach number in mixing layers and boundary layers shows that all is needed is an alternative to the Sarkar and Zeman functional dependencies of  $\epsilon_d$  upon  $M_t$ . Table 5.1 shows why the Sarkar term improves predictions for the mixing layer. The unmodified  $k$ - $\omega$  model predicts peak values of  $M_t$  in the mixing layer that are more than twice the values in the boundary layer for the same freestream Mach number. Using the Sarkar compressibility term reduces  $(M_t)_{max}$  by about one third for the mixing layer when  $M_\infty \geq 2$ . Even with this much reduction,  $(M_t)_{max}$  for the mixing layer remains higher than the largest value of  $(M_t)_{max}$  in the boundary layer all the way up to Mach 5.

For Mach 1, the Sarkar term reduces mixing-layer spreading rate below measured values (Figure 5.1). Zeman's term predicts a somewhat larger spreading rate at Mach 1, mainly because of the Mach number threshold in



Table 5.1: Maximum Turbulence Mach Number,  $(M_t)_{max}$ 

$M_\infty$	Boundary Layer		Mixing Layer	
	$\xi^* = 0$	$\xi^* = 1$	$\xi^* = 0$	$\xi^* = 1$
0	0	0	0	0
1	.061	.061	.180	.159
2	.114	.107	.309	.227
3	.149	.135	.384	.245
4	.174	.154	.424	.254
5	.191	.171	.453	.266

Zeman's model. That is, Zeman postulates that the compressibility effect is absent for  $M_t < M_{t_o}$ . Zeman's Mach number threshold also yields smaller differences between computed and measured boundary-layer skin friction at lower Mach numbers (see Figure 5.2). These observations show that an improved compressibility term can be devised by extending Zeman's threshold Mach number to a larger value of  $M_t$ . The Wilcox model simply combines the relative simplicity of Sarkar's functional form for  $F(M_t)$  with Zeman's Mach number threshold to accomplish this end.

## 5.6 Compressible Law of the Wall

In this section, we use perturbation methods to examine  $k$ - $\omega$  and  $k$ - $\epsilon$  model predicted, compressible log-layer structure. The results are particularly illuminating and clearly demonstrate why the Sarkar and Zeman compressibility terms adversely affect boundary-layer predictions.

Recall from Section 4.6.1 that the log layer is the region sufficiently close to the solid boundary for neglect of convective terms and far enough distant for molecular diffusion terms to be dropped. In the log layer, the equations of motion based on the  $k$ - $\omega$  model simplify to the following.

$$\mu_T \frac{d\tilde{u}}{dy} = \bar{\rho}_w u_\tau^2 \quad (5.70)$$

$$\mu_T \frac{d}{dy} \left[ \frac{C_p \tilde{T}}{Pr_T} + \frac{1}{2} \tilde{u}^2 + \sigma^* k \right] = -q_w \quad (5.71)$$

$$\sigma^* \frac{d}{dy} \left[ \mu_T \frac{dk}{dy} \right] + \mu_T \left( \frac{d\tilde{u}}{dy} \right)^2 - \beta^* \bar{\rho} \omega k = 0 \quad (5.72)$$

$$\sigma \frac{d}{dy} \left[ \mu_T \frac{d\omega}{dy} \right] + \alpha \bar{\rho} \left( \frac{d\tilde{u}}{dy} \right)^2 - \beta \bar{\rho} \omega^2 = 0 \quad (5.73)$$

$$\bar{\rho} \tilde{T} = \bar{\rho}_w \tilde{T}_w \quad (5.74)$$

The quantity  $u_\tau$  is friction velocity defined as  $\sqrt{\tau_w / \bar{\rho}_w}$  where  $\tau_w$  is surface shear stress and  $\bar{\rho}_w$  is density at the surface. Also,  $\tilde{T}_w$  is surface temperature,  $q_w$  is surface heat flux and  $C_p$  is specific heat at constant pressure. Finally,  $y$  is distance from the surface.

Following Saffman and Wilcox (1974), we change independent variables from  $y$  to  $\tilde{u}$ . Consequently, derivatives transform according to

$$\mu_T \frac{d}{dy} = \mu_T \frac{d\tilde{u}}{dy} \frac{d}{d\tilde{u}} = \bar{\rho}_w u_\tau^2 \frac{d}{d\tilde{u}} \quad (5.75)$$

With this change of variables, we replace Equations (5.71)-(5.73) by the following.

$$\frac{d}{d\tilde{u}} \left[ \frac{C_p \tilde{T}}{Pr_T} + \frac{1}{2} \tilde{u}^2 + \sigma^* k \right] = - \frac{q_w}{\bar{\rho}_w u_\tau^2} \quad (5.76)$$

$$\sigma^* \frac{d^2 k}{d\tilde{u}^2} + 1 - \frac{\beta^* \bar{\rho}^2 k^2}{\bar{\rho}_w^2 u_\tau^4} = 0 \quad (5.77)$$

$$\sigma \frac{d^2 \omega}{d\tilde{u}^2} + \alpha \frac{\omega}{k} - \frac{\beta \bar{\rho}^2 k \omega}{\bar{\rho}_w^2 u_\tau^4} = 0 \quad (5.78)$$

Integrating Equation (5.76) yields the temperature, and hence the density, as a function of velocity and Mach number based on friction velocity,  $M_\tau \equiv u_\tau / a_w$ .

$$\frac{\tilde{T}}{\tilde{T}_w} = \frac{\bar{\rho}_w}{\bar{\rho}} = 1 - (\gamma - 1) Pr_T M_\tau^2 \left[ \frac{1}{2} \left( \frac{\tilde{u}}{u_\tau} \right)^2 + \frac{q_w}{\bar{\rho}_w u_\tau^3} \left( \frac{\tilde{u}}{u_\tau} \right) + \sigma^* \left( \frac{k}{u_\tau^2} \right) \right] \quad (5.79)$$

Next, we assume a solution of the form:

$$\bar{\rho} k = \Gamma \bar{\rho}_w u_\tau^2 \quad (5.80)$$

where  $\Gamma$  is a constant to be determined. Substituting Equations (5.79) and (5.80) into Equation (5.77), and noting that  $M_t^2 = 2\Gamma M_\tau^2$ , leads to the following quartic equation for  $\Gamma$ .

$$\beta_o^* [1 + 2\xi^* M_\tau^2 \Gamma] [1 + (\gamma - 1)Pr_T \sigma^* M_\tau^2 \Gamma] \Gamma^2 = 1 \quad (5.81)$$

As can easily be verified, when  $M_\tau^2 \ll 1$ , the asymptotic solution for  $\Gamma$  is

$$\Gamma = \frac{1}{\sqrt{\beta_o^*}} - \left[ \frac{\xi^* + \frac{(\gamma-1)}{2} Pr_T \sigma^*}{\beta_o^*} \right] M_\tau^2 + \dots \quad (5.82)$$

Finally, in terms of  $\Gamma$ , Equation (5.78) simplifies to

$$\sigma \frac{d^2 \omega}{d\tilde{u}^2} + \{ \alpha - [\beta_o - 2\beta_o^* \xi^* M_\tau^2 \Gamma] \Gamma^2 \} \frac{\bar{\rho} \omega}{\bar{\rho}_w u_\tau^2 \Gamma} = 0 \quad (5.83)$$

Combining Equations (5.79) and (5.80) yields the density as a function of velocity and  $\Gamma$ .

$$\frac{\bar{\rho}_w}{\bar{\rho}} = \frac{1 - \frac{(\gamma-1)}{2} Pr_T M_\tau^2 \left[ \left( \frac{\tilde{u}}{u_\tau} \right)^2 + \frac{2q_w}{\rho_w u_\tau^3} \left( \frac{\tilde{u}}{u_\tau} \right) \right]}{1 + (\gamma - 1) Pr_T \sigma^* \Gamma M_\tau^2} \quad (5.84)$$

Equation (5.84) assumes a more compact form if we introduce the freestream velocity,  $U_\infty$ . A bit more algebra yields

$$\frac{\bar{\rho}_w}{\bar{\rho}} = \frac{1 + Bv - A^2 v^2}{1 + (\gamma - 1) Pr_T \sigma^* \Gamma M_\tau^2} \quad (5.85)$$

where

$$\left. \begin{aligned} v &= \tilde{u}/U_\infty \\ A^2 &= \frac{(\gamma-1)}{2} Pr_T M_\infty^2 (\tilde{T}_\infty/\tilde{T}_w) \\ B &= -Pr_T q_w U_\infty / (C_p \tilde{T}_w \tau_w) \end{aligned} \right\} \quad (5.86)$$

Using Equations (5.82), (5.85) and (5.86), and retaining terms up to  $O(M_\tau^2)$ , Equation (5.83) assumes the following form,

$$\frac{d^2 \omega}{dv^2} - \left[ \frac{K_\omega^2 (U_\infty/u_\tau)^2}{1 + Bv - A^2 v^2} \right] \omega = 0 \quad (5.87)$$

where the constant  $K_\omega$  is defined by

$$K_\omega^2 = \kappa^2 - \left[ \frac{(2 + \alpha + \beta_o/\beta_o^*)\xi^*}{\sigma} + \frac{(\gamma - 1) Pr_T (3\alpha - \beta_o/\beta_o^*)\sigma^*}{2\sigma} \right] M_\tau^2 + \dots \quad (5.88)$$

and  $\kappa$  is Kármán's constant. Because  $U_\infty/u_\tau \gg 1$ , we can use the WKB method [see Kevorkian and Cole (1981)] to solve Equation (5.87). Noting that  $\omega$  decreases as  $\tilde{u}/U_\infty$  increases, the asymptotic solution for  $\omega$  is

$$\omega \sim C [1 + Bv - A^2 v^2]^{1/4} \exp[-K_\omega u^*/u_\tau] \quad (5.89)$$

where  $C$  is a constant of integration and  $u^*$  is defined by

$$\frac{u^*}{U_\infty} = \frac{1}{A} \sin^{-1} \left( \frac{2A^2 v - B}{\sqrt{B^2 + 4A^2}} \right) \quad (5.90)$$

Combining Equations (5.70), (5.80) and (5.89), we can relate velocity and distance from the surface.

$$\int [1 + Bv - A^2 v^2]^{-1/4} \exp[K_\omega u^*/u_\tau] dv \sim \frac{Cy}{\Gamma U_\infty} \quad (5.91)$$

We integrate by parts to generate the asymptotic expansion of the integral in Equation (5.91) as  $U_\infty/u_\tau \rightarrow \infty$ . Hence,

$$[1 + Bv - A^2 v^2]^{1/4} \exp[K_\omega u^*/u_\tau] \sim \frac{K_\omega Cy}{\Gamma u_\tau} \quad (5.92)$$

Finally, we set the constant of integration  $C = \Gamma u_\tau^2 / (K_\omega \nu_w)$ . Taking the natural log of Equation (5.92), we conclude that

$$\frac{u^*}{u_\tau} \sim \frac{1}{K_\omega} \ln \left( \frac{u_\tau y}{\nu_w} \right) + B_\omega \quad (5.93)$$

The quantity  $B_\omega$  is the effective "constant" in the law of the wall defined by

$$B_\omega = B + \frac{1}{K_\omega} \ln \left( \frac{\bar{\rho}}{\bar{\rho}_w} \right)^{1/4} \quad (5.94)$$

where  $B$  is a true constant.

Most of the analysis above holds for the  $k$ - $\epsilon$  model. The only significant difference is in the  $\epsilon$  equation which is as follows.

$$\sigma_\epsilon^{-1} \frac{d}{dy} \left[ \mu_T \frac{d\epsilon}{dy} \right] + C_\mu C_{\epsilon 1} \bar{\rho} k \left( \frac{d\tilde{u}}{dy} \right)^2 - C_{\epsilon 2} \frac{\bar{\rho} \epsilon^2}{k} = 0 \quad (5.95)$$

Equations (5.80), (5.82) and (5.85) are still valid for the turbulence kinetic energy and density, provided  $\sigma^*$  is replaced by  $\sigma_k^{-1}$ . The transformed equation for  $\epsilon$  is

$$\frac{d^2 \epsilon}{dv^2} - \left[ \frac{K_\epsilon^2 (U_\infty/u_\tau)^2}{1 + Bv - A^2 v^2} \right] \epsilon = 0 \quad (5.96)$$

where the constant  $K_\epsilon$  is defined by

$$K_\epsilon^2 = \kappa^2 - \left[ (C_{\epsilon 1} + C_{\epsilon 2}) \sigma_\epsilon \xi^* + \frac{(\gamma - 1) Pr_T (3C_{\epsilon 1} - C_{\epsilon 2}) \sigma_\epsilon}{2\sigma_k} \right] M_\tau^2 + \dots \quad (5.97)$$

In arriving at Equation (5.97), recall from Equation (4.106) that the  $k$ - $\epsilon$  model's closure coefficients are related by

$$\kappa^2 = \sqrt{C_\mu} (C_{\epsilon 2} - C_{\epsilon 1}) \sigma_\epsilon \quad (5.98)$$

The asymptotic solution for  $\epsilon$  is

$$\epsilon \sim C [1 + Bv - A^2 v^2]^{1/4} \exp[-K_\epsilon u^*/u_\tau] \quad (5.99)$$

Velocity and distance from the surface are related by

$$\int [1 + Bv - A^2 v^2]^{3/4} \exp[K_\epsilon u^*/u_\tau] dv \sim C_0 y \quad (5.100)$$

where  $C_0$  is a constant of integration. Consequently, Equation (5.92) is replaced by

$$[1 + Bv - A^2 v^2]^{5/4} \exp[K_\epsilon u^*/u_\tau] \sim C_1 y \quad (5.101)$$

where  $C_1$  is another constant of integration. Finally, the law of the wall for the  $k$ - $\epsilon$  model is

$$\frac{u^*}{u_\tau} \sim \frac{1}{K_\epsilon} \ell n \left( \frac{u_\tau y}{\nu_w} \right) + B_\epsilon \quad (5.102)$$

where  $B_\epsilon$  is given by

$$B_\epsilon = B + \frac{1}{K_\epsilon} \ell n \left( \frac{\bar{\rho}}{\bar{\rho}_w} \right)^{5/4} \quad (5.103)$$

Equations (5.93) and (5.102) are very similar to the compressible law of the wall deduced by Van Driest (1951). There are two ways in which these equations differ from the Van Driest law.

The first difference is the effective Kármán constants,  $K_\omega$  and  $K_\epsilon$ , which vary with  $M_\tau$  according to Equation (5.88) for the  $k$ - $\omega$  model and Equation (5.97) for the  $k$ - $\epsilon$  model. In terms of each model's closure coefficients,  $K_\omega$  and  $K_\epsilon$  are given by (for  $M_\tau \ll 1$ ):

$$K_\omega^2 \sim \kappa^2 [1 - (40.29\xi^* + 0.87)M_\tau^2 + \dots] \quad (5.104)$$

and

$$K_\epsilon^2 \sim \kappa^2 [1 - (23.92\xi^* + 3.07)M_\tau^2 + \dots] \quad (5.105)$$

Table 5.2: Effective Kármán Constant

$M_\infty$	$M_\tau _{\xi^*=0}$	$K_\omega$	$M_\tau _{\xi^*=1}$	$K_\omega$
0	0	.410	0	.410
1	.032	.410	.031	.402
2	.048	.410	.046	.392
3	.052	.410	.049	.389
4	.050	.410	.046	.392
5	.048	.410	.043	.394

Table 5.2 summarizes results obtained in the boundary-layer computations of Section 5.5 for the unmodified  $k$ - $\omega$  model ( $\xi^* = 0$ ) and for the  $k$ - $\omega$  model with the Sarkar compressibility term ( $\xi^* = 1$ ). The value of  $K_\omega$  for the unmodified model deviates from the Kármán constant,  $\kappa = 0.41$ , by less than 0.12% for freestream Mach numbers between 0 and 5. By contrast, when  $\xi^* = 1$ , the deviation is as much as 5.10%. This large a deviation in the effective Kármán constant is consistent with the observed differences between computed and measured skin friction. Similarly, with  $M_\tau = .05$ ,  $K_\epsilon$  differs from  $\kappa$  by 0.5% and 3.5% for  $\xi^* = 0$  and 1, respectively. Thus the Sarkar compressibility term has a somewhat smaller effect on  $\kappa$  for the  $k$ - $\epsilon$  model relative to the effect on  $\kappa$  for the  $k$ - $\omega$  model.

To see why a small perturbation in  $\kappa$  corresponds to a larger perturbation in  $c_f$ , differentiate the law of the wall with respect to  $\kappa$ . Noting that  $c_f = \frac{1}{2}u_\tau^2/U_\infty^2$ , a little algebra shows that

$$\frac{dc_f}{d\kappa} \approx \frac{2}{\kappa}c_f \quad (5.106)$$

Thus, we should expect  $\Delta c_f/c_f$  to be double the value of  $\Delta\kappa/\kappa$ . The numerical results indicate somewhat larger differences in  $c_f$ , but the trend is clear.

The second way Equations (5.93) and (5.102) differ from the Van Driest compressible law of the wall is in the effective variation of the “constant” terms  $B_\omega$  and  $B_\epsilon$  with  $(\bar{\rho}/\bar{\rho}_w)$ . Because the exponent is only 1/4, the effect is minor for the  $k$ - $\omega$  model. By contrast, the exponent is 5/4 for the  $k$ - $\epsilon$  model. This large an exponent has a much stronger effect on predicted boundary layer properties. Figure 5.3 compares computed and measured [Fernholz and Finlay (1981)] velocity profiles for adiabatic-wall boundary layers at Mach numbers 4.5 and 10.3. The computed results are for the Wilcox (1988a)  $k$ - $\omega$  model and for Chien’s (1982) low-Reynolds-number

$k$ - $\epsilon$  model. Equations (5.93) and (5.102) are also shown (with  $B = 5.0$ ) to underscore the importance of the models' variable "constant" in the compressible law of the wall.

These results are consistent with the analysis of Huang, Bradshaw and Coakley (1992) that shows how poorly the  $k$ - $\epsilon$  model performs for compressible boundary layers. Since  $\bar{\rho}/\bar{\rho}_w > 1$  for all but strongly cooled walls, its effect is to increase the "constant" in the law of the wall with a corresponding decrease in  $c_f$ . The Sarkar and Zeman terms will thus amplify this inherent deficiency of the  $k$ - $\epsilon$  model.

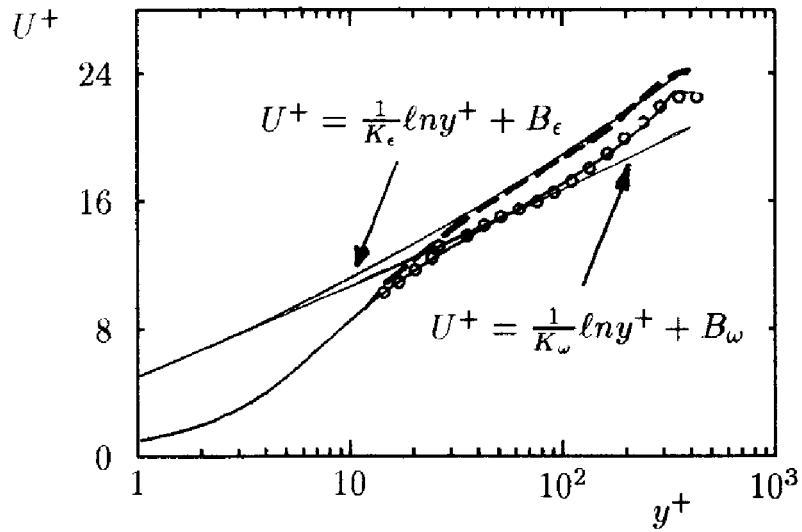
To put these results in proper perspective, we must not lose sight of the fact that the  $k$ - $\epsilon$  model requires the use of either wall functions or viscous damping functions in order to calculate wall-bounded flows. If these functions have an effect that persists well into the log layer, it may be possible to suppress the  $k$ - $\epsilon$  model's inherent flaws at low Reynolds numbers. However, the perturbation analysis shows that such a model will not be asymptotically consistent with the compressible law of the wall in the limit of infinite Reynolds number. In effect, such a model would have compensating errors that may fortuitously yield reasonably close agreement with the law of the wall at low Reynolds numbers.

As a final comment, if we had used  $\rho\epsilon$  as the dependent variable in Equation (5.95) in place of  $\epsilon$ , the exponent  $5/4$  in Equation (5.103) would be reduced to  $1/4$ . Presumably, this change would improve  $k$ - $\epsilon$  model predictions for compressible boundary layers. The effect of this rescaling on the mixing layer is unclear.

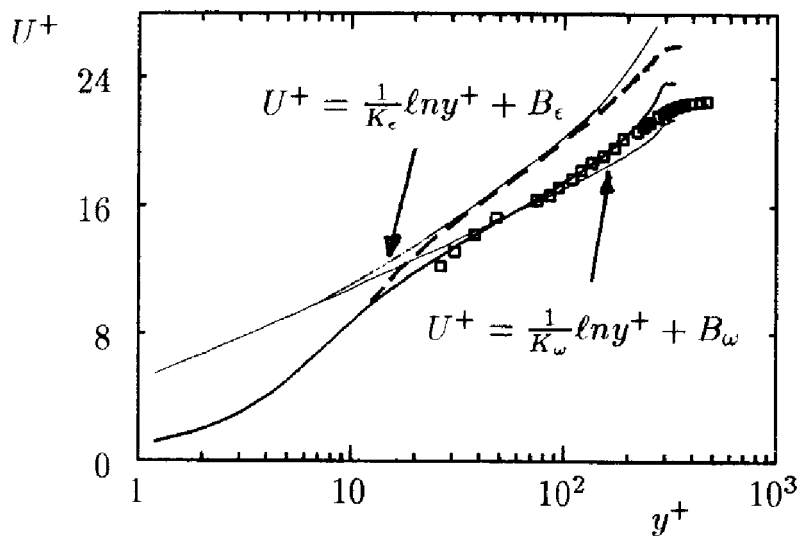
## 5.7 Compressible Boundary Layers

Most turbulence models are capable of providing reasonably accurate predictions for constant-pressure, adiabatic-wall boundary layers provided the Mach number does not exceed about 5. Similar to the incompressible situation, adverse pressure gradients continue to be anathema to the  $k$ - $\epsilon$  model, while presenting no major problem for the  $k$ - $\omega$  model. When surface heat transfer is present, model predictions often show nontrivial discrepancies from measured values for most turbulence models.

Algebraic models such as the Cebeci-Smith and Baldwin-Lomax models (see Subsections 3.4.1 and 3.4.2) require no special compressibility corrections. For the sake of clarity, recall that the Cebeci-Smith model uses the velocity thickness,  $\delta_v^*$ , defined in Equation (3.115) for both compressible and incompressible flow. The velocity thickness differs from the displacement



(a) Mach 4.5



(b) Mach 10.3

Figure 5.3: Comparison of computed and measured velocity profiles for compressible flat-plate boundary layers; — Wilcox  $k-\omega$ ; - - Chien  $k-\epsilon$ ;  $\circ$  Coles;  $\square$  Watson.



thickness,  $\delta^*$ , which is defined for compressible flows by

$$\delta^* = \int_0^\infty \left( 1 - \frac{\bar{\rho}}{\bar{\rho}_e} \frac{\tilde{u}}{\tilde{u}_e} \right) dy \quad (5.107)$$

The primary reason algebraic models should fare well for compressible boundary layers without special compressibility modifications is illustrated by Maise and McDonald (1967). Using the best experimental data of the time for compressible boundary layers, they inferred the mixing length variation. Their analysis shows that for Mach numbers up to 5:

- Velocity profiles for adiabatic walls correlate with the incompressible profile when the Van Driest (1951) scaling is used, i.e.,

$$\frac{u^*}{U_\infty} = \frac{1}{A} \sin^{-1} \left( A \frac{\tilde{u}}{U_\infty} \right), \quad A^2 = \frac{(\gamma - 1)}{2} M_\infty^2 (\tilde{T}_\infty / \tilde{T}_w) \quad (5.108)$$

- The Van Driest scaling fails to correlate compressible velocity profiles when surface heat transfer is present.
- The classical mixing length is independent of Mach number.

Using singular perturbation methods, Barnwell (1992) shows that algebraic models are consistent with the Maise-McDonald observations. Many researchers have applied the Cebeci-Smith model to compressible boundary layers, showing excellent agreement with measurements for adiabatic walls and somewhat larger differences when surface heat transfer is present. The Baldwin-Lomax model yields similar predictions.

Because the length scale employed in most one-equation models is patterned after the mixing length, they should also be expected to apply to compressible flows without ad hoc compressibility modifications. This is indeed the case, especially for newer models, which have been designed for compressible-flow applications. Figure 4.2, for example, shows how the Baldwin-Barth (1990) model performs for a Mach 2 flat-plate boundary layer.

As we have seen in the last subsection, the issue is more complicated for two-equation models. The log-layer solution indicates that the length scale for the  $k$ - $\omega$  and  $k$ - $\epsilon$  models varies linearly with distance from the surface, independent of Mach number. The models even predict the Van Driest velocity scaling. Thus, two-equation models are consistent with two of the most important observations made by Maise and McDonald, at least in the log layer. However, we have also seen that the  $\epsilon$  equation includes a nonphysical density effect that distorts the model's log-layer structure, and precludes a satisfactory solution. By contrast, the  $\omega$  equation is entirely

consistent with the Maise-McDonald observations. As shown in Figures 5.2 and 5.3, the  $k$ - $\omega$  model provides excellent quantitative agreement with measurements for Mach numbers up to about 5.

Turning to effects of pressure gradient, Figures 5.4 and 5.5 compare computed and measured skin friction and velocity profiles for two compressible boundary layers with adverse pressure gradient. Figure 5.4 corresponds to a Mach 4, adiabatic-wall experiment conducted by Zwarts [see Kline et al. (1981) — Flow 8411]. Computed results are shown for the Wilcox  $k$ - $\omega$  model without viscous corrections and for the Chien (1982)  $k$ - $\epsilon$  model. Although the effect is small for this flow, neither computation includes a dilatation-dissipation correction. As shown,  $k$ - $\omega$  model predictions fall within the scatter of the experimental data. By contrast, the  $k$ - $\epsilon$  model skin friction is about 8% lower than measured at the beginning of the computation where the Mach number is 4. This is consistent with results shown in Figure 5.3(a). Because the flow is decelerating, the Mach number decreases with distance, and falls to 3 by the end of the run. As a result,  $\bar{\rho}_e/\bar{\rho}_w$  is only half its upstream value, and the corresponding distortion of the  $k$ - $\epsilon$  model's log-layer velocity profile is greatly reduced. Consequently, the  $k$ - $\epsilon$  model's velocity profile is fortuitously in close agreement with the measured profile.

Figure 5.5 presents a similar comparison for a Mach 2.65 boundary layer with adverse pressure gradient and mild surface heating. The ratio of wall temperature to the adiabatic-wall temperature,  $T_w/T_{aw}$ , varies between 1.07 and 1.13 for the flow. Again, because the Mach number is in the low supersonic range, the density term in the  $k$ - $\epsilon$  model's law of the wall is small. The value of  $K_\epsilon^{-1} \ln(\bar{\rho}/\bar{\rho}_w)^{5/4}$  ranges between 0.50 at  $y^+ = 100$  to 1.45 at  $y^+ = 5000$ . By comparison, the distortion in the  $k$ - $\omega$  model's law of the wall is just a fifth of these values.

While the  $k$ - $\epsilon$  model solutions for both of these adverse pressure gradient cases are nearly as close to measurements as the  $k$ - $\omega$  model solutions, similar results should not be expected for higher Mach numbers. Many compressible-flow experiments have been conducted for Mach numbers of 3 and less. Far fewer experiments have been done at higher Mach numbers. Hence these results show how a model calibrated for the best data available may not apply at higher Mach numbers.

The  $k$ - $\epsilon$  model's near-wall behavior has a significant impact on model predictions, and Chien's model happens to be optimum for these two flows. The Jones-Launder (1972) and Launder-Sharma (1974) models, for example, predict skin friction values more than twice measured values for these two flows. Zhang et al. (1992) have developed a low-Reynolds-number  $k$ - $\epsilon$  model that yields close agreement with constant-pressure boundary layer data for Mach numbers up to 10. Interestingly, they note from the work

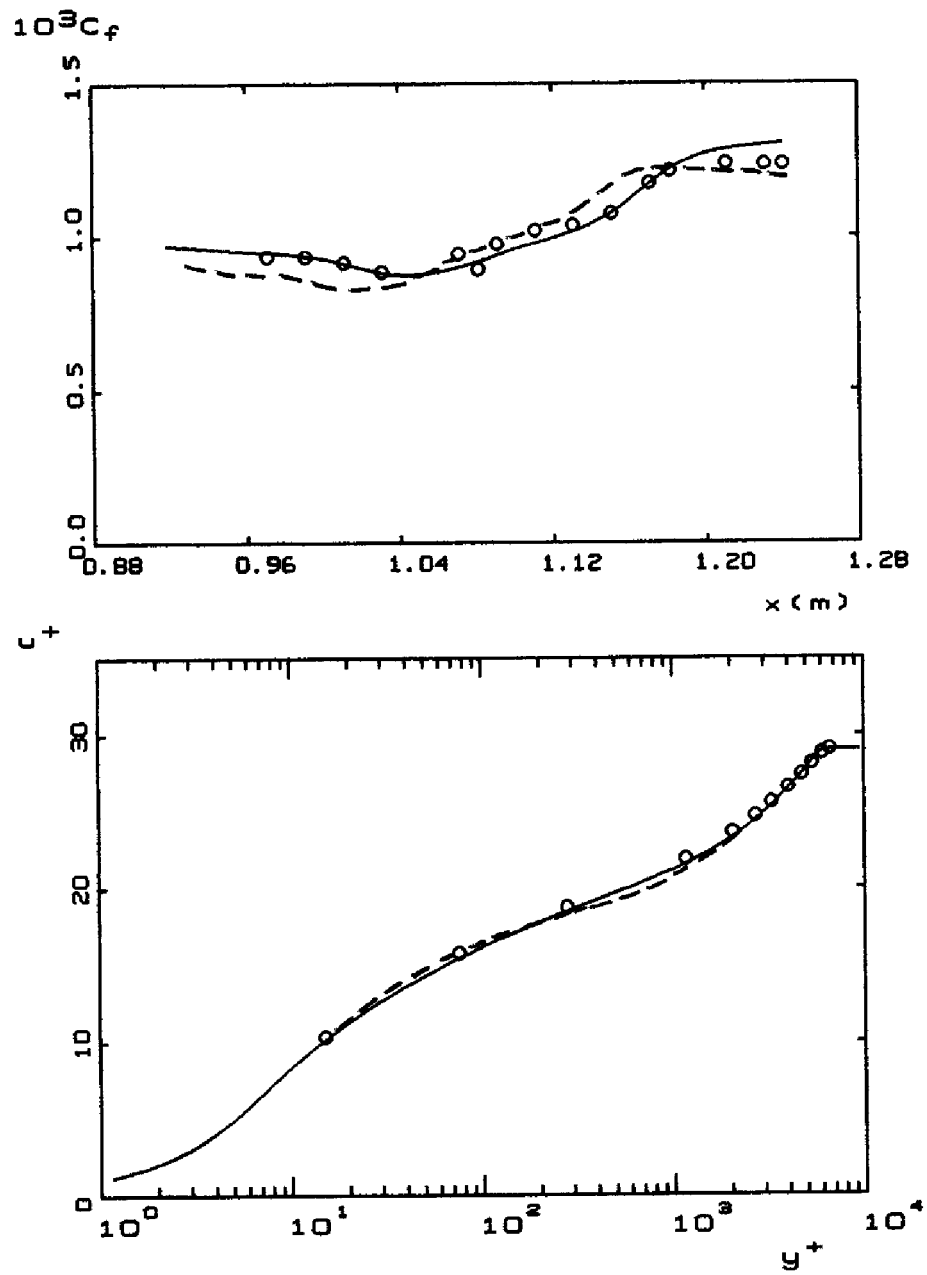


Figure 5.4: Computed and measured skin friction and velocity profile (at  $x = 1.18$  m.) for a Mach 4, adiabatic-wall boundary layer with an adverse pressure gradient; —  $k-\omega$  model; - - Chien  $k-\epsilon$  model;  $\circ$  Zwarts.

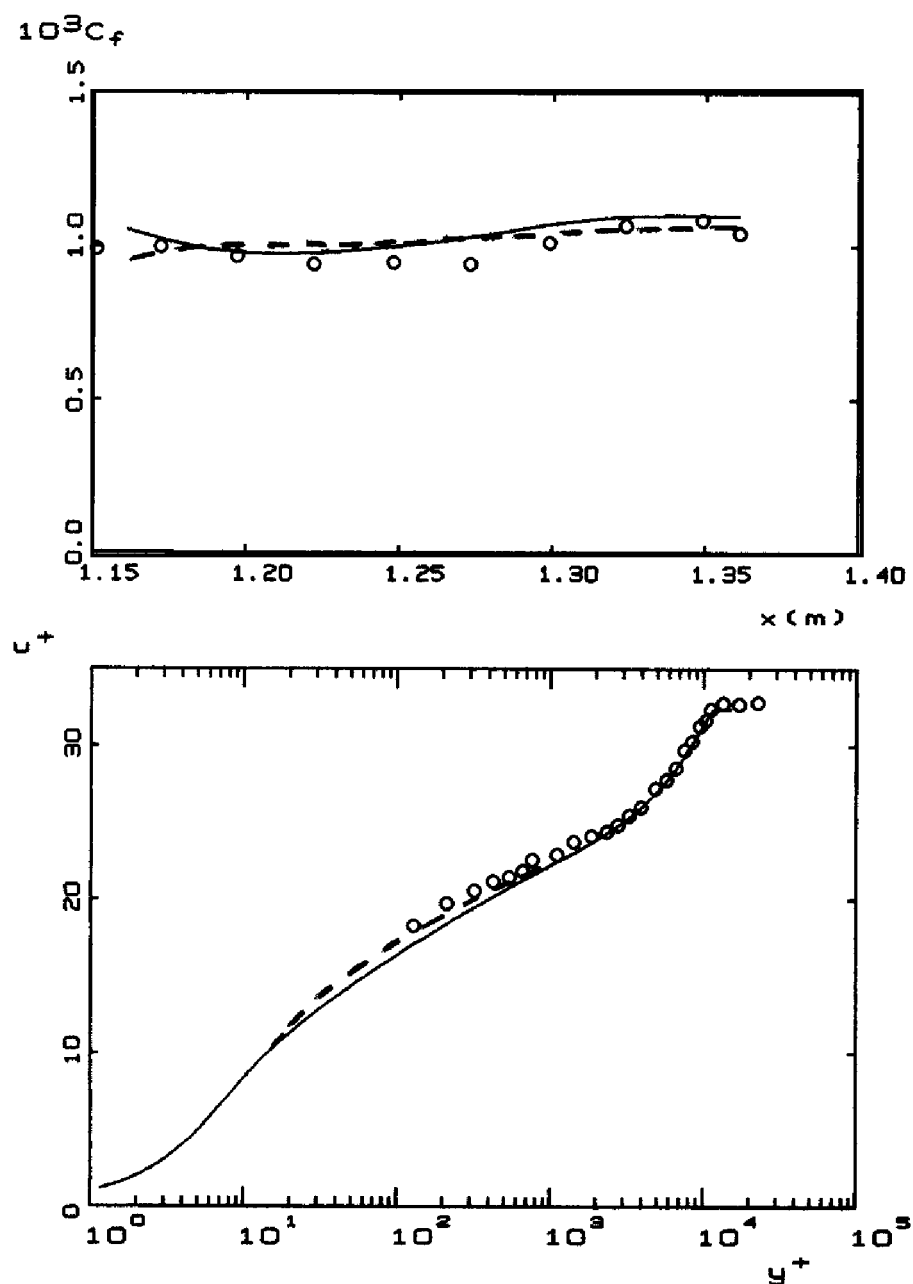


Figure 5.5: Computed and measured flow properties for a Mach 2.65, heated-wall boundary layer with an adverse pressure gradient; —  $k-\omega$  model; - - - Chien  $k-\epsilon$  model;  $\circ$  Fernando and Smits.

of Coleman and Mansour (1991) that the exact Favre-averaged equation for solenoidal dissipation,  $\epsilon_s$ , includes a term proportional to the rate of change of the kinematic viscosity,  $\bar{\nu}$ , as follows:

$$\bar{\rho} \frac{d\epsilon_s}{dt} = \frac{\bar{\rho}\epsilon_s}{\bar{\nu}} \frac{d\bar{\nu}}{dt} + \dots \quad (5.109)$$

which can be rewritten as

$$\bar{\rho}\bar{\nu} \frac{d}{dt} \left( \frac{\epsilon_s}{\bar{\nu}} \right) = \dots \quad (5.110)$$

This corresponds to an effective change of dependent variable in the  $\epsilon_s$  equation. Assuming a power-law viscosity law, i.e.,  $\bar{\mu} \propto \tilde{T}^n$ , the effective rescaled dependent variable would be  $\bar{\rho}^{(1+n)}\epsilon_s$ . Correspondingly, the exponent 5/4 in Equation (5.103) would become  $(n + 1/4)$ . For a typical value  $n = 7/10$ , the new coefficient would be 0.95. Hence this term should yield only a slight improvement for the model's distorted law of the wall. Actually, through a series of closure approximations, Zhang et al. combine this term with other terms and arrive at a rescaling that effectively leads to using  $\bar{\rho}^{-0.61}\epsilon_s$ . This would correspond to replacing the exponent 5/4 by 1.86 which would yield even more distortion. It is unclear how Zhang et al. have circumvented the inherent flaw in the  $k$ - $\epsilon$  model for compressible flows. Since virtually all of their applications to date have been for low-Reynolds-number flows, it is possible that their low-Reynolds-number damping functions penetrate far enough above the sublayer to offset the behavior indicated in Equation (5.103).

Turning to effects of surface heat transfer, Figure 5.6 compares computed skin friction with a correlation of measured values [see Kline, et al. (1981) — Flow 8201]. As shown, the  $k$ - $\omega$  model virtually duplicates the Van Driest correlation, although noticeable differences appear when wall temperature is reduced to one fifth of the adiabatic-wall temperature. The  $k$ - $\epsilon$  model predictions of Zhang et al. (1992) show a similar trend.

As the final application, consider compressible flow over roughened flat plates. Note that this provides a test of the  $k$ - $\omega$  model rough-surface boundary condition on flows for which it has not been calibrated. Figure 5.7 compares computed skin friction with the data summarized by Reda, Ketter and Fan (1974). Computations have been done for Mach numbers of 0, 1 and 5 and dimensionless roughness height,  $k_R^+$ , ranging from 0 to 100. For each Mach number, the reference smooth-wall skin friction coefficient,  $c_{f_o}$ , corresponds to a momentum-thickness Reynolds number,  $Re_\theta$ , of 10,000. As shown, computed skin friction falls well within experimental data scatter.

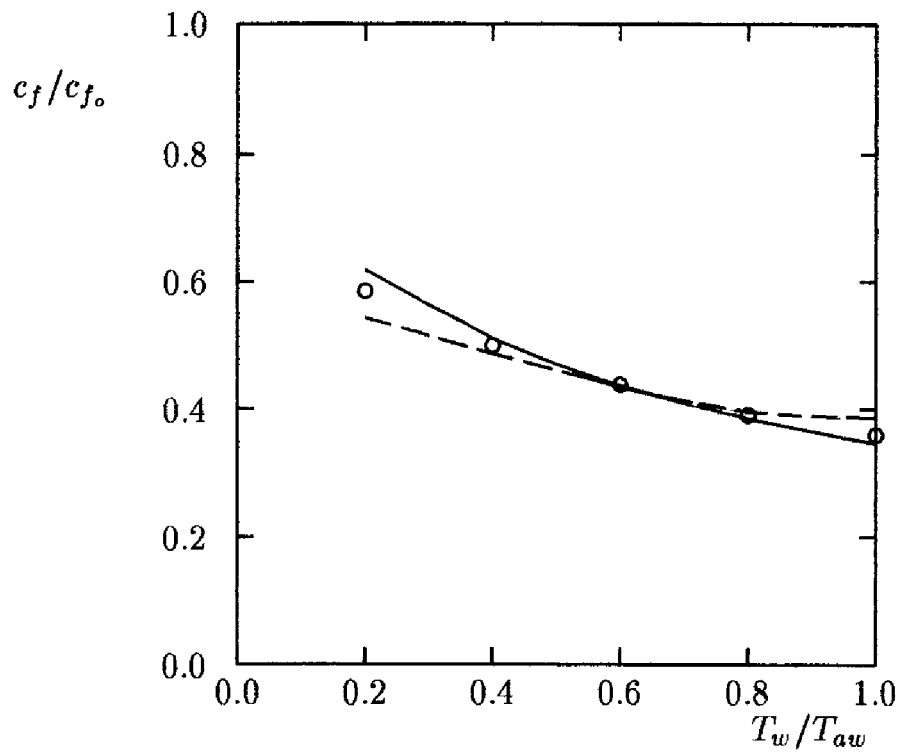


Figure 5.6: Computed and measured effects of surface cooling on skin friction for a Mach 5 flat-plate boundary layer; —  $k-\omega$  model; - - Zhang et al.  $k-\epsilon$  model;  $\circ$  Van Driest correlation.

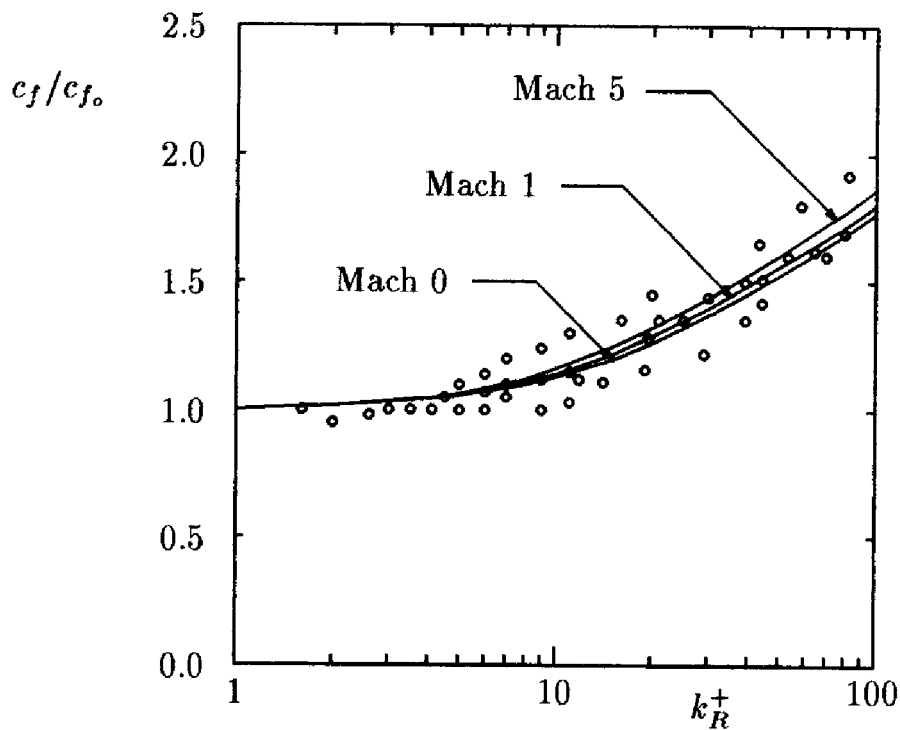


Figure 5.7: Computed and measured effects of surface roughness on skin friction for compressible flat-plate boundary layers; —  $k-\omega$  model;  $\circ$  Reda, Ketter and Fan.

The computations also demonstrate consistency with the observation originally made by Goddard (1959) that “the effect of surface roughness on skin-friction drag is localized deep within the boundary layer at the surface itself and is independent of the external flow, i.e., Mach number, per se, is eliminated as a variable.” Consistent with Goddard’s observation, Mach number has little effect on predicted  $c_f/c_{f_0}$ . Additionally, consistent with Reda’s findings, computed skin friction departs noticeably from the smooth-wall value for  $k_R^+$  values near 4 to 5 as opposed to Goddard’s correlation which indicates no effect for  $k_R^+$  less than 10.

## 5.8 Shock-Induced Boundary-Layer Separation

One of the most interesting and challenging CFD problems is the interaction of a turbulent boundary layer with a shock wave. Many researchers have analyzed this problem since the 1960’s, with varying degrees of success. The earliest efforts were confined to algebraic models, largely because of the long computing times required to solve the full Favre-averaged Navier-Stokes equation. The fastest computer of the late 1960’s and early 1970’s was the CDC 7600, a machine comparable in speed to a 50 MHz 80486 based microcomputer. Additionally, the best compressible-flow numerical algorithms of that era were explicit time-marching methods that required tens of thousands of timesteps to achieve a solution.

Wilcox (1974) did the first solutions to the Favre-averaged Navier-Stokes equation, using an advanced turbulence model, for shock-induced separation of a turbulent boundary layer. This early CFD study included six computations, three for reflection of an oblique shock from a flat plate and three for flow into a compression corner. Results of the study indicate that, using a two-equation turbulence model, a reasonably accurate description of the flowfield can be obtained for reflection of an oblique shock from a flat plate. However, the numerical flowfields for the compression corner cases differ significantly from the experimentally observed flowfields, even though Mach and Reynolds numbers and shock strength are identical to those of the flat-plate cases. Thus, a seemingly simple change in flow geometry causes a major difference in predictive accuracy. To put these computations in proper perspective, note that the turbulence model used was the Saffman-Wilcox (1974)  $k-\omega^2$  model with surface boundary conditions given by matching to the law of the wall. The numerical algorithm used was a first-order accurate explicit time-marching procedure.

Since that time, computational methods have improved dramatically

thanks to the innovative work of many researchers such as Beam and Warming (1976), Steger and Warming (1979), Roe (1981), Van Leer (1982), McCormack (1985), and Roache and Salari (1990), to name just a few. As a result of their innovations, converged solutions for separated flows can often be obtained in less than 200 timesteps. A two-equation turbulence model computation now takes about two hours of 80486-based microcomputer CPU time for a shock-separated flow.

While great advances have been made in developing accurate and efficient finite difference algorithms, far less improvement has been made with turbulence models for such flows. The work of Viegas and Horstman (1979), Viegas, Rubesin and Horstman (1985), Champney (1989) and Horstman (1992) provides clear substantiation of this claim. They have applied many turbulence models to shock-separated flows with almost universal results, viz.:

1. too little upstream influence as shown by pressure starting to rise well downstream of the measured beginning of adverse pressure gradient;
2. surface pressure in excess of measured values in the region directly above the separation bubble;
3. skin friction and heat transfer higher than measured downstream of reattachment;
4. velocity profiles downstream of reattachment that indicate flow deceleration in excess of corresponding measurements.

On the one hand, by using wall functions and the  $k-\epsilon$  model, Viegas, Horstman and Rubesin (1985) are able to remove Item 3 from this list. On the other hand, they achieve only modest improvements in the other items. This lack of success on the compression-corner problem, which has persisted for more than a decade, is excellent testimony to the oft quoted statement that **turbulence modeling is the pacing item in CFD**.

Most modern shock-separated computations are done without introducing wall functions. There is no evidence that the law of the wall holds on separated regions, and its use via wall functions is a questionable approximation. The primary motivation for using wall functions in large scale computations that require substantial computer resources is in reducing CPU time. Viegas, Horstman and Rubesin (1985), in effect, create a two-layer turbulence model where their wall functions apply in the sublayer, and the Standard  $k-\epsilon$  model applies above the sublayer. While their procedure yields significant reduction in computing time, numerical results are sensitive to the location of the grid point closest to the surface,  $y_2^+$ . In fact, there is no obvious convergence to a well defined limiting value as  $y_2^+ \rightarrow 0$ .



Consequently, the value of  $y_2^+$  is effectively an adjustable parameter in their model equations, to be selected by the user. In practice, it is typical for the user to fix  $y_2$  at each location, rather than modify it locally as the solution develops, which would be required to achieve a constant value of  $y_2^+$ . Thus, in practice,  $y_2^+$  actually varies throughout the flow in a manner that cannot be determined a priori, so that the sensitivity to its value is a computational liability.

The sensitivity can be removed by using perturbation methods to devise suitable wall functions. Wilcox (1989), for example, has deduced the following compressible-flow wall functions for the  $k$ - $\omega$  model:

$$\left. \begin{aligned} u^* &= u_\tau \left[ \frac{1}{\kappa} \ln \left( \frac{u_\tau y}{\nu_w} \right) + B - 0.48 \frac{u_\tau y}{\nu_w} \phi + O(\phi^2) \right] \\ k &= \frac{\bar{\rho}_w}{\bar{\rho}} \frac{u_\tau^2}{\sqrt{\beta^*}} \left[ 1 + 1.16 \frac{u_\tau y}{\nu_w} \phi + O(\phi^2) \right] \\ \omega &= \sqrt{\frac{\rho_w}{\bar{\rho}}} \frac{u_\tau}{\sqrt{\beta^* \kappa y}} \left[ 1 - 0.32 \frac{u_\tau y}{\nu_w} \phi + O(\phi^2) \right] \end{aligned} \right\} \quad (5.111)$$

where  $\phi$  is the dimensionless pressure gradient parameter defined by

$$\phi = \frac{\nu_w}{\rho u_\tau^3} \frac{dP}{dx} \quad (5.112)$$

As with the incompressible wall functions deduced for the incompressible  $k$ - $\omega$  model (see Subsection 4.7.1), the expansions in Equation (5.111) have been derived assuming  $\phi$  is a small parameter. Using these wall functions, numerical solutions show very little sensitivity to placement of the grid point closest to the surface.

Figure 5.8 compares computed and measured surface pressure for Mach 3 flow into a  $24^\circ$  compression corner using algebraic models, a one-equation model, several two-equation models, and a second-order closure model. As shown, none of the algebraic, one-equation or two-equation models provides a satisfactory solution. Figure 5.9 illustrates a critical problem regarding prediction of surface heating rates. Results are shown for three  $k$ - $\epsilon$  models, viz., the Jones-Launder (1972) model, the same model with compressibility corrections devised by Rubesin (1990), and a two-layer  $k$ - $\epsilon$  model developed by Rodi (1991) that uses a one-equation model rather than wall functions. As shown, the Jones-Launder model surface heat transfer,  $q_w$ , is off scale and is roughly triple the measured value. While the modified models predict peak heating rates closer to measured values, differences between computed and measured heat transfer are in excess of 25% throughout the flow.

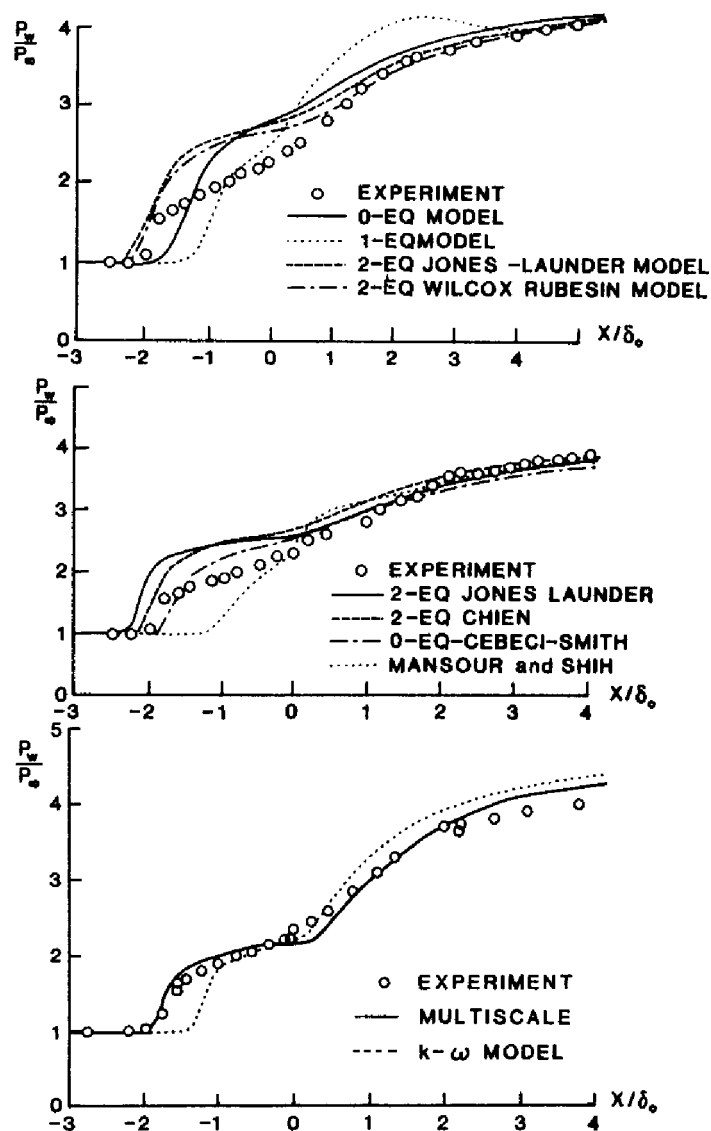


Figure 5.8: Comparison of computed and measured surface pressure for Mach 3 flow into a  $24^\circ$  compression corner for several turbulence models. [From Marshall and Dolling (1992) — Copyright © AIAA 1992 — Used with permission.]

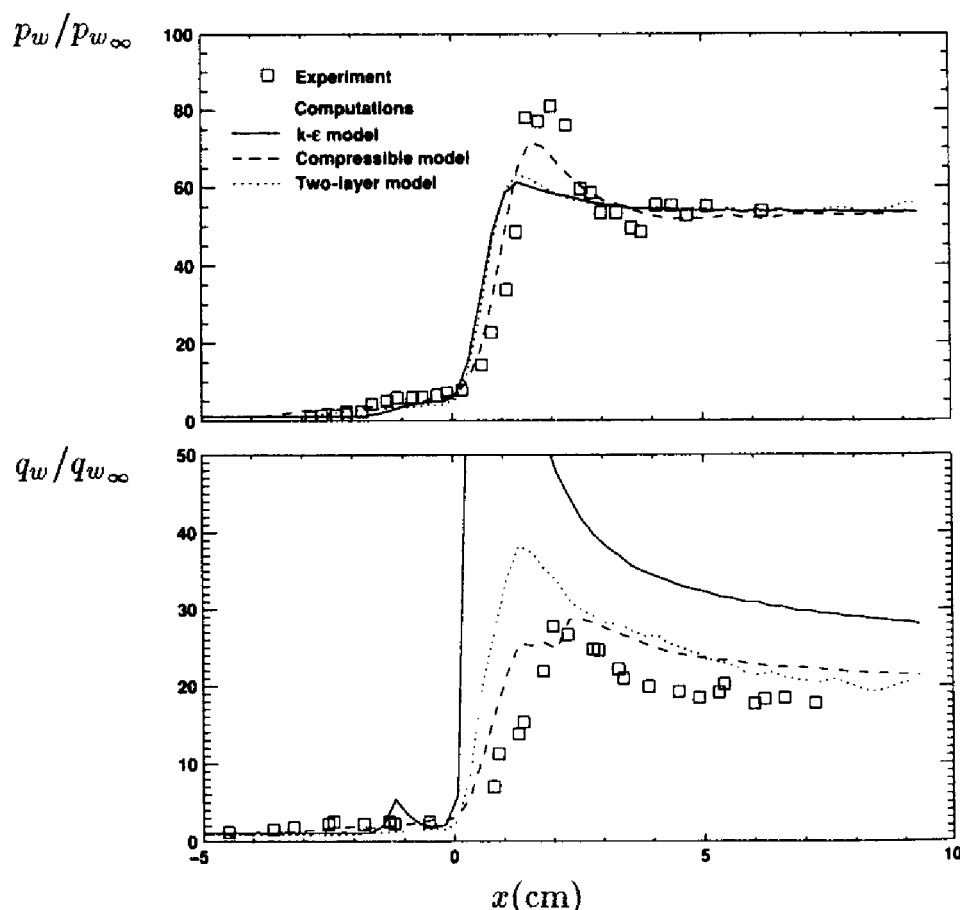


Figure 5.9: Comparison of computed and measured surface pressure and heat transfer for Mach 9.2 flow past a 40° cylinder flare. [From Horstman (1992) — Copyright © AIAA 1992 — Used with permission.]

There has been substantial progress in the capability for prediction of three-dimensional shock wave, turbulent boundary layer interactions. A recent review by Knight (1993) describes the status of research for five basic geometries. Figure 5.10(a) illustrates the three-dimensional single fin, arguably the most extensively studied such interaction. The deflection of the fin surface by an angle  $\alpha$  generates an oblique shock that interacts with the boundary layer on the flat plate. This interaction is of some practical interest, as it represents a geometric abstraction of a fin-body juncture for a high-speed aircraft. Figure 5.10(b) compares computed and measured surface pressure for  $M_\infty = 2.9$ ,  $\alpha = 20^\circ$ , and  $Re_{\delta_\infty} = 9 \cdot 10^5$ , where  $\delta_\infty$  is boundary-layer thickness upstream of the interaction. The comparison has been made at a spanwise distance,  $z = 6.8\delta_\infty$  from the plane of symmetry. Computations using the Baldwin-Lomax (1978) model (labeled “Knight”) and Rodi’s (1991)  $k$ - $\epsilon$  model (labeled “Horstman”) are in close agreement with measurements. Similar close agreement has been obtained with exper-

imental data for pitot pressure and yaw angle [Knight, et al. (1987)]. These results imply that the flowfield is predominantly rotational and inviscid, except within a thin region adjacent to the solid boundaries. This result is similar to the triple-deck theory developed for interacting boundary layers [e.g., Stewartson (1981)] and extended to non-separated three-dimensional shock wave, turbulent boundary layer interactions by Inger (1986). Consequently, the choice of turbulence model is unimportant for comparison with all but the inner (lower deck) provided the upstream boundary layer is correct. However, predicted skin friction and surface heat transfer are very sensitive to the turbulence model chosen, and can exhibit significant disagreement with experiment [Knight (1993)].

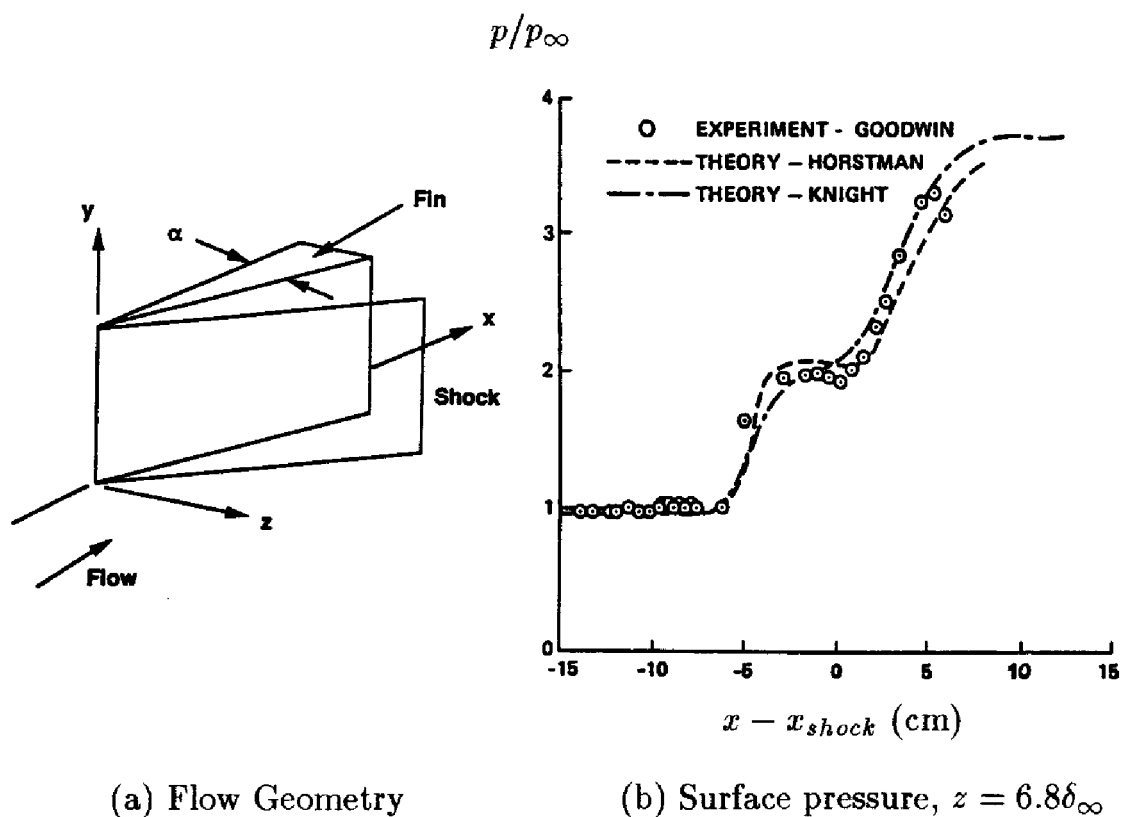


Figure 5.10: Single-fin shock wave, boundary layer interaction; Mach 2.9. [Figure provided by D. D. Knight.]

Figure 5.11(a) shows the double-fin geometry. This geometry is of practical interest as it represents a geometric simplification of a hypersonic inlet using sidewall compression, or a sidewall interaction for a supersonic mixed compression inlet. The two fins generate opposing shocks that intersect on the centerline, and interact with the boundary layers on the flat plate and fin. Figure 5.11(b) compares computed [Narayanswami, Horstman and

Knight (1993)] and measured peak surface pressure (on the centerline) for  $M_\infty = 8.3$ ,  $\alpha = 15^\circ$ , and  $Re_{\delta_\infty} = 1.7 \cdot 10^5$ . The turbulence models are the Baldwin-Lomax (1978) model and the Rodi (1991) version of the  $k-\epsilon$  model. The predictions are reasonably close except at the peak near  $x/\delta_\infty = 10$ . Baldwin-Lomax predictions are within about 20% of measurements, while  $k-\epsilon$  predictions differ by as much as 45%. It is interesting to note that the peak pressure is approximately half the theoretical inviscid level because of the viscous-inviscid interaction. Reasonable agreement is obtained between computed and measured pitot pressure and yaw-angle profiles. Comparison of computed eddy viscosity shows significant differences, however. As a result, Knight concludes that, similar to the single-fin case, the flow is dominantly rotational and inviscid, except within a thin region near the surface. The turbulence model has a very significant effect on computed heat transfer, and neither model yields acceptable results (Figure 5.12). Although the  $k-\omega$  model has not been applied to these flows, we can reasonably conclude that further research is needed in the development and application of turbulence models for three-dimensional shock wave, turbulent boundary layer interactions.

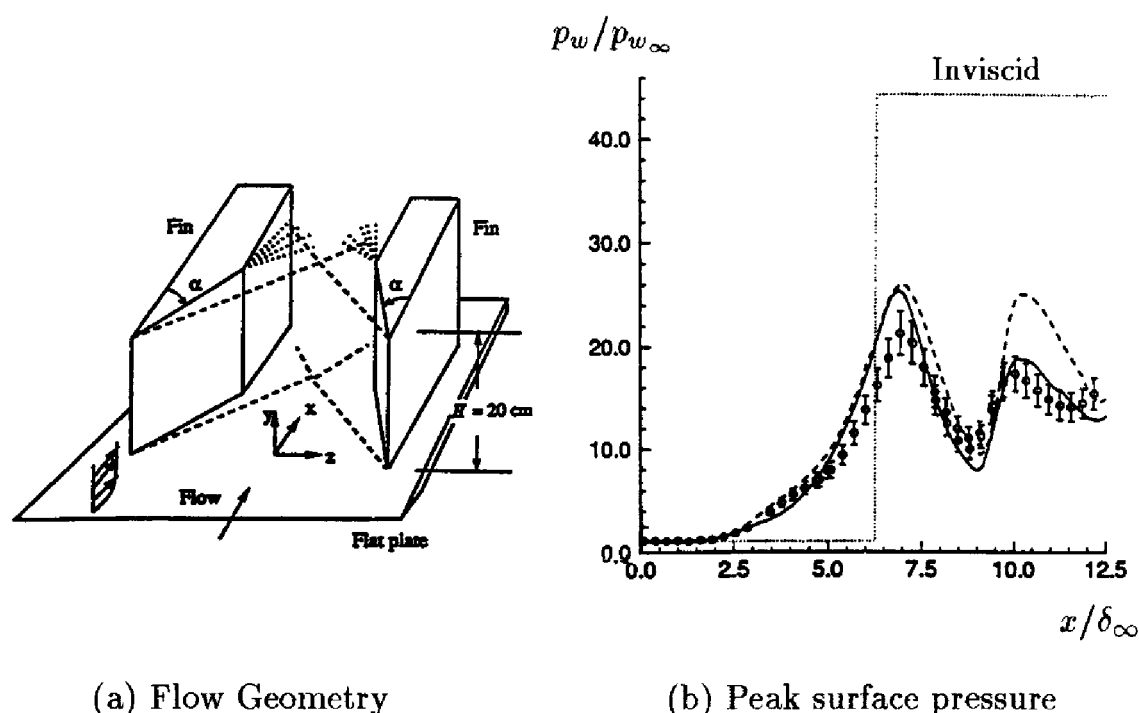


Figure 5.11: Double-fin shock wave, boundary layer interaction; Mach 8.3. • Experiment; — Baldwin-Lomax; - - - Rodi; [Figure provided by D. D. Knight.]

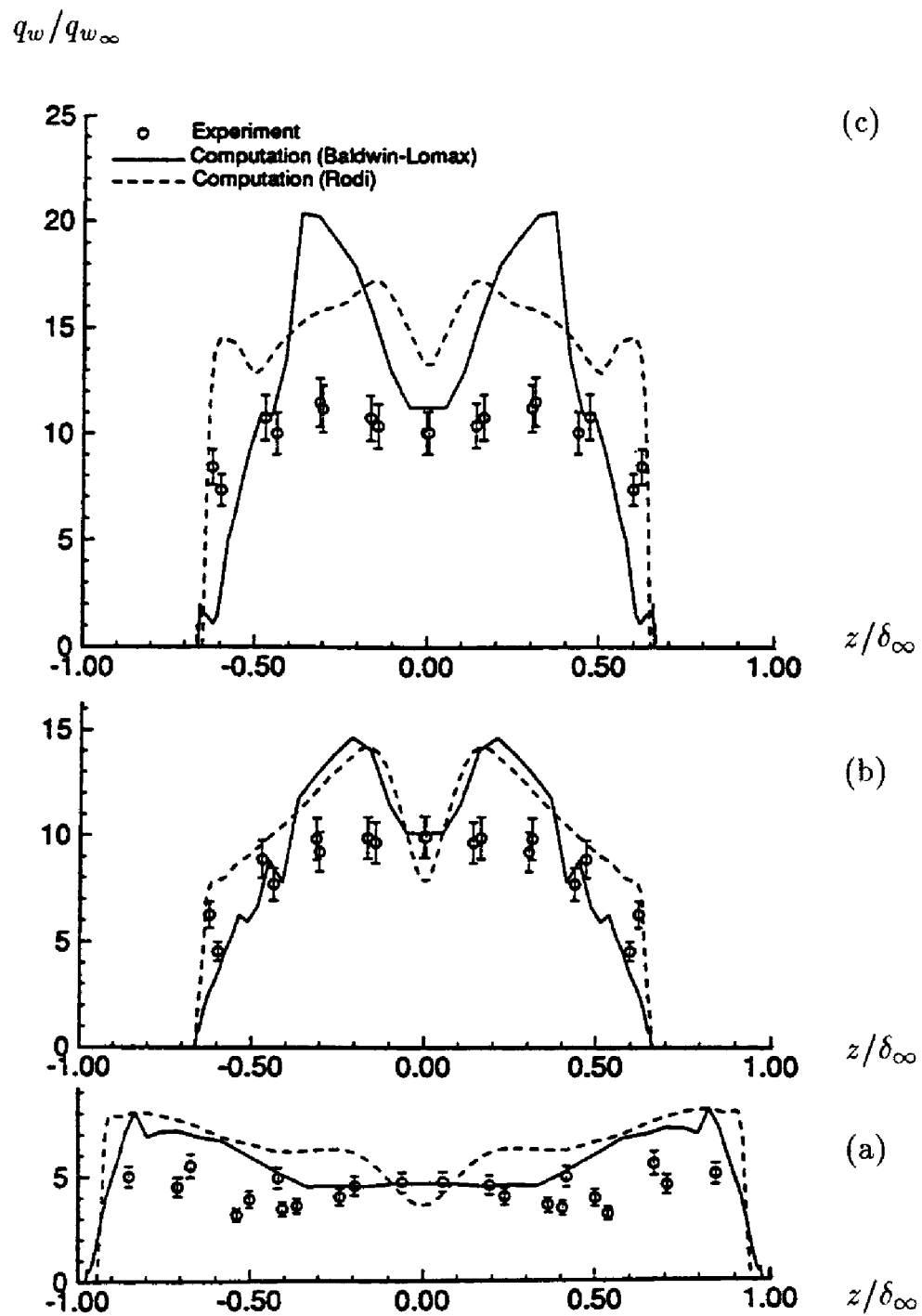


Figure 5.12: Transverse profiles of flat plate surface heat transfer at stream-wise locations of (a)  $x/\delta_\infty = 5.08$ , (b) 6.40 and (c) 7.78 for a double-fin shock wave, boundary layer interaction; Mach 8.3. [Figure provided by D. D. Knight.]

## Problems

**5.1** Derive the Reynolds-averaged momentum-conservation equation for compressible flow.

**5.2** Derive the Favre-averaged Reynolds-stress equation [Equation (5.39)].

**5.3** Verify that Equations (5.54) and (5.55) are equivalent.

**5.4** The classical Crocco temperature-velocity relationship for an adiabatic-wall boundary layer is

$$\frac{T}{T_w} = 1 - A^2 \left( \frac{\tilde{u}}{U_\infty} \right)^2$$

where  $A$  is a constant. Use this approximation to evaluate the following integral.

$$u^* = \int_0^{\tilde{u}} \sqrt{\frac{\rho}{\rho_w}} du$$

Compare your result with Equation (5.108).

**5.5** To use the WKB method in solving an equation such as

$$\frac{d^2\omega}{dv^2} - \lambda^2 f(v)\omega = 0, \quad \lambda \rightarrow \infty$$

we assume a solution of the form

$$\omega(v) \sim \exp \left[ \lambda \sum_{n=0}^{\infty} S_n(v) \lambda^{-n} \right] \sim \exp [\lambda S_0(v) + S_1(v) + O(\lambda^{-1})]$$

(a) Verify that  $S_0(v)$  and  $S_1(v)$  are given by

$$S_0(v) = \pm \int \sqrt{f(v)} dv + \text{constant}$$

$$S_1(v) = \ell n |f(v)|^{-1/4} + \text{constant}$$

(b) Use the result of Part (a) to show that the leading-order solution to Equation (5.87) is given by Equations (5.89) and (5.90).

(c) Now, complete the derivation of Equation (5.92).

**5.6** Derive the compressible law of the wall implied by the Cebeci-Smith model.

**5.7** Using the compressible log-layer solution, show that the turbulence length scale for the  $k$ - $\omega$  model defined by  $\ell = k^{1/2}/\omega$  varies linearly with distance from the surface in the compressible log layer.

**5.8** Using the compressible log-layer solution, show that the turbulence length scale for the  $k$ - $\epsilon$  model defined by  $\ell = k^{3/2}/\epsilon$  varies linearly with distance from the surface in the compressible log layer.



## Chapter 6

# Beyond the Boussinesq Approximation

The Boussinesq eddy-viscosity approximation assumes the principal axes of the Reynolds-stress tensor,  $\tau_{ij}$ , are coincident with those of the mean strain-rate tensor,  $S_{ij}$ , at all points in a turbulent flow. This is the analog of Stokes' approximation for laminar flows. The coefficient of proportionality between  $\tau_{ij}$  and  $S_{ij}$  is the eddy viscosity,  $\mu_T$ . Unlike the molecular viscosity which is a property of the fluid, the eddy viscosity depends upon many details of the flow under consideration. It is affected by the shape and nature (e.g., roughness height) of any solid boundaries, freestream turbulence intensity, and, perhaps most significantly, flow history effects. Experimental evidence indicates that flow history effects on  $\tau_{ij}$  often persist for long distances in a turbulent flow, thus casting doubt on the validity of a simple linear relationship between  $\tau_{ij}$  and  $S_{ij}$ . In this chapter, we examine several flows for which the Boussinesq approximation yields a completely unsatisfactory description. We then examine some of the remedies that have been proposed to provide more accurate predictions for such flows. Although our excursion into the realm beyond the Boussinesq approximation is brief, we will see how useful the analytical tools developed in preceding chapters are for even the most complicated turbulence models.

### 6.1 Boussinesq-Approximation Deficiencies

While models based on the Boussinesq eddy-viscosity approximation provide excellent predictions for many flows of engineering interest, there are some applications for which predicted flow properties differ greatly from

corresponding measurements. Generally speaking, such models are inaccurate for flows with sudden changes in mean strain rate and for flows with what Bradshaw (1973a) refers to as **extra rates of strain**. It is unsurprising that flows with sudden changes in mean strain rate pose a problem. The Reynolds stresses adjust to such changes at a rate unrelated to mean flow processes and time scales, so that the Boussinesq approximation must fail. Similarly, when a flow experiences extra rates of strain caused by rapid dilatation, out of plane straining, or significant streamline curvature, all of which give rise to unequal normal Reynolds stresses, the approximation again becomes suspect. Some of the most noteworthy types of applications for which models based on the Boussinesq approximation fail are:

1. flows with sudden changes in mean strain rate;
2. flow over curved surfaces;
3. flow in ducts with secondary motions;
4. flow in rotating and stratified fluids;
5. three-dimensional flows;
6. flows with boundary-layer separation.

As an example of a flow with a sudden change in strain rate, consider the experiment of Tucker and Reynolds (1968). In this experiment, a nearly isotropic turbulent flow is subjected to uniform mean normal strain rate attending the following mean velocity field:

$$U = \text{constant}, \quad V = -ay, \quad W = az \quad (6.1)$$

The coefficient  $a$  is the constant strain rate. The strain rate is maintained for a finite distance in the  $x$  direction in the experiment and then removed. The turbulence becomes anisotropic as a result of the uniform straining, and gradually approaches isotropy downstream of the point where the straining ceases. Wilcox and Rubesin (1980) have applied their  $k-\omega^2$  model to this flow to demonstrate the deficiency of the Boussinesq approximation for flows in which mean strain rate abruptly changes. Figure 6.1 compares the computed and measured distortion parameter,  $K$ , defined by

$$K \equiv \frac{\overline{v'^2} - \overline{w'^2}}{\overline{v'^2} + \overline{w'^2}} \quad (6.2)$$

As shown, when the strain rate is suddenly removed at  $x \approx 2.3$  m, the model predicts an instantaneous return to isotropy, i.e., all normal Reynolds

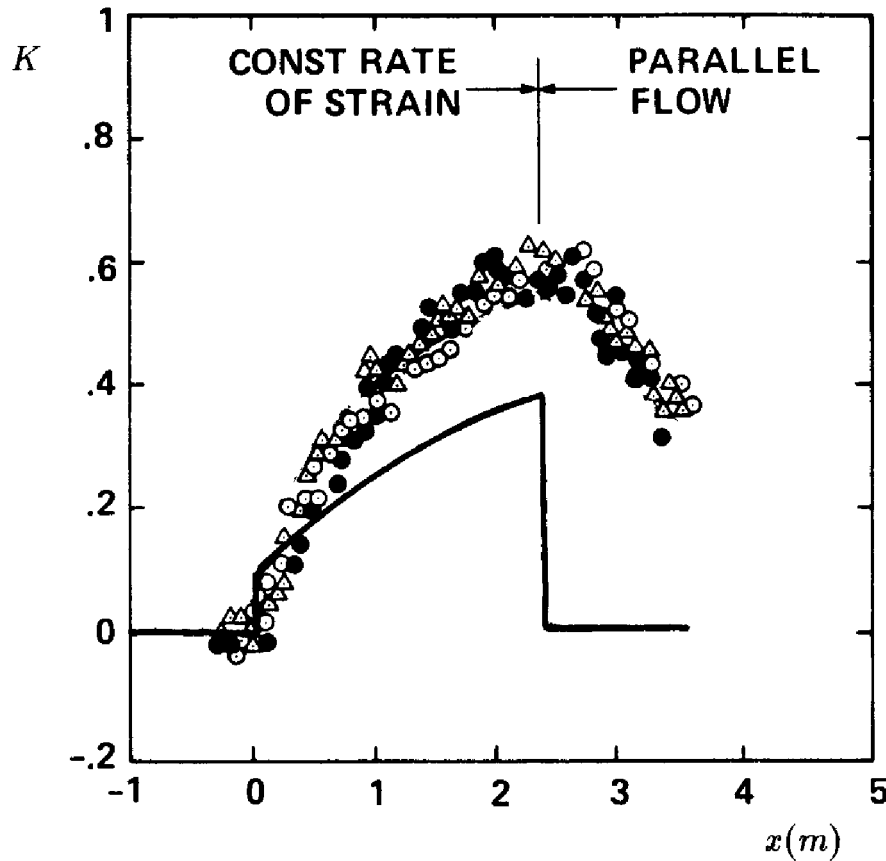


Figure 6.1: Computed and measured distortion parameter for the Tucker-Reynolds plane-strain flow; —  $k-\omega^2$  model;  $\circ \bullet \Delta$  Tucker-Reynolds. [From Wilcox and Rubesin (1980).]

stresses become equal. By contrast, the turbulence approaches isotropy at a finite rate. Note also that the model predicts a discontinuous jump in  $K$  when the straining begins at  $x = 0$  m. Interestingly, if the computation is extended downstream of  $x = 2.3$  m without removing the strain rate, the model predicted asymptotic value of  $K$  matches the measured value at  $x = 2.3$  m, but approaches this value at a slower than measured rate.

As an example of a flow with significant streamline curvature, consider flow over a curved surface. Meroney and Bradshaw (1975) find that for both convex and concave walls, when the radius of curvature,  $\mathcal{R}$ , is 100 times the local boundary-layer thickness,  $\delta$ , skin friction differs from its corresponding plane-wall value by as much as 10%. By contrast, laminar skin friction changes by about 1% for  $\delta/\mathcal{R} = .01$ . Similar results have been obtained by Thomann (1968) for supersonic boundary layers; for constant-pressure flow over surfaces with  $\delta/\mathcal{R} \sim .02$ , heat transfer changes by nearly 20%. Clearly, many practical aerodynamic surfaces are sufficiently curved to produce significant curvature effects. For such flows, a reliable turbulence

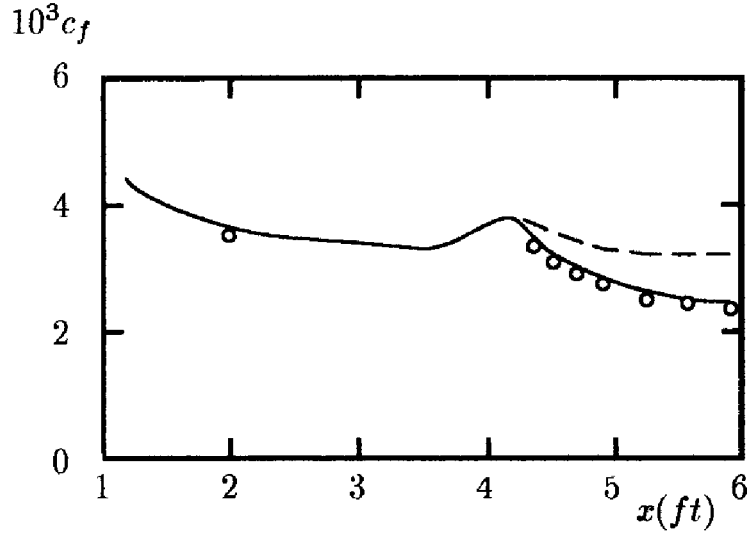


Figure 6.2: Computed and measured skin friction for flow over a convex surface with constant pressure; ---  $k$ - $\omega$  model without curvature correction; —  $k$ - $\omega$  model with curvature correction; o So and Mellor.

model must be capable of predicting effects of curvature on the turbulence.

Figure 6.2 compares computed and measured skin friction for flow over a convex wall. The flow, experimentally investigated by So and Mellor (1972), has nearly constant pressure. The wall is planar up to  $x = 4.375$  ft and has  $\delta/\mathcal{R} \sim .075$  beyond that location. As shown, computed skin friction is generally 30% to 40% higher than measured.

Wilcox and Chambers (1977) propose a curvature correction to the turbulence energy equation that provides an accurate prediction for flow over curved surfaces. Appealing to the classical stability arguments for flow over a curved wall advanced by von Kármán (1934), they postulate that the equation for  $k$  should more appropriately be thought of as the equation for  $\overline{v'^2}$ . Consequently, Wilcox and Chambers add a term originating from the centrifugal acceleration in the exact  $\overline{v'^2}$  equation. For the Standard  $k$ - $\omega$  model, the boundary layer form of the equations for flow over a curved surface with radius of curvature,  $\mathcal{R}$ , are as follows.

$$U \frac{\partial U}{\partial x} + V \frac{\partial U}{\partial y} = -\frac{1}{\rho} \frac{dP}{dx} + \frac{\partial}{\partial y} \left[ (\nu + \nu_T) \left( \frac{\partial U}{\partial y} - \frac{U}{\mathcal{R}} \right) \right], \quad \nu_T = \frac{k}{\omega} \quad (6.3)$$

$$U \frac{\partial k}{\partial x} + V \frac{\partial k}{\partial y} + \frac{9}{2} \nu_T \frac{U}{\mathcal{R}} \frac{\partial U}{\partial y} = \nu_T \left( \frac{\partial U}{\partial y} - \frac{U}{\mathcal{R}} \right)^2 - \beta^* \omega k + \frac{\partial}{\partial y} \left[ (\nu + \sigma^* \nu_T) \frac{\partial k}{\partial y} \right] \quad (6.4)$$

$$U \frac{\partial \omega}{\partial x} + V \frac{\partial \omega}{\partial y} = \alpha \left( \frac{\partial U}{\partial y} - \frac{U}{\mathcal{R}} \right)^2 - \beta \omega^2 + \frac{\partial}{\partial y} \left[ (\nu + \sigma \nu_T) \frac{\partial \omega}{\partial y} \right] \quad (6.5)$$

The last term on the left-hand side of Equation (6.4) is the Wilcox-Chambers curvature-correction term. As shown in Figure 6.2, including the curvature term brings model predictions into much closer agreement with measurements. A perturbation analysis of Equations (6.3) to (6.5) for the log layer (see Problems) shows that the model predicts a modified law of the wall given by

$$\left[ 1 - \beta_R \frac{y}{\mathcal{R}} \right] \frac{U}{u_\tau} = \frac{1}{\kappa} \ln \left( \frac{u_\tau y}{\nu} \right) + \text{constant} \quad (6.6)$$

with  $\beta_R \approx 8.8$ . This is very similar to the modified law of the wall deduced by Meroney and Bradshaw (1975), who conclude from correlation of measurements that  $\beta_R \approx 12.0$ .

Other curvature corrections have been proposed for two-equation models, and Lakshminarayana (1986) presents a comprehensive overview. Often, in the context of the  $k$ - $\epsilon$  model, a correction term is added to the  $\epsilon$  equation. Launder, Priddin and Sharma (1977), for example, replace the coefficient  $C_{\epsilon 2}$  [see Equation (4.42)] by

$$C_{\epsilon 2} \rightarrow C_{\epsilon 2} (1 - 0.2 Ri_T) \quad (6.7)$$

where  $Ri_T$  is the turbulence Richardson number defined by

$$Ri_T = \frac{2U}{\mathcal{R} \partial U / \partial y} \quad (6.8)$$

This type of correction yields improved accuracy comparable to that obtained with the Wilcox-Chambers curvature correction.

While two-equation model curvature-correction terms greatly improve predictive accuracy for flow over curved walls, they are *ad hoc* modifications that cannot be generalized for arbitrary flows. The Wilcox-Chambers curvature term is introduced by making analogy to the full Reynolds-stress equation and by assuming that  $k$  behaves more like  $\overline{v'^2}$  than the turbulence kinetic energy for such flows. This implicitly assumes that a full second-order closure model will naturally predict effects of streamline curvature. We will see in Section 6.3 that this is indeed the case.

These two applications alone are sufficient to serve as a warning that models based on the Boussinesq approximation will fail under some frequently encountered flow conditions. We have also seen in preceding chapters that such models are unreliable for separated flows, especially when the

flow is compressible. Such models also fail to predict secondary motions that commonly occur in ducts, and in the absence of ad hoc corrections, fail to predict salient features of rotating and stratified flows. While these are more subtle and specialized applications, each failure underscores the fact that models based on the Boussinesq approximation are not universal. The following sections explore some of the proposals made to remove many of these deficiencies in a less ad hoc fashion.

## 6.2 Nonlinear Constitutive Relations

One approach to achieving a more appropriate description of the Reynolds-stress tensor without introducing any additional differential equations is to assume the Boussinesq approximation is simply the leading term in a series expansion of functionals. Proceeding with this premise, Lumley (1970) and Saffman (1976) show that for incompressible flow the expansion must proceed through second order according to

$$\begin{aligned} \tau_{ij} = & -\frac{2}{3}\rho k\delta_{ij} + 2\mu_T S_{ij} - B\frac{\rho k}{\omega^2}S_{mn}S_{nm}\delta_{ij} - C\frac{\rho k}{\omega^2}S_{ik}S_{kj} \\ & - D\frac{\rho k}{\omega^2}(S_{ik}\Omega_{kj} + S_{jk}\Omega_{ki}) - F\frac{\rho k}{\omega^2}\Omega_{mn}\Omega_{nm}\delta_{ij} - G\frac{\rho k}{\omega^2}\Omega_{ik}\Omega_{kj} \end{aligned} \quad (6.9)$$

where  $B$ ,  $C$ ,  $D$ ,  $F$  and  $G$  are closure coefficients, and  $k/\omega^2$  may be equivalently written as  $k^3/\epsilon^2$ . Also,  $S_{ij}$  and  $\Omega_{ij}$  are the mean strain-rate and rotation tensors, viz.,

$$S_{ij} = \frac{1}{2} \left( \frac{\partial U_i}{\partial x_j} + \frac{\partial U_j}{\partial x_i} \right) \quad \text{and} \quad \Omega_{ij} = \frac{1}{2} \left( \frac{\partial U_i}{\partial x_j} - \frac{\partial U_j}{\partial x_i} \right) \quad (6.10)$$

In order to guarantee that the trace of  $\tau_{ij}$  is  $-2\rho k$ , we must have  $B = -C/3$  and  $F = -G/3$ . Equation (6.9) can be simplified by requiring it to conform with certain fundamental experimental observations. In the experiment of Tucker and Reynolds (1968), for example, the normal Reynolds stresses are related approximately by

$$\tau_{xx} \approx \frac{1}{2}(\tau_{yy} + \tau_{zz}) \quad (6.11)$$

Substituting Equations (6.1) and (6.11) into Equation (6.9) shows that necessarily  $C = 0$ . In addition, Ibbetson and Tritton (1975) show that homogeneous turbulence in rigid body rotation decays without developing anisotropy. This observation requires  $G = 0$ . Finally, if Equation (6.9) with  $C = G = 0$  is applied to a classical shear layer where the only significant

velocity gradient is  $\partial U/\partial y$ , Equation (6.11) again applies with  $\tau_{xx}$  and  $\tau_{zz}$  interchanged, independent of the value of  $D$ . Thus, Saffman's general expansion simplifies to:

$$\tau_{ij} = -\frac{2}{3}\rho k\delta_{ij} + 2\mu_T S_{ij} - D\frac{\rho k}{\omega^2}(S_{ik}\Omega_{kj} + S_{jk}\Omega_{ki}) \quad (6.12)$$

In analogy to this result, Wilcox and Rubesin (1980) propose the following simplified **nonlinear constitutive relation** for their  $k-\omega^2$  model.

$$\tau_{ij} = -\frac{2}{3}\rho k\delta_{ij} + 2\mu_T \left( S_{ij} - \frac{1}{3} \frac{\partial U_k}{\partial x_k} \delta_{ij} \right) + \frac{8}{9} \frac{\rho k (S_{ik}\Omega_{kj} + S_{jk}\Omega_{ki})}{(\beta^* \omega^2 + 2S_{mn}S_{nm})} \quad (6.13)$$

The primary usefulness of this prescription for the Reynolds-stress tensor is in predicting the normal stresses. The coefficient 8/9 is selected to guarantee

$$\overline{u'^2} : \overline{v'^2} : \overline{w'^2} = 4 : 2 : 3 \quad (6.14)$$

for the flat-plate boundary layer. Equation (6.14) is a good approximation throughout the log layer and much of the defect layer. The model faithfully predicts the ratio of the normal Reynolds stresses for boundary layers with adverse pressure gradient where the ratios are quite different from those given in Equation (6.14). Bardina, Ferziger and Reynolds (1983) have used an analog of this stress/strain-rate relationship in their Large Eddy Simulation studies. However, the model provides no improvement for flows over curved surfaces.

Speziale (1987b) proposes a nonlinear constitutive relation for the  $k-\epsilon$  model as follows (for incompressible flow):

$$\begin{aligned} \tau_{ij} = & -\frac{2}{3}\rho k\delta_{ij} + 2\mu_T S_{ij} + 4C_D C_\mu^2 \frac{\rho k^3}{\epsilon^2} \left( S_{ik}S_{kj} - \frac{1}{3}S_{mn}S_{nm}\delta_{ij} \right) \\ & + 4C_E C_\mu^2 \frac{\rho k^3}{\epsilon^2} \left( \overset{\circ}{S}_{ij} - \frac{1}{3}\overset{\circ}{S}_{mm}\delta_{ij} \right) \end{aligned} \quad (6.15)$$

where  $\overset{\circ}{S}_{ij}$  is the frame-indifferent Oldroyd derivative of  $S_{ij}$  defined by

$$\overset{\circ}{S}_{ij} = \frac{\partial S_{ij}}{\partial t} + U_k \frac{\partial S_{ij}}{\partial x_k} - \frac{\partial U_i}{\partial x_k} S_{kj} - \frac{\partial U_j}{\partial x_k} S_{ki} \quad (6.16)$$

The closure coefficients  $C_D$  and  $C_E$  are given by

$$C_D = C_E = 1.68 \quad (6.17)$$

In addition to its elegance and simplicity, this model satisfies three key criteria that assure consistency with properties of the exact Navier-Stokes

equation. **First**, like the Saffman and Wilcox-Rubesin models, it satisfies general coordinate and dimensional invariance. **Second**, it satisfies a limited form of the Lumley (1978) realizability constraints (i.e., positiveness of  $k \equiv -\frac{1}{2}\tau_{ii}$ ). **Third**, it satisfies material frame indifference in the limit of two-dimensional turbulence. The latter consideration leads to introduction of the Oldroyd derivative of  $S_{ij}$ .

The appearance of the rate of change of  $S_{ij}$  in the constitutive relation is appropriate for a viscoelastic-like medium. While, to some degree, the Speziale constitutive relation includes rate effects, it still fails to describe the gradual adjustment of the Reynolds stresses following a sudden change in strain rate. For example, consider the Tucker-Reynolds flow discussed above. The Oldroyd derivative of  $S_{ij}$  is given by

$$\overset{\circ}{S}_{yy} = \overset{\circ}{S}_{zz} = -2a^2; \quad \text{all other } \overset{\circ}{S}_{ij} = 0 \quad (6.18)$$

Clearly, when the strain rate is abruptly removed, the Speziale model predicts that the normal Reynolds stresses instantaneously return to isotropy. Hence, the model is no more accurate than the Wilcox-Rubesin model for such flows.

For flow over a curved surface, the contribution of the nonlinear terms in the Speziale model to the shear stress is negligible. Consequently, this model, like the Wilcox-Rubesin model, offers no improvement over the Boussinesq approximation for curved-wall flows.

While the model fails to improve model predictions for flows with sudden changes in strain rate and flows with curved streamlines, it does make a dramatic difference for flow through a rectangular duct [see Figure 6.3(a)]. For such a flow, the difference between  $\tau_{zz}$  and  $\tau_{yy}$  according to Speziale's relation is, to leading order,

$$\tau_{zz} - \tau_{yy} = C_D C_\mu^2 \frac{\rho k^3}{\epsilon^2} \left[ \left( \frac{\partial U}{\partial z} \right)^2 - \left( \frac{\partial U}{\partial y} \right)^2 \right] \quad (6.19)$$

while, to the same order, the shear stresses are

$$\tau_{xy} = \mu_T \frac{\partial U}{\partial y}, \quad \tau_{xz} = \mu_T \frac{\partial U}{\partial z}, \quad \tau_{yz} = C_D C_\mu^2 \frac{\rho k^3}{\epsilon^2} \frac{\partial U}{\partial y} \frac{\partial U}{\partial z} \quad (6.20)$$

Having a difference between  $\tau_{zz}$  and  $\tau_{yy}$  is critical in accurately simulating secondary motions. Using his model, Speziale (1987b) has computed flow through a rectangular duct. Figure 6.3(b) shows computed secondary flow streamlines, which clearly illustrates that there is an eight-vortex secondary flow structure as seen in experiments. Using the Boussinesq approximation, no secondary flow develops, so that the Speziale model obviously



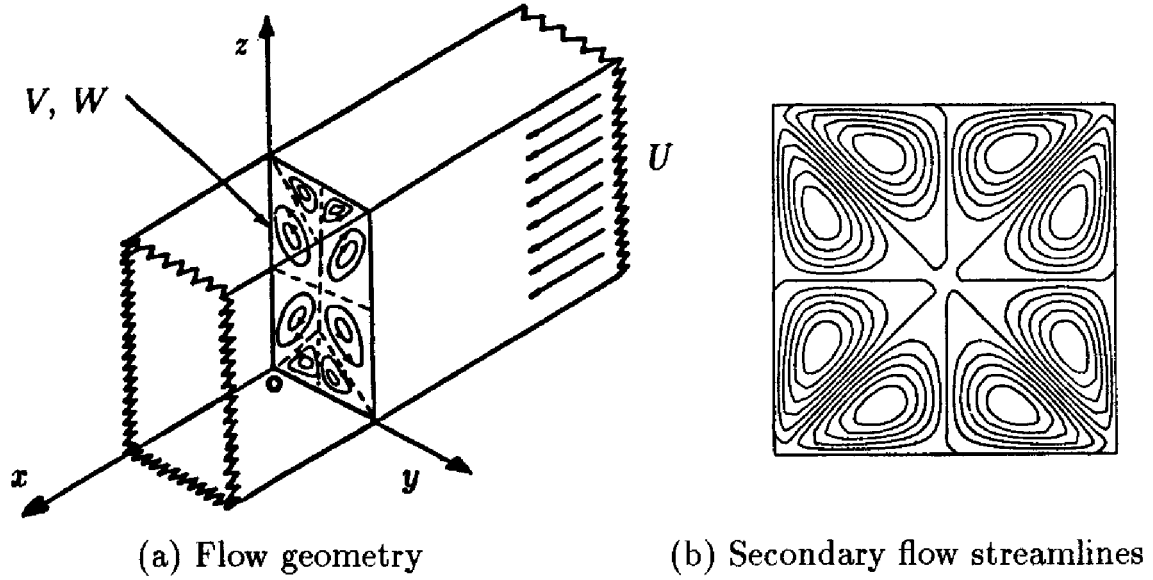


Figure 6.3: Fully developed turbulent flow in a rectangular duct. [From Speziale (1991) — Published with permission of author.]

does a better job of capturing this missing feature. Although Speziale presents no comparison of computed and measured results, the net effect of the nonlinear terms is very dramatic.

Speziale's nonlinear constitutive relation also improves  $k$ - $\epsilon$  model predictions for the backward-facing step. Focusing on the experiment of Kim, Kline and Johnston (1980), Thangam and Speziale (1992) have shown that using the nonlinear model with a low-Reynolds-number  $k$ - $\epsilon$  model increases predicted reattachment length for this flow from 6.3 step heights to 6.9 step heights. The measured length is 7.0 step heights.

Rodi (1976) deduces a nonlinear constitutive equation by working with a model for the full Reynolds-stress equation [Equation (2.34)]. Rodi begins by approximating the difference between convective and turbulent transport terms for incompressible flow as:

$$\begin{aligned} \frac{\partial \tau_{ij}}{\partial t} + U_k \frac{\partial \tau_{ij}}{\partial x_k} - \frac{\partial}{\partial x_k} \left[ \nu \frac{\partial \tau_{ij}}{\partial x_k} + C_{ijk} \right] \\ \approx \frac{\tau_{ij}}{k} \left\{ \frac{\partial k}{\partial t} + U_k \frac{\partial k}{\partial x_k} - \frac{\partial}{\partial x_k} \left[ \nu \frac{\partial k}{\partial x_k} + \frac{C_{jjk}}{2\rho} \right] \right\} \end{aligned} \quad (6.21)$$

This approximation yields a nonlinear algebraic equation that can be used to determine the Reynolds-stress tensor, viz.,

$$\frac{\tau_{ij}}{\rho k} \left\{ \tau_{mn} \frac{\partial U_m}{\partial x_n} - \rho \epsilon \right\} = -\tau_{ik} \frac{\partial U_j}{\partial x_k} - \tau_{jk} \frac{\partial U_i}{\partial x_k} + \epsilon_{ij} - \Pi_{ij} \quad (6.22)$$

With suitable closure approximations for the dissipation tensor,  $\epsilon_{ij}$ , and the pressure-strain correlation tensor,  $\Pi_{ij}$ , Equation (6.22) defines a nonlinear constitutive relation. More precisely, Gatski and Speziale (1992) regard such models as strain-dependent generalizations of nonlinear constitutive relations. That is, these models can be written in a form similar to Saffman's expansion [Equation (6.9)]. The various closure coefficients then become functions of certain Reynolds-stress tensor invariants. The complexity of the constitutive relation depends on the closure approximations, and alternative approximations have been tried by many researchers [see Lakshminarayana (1986)]. A model derived in this manner is known as an **Algebraic Stress Model** or, in abbreviated form, as an **ASM**.

When an ASM is used for a flow with zero mean strain rate, Equation (6.22) simplifies to

$$\tau_{ij} = \frac{k}{\epsilon} (\Pi_{ij} - \epsilon_{ij}) \quad (6.23)$$

As we will discuss in Subsection 6.3.1, in the limit of vanishing mean strain rate, the most common closure approximations for  $\epsilon_{ij}$  and  $\Pi_{ij}$  simplify to

$$\Pi_{ij} \rightarrow C_1 \frac{\epsilon}{k} \left( \tau_{ij} + \frac{2}{3} \rho k \delta_{ij} \right) \quad \text{and} \quad \epsilon_{ij} \rightarrow \frac{2}{3} \rho \epsilon \delta_{ij} \quad (6.24)$$

where  $C_1$  is a closure coefficient. Hence, when the mean strain rate vanishes, the algebraic stress model simplifies to

$$\tau_{ij} = -\frac{2}{3} \rho k \delta_{ij} \quad (6.25)$$

This shows that the ASM predicts an instantaneous return to isotropy in the Tucker-Reynolds flow discussed above. Hence, like the Wilcox-Rubesin and Speziale nonlinear constitutive relations, the ASM fails to properly account for sudden changes in the mean strain rate. The ASM does provide significant improvement for flows with streamline curvature however. So and Mellor (1978), for example, show that excellent agreement between computed and measured flow properties is possible using an ASM with the  $k$ - $\epsilon$  model for boundary layers on curved surfaces. The model predicts most qualitative features and provides fair quantitative agreement for flows with secondary motions as shown, for example, by Demuren (1991).

In summary, the primary advantage of nonlinear constitutive relations appears to be in predicting the anisotropy of the normal Reynolds stresses. The most important application for which this is of interest is for flow in ducts with secondary motions. In the case of algebraic stress models, greatly improved predictions can be obtained for flows with nontrivial streamline curvature. It is doubtful that the nonlinear stress models discussed in this

section yield any significant improvement for separating and reattaching flows. While the  $k$ - $\epsilon$  model's predicted reattachment length is closer to the measured length when the nonlinear model is used, it is not clear that a better description of the physics of this flow has been provided. The excellent solutions obtained with the Standard  $k$ - $\omega$  model [see Section 4.10] strongly suggest that the  $k$ - $\epsilon$  model's inaccuracy for such flows has nothing to do with the basic eddy-viscosity assumption. While the improvements attending use of a nonlinear constitutive relation with two-equation models are nontrivial, the models still retain many of their deficiencies.

### 6.3 Second-Order Closure Models

Although it poses a more formidable task with regard to establishing suitable closure approximations, there are potential gains in universality that can be realized by devising a second-order closure model. As we will see, such models naturally include effects of streamline curvature, sudden changes in strain rate, secondary motions, etc. We will also see that there is a significant price to be paid in complexity and computational difficulty for these gains.

Virtually all researchers use the same starting point for developing such a model, viz., the exact differential equation describing the behavior of the Reynolds-stress tensor,  $\tau_{ij} \equiv -\rho \overline{u'_i u'_j}$ . As shown in Chapter 2, the incompressible form of the exact equation is

$$\frac{\partial \tau_{ij}}{\partial t} + U_k \frac{\partial \tau_{ij}}{\partial x_k} = -\tau_{ik} \frac{\partial U_j}{\partial x_k} - \tau_{jk} \frac{\partial U_i}{\partial x_k} + \epsilon_{ij} - \Pi_{ij} + \frac{\partial}{\partial x_k} \left[ \nu \frac{\partial \tau_{ij}}{\partial x_k} + C_{ijk} \right] \quad (6.26)$$

where

$$\Pi_{ij} = \overline{p' \left( \frac{\partial u'_i}{\partial x_j} + \frac{\partial u'_j}{\partial x_i} \right)} \quad (6.27)$$

$$\epsilon_{ij} = 2\mu \overline{\frac{\partial u'_i}{\partial x_k} \frac{\partial u'_j}{\partial x_k}} \quad (6.28)$$

and

$$C_{ijk} = \overline{\rho u'_i u'_j u'_k} + \overline{p' u'_i} \delta_{jk} + \overline{p' u'_j} \delta_{ik} \quad (6.29)$$

Inspection of Equation (6.26) shows why we can expect a second-order closure model to correct some of the Boussinesq approximation's shortcomings. **First**, since the equation automatically accounts for the convection and diffusion of  $\tau_{ij}$ , a second-order closure model will include effects of flow history. The presence of dissipation and turbulent-transport terms indicates the presence of time scales unrelated to mean-flow time scales, so history

effects should be more realistically represented than with a two-equation model. **Second**, Equation (6.26) contains convection, production and (optionally) body-force terms that respond automatically to effects such as streamline curvature, system rotation and stratification, at least qualitatively. Thus, there is potential for naturally representing such effects with a well-formulated second-order closure model. **Third**, Equation (6.26) gives no a priori reason for the normal stresses to be equal even when the mean strain rate vanishes. Rather, their values will depend upon initial conditions and other flow processes, so that the model should behave properly for flows with sudden changes in strain rate.

Rotta (1951) was the first to accomplish closure of the Reynolds-stress equation, although he did not carry out numerical computations. Many researchers have made important contributions since the pioneering efforts of Rotta. Two of the most important conceptual contributions have been made by Donaldson and Lumley. Donaldson [c.f. Donaldson and Rosenbaum (1968)] was the first to advocate the concept of **invariant modeling**, i.e., establishing closure approximations that rigorously satisfy coordinate invariance. Lumley (1978) has developed a systematic procedure for representing closure approximations that guarantees **realizability**, i.e., that all physically positive-definite turbulence properties be computationally positive definite and that all computed correlation coefficients lie between  $\pm 1$ . The next subsection discusses these, and other, concepts and their impact on closure approximations.

### 6.3.1 Closure Approximations

To close Equation (6.26), we must model the dissipation tensor,  $\epsilon_{ij}$ , the turbulent-transport tensor,  $C_{ijk}$ , and the pressure-strain correlation tensor,  $\Pi_{ij}$ . Because each of these terms is a tensor, the approximations required for closure can assume much more elaborate forms compared to approximations used for the simpler scalar and vector terms in the  $k$  equation. In this subsection, we will discuss some of the most commonly used closure approximations.

**Dissipation:** Because dissipation occurs at the smallest scales, most modelers use the Kolmogorov (1941) hypothesis of local isotropy, which implies

$$\epsilon_{ij} = \frac{2}{3}\rho\epsilon\delta_{ij} \quad (6.30)$$

where

$$\epsilon = \nu \overline{\frac{\partial u'_i}{\partial x_k} \frac{\partial u'_i}{\partial x_k}} \quad (6.31)$$

The scalar quantity  $\epsilon$  is exactly the dissipation rate appearing in the turbulence kinetic energy equation. Contracting Equation (6.26) shows that this must be the case. As with simpler models, we must establish a procedure for determining  $\epsilon$ . In most of his work, for example, Donaldson has specified  $\epsilon$  algebraically, similar to what is done with a one-equation model. Most researchers use the  $\epsilon$  equation as formulated for the  $k$ - $\epsilon$  model. Wilcox and Rubesin (1980) and Wilcox (1988b) compute  $\epsilon$  by using an equation for the specific dissipation rate.

Since the dissipation is in reality anisotropic, particularly close to solid boundaries, some efforts have been made to model this effect. Generalizing a low-Reynolds-number proposal of Rotta (1951), Hanjalić and Launder (1976), for example, postulate that

$$\epsilon_{ij} = \frac{2}{3}\rho\epsilon\delta_{ij} + 2f_s\rho\epsilon b_{ij} \quad (6.32)$$

where  $b_{ij}$  is the dimensionless **Reynolds-stress anisotropy tensor**, viz.,

$$b_{ij} = - \left( \frac{\tau_{ij} + \frac{2}{3}\rho k\delta_{ij}}{2\rho k} \right) \quad (6.33)$$

and  $f_s$  is a low-Reynolds-number damping function, which they choose empirically to vary with turbulence Reynolds number,  $Re_T \equiv k^2/(\epsilon\nu)$ , according to

$$f_s = \left( 1 + \frac{1}{10}Re_T \right)^{-1} \quad (6.34)$$

**Turbulent Transport:** As with the turbulence energy equation, pressure fluctuations, as well as triple products of velocity fluctuations, appear in the tensor  $C_{ijk}$ . Definitive experimental data are unavailable to provide any guidance for modeling the pressure-correlation terms, and they are effectively ignored. The most common approach used in modeling  $C_{ijk}$  is to assume a gradient transport process. Donaldson (1972), for example, argues that the simplest tensor of rank three that can be obtained from the second-order correlation  $\tau_{ij}$  is  $\partial\tau_{ik}/\partial x_j$ . Since  $C_{ijk}$  is symmetric in all three of its indices, he concludes that

$$C_{ijk} \sim \frac{\partial\tau_{jk}}{\partial x_i} + \frac{\partial\tau_{ik}}{\partial x_j} + \frac{\partial\tau_{ij}}{\partial x_k} \quad (6.35)$$

This tensor has the proper symmetry, but is not dimensionally correct. We require a factor whose dimensions are length<sup>2</sup>/time — a gradient diffusivity — and the ratio of  $k^2/\epsilon$  has been employed by Mellor and Herring (1973)

and Launder, Reece and Rodi (1975). Using the notation of Launder et al., the final form of the closure approximation is

$$C_{ijk} = \frac{2}{3}C_s \frac{k^2}{\epsilon} \left[ \frac{\partial \tau_{jk}}{\partial x_i} + \frac{\partial \tau_{ik}}{\partial x_j} + \frac{\partial \tau_{ij}}{\partial x_k} \right] \quad (6.36)$$

where  $C_s \approx 0.11$  is a scalar closure coefficient.

Launder, Reece and Rodi also postulate a more general form based on analysis of the transport equation for  $C_{ijk}$ . Through a series of heuristic arguments, they infer the following alternative closure approximation:

$$C_{ijk} = -C'_s \frac{k}{\rho \epsilon} \left[ \tau_{im} \frac{\partial \tau_{jk}}{\partial x_m} + \tau_{jm} \frac{\partial \tau_{ik}}{\partial x_m} + \tau_{km} \frac{\partial \tau_{ij}}{\partial x_m} \right] \quad (6.37)$$

where  $C'_s \approx 0.25$  is also a scalar closure coefficient.

**Pressure-Strain Correlation:** The tensor  $\Pi_{ij}$ , which is often referred to as the **pressure-strain redistribution** term, has received the greatest amount of attention from turbulence modelers. The reason for this interest is twofold. First, being of the same order as production, the term plays a critical role in most flows of engineering interest. Second, because it involves essentially unmeasurable correlations, a great degree of cleverness and ingenuity is required to establish a rational closure approximation.

To determine pressure fluctuations in an incompressible flow we must, in principle, solve the following Poisson equation for  $p'$ .

$$\frac{1}{\rho} \nabla^2 p' = -2 \frac{\partial U_i}{\partial x_j} \frac{\partial u'_j}{\partial x_i} - \frac{\partial^2}{\partial x_i \partial x_j} \left( u'_i u'_j - \overline{u'_i u'_j} \right) \quad (6.38)$$

This equation follows from taking the divergence of the Navier-Stokes equation and subtracting the time-averaged equation from the instantaneous equation. The classical approach to solving this equation is to write  $p'$  as the sum of two contributions, viz.,

$$p' = p'_{slow} + p'_{rapid} \quad (6.39)$$

By construction, the **slow** and **rapid** pressure fluctuations satisfy the following equations.

$$\frac{1}{\rho} \nabla^2 p'_{slow} = - \frac{\partial^2}{\partial x_i \partial x_j} \left( u'_i u'_j - \overline{u'_i u'_j} \right) \quad (6.40)$$

$$\frac{1}{\rho} \nabla^2 p'_{rapid} = -2 \frac{\partial U_i}{\partial x_j} \frac{\partial u'_j}{\partial x_i} \quad (6.41)$$

The general notion implied by the nomenclature is changes in the mean strain rate contribute most rapidly to  $p'_{rapid}$  because the mean velocity gradient appears explicitly in Equation (6.41). By contrast, such effects are implicitly represented in Equation (6.40). The terminology **slow** and **rapid** should not be taken too literally, however, since the mean strain rate does not necessarily change more rapidly than  $u'_i u'_j$ .

For homogeneous turbulence, these equations can be solved in terms of appropriate Green's functions, and the resulting form of  $\Pi_{ij}$  is

$$\Pi_{ij} = A_{ij} + M_{ijkl} \frac{\partial U_k}{\partial x_l} \quad (6.42)$$

where  $A_{ij}$  is the **slow pressure strain** and the tensor  $M_{ijkl} \partial U_k / \partial x_l$  is the **rapid pressure strain**. The tensors  $A_{ij}$  and  $M_{ijkl}$  are given by the following.

$$A_{ij} = \frac{1}{4\pi} \iiint_V \overline{\left( \frac{\partial u'_i}{\partial x_j} + \frac{\partial u'_j}{\partial x_i} \right) \frac{\partial^2 (u'_k u'_l)}{\partial y_k \partial y_l} \frac{d^3 y}{|\mathbf{x} - \mathbf{y}|}} \quad (6.43)$$

$$M_{ijkl} = \frac{1}{2\pi} \iiint_V \overline{\left( \frac{\partial u'_i}{\partial x_j} + \frac{\partial u'_j}{\partial x_i} \right) \frac{\partial u'_l}{\partial y_k} \frac{d^3 y}{|\mathbf{x} - \mathbf{y}|}} \quad (6.44)$$

The integration range for Equations (6.43) and (6.44) is the entire flow-field. Additionally, for inhomogeneous turbulence, the second term in Equation (6.42) becomes an integral with the mean velocity gradient inside the integrand. This emphasizes a shortcoming of single-point closure schemes that has not been as obvious in any of the closure approximations we have discussed thus far. That is, we are postulating that we can accomplish closure based on correlations of fluctuating quantities at the same physical location. The pressure-strain correlation very clearly is not a localized process, but rather, involves contributions from every point in the flow. This would suggest that two-point correlations, i.e., products of fluctuating properties at two separate physical locations, are more appropriate. Nevertheless, we expect contributions from more than one or two large eddy sizes away to be negligible, and this would effectively define what is usually referred to as the **locally homogeneous approximation**. Virtually all modelers assume that turbulent flows behave as though they are locally homogeneous, and use Equation (6.42).

The forms of the tensors  $A_{ij}$  and  $M_{ijkl}$  must adhere to a variety of constraints resulting from the symmetry of indices, mass conservation and other kinematic constraints. We know, for example, that the trace of  $\Pi_{ij}$  must vanish and this is true for the slow and rapid parts individually. Rotta

(1951) postulates that the **slow pressure-strain** term, often referred to as the **return-to-isotropy** term, is given by

$$A_{ij} = C_1 \frac{\epsilon}{k} \left( \tau_{ij} + \frac{2}{3} \rho k \delta_{ij} \right) \quad (6.45)$$

where  $C_1$  is a closure coefficient whose value can be inferred from measurements [Uberoi (1956)] to lie in the range

$$1.4 < C_1 < 1.8 \quad (6.46)$$

Turning now to the **rapid pressure strain**, early research efforts of Donaldson [Donaldson and Rosenbaum (1968)], Daly and Harlow (1970), and Lumley (1972) assumed that the rapid pressure strain is negligible compared to the slow pressure strain. However, Crow (1968) and Reynolds (1970) provide simple examples of turbulent flows for which the effect of the rapid pressure strain far outweighs the slow pressure strain.

Launder, Reece and Rodi (1975) have devised a particularly elegant closure approximation based almost entirely on kinematical considerations. Building upon preliminary analysis of Rotta (1951), they write  $M_{ijkl}$  in terms of a tensor  $a_{ijkl}$  as follows.

$$M_{ijkl} = a_{ijkl} + a_{jikl} \quad (6.47)$$

This relation is strictly valid only for homogeneous turbulence. Rotta demonstrates that the tensor  $a_{ijkl}$  must satisfy the following constraints:

$$a_{ijkl} = a_{ljki} = a_{likj} \quad (6.48)$$

and

$$a_{iikl} = 0, \quad a_{ijjl} = -2\tau_{il} \quad (6.49)$$

Launder et al. propose that the fourth-rank tensor  $a_{ijkl}$  can be expressed as a linear function of the Reynolds-stress tensor. The most general tensor, linear in  $\tau_{ij}$ , satisfying the symmetry constraints of Equation (6.48) is

$$\begin{aligned} a_{ijkl} = & -\alpha \delta_{kj} \tau_{li} - \beta (\delta_{lk} \tau_{ij} + \delta_{lj} \tau_{ik} + \delta_{ik} \tau_{lj} + \delta_{ij} \tau_{lk}) \\ & - C_2 \delta_{li} \tau_{kj} + [\eta \delta_{li} \delta_{kj} + \nu (\delta_{lk} \delta_{ij} + \delta_{lj} \delta_{ik})] \rho k \end{aligned} \quad (6.50)$$

where  $\alpha$ ,  $\beta$ ,  $C_2$ ,  $\eta$  and  $\nu$  are closure coefficients. Invoking the conditions of Equation (6.49), all of the coefficients can be expressed in terms of  $C_2$ , viz.,

$$\alpha = \frac{4C_2 + 10}{11}, \quad \beta = -\frac{3C_2 + 2}{11}, \quad \eta = -\frac{50C_2 + 4}{55}, \quad \nu = \frac{20C_2 + 6}{55} \quad (6.51)$$



Finally, combining Equations (6.47) through (6.51), we arrive at the well-known LRR model for the rapid pressure strain.

### LRR Rapid Pressure-Strain Model:

$$M_{ijkl} \frac{\partial U_k}{\partial x_l} = -\hat{\alpha} \left( P_{ij} - \frac{1}{3} P_{kk} \delta_{ij} \right) - \hat{\beta} \left( D_{ij} - \frac{1}{3} D_{kk} \delta_{ij} \right) - \hat{\gamma} \rho k S_{ij} \quad (6.52)$$

$$P_{ij} = \tau_{im} \frac{\partial U_j}{\partial x_m} + \tau_{jm} \frac{\partial U_i}{\partial x_m} \quad \text{and} \quad D_{ij} = \tau_{im} \frac{\partial U_m}{\partial x_j} + \tau_{jm} \frac{\partial U_m}{\partial x_i} \quad (6.53)$$

$$\hat{\alpha} = \frac{8 + C_2}{11}, \quad \hat{\beta} = \frac{8C_2 - 2}{11}, \quad \hat{\gamma} = \frac{60C_2 - 4}{55}, \quad 0.4 < C_2 < 0.6 \quad (6.54)$$

Note that for compressible flows, the mean strain-rate tensor,  $S_{ij}$ , is usually replaced by  $S_{ij} - \frac{1}{3} S_{kk} \delta_{ij}$  in Equation (6.52).

One of the most remarkable features of this closure approximation is the presence of just one undetermined closure coefficient, namely,  $C_2$ . The value of  $C_2$  has been established by comparison of model predictions with measured properties of homogeneous turbulent flows. Launder, Reece and Rodi (1975) suggested using  $C_2 = 0.40$ . Morris (1984) revised its value upward to  $C_2 = 0.50$ , while Launder (1992) currently recommends  $C_2 = 0.60$ . Section 6.4 discusses the kind of flows used to calibrate this model.

Bradshaw (1973b) has shown that there is an additional contribution to Equations (6.43) and (6.44) that has a nontrivial effect close to a solid boundary. It is attributed to a surface integral that appears in the Green's function for Equation (6.38). This has come to be known as the **pressure-echo effect** or **wall-reflection effect**. Launder, Reece and Rodi (1975) propose a near-wall correction to their model for  $\Pi_{ij}$  that explicitly involves distance from the surface. Gibson and Launder (1978) and Craft and Launder (1992) propose alternative models to account for the pressure-echo effect. For example, the LRR wall-reflection term,  $\Pi_{ij}^{(w)}$ , is

$$\Pi_{ij}^{(w)} = \left[ 0.125 \frac{\epsilon}{k} (\tau_{ij} + \frac{2}{3} \rho k \delta_{ij}) - 0.015 (P_{ij} - D_{ij}) \right] \frac{k^{3/2}}{\epsilon n} \quad (6.55)$$

where  $n$  is distance normal to the surface.

More recent efforts at devising a suitable closure approximation for  $\Pi_{ij}$  have focused on developing a nonlinear expansion in terms of the anisotropy tensor,  $b_{ij}$ , defined in Equation (6.33). Lumley (1978) has systematically developed a general representation for  $\Pi_{ij}$  based on Equations (6.38) through (6.44). In addition to insisting upon coordinate invariance and other required symmetries, Lumley insists upon **realizability**. As noted earlier, this means that all quantities known to be strictly positive must be

guaranteed to be positive by the closure model. Additionally, all computed correlation coefficients must lie between  $\pm 1$ . This limits the possible form of the functional expansion for  $\Pi_{ij}$ . Lumley argues that the most general form of the complete tensor  $\Pi_{ij}$  for incompressible flow is as follows.

**Lumley Pressure-Strain Model:**

$$\begin{aligned}\Pi_{ij} = & a_0 \rho \epsilon b_{ij} + a_1 \rho \epsilon \left( b_{ik} b_{jk} - \frac{1}{3} II \delta_{ij} \right) + a_2 \rho k S_{ij} \\ & + \rho k (a_3 b_{kl} S_{lk} + a_4 b_{kl} b_{lm} S_{mk}) b_{ij} \\ & + \rho k (a_5 b_{kl} S_{lk} + a_6 b_{kl} b_{lm} S_{mk}) \left( b_{ik} b_{kj} - \frac{1}{3} II \delta_{ij} \right) \\ & + a_7 \rho k \left( b_{ik} S_{jk} + b_{jk} S_{ik} - \frac{2}{3} b_{kl} S_{lk} \delta_{ij} \right) \\ & + a_8 \rho k \left( b_{ik} b_{kl} S_{jl} + b_{jk} b_{kl} S_{il} - \frac{2}{3} b_{kl} b_{lm} S_{mk} \delta_{ij} \right) \\ & + a_9 \rho k (b_{ik} \Omega_{jk} + b_{jk} \Omega_{ik}) + a_{10} \rho k (b_{ik} b_{kl} \Omega_{jl} + b_{jk} b_{kl} \Omega_{il})\end{aligned}\quad (6.56)$$

The eleven closure coefficients are assumed to be functions of the **tensor invariants**  $II$  and  $III$ , i.e.,

$$a_i = a_i(II, III), \quad II = b_{ij} b_{ij}, \quad III = b_{ik} b_{kl} b_{li} \quad (6.57)$$

The tensor  $\Omega_{ij}$  is the mean rotation tensor. The LRR model can be shown to follow from Lumley's general expression when nonlinear terms in  $b_{ij}$  are neglected, i.e., when all coefficients except  $a_0$ ,  $a_2$ ,  $a_7$  and  $a_9$  are zero.

A similar, but simpler, nonlinear model has been postulated by Speziale, Sarkar and Gatski (1991). For incompressible flows, this model, known as the **SSG** model, is as follows.

**SSG Pressure-Strain Model:**

$$\begin{aligned}\Pi_{ij} = & - \left( C_1 \rho \epsilon + C_1^* \tau_{mn} \frac{\partial U_m}{\partial x_n} \right) b_{ij} + C_2 \rho \epsilon \left( b_{ik} b_{kj} - \frac{1}{3} b_{mn} b_{nm} \delta_{ij} \right) \\ & + \left( C_3 - C_3^* \sqrt{II} \right) \rho k S_{ij} + C_4 \rho k \left( b_{ik} S_{jk} + b_{jk} S_{ik} - \frac{2}{3} b_{mn} S_{mn} \delta_{ij} \right) \\ & + C_5 \rho k (b_{ik} \Omega_{jk} + b_{jk} \Omega_{ik})\end{aligned}\quad (6.58)$$

$$\left. \begin{aligned} C_1 = 3.4, \quad C_1^* = 1.8, \quad C_2 = 4.2, \quad C_3 = 0.8 \\ C_3^* = 1.3, \quad C_4 = 1.25, \quad C_5 = 0.4 \end{aligned} \right\} \quad (6.59)$$

Interestingly, the SSG model does not appear to require a correction for the pressure-echo effect in order to obtain a satisfactory log-layer solution.

Finally, combining Equations (6.47) through (6.51), we arrive at the well-known LRR model for the rapid pressure strain.

### LRR Rapid Pressure-Strain Model:

$$M_{ijkl} \frac{\partial U_k}{\partial x_l} = -\hat{\alpha} \left( P_{ij} - \frac{1}{3} P_{kk} \delta_{ij} \right) - \hat{\beta} \left( D_{ij} - \frac{1}{3} D_{kk} \delta_{ij} \right) - \hat{\gamma} \rho k S_{ij} \quad (6.52)$$

$$P_{ij} = \tau_{im} \frac{\partial U_j}{\partial x_m} + \tau_{jm} \frac{\partial U_i}{\partial x_m} \quad \text{and} \quad D_{ij} = \tau_{im} \frac{\partial U_m}{\partial x_j} + \tau_{jm} \frac{\partial U_m}{\partial x_i} \quad (6.53)$$

$$\hat{\alpha} = \frac{8 + C_2}{11}, \quad \hat{\beta} = \frac{8C_2 - 2}{11}, \quad \hat{\gamma} = \frac{60C_2 - 4}{55}, \quad 0.4 < C_2 < 0.6 \quad (6.54)$$

Note that for compressible flows, the mean strain-rate tensor,  $S_{ij}$ , is usually replaced by  $S_{ij} - \frac{1}{3} S_{kk} \delta_{ij}$  in Equation (6.52).

One of the most remarkable features of this closure approximation is the presence of just one undetermined closure coefficient, namely,  $C_2$ . The value of  $C_2$  has been established by comparison of model predictions with measured properties of homogeneous turbulent flows. Launder, Reece and Rodi (1975) suggested using  $C_2 = 0.40$ . Morris (1984) revised its value upward to  $C_2 = 0.50$ , while Launder (1992) currently recommends  $C_2 = 0.60$ . Section 6.4 discusses the kind of flows used to calibrate this model.

Bradshaw (1973b) has shown that there is an additional contribution to Equations (6.43) and (6.44) that has a nontrivial effect close to a solid boundary. It is attributed to a surface integral that appears in the Green's function for Equation (6.38). This has come to be known as the **pressure-echo effect** or **wall-reflection effect**. Launder, Reece and Rodi (1975) propose a near-wall correction to their model for  $\Pi_{ij}$  that explicitly involves distance from the surface. Gibson and Launder (1978) and Craft and Launder (1992) propose alternative models to account for the pressure-echo effect. For example, the LRR wall-reflection term,  $\Pi_{ij}^{(w)}$ , is

$$\Pi_{ij}^{(w)} = \left[ 0.125 \frac{\epsilon}{k} (\tau_{ij} + \frac{2}{3} \rho k \delta_{ij}) - 0.015 (P_{ij} - D_{ij}) \right] \frac{k^{3/2}}{\epsilon n} \quad (6.55)$$

where  $n$  is distance normal to the surface.

More recent efforts at devising a suitable closure approximation for  $\Pi_{ij}$  have focused on developing a nonlinear expansion in terms of the anisotropy tensor,  $b_{ij}$ , defined in Equation (6.33). Lumley (1978) has systematically developed a general representation for  $\Pi_{ij}$  based on Equations (6.38) through (6.44). In addition to insisting upon coordinate invariance and other required symmetries, Lumley insists upon **realizability**. As noted earlier, this means that all quantities known to be strictly positive must be

guaranteed to be positive by the closure model. Additionally, all computed correlation coefficients must lie between  $\pm 1$ . This limits the possible form of the functional expansion for  $\Pi_{ij}$ . Lumley argues that the most general form of the complete tensor  $\Pi_{ij}$  for incompressible flow is as follows.

**Lumley Pressure-Strain Model:**

$$\begin{aligned}\Pi_{ij} = & a_0 \rho \epsilon b_{ij} + a_1 \rho \epsilon \left( b_{ik} b_{jk} - \frac{1}{3} II \delta_{ij} \right) + a_2 \rho k S_{ij} \\ & + \rho k (a_3 b_{kl} S_{lk} + a_4 b_{kl} b_{lm} S_{mk}) b_{ij} \\ & + \rho k (a_5 b_{kl} S_{lk} + a_6 b_{kl} b_{lm} S_{mk}) \left( b_{ik} b_{kj} - \frac{1}{3} II \delta_{ij} \right) \\ & + a_7 \rho k \left( b_{ik} S_{jk} + b_{jk} S_{ik} - \frac{2}{3} b_{kl} S_{lk} \delta_{ij} \right) \\ & + a_8 \rho k \left( b_{ik} b_{kl} S_{jl} + b_{jk} b_{kl} S_{il} - \frac{2}{3} b_{kl} b_{lm} S_{mk} \delta_{ij} \right) \\ & + a_9 \rho k (b_{ik} \Omega_{jk} + b_{jk} \Omega_{ik}) + a_{10} \rho k (b_{ik} b_{kl} \Omega_{jl} + b_{jk} b_{kl} \Omega_{il})\end{aligned}\quad (6.56)$$

The eleven closure coefficients are assumed to be functions of the **tensor invariants**  $II$  and  $III$ , i.e.,

$$a_i = a_i(II, III), \quad II = b_{ij} b_{ij}, \quad III = b_{ik} b_{kl} b_{li} \quad (6.57)$$

The tensor  $\Omega_{ij}$  is the mean rotation tensor. The LRR model can be shown to follow from Lumley's general expression when nonlinear terms in  $b_{ij}$  are neglected, i.e., when all coefficients except  $a_0$ ,  $a_2$ ,  $a_7$  and  $a_9$  are zero.

A similar, but simpler, nonlinear model has been postulated by Speziale, Sarkar and Gatski (1991). For incompressible flows, this model, known as the **SSG** model, is as follows.

**SSG Pressure-Strain Model:**

$$\begin{aligned}\Pi_{ij} = & - \left( C_1 \rho \epsilon + C_1^* \tau_{mn} \frac{\partial U_m}{\partial x_n} \right) b_{ij} + C_2 \rho \epsilon \left( b_{ik} b_{kj} - \frac{1}{3} b_{mn} b_{nm} \delta_{ij} \right) \\ & + \left( C_3 - C_3^* \sqrt{II} \right) \rho k S_{ij} + C_4 \rho k \left( b_{ik} S_{jk} + b_{jk} S_{ik} - \frac{2}{3} b_{mn} S_{mn} \delta_{ij} \right) \\ & + C_5 \rho k (b_{ik} \Omega_{jk} + b_{jk} \Omega_{ik})\end{aligned}\quad (6.58)$$

$$\left. \begin{aligned} C_1 = 3.4, \quad C_1^* = 1.8, \quad C_2 = 4.2, \quad C_3 = 0.8 \\ C_3^* = 1.3, \quad C_4 = 1.25, \quad C_5 = 0.4 \end{aligned} \right\} \quad (6.59)$$

Interestingly, the SSG model does not appear to require a correction for the pressure-echo effect in order to obtain a satisfactory log-layer solution.

Many other proposals have been made for closing the Reynolds-stress equation, with most of the attention on  $\Pi_{ij}$ . Weinstock (1981), Shih and Lumley (1985), Haworth and Pope (1986), Reynolds (1987), Shih, Mansour and Chen (1987), Fu, Launder and Tselepidakis (1987) and Craft et al. (1989) have formulated nonlinear pressure-strain correlation models. As with the  $k$ - $\epsilon$  model, low-Reynolds-number damping functions are needed to integrate through the sublayer when the  $\epsilon$  equation is used. Damping functions appear in the pressure-strain correlation tensor as well as in the dissipation. So et al. (1991) give an excellent review of second-order closure models including low-Reynolds-number corrections. Compressibility, of course, introduces an extra complication, and a variety of new proposals are being developed.

While the discussion in this subsection is by design brief, it illustrates the nature of the closure problem for second-order closure models. Although dimensional analysis combined with physical insight still plays a role, there is a greater dependence upon the formalism of tensor calculus. To some extent, this approach focuses more on the differential equations than on the physics of turbulence. This appears to be necessary because the increased complexity mandated by having to model second and higher rank tensors makes it difficult to intuit the proper forms solely on the strength of physical reasoning. Fortunately, the arguments developed during the past decade have a stronger degree of rigor than the drastic surgery approach to modeling terms in the dissipation-rate equation discussed in Subsection 4.3.2.

### 6.3.2 Launder-Reece-Rodi Model

The model devised by Launder, Reece and Rodi (1975) is the most well known and most thoroughly tested second-order closure model based on the  $\epsilon$  equation. Most newer second-order closure models are based on the LRR model and differ primarily in the closure approximation chosen for  $\Pi_{ij}$ . Combining the closure approximations discussed in the preceding subsection, we have the following high-Reynolds-number form of the model.

#### Reynolds-Stress Tensor

$$\begin{aligned} \frac{\partial \tau_{ij}}{\partial t} + \frac{\partial}{\partial x_k} (U_k \tau_{ij}) = & -P_{ij} + \frac{2}{3} \rho \epsilon \delta_{ij} - \Pi_{ij} \\ & - C_s \frac{\partial}{\partial x_k} \left[ \frac{k}{\epsilon} \left( \tau_{im} \frac{\partial \tau_{jk}}{\partial x_m} + \tau_{jm} \frac{\partial \tau_{ik}}{\partial x_m} + \tau_{km} \frac{\partial \tau_{ij}}{\partial x_m} \right) \right] \end{aligned} \quad (6.60)$$

**Dissipation Rate**

$$\rho \frac{\partial \epsilon}{\partial t} + \rho U_j \frac{\partial \epsilon}{\partial x_j} = C_{\epsilon 1} \frac{\epsilon}{k} \tau_{ij} \frac{\partial U_i}{\partial x_j} - C_{\epsilon 2} \rho \frac{\epsilon^2}{k} - C_\epsilon \frac{\partial}{\partial x_k} \left[ \frac{k}{\epsilon} \tau_{km} \frac{\partial \epsilon}{\partial x_m} \right] \quad (6.61)$$

**Pressure-Strain Correlation**

$$\begin{aligned} \Pi_{ij} = & C_1 \frac{\epsilon}{k} \left( \tau_{ij} + \frac{2}{3} \rho k \delta_{ij} \right) - \hat{\alpha} \left( P_{ij} - \frac{2}{3} P \delta_{ij} \right) \\ & - \hat{\beta} \left( D_{ij} - \frac{2}{3} P \delta_{ij} \right) - \hat{\gamma} \rho k \left( S_{ij} - \frac{1}{3} S_{kk} \delta_{ij} \right) \\ & + \left[ 0.125 \frac{\epsilon}{k} \left( \tau_{ij} + \frac{2}{3} \rho k \delta_{ij} \right) - 0.015 (P_{ij} - D_{ij}) \right] \frac{k^{3/2}}{\epsilon n} \end{aligned} \quad (6.62)$$

**Auxiliary Relations**

$$P_{ij} = \tau_{im} \frac{\partial U_j}{\partial x_m} + \tau_{jm} \frac{\partial U_i}{\partial x_m}, \quad D_{ij} = \tau_{im} \frac{\partial U_m}{\partial x_j} + \tau_{jm} \frac{\partial U_m}{\partial x_i}, \quad P = \frac{1}{2} P_{kk} \quad (6.63)$$

**Closure Coefficients [Launder (1992)]**

$$\left. \begin{aligned} \hat{\alpha} &= (8 + C_2)/11, & \hat{\beta} &= (8C_2 - 2)/11, & \hat{\gamma} &= (60C_2 - 4)/55 \\ C_1 &= 1.8, & C_2 &= 0.60, & C_s &= 0.11 \\ C_\epsilon &= 0.18, & C_{\epsilon 1} &= 1.44, & C_{\epsilon 2} &= 1.92 \end{aligned} \right\} \quad (6.64)$$

Note that Equation (6.61) differs from the  $\epsilon$  equation used with the Standard  $k$ - $\epsilon$  model [Equation (4.42)] in the form of the diffusion term. Rather than introduce the eddy viscosity, Launder, Reece and Rodi opt to use the analog of the turbulent transport term,  $C_{ijk}$ . The values of the closure coefficients in Equation (6.64) are specific to the LRR model of course, and their values are influenced by the specific form assumed for  $\Pi_{ij}$ . In their original paper, Launder, Reece and Rodi recommend  $C_1 = 1.5$ ,  $C_2 = 0.4$ ,  $C_s = 0.11$ ,  $C_\epsilon = 0.15$ ,  $C_{\epsilon 1} = 1.44$  and  $C_{\epsilon 2} = 1.90$ . The values quoted in Equation (6.64) are those currently recommended by Launder (1992).

**6.3.3 Wilcox Multiscale Model**

Not all second-order closure models use the  $\epsilon$  equation to compute  $\epsilon$ . Wilcox and Rubesin (1980) postulate a second-order closure model based on their  $\omega^2$  equation and the LRR model for  $\Pi_{ij}$ . Although the model showed some promise for flows over curved surfaces and for swirling flows, its applications were very limited. By contrast, Wilcox (1988b) proposes a second-order closure model that has had a wide range of applications.

The model, known as the multiscale model, has some novel features that are worthy of mention. The model was intended to serve as an improved algebraic stress model. The intended improvement was to include real time dependent convective terms rather than using Rodi's Equation (6.22).

To accomplish this end, the model idealizes turbulent flows as consisting of two distinct types of eddies. The first type are large, or upper partition, eddies that contain most of the turbulence energy and primarily transport the Reynolds stresses. The second are small, or lower partition, eddies that are isotropic and primarily dissipative. The kinetic energy of the small eddies is  $e$  so that the kinetic energy of the large eddies is  $k - e$ . This notion is used in Large Eddy Simulation work (see Chapter 8) where small eddies (corresponding to the lower partition of the spectrum) are modeled and large eddies (corresponding to the upper partition of the spectrum) are numerically simulated. Both types of eddies are modeled in the multiscale model.

The model consists of a tensor equation governing the development of the small and large eddies, including an energy exchange process that governs their interaction. Because of the assumed form of the equations, the exchange tensor is essentially the pressure-strain correlation tensor,  $\Pi_{ij}$ . The model uses the LRR pressure-strain model, although the formulation is sufficiently general to permit the use of any plausible pressure-strain formulation.

Using a series of physical arguments, Wilcox arrives at a closed set of equations that can be combined to yield an equation for the Reynolds-stress tensor. Although the formulation differs in spirit from the conventional term-by-term closure approach, the model effectively uses the Kolmogorov (1941) hypothesis of local isotropy for the lower partition, while the effective closure approximation for  $C_{ijk}$  is given by

$$C_{ijk} + \nu \frac{\partial \tau_{ij}}{\partial x_k} \approx -\frac{2}{3} (\mu + \sigma^* \mu_T) \frac{\partial k}{\partial x_k} \delta_{ij} \quad (6.65)$$

This equation is the approximation that replaces Rodi's ASM approximation. The most important consequence is that the turbulent transport of the shear stresses is neglected. This is consistent with the idealized notion that the large eddies move in an inviscid manner. Computationally, most notably in boundary-layer computations, the multiscale model often behaves very much like an ASM. Using standard notation, the Wilcox multiscale model is as follows.

**Reynolds-Stress Tensor**

$$\begin{aligned} \frac{\partial \tau_{ij}}{\partial t} + \frac{\partial}{\partial x_k} (U_k \tau_{ij}) = & -P_{ij} + \frac{2}{3} \beta^* \rho \omega k \delta_{ij} - \Pi_{ij} \\ & - \frac{2}{3} \frac{\partial}{\partial x_k} \left[ (\mu + \sigma^* \mu_T) \frac{\partial k}{\partial x_k} \delta_{ij} \right] \end{aligned} \quad (6.66)$$

**Specific Dissipation Rate**

$$\begin{aligned} \rho \frac{\partial \omega}{\partial t} + \rho U_j \frac{\partial \omega}{\partial x_j} = & \alpha \frac{\omega}{k} \tau_{ij} \frac{\partial U_i}{\partial x_j} - \beta \rho \omega \left[ \omega + \hat{\xi} \sqrt{2 \Omega_{mn} \Omega_{mn}} \right] \\ & + \frac{\partial}{\partial x_k} \left[ (\mu + \sigma \mu_T) \frac{\partial \omega}{\partial x_k} \right] \end{aligned} \quad (6.67)$$

**Upper Partition Energy**

$$\rho \frac{\partial (k - e)}{\partial t} + \rho U_j \frac{\partial (k - e)}{\partial x_j} = \left( 1 - \hat{\alpha} - \hat{\beta} \right) P - \beta^* \rho \omega k \left( 1 - \frac{e}{k} \right)^{3/2} \quad (6.68)$$

**Pressure-Strain Correlation**

$$\begin{aligned} \Pi_{ij} = & \beta^* C_1 \omega \left( \tau_{ij} + \frac{2}{3} \rho k \delta_{ij} \right) - \hat{\alpha} \left( P_{ij} - \frac{2}{3} P \delta_{ij} \right) \\ & - \hat{\beta} \left( D_{ij} - \frac{2}{3} P \delta_{ij} \right) - \hat{\gamma} \rho k \left( S_{ij} - \frac{1}{3} S_{kk} \delta_{ij} \right) \end{aligned} \quad (6.69)$$

**Auxiliary Relations**

$$\mu_T = \rho k / \omega \quad (6.70)$$

$$P_{ij} = \tau_{im} \frac{\partial U_j}{\partial x_m} + \tau_{jm} \frac{\partial U_i}{\partial x_m}, \quad D_{ij} = \tau_{im} \frac{\partial U_m}{\partial x_j} + \tau_{jm} \frac{\partial U_m}{\partial x_i}, \quad P = \frac{1}{2} P_{kk} \quad (6.71)$$

**Closure Coefficients**

$$\left. \begin{aligned} \alpha &= 4/5, & \beta &= 3/40, & \beta^* &= 9/100, & \sigma &= 1/2, & \sigma^* &= 1/2 \\ \hat{\alpha} &= 42/55, & \hat{\beta} &= 6/55, & \hat{\gamma} &= 1/4, & \hat{\xi} &= 1 \\ C_1 &= 1 + 4(1 - e/k)^{3/2} \end{aligned} \right\} \quad (6.72)$$

The term proportional to  $\hat{\xi}$  in Equation (6.67) is the only formal difference from the  $k$ - $\omega$  model's Equation (4.35). Because of this term, the value of  $\alpha$  must increase from  $5/9$  to  $4/5$ . All other closure coefficients shared by the  $k$ - $\omega$  and multiscale models have the same values. The term proportional to  $\hat{\xi}$  follows from the LES work of Bardina, Ferziger and Reynolds (1983). In the context of homogeneous turbulence, it is required to accurately simulate effects of system rotation. The term also introduces subtle differences



between model-predicted effects of plane strain and uniform shear on homogeneous turbulence.

Note that the values chosen for  $\hat{\alpha}$  and  $\hat{\beta}$  are those used in the original Launder, Reece and Rodi (1975) model. However, a modified value of  $1/4$  rather than the LRR value of  $4/11$  has been selected for  $\hat{\gamma}$  to optimize model predictions for homogeneous turbulence. Also, in a the log layer of a flat-plate boundary layer, the model predicts  $e/k \approx 0.75$  so that the value of  $C_1$  is 1.5. This matches the value used in the original LRR model.

## 6.4 Application to Homogeneous Turbulent Flows

Homogeneous turbulent flows are useful for establishing the new closure coefficients introduced in modeling the pressure-strain correlation tensor,  $\Pi_{ij}$ . This is the primary type of flow normally used to calibrate a second-order closure model. Recall that homogeneous turbulence is defined as a turbulent flow that, on the average, is uniform in all directions. This means the diffusion terms in all of the equations of motion are identically zero, as is the pressure-echo correction. Hence, the primary remaining difference between the LRR and Wilcox multiscale models when applied to homogeneous turbulent flows is in the scale-determining equation. That is, both models use the LRR pressure-strain model and the Kolmogorov isotropy hypothesis, so that the equations for the Reynolds stresses are nearly identical. The only differences are: (a) the LRR model uses the  $\epsilon$  equation while the multiscale model uses the  $\omega$  equation; and, (b) the closure coefficient  $C_1$  is constant for the LRR model while it varies with large-eddy energy,  $(k - e)$ , for the multiscale model.

Additionally, since the diffusion terms vanish, the equations simplify to first-order, ordinary differential equations, which can sometimes be solved in closed form. At worst, a simple Runge-Kutta integration is required. Such flows are ideal for helping establish values of closure coefficients such as  $C_1$  and  $C_2$  in the LRR model, provided of course that we believe the same values apply to all turbulent flows.

The simplest of all homogeneous flows is the decay of isotropic turbulence. We discussed homogeneous isotropic turbulence in Section 4.4, and established the ratio of  $\beta^*$  to  $\beta$  for the  $k$ - $\omega$  model. The multiscale model equations for  $k$  and  $\omega$  simplify to

$$\frac{dk}{dt} = -\beta^* \omega k \quad \text{and} \quad \frac{d\omega}{dt} = -\beta \omega^2 \quad (6.73)$$

For large time, the asymptotic solution for  $k$  is given by

$$k \sim t^{-\beta^*/\beta} \quad (6.74)$$

Similarly, for the LRR model,  $k$  varies with  $t$  according to

$$k \sim t^{-1/(C_{\epsilon 2}-1)} \quad (6.75)$$

Experimental observations summarized by Townsend (1976) indicate that  $k \sim t^{-n}$  where  $n = 1.25 \pm 0.06$  for decaying homogeneous, isotropic turbulence. Hence, we can conclude that our closure coefficients must lie in the following ranges.

$$1.19 < \beta^*/\beta < 1.31, \quad 1.76 < C_{\epsilon 2} < 1.84 \quad (6.76)$$

Figures 6.4(a) and (b) compare computed and measured  $k$  for decaying homogeneous, isotropic turbulence as predicted by the Wilcox multiscale model. The experimental data in (a) and (b) are those of Comte-Bellot and Corrsin (1971) and Wigeland and Nagib (1978), respectively.

The second type of homogeneous turbulent flow that is useful for establishing the value of pressure-strain correlation closure coefficients is decaying anisotropic turbulence. Assuming dissipation follows the Kolmogorov (1941) isotropy hypothesis [Equation (6.30)], and using Rotta's (1951) slow pressure-strain term [Equation (6.45)], the Reynolds-stress equation is

$$\frac{d\tau_{ij}}{dt} = \frac{2}{3}\rho\epsilon\delta_{ij} - C_1 \frac{\epsilon}{k} \left( \tau_{ij} + \frac{2}{3}\rho k\delta_{ij} \right) \quad (6.77)$$

The solution is readily shown to be

$$\tau_{ij} + \frac{2}{3}\rho k\delta_{ij} = \left( \tau_{ij} + \frac{2}{3}\rho k\delta_{ij} \right)_o \left( \frac{k_o\epsilon}{k\epsilon_o} \right)^{C_1/(C_{\epsilon 2}-1)} \quad (6.78)$$

where subscript  $o$  denotes initial value. The experimental data of Uberoi (1956) indicate that the coefficient  $C_1$  lies in the range

$$1.4 < C_1 < 1.8 \quad (6.79)$$

Figures 6.4(e), (f), (g) and (h) compare computed  $k$  and normal Reynolds stresses with Uberoi's measurements for decaying homogeneous, anisotropic turbulence as predicted by the Wilcox multiscale model.

Note that  $C_1$  is not a constant in the multiscale model, but instead varies with  $e/k$ . The range of values for  $C_1$  in Equation (6.79) correspond to  $e/k$  lying in the range  $0.66 < e/k < 0.78$ . This is inconsistent with

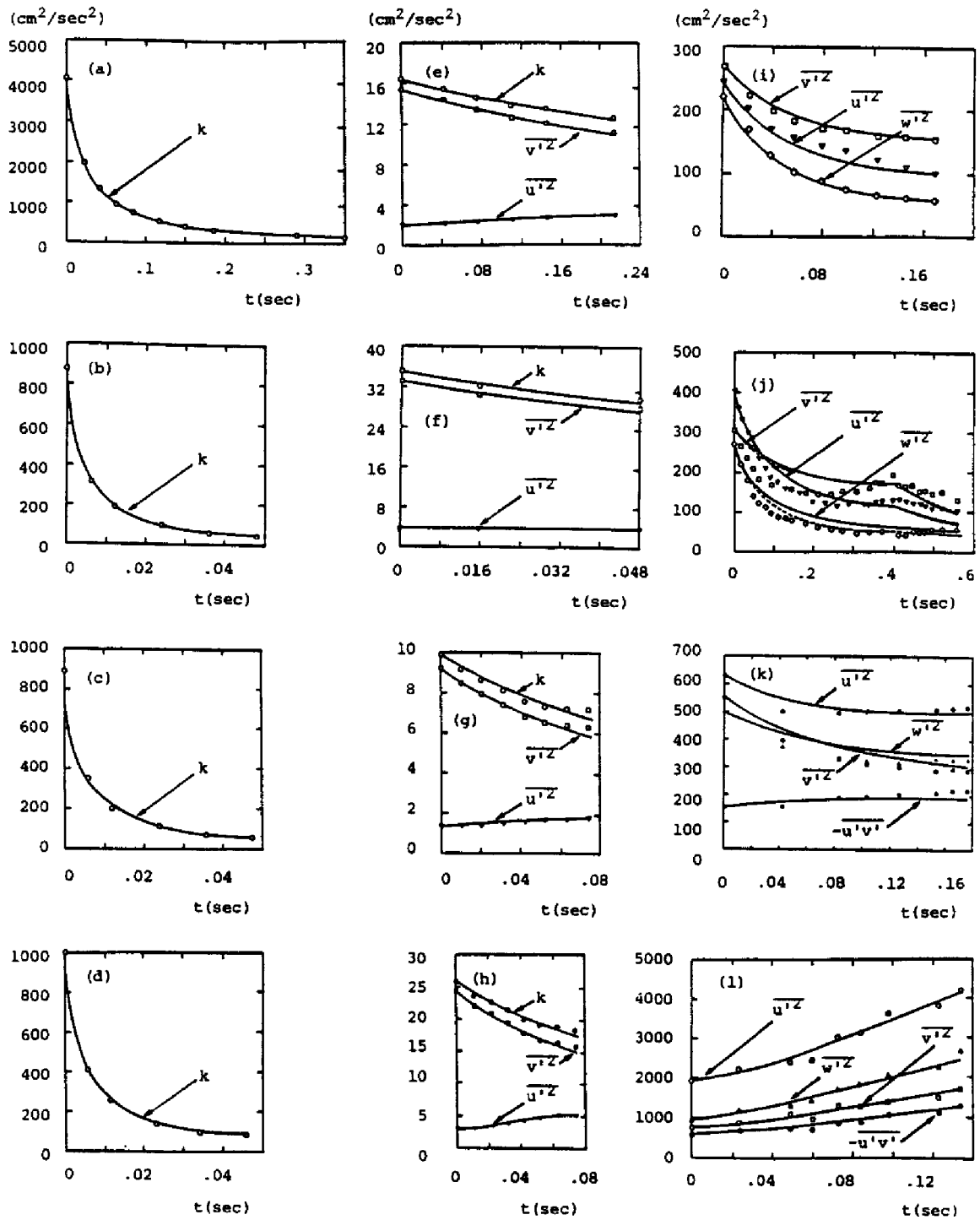


Figure 6.4: Computed and measured turbulence energy and Reynolds stresses for homogeneous turbulent flows; — Wilcox multiscale model;  $\circ \bullet \square \triangle \nabla$  measured. [From Wilcox (1988b) — Copyright © AIAA 1988 — Used with permission.]

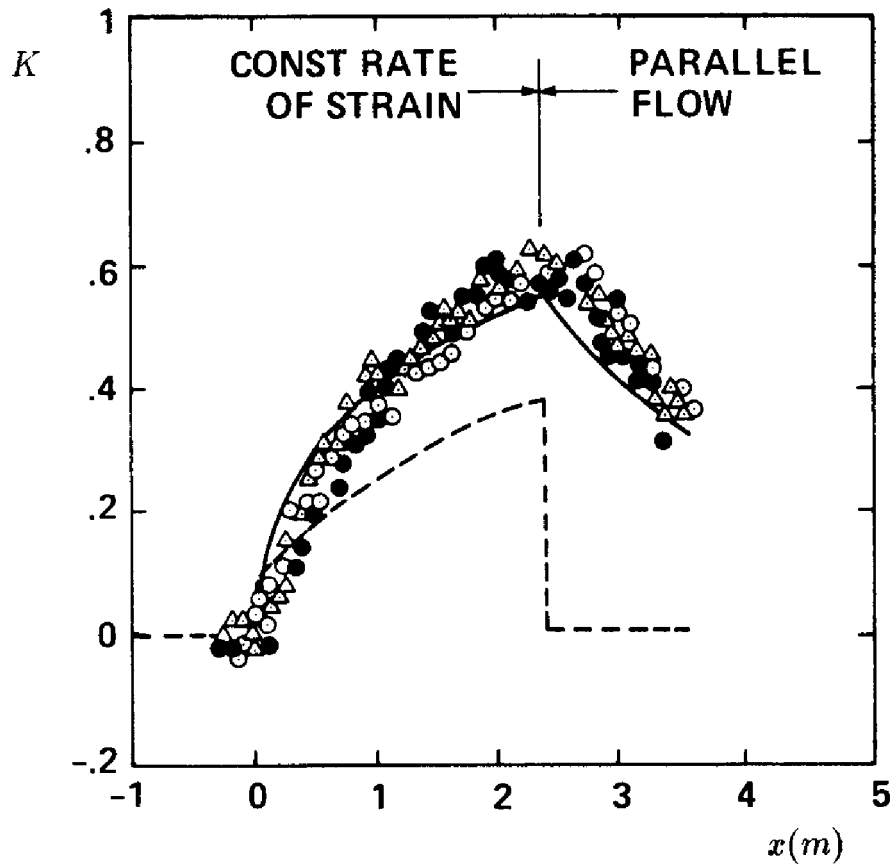


Figure 6.5: Computed and measured distortion parameter for the Tucker-Reynolds plane-strain flow; - - - Wilcox-Rubesin  $k-\omega^2$  model; — Wilcox-Rubesin second-order closure model;  $\circ \bullet \Delta$  Tucker-Reynolds. [From Wilcox and Rubesin (1980).]

Kolmogorov's notion that the large eddies contain most of the energy, and represents a conceptual flaw in the multiscale model. However, virtually all multiscale applications have been done using values of  $\epsilon/k$  that correspond to  $C_1$  lying in the range quoted in Equation (6.79). The model's predictions are not strongly affected by simply using a constant value of  $C_1$  and dropping Equation (6.68).

To illustrate how much of an improvement second-order closure models make for flows with sudden changes in mean strain rate, Figure 6.5 compares measured distortion parameter,  $K$ , for the Tucker-Reynolds experiment with computed results obtained using the Wilcox-Rubesin (1980)  $k-\omega^2$  and second-order closure models. As shown, the second-order closure model predicts a gradual approach to isotropy and the computed  $K$  more closely matches the experimental data.

Figure 6.6 compares computed and measured normal components of the Reynolds-stress anisotropy tensor,  $b_{ij}$ , for the experiment conducted by

Choi and Lumley (1984). This experiment is similar to the Tucker-Reynolds experiment, with turbulence initially subjected to plain strain and then returning to isotropy after the strain is removed. This computation has been done with the original LRR model using  $C_1 = 1.5$ .

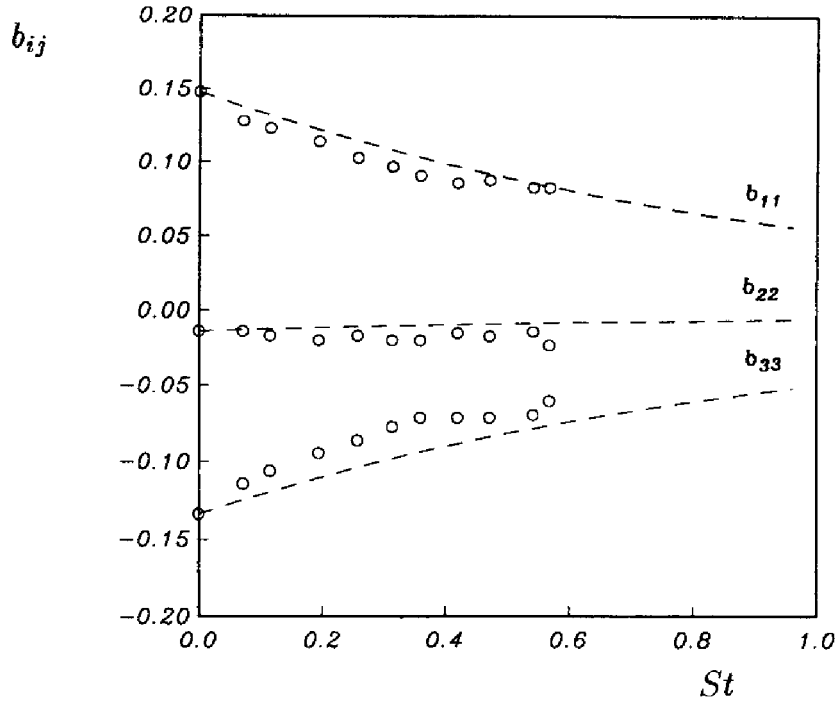


Figure 6.6: Comparison of computed and measured anisotropy tensor for decaying homogeneous, anisotropic turbulence; - - LRR model; o Choi and Lumley. [From Speziale (1991) — Published with permission of author.]

While discrepancies between computed and measured stresses are satisfactory, even closer agreement between theory and experiment can be obtained with a nonlinear model for the slow pressure-strain model. Sarkar and Speziale (1990), for example, propose a simple quadratic model for the slow pressure-strain given by

$$A_{ij} = -C_1 \rho \epsilon b_{ij} + C_2 \rho \epsilon \left( b_{ik} b_{kj} - \frac{1}{3} b_{mn} b_{nm} \delta_{ij} \right) \quad (6.80)$$

where  $C_1 = 3.4$  and  $C_2 = 4.2$  [see Equation (6.58)]. Figure 6.7 compares the so-called **phase-space portrait** of the return-to-isotropy problem. The figure shows the variation of the second tensor invariant  $II = b_{ij} b_{ji}$  as a function of the third tensor invariant,  $III = b_{ik} b_{kl} b_{li}$ . The nonlinear model clearly falls within the scatter of the experimental data, while the LRR model prediction provides a less satisfactory description.

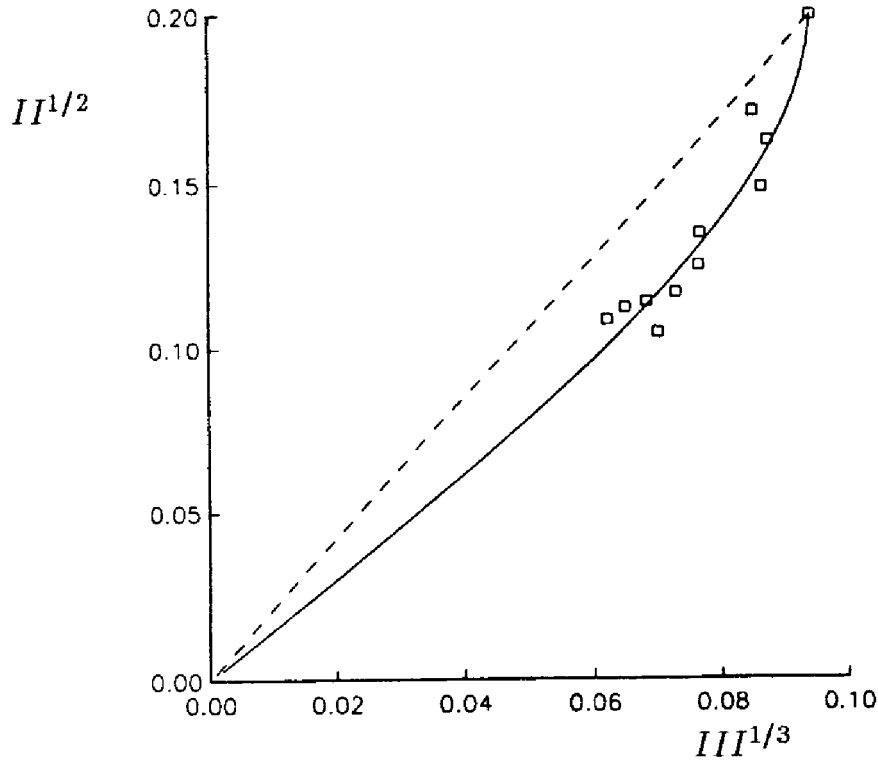


Figure 6.7: Phase-space portrait for decaying homogeneous, anisotropic turbulence; - - - LRR model; — Sarkar-Speziale model;  $\square$  Choi and Lumley. [From Speziale (1991) — Published with permission of author.]

Homogeneous turbulence experiments have also been performed that include irrotational plane strain [Townsend (1956) and Tucker and Reynolds (1968)] and uniform shear [Champagne, Harris and Corrsin (1970), Harris, Graham and Corrsin (1977), Tavoularis and Corrsin (1981), and Tavoularis and Karnik (1989)]. These flows can be used to establish closure coefficients such as  $C_2$  in the LRR pressure-strain model. The velocity gradient tensor for these flows is:

$$\frac{\partial U_i}{\partial x_j} = \begin{bmatrix} 0 & S & 0 \\ 0 & -a & 0 \\ 0 & 0 & a \end{bmatrix} \quad (6.81)$$

where  $a$  is the constant strain rate and  $S$  is the constant rate of mean shear.

While closed form solutions generally do not exist when mean strain rate and/or shear are present, analytical progress can be made for the asymptotic forms in the limit  $t \rightarrow \infty$ . In general, the specific dissipation rate,  $\omega \sim \epsilon/k$ , approaches a constant limiting value while  $k$  and the Reynolds stresses grow exponentially. Assuming solutions of this form yields closed-form expressions for the Reynolds stresses.

Using such analysis for uniform shear ( $a = 0, S \neq 0$ ), Abid and Speziale (1992) have analyzed the LRR and SSG pressure-strain models and two new nonlinear pressure-strain models developed by Shih and Lumley (1985) [SL model] and by Fu, Launder and Tselepidakis (1987) [FLT model]. Table 6.1 summarizes their results, along with results for the multiscale model (MS) and asymptotic values determined experimentally by Tavoularis and Karnik (1989). As shown, the SSG model most faithfully reproduces measured asymptotic values of the Reynolds stresses. Note that the multiscale model's modified value for  $\hat{\gamma}$  in the LRR rapid pressure-strain model yields a closer match to the measured  $b_{xy}$  than the original LRR model, while MS and LRR normal components are nearly identical.

Table 6.1: Anisotropy-Tensor Limiting Values for Uniform Shear

Property	MS	LRR	SL	FLT	SSG	Measured
$b_{xx}$	.156	.152	.120	.196	.218	.210
$b_{xy}$	-.154	-.186	-.121	-.151	-.164	-.160
$b_{yy}$	-.122	-.119	-.122	-.136	-.145	-.140
$b_{zz}$	-.034	-.033	.002	-.060	-.073	-.070
$Sk/\epsilon$	4.965	4.830	7.440	5.950	5.500	5.000

Figure 6.4(k) compares multiscale model Reynolds stresses with corresponding measured values for the Champagne, Harris and Corrsin (1970) uniform-shear experiment with  $S = 12.9 \text{ sec}^{-1}$ . Figure 6.4(l) makes a similar comparison with the measurements of Harris, Graham and Corrsin (1977) for which  $S = 48.0 \text{ sec}^{-1}$ . For both flows, the asymptotic value of  $e/k$  is  $4/5$ . Both computations use  $(e/k)_o = 4/5$ .

Turning to flows with irrotational strain rate ( $a \neq 0, S = 0$ ), Figure 6.4(i) and (j) compare multiscale model and measured [Townsend (1956) and Tucker and Reynolds (1968), respectively]  $k$  and Reynolds stresses. The strain rate for the Townsend case is  $a = 9.44 \text{ sec}^{-1}$ , while the Tucker-Reynolds case has  $a = 4.45 \text{ sec}^{-1}$ . Launder, Reece and Rodi (1975) report very similar results for the Tucker-Reynolds case. The multiscale model results are mildly sensitive to the initial value of  $e/k$ . Both cases have been done using  $(e/k)_o = 3/4$ , which turns out to be the long-time asymptotic value predicted by the model for uniform strain rate. Varying the initial ratio between  $1/2$  and  $9/10$  produces less than a 15% change overall in the Reynolds stresses. Figure 6.4(j) shows the results obtained for the Tucker-Reynolds case using initial  $e/k$  ratios of  $3/4$  (solid curves) and  $9/10$  (dashed

curves). As shown, the primary difference appears in  $\overline{w'^2}$ . Using the larger value produces closer agreement between theory and experiment.

Rotating homogeneous turbulent flow is of some interest as it includes Coriolis and centrifugal accelerations. The experiments of Wigeland and Nagib (1978), for example, involve decaying axisymmetric homogeneous turbulence that is subjected to constant angular rotation rate,  $\Omega$ . Figures 6.4(b), (c) and (d) compare computed and measured  $k$  for rotation rates of 0, 20  $\text{sec}^{-1}$  and 80  $\text{sec}^{-1}$ , respectively. These computations have been used to establish the value of  $\hat{\xi}$  in the Wilcox multiscale model. As noted earlier, this term was borrowed from the LES work of Bardina, Ferziger and Reynolds (1983). Speziale (1991) indicates that the nonlinear SSG pressure-strain model precludes the need for such rotation dependent terms in the  $\epsilon$  or  $\omega$  equation.

## 6.5 Application to Free Shear Flows

While second-order closure models eliminate many of the shortcomings of the Boussinesq eddy-viscosity approximation, they do not appear to solve the free shear flow problem. Table 6.2 summarizes computed and measured spreading rates for the Wilcox multiscale model and the LRR model. As shown in the table, while the multiscale model displays much less sensitivity to the freestream value of  $\omega$  than the  $k$ - $\omega$  model (see Table 4.2), its spreading rate is somewhat smaller than measured for the far wake. The LRR model's spreading rates are roughly 10% larger than those of the Standard  $k$ - $\epsilon$  model. As noted by Launder and Morse (1979), because the predicted round-jet spreading rate exceeds the predicted plane-jet spreading rate, the LRR model fails to resolve the round-jet/plane-jet anomaly.

Table 6.2: Free Shear Flow Spreading Rate

Flow	Multiscale Model	LRR Model	Measured
Far Wake	.248-.292	—	.365
Mixing Layer	.102-.115	.104	.115
Plane Jet	—	.123	.100-.110
Round Jet	—	.135	.086-.095

Figure 6.8 compares computed and measured width of a curved mixing layer. The computation was done using the LRR model [Rodi (1981)], and the measurements correspond to an experiment of Castro and Bradshaw



(1976) with stabilizing curvature. As shown, the LRR model predicts a greater reduction in width than the Standard  $k-\epsilon$  model. However, the LRR model's predicted width lies as far below the measured width as the  $k-\epsilon$  model's prediction lies above. Although not shown in the figure, Rodi's (1976) Algebraic Stress Model predicts a width about midway between, and thus in close agreement with measured values.

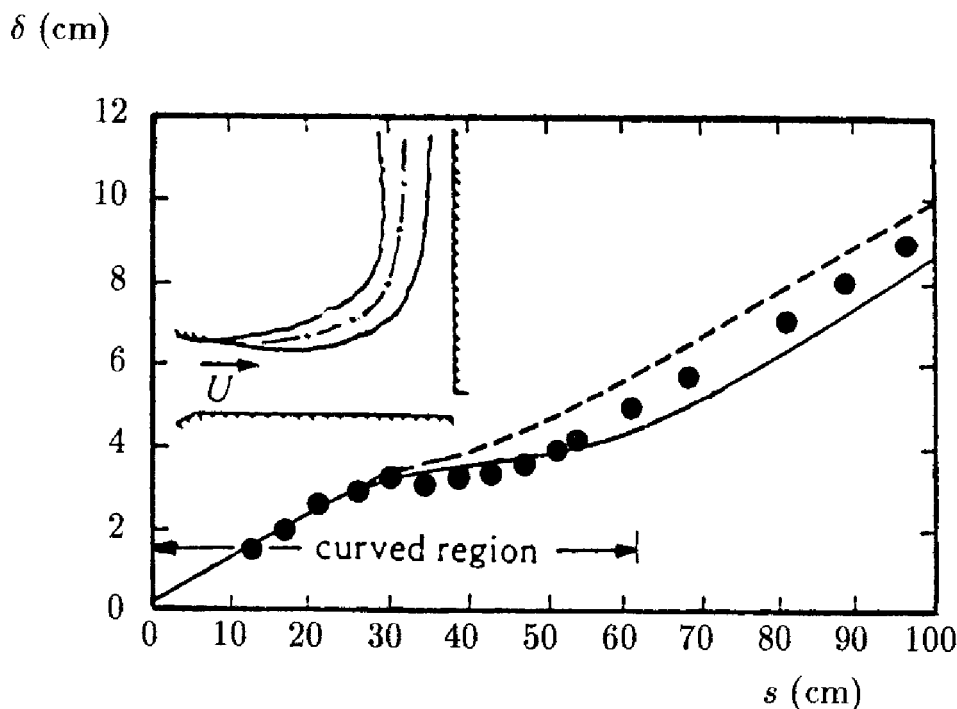


Figure 6.8: Comparison of computed and measured width for a curved mixing layer; — LRR model; - - - Standard  $k-\epsilon$  model; • Castro and Bradshaw. [From Rodi (1981) — Copyright © AIAA 1981 — Used with permission.]

As a final comment, with all of the additional new closure coefficients attending nonlinear pressure-strain models, it is very likely that such models can be fine tuned to correct the round-jet/plane-jet anomaly. However, we should keep in mind that the anomaly underscores a deficiency in our physical description and understanding of jets. Be aware that such fine tuning reveals nothing regarding the nature of these flows, and thus amounts to little more than a curve-fitting exercise.

## 6.6 Application to Wall-Bounded Flows

This section focuses upon wall-bounded flows, including channel and pipe flow, and boundary layers with a variety of complicating effects. Before

addressing such flows, however, we discuss surface boundary conditions. As with two-equation models, we have the option of using wall functions or integrating through the viscous sublayer.

### 6.6.1 Surface Boundary Conditions

Wall-bounded flows require boundary conditions appropriate to a solid boundary for the mean velocity and the scale-determining parameter, e.g.,  $\epsilon$  or  $\omega$ . Additionally, surface boundary conditions are needed for each component of the Reynolds-stress tensor (implying a boundary condition for  $k$ ). The exact surface boundary conditions follow from the no-slip condition:

$$\tau_{ij} = 0 \quad \text{at} \quad y = 0 \quad (6.82)$$

Second-order closure models, like two-equation models, may or may not predict a satisfactory value of the constant  $B$  in the law of the wall when the equations are integrated through the viscous sublayer. If the model fails to predict a satisfactory value for  $B$ , we have the choice of either introducing viscous damping factors or using wall functions to obviate integration through the sublayer. The near-wall behavior of second-order closure models is strongly influenced by the scale-determining equation. Models based on the  $\epsilon$  equation fail to predict an acceptable value of  $B$  and are very difficult to integrate through the sublayer. By contrast, models based on the  $\omega$  equation often predict an acceptable value of  $B$  and are generally quite easy to integrate through the sublayer.

The most rational procedure for devising wall functions is to analyze the log layer with perturbation methods. As with the  $k$ - $\epsilon$  model, the velocity,  $k$  and either  $\epsilon$  or  $\omega$  are given by

$$U = u_\tau \left[ \frac{1}{\kappa} \ln \left( \frac{u_\tau y}{\nu} \right) + B \right] \quad (6.83)$$

$$k = \frac{u_\tau^2}{\sqrt{\beta^*}}, \quad \omega = \frac{k^{1/2}}{(\beta^*)^{1/4} \kappa y}, \quad \epsilon = (\beta^*)^{3/4} \frac{k^{3/2}}{\kappa y} \quad (6.84)$$

Similar relations are needed for the Reynolds stresses, and the precise forms depend upon the approximations used to close the Reynolds-stress equation. The Problems section examines log-layer structure for the LRR and Wilcox multiscale models. Regardless of the model, the general form of the Reynolds-stress tensor is

$$\tau_{ij} = C_{ij} \rho k \quad \text{as} \quad y \rightarrow 0 \quad (6.85)$$

where  $C_{ij}$  is a constant tensor whose components depend upon the model's closure coefficients.

So, Lai, Zhang, and Hwang (1991) review low-Reynolds-number corrections for second-order closure models based on the  $\epsilon$  equation. The damping functions generally introduced are similar to those proposed for the  $k$ - $\epsilon$  model (see Section 4.9). As with the  $k$ - $\epsilon$  model, many authors have postulated low-Reynolds-number damping functions, and the topic remains in a continuing state of development.

As with the  $k$ - $\omega$  model, the surface value of specific dissipation rate,  $\omega_w$ , determines the value of the constant  $B$  in the law of the wall for the multiscale model. Perturbation analysis of the sublayer shows that the limit  $\omega_w \rightarrow \infty$  corresponds to a perfectly-smooth wall and, without low-Reynolds-number corrections, the asymptotic behavior of  $\omega$  approaching the surface for both the  $k$ - $\omega$  and multiscale models is

$$\omega \rightarrow \frac{6\nu_w}{\beta y^2} \quad \text{as} \quad y \rightarrow 0 \quad (\text{Smooth Wall}) \quad (6.86)$$

Using Program SUBLAY (Appendix C), the multiscale model's sublayer behavior can be readily determined. Most importantly, the constant,  $B$ , in the law of the wall is

$$B = 5.2 \quad (6.87)$$

Thus, the multiscale model can be integrated through the viscous sublayer without the aid of viscous damping functions. Figure 6.9(a) compares multiscale model smooth-wall velocity profiles with corresponding measurements of Laufer (1952), Andersen, Kays and Moffat (1972), and Wiegardt [as tabulated by Coles and Hirst (1969)]. Figure 6.9(b) compares computed turbulence production and dissipation terms with Laufer's (1952) near-wall pipe-flow measurements. In all cases, predictions are within experimental error bounds.

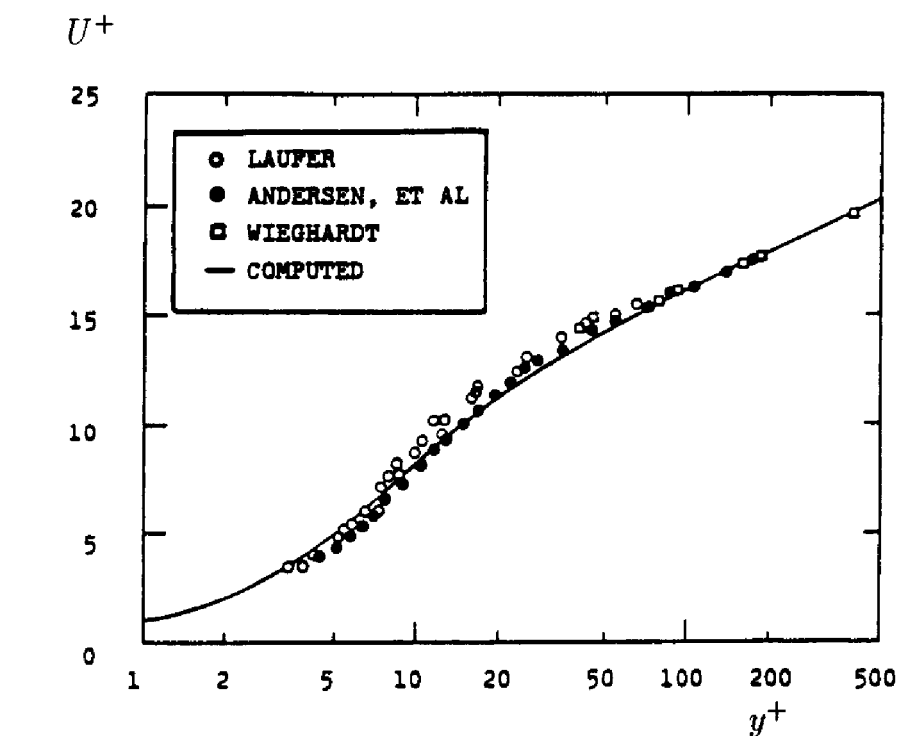
The multiscale model also has the property that the constant  $B$  varies with the surface value of  $\omega$ . We can thus correlate  $\omega_w$  with surface roughness height,  $k_R$ , and surface mass-injection velocity,  $v_w$ . The resulting correlations are a little different from those appropriate for the  $k$ - $\omega$  model. The surface boundary conditions based on these correlations are as follows.

**For rough surfaces:**

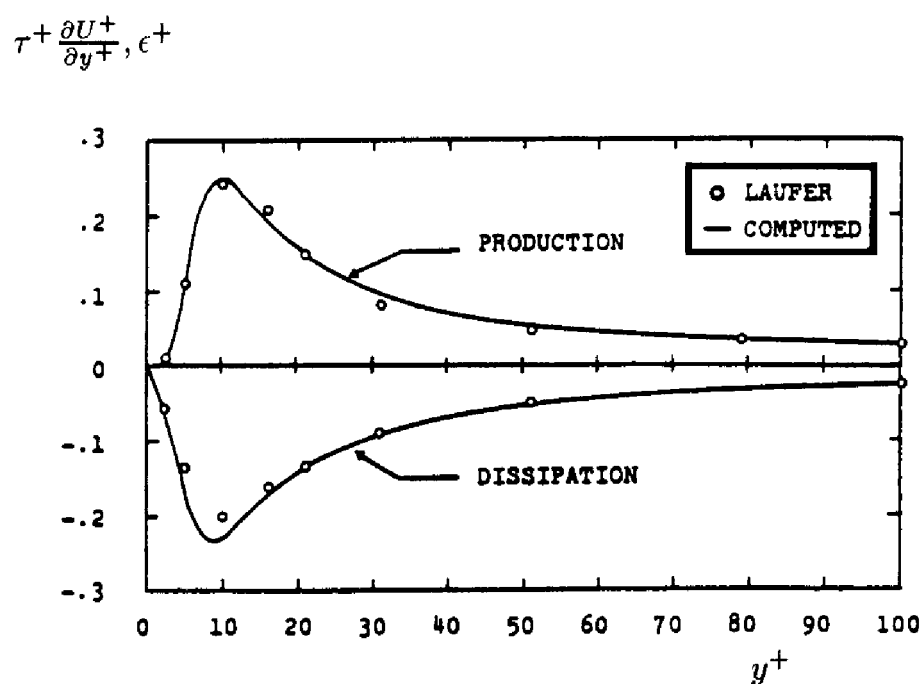
$$\omega = \frac{u_\tau^2 S_R}{\nu_w} \quad \text{at} \quad y = 0 \quad (\text{Rough Wall}) \quad (6.88)$$

where the dimensionless coefficient  $S_R$  is defined in terms of  $k_R^+ = u_\tau k_R / \nu_w$  by

$$S_R = \begin{cases} (50/k_R^+)^2, & k_R^+ \leq 25 \\ 500/(k_R^+)^{3/2} & k_R^+ > 25 \end{cases} \quad (6.89)$$



(a) Velocity



(b) Production and dissipation

Figure 6.9: Computed and measured sublayer properties; multiscale model. [From Wilcox (1988b) — Copyright © AIAA 1988 — Used with permission.]

**For surfaces with mass injection:**

$$\omega = \frac{u_\tau^2 S_B}{\nu_w} \quad \text{at} \quad y = 0 \quad (\text{Mass Injection}) \quad (6.90)$$

where the dimensionless coefficient  $S_B$  is defined in terms of  $v_w^+ = v_w/u_\tau$  by

$$S_B = \frac{16}{v_w^+(1 + 4v_w^+)} \quad (6.91)$$

As a final comment, while the multiscale model does not require viscous damping functions to achieve a satisfactory sublayer solution, introducing low-Reynolds-number corrections can improve model predictions for a variety of flows. Most importantly, with straightforward viscous damping functions very similar to those introduced for the  $k$ - $\omega$  model (see Subsection 4.9.2), the model's ability to predict transition can be greatly improved. As with the  $k$ - $\omega$  model, we let

$$\mu_T = \alpha^* \frac{\rho k}{\omega} \quad (6.92)$$

and the closure coefficients in Equations (6.72) are replaced by the following.

$$\left. \begin{aligned} \alpha^* &= \frac{\alpha_o^* + Re_T/R_k}{1 + Re_T/R_k} \\ \alpha &= \frac{4}{5} \cdot \frac{\alpha_o + Re_T/R_\omega}{1 + Re_T/R_\omega} \\ \beta^* &= \frac{9}{100} \cdot \frac{5/18 + (Re_T/R_\beta)^4}{1 + (Re_T/R_\beta)^4} \\ \hat{\gamma} &= \frac{1}{4} \cdot \frac{\hat{\gamma}_o + Re_T/R_k}{1 + Re_T/R_k} \end{aligned} \right\} \quad (6.93)$$

$$\left. \begin{aligned} \beta &= 3/40, \quad \sigma^* = \sigma = 1/2, \quad \hat{\alpha} = 42/55, \quad \hat{\beta} = 6/55, \quad \hat{\xi} = 1 \\ \alpha_o^* &= \beta/3, \quad \alpha_o = 1/10, \quad \hat{\gamma}_o = 9/500 \\ R_\beta &= 8, \quad R_k = 6, \quad R_\omega = 3/4, \quad C_1 = 1 + 4(1 - e/k)^{3/2} \end{aligned} \right\} \quad (6.94)$$

Note that, unlike the  $k$ - $\omega$  model, the factor  $(\alpha^*)^{-1}$  is not required in the equation for  $\alpha$  [see Equation (4.223) for comparison]. With these viscous corrections, the multiscale model reproduces all of the low-Reynolds-number  $k$ - $\omega$  model transition-predictions discussed in Subsection 4.9.2, and other subtle features such as asymptotic consistency. The values chosen for  $R_\beta$ ,  $R_k$  and  $R_\omega$  yield  $B = 5.0$ .

### 6.6.2 Channel and Pipe Flow

Figure 6.10 compares computed and measured velocity and Reynolds-stress profiles for the original Launder-Reece-Rodi model. The computation has been done using wall functions. Velocity profile data shown are those of Laufer (1951) and Hanjalić (1970), while the Reynolds-stress data are those of Comte-Bellot (1965). As shown, with the exception of  $\overline{u'^2}$ , computed and measured profiles differ by less than 5%. The computed and measured  $\overline{u'^2}$  profiles differ by no more than 20%. Although not shown, even closer agreement between computed and measured Reynolds stresses can be obtained with low-Reynolds-number versions of the LRR model [see So et al. (1991)].

One of the most controversial features of the LRR model solution for channel flow is the importance of the pressure-echo term throughout the flow. The pressure-echo contribution on the centerline is approximately 15% of its peak value. It is unclear that a supposed near-wall effect should have this large an impact at the channel centerline. However, some researchers argue that the echo effect scales with maximum eddy size which, for channel flow, would be about half the channel height.

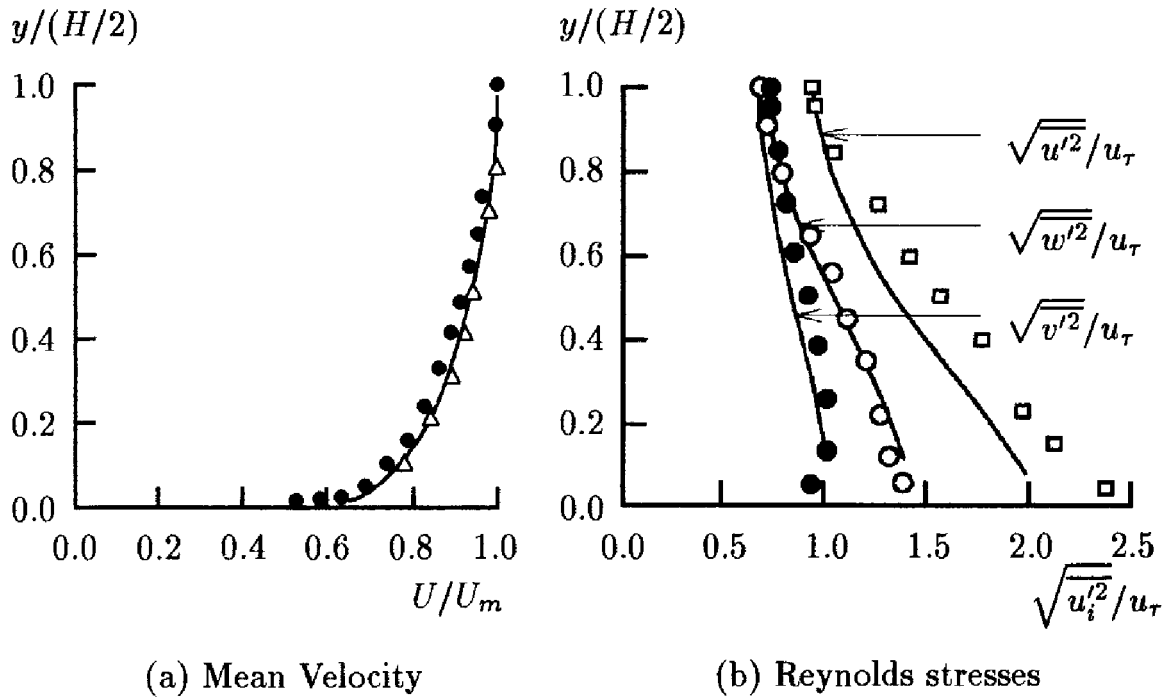


Figure 6.10: Computed and measured flow properties for channel flow; — LRR model; (a)  $\triangle$  Laufer,  $\bullet$  Hanjalić; (b)  $\square$   $\circ$   $\bullet$  Comte-Bellot.

Figures 6.11 and 6.12 compare computed and measured channel-flow and pipe-flow properties for the multiscale model with and without viscous corrections. As shown, computed skin friction is generally within 3% of the

Halleen and Johnston (1967) correlation [see Equation (3.137)] for channel flow. Similarly, computed  $c_f$  differs from Prandtl's universal law of friction [see Equation (3.138)] by less than 3% except at the lowest Reynolds numbers. For both channel and pipe flow, the velocity, Reynolds shear stress, and turbulence kinetic energy profiles differ by less than 6%. Most notably, the low-Reynolds-number model predicts the peak value of  $k$  near the wall to within 10% of the DNS value for channel flow and 4% of the measured value for pipe flow. For both cases, the turbulence-energy production,  $\tau_{xy}\partial U/\partial y$ , and dissipation,  $\epsilon$ , are within 10% of the DNS and measured results except very close to the surface.

Capturing subtle details such as the sharp peak in  $k$  near the surface has been done at the expense of 10% differences between computed and measured velocity profiles for  $y^+$  between 10 and 100, although the law of the wall is accurately predicted above  $y^+ = 100$ . This type of compromise is very typical of low-Reynolds-number versions of the LRR model as well. Unlike the multiscale model however, many low-Reynolds-number variants of the LRR model provide accurate descriptions of near-wall Reynolds stresses and dissipation while simultaneously giving nontrivial discrepancies between computed and measured skin friction. By contrast, the low-Reynolds-number corrections have virtually no effect on the multiscale model's predicted skin friction.

Interestingly, the multiscale model implements the LRR pressure-strain model for  $\Pi_{ij}$  without the pressure-echo correction. Hence, the strong effect this term has on LRR-model predictions may, to some extent, reflect shortcomings of the  $\epsilon$  equation's near-wall behavior.

Rotating channel flow is an interesting application of second-order closure models. As with flow over a curved surface, two-equation models require ad hoc corrections for rotating channel flow in order to make realistic predictions [e.g., Launder, Priddin and Sharma (1977) and Wilcox and Chambers (1977)]. To understand the problem, note that in a rotating coordinate frame, the Coriolis acceleration yields additional inertial terms in the Reynolds-stress equation. Specifically, in a coordinate system rotating with angular velocity,  $\Omega$ , the Reynolds-stress equation is

$$\begin{aligned} \frac{\partial \tau_{ij}}{\partial t} + U_k \frac{\partial \tau_{ij}}{\partial x_k} + 2(\epsilon_{jkm}\Omega_k \tau_{im} + \epsilon_{ikm}\Omega_k \tau_{jm}) \\ = -\tau_{ik} \frac{\partial U_j}{\partial x_k} - \tau_{jk} \frac{\partial U_i}{\partial x_k} + \epsilon_{ij} - \Pi_{ij} + \frac{\partial}{\partial x_k} \left[ \nu \frac{\partial \tau_{ij}}{\partial x_k} + C_{ijk} \right] \end{aligned} \quad (6.95)$$

where  $\epsilon_{jkm}$  is the permutation tensor. Note that if the rotation tensor,  $\Omega_{ij}$ , appears in any of the closure approximations for  $\epsilon_{ij}$ ,  $\Pi_{ij}$  or  $C_{ijk}$ , it must be replaced by  $\Omega_{ij} + \epsilon_{ikj}\Omega_k$ . Contracting Equation (6.95) yields the

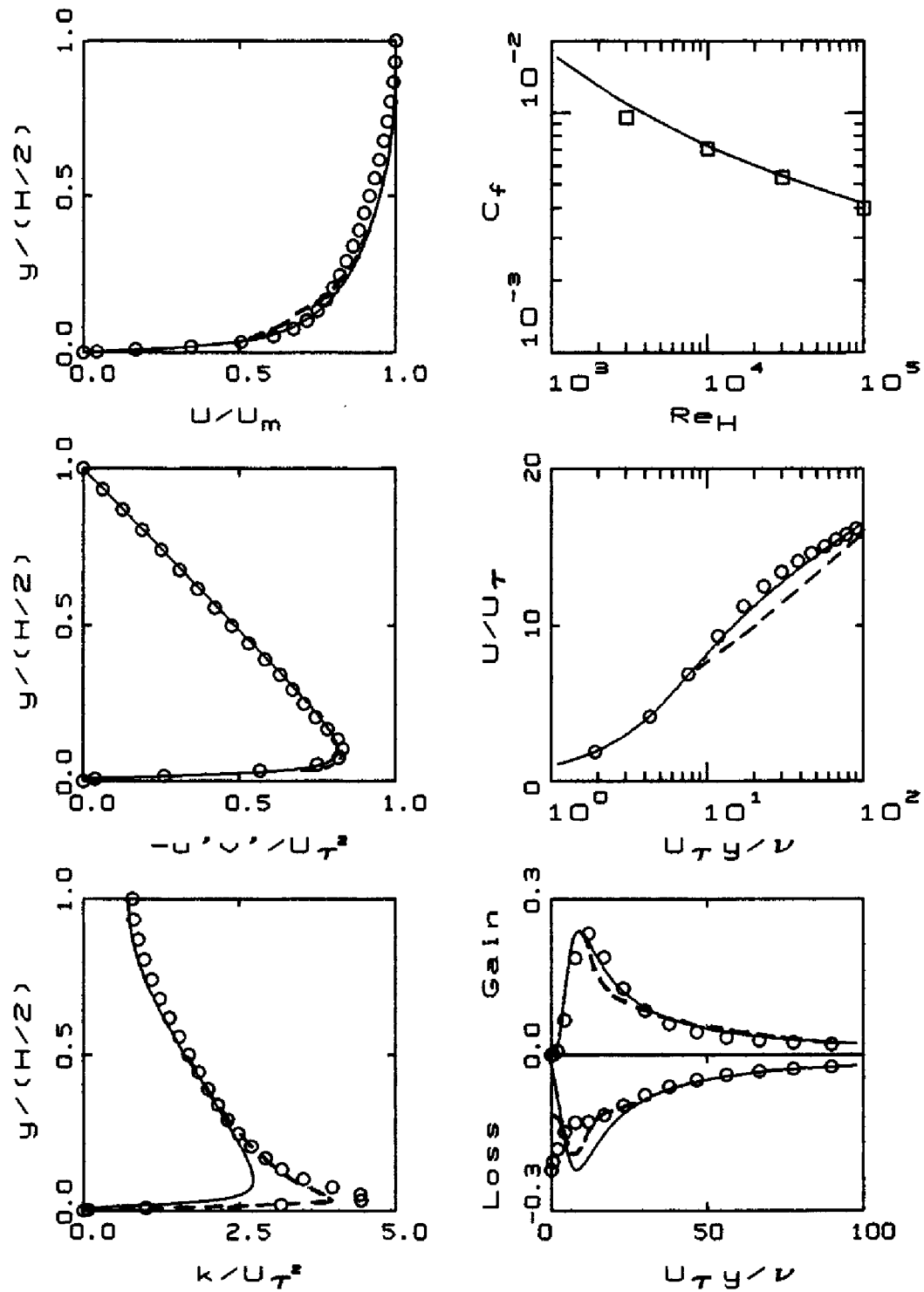


Figure 6.11: Comparison of computed and measured channel-flow properties,  $Re_H = 13,750$ . — High-Reynolds-number multiscale model; - - - Low-Reynolds-number multiscale model; o Mansour et al. (DNS); □ Halleen-Johnston correlation.



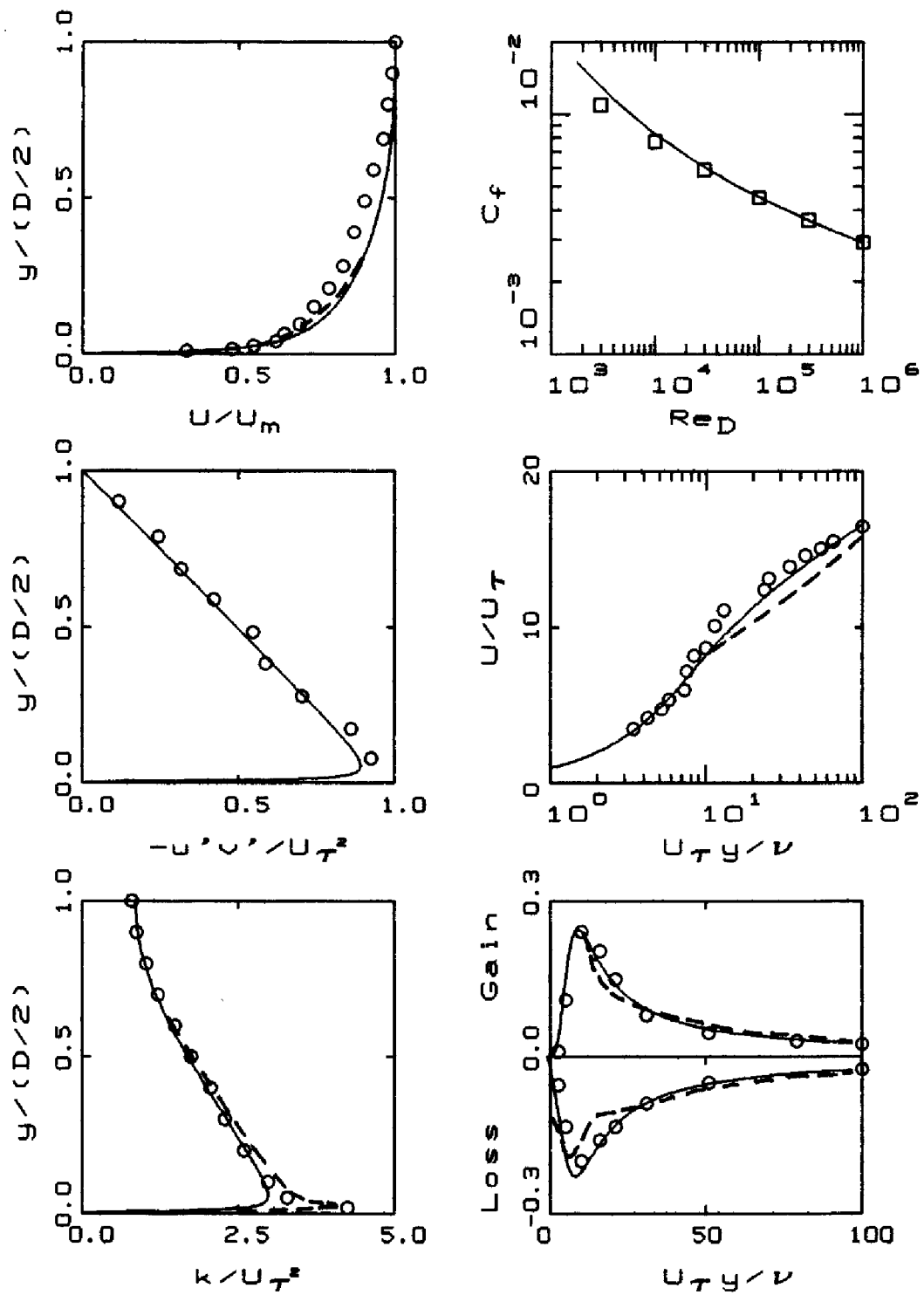


Figure 6.12: Comparison of computed and measured pipe-flow properties,  $Re_D = 40,000$ . — High-Reynolds-number multiscale model; - - - Low-Reynolds-number multiscale model;  $\circ$  Laufer;  $\square$  Prandtl correlation.

turbulence kinetic energy equation. Because the trace of the Coriolis term is zero, there is no explicit effect of rotation appearing in the equation for  $k$ . Since rotation has a strong effect on turbulence, this shows why ad hoc modifications are needed for a two-equation model.

Figure 6.13 compares a computed and measured velocity profile for a channel with a constant angular velocity about the spanwise ( $z$ ) direction. The computations have been done using the Gibson-Lauder (1978) second-order closure model and the Standard  $k$ - $\epsilon$  model. The experimental data are those of Johnston et al. (1972), and correspond to an inverse Rossby number,  $\Omega H/U_m = 0.21$ , where  $H$  is the height of the channel and  $U_m$  is the average velocity. As shown, the  $k$ - $\epsilon$  model predicts a velocity profile that is symmetric about the center line. Consistent with measurements, the Gibson-Lauder model predicts an asymmetric profile. However, as clearly shown in the figure, only qualitative agreement with measurements has been achieved.

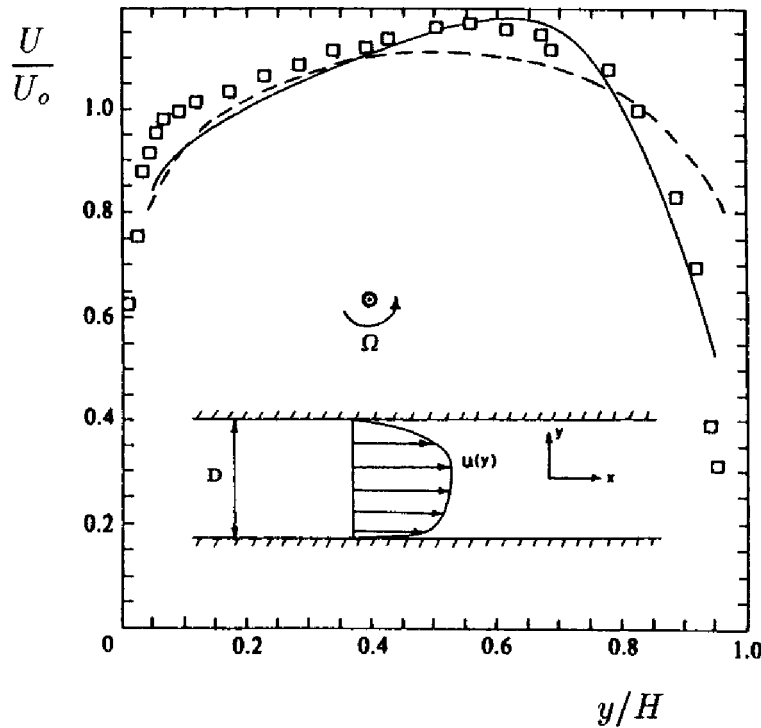


Figure 6.13: Computed and measured velocity profiles for rotating channel flow with  $\Omega H/U_m = 0.21$ ; — Gibson-Lauder model; - - -  $k$ - $\epsilon$  model;  $\square$  Johnston et al. [From Speziale (1991) — Published with permission of author.]

### 6.6.3 Boundary Layers

Figure 6.14 compares computed and measured skin friction and velocity profiles for three incompressible boundary layers. The cases include the constant-pressure case [Coles and Hirst (1969) - Flow 1400], Bradshaw's adverse gradient case [Coles and Hirst (1969) - Flow 3300], and the Samuel-Joubert flow with increasingly adverse pressure gradient [Kline et al. (1981) - Flow 0141]. Computations have been done with the Wilcox (1988b) multiscale model for all three cases and with the Hanjalić-Launder (1980) low-Reynolds-number second-order closure model for Samuel-Joubert case.

Figures 6.14(a) and 6.14(b) compare computed and measured flat-plate boundary layer skin friction and velocity profiles for the multiscale model. As expected, differences between theory and experiment are almost insignificant, with the largest differences being less than 3%. Although not shown, most variants of the LRR model are as close to measurements as the multiscale model.

For the Bradshaw case, Figures 6.14(c) and 6.14(d) compare computed and measured skin friction and a velocity profile at the final station. Differences between theory and experiment are almost undetectable. For the Samuel-Joubert case, Figures 6.14(e) through 6.14(g) compare computed and measured flow properties. As shown, multiscale model skin friction differs from measured values by less than 3%, while the Hanjalić-Launder model's skin friction shows increasing differences approaching the final station. For both models, velocity profiles are nearly identical, and Reynolds shear stress profiles differ by less than 7% and 15% for the multiscale and Hanjalić-Launder models, respectively.

Centrifugal and Coriolis accelerations attending flow over curved surfaces have a significant effect upon structural features of the turbulent boundary layer. As discussed in Section 6.1, in the absence of ad hoc modifications, such effects cannot be accurately predicted with a two-equation model as curvature has a trivial effect on the turbulence kinetic energy equation. In principle, second-order closure models should display none of these shortcomings. Thus, computing curved-wall boundary layers poses an interesting test of second-order closure models.

Figure 6.15 presents results of two computations done with the Wilcox multiscale model for flow over a convex surface. The two cases are the constant-pressure and adverse-pressure-gradient flows that So and Mellor (1972) have investigated experimentally. To insure accurate starting conditions, the measured momentum and displacement thickness at  $x = 2$  ft. have been matched to within 1% for both cases, a point well upstream of the beginning of the curved-wall portion of the flow at  $x = 4.375$  ft. For both computations, computed and measured flow properties differ by less

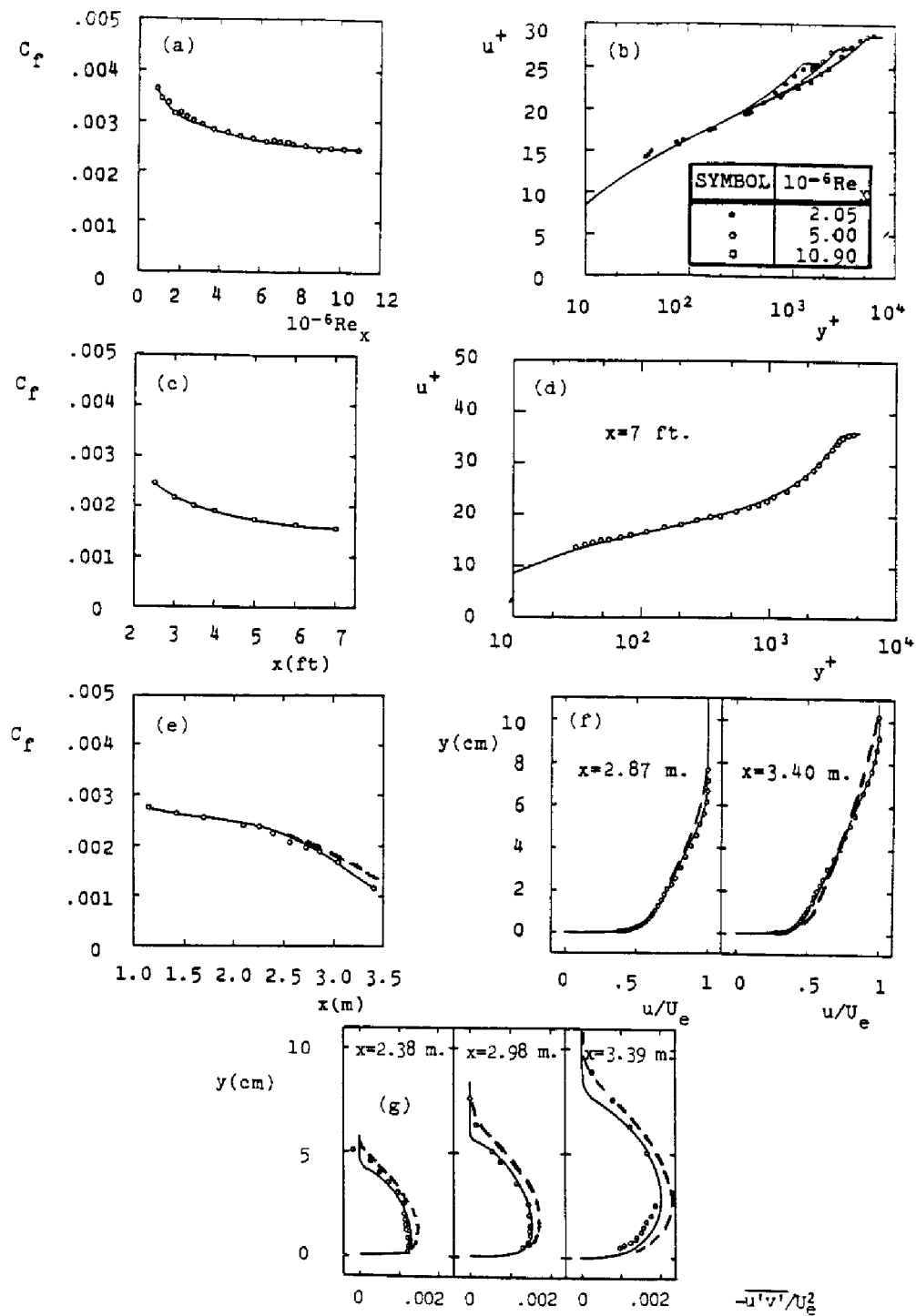


Figure 6.14: Comparison of computed and measured skin friction and profiles for incompressible boundary layers; — Wilcox multiscale model; - - - Hanjalic-Launer model;  $\circ \bullet \square$  Measured. [From Wilcox (1988b) — Copyright © AIAA 1988 — Used with permission.]

than 6%. The LRR model also offers important improvement in predictive accuracy relative to the  $k-\epsilon$  model for flows with curved streamlines. Lai et al. (1991), for example, have successfully applied three variants of the LRR model with wall functions to flow in a curved pipe. Consistent with measurements, their computations predict existence of secondary flows.

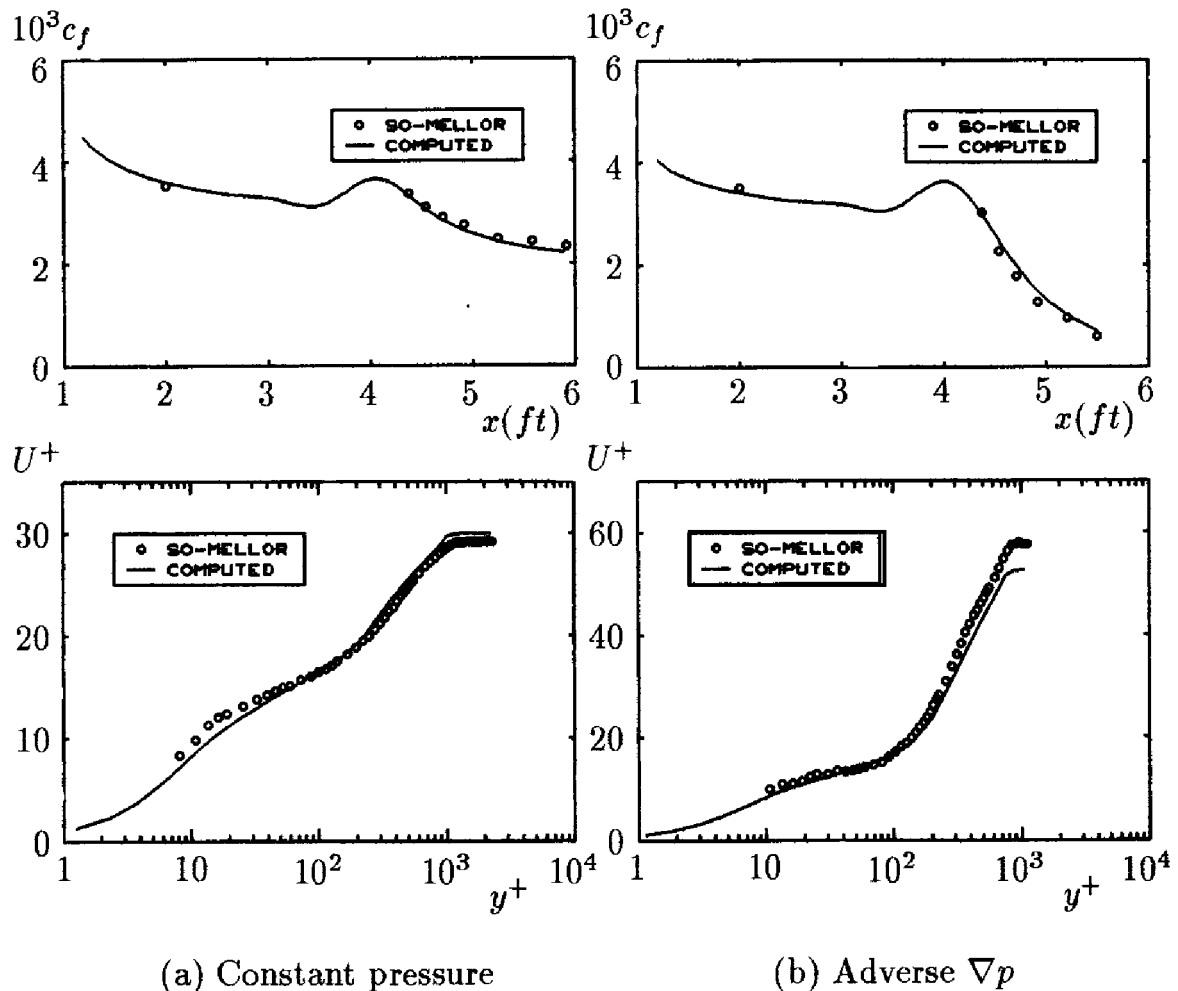


Figure 6.15: Comparison of computed and measured skin friction for flow over a convex wall.

Turning to effects of compressibility, a second-order closure model's performance is intimately tied to the scale-determining equation. Models based on the  $\epsilon$  equation will share the  $k-\epsilon$  model's incorrect density scaling (see Section 5.6). By contrast, models based on the  $\omega$  equation should share the  $k-\omega$  model's ability to accurately predict the compressible law of the wall. Figure 6.16 confirms this point for the Wilcox multiscale model. The figure compares computed effects of Mach number and surface cooling on flat-plate boundary layer skin friction. Figure 6.16(a) compares computed

ratio of skin friction to the incompressible value,  $c_f/c_{f_0}$ , as a function of Mach number with the Van Driest correlation. Differences between computed ratios and correlated values are trivial. Figure 6.16(b) focuses upon effects of surface temperature on flat-plate skin friction at Mach 5. Differences between predicted values and correlated values nowhere exceed 4%.

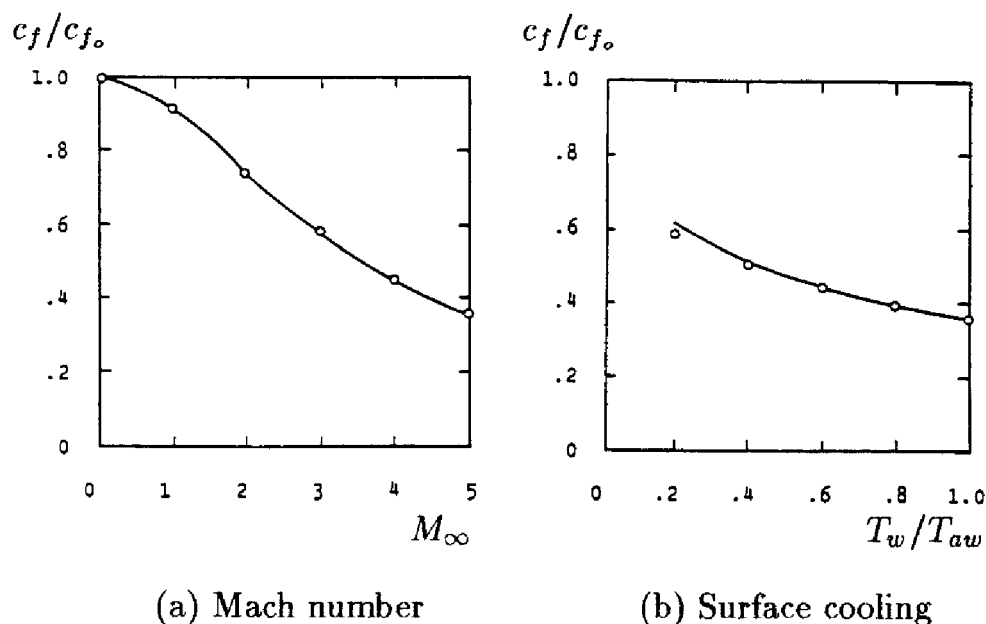


Figure 6.16: Comparison of computed and measured effect of freestream Mach number and surface cooling on flat-plate boundary-layer skin friction; — Wilcox multiscale model;  $\circ$  Van Driest correlation. [From Wilcox (1988b) — Copyright © AIAA 1988 — Used with permission.]

Second-order closure models hold promise of more accurate predictions for flows in which the surface shear force is not parallel to the freestream velocity. Figure 6.17 compares computed and measured skin friction for such a flow, a boundary layer on a segmented cylinder, part of which rotates about its axis. The experiment was performed by Higuchi and Rubesin (1978). As shown, the Wilcox-Rubesin (1980) second-order closure model most accurately describes both the axial ( $c_{f_x}$ ) and transverse ( $c_{f_z}$ ) skin friction components in the relaxation zone, i.e., the region downstream of the spinning segment. The Cebeci-Smith algebraic model and the Wilcox-Rubesin (1980) two-equation model yield skin friction components that differ from measured values by as much as 20% and 10%, respectively.

The final round of applications is for incompressible, unsteady turbulent boundary layers. These flows pose a difficult challenge to a turbulence model because many complicated frequency-dependent phenomena are generally present, including periodic separation and reattachment.

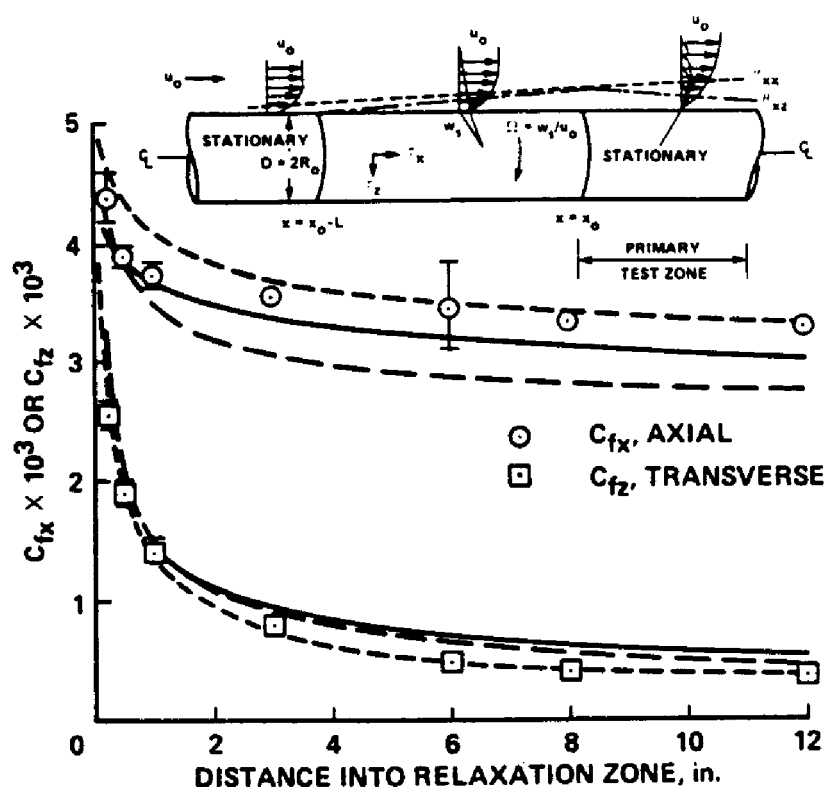


Figure 6.17: Skin friction on a segmented spinning cylinder; — Cebeci-Smith model; — — Wilcox-Rubesin  $k-\omega^2$  model; - - - Wilcox-Rubesin second-order closure model;  $\circ$   $\square$  Higuchi and Rubesin. [From Rubesin (1989) — Copyright ©AIAA — Used with permission.]

Wilcox (1988b) has simulated the experiments performed by Jayaraman, Parikh and Reynolds (1982). In these experiments, a well developed steady turbulent boundary layer enters a test section which has been designed to have freestream velocity that varies according to:

$$U_e = U_o \{1 - ax'[1 - \cos(2\pi ft)]\}, \quad x' = (x - x_0)/(x_1 - x_0) \quad (6.96)$$

The quantity  $x'$  is fractional distance through the test section where  $x_0$  and  $x_1$  are the values of streamwise distance,  $x$ , at the beginning and end of the test section, respectively. Thus, an initially steady turbulent boundary layer is subjected to a sinusoidally varying adverse pressure gradient. The experiments were performed for low- and high-amplitude unsteadiness characterized by having  $a \approx 0.05$  and  $0.25$ , respectively. For both amplitudes, experiments were conducted for five frequencies,  $f$ , ranging from  $0.1$  Hz to  $2.0$  Hz. Wilcox simulates nine of the experiments, including all of the low-amplitude cases and all four of the high-amplitude cases.

In order to compare computed and measured flow properties, we must decompose any flow property  $y(\mathbf{x}, t)$  in terms of three components, viz.,

$$y(\mathbf{x}, t) = \bar{y}(\mathbf{x}) + \tilde{y}(\mathbf{x}, t) + y'(\mathbf{x}, t) \quad (6.97)$$

where  $\bar{y}(\mathbf{x})$  is the long-time averaged value of  $y(\mathbf{x}, t)$ ,  $\tilde{y}(\mathbf{x}, t)$  is the organized response component due to the imposed unsteadiness, and  $y'(\mathbf{x}, t)$  is the turbulent fluctuation. Using an unsteady boundary layer program, Wilcox computes the phase averaged component,  $\langle y(\mathbf{x}, t) \rangle$ , defined by

$$\langle y(\mathbf{x}, t) \rangle = \bar{y}(\mathbf{x}) + \tilde{y}(\mathbf{x}, t) \quad (6.98)$$

Jayaraman et al. expand  $\langle y(\mathbf{x}, t) \rangle$  in a Fourier series according to

$$\langle y(\mathbf{x}, t) \rangle = \bar{y}(\mathbf{x}) + \sum_{n=1}^{\infty} A_{n,y}(\mathbf{x}) \cos[2n\pi ft + \phi_{n,y}(\mathbf{x})] \quad (6.99)$$

Velocity profile data, for example, are presented by Jayaraman et al. in terms of  $\bar{u}(\mathbf{x})$ ,  $A_{1,u}(\mathbf{x})$  and  $\phi_{1,u}(\mathbf{x})$ . These quantities can be extracted from the boundary-layer solution by the normal Fourier decomposition, viz., by computing the following integrals.

$$\bar{u}(\mathbf{x}) = f \int_0^{1/f} \langle u(\mathbf{x}, t) \rangle dt \quad (6.100)$$

$$A_{1,u}(\mathbf{x}) \cos \phi_{1,u} = f \int_0^{1/f} \langle u(\mathbf{x}, t) \rangle \cos(2\pi ft) dt \quad (6.101)$$

$$A_{1,u}(\mathbf{x}) \sin \phi_{1,u} = -f \int_0^{1/f} \langle u(\mathbf{x}, t) \rangle \sin(2\pi ft) dt \quad (6.102)$$

Figure 6.18 compares the computed and measured velocity profiles at  $x' = 0.88$  for the five low-amplitude cases. As shown, computed mean velocity profiles differ from corresponding measured profiles by no more than 5% of scale. Comparison of computed and measured  $A_{1,u}$  profiles shows that, consistent with measurements, unsteady effects are confined to the near-wall Stokes layer at the higher frequencies ( $f > .5$  Hz). By contrast, at the two lowest frequencies, the entire boundary layer is affected with significant amplification of the organized component occurring away from the surface. Differences between the numerical and experimental  $A_{1,u}$  profiles are less than 10%. Computed and measured phase,  $\phi_{1,u}$ , profiles are very similar with differences nowhere exceeding  $5^\circ$ .



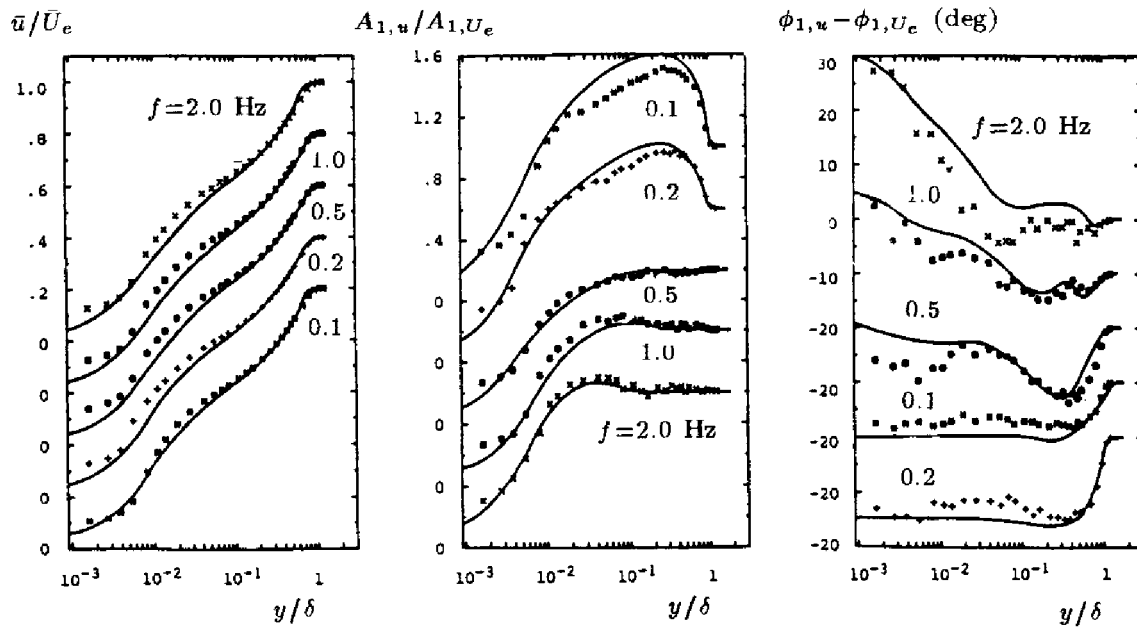


Figure 6.18: Comparison of computed and measured mean velocity,  $A_{1,u}$  and phase profiles at  $x' = 0.88$  for low amplitude; — multiscale model; • Jayaraman, et al. [From Wilcox (1988b) — Copyright © AIAA 1988 — Used with permission.]

Figure 6.19 compares the computed and measured velocity profiles at  $x' = 0.94$  for the high-amplitude cases. As for low amplitude, computed and measured  $\bar{u}(\mathbf{x})$  profiles lie within 5% of scale of each other. Similarly, computed  $A_{1,u}$  and  $\phi_{1,u}$  profiles differ from corresponding measurements by less than 10%. To provide a measure of how accurately temporal variations have been predicted, Figure 6.20 compares computed and measured shape factor through a complete cycle for all four frequencies. Differences between computed and measured shape factors are less than 5%.

The four high-amplitude cases have also been computed using the Standard  $k-\omega$  model. Results are included in Figure 6.20, which shows that  $k-\omega$  and multiscale-model predictions differ by only a few percent. Although it is possible the test cases are not as difficult as might be expected, this seems unlikely in view of the wide Strouhal number range and the fact that periodic separation and reattachment are present. More likely, the  $k-\omega$  model fares well because all of the cases have attached boundary layers through most of each cycle and in the mean.

As a closing comment, many recent turbulence modeling efforts focusing on unsteady boundary layers mistakenly credit their success (or lack of it) to achieving asymptotic consistency with the  $k-\epsilon$  model or with second-order closure models based on the  $\epsilon$  equation. The computations described

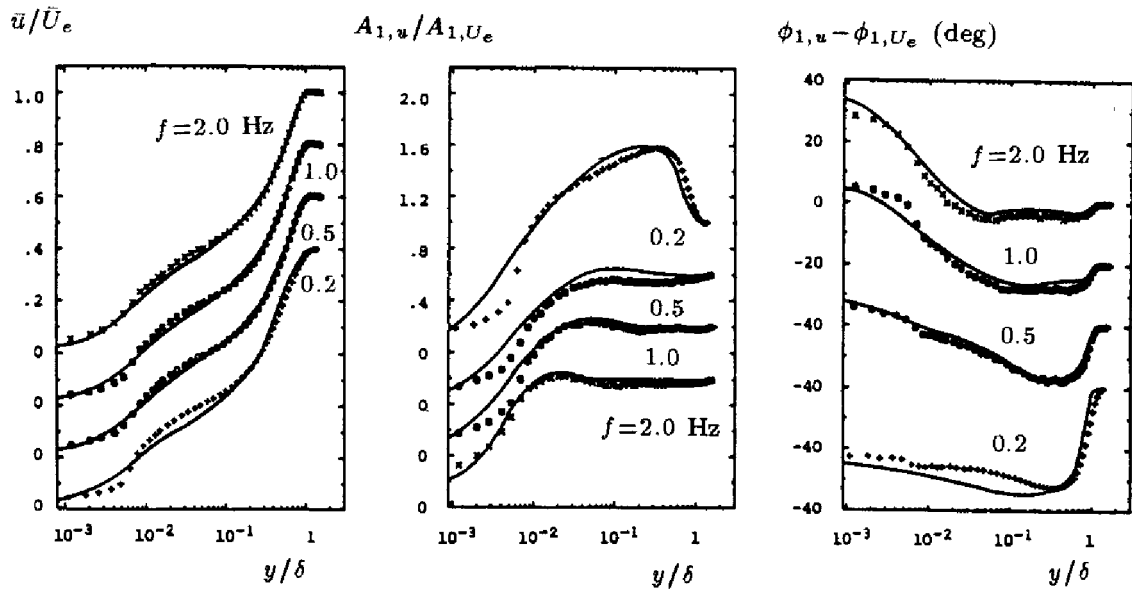


Figure 6.19: Comparison of computed and measured mean velocity,  $A_{1,u}$  and phase profiles at  $x' = 0.94$  for high amplitude; — multiscale model; • Jayaraman, et al. [From Wilcox (1988b) — Copyright © AIAA 1988 — Used with permission.]

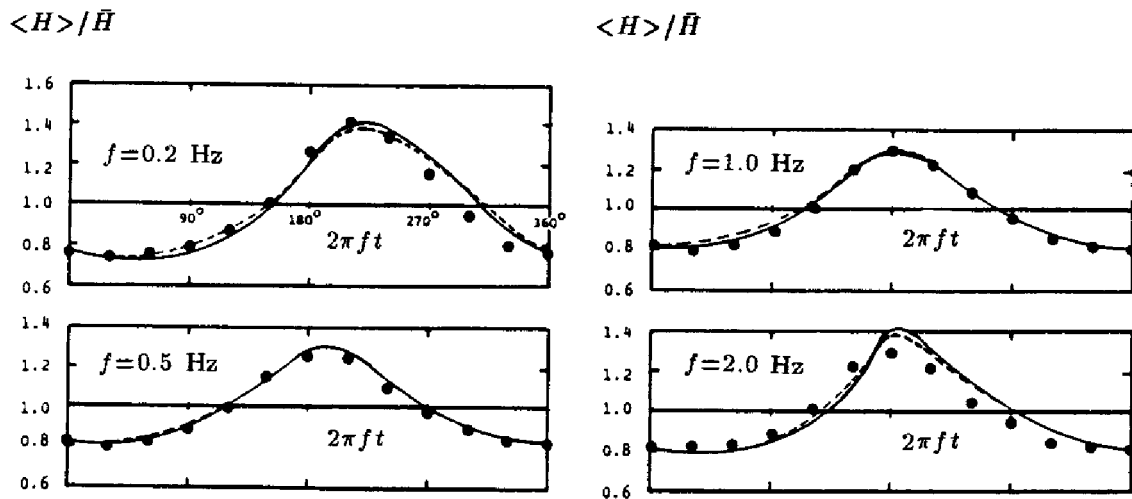


Figure 6.20: Comparison of computed and measured temporal variation of shape factor for the high-amplitude cases; - -  $k-\omega$  model; — multiscale model; • Jayaraman, et al. [From Wilcox (1988b) — Copyright © AIAA 1988 — Used with permission.]

above were done using the high-Reynolds-number versions of the  $k$ - $\omega$  and multiscale models, neither of which is asymptotically consistent. All that appears to be necessary is to achieve a satisfactory value for the constant,  $B$ , in the law of the wall. This makes sense physically as the dissipation time scale is so short in the sublayer that the sublayer responds to changes in the mean flow almost instantaneously and thus behaves as a quasi-steady region. Consequently, achieving asymptotically consistent behavior in the sublayer is neither more nor less important for unsteady flows than it is for steady flows.

## 6.7 Application to Separated Flows

As we have seen in preceding chapters, turbulence models that use the Boussinesq approximation generally are unreliable for separated flows, especially shock-induced separation. Figure 5.8, for example, illustrates how poorly such models perform for Mach 3 flow into a compression corner. The figure also shows the surface pressure computed with the Wilcox (1988b) multiscale model, and it lies much closer to measured values than any of the algebraic and two-equation models. In this section, we will take a close look at how well second-order closure models perform for several separated flows.

Because second-order closure models require more computer resources than algebraic and two-equation models, applications to such flows have not been made until recently. Consequently, only preliminary conclusions can be drawn from the limited work that has been done at present. Incompressible applications have generally been limited to the backward-facing step, while compressible-flow applications have been done for compression corners for a limited range of Mach numbers.

Focusing first on the backward-facing step, So et al. (1988) have done an interesting study using a variety of closure approximations. Their computations use Chien's (1982) low-Reynolds number version of the  $\epsilon$  equation. Most importantly, they have used three different models for the pressure-strain correlation, viz., the models of Rotta (1951) [Model A1], Launder, Reece and Rodi (1975) [Model A2], and Gibson and Younis (1986) [Model A4]. Using the Rotta model, computations have been done with wall functions as well [Model H-A1]. For reference, their computations also include the Chien (1982) low-Reynolds-number  $k$ - $\epsilon$  model [Model Lk- $\epsilon$ ]. These models differ mainly in their representation of the fast pressure-strain term, with the Rotta model ignoring it altogether. The computations simulate the experiments of Eaton and Johnston (1980), for which the measured reattachment length is 8 step heights.

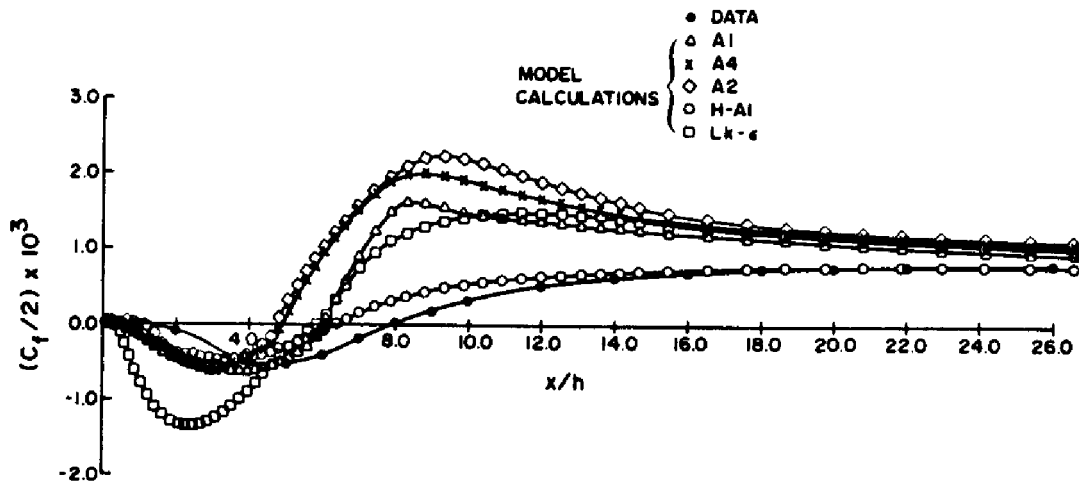


Figure 6.21: Computed and measured skin friction for flow past a backward-facing step; A1=Rotta model; A2=LRR model; A4=Gibson-Younis model; H-A1=Rotta model with wall functions; Lk- $\epsilon$ =Chien  $k$ - $\epsilon$  model;  $\bullet$ =Eaton and Johnston. [From So et al. (1988) — Published with permission.]

As shown in Figure 6.21, computed reattachment length for all of their computations lies between 5 and 6 step heights, so that their result closest to measurements differs from the measured value by 25%. All of the models show large discrepancies between computed and measured wall pressure, while peak skin friction values are as much as 3 times measured values downstream of reattachment for the low-Reynolds-number models. In general, the second-order closure model skin friction results are as far from measurements as those of the low-Reynolds-number  $k$ - $\epsilon$  model. Only when wall functions are used with the second-order closure model does the computed skin friction lie reasonably close to measured values. So et al. note that the smallest discrepancies between computed and measured flow properties are obtained with the Rotta pressure-strain model, which omits the rapid pressure-strain correlation. That is, the LRR and Gibson-Younis models for the rapid pressure strain appear to yield larger discrepancies between computed and measured values.

Recalling how close to measurements  $k$ - $\omega$  model predictions are for flow past a backward-facing step (Section 4.10), the So et al. computations strongly suggest that their poor predictions are caused by use of the  $\epsilon$  equation. On the one hand, comparison of Figures 4.29 and 6.21 show that for second-order closure model H-A1,  $c_f$  is very similar to  $k$ - $\epsilon$  model  $c_f$  when wall functions are used. Although the flows are a little different, in both cases the reattachment length is 25% smaller than measured. On the other

hand, using the same low-Reynolds-number  $\epsilon$  equation,  $c_f$  for second-order closure model A1 is very similar to the low-Reynolds-number  $k-\epsilon$  model  $c_f$ , except in the reverse flow region. Despite the latter difference, the reattachment length is the same in this case also. Thus, as with two-equation models, a second-order closure model's performance for the backward-facing step is intimately linked to the scale-determining equation. This strongly suggests that much closer agreement between computed and measured flow properties would be obtained with a second-order closure model based on the  $\omega$  equation, such as the Wilcox multiscale model. Unfortunately, the multiscale model has not been applied to the backward-facing step, so this must remain a point of conjecture until such a computation is done.

Turning to compressible flows, Wilcox (1990) has done a numerical study that provides a definitive measure of differences attending use of the multiscale model compared to the  $k-\omega$  model. The study includes results of three shock-separated turbulent boundary-layer computations using both the multiscale and  $k-\omega$  models. The flows considered include two planar compression-corner flows and an axisymmetric compression-corner flow.

The first of the three applications is for Mach 2.79 flow into a  $20^\circ$  compression corner. This flow has been experimentally investigated by Settles, Vas and Bogdonoff (1976) and includes a small region over which separation of the incident turbulent boundary layer occurs. Figure 6.22(a) compares computed and measured surface pressure,  $p_w/p_\infty$ , and skin friction,  $c_f$ . The multiscale model predicts more upstream influence, a lower pressure plateau at separation, and a more gradual increase in skin friction downstream of reattachment relative to the  $k-\omega$  results. All of these features represent significant improvement in predictive accuracy. Using the  $k-\epsilon$  model and specially devised wall functions, Viegas, Rubesin and Horstman (1985) are able to achieve similar accuracy for this flow.

The second of the three applications is for Mach 2.84 flow into a  $24^\circ$  compression corner. This flow has also been experimentally investigated by Settles, Vas and Bogdonoff (1976) and includes a larger region over which separation of the incident turbulent boundary layer occurs than in the  $20^\circ$  case of the preceding section. Figure 6.22(b) compares computed and measured surface pressure and skin friction. As in the  $20^\circ$  compression-corner computation, the multiscale model predicts much more upstream influence. Interestingly, the  $k-\omega$  predicted pressure plateau at separation is very close to the measured level, and there is little difference between  $k-\omega$  and multiscale predicted increase in skin friction downstream of reattachment. Note that, for this flow, Viegas, Rubesin and Horstman (1985) predict pressure plateau values about 20% higher than measured, and are unable to simultaneously make accurate predictions for skin friction downstream of reattachment and the initial rise in surface pressure. That is, their solutions

can match either skin friction or surface pressure, but not both.

The third application is for Mach 2.85 flow into a  $30^\circ$  axisymmetric compression corner. This flow has been experimentally investigated by Brown (1986) and includes a separation bubble of length comparable to the  $24^\circ$  planar compression corner. Figure 6.22(c) compares computed and measured surface pressure. Computed skin friction is also shown. Once again the multiscale model predicts much more upstream influence. For both models, the predicted pressure plateau at separation is about 10% higher than the measured level, and there is little difference between  $k-\omega$  and multiscale predicted increase in skin friction downstream of reattachment. The overall pressure rise is predicted by both models to be 4.7, while the measurements indicate a value of 4.0. The inviscid pressure rise for a  $30^\circ$  axisymmetric compression corner is 4.4, so that neither theory nor experiment appears to be completely consistent with the physics of this flow.

Clearly, for the three compression-corner cases considered, the multiscale model provides a flowfield more consistent with experimental observations than does the  $k-\omega$  model. The primary reason for the difference in the two models' predictions can be found by examining predicted behavior of the Reynolds shear stress near the separation point. Figure 6.22(d) shows the maximum Reynolds shear stress,  $\tau_{max}$ , throughout the interaction region for the three compression-corner computations. As shown, the  $k-\omega$  model predicts a more abrupt increase in  $\tau_{max}$  at separation and a much larger peak value than predicted by the multiscale model. For the axisymmetric case, the figure includes experimental data for points ahead of the measured separation point. As shown, the multiscale-model predicted  $\tau_{max}$  falls within experimental data scatter.

The physical implication of the pronounced difference in the rate of amplification of the Reynolds shear stress is clear. Using the Boussinesq approximation, the  $k-\omega$  model makes a far more rapid adjustment to the rotation of the mean strain rate tensor's principal axes than the multiscale model. Consequently, the predicted separation point and initial pressure rise lie closer to the corner with the  $k-\omega$  model than measured. Predicting more physically realistic growth of the Reynolds stresses, the multiscale model predicts overall flow properties which are in much closer agreement with measurements.

It is interesting to note that for the multiscale model, although the pressure is in such close agreement with measurements, the numerical separation points are further upstream than indicated by oil flow measurements for all three compression corner cases. Marshall and Dolling (1992) indicate that these flows include a low-frequency oscillation of the separation shock. The time-mean pressure distribution upstream of the corner is affected by these oscillations whose frequency content includes substantial energy at time

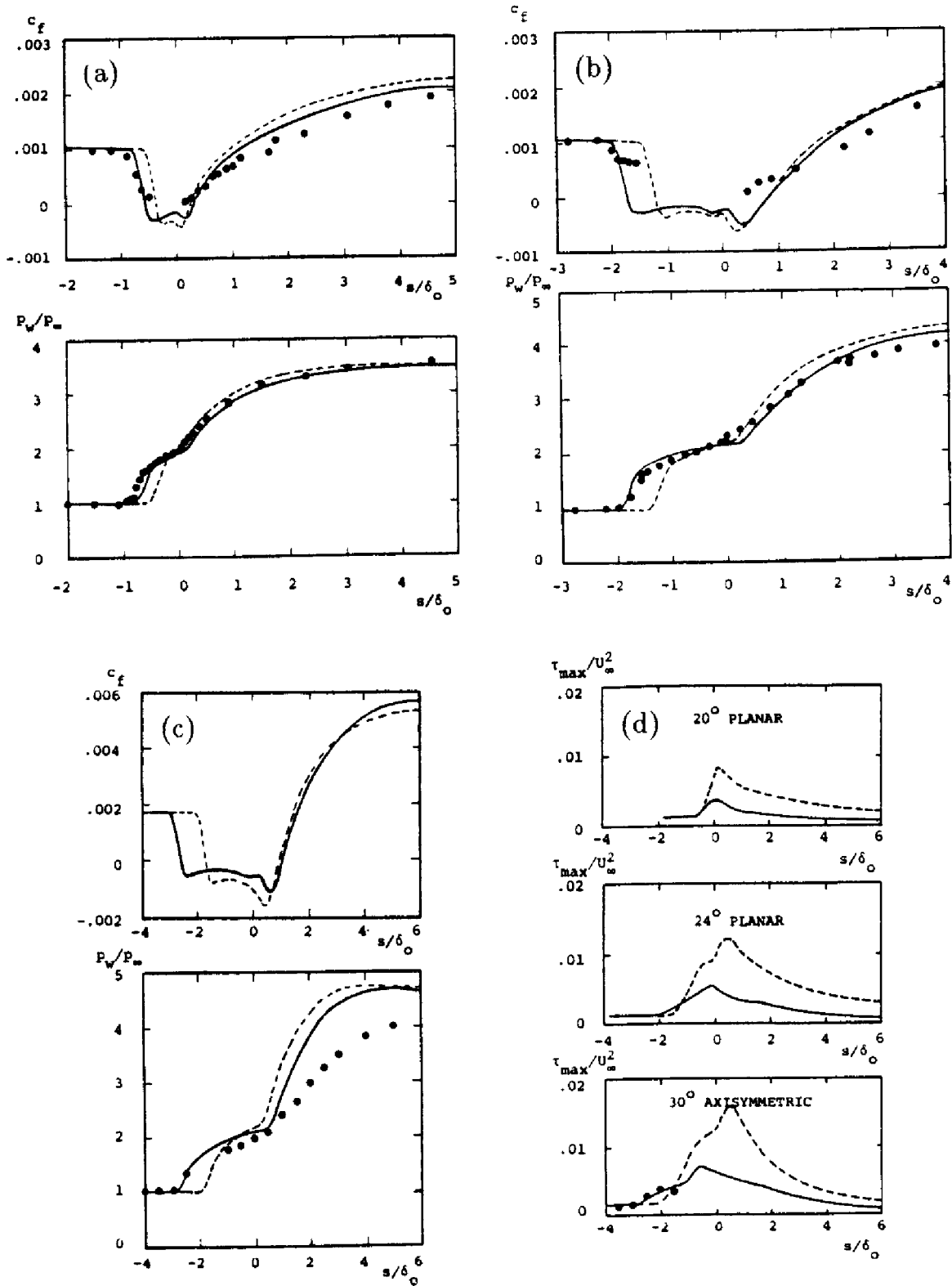


Figure 6.22: Computed and measured properties for supersonic compression corners;  $s$  is tangential distance from corner; ---  $k-\omega$  model; — multiscale model; (a) and (b) • Settles et al.; (c) and (d) • Brown. [From Wilcox (1990) — Copyright © AIAA 1990 — Used with permission.]

scales of the mean motion. This unsteadiness is responsible for the apparent mismatch between the beginning of the pressure rise and the separation point. Since computations with the multiscale model and the  $k-\omega$  model fail to display any low-frequency oscillation of the shock, more research is needed to arrive at a completely satisfactory solution.

## 6.8 Range of Applicability

The two primary approaches to removing the limitations of the Boussinesq approximation are to use either a **nonlinear constitutive relation** or a **second-order closure model**. As discussed in Section 6.2, nonlinear constitutive relations offer some advantage over the Boussinesq approximation, most notably for flows in which anisotropy of the normal Reynolds stresses is important. **Algebraic Stress Models** provide a straightforward method for accurately predicting effects of streamline curvature and system rotation, although ad hoc corrections to standard two-equation models are just as effective. However, nonlinear constitutive relations offer no improvement over the Boussinesq approximation for flows with sudden changes in mean strain rate.

Despite their complexity, second-order closure models have great potential for removing shortcomings of the Boussinesq approximation in a natural way. Without ad hoc corrections, second-order closure models provide physically realistic predictions for flows with curved streamlines, system rotation, stratification, sudden changes in mean strain rate, secondary motions, and anisotropic shear. While more research is needed for separated flows, these models may also improve predictions for shock-separated flows. However, to be completely objective in our assessment, we must also note that in many such applications only qualitative agreement between theory and experiment has been obtained.

Just as one-equation turbulence models share the shortcomings and successes of the mixing-length model, second-order closure models reflect the strengths and weaknesses of the scale-determining equation used with the model. There is an increasing pool of evidence that many of the shortcomings of second-order closure models are caused by the scale-determining equation. Results obtained for the Samuel-Joubert boundary layer (Subsection 6.6.3) and the backward-facing step (Section 6.7) strongly suggest that predictions of standard second-order closure models can be improved by using the  $\omega$  equation in place of the  $\epsilon$  equation.

From a numerical point of view, second-order closure models are at least as difficult to solve as the corresponding two-equation model. Models based on the  $\epsilon$  equation fail to predict a satisfactory law of the wall and require



complicated viscous damping functions. Correspondingly, such models are generally very difficult to integrate. By contrast, models based on the  $\omega$  equation require no special viscous corrections, and are much easier to integrate. In particular, the Wilcox multiscale model usually requires about 25% to 40% more computing time relative to corresponding two-equation models. Hence, the scale-determining equation may be even more important for second-order closure models than for two-equation models.

## Problems

**6.1** The objective of this problem is to derive the modified law of the wall for flow over a curved wall according to the  $k$ - $\omega$  model.

- (a) Verify that the dimensionless form of Equations (6.3) to (6.5) in the log layer is [with  $\epsilon \equiv \nu/(u_\tau \mathcal{R})$ ]:

$$\begin{aligned}\nu_T^+ \left( \frac{\partial U^+}{\partial y^+} - \epsilon U^+ \right) &= 1, \quad \nu_T^+ = \frac{k^+}{\omega^+} \\ \sigma^* \nu_T^+ \frac{\partial}{\partial y^+} \left[ \nu_T^+ \frac{\partial k^+}{\partial y^+} \right] &= \beta^* (k^+)^2 - 1 + \frac{9}{2} \epsilon (\nu_T^+)^2 U^+ \frac{\partial U^+}{\partial y^+} \\ \sigma \nu_T^+ \frac{\partial}{\partial y^+} \left[ \nu_T^+ \frac{\partial \omega^+}{\partial y^+} \right] &= \beta k^+ \omega^+ - \alpha \frac{\omega^+}{k^+}\end{aligned}$$

- (b) Assume a solution of the form

$$\begin{aligned}\frac{dU^+}{dy^+} &\sim \frac{1}{\kappa y^+} [1 + \epsilon a y^+ \ell n y^+ + O(\epsilon^2)] \\ k^+ &\sim \frac{1}{\sqrt{\beta^*}} [1 + \epsilon b y^+ \ell n y^+ + O(\epsilon^2)] \\ \omega^+ &\sim \frac{1}{\sqrt{\beta^* \kappa} y^+} [1 + \epsilon c y^+ \ell n y^+ + O(\epsilon^2)]\end{aligned}$$

with  $\epsilon \ll 1$ . Substitute into the equations for  $k^+$  and  $\omega^+$  and verify that the coefficients  $b$  and  $c$  are given by

$$b = -\frac{9/2}{2 - \sigma^* \kappa^2 / \sqrt{\beta^*}} \quad \text{and} \quad c = \frac{\alpha}{\alpha - \beta / \beta^*} b$$

**NOTE:** Use the fact that the  $k$ - $\omega$  model closure coefficients are related by  $\sigma \kappa^2 = (\beta / \beta^* - \alpha) \sqrt{\beta^*}$  and ignore terms proportional to  $y^+$  relative to terms proportional to  $y^+ \ell n y^+$ .

- (c) Substitute into the momentum equation and verify that

$$a + b - c = 1$$

- (d) Using  $\alpha = 5/9$ ,  $\beta = 3/40$ ,  $\beta^* = 9/100$ ,  $\sigma = 1/2$  and  $\sigma^* = 1/2$ , determine the numerical values of  $a$ ,  $b$  and  $c$ , and show that the modified law of the wall is of the form

$$\left[ 1 - \beta_R \frac{y}{\mathcal{R}} \right] \frac{U}{u_\tau} \sim \frac{1}{\kappa} \ell n \left( \frac{u_\tau y}{\nu} \right) + \dots$$

where  $\beta_R \approx 8.8$ .

**6.2** For incompressible flow, we wish to use Speziale's non-linear constitutive relation with the  $k$ - $\omega$  model. In terms of  $k$ - $\omega$  model parameters, the relation can be written as

$$\begin{aligned}\tau_{ij} = & -\frac{2}{3}\rho k\delta_{ij} + 2\mu_T S_{ij} + C_D \frac{\rho k}{\beta^* \omega^2} \left( S_{ik} S_{kj} - \frac{1}{3} S_{mn} S_{nm} \delta_{ij} \right) \\ & + C_E \frac{\rho k}{\beta^* \omega^2} \left( \overset{\circ}{S}_{ij} - \frac{1}{3} \overset{\circ}{S}_{mm} \delta_{ij} \right)\end{aligned}$$

where  $C_D$  and  $C_E$  are closure coefficients whose values are to be determined.

(a) Verify for incompressible boundary layers that

$$S_{xy} = S_{yx} = \frac{1}{2} \frac{\partial U}{\partial y}; \quad \text{all other } S_{ij} \approx 0$$

$$\overset{\circ}{S}_{xx} = - \left( \frac{\partial U}{\partial y} \right)^2; \quad \text{all other } \overset{\circ}{S}_{ij} \approx 0$$

- (b) Express the Reynolds-stress components  $\tau_{xy}$ ,  $\tau_{xx}$ ,  $\tau_{yy}$  and  $\tau_{zz}$  in terms of  $\rho$ ,  $k$ ,  $\mu_T$ ,  $\beta^*$ ,  $\omega$  and  $\partial U/\partial y$  for incompressible boundary layers.
- (c) Using the stresses derived in part (b), write the log-layer form of the mean-momentum,  $k$  and  $\omega$  equations.
- (d) Assuming a solution of the form  $\partial U/\partial y = u_\tau/(\kappa y)$  and  $k = \text{constant}$ , verify that

$$\left( \frac{\partial U}{\partial y} \right)^2 = \beta^* \omega^2$$

(e) Verify that

$$\overline{u'^2}/k = (8 - C_D + 8C_E)/12$$

$$\overline{v'^2}/k = (8 - C_D - 4C_E)/12$$

$$\overline{w'^2}/k = (8 + 2C_D - 4C_E)/12$$

- (f) Determine the values of  $C_D$  and  $C_E$  that are consistent with the normal Reynolds stresses standing in the ratio

$$\overline{u'^2} : \overline{v'^2} : \overline{w'^2} = 4 : 2 : 3$$

**6.3** Verify that in the log layer of an incompressible flat-plate boundary layer, the Wilcox-Rubesin nonlinear constitutive relation [Equation (6.13)] predicts that the normal Reynolds stresses stand in the ratio

$$\overline{u'^2} : \overline{v'^2} : \overline{w'^2} = 4 : 2 : 3$$

**HINT:** Recall that in the log layer,  $\partial U / \partial y \approx \sqrt{\beta^*} \omega$ .

**6.4** For incompressible flow in a rectangular duct, the strain rate and rotation tensors are approximately

$$S_{ij} = \begin{bmatrix} 0 & \frac{1}{2} \frac{\partial U}{\partial y} & \frac{1}{2} \frac{\partial U}{\partial z} \\ \frac{1}{2} \frac{\partial U}{\partial y} & 0 & 0 \\ \frac{1}{2} \frac{\partial U}{\partial z} & 0 & 0 \end{bmatrix} \quad \text{and} \quad \Omega_{ij} = \begin{bmatrix} 0 & \frac{1}{2} \frac{\partial U}{\partial y} & \frac{1}{2} \frac{\partial U}{\partial z} \\ -\frac{1}{2} \frac{\partial U}{\partial y} & 0 & 0 \\ -\frac{1}{2} \frac{\partial U}{\partial z} & 0 & 0 \end{bmatrix}$$

Determine  $\tau_{xy}$ ,  $\tau_{xz}$ ,  $\tau_{yz}$  and  $(\tau_{zz} - \tau_{yy})$  according to the Wilcox-Rubesin nonlinear constitutive relation [Equation (6.13)].

**6.5** Derive the Poisson equation [Equation(6.38)] for the fluctuating pressure.

**6.6** Consider the Launder-Reece-Rodi (LRR) rapid pressure strain closure approximation, Equation (6.50).

- (a) Verify that  $a_{ijkl}$  satisfies the symmetry constraints in Equation (6.48).
- (b) Invoke the constraints of Equation (6.49) and verify that  $\alpha$ ,  $\beta$ ,  $\eta$  and  $\nu$  are given by Equation (6.51).
- (c) Form the tensor product

$$M_{ijkl} \frac{\partial U_k}{\partial x_l} = (a_{ijkl} + a_{jikl}) \frac{\partial U_k}{\partial x_l}$$

and verify Equations (6.52) through (6.54).

**6.7** Consider Lumley's general representation for  $\Pi_{ij}$  in Equation (6.56). Show that the LRR pressure-strain model [including  $A_{ij}$  as defined in Equation (6.45)] is the limiting case where all coefficients other than  $a_0$ ,  $a_2$ ,  $a_7$  and  $a_9$  equal to zero. Also, assuming  $C_1 = 1.8$ , determine the values of  $a_0$ ,  $a_2$ ,  $a_7$  and  $a_9$  that correspond to  $C_2 = 0.4$ ,  $0.5$  and  $0.6$ . Assume the flow is incompressible.

**6.8** Consider the Launder, Reece and Rodi second-order closure model, Equations (6.60) - (6.64). This problem analyzes the model's predicted asymptotic solution for homogeneous plane shear, in which

$$\frac{\partial U_i}{\partial x_j} = \begin{bmatrix} 0 & S & 0 \\ 0 & 0 & 0 \\ 0 & 0 & 0 \end{bmatrix}$$

- (a) Assuming that  $\epsilon/k \rightarrow \text{constant}$  as  $t \rightarrow \infty$ , verify that

$$\frac{P}{\rho\epsilon} \rightarrow \frac{C_{\epsilon 2} - 1}{C_{\epsilon 1} - 1}$$

where  $P = S\tau_{xy}$ .

- (b) Neglecting the pressure-echo effect, verify that

$$P_{ij} = \begin{bmatrix} 2S\tau_{xy} & S\tau_{yy} & S\tau_{yz} \\ S\tau_{yy} & 0 & 0 \\ S\tau_{yz} & 0 & 0 \end{bmatrix}, \quad D_{ij} = \begin{bmatrix} 0 & S\tau_{xx} & 0 \\ S\tau_{xx} & 2S\tau_{xy} & S\tau_{xz} \\ 0 & S\tau_{xz} & 0 \end{bmatrix}$$

- (c) Assuming a solution of the form  $\tau_{ij} = C_{ij}e^{\lambda t}$  where  $C_{ij}$  is independent of time and  $\lambda$  is a constant, verify that if  $\tau_{xz}$  and  $\tau_{yz}$  are initially zero, they are always zero, provided  $\hat{\beta}(1 - \hat{\alpha}) > 0$ .
- (d) Determine  $\epsilon/k$  and  $P/(\rho k)$  as functions of  $C_{\epsilon 1}$ ,  $C_{\epsilon 2}$  and  $\lambda$  under the assumption that  $\tau_{ij} = C_{ij}e^{\lambda t}$ .
- (e) Using results of Parts (a) - (d), determine  $\overline{u'^2}/k$ ,  $\overline{v'^2}/k$  and  $\overline{w'^2}/k$  as algebraic functions of the closure coefficients. **HINT:** You can simplify your computations somewhat by first writing the equation for  $\tau_{ij}$  as an equation for  $\tau_{ij} + \frac{2}{3}\rho k\delta_{ij}$ .
- (f) Using the following two sets of closure coefficient values, compute the numerical values of  $\overline{u'^2}/k$ ,  $\overline{v'^2}/k$  and  $\overline{w'^2}/k$ .

1. Original LRR:  $C_1 = 1.5$ ,  $C_2 = 0.4$ ,  $C_{\epsilon 1} = 1.44$ ,  $C_{\epsilon 2} = 1.90$

2. Revised LRR:  $C_1 = 1.8$ ,  $C_2 = 0.6$ ,  $C_{\epsilon 1} = 1.44$ ,  $C_{\epsilon 2} = 1.92$

**6.9** Consider the Launder, Reece and Rodi second-order closure model, Equations (6.60) - (6.64).

- (a) State the limiting form of the equations for the incompressible, two-dimensional log layer.

- (b) Assuming a solution of the form

$$\frac{dU}{dy} \sim \frac{u_\tau}{\kappa y}, \quad k \sim \frac{u_\tau^2}{\sqrt{C_\mu}}, \quad \epsilon \sim \frac{u_\tau^3}{\kappa y}$$

determine  $\kappa$ ,  $-\overline{u'v'}/k$ ,  $\overline{u'^2}/k$ ,  $\overline{v'^2}/k$  and  $\overline{w'^2}/k$  as algebraic functions of the closure coefficients. **HINTS:** All are constant. Also, the  $\epsilon$  equation yields  $\kappa$  as a function of the closure coefficients and  $\overline{v'^2}/k$ . You needn't simplify further.

- (c) Using the closure coefficient values in Equation (6.64), verify that  $\kappa \approx 0.39$ ,  $-\overline{u'v'}/k \approx 0.36$ , and  $\overline{u'^2} : \overline{v'^2} : \overline{w'^2} \approx 4 : 2.2 : 3.2$ . **HINT:** Combining the simplified  $\epsilon$  and  $\tau_{yy}$  equations yields a cubic equation for  $\kappa$ . It can be solved in closed form by assuming  $\kappa = 0.4(1 + \delta)$ , linearizing and solving for  $\delta$ .

**6.10** Consider the Wilcox multiscale model, Equations (6.66) - (6.72).

- (a) State the limiting form of the equations for the incompressible, two-dimensional log layer.
- (b) Assuming a solution of the form

$$\frac{dU}{dy} \sim \frac{u_\tau}{\kappa y}, \quad k \sim \frac{u_\tau^2}{\sqrt{\beta^*}}, \quad \omega \sim \frac{u_\tau}{\sqrt{\beta^*} \kappa y}$$

determine  $\kappa$ ,  $-\overline{u'v'}/k$ ,  $\overline{u'^2}/k$ ,  $\overline{v'^2}/k$ ,  $\overline{w'^2}/k$  and  $e/k$  as algebraic functions of the closure coefficients. **HINT:** All are constant.

- (c) Using the closure coefficient values in Equation (6.72), verify that  $\kappa \approx 0.41$ ,  $-\overline{u'v'}/k \approx 0.30$ ,  $\overline{u'^2} : \overline{v'^2} : \overline{w'^2} \approx 4 : 2 : 2.6$ , and  $e/k \approx 0.75$ .

**6.11** Suppose we have flow in a coordinate frame rotating with angular velocity  $\boldsymbol{\Omega} = \Omega \mathbf{k}$ , where  $\mathbf{k}$  is a unit vector in the  $z$  direction. The incompressible Navier-Stokes equation is

$$\rho \frac{d\mathbf{u}}{dt} + 2\rho \boldsymbol{\Omega} \times \mathbf{u} = -\nabla p - \rho \boldsymbol{\Omega} \times \boldsymbol{\Omega} \times \mathbf{x} + \mu \nabla^2 \mathbf{u}$$

where  $\mathbf{x}$  is position vector and  $d/dt$  is the Eulerian derivative. Verify that the Reynolds-stress equation's inertial terms in a two-dimensional flow are as follows:

$$\frac{d}{dt} \begin{bmatrix} \tau_{xx} & \tau_{xy} & 0 \\ \tau_{xy} & \tau_{yy} & 0 \\ 0 & 0 & \tau_{zz} \end{bmatrix} + \begin{bmatrix} -4\Omega\tau_{xy} & 2\Omega(\tau_{xx} - \tau_{yy}) & 0 \\ 2\Omega(\tau_{xx} - \tau_{yy}) & 4\Omega\tau_{xy} & 0 \\ 0 & 0 & 0 \end{bmatrix} = \dots$$

# Chapter 7

## Numerical Considerations

Modern turbulence model equations pose special numerical difficulties that must be understood in order to obtain reliable numerical solutions, even for boundary-layer flows where the equations are parabolic. For one-equation, two-equation and second-order closure models, these difficulties include stiffness caused by the presence of an additional time scale, singular behavior near solid boundaries, and non-analytical behavior at sharp turbulent/nonturbulent interfaces. This chapter focuses on these difficulties and on the solution methods for turbulence-model equations that have evolved.

### 7.1 Multiple Time Scales and Stiffness

One key issue that must be addressed in developing a numerical algorithm for fluid-flow problems is that of the physically relevant time scales. Taking proper account of these time scales is a necessary condition for numerical accuracy. For example, when we deal with non-chemically-reacting laminar flow, there are two distinct time scales corresponding to different physical processes. If  $L$  and  $U$  denote characteristic length and velocity for the flowfield,  $a$  is sound speed and  $\nu$  is kinematic viscosity, the time scales are:

- Wave propagation,  $t_{wave} \sim L/|U \pm a|$
- Molecular diffusion,  $t_{diff} \sim L^2/\nu$

When we use turbulence transport equations, we have yet another time scale corresponding to the rate of decay of turbulence properties. In terms of the specific dissipation rate,  $\omega \sim \epsilon/k$ , this time scale is:

- Dissipation,  $t_{diss} \sim 1/\omega \sim k/\epsilon$

Any numerical algorithm designed for use with turbulence transport equations should reflect all three of these time scales.

In terms of the Reynolds number,  $Re_L = UL/\nu$ , and the Mach number,  $M = U/a$ , the ratio of  $t_{diff}$  to  $t_{wave}$  is given by

$$\frac{t_{diff}}{t_{wave}} \sim \frac{|M \pm 1|Re_L}{M} \quad (7.1)$$

Clearly, for high Reynolds number flows the diffusion time scale is much longer than the wave propagation time scale regardless of Mach number. Diffusion will generally be important over very short distances such as the thickness of a boundary layer,  $\delta$ , i.e., when  $L \sim \delta$ . For specified freestream Mach and Reynolds numbers, the relative magnitudes of the diffusion and wave propagation time scales are more-or-less confined to a limited range. This is not the case for the dissipation time scale.

The specific dissipation rate can vary by many orders of magnitude across a turbulent boundary layer. Consequently, in the same flow,  $t_{diss}$  can range from values much smaller than the other time scales to much larger. This is a crude reflection of the physical nature of turbulence, which consists of a wide range of frequencies. Thus, regardless of the flow speed, we should expect the dissipation time to have a nontrivial impact on numerical algorithms.

Because of the multiplicity of time scales attending use of turbulence transport equations, especially two-equation models and second-order closure models, we must contend with an unpleasant feature known as **stiffness**. An equation, or system of equations, is said to be stiff when there are two or more very different scales of the independent variable on which the dependent variables are changing. For example, consider the equation

$$\frac{d^2 y}{dt^2} = 100y \quad (7.2)$$

The general solution to this equation is

$$y(t) = Ae^{-10t} + Be^{10t} \quad (7.3)$$

If we impose the initial conditions

$$y(0) = 1 \quad \text{and} \quad \dot{y}(0) = -10 \quad (7.4)$$

the exact solution becomes

$$y_{exact}(t) = e^{-10t} \quad (7.5)$$



Unfortunately, any roundoff or truncation error in a numerical solution can excite the  $e^{10t}$  factor, viz., we can inadvertently wind up with

$$y_{\text{numerical}}(t) = e^{-10t} + \epsilon e^{10t}, \quad |\epsilon| \ll 1 \quad (7.6)$$

No matter how small  $\epsilon$  is, the second term will eventually dominate the solution. The equivalent situation for a system of equations is to have eigenvalues of the characteristic equation of very different magnitudes.

It is easy to see that most turbulence transport equations hold potential for being stiff. The  $k$ - $\epsilon$  model is notoriously stiff when some of the commonly used viscous damping functions are introduced. Second-order closure models that use the  $\epsilon$  equation are often so stiff as to almost preclude stable numerical solution. Some of the difficulty with the  $\epsilon$  equation occurs because the dissipation time scale is a function of both  $k$  and  $\epsilon$ . Transient solution errors in both parameters can yield large variations in  $k/\epsilon$ , so that the dissipation time scale can assume an unrealistic range of values. By contrast, near-wall solutions to models based on the  $\omega$  equation have well-defined algebraic solutions approaching a solid boundary, and are thus much easier to integrate.

## 7.2 Numerical Accuracy Near Boundaries

Proper treatment of boundary conditions is necessary for all numerical solutions, regardless of the equations being solved. Because of the special nature of turbulence transport equations, there are two types of boundary behavior that require careful treatment. Specifically, quantities such as dissipation rate,  $\epsilon$ , and specific dissipation rate,  $\omega$ , grow so rapidly approaching a solid boundary that they appear to be singular. In fact,  $\omega$  is singular for a perfectly-smooth wall. Also, at interfaces between turbulent and nonturbulent regions, velocity and other properties have nearly discontinuous slopes approaching the interface. Because wall-bounded flows typically involve both types of boundaries, accurate numerical solutions must account for the special problems presented by this unusual solution behavior.

### 7.2.1 Solid Surfaces

We know that for a perfectly-smooth wall, the specific dissipation rate varies in the sublayer as  $y^{-2}$  approaching the surface (see Subsection 4.6.3). Even if we choose to use wall functions to obviate integration through the viscous sublayer, analysis of the log layer (see Subsection 4.6.1) shows that both  $\epsilon$

and  $\omega$  are inversely proportional to distance from the surface. In either case, care must be taken to accurately compute derivatives of such functions.

To illustrate the difficulty imposed by singular behavior approaching a solid boundary, consider the function  $\phi$  defined by

$$\phi = \frac{1}{y^n}; \quad n = 1 \text{ or } 2 \quad (7.7)$$

The exact first and second derivatives are

$$\frac{d\phi}{dy} = -\frac{n}{y^{n+1}} \quad \text{and} \quad \frac{d^2\phi}{dy^2} = \frac{n(n+1)}{y^{n+2}} \quad (7.8)$$

Using central differences on a uniform grid with  $y_j = j\Delta y$ , a straightforward calculation shows that

$$\left(\frac{d\phi}{dy}\right)_j \approx \frac{\phi_{j+1} - \phi_{j-1}}{2\Delta y} = \left[\frac{j^2}{j^2 - 1}\right]^n \left(\frac{d\phi}{dy}\right)_{\text{exact}} \quad (7.9)$$

and

$$\left(\frac{d^2\phi}{dy^2}\right)_j \approx \frac{\phi_{j+1} - 2\phi_j + \phi_{j-1}}{(\Delta y)^2} \approx \left[\frac{j^2}{j^2 - 1}\right]^n \left(\frac{d^2\phi}{dy^2}\right)_{\text{exact}} \quad (7.10)$$

where subscript  $j$  denotes the value at  $y = y_j$ . Table 7.1 lists the errors attending use of central differences as a function of  $\Delta y/y_j$  for  $n = 1$  and  $n = 2$ .

Table 7.1: Central Difference Errors for  $\phi = y^{-n}$

$j$	$\Delta y/y_j$	(% Error) $_{n=1}$	(% Error) $_{n=2}$
2	.50	33	78
3	.33	13	27
5	.20	4	9
7	.14	2	4
10	.10	1	2

Clearly, significant numerical errors are introduced if the ratio  $\Delta y/y_j$  is not small. If wall functions are used (corresponding to  $n = 1$ ), regardless of how close the grid point nearest the surface lies, nontrivial numerical errors in derivatives result for  $j < 5$ . Consequently, simply using wall functions as effective boundary conditions applied at the first grid point above the

surface is unsatisfactory. Rather, the value for  $\omega$  or  $\epsilon$  should be specified for all points below  $j = 4$  (at a minimum) to insure numerical accuracy. This is undoubtedly the primary reason why most researchers find their numerical solutions to be sensitive to near-wall grid-point spacing when they use wall functions. As an alternative, a relatively large cell can be used next to the surface, so that for example,  $y_1 = 0$ ,  $y_2 = \Delta y$ ,  $y_3 = 1.2\Delta y$ , etc. As a result of using the Rubel-Melnik (1984) transformation, Program DEFECT (Appendix C) automatically generates such a grid.

When the  $k$ - $\omega$  or multiscale model is integrated through the viscous sublayer for a perfectly-smooth surface (corresponding to  $n = 2$ ), there is no practical way to avoid having  $\Delta y/y_2 \sim 1$ . The exact solution to the  $\omega$  equation in the viscous sublayer is

$$\omega \sim \frac{N_\omega \nu_w}{y^2}, \quad y^+ < 2.5 \quad (7.11)$$

where

$$N_\omega = \begin{cases} 6/\beta, & \text{without viscous corrections} \\ 2/\beta^*, & \text{with viscous corrections} \end{cases} \quad (7.12)$$

If we simply use the value of  $\omega$  according to Equation (7.11) at the first grid point above the surface, Table 7.1 shows that the molecular diffusion term will be in error by 78%. This, in turn, will increase values of  $\omega$  at larger values of  $y$ . Recall that the surface value of  $\omega$  has a strong effect on the additive constant,  $B$ , in the law of the wall (see Subsection 4.7.2). Thus, computing too large a value of  $\omega$  near the surface will distort the velocity profile throughout the sublayer and into the log layer. That is, numerically inaccurate near-wall  $\omega$  values can distort the entire boundary-layer solution.

The remedy that has proven very effective for eliminating this numerical error is to use Equation (7.11) for the first 7 to 10 grid points above the surface. Of course, these grid points must lie below  $y^+ = 2.5$  since Equation (7.11) is not valid above this point. This procedure has been used in Programs PIPE and SUBLAY (Appendix C) and Program EDDYBL (Appendix D).

An alternative procedure for accurately computing near-surface behavior of  $\omega$  is to use the rough-wall boundary condition. As shown in Subsection 4.7.2 for the  $k$ - $\omega$  model and Subsection 6.6.1 for the multiscale model,

$$\omega = \frac{u_\tau^2}{\nu_w} S_R \quad \text{at} \quad y = 0 \quad (7.13)$$

where

$$S_R = (50/k_R^+)^2, \quad k_R^+ < 25 \quad (7.14)$$

The quantity  $k_R^+ = u_\tau k_R / \nu_w$  is the scaled surface roughness height.

In order to simulate a smooth surface, we simply require that  $k_R^+$  be smaller than 5. Then, combining Equations (7.13) and (7.14), we arrive at the **slightly-rough-surface boundary condition** on  $\omega$ , viz.,

$$\omega = \frac{2500\nu_w}{k_R^2} \quad \text{at} \quad y = 0 \quad (7.15)$$

It is important to select a small enough value of  $k_R$  to insure that  $k_R^+ < 5$ . If too large a value is selected, the skin friction values will be larger than smooth-wall values.

As a final comment, the near-wall solution to the  $\omega$  equation for a rough wall is given by

$$\omega = \frac{\omega_w}{\left(1 + \sqrt{\frac{\omega_w}{N_\omega \nu_w}} y\right)^2}, \quad y^+ < 2.5 \quad (7.16)$$

where  $\omega_w$  is the surface value of  $\omega$  and  $N_\omega$  is given in Equation (7.12). An important test for numerical accuracy of any finite-difference program implementing the  $\omega$  equation is to verify that solutions match either Equation (7.11) or (7.16). If the program fails to accurately reproduce the near-wall  $\omega$  variation, the program is unlikely to yield accurate results.

Rapid variation of the dependent variable is not the only potential source of numerical error near solid boundaries. Another serious consideration is roundoff error resulting from the relatively small difference between two numbers of comparable magnitude. This problem is frequently encountered with low-Reynolds-number  $k$ - $\epsilon$  models. For example, damping functions such as

$$f_2 = 1 - e^{-Re_T^2} \quad \text{and} \quad f_\mu = 1 - e^{-0.0115y^+} \quad (7.17)$$

appear in the Lam-Bremhorst (1981) and Chien (1982) models. Approaching the surface, desired asymptotic behavior depends upon accurate values of these damping functions. If single-precision accuracy is used, it is advisable to use Taylor series expansions for the damping functions close to the surface. For example, Chien's  $f_\mu$  can be computed according to

$$f_\mu = \begin{cases} 1 - e^{-0.0115y^+}, & y^+ > 0.01 \\ 0.0115y^+, & y^+ \leq 0.01 \end{cases} \quad (7.18)$$

This procedure is used in Program EDDYBL (Appendix D) to insure numerically accurate solutions.

### 7.2.2 Turbulent/Nonturbulent Interfaces

More often than not, turbulence model equations that are in general usage appear to predict sharp interfaces between turbulent and nonturbulent regions, i.e., interfaces where discontinuities in derivatives of flow properties occur at the edge of the shear layer. As noted in earlier chapters, these interfaces bear no relation to the physical turbulent/nonturbulent interfaces that actually fluctuate in time and have smooth Reynolds-averaged properties. The mixing-length model, for example, exhibits a sharp interface for the far wake (see Subsection 3.3.1). That is, the predicted velocity profile is

$$U(x, y) = \begin{cases} U_\infty - 1.38\sqrt{\frac{D}{\rho x}} [1 - (y/\delta)^{3/2}]^2, & y < \delta \\ U_\infty, & y \geq \delta \end{cases} \quad (7.19)$$

where  $U_\infty$  is freestream velocity,  $D$  is drag per unit width,  $\rho$  is density,  $y$  is distance from the centerline and  $\delta$  is the half-width of the wake. Clearly, all derivatives of  $U$  above  $\partial^2 U / \partial y^2$  are discontinuous at  $y = \delta$ . Such a solution is called a **weak solution** to the differential equation.

By definition [see Courant and Hilbert (1966)], a weak solution to a partial differential equation

$$\mathcal{L}[u] = \frac{\partial}{\partial x} P(x, y, u) + \frac{\partial}{\partial y} Q(x, y, u) + S(x, y, u) = 0 \quad (7.20)$$

satisfies the following conditions.

1.  $u(x, y)$  is piecewise continuous and has piecewise continuous first derivatives in two adjacent domains,  $R_1$  and  $R_2$ .
2.  $\mathcal{L}[u] = 0$  in  $R_1$  and  $R_2$ .
3. For any test function  $\phi(x, y)$  that is differentiable to all orders and that is identically zero outside of  $R_1$  and  $R_2$ , the following integral over the combined region  $R = R_1 \cup R_2$  must be satisfied.

$$\iint_R \left[ P \frac{\partial \phi}{\partial x} + Q \frac{\partial \phi}{\partial y} - S \phi \right] dx dy = 0 \quad (7.21)$$

A similar result holds for a system of equations. Clearly, Equation (7.21) can be rewritten as

$$\iint_R \left[ \frac{\partial(\phi P)}{\partial x} + \frac{\partial(\phi Q)}{\partial y} \right] dx dy - \iint_R \phi \left[ \frac{\partial P}{\partial x} + \frac{\partial Q}{\partial y} + S \right] dx dy = 0 \quad (7.22)$$

The second integral vanishes since  $P$ ,  $Q$  and  $S$  satisfy the differential equation in both  $R_1$  and  $R_2$ . Then, using Gauss' theorem, if  $\Gamma$  is the curve of

discontinuity that divides  $R_1$  and  $R_2$  and  $\mathbf{n} = (n_x, n_y)$  is the unit normal to  $\Gamma$ , there follows:

$$\int_{\Gamma} \phi ([P]n_x + [Q]n_y) ds = 0 \quad (7.23)$$

The symbols  $[P]$  and  $[Q]$  denote the jumps in  $P$  and  $Q$  across  $\Gamma$ . Since the function  $\phi$  is arbitrary, we can thus conclude that the **jump condition** across the surface of discontinuity is given by

$$[P]n_x + [Q]n_y = 0 \quad (7.24)$$

For example, in the case of the far-wake solution given by the mixing length model, we have  $P = U_{\infty}U$ ,  $Q = -(\alpha\delta\partial U/\partial y)^2$  and  $S = 0$ . Inspection of Equation (7.19) shows that the jumps in  $P$  and  $Q$  are both zero, corresponding to the fact that the discontinuity appears in the second derivative rather than the first.

The occurrence of weak solutions causes problems on at least two counts. First, the jump condition is not unique. For example, if  $Q$  can be written as a function of  $P$ , we can always multiply Equation (7.20) by an arbitrary function  $\psi(P)$ , and rearrange as follows:

$$\frac{\partial F}{\partial x} + \frac{\partial G}{\partial y} + S\psi = 0 \quad (7.25)$$

where

$$F = \int \psi(P) dP \quad \text{and} \quad G = \int \psi(P)Q'(P) dP \quad (7.26)$$

The jump condition then becomes

$$[F]n_x + [G]n_y = 0 \quad (7.27)$$

In other words, we can have any jump condition we want (and don't want!). This means we have no guarantee that our solution is unique.

The second difficulty posed by the presence of weak solutions is an adverse effect on accuracy and convergence of numerical solution methods. For example, a central-difference approximation for a first derivative is second-order accurate provided the function of interest is twice differentiable. However, if the function has discontinuous first or second derivative, the accuracy of the central-difference approximation becomes indeterminate. Maintaining second-order accuracy is then possible only if we know the location of the curve of discontinuity in advance. For a hyperbolic equation, this curve is a characteristic curve so that the method of characteristics, for example, can provide a high degree of accuracy in the vicinity

of such discontinuities. Since we don't know the location of the characteristics a priori in standard finite-difference computations, accuracy is suspect when the equations have weak solutions.

Turbulence energy equation models have problems similar to the mixing length model near turbulent/nonturbulent interfaces. Spalart and Allmaras (1992), for example, demonstrate existence of weak solutions to their one-equation model at such interfaces. Saffman (1970) was the first to illustrate weak solutions for a two-equation model. He discusses the nature of solutions to his  $k$ - $\omega^2$  model approaching a turbulent/nonturbulent interface. In fact, he builds in weak-solution behavior by choosing his closure coefficients to insure that approaching the interface from within the turbulent region, the streamwise velocity and turbulence length scale vary as

$$U_e - U \propto (\delta - y) \quad \text{and} \quad \ell = k^{1/2}/\omega \propto \text{constant} \quad \text{as} \quad y \rightarrow \delta \quad (7.28)$$

where the interface lies at  $y = \delta$ . Vollmers and Rotta (1977) discuss solution behavior near a turbulent/nonturbulent interface for their  $k$ - $k\ell$  model, while Rubel and Melnik (1984) perform a similar analysis for the  $k$ - $\epsilon$  model. Cazalbou, Spalart and Bradshaw (1994) confirm existence of weak solutions for most  $k$ - $\epsilon$ ,  $k$ - $k\ell$  and  $k$ - $\omega$  models. Finally, inspection of the  $k$ - $\omega$  and  $k$ - $\epsilon$  model free shear flow velocity profiles [Figures 4.5 - 4.8] illustrates the nonanalytic behavior at the edge of the shear layer.

Rubel and Melnik (1984) offer an interesting solution for thin shear layer flows that effectively maps the turbulent/nonturbulent interface to infinity and implicitly clusters grid points near the interface. Their transformation consists of introducing a new independent variable,  $\xi$ , defined in terms of the normal distance,  $y$ , by

$$d\xi = \frac{dy}{\nu_T} \quad \text{or} \quad \frac{d}{d\xi} = \nu_T \frac{d}{dy} \quad (7.29)$$

where  $\nu_T$  is kinematic eddy viscosity. The Rubel-Melnik transformation, which is useful primarily for self-similar flows, improves numerical accuracy because the edge of the shear layer that occurs at a finite value of  $y$  moves to infinity in terms of the transformed independent variable  $\xi$  (provided  $\nu_T = 0$  in the freestream). Since  $\nu_T \rightarrow 0$ , the transformation produces fine resolution near the interface. For example, if the freestream velocity,  $U_e$ , is constant, close to the shear-layer edge, convection balances turbulent diffusion in the streamwise momentum equation. Hence,

$$V \frac{dU}{dy} = \frac{d}{dy} \left( \nu_T \frac{dU}{dy} \right) \quad (7.30)$$

where  $V$  is the entrainment velocity, which must also be constant in order to satisfy continuity. Since shear layers grow in thickness, necessarily  $V < 0$ .

Multiplying both sides of Equation (7.30) by  $\nu_T$  and using Equation (7.29), we arrive at

$$V \frac{dU}{d\xi} = \frac{d^2 U}{d\xi^2} \quad (7.31)$$

for which the solution is

$$U = U_e - \mathcal{U} e^{V\xi} \quad (7.32)$$

where  $\mathcal{U}$  is a constant of integration.

Using the Rubel-Melnik transformation, it is a straightforward matter to determine the nature of solutions to turbulence model equations approaching a turbulent/nonturbulent interface. Applying the transformation to the  $k$ - $\epsilon$  model, for example, we find

$$V \frac{dk}{d\xi} = \left( \frac{dU}{d\xi} \right)^2 - C_\mu k^2 + \frac{1}{\sigma_k} \frac{d^2 k}{d\xi^2} \quad (7.33)$$

$$V \frac{d\epsilon}{d\xi} = C_{\epsilon 1} \frac{\epsilon}{k} \left( \frac{dU}{d\xi} \right)^2 - C_{\epsilon 2} C_\mu k \epsilon + \frac{1}{\sigma_\epsilon} \frac{d^2 \epsilon}{d\xi^2} \quad (7.34)$$

Provided the closure coefficients  $\sigma_k$  and  $\sigma_\epsilon$  are both less than 2, the production and dissipation terms are negligible in both equations. The solution approaching the interface is

$$k \sim \mathcal{K} e^{\sigma_k V \xi}, \quad \epsilon \sim \mathcal{E} e^{\sigma_\epsilon V \xi} \quad (\sigma_k < 2, \quad \sigma_\epsilon < 2) \quad (7.35)$$

where  $\mathcal{K}$  and  $\mathcal{E}$  are integration constants. Thus, the eddy viscosity is

$$\nu_T \sim C_\mu \frac{\mathcal{K}^2}{\mathcal{E}} e^{(2\sigma_k - \sigma_\epsilon) V \xi} \quad (7.36)$$

Finally, substituting Equation (7.36) into Equation (7.29) and integrating yields

$$e^{V\xi} \propto (1 - y/\delta)^{(2\sigma_k - \sigma_\epsilon)^{-1}} \quad (7.37)$$

wherefore the solution to the  $k$ - $\epsilon$  model equations approaching a turbulent/nonturbulent interface from the turbulent side behaves according to

$$\left. \begin{aligned} U_e - U &\sim \mathcal{U} (1 - y/\delta)^{(2\sigma_k - \sigma_\epsilon)^{-1}} \\ k &\sim \mathcal{K} (1 - y/\delta)^{\sigma_k (2\sigma_k - \sigma_\epsilon)^{-1}} \\ \epsilon &\sim \mathcal{E} (1 - y/\delta)^{\sigma_\epsilon (2\sigma_k - \sigma_\epsilon)^{-1}} \end{aligned} \right\} \quad \text{as } y \rightarrow \delta \quad (7.38)$$

Using the standard values  $\sigma_k = 1.0$  and  $\sigma_\epsilon = 1.3$ , the  $k$ - $\epsilon$  model predicts

$$\left. \begin{aligned} U_e - U &\sim \mathcal{U} (1 - y/\delta)^{10/7} \\ k &\sim \mathcal{K} (1 - y/\delta)^{10/7} \\ \epsilon &\sim \mathcal{E} (1 - y/\delta)^{13/7} \end{aligned} \right\} \quad \text{as } y \rightarrow \delta \quad (7.39)$$



The solution for the  $k$ - $\omega$  model is a bit more complicated when  $\sigma$  and  $\sigma^*$  are both equal to  $1/2$ . As a result, only the dissipation terms are negligible, and the production term in the transformed  $k$  equation yields a secular term, which complicates the solution. That is, the approximate transformed equations for  $k$  and  $\omega$  are as follows.

$$\frac{d^2 k}{d\xi^2} - 2V \frac{dk}{d\xi} = 2V^2 \mathcal{U}^2 e^{2V\xi} \quad (7.40)$$

$$\frac{d^2 \omega}{d\xi^2} - 2V \frac{d\omega}{d\xi} = 2\alpha V^2 \mathcal{U}^2 \frac{\omega}{k} e^{2V\xi} \quad (7.41)$$

The solution for  $k$  and  $\omega$  is

$$k \sim \mathcal{U}^2 V \xi e^{2V\xi}, \quad \omega \sim \mathcal{W} \xi^{-\alpha} \quad (7.42)$$

where  $\mathcal{W}$  is an integration constant. Computing the eddy viscosity and substituting into Equation (7.29), we arrive at

$$y \sim \delta + \frac{\mathcal{U}^2 V}{\mathcal{W}} \int_{\xi}^{\infty} \xi^{1+\alpha} e^{2V\xi} d\xi \quad (7.43)$$

Integrating by parts, we can approximate the limiting form of the integral for  $\xi \rightarrow \infty$  as follows.

$$\delta - y \sim \frac{\mathcal{U}^2}{2\mathcal{W}} \xi^{1+\alpha} e^{2V\xi} \quad (7.44)$$

Now, we must solve this equation for  $\xi$  as a function of  $\delta - y$ . To do this, let

$$\eta = \frac{2\mathcal{W}}{\mathcal{U}^2} (\delta - y) \quad (7.45)$$

Then, Equation (7.44) simplifies to

$$\eta \sim \xi^{1+\alpha} e^{2V\xi} \quad (7.46)$$

This equation can be solved for  $\xi$  as a function of  $\eta$  by assuming

$$2V\xi \sim \ell n \eta + \phi(\eta) \quad (7.47)$$

where  $\phi(\eta)$  is a function to be determined. In the limit  $\xi \rightarrow \infty$ , which corresponds to  $\eta \rightarrow 0$ , the approximate solution for  $\phi(\eta)$  is

$$\phi(\eta) \sim -(1 + \alpha) \ell n \left( \frac{\ell n \eta}{2V} \right) \quad (7.48)$$

With a bit more algebra, there follows

$$e^{V\xi} \propto \eta^{1/2} \left( \frac{2V}{\ell n \eta} \right)^{(1+\alpha)/2} \quad (7.49)$$

Thus, the behavior of solutions to the  $k$ - $\omega$  model approaching a turbulent/nonturbulent interface from within the turbulent region is

$$\left. \begin{aligned} U_e - U &\sim \mathcal{U}\sqrt{\lambda} \\ k &\sim -\mathcal{K}\lambda\ell n\lambda \\ \omega &\sim \mathcal{W}(-\ell n\lambda)^{-\alpha} \\ \lambda &\sim \frac{(1 - y/\delta)}{[-\ell n(1 - y/\delta)]^{1+\alpha}} \end{aligned} \right\} \quad \text{as } y \rightarrow \delta \quad (7.50)$$

Clearly,  $\omega$  approaches zero very slowly from the turbulent side as compared to the variation of  $\epsilon/k \sim (\delta - y)^{3/7}$  predicted by the  $k$ - $\epsilon$  model.

Usually it is more convenient to assign small nonzero values to  $k$  and other turbulence parameters in the freestream, especially when the parameter appears in the denominator of the eddy viscosity. Cazalbou, Spalart and Bradshaw (1994) show that when this is done in boundary-layer computations with the  $k$ - $\epsilon$  model, the weak solution prevails below the interface. Small gradients in  $k$  and  $\epsilon$  appear above the interface that yield an asymptotic approach to the prescribed freestream values. There is “no significant influence on the predicted flow.”

By contrast, Menter (1992a) shows that for the far wake, in which the entrainment velocity increases in magnitude linearly with distance from the centerline, the  $k$ - $\omega$  model predicts that  $k$  and  $\omega$  decay exponentially with distance squared. However, they decay at the same rate so that the eddy viscosity remains constant. As a consequence, consistent with results presented in Section 4.5, the freestream value of  $\omega$  has a nontrivial effect on the solution. Menter indicates a smaller effect on boundary layers, primarily because of the large values of  $\omega$  prevailing near the surface. The behavior of  $\omega$  in Equation (7.50) is consistent with Menter’s observation that the  $k$ - $\omega$  model solutions appear to have discontinuous derivatives at the shear layer edge. However, the discontinuity in  $d\omega/dy$  would probably be difficult to detect.

In principle, solutions with discontinuous derivatives will not occur if molecular viscosity is included in the diffusion terms of the equations of motion. As shown by Saffman (1970), there is a thin **viscous-interface layer** of thickness

$$\delta \sim \nu/|V| \quad (7.51)$$

in which the discontinuities are resolved. This is a singular perturbation problem in the limit  $|V|\delta/\nu \rightarrow \infty$ , and the weak solution discussed above is the outer solution. The inner solution holds in the viscous-interface layer. For example, in the interface layer, Saffman's equations simplify to

$$\left. \begin{aligned} V \frac{dU}{dy} &= \frac{d}{dy} \left[ \left( \nu + \frac{k}{\omega} \right) \frac{dU}{dy} \right] \\ V \frac{dk}{dy} &= \frac{d}{dy} \left[ \left( \nu + \sigma^* \frac{k}{\omega} \right) \frac{dk}{dy} \right] \\ V \frac{d\omega^2}{dy} &= \frac{d}{dy} \left[ \left( \nu + \sigma \frac{k}{\omega} \right) \frac{d\omega^2}{dy} \right] \end{aligned} \right\} \quad (7.52)$$

These equations must be solved subject the following conditions that correspond to formal matching to the solutions on each side of the turbulent/nonturbulent interface:

$$U_e - U \rightarrow \mathcal{U}(\delta - y), \quad k \rightarrow \mathcal{K}(\delta - y)^2, \quad \omega \rightarrow \frac{\mathcal{K}}{|V|}(\delta - y) \quad \text{as} \quad \frac{|V|(\delta - y)}{\nu} \rightarrow \infty \quad (7.53)$$

and

$$U_e - U \rightarrow 0, \quad k \rightarrow 0, \quad \omega \rightarrow 0 \quad \text{as} \quad \frac{|V|(\delta - y)}{\nu} \rightarrow -\infty \quad (7.54)$$

As can be easily verified, for  $\sigma = \sigma^* = 1/2$ , the solution is given by

$$\left. \begin{aligned} U_e - U &= \frac{\mathcal{U}|V|^3}{\mathcal{K}^2\nu} \left( \frac{\omega^2}{1 + V^2\omega/\mathcal{K}\nu} \right) \\ k &= \frac{V^2\omega^2}{\mathcal{K}} \\ y - \delta &= \frac{|V|\omega}{\mathcal{K}} + \frac{2\nu}{|V|} \ln \left( \frac{V^2\omega}{\mathcal{K}\nu} \right) \end{aligned} \right\} \quad (7.55)$$

In practice, finite difference grids are never sufficiently fine to resolve the viscous-interface layer. Generally, grid points are packed close to the surface to permit accurate resolution of the sublayer. Hence, even when molecular viscosity is included in a typical finite-difference computation, turbulent/nonturbulent interfaces are not sufficiently resolved. As a consequence, the interfaces are sharp, and the weak solutions generally prevail. However, truncation error, numerical diffusion and dissipation will generally yield diffused solutions close to the interfaces. The most significant numerical problem typically encountered is the appearance of nonphysical

negative values of  $k$  and/or other normally positive turbulence parameters such as  $\omega$ ,  $\epsilon$  and  $\ell$ .

For self-similar flows such as the far wake, mixing layer, jet and defect layer, the Rubel-Melnik transformation cures the problem by mapping the interface to  $\infty$ . Programs WAKE, MIXER, JET and DEFECT described in Appendix C all use this transformation. In addition to eliminating difficulties associated with the turbulent/nonturbulent interface, the transformation linearizes the first and second derivative terms in the equations. This linearization tends to improve the rate of convergence of most numerical methods. The only shortcoming of the method is its sensitivity to the location of  $\infty$ . Using too large or too small a value of  $\xi_{max}$  (the far-field value of  $\xi$ ) sometimes impedes convergence of the numerical solution.

In general finite-difference computations, the correct jump condition will be obtained provided the diffusion terms in all equations are differenced in a conservative manner. For the same reasons, we use conservative differencing for the Navier-Stokes equation to guarantee that the exact shock relations are satisfied across a shock wave in a finite-difference computation. Program EDDYBL (Appendix D), for example, uses conservative differencing for diffusion terms and rarely ever encounters numerical difficulties attending the presence of sharp turbulent/nonturbulent interfaces.

For nonzero freestream values of  $k$ , etc., some researchers prefer zero-gradient boundary conditions at a boundary-layer edge. While such conditions are clean from a theoretical point of view, they are undesirable from a numerical point of view. That is, specified values at the edge are of the Neumann type while zero-gradient conditions are of the Dirichlet type. Almost universally, convergence of iterative schemes is much slower with Dirichlet conditions than with Neumann conditions.

In order to resolve this apparent dilemma, we can appeal directly to the equations of motion. Beyond the boundary-layer edge, we expect to have vanishing normal gradients so that the equations for  $k$  and  $\omega$  simplify to the following:

$$U_e \frac{dk_e}{dx} = -\beta^* \omega_e k_e \quad (7.56)$$

$$U_e \frac{d\omega_e}{dx} = -\beta \omega_e^2 \quad (7.57)$$

where subscript  $e$  denotes the value at the boundary-layer edge. The solution to Equations (7.56) and (7.57) can be obtained by simple quadrature, independent of integrating the equations of motion through the boundary layer. Once  $k_e$  and  $\omega_e$  are determined from Equations (7.56) and (7.57), it is then possible to specify Neumann-type boundary conditions that guarantee zero normal gradients. Clearly, the same procedure can be used for any turbulence model. Program EDDYBL (Appendix D) uses this procedure.

## 7.3 Parabolic Marching Methods

In general, numerical methods for solving parabolic systems of equations such as the boundary-layer equations are unconditionally stable. A second-order accurate scheme like the Blottner (1974) variable-grid method, for example, involves inversion of a tridiagonal matrix. If the matrix is diagonally dominant, the scheme will run stably with arbitrarily large streamwise stepsize,  $\Delta x$ . Turbulent boundary layer computations using algebraic models often run with  $\Delta x/\delta$  between 1 and 10, where  $\delta$  is boundary layer thickness. By contrast, early experience with two-equation models indicated that much smaller steps must be taken. Rastogi and Rodi (1978) found that their three-dimensional boundary-layer program based on the Jones-Launder (1972)  $k$ - $\epsilon$  model required initial steps of about  $\delta/100$ , and that ultimately  $\Delta x$  could not exceed  $\delta/2$ . Similar results hold for models based on the  $\omega$  equation.

Wilcox (1981b) found that the problem stems from a loss of diagonal dominance caused by the production terms in the turbulence model equations. To illustrate the essence of the problem, consider the  $k$ - $\omega$  model's turbulence energy equation for an incompressible two-dimensional boundary layer, viz.,

$$U \frac{\partial k}{\partial x} + V \frac{\partial k}{\partial y} = \left[ \frac{(\partial U / \partial y)^2}{\omega} - \beta^* \omega \right] k + \frac{\partial}{\partial y} \left[ (\nu + \sigma^* \nu_T) \frac{\partial k}{\partial y} \right] \quad (7.58)$$

The following analysis is based on the Blottner variable-grid method, which is the scheme implemented in Program EDDYBL (Appendix D). This algorithm uses a three-point forward difference formula [Adams-Bashforth — see Roache (1976)] in the streamwise direction, central differencing for the normal convection term, and conservative differencing for the diffusion terms. Hence, discretization approximations for all except the source terms are as follows:

$$U \frac{\partial k}{\partial x} \doteq \frac{U}{\Delta x} (3k_{m+1,n} - 4k_{m,n} + k_{m-1,n}) \quad (7.59)$$

$$V \frac{\partial k}{\partial y} \doteq \frac{V}{2\Delta y} (k_{m+1,n+1} - k_{m+1,n-1}) \quad (7.60)$$

$$\frac{\partial}{\partial y} \left[ (\nu + \sigma^* \nu_T) \frac{\partial k}{\partial y} \right] \doteq \frac{\nu^+ (k_{m+1,n+1} - k_{m+1,n}) - \nu^- (k_{m+1,n} - k_{m+1,n-1})}{(\Delta y)^2} \quad (7.61)$$

where  $k_{m,n}$  denotes the value of  $k$  at  $x = x_m$  and  $y = y_n$ , and  $\Delta y$  denotes the vertical distance between grid points. Unsubscripted quantities are assumed known during the typically iterative solution procedure. Also, the

quantity  $\nu^-$  denotes the value of  $(\nu + \sigma^* \nu_T)$  midway between  $y_{n-1}$  and  $y_n$ , while  $\nu^+$  denotes the value midway between  $y_n$  and  $y_{n+1}$ . For simplicity, we assume points are equally spaced in both the  $x$  and  $y$  directions, so that the grid consists of rectangular cells. Figure 7.1 shows the finite-difference molecule.

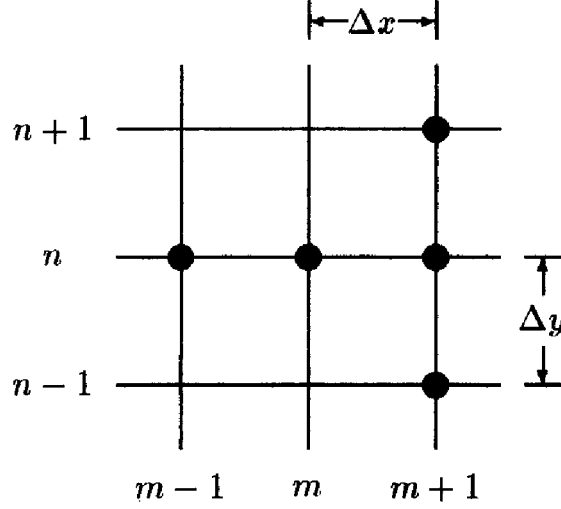


Figure 7.1: Finite-difference molecule for Blottner's variable-grid method.

Turning to the source terms, the simplest second-order accurate discretization approximation is

$$\left[ \frac{(\partial U / \partial y)^2}{\omega} - \beta^* \omega \right] k \doteq \left[ \frac{(\partial U / \partial y)^2}{\omega} - \beta^* \omega \right] k_{m+1,n} \quad (7.62)$$

Substituting Equations (7.59)-(7.62) into Equation (7.58) and regrouping terms leads to a tridiagonal matrix system as follows:

$$A_n k_{m+1,n-1} + B_n k_{m+1,n} + C_n k_{m+1,n+1} = D_n \quad (7.63)$$

where  $A_n$ ,  $B_n$ ,  $C_n$  and  $D_n$  are defined by

$$A_n = - \left[ \frac{V}{2\Delta y} + \frac{\nu^-}{(\Delta y)^2} \right] \quad (7.64)$$

$$B_n = 3 \frac{U}{\Delta x} + \frac{\nu^- + \nu^+}{(\Delta y)^2} - \frac{(\partial U / \partial y)^2}{\omega} + \beta^* \omega \quad (7.65)$$

$$C_n = \left[ \frac{V}{2\Delta y} - \frac{\nu^+}{(\Delta y)^2} \right] \quad (7.66)$$

$$D_n = \frac{U}{\Delta x} [4k_{m,n} - k_{m-1,n}] \quad (7.67)$$

Now, in order to have a diagonally dominant system, the condition

$$B_n \geq -(A_n + C_n) \quad (7.68)$$

must be satisfied. Substituting Equations (7.64)-(7.66) into Equation (7.68) yields the following condition.

$$3 \frac{U}{\Delta x} - \frac{(\partial U / \partial y)^2}{\omega} + \beta^* \omega \geq 0 \quad (7.69)$$

When dissipation exceeds production, so that  $\beta^* \omega > (\partial U / \partial y)^2 / \omega$ , Equation (7.69) is satisfied so long as we march in the direction of flow (i.e., so long as  $U$  and  $\Delta x$  are of the same sign). The system is then said to be **unconditionally stable**. However, when production exceeds dissipation, we have the following limit on stepsize.

$$\Delta x \leq (\Delta x)_{theory} \equiv \frac{3\omega U}{(\partial U / \partial y)^2 - \beta^* \omega^2} \quad (7.70)$$

Hence, the scheme is **conditionally stable**, the condition being that of Equation (7.70).

To demonstrate the validity of Equation (7.70), Wilcox (1981b) presents computed results for an incompressible flat-plate boundary layer using the Wilcox-Rubesin (1980)  $k-\omega^2$  model. At a plate-length Reynolds number,  $Re_x$ , of  $1.2 \cdot 10^6$ , stable computation is found empirically to be possible provided  $Re_{\Delta x} < 2.2 \cdot 10^4$ , which corresponds to  $\Delta x / \delta = 1.15$ . Figure 7.2 shows  $Re_{\Delta x}$  as predicted by Equation (7.70) throughout the boundary layer. As shown, the minimum value of  $Re_{\Delta x}$  according to Equation (7.70) is  $1.9 \cdot 10^4$  and occurs at  $y / \delta = 0.012$ . This close agreement verifies that the source of instability is lack of diagonal dominance in the tridiagonal matrix system defined in Equations (7.63)-(7.67).

To remedy this situation, note first that because of nonlinearity, Equation (7.63) always requires an iterative solution. Letting superscript  $i$  denote iteration number, we replace  $B_n$  and  $D_n$  by the following revised discretization approximations:

$$B_n = 3 \frac{U}{\Delta x} + \frac{\nu^- + \nu^+}{(\Delta y)^2} - \frac{(\partial U / \partial y)^2}{\omega} + (1 + \psi_k) \beta^* \omega \quad (7.71)$$

$$D_n = \frac{U}{\Delta x} [4k_{m,n} - k_{m-1,n}] + \psi_k \beta^* \omega k_{m+1,n}^{i-1} \quad (7.72)$$

where  $\psi_k$  will be defined below. Then, Equation (7.63) is replaced by

$$A_n k_{m+1,n-1}^i + B_n k_{m+1,n}^i + C_n k_{m+1,n+1}^i = D_n \quad (7.73)$$

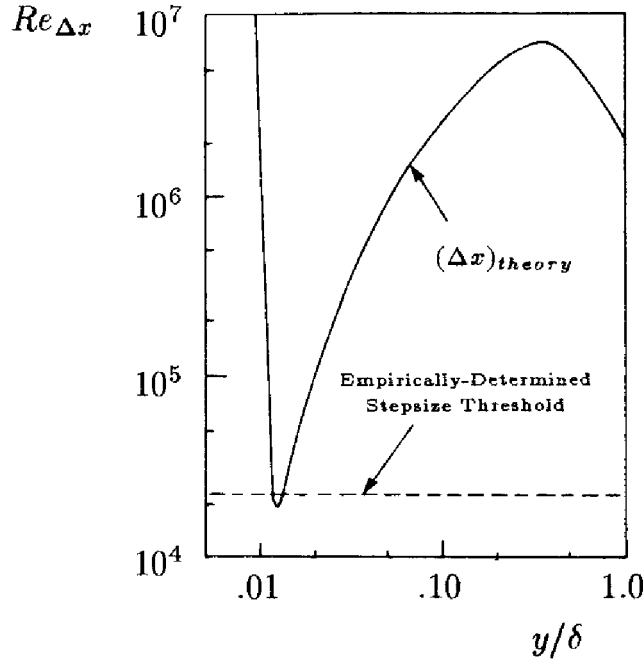


Figure 7.2: Theoretical and empirically determined stepsize threshold for a flat-plate boundary layer. [From Wilcox (1981b) — Copyright © AIAA 1981 — Used with permission.]

Inspection of Equations (7.71)-(7.73) shows that when convergence has been achieved (i.e., when  $k_{m+1,n}^i$  and  $k_{m+1,n}^{i-1}$  differ by a negligible amount), terms on the right- and left-hand sides of Equation (7.73) proportional to  $\psi_k$  cancel identically. Hence,  $k_{m+1,n}^i$  satisfies the correct equation. The advantage of this procedure becomes obvious upon inspection of the stability condition, which now becomes

$$3 \frac{U}{\Delta x} - \frac{(\partial U / \partial y)^2}{\omega} + (1 + \psi_k) \beta^* \omega \geq 0 \quad (7.74)$$

Clearly,  $\psi_k$  can be chosen to insure that this inequality is always satisfied, regardless of the value of  $\Delta x$ . This corresponds to unconditional stability.

Numerical experimentation shows that the best results are obtained when  $(1 + \psi_k) \beta^* \omega$  exceeds  $(\partial U / \partial y)^2 / \omega$  by about 30%, a condition that is insured by defining  $\psi_k$  as follows.

$$\psi_k = \begin{cases} \frac{3}{10}, & (\partial U / \partial y)^2 \leq \beta^* \omega^2 \\ \frac{(\partial U / \partial y)^2}{\beta^* \omega^2} - \frac{7}{10}, & (\partial U / \partial y)^2 > \beta^* \omega^2 \end{cases} \quad (7.75)$$

A similar factor,  $\psi_\omega$ , must be introduced for the  $\omega$  equation, and experience



has shown that selecting

$$\psi_\omega = \psi_k \quad (7.76)$$

is satisfactory to achieve both unconditional stability and rapid convergence.

The prescription for  $\psi_k$  and  $\psi_\omega$  given in Equations (7.75) and (7.76) permits stepsizes comparable to those used with algebraic models. While the numerical procedure is unconditionally stable for other values of  $\psi_k$ , using these values for  $\psi_k$  and  $\psi_\omega$  optimizes  $k$ - $\omega^2$  and  $k$ - $\omega$  model computations with respect to the number of iterations required for the solution to converge. Interestingly, if  $\psi_k$  is too large, say  $\psi_k = 2$ , stable integration is inhibited. The value of  $\psi_\omega$  cannot be too large either, although the upper bound appears to be dependent upon details of the specific model.

The same analysis applies to the  $k$ - $\epsilon$  model. For the  $k$  equation, writing Equation (7.75) in terms of the model's variables leads to the following entirely equivalent form.

$$\psi_k = \begin{cases} \frac{3}{10}, & \nu_T(\partial U/\partial y)^2 \leq \epsilon \\ \frac{\nu_T(\partial U/\partial y)^2}{\epsilon} - \frac{7}{10}, & \nu_T(\partial U/\partial y)^2 > \epsilon \end{cases} \quad (7.77)$$

By contrast, the value of the corresponding factor for the  $\epsilon$  equation,  $\psi_\epsilon$ , is very much dependent upon details of the model. Low-Reynolds-number viscous damping functions have a pronounced effect on the most appropriate value. Table 7.2 lists the values of  $\psi_\epsilon$  used in Program EDDYBL (Appendix D) for six different low-Reynolds-number  $k$ - $\epsilon$  models. The values listed have been found empirically to yield optimum convergence rates for incompressible boundary layers.

Table 7.2: Values of  $\psi_\epsilon$  for low-Reynolds-number  $k$ - $\epsilon$  models

Model	$\psi_\epsilon$
Jones-Launder (1972)	0.50
Launder-Sharma (1974)	0.50
Lam-Bremhorst (1981)	0.50
Chien (1982)	-0.25
Yang-Shih (1993)	-0.25
Fan-Lakshminarayana-Barnett (1993)	-0.25

## 7.4 Elementary Time-Marching Methods

One of the most effective procedures for solving complex flowfields is the use of time-marching methods. If the desired solution is unsteady, time-marching solutions yield a true time history. Time-marching methods can also be used for steady-flow problems by letting the solution evolve in time until temporal variations become negligibly small. That is, we begin with an initial approximation and update the solution at each timestep until the solution differs between timesteps by less than a prescribed tolerance level. Prior to discussing the impact of turbulence-model source terms on explicit and implicit methods, this section presents a brief overview of these methods. For more complete details see a general text on Computational Fluid Dynamics such as Roache (1976), Peyret and Taylor (1983), Anderson et al. (1984) or Minkowycz et al. (1988).

The simplest time-marching schemes are **explicit methods**, such as the DuFort-Frankel (1953), Godunov (1959), Lax-Wendroff (1960) and McCormack (1969) methods. Most explicit schemes were developed prior to 1970. In an explicit scheme, the solution at time  $t^{n+1}$  depends only on the past history, i.e., the solution at time  $t^n$ . For example, consider the one-dimensional wave equation:

$$\frac{\partial k}{\partial t} + U \frac{\partial k}{\partial x} = 0, \quad U > 0 \quad (7.78)$$

where  $k$  is a flow property,  $U$  is velocity,  $t$  is time and  $x$  is streamwise direction. Letting  $k_j^n$  denote  $k(x_j, t^n)$ , we approximate  $\partial k / \partial t$  with a **forward-difference approximation** so that

$$\frac{\partial k}{\partial t} \doteq \frac{k_j^{n+1} - k_j^n}{\Delta t} + O(\Delta t) \quad (7.79)$$

where  $\Delta t = t^{n+1} - t^n$ . For simplicity, consider simple **upwind differencing** in which we approximate  $\partial k / \partial x$  according to

$$\frac{\partial k}{\partial x} \doteq \frac{k_j^n - k_{j-1}^n}{\Delta x} + O(\Delta x) \quad (7.80)$$

Using these discretization approximations, we arrive at the following first-order accurate difference equation that approximates Equation (7.78).

$$k_j^{n+1} = k_j^n - \frac{U \Delta t}{\Delta x} (k_j^n - k_{j-1}^n) \quad (7.81)$$

This is not a particularly accurate method, but nevertheless illustrates the general nature of explicit schemes. Note that all terms on the right-hand

side of Equation (7.81) are known from time  $t^n$ . Hence,  $k_j^{n+1}$  is obtained from simple algebraic operations. Because only algebraic operations are needed (as opposed to inversion of a large matrix), explicit methods are easy to implement.

The primary shortcoming of explicit schemes is a limit on the timestep that can be used. For too large a timestep, solution errors will grow with increasing iterations and the computation becomes unstable. The most commonly used method for determining the stability properties of a time-marching finite-difference scheme is von Neumann stability analysis [see Roache (1976) or Anderson et al. (1984)]. In this method, we introduce a discrete Fourier series solution to the finite-difference equation under study, and determine the growth rate of each mode. If all Fourier modes decay as we march in time, the scheme is stable. However, if even a single mode grows, the scheme is unstable. We write each Fourier component as

$$k_j^n = G^n e^{i(j\kappa\Delta x)} \quad (7.82)$$

where  $G$  is called the **amplitude factor**,  $i = \sqrt{-1}$  and  $\kappa$  is wavenumber. The stability of a scheme is determined as follows:

$$\left. \begin{array}{ll} |G| < 1, & \text{Stable} \\ |G| = 1, & \text{Neutrally Stable} \\ |G| > 1, & \text{Unstable} \end{array} \right\} \quad (7.83)$$

In general,  $G$  is complex, and the notation  $G^n$  means  $G$  raised to the power  $n$ . The amplitude factor for Equation (7.81) is

$$G = 1 - \frac{U\Delta t}{\Delta x} (1 - e^{-i\theta}), \quad \text{where} \quad \theta = \kappa\Delta x \quad (7.84)$$

Thus,

$$|G|^2 = 1 + 2(1 - \cos\theta) \frac{U\Delta t}{\Delta x} \left( \frac{U\Delta t}{\Delta x} - 1 \right) \quad (7.85)$$

In order to have a stable scheme,  $|G|$  must be less than or equal to 1 for all possible values of  $\theta$ . Clearly, for the upwind-difference scheme, errors will not grow provided the condition

$$\Delta t < \frac{\Delta x}{U} \quad \text{or} \quad N_{CFL} = \frac{U\Delta t}{\Delta x} < 1 \quad (7.86)$$

is satisfied. This is the famous Courant-Friedrichs-Lewy (1967), or CFL condition, which means a wave cannot propagate a distance exceeding  $\Delta x$  in a single timestep.  $N_{CFL}$  is known as the **CFL Number**.

Explicit methods are of interest in modern CFD applications mainly for time-dependent flows. There has been renewed interest in these methods because of their suitability for massively-parallel computers. In summary, their algebraic simplicity makes them especially easy to implement on any computer. Their primary drawback is their conditional stability, and thousands of timesteps are often needed to achieve steady-flow conditions.

**Implicit methods** date back to 1947 when the Crank-Nicolson (1947) method first appeared. Other methods such as the Euler [Lilley (1965)] and Alternating Direction Implicit (ADI) schemes [Peaceman and Rachford (1955)] are implicit. The solution at time  $t^{n+1}$  and location  $x_j$  in this type of scheme depends not only upon the solution at the earlier timestep, but upon the solution at other spatial locations at time  $t^{n+1}$  as well. For example, the Crank-Nicolson method uses

$$\frac{\partial k}{\partial x} \doteq \frac{1}{2} \left( \frac{k_{j+1}^n - k_{j-1}^n}{2\Delta x} + \frac{k_{j+1}^{n+1} - k_{j-1}^{n+1}}{2\Delta x} \right) + O[(\Delta x)^2] \quad (7.87)$$

Thus, Equation (7.78) is approximated by the following second-order accurate difference equation:

$$-\lambda k_{j-1}^{n+1} + k_j^{n+1} + \lambda k_{j+1}^{n+1} = k_j^n - \lambda (k_{j+1}^n - k_{j-1}^n) \quad (7.88)$$

where

$$\lambda = \frac{U\Delta t}{4\Delta x} \quad (7.89)$$

Hence, as with the Blottner method discussed in the preceding section, a tridiagonal matrix system of equations must be solved. Although inverting any matrix is more time consuming than solving a simple algebraic equation, the increased complexity is attended by a significant increase in the maximum permissible timestep. That is, stability analysis shows that the scheme defined in Equation (7.88) is unconditionally stable.

Implicit schemes have proven to be especially useful for steady-flow computations where the CFL limit can be exceeded by factors as large as 5. While these schemes will run at a larger CFL number, using larger values of  $\Delta t$  sometimes introduces significant truncation errors if convective effects have a significant effect on the physics of the flow. The number of timesteps required, relative to explicit methods, to achieve steady-flow conditions typically is reduced, although the factor is  $N_{CFL}^{-n}$  where  $n < 1$ .

Recall from Section 7.1 that there are three physically relevant time scales when turbulence model equations are used. If we use an explicit finite-difference scheme to approximate the Favre-averaged Navier-Stokes equation, stability analysis shows that the wave speed is  $|\tilde{u}| + a$ , where  $\tilde{u}$

is mass averaged velocity and  $a$  is sound speed. If  $\nu$  denotes kinematic viscosity, the wave-propagation and diffusion timestep limitations are as follows.

$$\Delta t \leq \frac{\Delta x}{|\tilde{u}| + a} \quad \text{and} \quad \Delta t \leq \frac{(\Delta x)^2}{2\nu} \quad (7.90)$$

We might also anticipate that including source terms in the stability analysis would lead to an additional timestep constraint such as  $\Delta t \leq t_{diss}$ . This is indeed the case, and this timestep limitation is sometimes more restrictive than either condition in Equation (7.90).

To illustrate the problem, we add a source term,  $Sk$ , to Equation (7.78), wherefore

$$\frac{\partial k}{\partial t} + U \frac{\partial k}{\partial x} = Sk \quad (7.91)$$

The condition  $S > 0$  corresponds to production exceeding dissipation, and vice versa for  $S < 0$ . To cast this equation in discretized form, we use Crank-Nicolson differencing and we approximate the source term as follows:

$$Sk \doteq S [\psi k_j^n + (1 - \psi)k_j^{n+1}] + O[(\psi - \frac{1}{2})\Delta t, (\Delta t)^2] \quad (7.92)$$

where  $\psi$  lies between 0 and 1. Hence, our finite-difference approximation to Equation (7.91) is

$$k_j^{n+1} = k_j^n - \lambda (k_{j+1}^{n+1} + k_{j+1}^n - k_{j-1}^{n+1} - k_{j-1}^n) + S\Delta t [\psi k_j^n + (1 - \psi)k_j^{n+1}] \quad (7.93)$$

The complex amplification factor for this scheme is

$$G = \frac{1 + \psi S\Delta t - 2i\lambda \sin \theta}{1 - (1 - \psi)S\Delta t + 2i\lambda \sin \theta} \quad (7.94)$$

Hence, in order for this scheme to be stable, we must require

$$|G|^2 = \frac{[1 + \psi S\Delta t]^2 + 4\lambda^2 \sin^2 \theta}{[1 - (1 - \psi)S\Delta t]^2 + 4\lambda^2 \sin^2 \theta} \leq 1 \quad (7.95)$$

After a little algebra, the stability condition simplifies to

$$S\Delta t [1 + (\psi - \frac{1}{2})S\Delta t] \leq 0 \quad (7.96)$$

When  $S < 0$ , we find

$$\begin{cases} \Delta t \leq \frac{1}{(\psi - \frac{1}{2})|S|}; & \psi > \frac{1}{2}, \quad S < 0 \\ \text{Unconditionally Stable;} & \psi \leq \frac{1}{2}, \quad S < 0 \end{cases} \quad (7.97)$$

When  $S > 0$ , upon first inspection, von Neumann stability analysis indicates this scheme is unstable when  $\psi \geq \frac{1}{2}$  and that  $\Delta t$  must have a lower bound (as opposed to an upper bound) to insure stable computation when  $\psi < \frac{1}{2}$ . However, these results are irrelevant. This is true because the exact solution to Equation (7.91) is proportional to  $e^{St}$ , and is thus unbounded as  $t \rightarrow \infty$ . When this occurs, even if the error is a small fraction of the exact solution, it will also be unbounded. The requirement  $|G| \leq 1$  is thus too stringent for an unbounded function. According to von Neumann, the condition for stability when the exact solution is unbounded is:

$$|G| \leq 1 + O(\Delta t) \quad (7.98)$$

With a little rearrangement of terms, Equation (7.95) can be written as

$$|G|^2 = 1 + \left( \frac{2[1 + (\psi - \frac{1}{2})S\Delta t]}{[1 - (1 - \psi)S\Delta t]^2 + 4\lambda^2 \sin^2 \theta} \right) S\Delta t \quad (7.99)$$

Since the factor proportional to  $\sin^2 \theta$  serves only to increase the denominator, we can omit it and say that

$$|G|^2 \leq 1 + \left( \frac{2[1 + (\psi - \frac{1}{2})S\Delta t]}{[1 - (1 - \psi)S\Delta t]^2} \right) S\Delta t \quad (7.100)$$

Clearly, the function in parentheses is bounded as  $\Delta t \rightarrow 0$  as long as the denominator doesn't vanish, so that Equation (7.98) is satisfied provided:

$$\Delta t \leq \frac{1}{(1 - \psi)S}, \quad S > 0 \quad (7.101)$$

Although this analysis has been done for implicit Crank-Nicolson differencing of the convective term, the same result holds for explicit methods. While Equation (7.92) involves  $k_j^{n+1}$ , the terms in an explicit scheme can be rearranged to preserve its explicit nature. For example, if we use upwind differencing for the convective term in Equation (7.91), the discretized equation becomes

$$k_j^{n+1} = \frac{[1 + \psi S\Delta t - \frac{U\Delta t}{\Delta x}] k_j^n + \frac{U\Delta t}{\Delta x} k_{j-1}^n}{1 - (1 - \psi)S\Delta t} \quad (7.102)$$

We now have sufficient information to discuss the most suitable discretization approximations for source terms in both explicit and implicit methods. If second-order accuracy is required, as it would be for numerical simulation of an unsteady flow,  $\psi$  must be  $1/2$ . On the other hand, if only steady-state solutions are needed, we can take advantage of the fact that

using  $\psi = 0$  when  $S < 0$  and  $\psi = 1$  when  $S > 0$  yields an unconditionally stable (albeit first-order accurate in time) scheme. In summary, the following has proven satisfactory for turbulence model equations.

#### Second-Order Time Accuracy — Conditional Stability

$$Sk \doteq \frac{1}{2}S(k_j^n + k_j^{n+1}), \quad \Delta t \leq \frac{2}{|S|} \quad (7.103)$$

#### First-Order Time Accuracy — Unconditional Stability

$$Sk \doteq \begin{cases} Sk_j^{n+1} & \text{for } S < 0 \\ Sk_j^n & \text{for } S > 0 \end{cases} \quad (7.104)$$

All of the programs in Appendix C use Equation (7.104).

## 7.5 Block-Implicit Methods

The most efficient numerical methods currently available for complex flow-fields are **block-implicit** methods. They differ from elementary implicit methods in one very important respect. Specifically, when an elementary implicit scheme is applied to a coupled set of equations, each equation is solved in sequence. In the context of a system of equations, this is usually referred to as a **sequentially-implicit** method. By contrast, a block-implicit scheme solves all of the equations simultaneously at each grid point. The block-implicit formulation, generally requiring inversion of block-tridiagonal matrices, entails more computational effort than a sequentially-implicit method. The additional computation at each grid point and timestep is usually compensated for by a dramatically improved convergence rate. Block-implicit solvers can achieve CFL numbers in excess of 100, and often converge in 100 to 200 timesteps for flows including boundary-layer separation. For example, using a block-implicit method, a supersonic two-dimensional shock-separated turbulent flow can be simulated on an 80486-based microcomputer in about 3 hours of CPU time [Wilcox (1991)]. On the same computer, a similar computation would take about 25 hours using a sequentially-implicit method [Wilcox (1990)] and 75 hours using an explicit method [Wilcox (1974)].

As in the preceding section, we begin with a brief overview of block-implicit methods. For simplicity, we focus on a one-dimensional system. The primary concern in this section is, of course, upon how turbulence model source terms impact such methods.

Consider the one-dimensional conservation equations for flow of a viscous, perfect gas, written in vector form, viz.,

$$\frac{\partial \mathbf{Q}}{\partial t} + \frac{\partial}{\partial x} (\mathbf{F} - \mathbf{F}_v) = \mathbf{0} \quad (7.105)$$

where

$$\mathbf{Q} = \begin{Bmatrix} \bar{\rho} \\ \bar{\rho}\tilde{u} \\ \bar{\rho}E \end{Bmatrix}, \quad \mathbf{F} = \begin{Bmatrix} \bar{\rho}\tilde{u} \\ \bar{\rho}\tilde{u}^2 + P \\ (\bar{\rho}E + P)\tilde{u} \end{Bmatrix}, \quad \mathbf{F}_v = \begin{Bmatrix} 0 \\ \hat{\tau}_{xx} \\ \tilde{u}\hat{\tau}_{xx} - \hat{q}_x \end{Bmatrix} \quad (7.106)$$

where  $\hat{\tau}_{xx}$  and  $\hat{q}_x$  denote total stress and heat flux, respectively. Also, the total energy for one-dimensional flow is  $E = \tilde{e} + \frac{1}{2}\tilde{u}^2$  and the pressure is given by  $P = (\gamma - 1)\bar{\rho}\tilde{e}$ .

The first step often taken in establishing a block-implicit scheme for this system of equations is to introduce a first-order backward-difference (implicit backward-Euler) scheme, which can be written symbolically as follows.

$$\frac{\mathbf{Q}^{n+1} - \mathbf{Q}^n}{\Delta t} + \left[ \frac{\partial}{\partial x} (\mathbf{F} - \mathbf{F}_v) \right]^{n+1} = \mathbf{0} \quad (7.107)$$

Now, we expand the flux vectors  $\mathbf{F}$  and  $\mathbf{F}_v$  in a Taylor series about time level  $n$ , wherefore

$$\mathbf{F}^{n+1} \doteq \mathbf{F}^n + \frac{\partial \mathbf{F}}{\partial t} \Delta t + O[(\Delta t)^2] \quad (7.108)$$

and similarly for  $\mathbf{F}_v$ . Then, using the chain rule of calculus, we have

$$\frac{\partial \mathbf{F}}{\partial t} = \frac{\partial \mathbf{F}}{\partial \mathbf{Q}} \frac{\partial \mathbf{Q}}{\partial t} \quad (7.109)$$

where  $\partial \mathbf{F} / \partial \mathbf{Q}$  is the **inviscid-flux Jacobian matrix**. The incremental change in the dependent-variable vector,  $\Delta \mathbf{Q}$ , is defined by

$$\Delta \mathbf{Q} = \mathbf{Q}^{n+1} - \mathbf{Q}^n \quad (7.110)$$

Since we approximate the unsteady term according to  $\partial \mathbf{Q} / \partial t \doteq \Delta \mathbf{Q} / \Delta t$ , we can rewrite Equation (7.108) as

$$\mathbf{F}^{n+1} \doteq \mathbf{F}^n + \frac{\partial \mathbf{F}}{\partial \mathbf{Q}} \Delta \mathbf{Q} + O[(\Delta t)^2] \quad (7.111)$$

Because of the prominent role played by  $\Delta \mathbf{Q}$ , this approach is usually referred to as the **delta formulation**.



Finally, we must introduce a discretization approximation for the spatial derivatives of the vectors  $\mathbf{F}$  and  $\mathbf{F}_v$ . In general, this means forming a matrix that multiplies  $(\mathbf{F} - \mathbf{F}_v)$ , and yields a desired degree of accuracy. Details of this matrix are unimportant for our discussion, and it is sufficient to introduce symbolic notation with the understanding that an approximation to spatial differentiation is implied. Thus, we introduce a finite-difference matrix operator,  $\delta_x$ , so that

$$\left[ \frac{\partial}{\partial x} (\mathbf{F} - \mathbf{F}_v) \right]^{n+1} \doteq \delta_x (\mathbf{F}^n - \mathbf{F}_v^n) + \delta_x \left( \frac{\partial \mathbf{F}}{\partial \mathbf{Q}} - \frac{\partial \mathbf{F}_v}{\partial \mathbf{Q}} \right) \Delta \mathbf{Q} \quad (7.112)$$

where  $\partial \mathbf{F}_v / \partial \mathbf{Q}$  is the **viscous-flux Jacobian matrix**. Collecting all of this, we arrive at the symbolic form of a typical block-implicit method:

$$\left[ \frac{I}{\Delta t} + \delta_x \left( \frac{\partial \mathbf{F}}{\partial \mathbf{Q}} - \frac{\partial \mathbf{F}_v}{\partial \mathbf{Q}} \right) \right] \Delta \mathbf{Q} = -\delta_x (\mathbf{F}^n - \mathbf{F}_v^n) \quad (7.113)$$

where  $I$  is the unit (identity) matrix. The matrix multiplying  $\Delta \mathbf{Q}$  in Equation (7.113) is of block-tridiagonal form. In the present example, the blocks are 3 by 3, corresponding to the three equations being solved simultaneously at each mesh point.

Now, suppose we choose to use a two-equation turbulence model to determine the Reynolds stress. The following three points that must be considered in modifying a block-implicit solution scheme.

1. Decide whether to solve all equations simultaneously or to solve the model equations and mean-flow equations sequentially.
2. If the preferred option is to solve all equations simultaneously, determine the changes to the flux-Jacobian matrices.
3. Make provision for handling source terms.

In principle, solving all equations simultaneously will yield the most rapidly convergent scheme in the number of iterations, but not necessarily in CPU time. However, the coupling between the turbulence-model equations and the mean-flow equations appears to be relatively weak. The primary coupling is through the diffusion terms, and the eddy viscosity is usually treated as a constant in forming the viscous-flux Jacobian matrix. Limited experience to date seems to indicate there is little advantage to solving all equations simultaneously as opposed to solving the model equations and mean-flow equations sequentially.

If all equations are solved simultaneously, the basic system of equations for the  $k$ - $\omega$  model would be as follows:

$$\frac{\partial \mathbf{Q}}{\partial t} + \frac{\partial}{\partial x} (\mathbf{F} - \mathbf{F}_v) = \mathbf{S} \quad (7.114)$$

where the dependent-variable and inviscid-flux vectors are

$$\mathbf{Q} = \begin{Bmatrix} \bar{\rho} \\ \bar{\rho}\tilde{u} \\ \bar{\rho}E \\ \bar{\rho}k \\ \bar{\rho}\omega \end{Bmatrix}, \quad \mathbf{F} = \begin{Bmatrix} \bar{\rho}\tilde{u} \\ \bar{\rho}\tilde{u}^2 + P \\ (\bar{\rho}E + P)\tilde{u} \\ \bar{\rho}\tilde{u}k \\ \bar{\rho}\tilde{u}\omega \end{Bmatrix} \quad (7.115)$$

The viscous-flux and source-term vectors are given by

$$\mathbf{F}_v = \begin{Bmatrix} 0 \\ \frac{4}{3}\mu\frac{\partial\tilde{u}}{\partial x} + \tau_{xx} \\ \tilde{u}(\frac{4}{3}\mu\frac{\partial\tilde{u}}{\partial x} + \tau_{xx}) - \hat{q}_x \\ (\mu + \sigma^*\mu_T)\frac{\partial k}{\partial x} \\ (\mu + \sigma\mu_T)\frac{\partial\omega}{\partial x} \end{Bmatrix}, \quad \mathbf{S} = \begin{Bmatrix} 0 \\ 0 \\ 0 \\ \tau_{xx}\frac{\partial\tilde{u}}{\partial x} - \beta^*\bar{\rho}\omega k \\ \alpha\left(\frac{\omega}{k}\right)\tau_{xx}\frac{\partial\tilde{u}}{\partial x} - \beta\bar{\rho}\omega^2 \end{Bmatrix} \quad (7.116)$$

There are two places where the turbulence kinetic energy appears that has an impact on the flux-Jacobian matrices. Specifically, the total energy,  $E$ , should be written as

$$E = \tilde{e} + \frac{1}{2}\tilde{u}^2 + k \quad (7.117)$$

and the Reynolds stress tensor is

$$\tau_{xx} = \frac{4}{3}\mu_T\frac{\partial\tilde{u}}{\partial x} - \frac{2}{3}\bar{\rho}k \quad (7.118)$$

Hence, since the vector  $\mathbf{Q}$  contains  $\bar{\rho}k$  as one of its elements, the inviscid- and viscous-flux Jacobian matrices must be evaluated from scratch. Some of the original 9 elements appropriate for laminar flow or an algebraic model will be affected by the appearance of  $k$  in  $E$  and  $\hat{\tau}_{xx}$ . For this system, the inviscid-flux Jacobian matrix assumes the following form:

$$\frac{\partial\mathbf{F}}{\partial\mathbf{Q}} = \begin{bmatrix} 0 & 1 & 0 & 0 & 0 \\ \left(\frac{\gamma-3}{2}\right)\tilde{u}^2 & (3-\gamma)\tilde{u} & (\gamma-1) & -(\gamma-1) & 0 \\ -\left[H - \frac{\gamma-1}{2}\tilde{u}^2\right]\tilde{u} & [H - (\gamma-1)\tilde{u}^2] & \gamma\tilde{u} & -(\gamma-1)\tilde{u} & 0 \\ -\tilde{u}k & k & 0 & \tilde{u} & 0 \\ -\tilde{u}\omega & \omega & 0 & 0 & \tilde{u} \end{bmatrix} \quad (7.119)$$

where  $H$  is the total enthalpy defined by

$$H = \tilde{h} + \frac{1}{2}\tilde{u}^2 + k \quad (7.120)$$

As shown in Equation (7.119), the first two components on row 3 involve  $H$ , and are thus affected by  $k$ . In modifying an existing computer program

based on this block-implicit scheme, all that would be required to modify the inviscid-flux Jacobian matrix components would be to have  $H$  appear as indicated, and to include  $k$  in the computation of  $H$ .

By contrast, if we choose to solve the mean-flow and turbulence model equations sequentially, we retain the original conservation equations [Equation (7.105)]. All of the flux-Jacobian matrices and, in fact, the entire algorithm remain the same. To determine  $k$  and  $\omega$ , we then consider the following vector equation:

$$\frac{\partial \mathbf{q}}{\partial t} + \frac{\partial}{\partial x} (\mathbf{f} - \mathbf{f}_v) = \mathbf{s} \quad (7.121)$$

where

$$\mathbf{q} = \begin{Bmatrix} \bar{\rho}k \\ \bar{\rho}\omega \end{Bmatrix}, \quad \mathbf{f} = \begin{Bmatrix} \bar{\rho}\tilde{u}k \\ \bar{\rho}\tilde{u}\omega \end{Bmatrix}, \quad \mathbf{f}_v = \begin{Bmatrix} (\mu + \sigma^* \mu_T) \frac{\partial k}{\partial x} \\ (\mu + \sigma \mu_T) \frac{\partial \omega}{\partial x} \end{Bmatrix} \quad (7.122)$$

$$\mathbf{s} = \begin{Bmatrix} \tau_{xx} \frac{\partial \tilde{u}}{\partial x} - \beta^* \bar{\rho} \omega k \\ \alpha \left( \frac{\omega}{k} \right) \tau_{xx} \frac{\partial \tilde{u}}{\partial x} - \beta \bar{\rho} \omega^2 \end{Bmatrix} \quad (7.123)$$

Consistent with the block-implicit approach, we linearize the flux and source vectors according to

$$(\mathbf{f} - \mathbf{f}_v)^{n+1} \doteq (\mathbf{f} - \mathbf{f}_v)^n + \left( \frac{\partial \mathbf{f}}{\partial \mathbf{q}} - \frac{\partial \mathbf{f}_v}{\partial \mathbf{q}} \right) \Delta \mathbf{q} \quad (7.124)$$

$$\mathbf{s} \doteq \mathbf{s}^n + \frac{\partial \mathbf{s}}{\partial \mathbf{q}} \Delta \mathbf{q} \quad (7.125)$$

where  $\partial \mathbf{s} / \partial \mathbf{q}$  is the **source-Jacobian matrix**. The flux-Jacobian matrices are generally much simpler than their counterparts in the mean-flow equations. For example, the inviscid-flux Jacobian matrix is

$$\frac{\partial \mathbf{f}}{\partial \mathbf{q}} = \begin{bmatrix} \tilde{u} & 0 \\ 0 & \tilde{u} \end{bmatrix} \quad (7.126)$$

This brings us to the all important question of how to handle the source-term vector  $\mathbf{s}$ . Several prescriptions are possible, and the primary considerations are to: maintain numerical stability; achieve rapid convergence rate; and guarantee that  $k$  and  $\omega$  are positive definite. Wilcox (1991) has found the following linearization of the source terms to be quite satisfactory for the  $k$ - $\omega$  model, within the framework of MacCormack's (1985) block-implicit method. Specifically, the source-term vector is rearranged as follows.

$$\mathbf{s} = \begin{Bmatrix} \tau_{xx} \frac{\partial \tilde{u}}{\partial x} - \beta^* \left( \frac{\omega}{k} \right) \frac{(\bar{\rho}k)^2}{\bar{\rho}} \\ \alpha \left( \frac{\omega}{k} \right) \tau_{xx} \frac{\partial \tilde{u}}{\partial x} - \beta \frac{(\bar{\rho}\omega)^2}{\bar{\rho}} \end{Bmatrix} \quad (7.127)$$

Then, treating  $\tau_{xx}\partial\tilde{u}/\partial x$  and  $\omega/k$  as constant in computing the source-Jacobian matrix, we arrive at

$$\mathbf{s}^n = \left\{ \begin{array}{c} \tau_{xx}\frac{\partial\tilde{u}}{\partial x} - \beta^*\bar{\rho}\omega k \\ \alpha\left(\frac{\omega}{k}\right)\tau_{xx}\frac{\partial\tilde{u}}{\partial x} - \beta\bar{\rho}\omega^2 \end{array} \right\}, \quad \frac{\partial\mathbf{s}}{\partial\mathbf{q}} = \left[ \begin{array}{cc} -2\beta^*\omega & 0 \\ 0 & -2\beta\omega \end{array} \right] \quad (7.128)$$

In this treatment of the source-term vector the production terms are evaluated explicitly (i.e., computed at time level  $n$ ), and the dissipation terms are treated implicitly (computed at time level  $n+1$ ). The block-tridiagonal scheme for the turbulence model equations becomes

$$\left[ \frac{I}{\Delta t} + \delta_x \left( \frac{\partial\mathbf{f}}{\partial\mathbf{q}} - \frac{\partial\mathbf{f}_v}{\partial\mathbf{q}} \right) - \frac{\partial\mathbf{s}}{\partial\mathbf{q}} \right] \Delta\mathbf{q} = -\delta_x(\mathbf{f}^n - \mathbf{f}_v^n) + \mathbf{s}^n \quad (7.129)$$

Since  $\partial\mathbf{s}/\partial\mathbf{q}$  is a diagonal matrix and its diagonal elements are always negative, its contribution is guaranteed to enhance diagonal dominance of the matrix multiplying  $\Delta\mathbf{q}$ . Additionally, Spalart and Allmaras (1992) show that this form guarantees that  $k$  and  $\omega$  (or  $\epsilon$  for a  $k$ - $\epsilon$  model) will always be positive.

However, Spalart and Allmaras also point out that in regions where production and dissipation are both large and dominate the overall balance of terms in the equation, this form can result in slow convergence. This appears to be a more serious problem for the  $k$ - $\epsilon$  model than it is for the  $k$ - $\omega$  model. Wilcox (1991), for example, has shown that the scheme described above yields very rapid convergence in flows with attached equilibrium boundary layers and in flows with large regions of separation. The procedure recommended by Spalart and Allmaras is similar to the procedure recommended for elementary implicit methods in Equation (7.104). That is, they recommend linearizing the source term according to

$$\mathbf{s} \doteq \mathbf{s}^n + \text{neg} \left( \frac{\partial\mathbf{s}}{\partial\mathbf{q}} \right) \Delta\mathbf{q} \quad (7.130)$$

where the function  $\text{neg}(x)$  is defined as

$$\text{neg}(x) = \begin{cases} x, & x < 0 \\ 0, & x \geq 0 \end{cases} \quad (7.131)$$

The production terms are then included in computing the source-Jacobian matrix. The  $\text{neg}$  operator is understood to apply to each element of the resulting (diagonal) matrix. Thus, as long as dissipation exceeds production, both production and dissipation are treated implicitly, and explicitly when production exceeds dissipation. Huang and Coakley (1992) have successfully applied a linearization similar to that recommended by Spalart and Allmaras.

## 7.6 Solution Convergence and Grid Sensitivity

Regardless of the application, there is a need for control of numerical accuracy in CFD [Roache (1990)]. This need is just as critical in CFD work as it is in experiments where the experimenter is expected to provide estimates for the accuracy of his or her measurements. All CFD texts of any value stress this need.

One key issue determining numerical accuracy is **iteration convergence**. Most numerical methods used in CFD applications require many iterations to converge. The iteration convergence error is defined as the difference between the current iterate and the exact solution to the difference equations. Often, the difference between successive iterates is used as a measure of the error in the converged solution, although this in itself is inadequate. A small relaxation factor can always give a false indication of convergence [Anderson et al. (1984)]. Whatever the algorithm is, you should always be careful to check that a converged solution has been obtained. This can be done by trying a stricter than usual convergence criterion, and demonstrating that there is a negligible effect on the solution. Most reputable engineering journals require demonstration of iteration convergence as a condition for publication. This is not specific to turbulence-model applications — all of the usual criteria for standard CFD applications apply.

Specific to turbulence-model computations, the approach to iteration convergence often is more erratic, and typically much slower, than for laminar-flow computations. A variety of factors including stiffness and non-linearity of the equations, as well as the severely stretched finite-difference grids needed to resolve thin viscous layers, yield less rapid and less monotone convergence. Ferziger (1989) explains the slow convergence often observed in terms of the eigenvalues of the matrix system corresponding to the discretized equations. He notes that any iteration scheme for a linear system can be written as

$$\phi^{n+1} = A\phi^n + S \quad (7.132)$$

where  $\phi^n$  is the solution after the  $n^{th}$  iteration,  $A$  is a matrix, and  $S$  is a source term. He then shows that the actual solution error is given by

$$\phi_{exact} - \phi^n \approx \frac{\phi^{n+1} - \phi^n}{1 - \lambda_{max}} \quad (7.133)$$

where  $\phi_{exact}$  denotes the **exact solution to the discretized equations** and  $\lambda_{max}$  is the largest eigenvalue of the matrix  $A$ . Of course, all eigenvalues of  $A$  must be less than 1 for the solution to converge. This result

shows that the solution error is larger than the difference between iterates. Furthermore, the closer  $\lambda_{max}$  is to 1, the larger the ratio of solution error to the difference between iterates. In other words, the slower the rate of convergence of the method, the smaller the difference between iterates must be to guarantee iteration convergence.

A second key issue is **grid convergence** or **grid insensitivity**. Because of the finite size of finite-difference cells, discretization errors exist that represent the difference between the solution to the difference equations and the **exact (continuum) solution to the differential equations**. It is important to know the magnitude of these discretization errors and to insure that a fine enough grid has been used to reduce the error to an acceptable level.

As with iteration convergence, all CFD work should demonstrate grid convergence, regardless of what equations are being solved. In most engineering journals, it is no longer sufficient to publish results performed on a single fixed grid. While grid sensitivity studies should be done for all CFD work, they are even more crucial for turbulence-model computations because of the need to separate numerical error from turbulence-model error. This issue came into sharp focus at the 1980-81 AFOSR-HTTM-Stanford Conference on Complex Turbulent Flows [see Kline, Cantwell, and Lilley (1981)]. Clearly, no objective evaluation of the merits of different turbulence models can be made unless the discretization error of the numerical algorithm is known.

The most common way to demonstrate grid convergence is to repeat a computation on a grid with twice as many grid points, and compare the two solutions. If computer resources are unavailable to facilitate a grid doubling, a grid halving is also appropriate, although the error bounds will not be as sharp. Using results for two different grids, techniques such as **Richardson extrapolation** [see Roache (1976)] can be used to determine discretization error. This method is very simple to implement, and should be used whenever possible. For a second-order accurate method with central differences, Richardson extrapolation assumes the error,  $E_h \equiv \phi_{exact} - \phi_h$ , where  $\phi_h$  denotes the solution when the grid-point spacing is  $h$ , can be expanded as a Taylor series in  $h$ , wherefore

$$E_h = e_2 h^2 + e_4 h^4 + e_6 h^6 + \dots \quad (7.134)$$

Note that for three-point upwind differences the leading term is still  $e_2 h^2$ , but the next term is  $e_3 h^2$ , and Richardson extrapolation is only  $O(h^3)$  rather than  $O(h^4)$ . By hypothesis, the  $e_i$  are, at worst, functions of the coordinates, but are nevertheless independent of  $h$ . Now, if we halve the

number of grid points so that  $h$  is doubled, the error is given by

$$E_{2h} = 4e_2h^2 + 16e_4h^4 + 64e_6h^6 + \dots \quad (7.135)$$

For small values of  $h$ , we can drop all but the leading terms, whence the discretization error is given by

$$E_h \approx \frac{1}{3}(\phi_h - \phi_{2h}) \quad (7.136)$$

As a final comment, Richardson extrapolation has limitations. First, if it is applied to primitive variables such as velocity and internal energy, its implications regarding momentum and energy conservation may be inaccurate. Second, the method implicitly assumes the solution has continuous derivatives to all orders. Hence, its results are not meaningful near shock waves or turbulent/nonturbulent interfaces of the type discussed in Subsection 7.2.2.

There is another grid-related factor affecting solution accuracy. In order to resolve thin viscous layers, for example, highly stretched grids are normally used. Conventional central-difference approximations are only first-order accurate on such a grid, and care must be taken to account for this. Also, the location of the grid point nearest the surface has a nontrivial effect on the accuracy of skin friction and surface heat flux. Wilcox (1989), for example, has found that grid-insensitive computations using wall functions that account for pressure gradient [e.g., Equation (5.111)] can be obtained with block-implicit methods provided:

$$10 < y_2^+ < 100, \quad (\text{wall functions}) \quad (7.137)$$

where  $y_2^+$  is the sublayer-scaled value of the first grid point above the surface. This range appears to hold for boundary-layer computations as well [Chambers and Wilcox (1977)], again provided pressure gradient is accounted for. When turbulence-model equations are integrated through the viscous sublayer, many researchers have shown that it is imperative to require:

$$y_2^+ < 1, \quad (\text{integration through the sublayer}) \quad (7.138)$$

When these limits are not adhered to, consistent with the discussion in Subsection 7.2.1, solution errors throughout the boundary layer generally are large.

## Problems

**7.1** For a Mach 3 turbulent flat-plate boundary layer, it is a fact that  $Mc_f Re_L \approx Re_{\delta^*}$ .

- (a) In the viscous sublayer, the appropriate scaling for the specific dissipation rate is  $\omega \sim u_\tau^2/\nu$ . Noting that  $u_\tau \approx U\sqrt{c_f}$ , express the ratio of  $t_{diss}$  to  $t_{wave}$  as a function of  $Re_{\delta^*}$  in the sublayer.
- (b) In the defect layer, the appropriate scaling for the specific dissipation rate is  $\omega \sim u_\tau/\Delta$  where  $\Delta = U\delta^*/u_\tau$ . Express the ratio of  $t_{diss}$  to  $t_{wave}$  as a function of  $Re_{\delta^*}$  in the defect layer.
- (c) Comment on the implications of your estimates in Parts (a) and (b).

**7.2** Determine whether or not the following systems of equations are stiff with regard to the specified initial conditions.

(a)

$$\frac{d}{dt} \begin{Bmatrix} x \\ y \end{Bmatrix} = \begin{bmatrix} -3 & 4 \\ 4 & 3 \end{bmatrix} \begin{Bmatrix} x \\ y \end{Bmatrix}, \quad \begin{Bmatrix} \dot{x}(0) \\ \dot{y}(0) \end{Bmatrix} = -5 \begin{Bmatrix} x(0) \\ y(0) \end{Bmatrix}$$

(b)

$$\frac{d}{dt} \begin{Bmatrix} x \\ y \end{Bmatrix} = \begin{bmatrix} -3 & 1 \\ 4 & -3 \end{bmatrix} \begin{Bmatrix} x \\ y \end{Bmatrix}, \quad \begin{Bmatrix} \dot{x}(0) \\ \dot{y}(0) \end{Bmatrix} = - \begin{Bmatrix} x(0) \\ y(0) \end{Bmatrix}$$

**7.3** Consider the high-Reynolds-number  $k$ - $\omega$  model's near-wall variation of specific dissipation rate,  $\omega$ , for a rough wall, i.e.,

$$\omega = \frac{\omega_w}{[1 + Ay]^2}, \quad A = \sqrt{\frac{\beta\omega_w}{6\nu_w}}$$

- (a) Assuming equally spaced grid points, show that the central-difference approximation to  $d^2\omega/dy^2$  at the first grid point above the surface (i.e., at  $y = \Delta y$ ) is given by

$$\left(\frac{d^2\omega}{dy^2}\right)_2 \approx \Phi(\Delta y) \left(\frac{d^2\omega}{dy^2}\right)_{exact}$$

where

$$\Phi(\Delta y) = \frac{[1 + A\Delta y]^2[1 + 2A\Delta y + \frac{2}{3}(A\Delta y)^2]}{[1 + 2A\Delta y]^2}$$



(b) Assuming a slightly-rough wall so that

$$\omega_w = \frac{2500\nu_w}{k_R^2}$$

and that  $\beta = 3/40$ , show that

$$A\Delta y = \frac{5\sqrt{5}}{2} \frac{\Delta y^+}{k_R^+}$$

(c) Determine the percentage error introduced by the central-difference approximation in computing  $d^2\omega/dy^2$  when we assume a hydraulically smooth wall so that  $k_R^+ = 5$ , and set  $\Delta y^+ = 1/\sqrt{5} = 0.447$ .

**7.4** This problem shows that while trapezoidal-rule integration is second-order accurate for a piecewise continuous function with a discontinuous first derivative, the truncation error depends upon placement of the nodes. Using the trapezoidal rule, the integral of a function  $f(x)$  is

$$\int_a^b f(x) dx \approx \sum_{k=1}^N f(x_k)\Delta x + \frac{1}{2}[f(a) - f(b)]\Delta x$$

where

$$x_k = k\Delta x \quad \text{and} \quad \Delta x = \frac{b-a}{N}$$

Consider the following piecewise continuous function  $f(x)$ :

$$f(x) = \begin{cases} x^2, & 0 \leq x \leq 1 \\ 1, & 1 < x \leq 2 \end{cases}$$

Note that a node lies at  $x = 1$  only for even values of  $N$ .

(a) Verify that the exact integral of  $f(x)$  for  $x$  ranging from 0 to 2 is

$$I \equiv \int_0^2 f(x) dx = \frac{4}{3}$$

(b) Assuming  $N$  is odd show that the trapezoidal rule yields

$$I \approx \frac{4}{3} \left[ 1 - \frac{1}{16}(\Delta x)^2 \right]$$

(c) Assuming  $N$  is even show that the trapezoidal rule yields

$$I \approx \frac{4}{3} \left[ 1 + \frac{1}{8}(\Delta x)^2 \right]$$

**HINT:** Use the fact that  $\sum_{k=1}^M k^2 = \frac{1}{6}M(M+1)(2M+1)$ .

**7.5** Consider the mixing-length model with  $\ell_{mix} = \alpha\delta$ , where  $\alpha$  is a constant and  $\delta$  is shear layer thickness.

- (a) Assuming that  $dU/dy > 0$ , verify that according to the Rubel-Melnik transformation,

$$\nu_T = \ell_{mix} \sqrt{\frac{dU}{d\xi}}$$

- (b) For flow near a turbulent/nonturbulent interface with constant entrainment velocity,  $V < 0$ , determine the velocity difference,  $U_e - U$ , as  $y \rightarrow \delta$ . Express your answer as a function of  $|V|$ ,  $\alpha$  and  $y/\delta$ .

**7.6** The object of this problem is to verify that Equation (7.55) is the solution to Equations (7.52) - (7.54).

- (a) Integrate Equations (7.52) once and impose the freestream boundary condition [Equation (7.54)].
- (b) Observing that  $\sigma = \sigma^* = 1/2$  for Saffman's model, combine the  $k$  and  $\omega^2$  equations to show that

$$\frac{dk}{d\omega^2} = \frac{k}{\omega^2}$$

Solve this equation subject to the boundary conditions.

- (c) Introduce the dimensionless variables

$$\bar{y} = \frac{|V|(\delta - y)}{\nu} \quad \text{and} \quad \bar{\omega} = \frac{V^2 \omega}{K\nu}$$

and substitute the solution for  $k$  into the equation for  $\omega$ . Set any arbitrary constant of integration equal to zero, and verify the solution for  $y \rightarrow \delta$ .

- (d) Letting  $\bar{U} = U/|V|$ , rewrite the momentum equation. Using the dimensionless equation for  $\bar{\omega}$  derived in Part (c), verify that

$$\left( \frac{1 + \bar{\omega}}{2 + \bar{\omega}} \right) \frac{d\bar{U}}{d\bar{\omega}} = \frac{\bar{U} - \bar{U}_e}{\bar{\omega}}$$

and verify the solution for  $U_e - U$ .

**7.7** This problem illustrates how nonlinear terms affect numerical stability for parabolic marching methods. Consider the following limiting form of the  $k$ - $\omega$  model.

$$U \frac{\partial \omega}{\partial x} = \alpha \left( \frac{\partial U}{\partial y} \right)^2 - \beta \omega^2$$

We wish to analyze the stability of the solution to this equation under the following discretization approximations.

$$U \frac{\partial \omega}{\partial x} \doteq \frac{U}{\Delta x} [3\omega_{m+1}^i - 4\omega_m + \omega_{m-1}]$$

$$\alpha \left( \frac{\partial U}{\partial y} \right)^2 \doteq \frac{\alpha (\partial U / \partial y)^2}{\omega_{m+1}^{i-1}} \omega_{m+1}^i$$

$$\beta \omega^2 \doteq (1 + \psi_\omega) \beta \omega_{m+1}^{i-1} \omega_{m+1}^i - \psi_\omega \beta (\omega_{m+1}^{i-1})^2$$

- (a) Assuming that  $\omega_{m+1}^i$  is the sum of the exact solution to the discretized equation,  $\omega_{m+1}$ , and an error term,  $\delta \omega^i$ , viz.,

$$\omega_{m+1}^i = \omega_{m+1} + \delta \omega^i$$

linearize the discretized equation for  $\omega$  and verify that

$$\frac{\delta \omega^i}{\delta \omega^{i-1}} = \frac{(\psi_\omega - 1) \beta \omega_{m+1}^2 - \alpha (\partial U / \partial y)^2}{3U \omega_{m+1} / \Delta x - \alpha (\partial U / \partial y)^2 + (\psi_\omega + 1) \beta \omega_{m+1}^2}$$

- (b) Using the fact that  $\omega_{m+1}$  satisfies the exact discretized equation, simplify the denominator and show that

$$\frac{\delta \omega^i}{\delta \omega^{i-1}} = \frac{(\psi_\omega - 1) - \alpha (\partial U / \partial y)^2 / (\beta \omega_{m+1}^2)}{\psi_\omega + U(4\omega_m - \omega_{m-1}) / (\omega_{m+1}^2 \Delta x)}$$

- (c) Assuming the term proportional to  $U$  is negligible, determine the condition that  $\psi_\omega$  must satisfy in order to insure that  $|\delta \omega^i / \delta \omega^{i-1}| < 1$ .

**7.8** Using von Neumann stability analysis, determine  $G$  and any condition required for stability of the following finite-difference schemes. Assume  $U > 0$ ,  $\nu > 0$  and  $S < 0$ .

(a) Euler's method:

$$k_j^{n+1} = k_j^n - \frac{U \Delta t}{2 \Delta x} (k_{j+1}^{n+1} - k_{j-1}^{n+1})$$

(b) Richardson's method:

$$k_j^{n+1} = k_j^{n-1} + \frac{2\nu \Delta t}{(\Delta x)^2} (k_{j+1}^n - 2k_j^n + k_{j-1}^n)$$

(c) Crank and Nicolson's method:

$$k_j^{n+1} = k_j^n - \frac{U \Delta t}{4 \Delta x} (k_{j+1}^{n+1} + k_{j+1}^n - k_{j-1}^{n+1} - k_{j-1}^n) + \frac{1}{2} S \Delta t (k_j^{n+1} + k_j^n)$$

**7.9** Consider the following one-dimensional wave equation with source and diffusion terms.

$$\frac{\partial k}{\partial t} + U \frac{\partial k}{\partial x} = S k + \nu \frac{\partial^2 k}{\partial x^2}$$

where  $U > 0$ ,  $\nu > 0$  and  $S$  can be either positive or negative.

(a) Cast this equation in finite-difference form using Crank-Nicolson differencing and the following approximation for the source term.

$$S k \doteq S [\psi k_j^n + (1 - \psi) k_j^{n+1}], \quad 0 \leq \psi \leq 1$$

(b) Using von Neumann stability analysis, determine  $G$  and any condition required for stability of this finite-difference scheme. How do your results compare to the analysis of Equation (7.91) in Section 7.4?

**7.10** Verify that the dependent-variable and inviscid-flux vectors in Equation (7.115) can be written as

$$\mathbf{Q} = \begin{Bmatrix} Q_1 \\ Q_2 \\ Q_3 \\ Q_4 \\ Q_5 \end{Bmatrix}, \quad \mathbf{F} = \begin{Bmatrix} Q_2 \\ (\frac{3-\gamma}{2}) Q_2^2 / Q_1 + (\gamma - 1) Q_3 - (\gamma - 1) Q_4 \\ \gamma Q_2 Q_3 / Q_1 - (\frac{\gamma-1}{2}) Q_2^3 / Q_1^2 - (\gamma - 1) Q_2 Q_4 / Q_1 \\ Q_2 Q_4 / Q_1 \\ Q_2 Q_5 / Q_1 \end{Bmatrix}$$

and show that the flux-Jacobian matrix is given by Equation (7.119).

**7.11** The following table represents partial results for a one-dimensional finite-difference computation using a second-order accurate, time-marching method. The computation was done on grids with 50, 100 and 200 points. Use Richardson extrapolation to estimate the discretization error at each point for the two finest grids. Based on your results, make a table of the results below and add a column with your best estimate of the continuum solution (grid-point spacing  $\rightarrow 0$ ) to the differential equation.

$j$	$\phi_{50}$	$j$	$\phi_{100}$	$j$	$\phi_{200}$
1	.5592	1	.5628	1	.5607
2	.5700	3	.5740	5	.5726
3	.5737	5	.5748	9	.5745
4	.5615	7	.5557	13	.5573

# Chapter 8

## New Horizons

The focus of the previous chapters has been on approximate models for use in general engineering applications. Throughout this text, we have stressed the virtue of using the minimum amount of complexity while capturing the essence of the relevant physics. This is the same notion that G. I. Taylor described as the “simple model/simple experiment” approach. Nevertheless, no pretense has been made that any of the models devised in this spirit applies universally to all turbulent flows. We must always proceed with some degree of caution since there is no guarantee that such models are accurate beyond their established data base. Thus, while simplicity has its virtues for many practical engineering applications, there is a danger that must not be overlooked. Specifically, as quipped by H. L. Mencken, “to every difficult question there is a simple answer — which is wrong.”

This chapter discusses modern efforts that more directly address the physics of turbulence without introducing Reynolds closure approximations. We begin by discussing Direct Numerical Simulation (DNS) in which the exact Navier-Stokes and continuity equations are solved, albeit at relatively low Reynolds numbers. Next, we turn to Large Eddy Simulation (LES) in which the largest eddies are computed exactly and the smallest eddies are modeled, hopefully with a non-critical impact on the simulation. Finally, we discuss current efforts in chaos studies, and their possible relevance to turbulence.

### 8.1 Background Information

Before plunging into these topics, it is worthwhile to pause and discuss certain aspects of turbulence that we haven’t explicitly addressed in preceding

chapters. The first important point we must consider is that of the smallest scales of turbulence. Our primary focus in devising closure approximations has been on the dynamics of the largest eddies, which account for most of the transport of properties in a turbulent flow. Our use of dimensional analysis, in which molecular viscosity has been ignored, guarantees that the closure approximations involve length scales typical of the energy-bearing eddies whose Reynolds number — however defined — is much larger than one except close to a solid surface, i.e., in the viscous wall region,  $y^+ < 3$ , say. (This is the reason that viscous damping functions are often needed close to a solid boundary where the dissipating eddies dominate, and even the energy-bearing eddies have Reynolds numbers of order one.) To achieve a more complete description of turbulence, we must determine what the smallest length scale in a turbulent flow is.

Interestingly, we can estimate the magnitude of the smallest scales by again appealing to dimensional analysis. Of course, to establish the relevant dimensional parameters, we must first consider the physics of turbulence at very small length scales. We begin by recalling that the cascading process present in all turbulent flows involves a transfer of kinetic energy from larger eddies to smaller eddies. Dissipation of kinetic energy to heat through the action of molecular viscosity occurs at the scale of the smallest eddies. Because small-scale motion tends to occur on a short time scale, we can reasonably assume that such motion is independent of the relatively slow dynamics of the large eddies and of the mean flow. Hence, the smaller eddies should be in a state where the rate of receiving energy from the larger eddies is very nearly equal to the rate at which the smallest eddies dissipate the energy to heat. This is known as Kolmogorov's (1941) **universal equilibrium theory**, a corollary of which is his **hypothesis of local isotropy** that we appealed to in developing some of the closure approximations in Chapter 6. Hence, the motion at the smallest scales should depend only upon: (a) the rate at which the larger eddies supply energy,  $\epsilon$ , and (b) the kinematic viscosity,  $\nu$ .

Having established  $\epsilon$  and  $\nu$  as the appropriate dimensional parameters, it is a simple matter to form the following length ( $\eta$ ), time ( $\tau$ ) and velocity ( $v$ ) scales.

$$\eta \equiv (\nu^3/\epsilon)^{1/4}, \quad \tau \equiv (\nu/\epsilon)^{1/2}, \quad v \equiv (\nu\epsilon)^{1/4} \quad (8.1)$$

These are the **Kolmogorov scales** of length, time and velocity. To appreciate how small the Kolmogorov length scale is for example, recall that the length scale appropriate to the energy-bearing eddies,  $\ell$ , (often referred to as the **integral scale** in statistical turbulence theory) is related to  $\epsilon$  by

Equation (4.8), so that

$$\frac{\eta}{\ell} \sim Re_T^{-3/4} \quad (8.2)$$

where  $Re_T = k^{1/2}\ell/\nu$  is the usual turbulence Reynolds number. Since values of  $Re_T$  in excess of  $10^4$  are typical of fully-developed turbulent boundary layers and  $\ell \sim 0.1\delta$  where  $\delta$  is boundary-layer thickness, the Kolmogorov length scale,  $\eta$ , outside the viscous wall region is less than one ten-thousandth times the thickness of the boundary layer.

Another turbulence length scale often referred to in the statistical theory of turbulence is the **Taylor microscale**,  $\lambda$  [c.f., Tennekes and Lumley (1983) or Hinze (1975)]. For isotropic turbulence, it is defined by

$$\epsilon = 15\nu \overline{\left(\frac{\partial u'}{\partial x}\right)^2} \equiv 15\nu \frac{\overline{u'^2}}{\lambda^2} \quad (8.3)$$

Again, using Equation (4.8), and assuming  $k \sim \overline{u'^2}$ , we conclude that

$$\frac{\lambda}{\ell} \sim Re_T^{-1/2} \quad \text{or} \quad \lambda \sim (\ell\eta^2)^{1/3} \quad (8.4)$$

Thus, in general we can say that for high-Reynolds-number turbulence there is a distinct separation of these scales, i.e.,

$$\eta \ll \lambda \ll \ell \quad (8.5)$$

Results of numerical simulations are often characterized in terms of the **microscale Reynolds number**,  $Re_\lambda$ , defined by

$$Re_\lambda = k^{1/2}\lambda/\nu \quad (8.6)$$

Finally, the **eddy turnover time**,  $\tau_{turnover}$ , is simply the ratio of the macroscales for length,  $\ell$ , and velocity,  $k^{1/2}$ , and is given by

$$\tau_{turnover} \sim \ell/k^{1/2} \quad (8.7)$$

The eddy turnover time is a measure of the time it takes an eddy to interact with its surroundings. It is also the reciprocal of the specific dissipation rate,  $\omega$ .

A second important consideration is the spectral representation of turbulence properties. That is, since turbulence contains a continuous spectrum of scales, it is often convenient to cast our analysis in terms of the **spectral distribution** of energy. If  $\kappa$  denotes wavenumber and  $E(\kappa)d\kappa$  is the turbulence kinetic energy contained between wavenumbers  $\kappa$  and  $\kappa+d\kappa$ , we can say

$$k \equiv \frac{1}{2}\overline{u'_i u'_i} = \int_0^\infty E(\kappa) d\kappa \quad (8.8)$$



Recall that  $k$  is half the trace of the autocorrelation tensor,  $\mathcal{R}_{ij}$ , defined in Equation (4.50). Correspondingly, the **energy spectral density** or **energy spectrum function**,  $E(\kappa)$ , is the Fourier transform of half the trace of  $\mathcal{R}_{ij}$ . In general, we regard a spectral representation as a decomposition into wavenumbers ( $\kappa$ ) or, equivalently, wavelengths ( $2\pi/\kappa$ ). See Tennekes and Lumley (1983) for a detailed discussion of energy spectra. In the present context, we think of the reciprocal of  $\kappa$  as the eddy size.

In general,  $E(\kappa)$  is a function of  $\nu$ ,  $\epsilon$ ,  $\ell$ ,  $\kappa$  and the mean strain rate,  $S$ . We needn't consider  $k$  as it can be expressed in terms of  $\epsilon$  and  $\ell$ . As part of his universal equilibrium theory, Kolmogorov also made the hypothesis that for very large Reynolds number, there is a range of eddy sizes between the largest and smallest for which the cascade process is independent of the statistics of the energy-containing eddies (so that  $S$  and  $\ell$  can be ignored) and of the direct effects of molecular viscosity (so that  $\nu$  can be ignored). The idea is that a range of wavenumbers exists in which the energy transferred by inertial effects dominates, wherefore  $E(\kappa)$  depends only upon  $\epsilon$  and  $\kappa$ . On dimensional grounds, he thus concluded that

$$E(\kappa) = C_K \epsilon^{2/3} \kappa^{-5/3}, \quad \frac{1}{\ell} \ll \kappa \ll \frac{1}{\eta} \quad (8.9)$$

where  $C_K$  is the Kolmogorov constant. Because inertial transfer of energy dominates, Kolmogorov identified this range of wavenumbers as the **inertial subrange**. The existence of the inertial subrange has been verified by many experiments and numerical simulations, although many years passed before definitive data were available to confirm its existence. Figure 8.1 shows a typical energy spectrum for a turbulent flow.

The Kolmogorov  $-5/3$  law is so well established that, as noted by Rogallo and Moin (1984), theoretical or numerical predictions are regarded with skepticism if they fail to reproduce it. Its standing is as important as the law of the wall. With these preliminary remarks in hand, we are now in a position to discuss DNS and LES in the next two sections.

## 8.2 Direct Numerical Simulation

A direct numerical simulation, or DNS for short, means a complete time-dependent solution of the Navier-Stokes and continuity equations. The value of such simulations is obvious. From a practical standpoint, computed statistics can be used to test proposed closure approximations in engineering models. At the most fundamental level, they can be used to obtain understanding of turbulence structure and processes that can be of value in developing turbulence control methods (e.g., drag reduction) or prediction

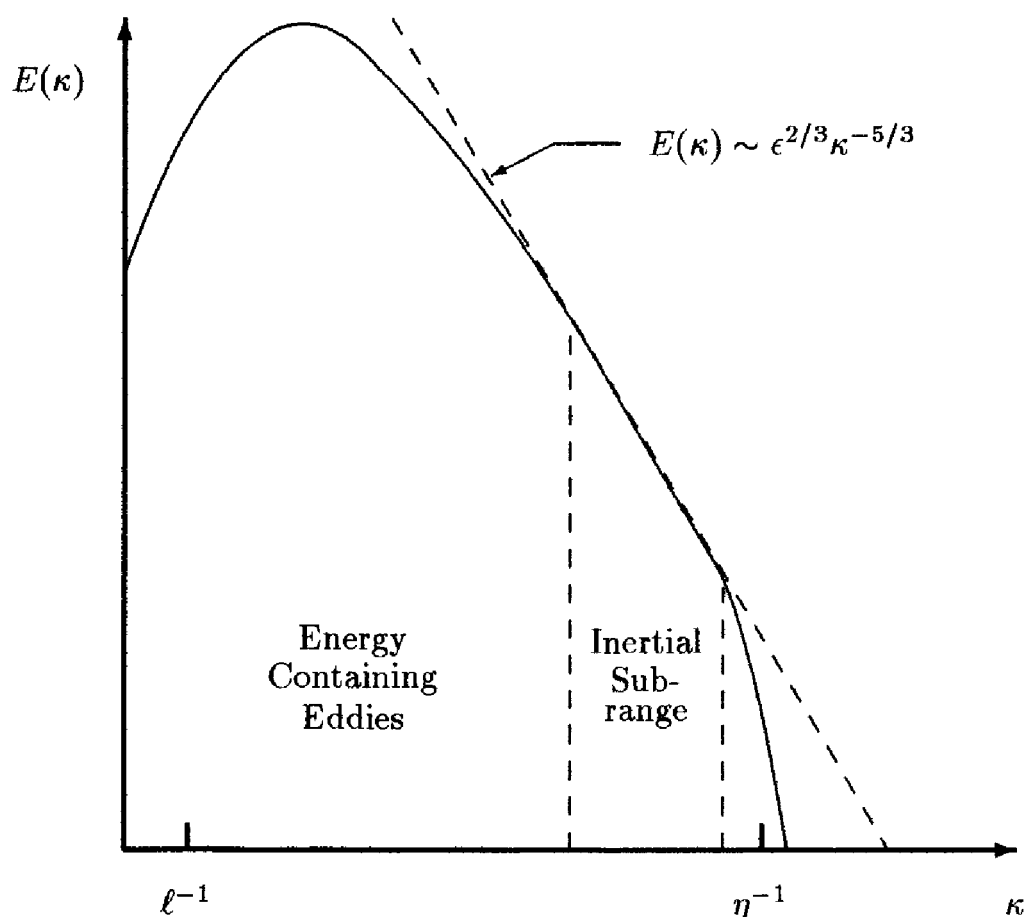


Figure 8.1: Energy spectrum for a turbulent flow — log-log scales.

methods. They can also be viewed as an additional source of experimental data that have been taken with unobtrusive measuring techniques. This is especially desirable in obtaining information about essentially unmeasurable properties like pressure fluctuations.

All of these comments assume the DNS is free of significant numerical, and other, forms of error. This is a nontrivial consideration, and the primary concerns in DNS are related to numerical accuracy, specification of boundary and initial conditions, and making optimum use of available computer resources. This section will discuss these issues briefly. For more detail at an introductory level, see the excellent (although a bit dated) review article by Rogallo and Moin (1984).

Estimating the number of grid points and timesteps needed to perform an accurate DNS reveals the complexity of the problem from a computational point of view. As an example, consider incompressible turbulent flow in a channel of height  $H$ . The computational domain must be of sufficient extent to accommodate the largest turbulence scales. In channel flow, eddies are elongated in the direction parallel to the channel walls, and their

length  $\Lambda$  is known to be about  $2H$ . Also, in principle, the grid must be fine enough to resolve the smallest eddies whose size is of the order of the Kolmogorov length scale,  $\eta$ . Assuming that at least 4 grid points in each direction are needed to resolve an eddy (since we need adequate resolution of derivatives), we estimate that the total number of grid points for uniform spacing,  $N_{uniform}$ , is

$$N_{uniform} \approx \left[4 \frac{\Lambda}{\eta}\right]^3 = \left[8H \left(\frac{\epsilon}{\nu^3}\right)^{1/4}\right]^3 \quad (8.10)$$

Now, in channel flow, the average dissipation is  $\epsilon \approx 2u_\tau^2 U_m / H$  where  $U_m$  is the average velocity across the channel, and  $U_m / u_\tau \approx 20$ . Substituting these estimates into Equation (8.10), we arrive at

$$N_{uniform} \approx (110 Re_\tau)^{9/4}, \quad Re_\tau = \frac{u_\tau H / 2}{\nu} \quad (8.11)$$

In practice, it is wasteful to use uniformly spaced grid points since there are regions where  $\epsilon$  is small and the Kolmogorov length scale is much larger than it is near the surface where  $\epsilon$  is largest. By using stretched grids to concentrate points where the smallest eddies reside, experience [Moser and Moin (1984), Kim, Moin and Moser (1987)] shows that the factor of 110 in Equation (8.11) can be replaced by about 3. Thus, the actual number of grid points typically used in a DNS of channel flow,  $N_{DNS}$ , is

$$N_{DNS} \approx (3 Re_\tau)^{9/4} \quad (8.12)$$

Similarly, the timestep in the computation,  $\Delta t$ , should be of the same order as the Kolmogorov time scale,  $\tau = (\nu/\epsilon)^{1/2}$ . Based on the results of Kim, et al. (1987), the timestep must be

$$\Delta t \approx \frac{.003}{\sqrt{Re_\tau}} \frac{H}{u_\tau} \quad (8.13)$$

To appreciate how prohibitive these constraints are, consider the channel flow experiments done by Laufer (1951) at Reynolds numbers of 12,300, 30,800 and 61,600 and the experiment of Comte-Bellot (1963) at a Reynolds number of 230,000. Table 8.1 lists the number of grid points and timesteps required to perform a DNS, assuming the time required to reach a statistically steady state is  $100H/U_m \sim 5H/u_\tau$ . Clearly, computer memory limitations make all but the lowest Reynolds number considered by Laufer impractical with computers of the early 1990's. However, it is very impressive indeed that a simulation is feasible for at least one of Laufer's cases.

Table 8.1: Grid point and timestep requirements for channel-flow DNS

$Re_H$	$Re_\tau$	$N_{DNS}$	Timesteps
12,300	360	$6.7 \cdot 10^6$	32,000
30,800	800	$4.0 \cdot 10^7$	47,000
61,600	1,450	$1.5 \cdot 10^8$	63,000
230,000	4,650	$2.1 \cdot 10^9$	114,000

The computations of Kim, et al. (1987) provide an example of the computer resources required for DNS of channel flow. To demonstrate grid convergence of their methods, they compute channel flow with  $Re_\tau = 180$ , corresponding to  $Re_H \approx 6,000$  using grids with  $2 \cdot 10^6$  and  $4 \cdot 10^6$  points. For the finer grid, the CPU time on a Cray X/MP was 40 seconds per timestep, was run for a total time  $5H/u_\tau$ , and required 250 CPU hours.

Both second-order accurate and fourth-order accurate numerical algorithms have been used in DNS research to advance the solution in time. There are two primary concerns regarding numerical treatment of the spatial directions. The first is achieving accurate representations of derivatives, especially at the smallest scales (or, equivalently, the highest wavenumbers). Spectral methods — Fourier series in the spatial directions — are used to insure accurate computation of derivatives. If derivatives are inaccurate at the smallest scales, excessive energy accumulates in the smallest finite-difference cells, resulting in excessive dissipation. Consequently, the primary issue in demonstrating grid convergence of a DNS is to verify that the energy spectrum,  $E(\kappa)$ , displays a rapid decay, often referred to as the **rolloff**, near the Kolmogorov length scale,  $\eta$ . While spectral methods are more accurate for computing derivatives at the smallest scales, they are not amenable to arbitrary grid-point spacing. The second issue is to avoid a phenomenon known as **aliasing**. This occurs when nonlinear interactions among the resolved wavenumbers produce waves with wavenumbers greater than  $\kappa_{max}$ , which can be misinterpreted numerically. If special precautions are not taken, this can result in a spurious transfer of energy to small wavenumbers [Ferziger (1976)].

In their grid-convergence study, Kim, et al. (1987) show that their energy spectra display the characteristic rolloff approaching the Kolmogorov length scale. This is true even though their computations actually resolve the flow down to about  $2\eta$ , rather than to  $\eta$ . This means the actual dissipation results from a combination of the true viscosity and some amount of

numerical viscosity. Although the smallest eddies are not resolved in regions such as the viscous superlayer near the edge of a turbulent/nonturbulent interface, the resolution is fine enough to insure that the rate of dissipation is correctly predicted. Most importantly, the peak dissipation near the surface occurs between  $6\eta$  and  $10\eta$ , which is well resolved in the simulation. As in physical turbulence, the smallest eddies in the DNS apparently achieve an equilibrium state in which they dissipate the kinetic energy cascaded from the larger eddies.

As an example of the type of numerical algorithm used in DNS research to advance the solution in time, Kim, et al. (1987), use a procedure very similar to that used in Program EDDYBL (Section 7.3 and Appendix C), viz., Crank-Nicolson differencing for the viscous terms, and the three-point forward difference formulation (Adams-Bashforth) for the convective terms. To improve numerical accuracy for the smallest eddies, the equations are Fourier transformed in the streamwise and spanwise directions. This also permits use of the Fast Fourier Transform (FFT) [Cooley and Tukey (1965)], which is extremely efficient on a computer. Fourier transforms are suitable as the flow can be treated as though it is periodic in these directions. This cannot be done in the direction normal to the surface because of the no-slip boundary condition. Rather, a Chebychev polynomial expansion is used, which yields similar gains in numerical accuracy and computational efficiency. Using Fourier, Chebychev and other eigenfunction expansions, is known as the **spectral method** in its most precise form. A more-efficient approximation exists known as the **pseudo-spectral method**. Spectral and pseudo-spectral methods were pioneered by Orszag, et al. [Patterson and Orszag (1971), Orszag (1972), and Gottlieb and Orszag (1977)].

The primary difficulty with boundary conditions in a DNS is at open boundaries. Because of the elliptic nature of the problem, the flow at such boundaries depends on the unknown flow outside the computational domain. This problem is circumvented by imposing periodic boundary conditions for directions in which the flow is statistically homogeneous (e.g., the streamwise and spanwise directions in channel flow). Flows that grow in the streamwise direction in a nearly self-similar manner (e.g., equilibrium boundary layers) can be reduced to approximate homogeneity by a coordinate transformation [Spalart (1986), Spalart (1988), Spalart (1989)]. Most simulations done to date are homogeneous or periodic in at least two spatial directions. Boundary conditions at a solid boundary pose no special problems where the no-slip velocity boundary condition applies.

Initial conditions are often obtained from results of a previous simulation if available. If no such results are available, a random fluctuating velocity field can be added to a prescribed mean-velocity field. After a few eddy turnover times, the correct statistics ultimately evolve. Interestingly, the

work done to date shows a feature of turbulence that illustrates one of its mysteries. Suppose we have generated a solution from some given set of initial conditions. Suppose further that we make a small perturbation in the initial conditions and repeat the computation. We find that, after a few eddy-turnover times, the second solution, or **realization**, is very different from the first. However, in terms of all statistical measures, the two flows are identical!

This is the classical problem of **predictability** discussed, for example, by Sandham and Kleiser (1992). As a simple example, two strangers in a crowd tend to drift apart. If one steps on another's foot twice, the steppeer thinks the stepor does it on purpose, although the cause and effect are completely random. Thus, while somewhat disconcerting to the mathematician, this phenomenon should come as no great surprise to the engineer.

DNS matured rapidly during the 1980's and continues to develop as more and more powerful computers appear. As an example, DNS data are currently available for the following flows, and the list of applications continues to grow.

- Curved channel flow
- Channel flow, with and without heat transfer — values of  $Re_H$  as high as 13,750 have been achieved
- Two-dimensional boundary layers in various pressure gradients — values of  $Re_\theta$  as high as 1,410 have been achieved
- Three-dimensional flows including flow over a swept wing
- Two-dimensional separating and reattaching flows
  - (a) shallow separation bubble on a flat surface
  - (b) flow over a backward-facing step
- Two-dimensional time- and spatially-developing mixing layers
- Three-dimensional Ekman layer
- Two-dimensional buoyant flows
- Two-dimensional homogeneously-strained flows
- Two-dimensional homogeneous flows with constant-density chemical reactions
- Compressible homogeneous flows with bulk compression in one, two or three directions
- Transitional compressible flows

### 8.3 Large Eddy Simulation

A Large Eddy Simulation, or LES for short, is a computation in which the large eddies are computed and the smallest eddies are modeled. The underlying premise is that the largest eddies are directly affected by the boundary conditions and must be computed. By contrast, the small-scale turbulence is more nearly isotropic and has universal characteristics; it is thus more amenable to modeling.

Because LES involves modeling the smallest eddies, the smallest finite-difference cells can be much larger than the Kolmogorov length, and much larger timesteps can be taken than are possible in a DNS. Hence, for a given computing cost, it is possible to achieve much higher Reynolds numbers with LES than with DNS. Based on a combination of estimates given by Rogallo and Moin (1984) and recent channel-flow LES results of Yang and Ferziger (1993), the number of grid points required for channel flow,  $N_{LES}$  should be

$$N_{LES} \approx \left( \frac{0.4}{Re_\tau^{1/4}} \right) N_{DNS} \quad (8.14)$$

Table 8.2 compares grid point requirements based on this estimate. Credible channel-flow results have been obtained with fewer grid points by using the law of the wall to obviate integration through the viscous sub-layer. Deardorff (1970), for example has done a LES of Laufer's (1951)  $Re_H = 61,600$  channel-flow experiment using just 6,720 mesh points. Schumann (1975) has computed channel flow with  $Re_H > 10^4$  using 65,536 points, and the computations even include temperature fluctuations and heat transfer. Grotzbach (1979) has done a LES for buoyancy-driven mixing in a nuclear reactor with  $16 \times 16 \times 8 = 2,048$  grid points. In all cases, sensible statistics have been obtained for the largest eddies, although mean-flow properties such as velocity sometimes differ from measurements by as much as 15%. While using the law of the wall as a boundary condition is attractive from a computing-cost point of view, this approach has been abandoned in most recent LES work. No viable scheme has been developed to establish the fluctuating quantities in the log layer, which are needed along with the overall statistics to achieve a suitable boundary condition. As a final comment, although LES is more economical than DNS (typically requiring 5 to 10% of the CPU time needed for DNS), the method still requires large computer resources.

Aside from the issue of the need to resolve the smallest eddies, the comments regarding DNS numerics, boundary and initial conditions in the previous section hold for LES as well. The primary issue in accuracy remains that of computing derivatives at the smallest scales (highest wavenumbers) resolved. The ultimate test of grid convergence is again the requirement

Table 8.2: Grid point requirements for channel-flow DNS and LES

$Re_H$	$Re_\tau$	$N_{DNS}$	$N_{LES}$
12,300	360	$6.7 \cdot 10^6$	$6.1 \cdot 10^5$
30,800	800	$4.0 \cdot 10^7$	$3.0 \cdot 10^6$
61,600	1,450	$1.5 \cdot 10^8$	$1.0 \cdot 10^7$
230,000	4,650	$2.1 \cdot 10^9$	$1.0 \cdot 10^8$

that excessive energy must not accumulate in the smallest scales. The primary requirement is to get the dissipation rate right; details of the dissipating eddies are unimportant in LES. (By contrast, DNS requires accurate simulation of the dissipating eddies.) If spectral or pseudo-spectral methods are used, the same boundary-condition difficulties hold in both DNS and LES.

To understand the primary difference between DNS and LES, we must introduce the concept of **filtering**. To understand this concept, note first that the values of flow properties at discrete points in a numerical simulation represent averaged values. To see this explicitly, consider the central-difference approximation for the first derivative of a continuous variable,  $u(x)$ , in a grid with points spaced a distance  $h$  apart. We can write this as follows.

$$\frac{u(x+h) - u(x-h)}{2h} = \frac{d}{dx} \left[ \frac{1}{2h} \int_{x-h}^{x+h} u(\xi) d\xi \right] \quad (8.15)$$

This shows that the central-difference approximation can be thought of as an operator that **filters out scales smaller than the mesh size**. Furthermore, the approximation yields the derivative of an averaged value of  $u(x)$ .

There are many kinds of filters that can be used. The simplest type of filter is the **volume-average box filter** used by Deardorff (1970), one of the earliest LES researchers. The filter is:

$$\bar{u}_i(\mathbf{x}, t) = \frac{1}{\Delta^3} \int_{x-\frac{1}{2}\Delta x}^{x+\frac{1}{2}\Delta x} \int_{y-\frac{1}{2}\Delta y}^{y+\frac{1}{2}\Delta y} \int_{z-\frac{1}{2}\Delta z}^{z+\frac{1}{2}\Delta z} u_i(\xi, t) d\xi d\eta d\zeta \quad (8.16)$$

The quantity  $\bar{u}_i$  denotes the **resolvable-scale filtered velocity**. The **subgrid scale (SGS) velocity**,  $u'_i$ , and the **filter width**,  $\Delta$ , are given by

$$u'_i = u_i - \bar{u}_i \quad \text{and} \quad \Delta = (\Delta x \Delta y \Delta z)^{1/3} \quad (8.17)$$



Leonard (1974) defines a generalized filter as a convolution integral, viz.,

$$\bar{u}_i(\mathbf{x}, t) = \iiint G(\mathbf{x} - \boldsymbol{\xi}; \Delta) u_i(\boldsymbol{\xi}, t) d^3\boldsymbol{\xi} \quad (8.18)$$

The **filter function**,  $G$ , is normalized by requiring that

$$\iiint G(\mathbf{x} - \boldsymbol{\xi}; \Delta) d^3\boldsymbol{\xi} = 1 \quad (8.19)$$

In terms of the filter function, the volume-average box filter as defined in Equation (8.16) is:

$$G(\mathbf{x} - \boldsymbol{\xi}; \Delta) = \begin{cases} 1/\Delta^3, & |\mathbf{x} - \boldsymbol{\xi}| < \Delta/2 \\ 0, & \text{otherwise} \end{cases} \quad (8.20)$$

The Fourier transform of Equation (8.18) is  $\bar{U}_i(\boldsymbol{\kappa}, t) = \mathcal{G}(\boldsymbol{\kappa})\mathcal{U}_i(\boldsymbol{\kappa}, t)$  where  $\mathcal{U}_i$  and  $\mathcal{G}$  represent the Fourier transforms of  $u_i$  and  $G$ . Fourier spectral methods implicitly filter with

$$\mathcal{G}(\boldsymbol{\kappa}; \Delta) = 0 \quad \text{for} \quad |\boldsymbol{\kappa}| > \kappa_{max} = 2\pi/\Delta \quad (8.21)$$

As an example, Orszag et al. [see Ferziger (1976)] use

$$G(\mathbf{x} - \boldsymbol{\xi}; \Delta) = \frac{1}{\Delta^3} \prod_{i=1}^3 \frac{\sin(x_i - \xi_i)/\Delta}{(x_i - \xi_i)/\Delta} \quad (8.22)$$

The **Gaussian filter** [Ferziger (1976)] is popular in LES research, and is defined by

$$G(\mathbf{x} - \boldsymbol{\xi}; \Delta) = \left( \frac{6}{\pi\Delta^2} \right)^{3/2} \exp \left( -6 \frac{|\mathbf{x} - \boldsymbol{\xi}|^2}{\Delta^2} \right) \quad (8.23)$$

Many other filters have been proposed and used, some of which are neither isotropic nor homogeneous. In all cases however, the filter introduces a scale  $\Delta$  that represents the smallest turbulence scale allowed by the filter.

The filter provides a formal definition of the averaging process and separates the **resolvable scales** from the **subgrid scales**. We use filtering to derive the **resolvable-scale equations**. For incompressible flow, the continuity and Navier-Stokes equations assume the following form.

$$\frac{\partial \bar{u}_i}{\partial x_i} = 0 \quad (8.24)$$

$$\frac{\partial \bar{u}_i}{\partial t} + \frac{\partial}{\partial x_j} (\bar{u}_i \bar{u}_j) = -\frac{1}{\rho} \frac{\partial \bar{p}}{\partial x_i} + \nu \frac{\partial^2 \bar{u}_i}{\partial x_k \partial x_k} \quad (8.25)$$

Now, the convective flux is given by

$$\overline{u_i u_j} = \bar{u}_i \bar{u}_j + L_{ij} + C_{ij} + R_{ij} \quad (8.26)$$

where

$$\left. \begin{aligned} L_{ij} &= \overline{\bar{u}_i \bar{u}_j} - \bar{u}_i \bar{u}_j \\ C_{ij} &= \overline{\bar{u}_i u'_j} + \overline{\bar{u}_j u'_i} \\ R_{ij} &= \overline{u'_i u'_j} \end{aligned} \right\} \quad (8.27)$$

Note that filtering differs from standard averaging in one important respect:

$$\bar{\bar{u}}_i \neq \bar{u}_i \quad (8.28)$$

i.e., a second averaging yields a different result from the first averaging. The tensors  $L_{ij}$ ,  $C_{ij}$  and  $R_{ij}$  are known as the **Leonard stress**, **cross-term stress** and the **SGS Reynolds stress**, respectively.

Leonard (1974) shows that the Leonard stress term removes significant energy from the resolvable scales. It can be computed directly and needn't be modeled. This is sometimes inconvenient however, depending on the numerical method used. Leonard also demonstrates that since  $\bar{u}_i$  is a smooth function,  $L_{ij}$  can be computed in terms of its Taylor series expansion, the first term of which is

$$L_{ij} \approx \frac{\gamma_\ell}{2} \nabla^2 (\bar{u}_i \bar{u}_j), \quad \gamma_\ell = \iiint |\xi|^2 G(\xi) d^3 \xi \quad (8.29)$$

Clark, et al. (1979) verify that this representation is very accurate at low Reynolds number by comparing with DNS results. However, as shown by Shaanan, Ferziger and Reynolds (1975), the Leonard stresses are of the same order as the truncation error when a finite-difference scheme of second-order accuracy is used, and are thus implicitly represented.

The cross-term stress tensor,  $C_{ij}$ , also drains significant energy from the resolvable scales. An expansion similar to Equation (8.29) can be made for  $C_{ij}$ . However, most current efforts model the sum of  $C_{ij}$  and  $R_{ij}$ . Clearly, the accuracy of a LES depends critically upon the model used for these terms.

We can now rearrange Equation (8.25) into a more conventional form, i.e.,

$$\frac{\partial \bar{u}_i}{\partial t} + \frac{\partial}{\partial x_j} (\bar{u}_i \bar{u}_j) = -\frac{1}{\rho} \frac{\partial P}{\partial x_i} + \frac{\partial}{\partial x_j} \left[ \nu \frac{\partial \bar{u}_i}{\partial x_j} + \frac{\tau_{ij}}{\rho} \right] \quad (8.30)$$

where

$$\left. \begin{aligned} \frac{\tau_{ij}}{\rho} &= - \left( Q_{ij} - \frac{1}{3} Q_{kk} \delta_{ij} \right) \\ P &= \bar{p} + \frac{1}{3} \rho Q_{kk} \delta_{ij} \\ Q_{ij} &= R_{ij} + C_{ij} \end{aligned} \right\} \quad (8.31)$$

At this point, the **fundamental problem of Large Eddy Simulation** is evident. Specifically, we must establish a satisfactory model for the SGS stresses as represented by the tensor  $Q_{ij}$ . To emphasize the importance of achieving an accurate SGS stress model, consider the following. In simulating the decay of homogeneous isotropic turbulence with  $16^3 = 4,096$  and  $32^3 = 32,768$  grid points, Ferziger (1976) reports that the SGS turbulence energy is 29% and 20%, respectively, of the total. Thus, the subgrid scales constitute a significant portion of the turbulence spectrum. The various attempts at developing a satisfactory SGS stress model during the past four decades resemble the research efforts on engineering models discussed in Chapters 3 - 6. That is, models have been postulated that range from a simple gradient-diffusion model [Smagorinsky (1963)], to a one-equation model [Lilly (1966)], to the analog of a second-order closure model [Deardorff (1973)]. Nonlinear stress-strain rate relationships have even been postulated [Bardina, Ferziger and Reynolds (1983)]. Only the analog of the two-equation model appears to have been overlooked, most likely because the filter width serves as a readily available length scale.

Smagorinsky (1963) was the first to postulate a model for the SGS stresses. The model assumes the SGS stresses follow a gradient-diffusion process, similar to molecular motion. Consequently,  $\tau_{ij}$  is given by

$$\tau_{ij} = 2\mu_T S_{ij}, \quad S_{ij} = \frac{1}{2} \left( \frac{\partial \bar{u}_i}{\partial x_j} + \frac{\partial \bar{u}_j}{\partial x_i} \right) \quad (8.32)$$

where the **Smagorinsky eddy viscosity** is

$$\mu_T = \rho(C_S \Delta)^2 \sqrt{S_{ij} S_{ij}} \quad (8.33)$$

and  $C_S$  is the Smagorinsky coefficient.

For all of the reasons discussed in Chapter 3, the approximation that the smallest eddies behave like molecules is just not true. They are constantly interacting in a much more complicated manner than the infrequent collisions of molecules. Nevertheless, just as the mixing-length model can be readily calibrated for a given class of flows, so can the Smagorinsky coefficient,  $C_S$ . As with the mixing-length model, the value of  $C_S$  is not universal. Its value varies from flow to flow, and various applications have been done with [Rogallo and Moin (1984)]:

$$0.10 < C_S < 0.24 \quad (8.34)$$

There are two key reasons why the Smagorinsky model has enjoyed some degree of success. First, the model yields sufficient diffusion and dissipation to stabilize the numerical computations. Second, low-order statistics of the larger eddies are usually insensitive to the SGS motions.

In an attempt to incorporate some representation of the dynamics of the subgrid scales and to account for **backscatter** (reverse cascading of energy from smaller to larger eddies), Lilly (1966) postulates that

$$\mu_T = \rho C_L \Delta q \quad (8.35)$$

where  $q^2$  is the SGS kinetic energy, and  $C_L$  is a closure coefficient. An equation for  $q^2$  can be derived from a moment of the Navier-Stokes equation, which involves several terms that must be modeled. This model is very similar to Prandtl's one-equation model (Section 4.2), both in spirit and in results obtained. As pointed out by Schumann (1975) who used the model in his LES research, it is difficult to conclude that any significant improvement over the Smagorinsky model can be obtained with such a model.

The most complicated SGS model has been created by Deardorff (1973) for application to the atmospheric boundary layer. The model consists of 10 partial differential equations and bears a strong resemblance to a second-order closure model. While the model leads to improved predictions, its complexity has discouraged many researchers. This is similar to the situation with the second-order closure models discussed in Chapter 6.

Germano, et al. (1990) [see also Ghosal et al. (1992)], have devised an interesting new concept that they describe as a **Dynamic SGS Model**. Their formulation begins with the Smagorinsky eddy-viscosity approximation. However, rather than fixing the value of  $C_S$  a priori, they permit it to be computed as the LES proceeds. This is accomplished by using two filters. Yang and Ferziger (1993) present compelling evidence that this approach has great potential in their recent computations of flow over a rectangular obstacle in a channel.

Erlebacher, et al. (1987) have pushed the frontiers of LES research into compressible flows. They have formulated a compressible flow SGS model and exercised it in computation of compressible isotropic turbulence. Results obtained are in excellent agreement with DNS results.

In conclusion, LES holds promise as a future design tool, especially as computers continue to increase in speed and memory. Intense efforts are currently focused on devising a satisfactory SGS stress model, which is the primary deficiency of the method at this time. Even if LES is too expensive for modern design efforts, results of LES research can certainly be used to help improve engineering models of turbulence. The future of LES research appears very bright.

## 8.4 Chaos

Our final topic is chaos, a mathematical theory that has attracted considerable attention in recent years. At the present time, no quantitative predictions for properties such as the reattachment length behind a backward-facing step or even the skin friction on a flat plate have been made. Hence, its relevance to turbulence modeling thus far has not been as a competing predictive tool. Rather, the theory's value is in developing qualitative understanding of turbulent flow phenomena.

Chaos abounds with colorful terminology including **fractals**, **folded towel diffeomorphisms**, **smooth noodle maps**, **homeomorphisms**, **Hopf bifurcation** and the all important **strange attractor**. Chaos theory stretches our imagination to think of noninteger dimensional space, and abounds with marvelous geometrical patterns with which the name Mandelbrot is intimately connected.

In the context of turbulence, the primary focus in chaos is upon **nonlinear dynamical systems**, i.e., a coupled system of nonlinear ordinary differential equations. Mathematicians have discovered that certain dynamical systems with a very small number of equations (degrees of freedom) possess extremely complicated (chaotic) solutions. Very simple models have been created that simulate observed physical behavior for nontrivial problems. For example, consider an initially motionless fluid between two horizontal heat-conducting plates in a gravitational field. Now suppose the lower plate is heated slightly. For small temperature difference, viscous forces are sufficient to suppress any mass motion. As the temperature is increased, a threshold is reached where fluid motion begins. A series of convective rolls forms that becomes more and more complicated as the temperature increases, and the flow ultimately becomes turbulent. This is known as **Rayleigh-Bénard instability** or **Rayleigh-Bénard convection**.

One of the famous successes of chaos theory is in describing this phenomenon with the following three coupled **ordinary** differential equations.

$$\left. \begin{aligned} \frac{dX}{dt} &= (Y - X)/Pr_L \\ \frac{dY}{dt} &= -XZ + rX - Y \\ \frac{dZ}{dt} &= XY - bZ \end{aligned} \right\} \quad (8.36)$$

The quantity  $Pr_L$  is the Prandtl number,  $b$  and  $r$  are constants, and  $X$ ,  $Y$  and  $Z$  are related to the streamfunction and temperature. The precise details of the model are given by Bergé, Pomeau and Vidal (1984), and are not important for the present discussion. What is important is the

following. This innocent looking set of equations yields a qualitative analog to the Rayleigh-Bénard convection problem, including the geometry of the convection rolls and a solution that resembles turbulent flow.

The central feature of these equations is that they describe what is known as a strange attractor. This particular attractor was the first to be discovered and is more specifically referred to as the **Lorenz attractor**. For the general case, in some suitably defined **phase space** in which each point characterizes the velocity field within a three-dimensional volume ( $X$ ,  $Y$  and  $Z$  for the Lorenz attractor), the dynamical system sweeps out a curve that we call the attractor. The concept of a phase space is an extension of classical phase-plane analysis of ordinary differential equations [c.f. Bender and Orszag (1978)]. In phase-plane analysis, for example, linear equations have critical points such as the focus, the node and the saddle point. For a dynamical system, if the flow is steady, the curve is a single point, as the velocity is independent of time. If the flow is periodic the curve is closed and we have the familiar limit cycle. The interesting case in chaos is the unsteady, aperiodic case in which the curve asymptotically approaches the strange attractor. If the dynamical system is dissipative, as the Lorenz equations are, the solution trajectories always converge toward an attractor. Additionally, a slight change in the initial conditions for  $X$ ,  $Y$  and  $Z$  causes large changes in the solution.

Chaos theory puts great emphasis on the strange attractor, and one of the primary goals of chaos research is to find a set of equations that correspond to the **turbulence attractor**. A dynamical regime is chaotic if two key conditions are satisfied:

1. Its power spectrum contains a continuous part, i.e., a broad band, regardless of the possible presence of peaks.
2. The autocorrelation function goes to zero in finite time.

Of course, both of these conditions are characteristic of turbulence. The latter condition means there is ultimately a loss of memory of the signal with respect to itself. This feature of chaos accounts for the strange attractor's **sensitive dependence on initial conditions**. That is, on a strange attractor, two neighboring trajectories always diverge, regardless of their initial proximity, so that the trajectory actually followed by the system is very sensitive to initial conditions. In chaos, this is known as the **butterfly effect** — the notion that a butterfly flapping its wings in Beijing today can change storm systems in New York next month. It is also precisely what has been observed about the sensitivity of DNS and LES to initial conditions.

While all of these observations indicate there may be promise in using chaos to tackle the turbulence problem, there are some sobering realities

that must be faced. The broad spectrum of wavelengths in the turbulence spectrum, ranging from the Kolmogorov length scale to the dimension of the flow, is far greater than that of the dynamical systems that have been studied. Hence, as deduced by Keefe (1990) from analysis of DNS data, the dimension of the turbulence attractor (in essence, the number of equations needed to describe the attractor) must be several hundreds for Reynolds numbers barely large enough for turbulence to exist. As noted by Bradshaw (1992), “the most ambitious efforts require an amount of computing time which is not much less than that of a large-eddy simulation.”

The layman oriented book by Gleick (1988) provides an excellent introduction to this fascinating theory in general. As a more focused reference, Deissler (1989) presents a review of chaos studies in fluid mechanics.

# Appendix A

## Cartesian Tensor Analysis

The central point of view of tensor analysis is to provide a systematic way for transforming quantities such as vectors and matrices from one coordinate system to another. Tensor analysis is a very powerful tool for making such transformations, although the analysis generally is very involved. For our purposes, working with Cartesian coordinates is sufficient so that we only need to focus on issues of notation, nomenclature and some special tensors. This appendix presents rudiments of Cartesian tensor analysis.

We begin by addressing the question of notation. In Cartesian tensor analysis we make extensive use of subscripts. For consistency with general tensor analysis nomenclature we will use the terms subscript and index interchangeably. The components of an  $n$ -dimensional vector  $\mathbf{x}$  are denoted as  $x_1, x_2, \dots, x_n$ . For example, in three-dimensional space, we rewrite the coordinate vector  $\mathbf{x} = (x, y, z)$  as  $\mathbf{x} = (x_1, x_2, x_3)$ . Now consider an equation describing a plane in three-dimensional space, viz.,

$$a_1x_1 + a_2x_2 + a_3x_3 = c \quad (\text{A.1})$$

where  $a_i$  and  $c$  are constants. This equation can be written as

$$\sum_{i=1}^3 a_i x_i = c \quad (\text{A.2})$$

In tensor analysis, we introduce the Einstein summation convention and rewrite Equation (A.2) in the shorthand form

$$a_i x_i = c \quad (\text{A.3})$$



The Einstein summation convention is as follows:

**Repetition of an index in a term denotes summation with respect to that index over its range.**

The **range** of an index  $i$  is the set of  $n$  integer values 1 to  $n$ . An index that is summed over is called a **dummy index**; one that is not summed is called a **free index**.

Since a dummy index simply indicates summation, it is immaterial what symbol is used. Thus,  $a_i x_i$  may be replaced by  $a_j x_j$ , which is obvious if we simply note that

$$\sum_{i=1}^3 a_i x_i = \sum_{j=1}^3 a_j x_j \quad (\text{A.4})$$

As an example of an equation with a free index, consider a unit normal vector  $\mathbf{n}$  in three-dimensional space. If the unit normals in the  $x_1$ ,  $x_2$  and  $x_3$  directions are  $\mathbf{i}_1$ ,  $\mathbf{i}_2$  and  $\mathbf{i}_3$ , then the direction cosines  $\alpha_1$ ,  $\alpha_2$  and  $\alpha_3$  for the vector  $\mathbf{n}$  are given by

$$\alpha_k = \mathbf{n} \cdot \mathbf{i}_k \quad (\text{A.5})$$

There is no implied summation in Equation (A.5). Rather, it is a shorthand for the three equations defining the direction cosines. Because the length of a unit vector is one, we can take the dot product of  $(\alpha_1, \alpha_2, \alpha_3)$  with itself and say that

$$\alpha_i \alpha_i = 1 \quad (\text{A.6})$$

As another example, consider the total differential of a function of three variables,  $p(x_1, x_2, x_3)$ . We have

$$dp = \frac{\partial p}{\partial x_1} dx_1 + \frac{\partial p}{\partial x_2} dx_2 + \frac{\partial p}{\partial x_3} dx_3 \quad (\text{A.7})$$

In tensor notation, this is replaced by

$$dp = \frac{\partial p}{\partial x_i} dx_i \quad (\text{A.8})$$

Equation (A.8) can be thought of as the dot product of the gradient of  $p$ , namely  $\nabla p$ , and the differential vector  $d\mathbf{x} = (dx_1, dx_2, dx_3)$ . Thus, we can also say that the  $i$  component of  $\nabla p$ , which we denote as  $(\nabla p)_i$ , is given by

$$(\nabla p)_i = \frac{\partial p}{\partial x_i} = p_{,i} \quad (\text{A.9})$$

where a comma followed by an index is tensor notation for differentiation with respect to  $x_i$ . Similarly, the divergence of a vector  $\mathbf{u}$  is given by

$$\nabla \cdot \mathbf{u} = \frac{\partial u_i}{\partial x_i} = u_{i,i} \quad (\text{A.10})$$

where we again denote differentiation with respect to  $x_i$  by “ $,i$ ”.

Thus far, we have dealt with scalars and vectors. The question naturally arises about how we might handle a matrix. The answer is we denote a matrix by using two subscripts, or indices. The first index corresponds to row number while the second corresponds to column number. For example, consider the  $3 \times 3$  matrix  $[A]$  defined by

$$[A] = \begin{bmatrix} A_{11} & A_{12} & A_{13} \\ A_{21} & A_{22} & A_{23} \\ A_{31} & A_{32} & A_{33} \end{bmatrix} \quad (\text{A.11})$$

In tensor notation, we represent the matrix  $[A]$  as  $A_{ij}$ . If we post-multiply an  $m \times n$  matrix  $B_{ij}$  by an  $n \times 1$  column vector  $x_j$ , their product is an  $m \times 1$  column vector  $y_i$ . Using the summation convention, we write

$$y_i = B_{ij}x_j \quad (\text{A.12})$$

Equation (A.12) contains both a free index ( $i$ ) and a dummy index ( $j$ ). The product of a square matrix  $A_{ij}$  and its inverse is the unit matrix, i.e.,

$$[A][A]^{-1} = \begin{bmatrix} 1 & 0 & 0 \\ 0 & 1 & 0 \\ 0 & 0 & 1 \end{bmatrix} \quad (\text{A.13})$$

Equation (A.13) is rewritten in tensor notation as follows:

$$A_{ik}(A^{-1})_{kj} = \delta_{ij} \quad (\text{A.14})$$

where  $\delta_{ij}$  is the Kronecker delta defined by

$$\delta_{ij} = \begin{cases} 1, & i = j \\ 0, & i \neq j \end{cases} \quad (\text{A.15})$$

We can use the Kronecker delta to rewrite Equation (A.6) as

$$\alpha_i \delta_{ij} \alpha_j = 1 \quad (\text{A.16})$$

This corresponds to pre-multiplying the  $3 \times 3$  matrix  $\delta_{ij}$  by the row vector  $(\alpha_1, \alpha_2, \alpha_3)$  and then post-multiplying their product by the column vector  $(\alpha_1, \alpha_2, \alpha_3)^T$ , where superscript  $T$  denotes transpose.

The determinant of a  $3 \times 3$  matrix  $A_{ij}$  is

$$\begin{vmatrix} A_{11} & A_{12} & A_{13} \\ A_{21} & A_{22} & A_{23} \\ A_{31} & A_{32} & A_{33} \end{vmatrix} = \begin{matrix} A_{11}A_{22}A_{33} + A_{21}A_{32}A_{13} + A_{31}A_{12}A_{23} \\ -A_{11}A_{32}A_{23} - A_{12}A_{21}A_{33} - A_{13}A_{22}A_{31} \end{matrix} \quad (\text{A.17})$$

Tensor analysis provides a shorthand for this operation as well. Specifically, we replace Equation (A.17) by

$$\det(A_{ij}) = |A_{ij}| = \epsilon_{rst} A_{r1} A_{s2} A_{t3} \quad (\text{A.18})$$

where  $\epsilon_{rst}$  is the **permutation tensor** defined by

$$\left. \begin{aligned} \epsilon_{123} &= \epsilon_{231} = \epsilon_{312} = 1 \\ \epsilon_{213} &= \epsilon_{321} = \epsilon_{132} = -1 \\ \epsilon_{111} &= \epsilon_{222} = \epsilon_{333} = \epsilon_{112} = \epsilon_{113} = \epsilon_{221} = \epsilon_{223} = \epsilon_{331} = \epsilon_{332} = 0 \end{aligned} \right\} (\text{A.19})$$

In other words,  $\epsilon_{ijk}$  vanishes whenever the values of any two indices are the same;  $\epsilon_{ijk} = 1$  when the indices are a permutation of 1, 2, 3; and  $\epsilon_{ijk} = -1$  otherwise.

As can be easily verified, the cross product of two vectors **a** and **b** can be expressed as follows.

$$(\mathbf{a} \times \mathbf{b})_i = \epsilon_{ijk} a_j b_k \quad (\text{A.20})$$

In particular, the curl of a vector **u** is

$$(\nabla \times \mathbf{u})_i = \epsilon_{ijk} \frac{\partial u_k}{\partial x_j} = \epsilon_{ijk} u_{k,j} \quad (\text{A.21})$$

The Kronecker delta and permutation tensor are very important quantities that appear throughout this book. They are related by the  $\epsilon$ - $\delta$  identity, which is the following.

$$\epsilon_{ijk} \epsilon_{ist} = \delta_{js} \delta_{kt} - \delta_{jt} \delta_{ks} \quad (\text{A.22})$$

All that remains to complete our brief introduction to tensor analysis is to define a tensor. Tensors are classified in terms of their rank. To determine the rank of a tensor, we simply count the number of indices.

The lowest rank tensor is rank zero which corresponds to a scalar, i.e., a quantity that has magnitude only. Thermodynamic properties such as pressure and density are scalar quantities. Vectors such as velocity, vorticity and pressure gradient are tensors of rank one. They have both magnitude and direction. Matrices are rank two tensors. The stress tensor is a good example for illustrating physical interpretation of a second rank tensor.

It defines a force per unit area that has a magnitude and two associated directions, the direction of the force and the direction of the normal to the plane on which the force acts. For a normal stress, these two directions are the same; for a shear stress, they are (by convention) normal to each other.

As we move to tensors of rank three and beyond, the physical interpretation becomes more difficult to ascertain. This is rarely an issue of great concern since virtually all physically relevant tensors are of rank 2 or less. The permutation tensor is of rank 3, for example, and is simply defined by Equation (A.19).

A tensor  $a_{ij}$  is **symmetric** if  $a_{ij} = a_{ji}$ . Many important tensors in mathematical physics are symmetric, e.g., stress, strain and strain-rate tensors, moment of inertia tensor, virtual-mass tensor. A tensor is **skew symmetric** if  $a_{ij} = -a_{ji}$ . The rotation tensor,  $\Omega_{ij} = \frac{1}{2}(u_{i,j} - u_{j,i})$  is skew symmetric.

As a final comment, in performing tensor analysis operations with tensors that are not differential operators, we rarely have to worry about preserving the order of terms as we did in Equation (A.16). There is no confusion in writing  $\delta_{ij}\alpha_i\alpha_j$  in place of  $\alpha_i\delta_{ij}\alpha_j$ . This is only an issue when the indicated summations actually have to be done. However, care should be exercised when differentiation occurs. As an example,  $\nabla \cdot \mathbf{u} = \partial u_i / \partial x_i$  is a scalar number while  $\mathbf{u} \cdot \nabla = u_i \partial / \partial x_i$  is a scalar differential operator.

## Problems

**A.1** Use the  $\epsilon$ - $\delta$  identity to verify the well known vector identity

$$\mathbf{A} \times (\mathbf{B} \times \mathbf{C}) = (\mathbf{A} \cdot \mathbf{C})\mathbf{B} - (\mathbf{A} \cdot \mathbf{B})\mathbf{C}$$

**A.2** Show that, when  $i, j, k$  range over 1, 2, 3

(a)  $\delta_{ij}\delta_{ji} = 3$

(b)  $\epsilon_{ijk}\epsilon_{jki} = 6$

(c)  $\epsilon_{ijk}A_jA_k = 0$

(d)  $\delta_{ij}\delta_{jk} = \delta_{ik}$

**A.3** Verify that  $2S_{ij,j} = \nabla^2 u_i$  for incompressible flow, where  $S_{ij}$  is the strain-rate tensor, i.e.,  $S_{ij} = \frac{1}{2}(u_{i,j} + u_{j,i})$ .

**A.4** Show that the scalar product  $S_{ij}\Omega_{ji}$  vanishes identically if  $S_{ij}$  is a symmetric tensor and  $\Omega_{ij}$  is skew symmetric.

**A.5** If  $u_j$  is a vector, show that the tensor  $\omega_{ik} = \epsilon_{ijk}u_j$  is skew symmetric.

**A.6** Show that if  $A_{jk}$  is a skew-symmetric tensor, the unique solution of the equation  $\omega_i = \frac{1}{2}\epsilon_{ijk}A_{jk}$  is  $A_{mn} = \epsilon_{mni}\omega_i$ .

**A.7** The incompressible Navier-Stokes equation in a coordinate system rotating with constant angular velocity  $\boldsymbol{\Omega}$  and with position vector  $\mathbf{x} = x_k \mathbf{i}_k$  is

$$\frac{\partial \mathbf{u}}{\partial t} + \mathbf{u} \cdot \nabla \mathbf{u} + 2\boldsymbol{\Omega} \times \mathbf{u} = -\nabla \left( \frac{p}{\rho} \right) - \boldsymbol{\Omega} \times \boldsymbol{\Omega} \times \mathbf{x} + \nu \nabla^2 \mathbf{u}$$

(a) Rewrite this equation in tensor notation.

(b) Using tensor analysis, show that for  $\boldsymbol{\Omega} = \Omega \mathbf{k}$  ( $\mathbf{k}$  is a unit vector aligned with  $\boldsymbol{\Omega}$ ), the centrifugal force per unit mass is given by

$$-\boldsymbol{\Omega} \times \boldsymbol{\Omega} \times \mathbf{x} = \nabla \left( \frac{1}{2} \Omega^2 x_k x_k \right) - [\mathbf{k} \cdot \nabla \left( \frac{1}{2} \Omega^2 x_k x_k \right)] \mathbf{k}$$

**A.8** Using tensor analysis, prove the vector identity

$$\mathbf{u} \cdot \nabla \mathbf{u} = \nabla \left( \frac{1}{2} \mathbf{u} \cdot \mathbf{u} \right) - \mathbf{u} \times (\nabla \times \mathbf{u})$$

## Appendix B

# Rudiments of Perturbation Methods

When we work with perturbation methods, we are constantly dealing with the concept of **order of magnitude**. There are three conventional **order symbols** that provide a mathematical measure of the order of magnitude of a given quantity, viz., **Big O**, **Little o**, and  $\sim$ . They are defined as follows.

**Big O** :  $f(\delta) = O[g(\delta)]$  as  $\delta \rightarrow \delta_o$  if a neighborhood of  $\delta_o$  exists and a constant  $M$  exists such that  $|f| \leq M|g|$ , i.e.,  $f(\delta)/g(\delta)$  is bounded as  $\delta \rightarrow \delta_o$ .

**Little o** :  $f(\delta) = o[g(\delta)]$  as  $\delta \rightarrow \delta_o$  if, given any  $\epsilon > 0$ , there exists a neighborhood of  $\delta_o$  such that  $|f| \leq \epsilon|g|$ , i.e.,  $f(\delta)/g(\delta) \rightarrow 0$  as  $\delta \rightarrow \delta_o$ .

$\sim$  :  $f(\delta) \sim g(\delta)$  as  $\delta \rightarrow \delta_o$  if  $f(\delta)/g(\delta) \rightarrow 1$  as  $\delta \rightarrow \delta_o$ .

For example, the Taylor series for the exponential function is

$$e^{-x} = 1 - x + \frac{1}{2}x^2 - \frac{1}{6}x^3 + \dots \quad (\text{B.1})$$

where “...” is conventional shorthand for the rest of the Taylor series, i.e.,

$$\dots = \sum_{n=4}^{\infty} \frac{(-1)^n x^n}{n!} \quad (\text{B.2})$$

In terms of the ordering symbols, we can replace “...” as follows.

$$e^{-x} = 1 - x + \frac{1}{2}x^2 - \frac{1}{6}x^3 + O(x^4) = 1 - x + \frac{1}{2}x^2 - \frac{1}{6}x^3 + o(x^3) \quad (\text{B.3})$$

We define an **asymptotic sequence of functions** as a sequence  $\phi_n(\delta)$ ,  $n = 1, 2, 3, \dots$  satisfying the condition

$$\phi_{n+1}(\delta) = o[\phi_n(\delta)] \quad \text{as} \quad \delta \rightarrow \delta_o \quad (\text{B.4})$$

Examples of asymptotic sequences are:

$$\left. \begin{aligned} \phi_n(\delta) &= 1, (\delta - \delta_o), (\delta - \delta_o)^2, (\delta - \delta_o)^3, \dots & \delta \rightarrow \delta_o \\ \phi_n(\delta) &= 1, \delta^{1/2}, \delta, \delta^{3/2}, \dots & \delta \rightarrow 0 \\ \phi_n(\delta) &= 1, \delta, \delta^2 \ln \delta, \delta^2, \dots & \delta \rightarrow 0 \\ \phi_n(x) &= x^{-1}, x^{-2}, x^{-3}, x^{-4}, \dots & x \rightarrow \infty \end{aligned} \right\} \quad (\text{B.5})$$

We say that  $g(\delta)$  is **transcendentally small** if  $g(\delta)$  is  $o[\phi_n(\delta)]$  for all  $n$ . For example,

$$e^{-1/\delta} = o(\delta^n) \quad \text{for all } n \quad (\text{B.6})$$

An **asymptotic expansion** is the sum of the first  $N$  terms in an asymptotic sequence. It is the asymptotic expansion of a function  $F(\delta)$  as  $\delta \rightarrow \delta_o$  provided

$$F(\delta) = \sum_{n=1}^N a_n \phi_n(\delta) + o[\phi_N(\delta)] \quad (\text{B.7})$$

The following are a few useful asymptotic expansions generated from simple Taylor series expansions, all of which are convergent as  $\delta \rightarrow 0$ .

$$\left. \begin{aligned} (1 + \delta)^n &\sim 1 + n\delta + \frac{n(n-1)}{2}\delta^2 + O(\delta^3) \\ \ln(1 + \delta) &\sim \delta - \frac{1}{2}\delta^2 + \frac{1}{3}\delta^3 + O(\delta^4) \\ (1 - \delta)^{-1} &\sim 1 + \delta + \delta^2 + O(\delta^3) \\ \cos \delta &\sim 1 - \frac{1}{2}\delta^2 + \frac{1}{24}\delta^4 + O(\delta^6) \\ \sin \delta &\sim \delta - \frac{1}{6}\delta^3 + \frac{1}{120}\delta^5 + O(\delta^7) \\ \tan \delta &\sim \delta + \frac{1}{3}\delta^3 + \frac{2}{15}\delta^5 + O(\delta^7) \end{aligned} \right\} \quad (\text{B.8})$$

Not all asymptotic expansions are developed as a Taylor series, nor are they necessarily convergent. For example, consider the complementary error function,  $\text{erfc}(x)$ , i.e.,

$$\text{erfc}(x) = \frac{2}{\sqrt{\pi}} \int_x^\infty e^{-t^2} dt \quad (\text{B.9})$$

We can generate an asymptotic expansion using a succession of integration by parts operations. (To start the process, for example, multiply and divide

the integrand by  $t$  so that  $t \exp(-t^2)$  becomes integrable in closed form.) The expansion is:

$$\begin{aligned} \operatorname{erfc}(x) &\sim \frac{2}{\sqrt{\pi}} e^{-x^2} \sum_{n=0}^{\infty} (-1)^n \frac{(1)(3) \dots (2n-1)}{2^{n+1} x^{2n+1}} \quad \text{as } x \rightarrow \infty \\ &\sim \frac{2}{\sqrt{\pi}} e^{-x^2} \left\{ \frac{x^{-1}}{2} - \frac{x^{-3}}{4} + O(x^{-5}) \right\} \end{aligned} \quad (\text{B.10})$$

A simple ratio test shows that this series is divergent for all values of  $x$ . However, if we define the remainder after the first  $N$  terms of the series as  $R_N(x)$ , there are two limits we can consider, viz.,

$$\lim_{x \rightarrow \infty} |R_N(x)|_{\text{Fixed } N} = 0 \quad \text{and} \quad \lim_{N \rightarrow \infty} |R_N(x)|_{\text{Fixed } x} = \infty \quad (\text{B.11})$$

Thus this divergent series gives a good approximation to  $\operatorname{erfc}(x)$  provided we don't keep too many terms! This is often the case for an asymptotic series.

Part of our task in developing a perturbation solution is to determine the appropriate asymptotic sequence. It is usually obvious, but not always. Also, more than one set of  $\phi_n(\delta)$  may be suitable, i.e., we are not guaranteed uniqueness in perturbation solutions. These problems, although annoying from a theoretical viewpoint, by no means diminish the utility of perturbation methods. Usually, we have physical intuition to help guide us in developing our solution. This type of mathematical approach is, after all, standard operating procedure for the engineer. We are, in essence, using the methods Prandtl and von Kármán used before perturbation analysis was given a name.

A **singular perturbation problem** is one in which no single asymptotic expansion is uniformly valid throughout the field of interest. For example, while  $\delta/x^{1/2} = O(\delta)$  as  $\delta \rightarrow 0$ , the singularity as  $x \rightarrow 0$  means this expression is not uniformly valid. Similarly,  $\delta \ln x = O(\delta)$  as  $\delta \rightarrow 0$  and is not uniformly valid as  $x \rightarrow 0$  and as  $x \rightarrow \infty$ . The two most common situations that lead to a singular perturbation problem are:

- (a) the coefficient of the highest derivative in a differential equation is very small;
- (b) difficulties arise in behavior near boundaries.

Case (b) typically arises in analyzing the turbulent boundary layer where logarithmic behavior of the solution occurs close to a solid boundary. The following second-order ordinary differential equation illustrates Case (a).

$$\delta \frac{d^2 F}{ds^2} + \frac{dF}{ds} + F = 0; \quad 0 \leq s \leq 1 \quad (\text{B.12})$$



We want to solve this equation subject to the following boundary conditions.

$$F(0) = 0 \quad \text{and} \quad F(1) = 1 \quad (\text{B.13})$$

We also assume that  $\delta$  is very small compared to 1, i.e.,

$$\delta \ll 1 \quad (\text{B.14})$$

This equation is a simplified analog of the Navier-Stokes equation. The second-derivative term has a small coefficient just as the second-derivative term in the Navier-Stokes equation, in nondimensional form, has the reciprocal of the Reynolds number as its coefficient. An immediate consequence is that only one boundary condition can be satisfied if we set  $\delta = 0$ . This is similar to setting viscosity to zero in the Navier-Stokes equation, which yields Euler's equation, and the attendant consequence that only the normal velocity surface boundary condition can be satisfied. That is, we cannot enforce the no-slip boundary condition for Euler-equation solutions.

The exact solution to this equation is

$$F(s; \delta) = \frac{e^{1-s} - e^{1-s/\delta}}{1 - e^{1-1/\delta}} \quad (\text{B.15})$$

which clearly satisfies both boundary conditions. If we set  $\delta = 0$  in Equation (B.12), we have the following first-order equation:

$$\frac{dF}{ds} + F = 0 \quad (\text{B.16})$$

and the solution,  $F(s; 0)$ , is

$$F(s; 0) = e^{1-s} \quad (\text{B.17})$$

where we use the boundary condition at  $s = 1$ . However, the solution fails to satisfy the boundary condition at  $s = 0$  because  $F(0; 0) = e = 2.71828 \dots$ . Figure B.1 illustrates the solution to our simplified equation for several values of  $\delta$ .

As shown, the smaller the value of  $\delta$ , the more closely  $F(s; 0)$  represents the solution throughout the region  $0 < s \leq 1$ . Only in the immediate vicinity of  $s = 0$  is the solution inaccurate. The thin layer where  $F(s; 0)$  departs from the exact solution is called a boundary layer, in direct analogy to its fluid-mechanical equivalent.

To solve this problem using perturbation methods, we seek a solution that consists of two separate asymptotic expansions, one known as the

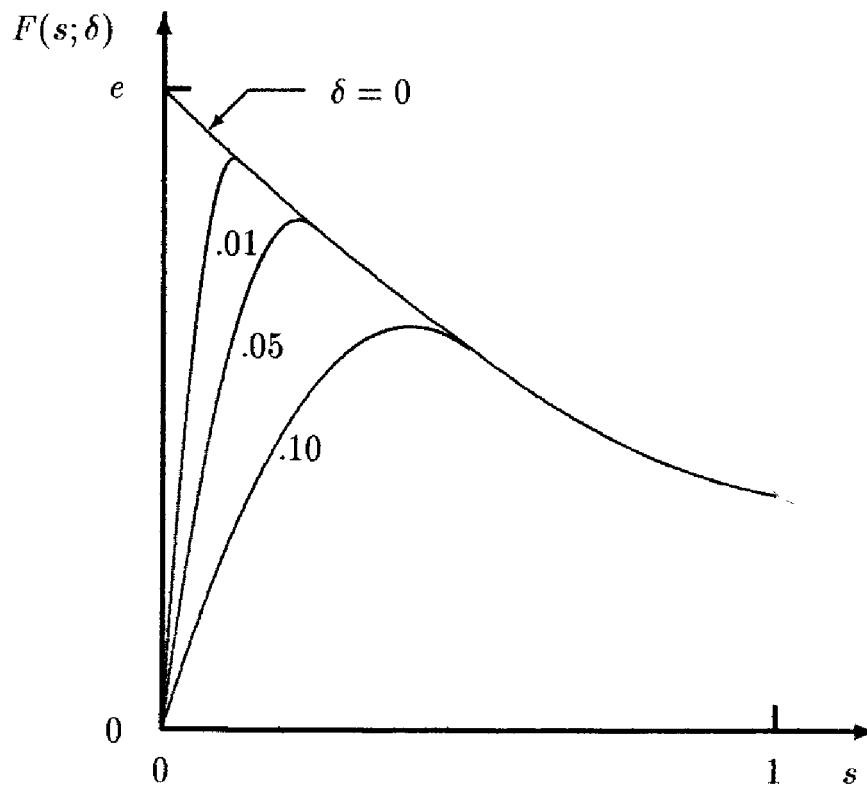


Figure B.1: Solutions to the model equation for several values of  $\delta$ .

**outer expansion** and the other as the **inner expansion**. For the outer expansion, we assume a solution of the form

$$F_{outer}(s; \delta) \sim \sum_{n=0}^N F_n(s) \phi_n(\delta) \quad (\text{B.18})$$

where the asymptotic sequence functions,  $\phi_n(\delta)$ , will be determined as part of the solution. Substituting Equation (B.18) into Equation (B.12) yields the following.

$$\sum_{n=0}^N \left\{ \frac{d^2 F_n}{ds^2} \delta \phi_n(\delta) + \frac{dF_n}{ds} \phi_n(\delta) + F_n \phi_n(\delta) \right\} = 0 \quad (\text{B.19})$$

Clearly, if we select

$$\phi_n(\delta) = \delta^n \quad (\text{B.20})$$

we, in effect, have a power-series expansion. Equating like powers of  $\delta$ , the **leading-order** ( $n = 0$ ) problem is Equation (B.16), while the second-derivative term makes its first appearance in the **first-order** ( $n = 1$ ) problem. Our perturbation solution yields the following series of problems for

the **outer expansion**.

$$\left. \begin{aligned} \frac{dF_0}{ds} + F_0 &= 0 \\ \frac{dF_1}{ds} + F_1 &= -\frac{d^2 F_0}{ds^2} \\ \frac{dF_2}{ds} + F_2 &= -\frac{d^2 F_1}{ds^2} \\ &\vdots \end{aligned} \right\} \quad (\text{B.21})$$

Provided we solve the equations in sequence starting at the lowest order ( $n = 0$ ) equation, the right-hand side of each equation is known from the preceding solution and serves simply to make each equation for  $n \geq 1$  non-homogeneous. Consequently, to all orders, the equation for  $F_n(s)$  is of first order. Hence, no matter how many terms we include in our expansion, we can satisfy only one of the two boundary conditions. As in the introductory remarks, we elect to satisfy  $F(1) = 1$ . In terms of our expansion [Equations (B.18) and (B.20)], the boundary conditions for the  $F_n$  are

$$F_0(1) = 1 \quad \text{and} \quad F_n(1) = 0 \quad \text{for} \quad n \geq 1 \quad (\text{B.22})$$

The solution to Equations (B.21) subject to the boundary conditions specified in Equation (B.22) is as follows.

$$\left. \begin{aligned} F_0(s) &= e^{1-s} \\ F_1(s) &= (1-s)e^{1-s} \\ &\vdots \end{aligned} \right\} \quad (\text{B.23})$$

Hence, our **outer expansion** assumes the following form.

$$F_{outer}(s; \delta) \sim e^{1-s} [1 + (1-s)\delta + O(\delta^2)] \quad (\text{B.24})$$

In general, for singular perturbation problems, we have no guarantee that continuing to an infinite number of terms in the outer expansion yields a solution that satisfies both boundary conditions. That is, our expansion may or may not be convergent. Hence, we try a different approach to resolve the region near  $s = 0$ . We now generate an **inner expansion** in which we **stretch** the  $s$  coordinate. That is, we define a new independent variable  $\sigma$  as follows.

$$\sigma = \frac{s}{\mu(\delta)} \quad (\text{B.25})$$

We assume an inner expansion in terms of a new set of asymptotic-sequence functions,  $\psi_n(\delta)$ , i.e.,

$$F_{inner}(\sigma; \delta) \sim \sum_{n=0}^N f_n(\sigma) \psi_n(\delta) \quad (\text{B.26})$$

To best illustrate how we determine the appropriate stretching function,  $\mu(\delta)$ , consider the leading-order terms in the original differential equation, viz.,

$$\frac{d^2 f_0}{d\sigma^2} \left( \frac{\delta \psi_0}{\mu^2} \right) + \frac{df_0}{d\sigma} \left( \frac{\psi_0}{\mu} \right) + f_0 \psi_0 = O \left( \frac{\delta \psi_1}{\mu^2}, \frac{\psi_1}{\mu}, \psi_1 \right) \quad (\text{B.27})$$

First of all, we must consider the three possibilities for the order of magnitude of  $\mu(\delta)$ , viz.,  $\mu \gg 1$ ,  $\mu \sim 1$  and  $\mu \ll 1$ . If  $\mu \gg 1$ , inspection of Equation (B.27) shows that  $f_0 = 0$  which is not a useful solution. If  $\mu \sim 1$ , we have the outer expansion. Thus, we conclude that  $\mu \ll 1$ .

We are now faced with three additional possibilities:  $\delta \psi_0 / \mu^2 \gg \psi_0 / \mu$ ;  $\delta \psi_0 / \mu^2 \sim \psi_0 / \mu$ ; and  $\delta \psi_0 / \mu^2 \ll \psi_0 / \mu$ . Using the boundary condition at  $s = 0$ , assuming  $\delta \psi_0 / \mu^2 \gg \psi_0 / \mu$  yields  $f_0 = A\sigma$  where  $A$  is a constant of integration. While this solution might be useful, we have learned nothing about the stretching function,  $\mu(\delta)$ . At the other extreme,  $\delta \psi_0 / \mu^2 \ll \psi_0 / \mu$ , we obtain the trivial solution,  $f_0 = 0$ , which doesn't help us in our quest for a solution. The final possibility,  $\delta \psi_0 / \mu^2 \sim \psi_0 / \mu$ , is known as the **distinguished limit**, and this is the case we choose. Thus,

$$\mu(\delta) = \delta \quad (\text{B.28})$$

Again, the most appropriate choice for the  $\psi_n(\delta)$  is

$$\psi_n(\delta) = \delta^n \quad (\text{B.29})$$

The following sequence of equations and boundary conditions define the **inner expansion**.

$$\left. \begin{aligned} \frac{d^2 f_0}{d\sigma^2} + \frac{df_0}{d\sigma} &= 0 \\ \frac{d^2 f_1}{d\sigma^2} + \frac{df_1}{d\sigma} &= -f_0 \\ \frac{d^2 f_2}{d\sigma^2} + \frac{df_2}{d\sigma} &= -f_1 \\ &\vdots \end{aligned} \right\} \quad (\text{B.30})$$

$$f_n(0) = 0 \quad \text{for all } n \geq 0 \quad (\text{B.31})$$

Solving the leading, or **zeroth**, order problem ( $n = 0$ ) and the **first** order problem ( $n = 1$ ), we find

$$\left. \begin{aligned} f_0(\sigma) &= A_0(1 - e^{-\sigma}) \\ f_1(\sigma) &= (A_1 - A_0\sigma) - (A_1 + A_0\sigma)e^{-\sigma} \\ &\vdots \end{aligned} \right\} \quad (\text{B.32})$$

where  $A_0$  and  $A_1$  are constants of integration. These integration constants arise because each of Equations (B.30) is of second order and we have used only one boundary condition.

To complete the solution, we perform an operation known as **matching**. To motivate the matching procedure, note that on the one hand, the boundary  $s = 1$  is located at  $\sigma = 1/\delta \rightarrow \infty$  as  $\delta \rightarrow 0$ . Hence, we need a boundary condition for  $F_{inner}(\sigma; \delta)$  valid as  $\sigma \rightarrow \infty$ . On the other hand, the independent variable in the outer expansion is related to  $\sigma$  by  $s = \delta\sigma$ . Thus, for any finite value of  $\sigma$ , the inner expansion lies very close to  $s = 0$ . We **match** these two asymptotic expansions by requiring that

$$\lim_{\sigma \rightarrow \infty} F_{inner}(\sigma; \delta) = \lim_{s \rightarrow 0} F_{outer}(s; \delta) \quad (\text{B.33})$$

The general notion is that on the scale of the outer expansion, the inner expansion is valid in an infinitesimally thin layer. Similarly, on the scale of the inner expansion, the outer expansion is valid for a region infinitely distant from  $s = 0$ . For the problem at hand,

$$\lim_{\sigma \rightarrow \infty} f_0(\sigma) = A_0 \quad \text{and} \quad \lim_{s \rightarrow 0} F_0(s) = e \quad (\text{B.34})$$

Thus, we conclude that

$$A_0 = e \quad (\text{B.35})$$

Equivalently, we can visualize the existence of an **overlap region** between the inner and outer solutions. In the overlap region, we stretch the  $s$  coordinate according to

$$s^* = \frac{s}{\nu(\delta)}; \quad \delta \ll \nu(\delta) \ll 1 \quad (\text{B.36})$$

In terms of this intermediate variable, for any finite value of  $s^*$ ,

$$s \rightarrow 0 \quad \text{and} \quad \sigma \rightarrow \infty \quad \text{as} \quad \nu(\delta) \rightarrow 0 \quad (\text{B.37})$$

Using this method, we can match to as high an order as we wish. For example, matching to  $n^{th}$  order, we perform the following limit operation.

$$\lim_{\delta \rightarrow 0} \left[ \frac{F_{inner} - F_{outer}}{\delta^n} \right] = 0 \quad (\text{B.38})$$

For the problem at hand, the independent variables  $s$  and  $\sigma$  become

$$s = \nu(\delta)s^* \quad \text{and} \quad \sigma = \frac{\nu(\delta)s^*}{\delta} \quad (\text{B.39})$$

Hence, replacing  $e^{-\nu(\delta)s^*}$  by its Taylor series expansion, we find

$$F_{outer} \sim e \{1 - \nu(\delta)s^* + \delta + O[\delta\nu(\delta)]\} \quad (\text{B.40})$$

Similarly, noting that  $e^{-\nu(\delta)s^*/\delta}$  is transcendentally small as  $\delta \rightarrow 0$ , we have

$$F_{inner} \sim A_0 - A_0\nu(\delta)s^* + A_1\delta + O(\delta^2) \quad (\text{B.41})$$

Thus, holding  $s^*$  constant,

$$\lim_{\delta \rightarrow 0} \left[ \frac{F_{inner} - F_{outer}}{\delta} \right] \sim \frac{(A_0 - e)(1 - \nu(\delta)s^*) + (A_1 - e)\delta + o(\delta)}{\delta} \quad (\text{B.42})$$

Clearly, **matching to zeroth and first orders** can be achieved only if

$$A_0 = A_1 = e \quad (\text{B.43})$$

In summary, the **inner and outer expansions** are given by

$$\left. \begin{aligned} F_{outer}(s; \delta) &\sim e^{1-s} [1 + (1-s)\delta + O(\delta^2)] \\ F_{inner}(\sigma; \delta) &\sim e \{ (1 - e^{-\sigma}) + [(1-\sigma) - (1+\sigma)e^{-\sigma}]\delta + O(\delta^2) \} \\ \sigma &= s/\delta \end{aligned} \right\} \quad (\text{B.44})$$

Finally, we can generate a single expansion, known as a **composite expansion**, that can be used throughout the region  $0 \leq s \leq 1$ . Recall that in the matching operations above, we envisioned an **overlap region**. In constructing a composite expansion, we note that the inner expansion is valid in the inner region, the outer expansion is valid in the outer region, and both are valid in the overlap region. Hence, we define

$$F_{composite} \equiv F_{inner} + F_{outer} - F_{cp} \quad (\text{B.45})$$

where  $F_{cp}$  is the **common part**, i.e., the part of the expansions that cancel in the matching process. Again, for the case at hand, comparison of Equations (B.40) and (B.41) with  $A_0$  and  $A_1$  given by Equation (B.43) shows that

$$F_{cp} \sim e [1 + (1-\sigma)\delta + O(\delta^2)] \quad (\text{B.46})$$

where we use the fact that  $\nu(\delta)s^* = \delta\sigma$ . Hence, the **composite expansion** is

$$F_{\text{composite}} \sim \left[ e^{1-s} - e^{1-s/\delta} \right] + \left[ (1-s)e^{1-s} - (1+s/\delta)e^{1-s/\delta} \right] \delta + O(\delta^2) \quad (\text{B.47})$$

Retaining just the zeroth order term of the composite expansion yields an approximation to the exact solution that is accurate to better than 3% for  $\delta$  as large as 0.2! This is actually a bit fortuitous since the leading term in Equation (B.47) and the exact solution differ by a transcendently small term. What we have done is combine two non-uniformly valid expansions to achieve a **uniformly valid approximation** to the exact solution.

For the obvious reason, perturbation analysis is often referred to as the theory of **matched asymptotic expansions**. The discussion here, although sufficient for our needs, is brief and covers only the bare essentials of the theory. For additional information, see the excellent books by Van Dyke (1964), Bender and Orszag (1978) or Kevorkian and Cole (1981) on this powerful mathematical theory.

## Problems

**B.1** Consider the polynomial

$$x^3 - x^2 + \delta = 0$$

- (a) For nonzero  $\delta < 4/27$  this equation has three real and unequal roots. Why is this a singular perturbation problem in the limit  $\delta \rightarrow 0$ ?
- (b) Use perturbation methods to solve for the first two terms in the expansions for the roots.

**B.2** The following is an example of a perturbation problem that is singular because of nonuniformity near a boundary. Consider the following first-order equation in the limit  $\epsilon \rightarrow 0$ .

$$x^3 \frac{dy}{dx} = \epsilon y^2; \quad y(1) = 1$$

The solution is known to be finite on the closed interval  $0 \leq x \leq 1$ .

- (a) Solve for the first two terms in the outer expansion and show that the solution has a singularity as  $x \rightarrow 0$ .
- (b) Show that there is a boundary layer near  $x = 0$  whose thickness is of order  $\epsilon^{1/2}$ .
- (c) Solve for the first two terms of the inner expansion. Note that the algebra simplifies if you do the zeroth-order matching before attempting to solve for the next term in the expansion.

**B.3** Generate the first two terms of the inner and outer expansions for the following boundary-value problem. Also, construct a composite expansion.

$$\delta \frac{d^2 y}{dx^2} + \frac{dy}{dx} - xy = 0; \quad \delta \ll 1$$

$$y(0) = 0 \quad \text{and} \quad y(1) = e^{1/2}$$



**B.4** Generate the first two terms of the inner and outer expansions for the following boundary-value problem. Also, construct a composite expansion.

$$\delta \frac{d^2 y}{dx^2} + \frac{dy}{dx} = \frac{1}{2} x^2; \quad \delta \ll 1$$

$$y(0) = 1 \quad \text{and} \quad y(1) = 1/6$$

**B.5** This problem demonstrates that the **overlap region** is not a layer in the same sense as the boundary layer. Rather, its thickness depends upon how many terms we retain in the matching process. Suppose we have solved a boundary-layer problem and the first three terms of the inner and outer expansions valid as  $\epsilon \rightarrow 0$  are:

$$y_{outer}(x; \epsilon) \sim 1 + \epsilon e^{-x^2} + \epsilon^2 e^{-2x^2} + O(\epsilon^3)$$

$$y_{inner}(x; \epsilon) \sim A(1 - e^{-\xi}) + \epsilon B(1 - e^{-\xi}) + \epsilon^2 C(1 - \xi^2) + O(\epsilon^3)$$

where

$$\xi \equiv \frac{x}{\epsilon^{1/2}}$$

Determine the coefficients  $A$ ,  $B$  and  $C$ . Explain why the thickness of the overlap region,  $\nu(\epsilon)$ , must lie in the range

$$\epsilon^{1/2} \ll \nu(\epsilon) \ll \epsilon^{1/4}$$

as opposed to the normally assumed range  $\epsilon^{1/2} \ll \nu(\epsilon) \ll 1$ .

# Appendix C

## Companion Software

### C.1 Overview

The software described in this appendix solves for: (a) free shear flow far-field behavior; (b) pipe and channel flow; and, (c) detailed sublayer and defect-layer behavior. In all cases, accurate algorithms are used that guarantee grid-independent solutions on any computer from an IBM PC to a Cray Y/MP. These programs serve two purposes. First, they solve basic **building-block** flow problems and can thus be helpful in developing or modifying a turbulence model. Second, these programs provide a definitive separation of turbulence-model error and numerical error.

As computers have increased in power, there has been a tendency away from analytical methods such as similarity solutions and singular perturbation methods. The mathematics of these procedures can be tedious, and it can be a lot easier to use a parabolic marching program for the types of flows described above. Eventually, marching far enough in space, self-similarity is achieved with such a program. However, complete avoidance of analytical methods can lead to an ignorance of important flow details such as singularities and important asymptotic behavior that can be masked by numerical error. More alarmingly, improper treatment of such flow detail can be the source of numerical error.

While the view presented here may appear to be a bit overcautious, it is justified by the difficulties so often encountered in solving turbulence transport equations. Exact solutions are virtually nonexistent. Experimental measurements cannot objectively be used to test for numerical accuracy. Consequently, it is difficult to assess the accuracy of a new turbulent-flow program. The programs described in this appendix generate very accurate

solutions for a variety of simple turbulent flows and turbulence models, and can be used to assess numerical accuracy of more complicated programs.

The accompanying diskette includes source code for all of the programs, as well as several auxiliary routines referenced by the programs. Plotting programs are included that can be used on IBM PC and compatible computers with support for a variety of video displays and hardcopy devices. Only the executable versions of the plotting programs are included as they are based on proprietary plotting software. Section C.6 lists the files included on the distribution diskette. Appendix E presents details of the hardware supported by the plotting programs.

### C.1.1 Program Structure

All of the programs use time-marching methods to solve the nonlinear two-point boundary-value problems attending use of the similarity-solution method for simple turbulent flows. The solution algorithm used is based on implicit Crank-Nicolson differencing. To render straightforward and easy to modify programs, each equation of a given turbulence model is solved independently using a standard tridiagonal matrix inversion algorithm.

In the interest of portability, the programs have been written so that they run on IBM PC and compatible microcomputers, SUN Workstations, VAX (VMS based) computers, the Silicon Graphics IRIS and Cray super computers. The programs all use an **include** file named **cpuid** that defines a single parameter called *icpu*. This parameter is passed to a subroutine named **NAMSYS** that returns system-dependent and compiler-specific parameters. The file **cpuid** contains the following statements.

```

c-----
c   S E L E C T   A P P R O P R I A T E   C O M P I L E R / C P U
c-----
c   icpu =  0...SVS Fortran (680x0/80x86)
c           =  1...Lahey Fortran/Microsoft Fortran (80x86)
c           =  2...VAX/VMS
c           =  3...SUN Fortran (68020/SPARC)
c           =  4...Cray/Unicos
c           =  5...Silicon Graphics Iris
c-----
      icpu=1

```

Set *icpu* to the value appropriate for your system. If your computer and/or Fortran compiler is not listed, you will have to modify subroutine **NAMSYS**. See Subsection C.5.2 for a detailed explanation of what is required as well as a listing of subroutine **NAMSYS**.

The same basic structure has been used for all of the programs. A standardized set of subroutine, input and output file, variable and common

block names has been used throughout. For example, if the program name is **PROGNAME**, the input data file is **progrname.dat** and the main output disk file is **progrname.prt**.

The main program coordinates all computations and program logic by calling a collection of subroutines. In all programs, the computational sequence is as follows:

1. Call **NAMIN** to coordinate reading the input data file. Note that **NAMIN** calls **NAMSYS** to set all system-dependent and compiler-specific parameters.
2. Call **GRID** to set up the finite-difference grid.
3. Call **START** to set closure coefficients and initial conditions.
4. Enter the main computation loop and repeat the following steps until convergence is achieved.
  - Call **GETETA** to compute  $\eta = \int \mu_T d\xi$  for programs that use the Rubel-Melnik (1984) transformation.
  - Call **CALCS** to compute eddy viscosity, vertical velocity, etc.
  - Call **TMESTP** to compute the timestep.
  - Call **EDDY** to advance the solution in time.
5. When the solution has either converged or the maximum allowable number of timesteps has been reached, call **EDIT** to either write program output to a disk file or directly to the printer. For the free shear layer programs, call **GROW** to compute spreading rate.
6. Write a disk file that can be used for making a plot of program output.

### C.1.2 Program Input

A standardized method, reminiscent of the non-Ansi-Standard NAMELIST scheme, has been used to provide input to the programs. As noted above, if the program name is **PROGNAME**, input is provided in a disk file named **progrname.dat** (sample input for each program is provided on the distribution diskette). The format for integer quantities is (1x,a12,i4) while the format for floating-point quantities is (1x,a12,e13.6). The (1x,a12) permits entering the variable name and an equal sign. Typical input thus appears as follows.

	<b>iunit1</b>	=	2	
	<b>iunit2</b>	=	7	
	<b>model</b>	=	0	
	<b>etin</b>	=	1.000000e-07	
	<b>wtin</b>	=	4.000000e-01	
<b>Column number:</b>	2	12	15	17
				26

### C.1.3 Program Output

The output from program **PROGNAME** consists of a disk file that can be used to plot computed results and, depending upon user preference, printed output that is directed to either the system printer, or to a disk file named **progrname.prt**. The name of the plotting-data disk file depends upon the turbulence model used as follows.

<b>komega.dat</b>	$k$ - $\omega$ model [Wilcox (1988a)]
<b>multi.dat</b>	Multiscale model [Wilcox (1988b)]
<b>kepsln.dat</b>	$k$ - $\epsilon$ model [Launder and Sharma (1974)]
<b>mixlen.dat</b>	Mixing-length model with $\ell_{mix} = \alpha\delta(x)$
<b>csmith.dat</b>	Cebeci-Smith model [Smith and Cebeci (1967)]
<b>blomax.dat</b>	Baldwin-Lomax model [Baldwin and Lomax (1978)]
<b>newmod.dat</b>	User-Defined model

All of the programs make provision for a user-defined model so that the supplied plotting utilities can be used for customized versions of the various programs. Only a subset of the models listed above is supported by any one program. Also, the contents of the plotting-data file are a bit different for each program. See the appropriate section to determine which models are supported by the program of interest and to determine the format of the plotting-data disk file.

The first input parameter for all of the programs is an integer variable named *iunit1*. Setting *iunit1* = 6 will cause the printed output to go to the system line printer for IBM PC implementations. Any other integer will send the printed output to a disk file whose name is **progrname.prt**.

Printed output consists of three segments. First, all input data are printed. Next, the maximum error and other flow properties such as spreading rate for free shear flows are printed; this information is also shown on the video display as the run proceeds. Finally, profiles of computed mean-flow and turbulence properties are printed in a self-explanatory manner. The precise format of the printed information differs slightly from one program to the next.

## C.2 Free Shear Flows

There are three free shear flow programs on the distribution diskette, viz., Programs **WAKE**, **MIXER** and **JET**. These programs solve the self-similar form of the turbulent-flow equations that are asymptotically approached far downstream. Section 4.5 of the main text presents the equations of motion in physical variables and in similarity form. An additional transformation devised by Rubel and Melnik (1984) has been used that greatly improves numerical accuracy. Specifically, we introduce a new independent variable,  $\xi$ , defined in terms of the similarity variable,  $\eta$ , by

$$d\xi = \frac{d\eta}{N(\eta)} \quad \text{or} \quad \frac{d}{d\xi} = N(\eta) \frac{d}{d\eta} \quad (\text{C.1})$$

where  $N(\eta)$  is the dimensionless eddy viscosity appearing in the similarity solution. In terms of this variable, the equations assume the following form:

**Mean Momentum:**

$$\nu \frac{dU}{d\xi} - \frac{1}{\eta^j} \frac{d}{d\xi} \left[ \eta^j \frac{dU}{d\xi} \right] = S_u N U \quad (\text{C.2})$$

**Turbulence Kinetic Energy:**

$$\nu \frac{dK}{d\xi} - \frac{1}{\eta^j} \frac{d}{d\xi} \left[ \sigma^* \eta^j \frac{dK}{d\xi} \right] = S_k N K + \left( \frac{dU}{d\xi} \right)^2 - \beta^* K^2 \quad (\text{C.3})$$

**$k$ - $\omega$  Model:**

$$\nu \frac{dW}{d\xi} - \frac{1}{\eta^j} \frac{d}{d\xi} \left[ \sigma \eta^j \frac{dW}{d\xi} \right] = S_w N W + \alpha \frac{W}{K} \left( \frac{dU}{d\xi} \right)^2 - \beta K W \quad (\text{C.4})$$

$$N = \frac{K}{W} \quad (\text{C.5})$$

**$k$ - $\epsilon$  Model:**

$$\nu \frac{dE}{d\xi} - \frac{1}{\eta^j} \frac{d}{d\xi} \left[ \frac{\eta^j}{\sigma_\epsilon} \frac{dE}{d\xi} \right] = S_\epsilon N E + C_{\epsilon 1} \frac{E}{K} \left( \frac{dU}{d\xi} \right)^2 - C_\mu C_{\epsilon 2} K E \quad (\text{C.6})$$

$$N = C_\mu \frac{K^2}{E} \quad (\text{C.7})$$

**Mixing-Length Model:**

$$N = \alpha \sqrt{\left| \frac{dU}{d\xi} \right|} \quad (\text{C.8})$$

where  $U$ ,  $V$ ,  $K$ ,  $W$  and  $E$  are the transformed velocity components, turbulence energy, specific dissipation rate and dissipation rate, respectively. See Section 4.5 of the main text for additional details on notation and other features of the similarity solution.

This transformation greatly improves numerical accuracy primarily because it removes numerical difficulties associated with the presence of sharp turbulent-nonturbulent interfaces. The edge of the shear layer that occurs at a finite value of  $\eta$  is moved to infinity in terms of the transformed independent variable  $\xi$ . Inspection of converged solutions shows a well behaved asymptotic approach to freestream conditions, a feature rarely observed when the equations are solved without the transformation. Consequently, a much tighter convergence criterion can be satisfied. Additionally, there is weaker coupling amongst the turbulence-model equations which also improves the convergence rate.

The only drawback to this transformation is the need to determine an appropriate maximum value of  $\xi$ . Using too large or too small a value can slow convergence and even cause the solution to blow up. All of the programs automatically compute the value of  $\xi_{max}$  that is suitable for the turbulence models implemented. If you add a new turbulence model, it may be necessary to empirically determine a suitable value for  $\xi_{max}$ .

Boundary conditions for these equations must be satisfied at  $\xi = 0$  and as  $\xi \rightarrow \infty$ , so that we must solve a two-point boundary-value problem. This is conveniently done by adding unsteady terms to the left-hand sides of Equations (C.2), (C.3), (C.4) and (C.6), making an initial guess, and letting the solution evolve in time. The solution to the desired two-point boundary-value problem is obtained when temporal variations vanish. Thus, for example, we replace the mean-momentum equation by the following.

$$\frac{\partial U}{\partial t} + V \frac{\partial U}{\partial \xi} - \frac{1}{\eta^j} \frac{\partial}{\partial \xi} \left[ \eta^j \frac{\partial U}{\partial \xi} \right] = S_u N U \quad (\text{C.9})$$

The resulting time-dependent system of equations is solved using implicit Crank-Nicolson differencing that is second-order accurate in both  $t$  and  $\xi$ . Using 101 mesh points, all of the free shear flow programs require computing times of less than 10 seconds on a 33 MHz 80486-based microcomputer and two minutes on a 10 MHz 8086-based laptop computer with an 8087 math chip.

### C.2.1 Program WAKE: Far Wake

Program **WAKE** computes two-dimensional flow in the far wake of an object in an incompressible stream.

#### Input-parameter description:

Program **WAKE** reads the following input parameters in the order listed below from disk file **wake.dat**. Integer quantities must be formatted according to (1x,a12,i4) while floating-point quantities must be formatted as (1x,a12,e13.6). See Subsection C.1.2 for a sample input-data file.

<i>iunit1</i>	Output-file unit number
	= 6 Printed output sent to printer
	≠ 6 Printed output saved in disk file <b>wake.prt</b>
<i>iunit2</i>	Plotting-data disk file unit number
<i>model</i>	Turbulence-model identification flag
	0 Wilcox $k$ - $\omega$ model
	2 Standard $k$ - $\epsilon$ model
	9 Mixing-length model with $\ell_{mix} = \alpha\delta(x)$
	99 User-defined model
<i>etin</i>	Freestream value of transformed turbulence kinetic energy
<i>wtin</i>	Freestream value of transformed specific dissipation rate
<i>xih</i>	$\omega$ -equation closure coefficient $\hat{\xi}$
<i>jmax</i>	Number of grid points
<i>maxn</i>	Maximum number of timesteps
<i>nedit</i>	Profile-print modulus; profiles are printed every <i>nedit</i> steps
<i>nfreq</i>	Short-print modulus; maximum error, shear-layer growth rate, etc. are printed every <i>nfreq</i> steps

#### Output description:

VIDEO OUTPUT includes the timestep number, maximum error and spreading rate every *nfreq* timesteps. PRINTED OUTPUT is sent to the line printer throughout the run if *iunit1* = 6. DISK-FILE OUTPUT is saved in the appropriate plotting-data disk file (see Subsection C.1.3 for file names). The file is **unformatted** and is created using the following statements:

```
jaxi=10
write(iunit2) jmax,jaxi
write(iunit2) (eta(j),uoum(j),j=1,jmax)
```

where eta(j) is  $\eta_j$  and uoum(j) is  $\mathcal{U}(\eta_j)$ . The parameter *jaxi* is used by plotting program **PLOTF**. Additionally, for any value of *iunit1* other than



6, printed output is saved in disk file **wake.prt** at the conclusion of the run.

**Comments:**

- $k$ - $\omega$  model far-wake predictions are very sensitive to the value of  $w_{tin}$ ; optimum agreement with measurements occurs for  $w_{tin} = 0.4$ .
- Program **WAKE** runs most efficiently for  $j_{max} \geq 101$ . A smaller number of grid points tends to slow convergence.

### C.2.2 Program MIXER: Mixing Layer

Program **MIXER** computes two-dimensional flow in the mixing layer between two streams of differing velocity, including effects of compressibility.

#### Input-parameter description:

Program **MIXER** reads the following input parameters in the order listed below from disk file **mixer.dat**. Integer quantities must be formatted according to (1x,a12,i4) while floating-point quantities must be formatted as (1x,a12,e13.6). See Subsection C.1.2 for a sample input-data file.

<i>iunit1</i>	Output-file unit number = 6 Printed output sent to printer ≠ 6 Printed output saved in disk file <b>mixer.prt</b>
<i>iunit2</i>	Plotting-data disk file unit number
<i>model</i>	Turbulence-model identification flag 0 Wilcox $k$ - $\omega$ model 2 Standard $k$ - $\epsilon$ model 9 Mixing-length model with $\ell_{mix} = \alpha\delta(x)$ 99 User-defined model
<i>etin</i>	Freestream value of transformed turbulence kinetic energy
<i>gam</i>	Specific heat ratio, $\gamma$
<i>prt</i>	Turbulent Prandtl number, $Pr_T$
<i>rho2</i>	Density ratio, $\rho_2/\rho_1$ where subscript 2 corresponds to the slow stream; required only for incompressible flow
<i>u2ou1</i>	Velocity ratio, $U_2/U_1$ where subscript 2 corresponds to the slow stream; required only for incompressible flow
<i>wtin</i>	Freestream value of transformed specific dissipation rate
<i>xih</i>	$\omega$ -equation closure coefficient $\hat{\xi}$
<i>xis</i>	Dilatation-dissipation closure coefficient $\xi^*$
<i>xma1</i>	Mach number of the fast stream, $M_1$
<i>xma2</i>	Mach number of the slow stream, $M_2$
<i>xmt0</i>	Dilatation-dissipation closure coefficient $M_{t0}$
<i>imach</i>	Dilatation-dissipation model flag 0 Sarkar's model 1 Wilcox's model 2 Zeman's model
<i>jmax</i>	Number of grid points
<i>jzero</i>	Index of grid point at the dividing streamline ( $\eta = 0$ )
<i>maxn</i>	Maximum number of timesteps
<i>nedit</i>	Profile-print modulus; profiles are printed every <i>nedit</i> steps
<i>nfreq</i>	Short-print modulus; maximum error, shear-layer growth rate, etc. are printed every <i>nfreq</i> steps

*nthick* Mixing-layer thickness definition flag for short print  
     -1 Bogdanoff's vorticity thickness  
     0 Birch's energy thickness  
     1 Roshko's pitot thickness  
     2 Sullin's momentum thickness

### Output description:

VIDEO OUTPUT includes the timestep number, maximum error and spreading rate every *nfreq* timesteps. PRINTED OUTPUT is sent to the line printer throughout the run if *iunit1* = 6. DISK-FILE OUTPUT is saved in the appropriate plotting-data disk file (see Subsection C.1.3 for file names). The file is **unformatted** and is created using the following statements:

```
jaxi=99
write(iunit2) jmax,jaxi
write(iunit2) (yox(j),u(j),j=1,jmax)
```

where *yox(j)* is  $\eta_j$  and *u(j)* is  $\mathcal{U}(\eta_j)$ . The parameter *jaxi* is used by plotting program **PLOTF**. Additionally, for any value of *iunit1* other than 6, printed output is saved in disk file **mixer.prt** at the conclusion of the run.

### Comments:

- *k- $\omega$*  model mixing-layer predictions are very sensitive to the value of *wtin*; optimum agreement with measurements occurs for *wtin* = 0.5.
- Program **MIXER** runs most efficiently for *jmax*  $\geq$  101. A smaller number of grid points tends to slow convergence.
- Program **MIXER** runs most efficiently for Mach numbers up to 5. It will run for larger values, although smaller timesteps are needed. The timestep can be reduced by changing the value of *cflmax* in the main program. The parameter *cflmax* is the maximum value of the Courant-Friedrichs-Lewy number; the timestep is computed as the product of a number less than or equal to 1, *cflmax* and the maximum timestep required for stability of an explicit scheme. Its default value is 1 for the *k- $\omega$*  and *k- $\epsilon$*  models and 2 for the mixing-length model.

### C.2.3 Program JET: Plane, Round and Radial Jet

Program **JET** computes far-field flow for plane, round and radial jets issuing into a quiescent incompressible fluid.

#### Input-parameter description:

Program **JET** reads the following input parameters in the order listed below from disk file **jet.dat**. Integer quantities must be formatted according to (1x,a12,i4) while floating-point quantities must be formatted as (1x,a12,e13.6). See Subsection C.1.2 for a sample input-data file.

<i>iunit1</i>	Output-file unit number
	= 6 Printed output sent to printer
	≠ 6 Printed output saved in disk file <b>jet.prt</b>
<i>iunit2</i>	Plotting-data disk file unit number
<i>model</i>	Turbulence-model identification flag
	0 Wilcox $k$ - $\omega$ model
	2 Standard $k$ - $\epsilon$ model
	9 Mixing-length model with $\ell_{mix} = \alpha\delta(x)$
	99 User-defined model
<i>etin</i>	Freestream value of transformed turbulence kinetic energy
<i>wtin</i>	Freestream value of transformed specific dissipation rate
<i>xih</i>	$\omega$ -equation closure coefficient $\hat{\xi}$
<i>ipope</i>	Round-jet modification flag
	0 Omit Pope's round-jet correction
	1 Use Pope's round-jet correction
<i>jaxi</i>	Geometry flag
	-1 Radial jet
	0 Plane jet
	1 Round jet
<i>jmax</i>	Number of grid points
<i>maxn</i>	Maximum number of timesteps
<i>nedit</i>	Profile-print modulus; profiles are printed every <i>nedit</i> steps
<i>nfreq</i>	Short-print modulus; maximum error, shear-layer growth rate, etc. are printed every <i>nfreq</i> steps

#### Output description:

VIDEO OUTPUT includes the timestep number, maximum error and spreading rate every *nfreq* timesteps. PRINTED OUTPUT is sent to the line printer throughout the run if *iunit1* = 6. DISK-FILE OUTPUT is saved in the appropriate plotting-data disk file (see Subsection C.1.3 for file names). The file is **unformatted** and is created using the following statements:

```

write(iunit2) jmax,jaxi
write(iunit2) (eta(j),uoum(j),j=1,jmax)

```

where  $\text{eta}(j)$  is  $\eta_j$  and  $\text{uoum}(j)$  is  $\mathcal{U}(\eta_j)$ . The parameter  $jaxi$  is used by plotting program **PLOTf**. Additionally, for any value of  $iunit1$  other than 6, printed output is saved in disk file **jet.prt** at the conclusion of the run.

**Comments:**

- $k$ - $\omega$  model jet predictions are very sensitive to the value of  $w_{tin}$ ; optimum agreement with measurements occurs for the following values of  $w_{tin}$ :

Radial jet,	$w_{tin} = 3$
Plane jet,	$w_{tin} = 5$
Round jet,	$w_{tin} = 50$

- Program **JET** runs most efficiently for  $jmax \geq 101$ . A smaller number of grid points tends to slow convergence.

### C.2.4 Program PLOTf: Plotting Utility

Program **PLOTf** creates video and hardcopy plots of free shear flow velocity profiles computed with programs **WAKE**, **MIXER** and **JET** on IBM PC's and compatibles. The program automatically detects the turbulence model used and the type of shear flow for which computations have been done.

#### Input-parameter description:

Program **PLOTf** reads the following nine input parameters in the order listed below from disk file **plotf.dat**. Integer quantities must be formatted according to (7x,i6) while floating-point quantities must be formatted as (7x,f6.2). This is similar to the format used for Programs **WAKE**, **MIXER** and **JET**.

<i>mon</i>	Monitor type (see Appendix E)
<i>ifore</i>	Foreground color (see Appendix E)
<i>iback</i>	Background color (see Appendix E)
<i>nprin</i>	Printer type (see Appendix E)
<i>mode</i>	Graphics-mode flag for printers; number of pens for plotters (see Appendix E)
<i>ksize</i>	Plot scaling factor. Using 100 yields a 5" by 5" hardcopy plot. Smaller values yield a hardcopy plot reduced by <i>ksize</i> per cent. Thus, <i>ksize</i> = 50 yields a 2.5" by 2.5" plot.
<i>symsiz</i>	Size of experimental data symbols, in inches
<i>height</i>	Physical height, in inches, of the video display
<i>width</i>	Physical width, in inches, of the video display

Next, Program **PLOTf** reads a single, free formatted, line to indicate where hardcopy print is directed and where required font files are located. This line comes immediately after the specified value for *width* and defines the following six additional parameters.

<i>devid</i>	Device name of type character*4; valid devices are LPT1, LPT2, LPT3, COM1, COM2, COM3, COM4
<i>nbaud</i>	Baud rate for a serial port; valid baud rates are 110, 150, 300, 600, 1200, 2400, 4800, 9600
<i>parity</i>	Parity of type character*3 or character*4 for a serial port; valid parity settings are 'even', 'odd' and 'none'
<i>nstop</i>	Number of stop bits for a serial port; either 1 or 2
<i>lword</i>	Word length for a serial port; either 7 or 8
<i>path</i>	Path to font files of type character*n where $n \leq 40$

**Output description:**

A 5" by 5" video plot (see Figure C.1) is created centered on the screen. When the plot is complete, the following message appears:

**Hardcopy output (y/n)?**

Enter a *y* or a *Y* to create a hardcopy plot. Pressing any other key terminates the run without creating a hardcopy plot.

**Comments:**

- The following is a sample input data file for a machine with a standard VGA monitor and an HP DeskJet connected to serial port COM1:

```

mon    =    18                (Standard VGA monitor)
ifore  =    15                (Bright-white foreground)
iback  =     1                (Blue background)
nprin  =     2                (HP DeskJet)
mode   =     3                (300 dots per inch resolution)
ksize  =   100                (Full size plot)
symsiz =  .080                (.08" experimental data symbols)
height =  7.500              (7.5" high video display)
width  =  9.250              (9.25" wide video display)
'com1' , 9600 , 'none' , 1 , 8, 'd:\fonts\'

```

The last line indicates the printer is connected to serial port COM1: and the port is set at 9600 baud, no parity, 1 stop bit and 8 data bits. Also, the plotting font file **sppfnt.002** is located in directory **fonts** on drive **d:**.

**IMPORTANT:** The terminating character in the path name must be a backslash, i.e., \.

- If disk file **plotf.dat** is not available, Program **PLOTF** uses the following set of default values :

```

mon = 18, ifore = 15, iback = 1, nprin = 24, mode = 39, ksize = 100,
symsiz = .08, height = 7.5, width = 9.25, devid = 'LPT1', path = '\

```

Note that *nbaud*, *parity*, *nstop* and *lword* are not used for parallel ports. Note also that the default path is the **root directory** of the current drive.

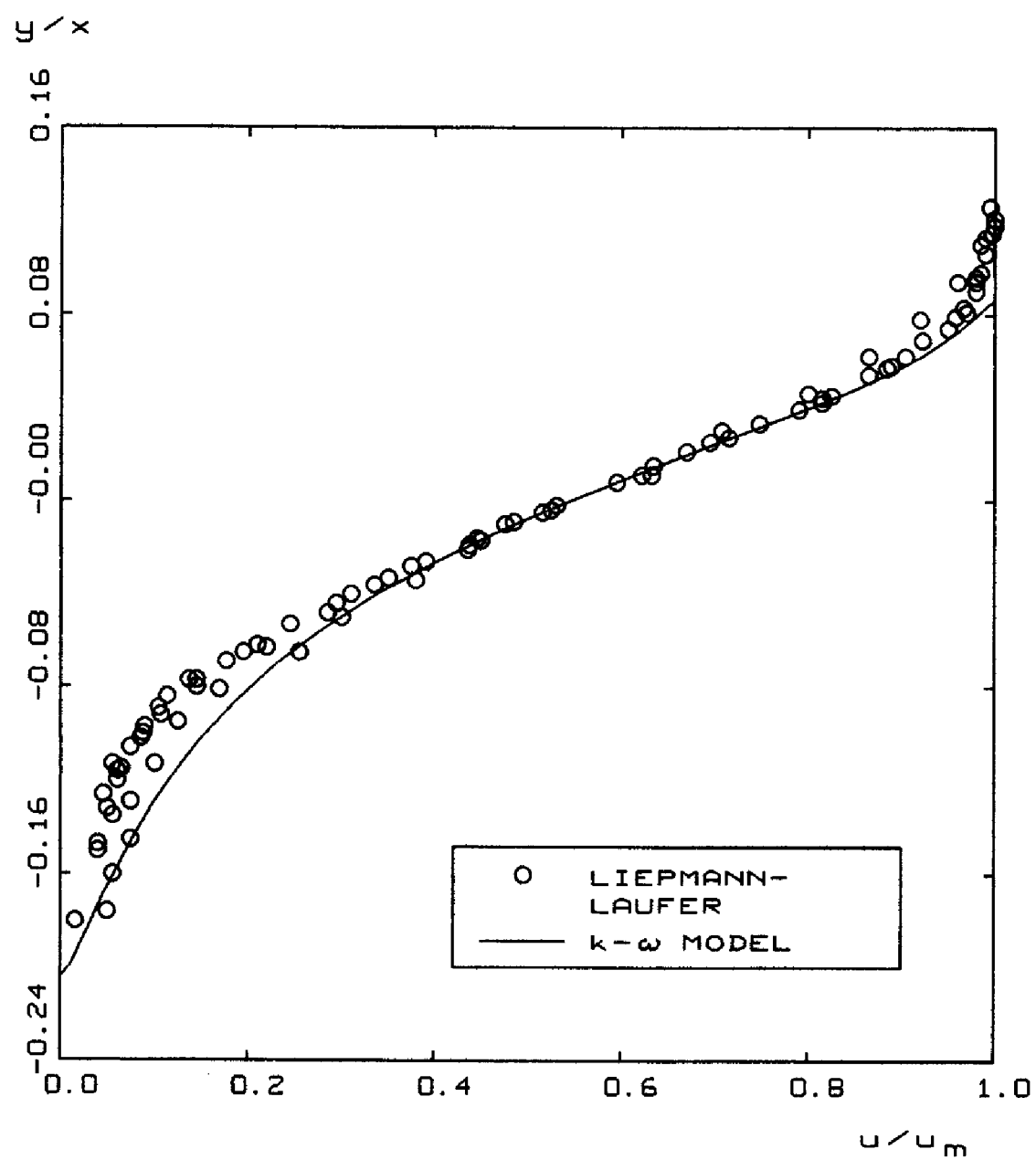


Figure C.1: Sample plot created by Program PLOTf.



### C.3 Channel and Pipe Flow

Program **PIPE** can be used to compute incompressible channel flow or pipe flow with several turbulence models. Subsections 3.5.1 and 4.8.1 of the main text describe the channel- and pipe-flow equations. No additional transformations are introduced in Program **PIPE**.

As with the free shear flow programs, we add unsteady terms to the turbulence-model equations to facilitate solution of the two-point boundary-value problem. However, the momentum equation is solved at each timestep by trapezoidal-rule integration. For example, in the case of a two-equation model, we advance the turbulence parameters in time. Then, after updating the eddy viscosity, we determine the velocity by integration of the following equation.

$$\frac{dU^+}{dy^+} = \frac{1 - y^+/R^+}{1 + \mu_T^+} \quad (\text{C.10})$$

All notation in Equation (C.10) is identical to that used in Subsections 3.5.1 and 4.8.1 of the main text.

The only other subtle feature of the program is the way the specific dissipation rate,  $\omega$ , in the Wilcox (1988a)  $k$ - $\omega$  model and the Wilcox (1988b) multiscale model is computed close to the solid boundary. To eliminate numerical error associated with computing the singular behavior of  $\omega$  for perfectly-smooth and slightly-rough surfaces, the exact asymptotic behavior of  $\omega$  is prescribed close to the surface (see Subsection 7.2.1). That is, we use the fact that, for  $y^+ < 2.5$ ,  $\omega^+ = \nu\omega/u_\tau^2$  is given by:

$$\omega^+ \rightarrow \frac{N_\omega}{(y^+)^2} \quad \text{as } y \rightarrow 0 \quad (\text{smooth wall}) \quad (\text{C.11})$$

$$\omega^+ \rightarrow \frac{\omega_w^+}{\left[1 + \sqrt{\frac{\omega_w^+}{N_\omega}} y^+\right]^2} \quad \text{as } y \rightarrow 0 \quad (\text{rough wall}) \quad (\text{C.12})$$

where

$$N_\omega = \begin{cases} 6/\beta, & \text{without viscous corrections} \\ 2/\beta^*, & \text{with viscous corrections} \end{cases} \quad (\text{C.13})$$

The exact analytical behavior of  $\omega$  is imposed for a prescribed number of mesh points,  $j_{skip}$ , next to the surface. Using 201 mesh points, Program **PIPE** requires computing times of less than 10 seconds on a 33 MHz 80486-based microcomputer and two minutes on a 10 MHz 8086-based laptop computer with an 8087 math chip.

### C.3.1 Program PIPE: Channel and Pipe Flow

Program **PIPE** computes incompressible, fully-developed flow in either a two-dimensional channel or a pipe of circular cross section.

#### Input-parameter description:

Program **PIPE** reads the following input parameters from disk file **pipe.dat** in the order listed below. Integer quantities must be formatted according to (1x,a12,i4) while floating-point quantities must be formatted as (1x,a12,e13.6). See Subsection C.1.2 for a sample input-data file.

- iunit1* Output-file unit number
  - = 6 Printed output sent to printer
  - ≠ 6 Printed output saved in disk file **pipe.prt**
- iunit2* Plotting-data disk file unit number
- model* Turbulence-model identification flag
  - 0 Wilcox  $k$ - $\omega$  model
  - 1 Wilcox multiscale model
  - 10 Cebeci-Smith model
  - 11 Baldwin-Lomax model
  - 99 User-defined model
- omegaw* Surface value of dimensionless specific dissipation rate,  $\omega_w^+$
- retau*  $Re_\tau = R^+ = u_\tau R/\nu$ , dimensionless channel half height or pipe radius
- xih*  $\omega$ -equation closure coefficient  $\hat{\xi}$
- yone* Value of  $y^+$  at the first grid point above the wall
- iruff* Surface-roughness flag
  - 0 Rough surface
  - 1 Smooth surface
- jaxi* Geometry flag
  - 0 Channel flow
  - 1 Pipe flow
- jmax* Number of grid points
- jskip* Grid-point number below which the exact asymptotic solution for specific dissipation rate is used
- maxn* Maximum number of timesteps
- nedit* Profile-print modulus; profiles are printed every *nedit* steps
- nfreq* Short-print modulus; maximum error, Reynolds number, skin friction, etc. are printed every *nfreq* steps
- nvisc* Viscous-modification flag
  - = 0 No  $k$ - $\omega$ /multiscale model viscous modifications
  - ≠ 0 Use  $k$ - $\omega$ /multiscale model viscous modifications

**Output description:**

VIDEO OUTPUT includes timestep number, maximum error, Reynolds number and skin friction every *nfreq* timesteps. PRINTED OUTPUT is sent to the line printer throughout the run if *iunit1* = 6. DISK-FILE OUTPUT is saved in the appropriate plotting-data disk file (see Subsection C.1.3 for file names). The file is **unformatted** and is created using the following statements.

```

      write(iunit2) jmax,jaxi,retau,reh,cf
      if(model.eq.10.or.model.eq.11) then
        write(iunit2) (yoh(j),uoum(j),yplus(j),uplus(j),
*                   upvp(j),j=1,jmax)
      else
        do 60 j=2,jmax
          diss(j)=-betas*bbeta(j)*et(j)*wt(j)
          prod(j)=upvp(j)*dudy(j)
60      continue
          if(nvisc.ne.0) diss(1)=2.*diss(2)-diss(3)
          prod(1)=0.
          write(iunit2) (yoh(j),uoum(j),yplus(j),uplus(j),
*                   upvp(j),et(j),diss(j),prod(j),j=1,jmax)
        endif

```

The quantity *reh* is Reynolds number based on the average velocity and channel height/pipe diameter, while *cf* is skin friction based on average velocity. Also, *yoh(j)* is  $y/R$ , *uoum(j)* is  $U(y)/U(0)$ , *yplus(j)* is  $y^+$ , *uplus(j)* is  $U^+$ , *upvp(j)* is  $\tau_{xy}/\tau_w$ , *et(j)* is  $k/u_\tau^2$ , *diss(j)* is  $\beta^* \nu \omega k / u_\tau^4$ , and *prod(j)* is  $\nu \tau_{xy} (dU/dy) / u_\tau^4$ . Additionally, for any value of *iunit1* other than 6, printed output is saved in disk file **pipe.prt** at the conclusion of the run.

### C.3.2 Program PLOTP: Plotting Utility

Program **PLOTP** creates video and hardcopy plots of channel- or pipe-flow properties computed with program **PIPE** on IBM PC's and compatibles. The program automatically detects the turbulence model used and the type flow for which computations have been done.

#### Input-parameter description:

Program **PLOTP** reads the following seven input parameters in the order listed below from disk file **plotp.dat**. Integer quantities must be formatted according to (7x,i6) while floating-point quantities must be formatted as (7x,f6.2). This is similar to the format used for Program **PIPE**.

<i>mon</i>	Monitor type (see Appendix E)
<i>ifore</i>	Foreground color (see Appendix E)
<i>iback</i>	Background color (see Appendix E)
<i>nprin</i>	Printer type (see Appendix E)
<i>mode</i>	Graphics-mode flag for printers; number of pens for plotters (see Appendix E)
<i>ksize</i>	Plot scaling factor. Using 100 yields a full-size hardcopy plot. Smaller values yield a hardcopy plot reduced by <i>ksize</i> per cent. Thus, <i>ksize</i> = 50 yields a half-size plot.
<i>symsiz</i>	Size of experimental data symbols, in inches

Next, Program **PLOTP** reads a single, free formatted, line to indicate where hardcopy print is directed and where required font files are located. This line comes immediately after the specified value for *symsiz* and defines the following six additional parameters.

<i>devid</i>	Device name of type character*4; valid devices are LPT1, LPT2, LPT3, COM1, COM2, COM3, COM4
<i>nbaud</i>	Baud rate for a serial port; valid baud rates are 110, 150, 300, 600, 1200, 2400, 4800, 9600
<i>parity</i>	Parity of type character*3 or character*4 for a serial port; valid parity settings are 'even', 'odd' and 'none'
<i>nstop</i>	Number of stop bits for a serial port; either 1 or 2
<i>lword</i>	Word length for a serial port; either 7 or 8
<i>path</i>	Path to font files of type character*n where $n \leq 40$

In addition to disk file **plotp.dat**, an optional disk file including skin-friction data can be included. This information includes results from a series of runs and must be prepared by the user. The name of the optional disk file depends upon the turbulence model used, viz.:

<b>cfkw.dat</b>	Wilcox $k$ - $\omega$ model
<b>cfms.dat</b>	Wilcox multiscale model
<b>cfcs.dat</b>	Cebeci-Smith model
<b>cfbl.dat</b>	Baldwin-Lomax model
<b>cfus.dat</b>	User-supplied model

The first line of the disk file must contain the number of input data pairs with format (i4). This line is followed by Reynolds number/skin friction data pairs with format (2e13.6). For example, a series of 10 runs with the Baldwin-Lomax model for channel flow yields the following results.

```

10
1.021000e 03 1.919000e-02
2.625000e 03 1.161000e-02
5.510000e 03 8.538000e-03
1.020000e 04 6.922000e-03
1.413000e 04 6.252000e-03
2.718000e 04 5.308000e-03
4.071000e 04 4.828000e-03
6.429000e 04 4.355000e-03
8.835000e 04 4.100000e-03
1.003000e 05 3.990000e-03

```

For channel flow, confine Reynolds number to the range  $10^3 \leq Re_H \leq 10^5$ . For pipe flow, Reynolds number should be in the range  $10^3 \leq Re_D \leq 10^6$ .

#### Output description:

A video plot with six graphs (see Figure C.2) is created on the screen. When the plot is complete, the following message appears:

**Hardcopy output (y/n)?**

Enter a *y* or a *Y* to create a hardcopy plot. Pressing any other key terminates the run without creating a hardcopy plot.

#### Comments:

- The following is a sample input data file for a machine with a standard VGA monitor and an HP DeskJet connected to serial port COM1:.

```

mon   =    18           (Standard VGA monitor)
ifore =    15           (Bright-white foreground)
iback =     1           (Blue background)
nprin =     2           (HP DeskJet)

```

```

mode =      3              (300 dots per inch resolution)
ksize =    100             (Full size plot)
symsiz=   .080             (.08" experimental data symbols)
'com1' , 9600 , 'none' , 1 , 8, 'd:\fonts\'

```

The last line indicates the printer is connected to serial port COM1: and the port is set at 9600 baud, no parity, 1 stop bit and 8 data bits. Also, the plotting font file **sppfnt.002** is located in directory **fonts** on drive **d:**.

**IMPORTANT:** The terminating character in the path name must be a backslash, i.e., \.

- If disk file **plotp.dat** is not available, Program **PLOTP** uses the following set of default values :

```

mon = 18, ifore = 15, iback = 1, nprin = 24, mode = 39, ksize = 100,
symsiz = .08, devid = 'LPT1', path = '\

```

Note that *nbaud*, *parity*, *nstop* and *lword* are not used for parallel ports. Note also that the default path is the **root directory** of the current drive.

- The following data are used for comparison with computed results:

Channel Flow — $Re_\tau < 287$ ,	Mansour, et al. (1988) [ $Re_\tau = 180$ ]
Channel Flow — $Re_\tau \geq 287$ ,	Mansour, et al. (1988) [ $Re_\tau = 395$ ]
Pipe Flow — All $Re_\tau$ ,	Laufer (1952) [ $Re_\tau = 1058$ ]

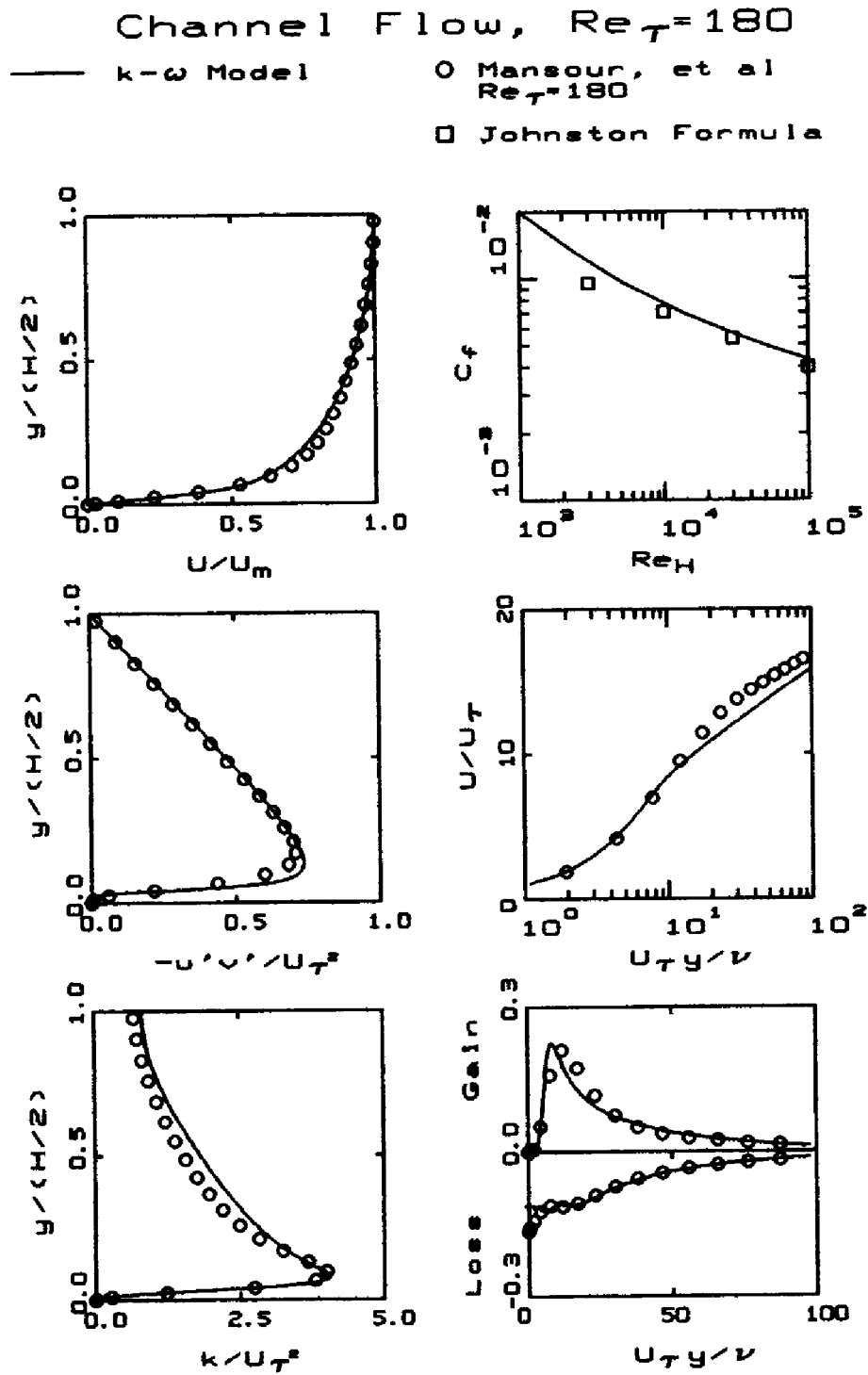


Figure C.2: Sample plot created by Program PLOTP.

## C.4 Boundary-Layer Perturbation Analysis

Programs **SUBLAY** and **DEFECT** can be used to compute turbulence-model predicted flow properties in the incompressible viscous sublayer and defect layer, respectively. Section 4.6 of the main text describes the sublayer and defect-layer equations. No additional transformations are introduced in Program **SUBLAY**. Program **DEFECT** uses the Rubel-Melnik (1984) transformation.

As with the free shear flow and pipe-flow programs, we add unsteady terms to the turbulence-model equations to facilitate solution of the two-point boundary-value problems appropriate for the sublayer and the defect layer. In Program **SUBLAY**, the momentum equation is solved at each timestep by trapezoidal-rule integration. For example, in the case of a two-equation model, we advance the turbulence parameters in time. Then, after updating the eddy viscosity, we determine the velocity by integration of the following equation.

$$\frac{dU^+}{dy^+} = \frac{1}{1 + \mu_T^+} \quad (\text{C.14})$$

All notation in Equation (C.14) is identical to that used in Section 4.6 of the main text.

The only other subtle feature of Program **SUBLAY** is the way the specific dissipation rate,  $\omega$ , in the Wilcox (1988a)  $k$ - $\omega$  model and the Wilcox (1988b) multiscale model is computed close to the solid boundary. To eliminate numerical error associated with computing the singular behavior of  $\omega$  for perfectly-smooth and slightly-rough surfaces, the exact asymptotic behavior of  $\omega$  is prescribed close to the surface (see Subsection 7.2.1). That is, we use the fact that, for  $y^+ < 2.5$ ,  $\omega^+ = \nu\omega/u_\tau^2$  is given by:

$$\omega^+ \rightarrow \frac{N_\omega}{(y^+)^2} \quad \text{as } y \rightarrow 0 \quad (\text{smooth wall}) \quad (\text{C.15})$$

$$\omega^+ \rightarrow \frac{\omega_w^+}{\left[1 + \sqrt{\frac{\omega_w^+}{N_\omega}} y^+\right]^2} \quad \text{as } y \rightarrow 0 \quad (\text{rough wall}) \quad (\text{C.16})$$

where

$$N_\omega = \begin{cases} 6/\beta, & \text{without viscous corrections} \\ 2/\beta^*, & \text{with viscous corrections} \end{cases} \quad (\text{C.17})$$

The exact analytical behavior of  $\omega$  is imposed for a prescribed number of mesh points,  $j_{skip}$ , next to the surface.



In terms of the transformation devised by Rubel and Melnik, the defect-layer equations are as follows. Note that to avoid numerical difficulties, Program **DEFECT** uses a small nonzero value for  $K_0(\xi)$  when  $\xi \rightarrow \infty$ . The nonvanishing boundary conditions quoted for  $W_0(\xi)$  and  $E_0(\xi)$  as  $\xi \rightarrow \infty$  are the only choices consistent with the similarity solution.

**All Models:**

$$\eta = \int_{-\infty}^{\xi} N_0(\xi') d\xi' \quad (\text{C.18})$$

$$\frac{d^2 U_1}{d\xi^2} + (1 + \beta_T) \eta \frac{dU_1}{d\xi} + \beta_T N_0 U_1 = 0 \quad (\text{C.19})$$

$$\sigma^* \frac{d^2 K_0}{d\xi^2} + (1 + \beta_T) \eta \frac{dK_0}{d\xi} + \sqrt{\beta^*} \left[ \left( \frac{dU_1}{d\xi} \right)^2 - K_0^2 \right] = 0 \quad (\text{C.20})$$

**$k$ - $\omega$  Model:**

$$\begin{aligned} \sigma \frac{d^2 W_0}{d\xi^2} + (1 + \beta_T) \eta \frac{dW_0}{d\xi} + (1 + 2\beta_T) N_0 W_0 \\ + \frac{\sqrt{\beta^*}}{K_0} \left[ \alpha \left( \frac{dU_1}{d\xi} \right)^2 - \frac{\beta}{\beta^*} K_0^2 \right] W_0 = 0 \end{aligned} \quad (\text{C.21})$$

$$W_0(\xi) \rightarrow \frac{(1 + 2\beta_T) \sqrt{\beta^*}}{\beta} \quad \text{as} \quad \xi \rightarrow \infty \quad (\text{C.22})$$

$$N_0 = K_0 / W_0 \quad (\text{C.23})$$

**$k$ - $\epsilon$  Model:**

$$\begin{aligned} \sigma_\epsilon^{-1} \frac{d^2 E_0}{d\xi^2} + (1 + \beta_T) \eta \frac{dE_0}{d\xi} + (1 + 2\beta_T) N_0 E_0 \\ + \frac{\sqrt{C_\mu}}{K_0} \left[ C_{\epsilon 1} \left( \frac{dU_1}{d\xi} \right)^2 - C_{\epsilon 2} K_0^2 \right] E_0 = 0 \end{aligned} \quad (\text{C.24})$$

$$E_0(\xi) / K_0(\xi) \rightarrow \frac{(1 + 2\beta_T)}{C_{\epsilon 2} \sqrt{C_\mu}} \quad \text{as} \quad \xi \rightarrow \infty \quad (\text{C.25})$$

$$N_0 = K_0^2 / E_0 \quad (\text{C.26})$$

### C.4.1 Program SUBLAY: Viscous Sublayer

Program **SUBLAY** computes incompressible viscous sublayer flow, including surface roughness and surface mass transfer.

#### Input-parameter description:

Program **SUBLAY** reads the following input parameters from disk file **sublay.dat** in the order listed below. Integer quantities must be formatted according to (1x,a12,i4) while floating-point quantities must be formatted as (1x,a12,e13.6). See Subsection C.1.2 for a sample input-data file.

- iunit1* Output-file unit number
  - = 6 Printed output sent to printer
  - ≠ 6 Printed output saved in disk file **sublay.prt**
- iunit2* Plotting-data disk file unit number
- model* Turbulence-model identification flag
  - 0 Wilcox  $k$ - $\omega$  model
  - 1 Wilcox multiscale model
  - 99 User-defined model
- omegw* Surface value of dimensionless specific dissipation rate,  $\omega_w^+$
- vwplus* Dimensionless vertical velocity at the surface,  $v_w/u_\tau$ .
- xih*  $\omega$ -equation closure coefficient  $\hat{\xi}$
- ymax* Maximum value of  $y^+$
- yone* Value of  $y^+$  at the first grid point above the wall
- iruff* Surface-roughness flag
  - 0 Rough surface
  - 1 Smooth surface
- jmax* Number of grid points
- jskip* Grid-point number below which the exact asymptotic solution for specific dissipation rate is used
- maxn* Maximum number of timesteps
- nedit* Profile-print modulus; profiles are printed every *nedit* steps
- nfreq* Short-print modulus; maximum error and  $B = u^+ - \frac{1}{\kappa} \ln y^+$  at  $y^+ = y_{max}$  are printed every *nfreq* steps
- nvisc* Viscous-modification flag
  - = 0 No  $k$ - $\omega$ /multiscale model viscous modifications
  - ≠ 0 Use  $k$ - $\omega$ /multiscale model viscous modifications

#### Output description:

VIDEO OUTPUT includes the timestep number, maximum error, and the constant in the law of the wall,  $B = u^+ - \frac{1}{\kappa} \ln y^+$ , at  $y^+ = y_{max}$  every *nfreq* timesteps. PRINTED OUTPUT is sent to the line printer throughout the run if *iunit1* = 6. DISK-FILE OUTPUT is saved in the appropriate

plotting-data disk file (see Subsection C.1.3 for file names). The file is **unformatted** and is created using the following statements.

```

      do 50 j=2,jmax
        wtm(j)=-betas*bbeta(j)*et(j)*wt(j)
        if(model.ne.1) tau(j)=eps(j)*dudy(j)
        etm(j)=tau(j)*dudy(j)
50    continue
      if(nvisc.ne.0) wtm(1)=2.*wtm(2)-wtm(3)
      etm(1)=0.
      write(iunit2) jmax
      write(iunit2) (yplus(j),uplus(j),wtm(j),
                    etm(j),j=1,jmax)

```

The quantity  $yplus(j)$  is  $y^+$ ,  $uplus(j)$  is  $U^+$ ,  $wtm(j)$  is  $\beta^* \nu \omega k / u_\tau^4$ , and  $etm(j)$  is  $\nu \tau_{xy} (dU/dy) / u_\tau^4$ . Additionally, for any value of *iunit1* other than 6, printed output is saved in disk file **sublay.prt** at the conclusion of the run.

### C.4.2 Program DEFECT: Defect Layer

Program **DEFECT** computes properties of the incompressible defect-layer including effects of pressure gradient.

#### Input-parameter description:

Program **DEFECT** reads the following input parameters from disk file **defect.dat** in the order listed below. Integer quantities must be formatted according to (1x,a12,i4) while floating-point quantities must be formatted as (1x,a12,e13.6). See Subsection C.1.2 for a sample input-data file.

*iunit1* Output-file unit number  
           = 6 Printed output sent to printer  
            $\neq$  6 Printed output saved in disk file **defect.prt**  
*iunit2* Plotting-data disk file unit number  
*model* Turbulence-model identification flag  
           0 Wilcox  $k$ - $\omega$  model  
           2 Standard  $k$ - $\epsilon$  model  
           99 User-defined model  
*betat* Pressure-gradient parameter,  $\beta_T$   
*jmax* Number of grid points  
*maxn* Maximum number of timesteps  
*nedit* Profile-print modulus; profiles are printed every *nedit* steps  
*nfreq* Short-print modulus; maximum error, wake strength, etc. are printed every *nfreq* steps

#### Output description:

VIDEO OUTPUT includes the timestep number, maximum error, wake strength, etc. every *nfreq* timesteps. PRINTED OUTPUT is sent to the line printer throughout the run if *iunit1* = 6. DISK-FILE OUTPUT is saved in the appropriate plotting-data disk file (see Subsection C.1.3 for file names). The file is **unformatted** and is created using the following statements.

```
write(iunit2) jmax,betat
write(iunit2) (eta(j),u(j),j=1,jmax)
```

where *betat* is  $\beta_T$ , *eta(j)* is  $\eta_j$  and *u(j)* is  $[U_e - U(\eta_j)]/u_\tau$ . Additionally, for any value of *iunit1* other than 6, printed output is saved in disk file **defect.prt** at the conclusion of the run.

#### Comments:

- The program has been optimized for  $-0.5 \leq \beta_T \leq 15$ .

### C.4.3 Program PLOTS: Sublayer Plotting Utility

Program **PLOTS** creates video and hardcopy plots of viscous sublayer properties computed with program **SUBLAY** on IBM PC's and compatibles. The program automatically detects the turbulence model used.

#### Input-parameter description:

Program **PLOTS** reads the following seven input parameters from disk file **plots.dat** in the order listed below. Integer quantities must be formatted according to (7x,i6) while floating-point quantities must be formatted as (7x,f6.2). This is similar to the format used for Program **SUBLAY**.

<i>mon</i>	Monitor type (see Appendix E)
<i>ifore</i>	Foreground color (see Appendix E)
<i>iback</i>	Background color (see Appendix E)
<i>nprin</i>	Printer type (see Appendix E)
<i>mode</i>	Graphics-mode flag for printers; number of pens for plotters (see Appendix E)
<i>ksize</i>	Plot scaling factor. Using 100 yields a full-size hardcopy plot. Smaller values yield a hardcopy plot reduced by <i>ksize</i> per cent. Thus, <i>ksize</i> = 50 yields a half-size plot.
<i>symsiz</i>	Size of experimental data symbols, in inches

Next, Program **PLOTS** reads a single, free formatted, line to indicate where hardcopy print is directed and where required font files are located. This line comes immediately after the specified value for *symsiz* and defines the following six additional parameters.

<i>devid</i>	Device name of type character*4; valid devices are LPT1, LPT2, LPT3, COM1, COM2, COM3, COM4
<i>nbaud</i>	Baud rate for a serial port; valid baud rates are 110, 150, 300, 600, 1200, 2400, 4800, 9600
<i>parity</i>	Parity of type character*3 or character*4 for a serial port; valid parity settings are 'even', 'odd' and 'none'
<i>nstop</i>	Number of stop bits for a serial port; either 1 or 2
<i>lword</i>	Word length for a serial port; either 7 or 8
<i>path</i>	Path to font files of type character*n where $n \leq 40$

#### Output description:

A video plot with two graphs (see Figure C.3) is created on the screen. When the plot is complete, the following message appears:

**Hardcopy output (y/n)?**

Enter a *y* or a *Y* to create a hardcopy plot. Pressing any other key terminates the run without creating a hardcopy plot.

**Comments:**

- The following is a sample input data file for a machine with a standard VGA monitor and an HP DeskJet connected to serial port COM1:.

```

mon    =    18                (Standard VGA monitor)
ifore  =    15                (Bright-white foreground)
iback  =     1                (Blue background)
nprin  =     2                (HP DeskJet)
mode   =     3                (300 dots per inch resolution)
ksize  =   100                (Full size plot)
symsiz =   .080              (.08" experimental data symbols)
'com1' , 9600 , 'none' , 1 , 8, 'd:\fonts\'

```

The last line indicates the printer is connected to serial port COM1: and the port is set at 9600 baud, no parity, 1 stop bit and 8 data bits. Also, the plotting font file **sppfnt.002** is located in directory **fonts** on drive **d:**.

**IMPORTANT:** The terminating character in the path name must be a backslash, i.e., \.

- If disk file **plots.dat** is not available, Program **PLOTS** uses the following set of default values :

```

mon = 18, ifore = 15, iback = 1, nprin = 24, mode = 39, ksize = 100,
symsiz = .08, devid = 'LPT1', path = '\'

```

Note that *nbaud*, *parity*, *nstop* and *lword* are not used for parallel ports. Note also that the default path is the **root directory** of the current drive.

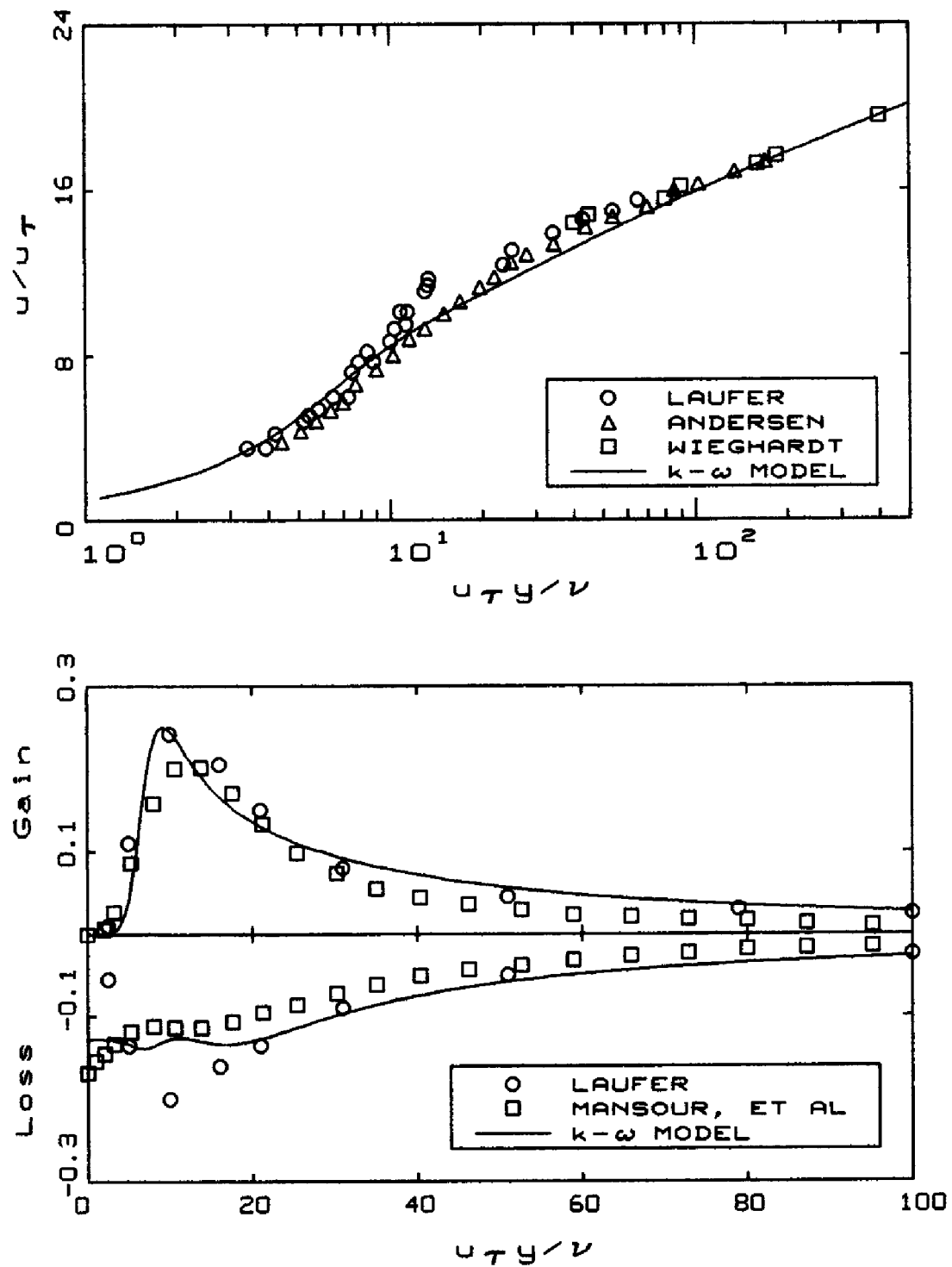


Figure C.3: Sample plot created by Program PLOTS.

### C.4.4 Program PLOTD: Defect-Layer Plotting Utility

Program **PLOTD** creates video and hardcopy plots of the defect-layer velocity profile computed with program **DEFECT** on IBM PC's and compatibles. The program automatically detects the turbulence model used.

#### Input-parameter description:

Program **PLOTD** reads the following nine input parameters from disk file **plotd.dat** in the order listed below. Integer quantities must be formatted according to (7x,i6) while floating-point quantities must be formatted as (7x,f6.2). This is similar to the format used for Program **DEFECT**.

<i>mon</i>	Monitor type (see Appendix E)
<i>ifore</i>	Foreground color (see Appendix E)
<i>iback</i>	Background color (see Appendix E)
<i>nprin</i>	Printer type (see Appendix E)
<i>mode</i>	Graphics-mode flag for printers; number of pens for plotters (see Appendix E)
<i>ksize</i>	Plot scaling factor. Using 100 yields a 5" by 5" hardcopy plot. Smaller values yield a hardcopy plot reduced by <i>ksize</i> per cent. Thus, <i>ksize</i> = 50 yields a 2.5" by 2.5" plot.
<i>symsiz</i>	Size of experimental data symbols, in inches
<i>height</i>	Physical height, in inches, of the video display
<i>width</i>	Physical width, in inches, of the video display

Next, Program **PLOTD** reads a single, free formatted, line to indicate where hardcopy print is directed and where required font files are located. This line comes immediately after the specified value for *width* and defines the following six additional parameters.

<i>devicd</i>	Device name of type character*4; valid devices are LPT1, LPT2, LPT3, COM1, COM2, COM3, COM4
<i>nbaud</i>	Baud rate for a serial port; valid baud rates are 110, 150, 300, 600, 1200, 2400, 4800, 9600
<i>parity</i>	Parity of type character*3 or character*4 for a serial port; valid parity settings are 'even', 'odd' and 'none'
<i>nstop</i>	Number of stop bits for a serial port; either 1 or 2
<i>lword</i>	Word length for a serial port; either 7 or 8
<i>path</i>	Path to font files of type character*n where $n \leq 40$

#### Output description:

A 5" by 5" video plot (see Figure C.4) is created centered on the screen. When the plot is complete, the following message appears:



**Hardcopy output (y/n)?**

Enter a *y* or a *Y* to create a hardcopy plot. Pressing any other key terminates the run without creating a hardcopy plot.

**Comments:**

- The following is a sample input data file for a machine with a standard VGA monitor and an HP DeskJet connected to serial port COM1:

```

mon    =    18                (Standard VGA monitor)
ifore  =    15                (Bright-white foreground)
iback  =     1                (Blue background)
nprin  =     2                (HP DeskJet)
mode   =     3                (300 dots per inch resolution)
ksize  =   100                (Full size plot)
symsiz =  .080                (.08" experimental data symbols)
height =  7.500              (7.5" high video display)
width  =  9.250              (9.25" wide video display)
'com1' , 9600 , 'none' , 1 , 8, 'd:\fonts\'

```

The last line indicates the printer is connected to serial port COM1: and the port is set at 9600 baud, no parity, 1 stop bit and 8 data bits. Also, the plotting font file **sppfnt.002** is located in directory **fonts** on drive **d**:

**IMPORTANT:** The terminating character in the path name must be a backslash, i.e., \.

- If disk file **plotd.dat** is not available, Program **PLOTD** uses the following set of default values :

```

mon = 18, ifore = 15, iback = 1, nprin = 24, mode = 39, ksize = 100,
symsiz = .08, height = 7.5, width = 9.25, devid = 'LPT1', path = '\

```

Note that *nbaud*, *parity*, *nstop* and *lword* are not used for parallel ports. Note also that the default path is the **root directory** of the current drive.

- The following experimental data from Coles and Hirst (1969) are used:

```

 $\beta_T < 0$ ,      Flow 2800: Herring-Norbury ( $\beta_T = -0.5$ )
 $0 \leq \beta_T \leq 2$ , Flow 1400: Wieghardt ( $\beta_T = 0.0$ )
 $2 < \beta_T < 7$ ,   Flow 2600: Bradshaw ( $\beta_T = 5.2$ )
 $\beta_T \geq 7$ ,     Flow 2300: Clauser ( $\beta_T = 8.7$ )

```

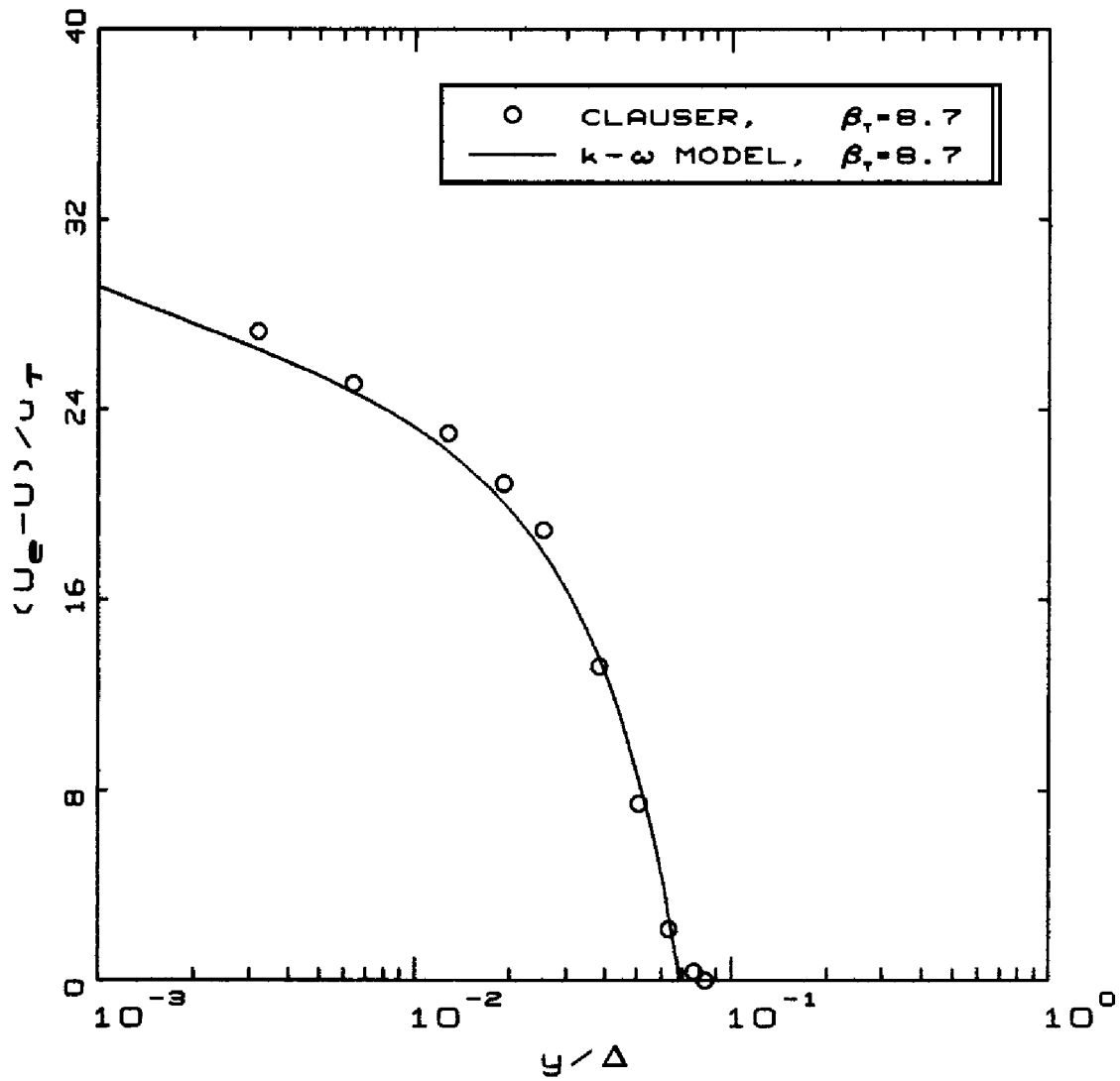


Figure C.4: Sample plot created by Program PLOTD.

## C.5 Miscellaneous Routines

This section includes several utility routines called by the various programs described in the preceding sections. They implement several standard mathematical procedures such as the Runge-Kutta predictor-corrector method for integrating a system of ordinary differential equations, the Newton iteration method for solving transcendental equations and Thomas' algorithm for solving a tridiagonal matrix system. These routines are of general usefulness in computational fluid mechanics as well as for the programs that are the main topic of this appendix. We assume the user is familiar with these algorithms and thus include only instructions on use of the subroutines. Users unfamiliar with the techniques should refer to texts such as Abramowitz and Stegun (1965), Hildebrand (1976), Chapra and Canale (1985) and Press, Flannery, Teukolsky and Vetterling (1987).

There is one routine, **NAMSYS**, that is called by all of the programs. The purpose of this routine is to make the programs portable to a variety of computers. The routine sets several system-dependent variables used in opening files, assigning video and hardcopy units, etc. The standardization of Fortran-77, including VAX extensions, by most compiler writers makes it possible to confine virtually all system-dependent parameters to this single subroutine.

For the convenience of users with IBM PC and compatible microcomputers, a library named **dcw.lib** containing the routines described in this section is included on the distribution diskette. The library is compatible with Microsoft Fortran, Version 5.00. The routines have been compiled with the **/FPI** option that generates code that will use a math coprocessor if it is available and provide software emulation if no coprocessor is available. To link the programs described in the preceding chapters (say, for example, **progrname**) use the following command.

**link progrname,,nul,dcw /e;**

**C.5.1 Function ERF: Error Function**

Function **ERF** computes the error function  $erf(x)$  defined by

$$erf(x) = \frac{2}{\sqrt{\pi}} \int_0^{\infty} e^{-t^2} dt$$

**Usage:** <real variable> =  $erf(x)$

**Input-parameter description:**

$x$       Error function argument,  $x$

**Output-parameter description:**

$erf$       Computed value,  $erf(x)$

**Comments:**

- A polynomial approximation is used. When  $x < 0$ , the function uses the fact that

$$erf(-x) = -erf(x)$$

### C.5.2 Subroutine NAMSYS: Fortran Portability

Subroutine **NAMSYS** returns several system-dependent and compiler-specific parameters to aid in portability of Fortran programs.

**Usage:** call `namsys(icpu,iin,iv,msdos,newfil,pform)`

#### Input-parameter description:

*icpu* CPU identification flag  
0 SVS Fortran (680x0, 80x86)  
1 Lahey/Microsoft Fortran (8088, 80x86)  
2 VAX/VMS  
3 SUN Fortran (SUN Workstation, Definicon SPARC)  
4 Cray Fortran/Unicos (Cray X/MP, Y/MP)  
5 Silicon Graphics Iris

#### Output-parameter description:

*iin* Input data file logical unit number; set to unit 15 for all CPU's  
*iv* Standard console unit number; set to 5 for all CPU's  
*msdos* Open-printer flag  
0 Printer opened as '*prn*'  
1 Don't open '*prn*'  
*newfil* Character\*7 string used in opening new files  
'*new*' if compiler writes over an existing file  
'*unknown*' for Ansi-77 standard operation  
*pform* Character\*9 string used as format type for printer output that is redirected to a disk file  
'*printer*' for SVS Fortran  
'*print*' for SUN Fortran  
'*formatted*' for all others

#### Comments:

- This routine is currently configured for the CPU's and Fortran compilers listed in the Input-parameter description. Other CPU's and compilers can be included by adding the appropriate statements to the routine. The following page includes an abbreviated listing of **NAMSYS**.

```

      subroutine namsys(icpu,iin,iv,msdos,newfil,pform)
      character newfil*7,pform*9
      iin=15
      iv=5
c-----
c   SVS Fortran (680x0 and 80x86)
      if(icpu.eq.0) then
         msdos=0
         pform='printer'
         newfil='new'
c-----
c   Lahey/Microsoft Fortran (80x86)
      elseif(icpu.eq.1) then
         msdos=0
         pform='formatted'
         newfil='unknown'
c-----
c               VAX/VMS
      elseif(icpu.eq.2) then
         msdos=1
         pform='formatted'
         newfil='new'
c-----
c   SUN Fortran...SUN Workstation
      elseif(icpu.eq.3) then
         msdos=0
         pform='print'
         newfil='unknown'
c-----
c   Cray Fortran...Unicos
      elseif(icpu.eq.4) then
         msdos=1
         pform='formatted'
         newfil='unknown'
c-----
c   Silicon Graphics Iris
      elseif(icpu.eq.5) then
         msdos=0
         pform='formatted'
         newfil='unknown'
c-----
c   Error...say so and quit
      else
         write(*,*) 'icpu = ',icpu,' is not supported!!!'
         stop
      endif
      return
      end

```

### C.5.3 Subroutine RKGS: Runge-Kutta Integration

Subroutine **RKGS** solves a system of first-order ordinary differential equations defined in an external subroutine with given initial values. The system of equations is of the form

$$\frac{dy_i}{dx} = f_i(x, y_j) \quad \text{for} \quad x_0 \leq x \leq x_1$$

**Usage:** call rkgs(prmt,y,yp,ndim,ihlf,fct,otp,aux)

#### Input-parameter description:

- fct* The name of an external subroutine used to compute the right hand side vector,  $f = yp$ . The argument list to this subroutine must be  $(x, y, yp)$ , and the subroutine must leave the values of  $x$  and  $y$  unchanged.
- ndim* Number of equations in the system
- prmt* Input and output array with dimension  $\geq 5$ , that specifies interval and accuracy parameters and that serves for communication between output subroutine *otp* (furnished by the user) and subroutine **RKGS**. With the exception of *prmt*(5), the components are not destroyed by subroutine **RKGS** and they are:
- prmt*(1) Lower bound of the interval,  $x_0$
  - prmt*(2) Upper bound of the interval,  $x_1$
  - prmt*(3)  $\Delta x_0$ , initial increment of  $x$
  - prmt*(4) Upper error bound. If the absolute error is greater than *prmt*(4), the increment is halved. If the increment is less than  $\Delta x_0$  and the absolute error is less than *prmt*(4)/50, the increment is doubled. If desired, the user can change *prmt*(4) in output subroutine *otp*.
  - prmt*(5) Termination parameter. Subroutine **RKGS** initially sets *prmt*(5) = 0. In order to terminate subroutine **RKGS** at any output point, change *prmt*(5) to a nonzero value in subroutine *otp*.
- y* Input vector of initial values,  $y_0$ .
- yp* Input vector of error weights; the sum of its components must be equal to 1.

#### Output-parameter description:

- aux* An  $(8 \times ndim)$  auxiliary storage array

- ihlf* Number of bisections of the initial increment. If *ihlf* exceeds 10, subroutine **RKGS** returns *ihlf* = 11. Additionally, if  $\Delta x_0 = 0$ , **RKGS** returns with *ihlf* = 12 while if  $\Delta x_0$  and  $(x_1 - x_0)$  differ in sign, **RKGS** returns *ihlf* = 13.
- outp* The name of an external subroutine used for program output. The form of its argument list must be  $(x, y, yp, ihlf, ndim, prmt)$ . None of these parameters (except, if necessary, *prmt*(4), *prmt*(5), ...) should be changed by subroutine *outp*. If *prmt*(5) is changed to a nonzero value, subroutine **RKGS** is terminated.
- prmt* Input and output array with dimension  $\geq 5$ , that specifies interval and accuracy parameters and that serves for communication between output subroutine *outp* (furnished by the user) and subroutine **RKGS**.
- prmt*(6) Although not required by subroutine **RKGS**, additional parameters can be included in array *prmt* provided its dimension is declared to be  $> 5$ . Such parameters may be useful for passing values to the routine calling **RKGS** which are obtained by special manipulations of output data in subroutine *outp*.
- y* Output vector of computed values, **y**, at intermediate points.
- yp* Output vector of derivatives, corresponding to function values **y** at point *x*.

**Comments:**

- Computation is done using the fourth-order accurate Runge-Kutta method with Gill's modification. Accuracy is tested by comparing the results of the procedure with single and double increments of the independent variable,  $\Delta x$ . Subroutine **RKGS** automatically adjusts the increment during the computation by halving or doubling  $\Delta x$ . The procedure terminates and returns to the calling routine, if any of the following conditions occur.
  1. More than 10 bisections of the initial increment are necessary to achieve satisfactory accuracy (error flag *ihlf* = 11);
  2. Either the initial increment  $\Delta x_0 = 0$  or has the wrong sign (error flags *ihlf* = 12 or *ihlf* = 13);
  3. The end of the integration interval,  $x = x_1$ , reached;
  4. Subroutine *outp* has changed *prmt*(5) to a nonzero value.
- The calling routine must declare the two user-supplied subroutines *outp*(*x, y, yp, ihlf, ndim, prmt*) and *fct*(*x, y, yp*) as external by including the statements **EXTERNAL FCT** and **EXTERNAL OUTP**.



### C.5.4 Subroutine RTNI: Newton's Iterations

Subroutine **RTNI** solves a general equation of the form  $f(x) = 0$  using Newton's iteration method. The function  $f(x)$  is specified by the user in a **SUBROUTINE** subprogram.

**Usage:** call `rtni(x,f,fp,fct,xst,eps,iend,ier)`

#### Input-parameter description:

<i>eps</i>	Upper bound on the error in $x$
<i>fct</i>	Name of the external subroutine used. It computes $f = f(x)$ and $fp = df/dx$ for a given value of $x$ . Its argument list must be $(x,f,fp)$ .
<i>iend</i>	Maximum number of iterations allowed
<i>xst</i>	Initial guess of the root $x_{st}$

#### Output-parameter description:

<i>f</i>	Computed value of $f(x)$ at root $x$
<i>fp</i>	Computed value of $df/dx$ at root $x$
<i>ier</i>	Error flag
	0 No error
	1 No convergence after <i>iend</i> iterations
	2 $df/dx = 0$ encountered
<i>x</i>	Computed root of $f(x) = 0$

#### Comments:

- Solution of the equation  $f(x) = 0$  is obtained using Newton's iteration method, which starts at the initial guess  $x_{st}$  of the root  $x$ . Convergence is quadratic if the value of  $df/dx$  at root  $x$  is not equal to zero. One iteration step requires one evaluation of  $f(x)$  and one evaluation of  $df/dx$ .
- The subroutine returns with the error flag  $ier = 2$  if, at any iteration step,  $df/dx$  vanishes.
- The calling routine must declare the subroutine  $fct(x,f,fp)$  as external by including an **EXTERNAL FCT** statement.

**C.5.5 Subroutine TRI: Tridiagonal Matrix Inversion**

Subroutine **TRI** solves the tridiagonal matrix equation

$$a_i x_{i-1} + b_i x_i + c_i x_{i+1} = d_i \quad \text{for} \quad I_l + 1 \leq i \leq I_u - 1$$

subject to either Dirichlet or Neumann boundary conditions.

**Usage:** call tri(a,b,c,d,il,iu,ibcl,dl,ibcu,du)

**Input-parameter description:**

- a*      Array of matrix elements left of the diagonal,  $a_i$ ; destroyed in the computation.
- b*      Array of matrix diagonal elements,  $b_i$ ; destroyed in the computation.
- c*      Array of matrix elements right of the diagonal,  $c_i$ .
- d*      Input right-hand-side vector,  $d_i$ . This vector is replaced by the solution vector,  $x_i$ .
- dl*      $d_{I_l}$ , lower boundary-condition value
- du*      $d_{I_u}$ , upper boundary-condition value
- ibcl*    Lower boundary-condition flag
  - 0 Dirichlet,  $x_{I_l} = d_{I_l}$
  - 1 Neumann,  $x_{I_l+1} - x_{I_l} = d_{I_l}$
- ibcu*    Upper boundary-condition flag
  - 0 Dirichlet,  $x_{I_u} = d_{I_u}$
  - 1 Neumann,  $x_{I_u} - x_{I_u-1} = d_{I_u}$
- il*       $I_l$ , lower bound on  $i$
- iu*       $I_u$ , upper bound on  $i$ ; also length of  $a_i$ ,  $b_i$ ,  $c_i$  and  $d_i$ .

**Output-parameter description:**

- d*      Solution vector,  $x_i$ . This vector replaces input vector  $d_i$ .

**Comments:**

- The solution is obtained using Thomas' algorithm. The input arrays  $a_i$ ,  $b_i$ ,  $c_i$  and  $d_i$  need only be specified for indices in the range

$$I_l + 1 \leq i \leq I_u - 1$$

## C.6 Diskette Contents

### Flowfield Program Source:

<b>cpuid</b>	Include file specifying CPU type
<b>defect.for</b>	Source code for Program <b>DEFECT</b>
<b>jet.for</b>	Source code for Program <b>JET</b>
<b>mixer.for</b>	Source code for Program <b>MIXER</b>
<b>pipe.for</b>	Source code for Program <b>PIPE</b>
<b>sublay.for</b>	Source code for Program <b>SUBLAY</b>
<b>wake.for</b>	Source code for Program <b>WAKE</b>

### Miscellaneous Routine Source:

<b>erf.for</b>	Source code for Function <b>ERF</b>
<b>namsys.for</b>	Source code for Subroutine <b>NAMSYS</b>
<b>rkgs.for</b>	Source code for Subroutine <b>RKGS</b>
<b>rtni.for</b>	Source code for Subroutine <b>RTNI</b>
<b>tri.for</b>	Source code for Subroutine <b>TRI</b>

### Input Data for Flowfield Programs:

<b>defect.dat</b>	Input data for Program <b>DEFECT</b>
<b>jet.dat</b>	Input data for Program <b>JET</b>
<b>mixer.dat</b>	Input data for Program <b>MIXER</b>
<b>pipe.dat</b>	Input data for Program <b>PIPE</b>
<b>sublay.dat</b>	Input data for Program <b>SUBLAY</b>
<b>wake.dat</b>	Input data for Program <b>WAKE</b>

### IBM PC Executable Plotting Programs:

<b>plotd.exe</b>	Plotting program for Program <b>DEFECT</b>
<b>plotf.exe</b>	Plotting program for <b>JET</b> , <b>MIXER</b> and <b>WAKE</b>
<b>plotp.exe</b>	Plotting program for Program <b>PIPE</b>
<b>plots.exe</b>	Plotting program for Program <b>SUBLAY</b>

### Input Data for Plotting Programs:

<b>plotd.dat</b>	Input data for Program <b>PLOTD</b>
<b>plotf.dat</b>	Input data for Program <b>PLOTF</b>
<b>plotp.dat</b>	Input data for Program <b>PLOTP</b>
<b>plots.dat</b>	Input data for Program <b>PLOTS</b>

### Miscellaneous Files:

<b>dcw.lib</b>	Miscellaneous routines library
<b>sppfmt.002</b>	Scientific font file for plotting programs

# Appendix D

## Program EDDYBL

### D.1 Overview

This appendix is the user's guide for Program **EDDYBL**, a two dimensional and axisymmetric, compressible boundary-layer program for turbulent boundary layers that is included on the distribution diskette. An overview of the program's evolution and operation is given, along with details on installing the program on your computer. Two bench-mark runs are described that can be used to make sure the program is operating properly on your computer. The software includes a plotting utility for both video and hardcopy plots on IBM PC and compatible computers.

#### D.1.1 Acknowledgments

Program **EDDYBL** is a compressible, two-dimensional and axisymmetric boundary-layer program that embodies the Wilcox (1988a)  $k-\omega$  model, the Wilcox (1988b) multiscale model, and several low-Reynolds-number variants of the  $k-\epsilon$  model. This program has evolved over the past 20 years and can thus be termed a mature software package. Many U. S. Government Agencies have contributed to development of the program that is based on a program originally developed by Price and Harris (1972). Most notably, various stages of the program's development can be attributed to support by the following agencies.

U. S. Army Research Office  
NASA Ames, Langley and Lewis Research Centers  
Air Force Office of Scientific Research  
Office of Naval Research

Defense Advanced Research Projects Agency  
Air Force Weapons Laboratory  
Naval Ship Research and Development Center

Additionally, important improvements have been made to this software package as a result of feedback from users, most notably from the outstanding fluid mechanics students at UCLA and USC. The author owes special thanks to Dr. G. Brereton of the University of Michigan whose personal efforts resulted in the addition of the option to use either English or SI units, and to J. Morrison of AS&M for adapting the software to a SUN Workstation.

### D.1.2 Required Hardware and Software

Versions of the program are available for the following computers.

Cray X-MP and Y-MP  
VAX 11 and 8600  
SUN Workstations  
Silicon Graphics Iris  
Intel 80386, 80486 and Pentium Based Microcomputers  
Definicon 68020 and 68030 Coprocessor Boards  
Definicon SPARC Coprocessor Boards  
IBM PC/XT/AT and Compatibles  
Heath/Zenith 100

The program requires at least 320 kilobytes of memory. To achieve sensible computing times, IBM PC/XT/AT and compatibles should have an 8087 or 80287 math coprocessor, and must use Microsoft Fortran Version 5.0 or higher. Intel 80386 based machines must have either an 80387 or Weitek math coprocessor.

## D.2 Getting Started Quickly

Because **EDDYBL** and its input-data preparation utility, **SETEBL**, run on many different computers, installation of the software is a little different for each machine. The main difference occurs in the commands needed to compile and link the programs. To install the software on a computer other than an IBM PC or compatible, you must skip ahead to Sections D.3 and D.4. If you have an IBM PC or compatible microcomputer running under the MS-DOS operating system, executable versions of the software package are included on the distribution diskette. Regardless of the computer you

are using, once you have executable programs, complete the installation as follows.

1. Read the contents of the file **read.me** in subdirectory **eddybl** on the distribution diskette. This file will tell you of any program revisions as well as the location of all pertinent program files on the diskette. Then, copy the following files to your working directory:

<b>eddybl.exe</b>	<b>blocrv.dat</b>	<b>plotb.exe</b>
<b>instl.exe</b>	<b>heater.dat</b>	<b>plotb.dat</b>
<b>setebl.exe</b>	<b>presur.dat</b>	<b>exper.dat</b>

Omit the files **plotb.exe**, **plotb.dat** and **exper.dat** if you are using a computer other than an IBM PC or compatible.

2. Run Program **INSTL** and answer all questions posed by the program. This program generates a file named **grafic.dat** that should be saved in your working directory.
3. If your computer is an IBM PC or compatible, install the **ansi.sys** driver supplied with your MS-DOS operating system by adding the following command to your **config.sys** file:

**device=ansi.sys**

Make sure the file **ansi.sys** is available in your path. If you have not previously had this command in your **config.sys** file, you must now re-boot your computer to install the **ansi.sys** driver.

A simple bench-mark case is built into the software package to allow you to quickly determine that everything is operating properly, and to see how easy it is to use Program **EDDYBL**. Because the input-data preparation utility, **SETEBL**, is menu driven, you will find that very little explanation of the program's operation is needed. After successfully completing the following bench-mark run, the first time user should nevertheless do the example of Section D.5 to be sure the software is properly installed and to learn some of the more subtle features of Program **SETEBL**.

1. The first step is to run **SETEBL**. If you have not installed **SETEBL**, you will be notified with a brief message after which the program will immediately terminate. If this happens, refer to Section D.3 and perform the installation procedure.

2. Assuming the program is properly installed, you will see a message informing you that file **eddybl.dat** does not exist. The message asks if you want to create a new file named **eddybl.dat**. For this sample session, you should answer yes by typing the letter *Y* or *y* followed by pressing the *ENTER* key.
3. Having performed Step 2, you will now be presented with the main menu (Figure D.1) on which ten options are listed. **SETEBL** has built-in default values for all input parameters that correspond to an incompressible (Mach .096) flat-plate boundary layer. When you eventually exit **SETEBL**, these data will be written into an Ascii data file named **eddybl.dat**. For this bench-mark case, if you selected English units as the default when you ran Program **INSTL**, you have no need to change any data. However, this case must be done using English units. If you selected SI units as the default when you ran **INSTL**, you must change to English units. Type either a *U* or a *u* (for Units - note that the *U* is in reverse video on your display) and press the *ENTER* key to make the change. The menu will change to indicate which units are in effect. Before exiting, you must generate two other data files, viz., **table.dat** and **input.dat** that are needed in order to run Program **EDDYBL**.

**E D D Y B L...America's Boundary Layer Code**  
 Dr. David C. Wilcox, DCW Industries  
 (C) Copyright 1986-92. All rights reserved.

INPUT DATA ORGANIZER  
 Version 6.8 1 Oct 92  
 English Units

Required Input:	Optional Input:
<b>M</b> MAIN PARAMETERS	<b>T</b> TURBULENCE MODEL
<b>E</b> EDGE/WALL CONDITIONS	<b>G</b> GAS PROPERTIES
<b>I</b> INITIAL PROFILES	<b>L</b> LOGICAL UNIT NUMBERS
<b>U</b> UNITS SELECTION	<b>P</b> PROFILE PRINTING
<b>W</b> WRITE DATA FILES	<b>R</b> RESTART RUN

Specify option desired or **X** to eXit...

Figure D.1: Opening menu of Program **SETEBL**.

4. To generate these files, select the **Write Data Files** option. To do this, type a *W* or a *w* followed by pressing the *ENTER* key. After a

short wait, you will be notified that the binary data file **table.dat** has been successfully written. You are now presented with the following query in reverse video.

**Save the profiles in Ascii form? (X=eXit, Y=Yes, ENTER=No)...**

If you desire a copy of the initial profiles to be saved in a disk file named **setebl.prt** for inspection at a later time, respond with a *Y*, *ENTER* sequence; otherwise press the *ENTER* key. After you have responded to this query, a second query will appear, viz.,

**Display the profiles on the video? (X=eXit, Y=Yes, ENTER=No)...**

If you want to see the profiles on your video display, respond accordingly. Otherwise, press *ENTER*. After you have responded, your screen clears again and a message appears indicating initial profiles are being generated. If you elected to display profiles on your video display, they will now be displayed, a screen at a time. Press *ENTER* to advance to the next screen. Regardless of the options you have chosen, the precise values of the integral parameters for your computed initial profiles are displayed. Finally, a message appears indicating the binary data file **input.dat** has been successfully written and that you must press *ENTER* in order to continue.

5. After you press *ENTER*, control returns to the main menu. At this point you have prepared all input-data files for the bench-mark run. Exit by typing an *X*, *ENTER* sequence.
6. All that remains now is to run Program **EDDYBL**. Program output will be directed to a disk file named **eddybl.prt**. The file **eddybl.prt** supplied on the distribution diskette contains the printout for the bench-mark run on an 80486/Weitek 4167 based microcomputer. Your results should agree to within several decimal places with those in the sample printout. For reference, Table D.1 summarizes approximate computing times (including disk I/O) required for several computers.
7. If you are using an IBM PC or compatible computer, you can generate a video and hardcopy plot of the computational results by running Program **PLOTEB**. Before executing this program, be sure to modify the input-data file, **plotb.dat**, as required for your system. Section D.8 describes all input parameters in the file.



Table D.1: Computing time for the bench-mark case

Computer	CPU (MHz)	FPU (MHz)	CPU Time(sec)
Cray 2	-	-	1
GA-486L	80486 (25.0)	mW4167 (25.0)	4
Notebook 486DX	80486 (33.0)	80487 (33.0)	5
GA-486L	80486 (25.0)	80487 (25.0)	6
M-317B	80386 (33.0)	mW3167 (33.0)	7
VAX 8600	-	-	10
SPARC	7C601 (20.0)	8847 (20.0)	12
Tandy 4000	80386 (16.0)	mW1167 (16.0)	17
DSI-785+	68020 (25.0)	68882 (25.0)	19
DSI-785+	68020 (20.0)	68882 (20.0)	24
DSI-020	68020 (16.7)	68882 (16.7)	29
VAX 11/785	-	-	36
DSI-020	68020 (16.7)	68881 (16.7)	39
VAX 11/750	-	-	46
DSI-020	68020 (12.5)	68881 (12.5)	52
Tandy 4000	80386 (16.0)	80287 ( 8.0)	120
Toshiba T1200	8086 (10.0)	8087 (10.0)	143
Turbo 286	80286 (12.0)	80287 ( 8.0)	154
M-317B	80386 (33.0)	None	232
Tandy 4000	80386 (16.0)	None	624
Turbo 286	80286 (12.0)	None	698
TRS-80 Mod 16	68000 ( 6.0)	None	890

**SPECIAL NOTE**

All input to Program SETEBL is case insensitive, i.e., all commands and input can be entered in either upper or lower case.

## D.3 Installing SETEBL

To use the supplied executable version of **SETEBL** on an IBM PC or compatible microcomputer, including the default values specified for all input-data parameters, simply copy the executable file to your working directory. Otherwise, if you wish to change some of the default values, or if you are using a computer other than an IBM PC, the first step required to install Program **SETEBL** is to compile and link the program. The main program is the file named **setebl.for**, and the various subroutines are listed in Section D.12. All routines reference three **include** files, **chars**, **comeb1** and **comeb2**. Section D.10 summarizes the commands required to compile and link Program **SETEBL**.

**The first step required to install SETEBL for your computer is to either copy the executable file to your working directory or to compile and link Program SETEBL.**

In order to use Program **SETEBL**, you must first install it for your particular console. The program makes extensive use of reverse video, direct cursor positioning, and some graphics characters. Since no uniform standard exists for such console characteristics, the appropriate sequences used by your console must be defined for Program **SETEBL**.

### D.3.1 Boot-Console Installation

In order to install **SETEBL** on your main (or boot) console, you must generate a binary data file named **grafic.dat** that contains all of the information needed by **SETEBL**. The source code for a program that generates **grafic.dat** customized for your console has been supplied as part of this software package. The program is called **INSTL**, and the source is contained in **instl.for**. If you customize Program **INSTL** or if you are using a computer other than an IBM PC, you must first compile and link Program **INSTL**. Then:

**The second step required to install SETEBL for your console is to run Program INSTL.**

When you run Program **INSTL**, you will be given the option of specifying whether you want the default units to be English or SI. Make the choice best suited to your needs. You will also have to specify the type of computer you have and, in some cases, the type of console.

When you have successfully run Program **INSTL**, the required binary data file **grafic.dat** will be created and **INSTL** will print a message to that

effect. Whenever you wish to run **SETEBL**, simply make sure **grafic.dat** is present in your directory. If it is not present, **SETEBL** displays a message informing you that you are attempting to run an uninstalled version of **SETEBL** and promptly terminates. If you are running Program **SETEBL** on an IBM PC based system, you must also install the **ansi.sys** driver. Thus,

**The third step required to install SETEBL on an IBM PC based system is to install the ansi.sys driver by adding the following command to your config.sys file.**

**device=ansi.sys**

If you have not previously had this command in your **config.sys** file, it will not take effect until you re-boot your computer.

### D.3.2 Remote-Terminal Installation

For a remote terminal whose characteristics are different from those of your boot console, you can create another **grafic.dat** by making appropriate changes to Program **INSTL**. The program is heavily commented, and customization should be straightforward.

## D.4 Installing EDDYBL

To use the supplied executable version of **EDDYBL** on an IBM PC or compatible microcomputer, simply copy the executable file to your working directory. Otherwise, if you wish to make program changes, or if you are using a computer other than an IBM PC, the first step required to install Program **EDDYBL** is to compile and link the program. The main program is the file **eddybl.for** that also makes use of the include files **common** and **cpuid**. Be sure to link with the **/e** option for the Microsoft Fortran version or the **-pack** option with SVS Fortran-386/Phar Lap to reduce the size of the executable file.

**The only step required to install EDDYBL for your computer is to either copy the executable file to your working directory or to compile and link Program EDDYBL.**

## D.5 Running a General Case

This section explores, in detail, all of the salient features of the input-data preparation utility, **SETEBL**. You will be guided through the various menus and, in the process, you will set up a constant-pressure boundary layer computation for a Mach 1 freestream. For the case you will do, freestream conditions are as follows.

$$\begin{aligned}\text{Total pressure, } p_{t\infty} &= 482.7 \text{ lb/ft}^2 \text{ (23112 N/m}^2\text{)} \\ \text{Total temperature, } T_{t\infty} &= 468^\circ\text{R (260 K)} \\ \text{Mach number, } M_\infty &= 1\end{aligned}$$

The surface will be slightly cooled so that surface temperature is 95% of the adiabatic-wall temperature.

Your goal is to initiate the computation at a plate-length Reynolds number,  $Re_x$ , of one million and determine the point where the momentum-thickness Reynolds number,  $Re_\theta$ , is 6000. You might want to do this, for example, in order to provide upstream profiles for a Navier-Stokes computation. You know from a correlation of experimental data that when  $Re_x = 1.0 \cdot 10^6$ , the boundary layer has the following integral properties:

$$\begin{aligned}\text{Skin friction, } c_f &= .0038 \\ \text{Shape factor, } H &= 1.80 \\ \text{B.L. Thickness, } \delta &= 11.9 \theta \\ \text{Reynolds number, } Re_\theta &= 1500\end{aligned}$$

Finally, the surface is perfectly smooth, there is no surface mass transfer, and the  $k$ - $\omega$  model will be used.

### D.5.1 Preliminary Operations

To perform this exercise, delete any existing **eddybl.dat** data file that might be in your directory. Although this is not generally necessary, for the purposes of this section it will be easier if you begin with the default values.

As with the bench-mark case of Section D.2, the very first step is to run Program **SETEBL**. If you have not installed the program, you will be notified with a brief message after which the program will immediately terminate. If this happens, go back to Section D.3 and perform the installation procedure.

Assuming the program is properly installed, you will see a message informing you that file **eddybl.dat** does not exist. You will be asked if you want to create a new file named **eddybl.dat**. For this sample session, you should answer yes by typing the letter *Y* followed by pressing the *ENTER* key.

### D.5.2 Units Selection

This case can be done in either English or SI units. Examine the main menu to determine which units are in effect. If you wish to change units, type a *U* followed by pressing *ENTER*. The menu will reflect the change in units immediately. If you change your mind and wish to go back to the original units, repeat the *U*, *ENTER* sequence. In the following sections, values are quoted in English units followed by corresponding SI values in parentheses.

### D.5.3 Main Parameters

At this point, you will be presented with the main menu on which ten options are listed. Begin by entering the **Main Parameters** sub-menu. To enter this sub-menu, type an *M* followed by pressing the *ENTER* key.

Yet another sub-menu will now appear that gives you the choice of entering input data for either **Freestream Conditions** or **Body Parameters**. There is a third option that allows you to **eXit**. The latter option permits you to return to the previous menu. You will eventually do so, but first you will do some actual data preparation.

**Freestream Parameters.** Type an *F* followed by pressing the *ENTER* key to descend to the **Freestream Conditions** menu. You will now see a display that includes seven of the primary quantities that specify freestream flow conditions, including freestream total pressure, total temperature, Mach number, shock-wave angle, and some turbulence parameters. The bottom row provides instructions on how to proceed. Press the *ENTER* key several times, for example, and you will see the arrow move from one input variable name to the next. When you reach the last variable, pressing the *ENTER* key again will cause the arrow to move to the uppermost variable. You may make as many passes through the list of variables as you wish.

This particular menu includes a **Help** option to further explain the meaning of the more obscure input quantities. To display the **Help** menu, type an *H* followed by pressing the *ENTER* key. After reading this **Help** menu, pressing the *ENTER* key returns you to the **Freestream Conditions** data-entry menu.

Having returned from the **Help** menu, you will now exercise the **Change** option. First, position the arrow in front of **Mach number**. You accomplish this by pressing *ENTER* twice. Now, type the letter *C* (for **Change**) followed by pressing *ENTER*. The bottom line of the menu will now change. You are told to specify the new value, and that the **FORMAT** must be

the standard FORTRAN floating-point format E13.6. The default value assigned to the Mach number is .096, corresponding to essentially incompressible flow conditions. Change the Mach number to one by typing 1. (the exponent E+00 is unnecessary but the decimal point is mandatory — this is normal FORTRAN I/O). As with all commands to **SETEBL**, nothing will happen until you press the *ENTER* key. Before you do however, watch the line near the bottom of your display entitled **Static Conditions**. Keeping your eyes on the static conditions line, press the *ENTER* key. If you have done this step correctly, the new static conditions should appear in place of the old. Also, if you look at the value assigned to the Mach number you will find it has been changed to one.

At this point, you can change any of the seven input quantities. In addition to Mach number, you must change total pressure and temperature. Press the *ENTER* key five times in order to position the arrow in front of PT1, the total pressure. Using the change procedure, i.e., type a *C* followed by *ENTER*, insert the desired total pressure of 482.7 lb/ft<sup>2</sup> (23112 N/m<sup>2</sup>). You may enter 4.827e+02 (2.3112e+04) or 4.827E2 (2.3112E4), etc. if you wish. Note that your keyboard's normal destructive backspace key can be used to correct typing errors. When your desired new total pressure is correctly entered, press *ENTER* and the change will be made. Verify that the new value for PT1 shown on the display is 4.827000E+02 (2.311200E+04). If you made any mistakes, repeat the change operation until you get it right.

Now press *ENTER* to position the arrow in front of TT1, the total temperature. Using the change procedure, change the value of TT1 to 468. (260.). Don't forget the decimal point or else your total temperature will be .000468 (.000260). Verify that the new value for TT1 shown on the display is 4.680000E+02 (2.600000E+02).

If you have changed Mach number, total pressure and total temperature correctly, the value listed below for static pressure will be very close to 255 lb/ft<sup>2</sup> (12209 N/m<sup>2</sup>) and the unit Reynolds number should be approximately  $1.24 \cdot 10^6 \text{ ft}^{-1}$  ( $4.07 \cdot 10^6 \text{ m}^{-1}$ ). Verify that your static conditions match these two values. If they do not, find and correct any errors you have made.

jot the values of static pressure and freestream unit Reynolds number on a slip of paper for reference later. In general, knowing these values often helps expedite preparation of your input data. Later on, we will see an example of using both parameters.

You have now finished this sub-menu. In order to exit, simply type an *X* followed by pressing the *ENTER* key. Note that, with the exception of Help menus for which only *ENTER* is needed, you return to the previous menu by the *X*, *ENTER* sequence. Also, if you are ever in doubt about

what to do, look at the last line of the display for instructions.

**Body Parameters, Etc.** Now you are back to the **Main Parameters** sub-menu that provides the options of altering freestream conditions, body parameters, etc. Descend to the **Body Parameters** sub-menu by typing the letter *B* followed by pressing *ENTER*. You will be presented with a menu similar to the **Freestream Conditions** sub-menu. As before, press *ENTER* several times to move the arrow. Scan the input variable definitions and default values. Examine the Help menu. In other words, begin discovering that you already know most of what is needed in order to operate **SETEBL**!

There are only two input quantities you need to change, viz., *ISHORT* and *SSTOP*. Because you are looking for the point where momentum thickness Reynolds number is 6000, you have no need for the long printout that gives far more detail than you are interested in. Consequently, you should position the arrow next to *ISHORT* and change its value to 0. This is done by typing *C* and a carriage return; no value need be entered. As an experiment, you might want to try repeating this sequence. If you do, the value of *ISHORT* will change back to 1. Be sure you have changed *ISHORT* to 0 after you finish experimenting.

Turning now to *SSTOP*, use the *ENTER* key to position the arrow next to *SSTOP*. This is the maximum value of plate length to which you will permit computation to proceed. You are certain that momentum thickness Reynolds number will reach 6000 at a plate-length Reynolds number somewhere between three and five million. Hence, you might want to terminate your run when Reynolds number reaches five million. Referring to the unit Reynolds number of  $1.24 \cdot 10^6 \text{ ft}^{-1}$  ( $4.07 \cdot 10^6 \text{ m}^{-1}$ ) that you jotted down earlier, a quick computation shows that a plate-length Reynolds number of five million occurs when plate length is 4.03 ft (1.23 m). Thus, change *SSTOP* to 4.03 (1.23).

There are no further changes you need to make at this time on this menu, so you should now exit by typing *X* followed by pressing the *ENTER* key.

At this point, you are done with the **Main Parameters** sub-menu. In order to return to the main menu, type another *X* followed by pressing the *ENTER* key. Remember, nothing happens in **SETEBL** until you press the *ENTER* key.

### D.5.4 Taking a Lunch Break

Before continuing setting up a new run, you are going to simulate a lunch break. Imagine that it's time to break for lunch and the systems people upstairs are notorious for causing your VAX 8600 to crash during the lunch

hour. Any file you leave open will be lost as a result of a crash. In order to protect your work from such a disaster, simply exercise the exit option by typing yet another *X* followed by pressing the *ENTER* key.

Inspection of your directory will show that a new file named **eddybl.dat** has been created. Verify that the file exists at this time. If it does not, go back to Subsection D.5.1 and omit the mistake you made that caused you to reach this point unsuccessfully.

Now imagine you have returned from lunch, and your microcomputer (which never crashes during lunch because there are no system people to cause it to) is ready to continue serving your data processing needs. At this point, run Program **SETEBL** again. Because the data file **eddybl.dat** exists, the program will go directly to the main menu.

### D.5.5 Edge/Wall Conditions

From the main menu, you should now proceed to the **Edge/Wall Conditions** sub-menu by typing an *E* followed by pressing *ENTER*.

This sub-menu contains five options, viz., Pressure Distribution, Heat Transfer, Mass Transfer, Body Geometry and *eXit*. Type a *P* followed by *ENTER*. The **Pressure Distribution** sub-menu explains that you must prepare a file **presur.dat** that defines the pressure distribution. You must prepare the file with an editor such as MS-DOS 5.0's *EDIT*, DEC's *EDT*, UNIX's *vi*, etc. All you can change in this menu is the number of points you plan on using. You will not change **NUMBER** because your run will have constant pressure. Thus, you need to specify pressure at two values of plate length. Note that this menu describes in detail the contents and format of **presur.dat**. Exit this menu with the usual *X*, *ENTER* sequence.

Now go to the **Heat Transfer** sub-menu. You are presented with a description of data file **heater.dat** that must be created with your own editor. Note that the adiabatic-wall temperature is given for your information and the value listed should be 459.4°R (255.2 K). The one parameter you can change on this menu is **KODWAL** which determines whether you plan on specifying surface heat flux or surface temperature. Type a *C* followed by *ENTER* to change **KODWAL**. Note that the display now indicates temperature is prescribed at the surface. Jot down the adiabatic-wall temperature for later reference. Exit this sub-menu by typing an *X* followed by *ENTER*.

Now go to the **Mass Transfer** sub-menu. This sub-menu describes a file, **blocrv.dat**, that must be prepared externally. You can alter the one parameter **NFLAG**. The default value is 0, which means **blocrv.dat** is not required to prepare your edge and surface conditions. You have no need to change its value for this application. Note that your display indicates the file **blocrv.dat** will not be required. Exit this sub-menu.



Having exited the **Mass Transfer** sub-menu, you are now back at the **Edge/Wall Conditions** sub-menu. Proceed to the **Body Geometry** sub-menu. No, you didn't make a typing error. This is the same menu you just completed. It has been included for planned future enhancements to **SETEBL**. Exit back to the **Edge/Wall Conditions** sub-menu with an *X*, *ENTER* sequence.

The final option is to eXit. Do so by typing another *X*, *ENTER* sequence.

You are now back at the main menu. You cannot continue until you have prepared input-data files **presur.dat** and **heater.dat** (**blocrv.dat** is not needed because *NFLAG* is 0). Hence, it is time to exit **SETEBL** and save all the work you have done so far.

### D.5.6 Preparing Edge/Wall Condition Data Files

The easiest way to prepare the data files **presur.dat** and **heater.dat** (and **blocrv.dat** as well) is to use an editor such as EDIT, EDT, vi, etc. to modify existing files from a previous run. That is why you left the files from the bench-mark run in your directory. You can delete **blocrv.dat** now if you wish as it won't be needed.

If you have followed all of the instructions correctly, you have the static pressure of 255 lb/ft<sup>2</sup> (12209 N/m<sup>2</sup>) and the adiabatic-wall temperature of 459.4°R (255.2 K) jotted down somewhere. Using your favorite editor, change **presur.dat** to the following:

English Units:

```
0.000000E 00  2.550000E 02
1.000000E 01  2.550000E 02
0.000000E 00  0.000000E 00
```

SI Units:

```
0.000000E 00  1.220900E 04
1.000000E 01  1.220900E 04
0.000000E 00  0.000000E 00
```

As explained in the **Pressure Distribution** sub-menu, the first two lines of this file are arc-length/pressure pairs presented in format (2E14.6). The final line is the pressure gradient at the beginning and end of the interval and the data are given in the (2E14.6) format also. You have specified pressure at a plate length of zero and ten feet (meters). This interval must at least cover the planned integration range. The value of the pressure is the static pressure you jotted down earlier.

Turning now to surface temperature, note that 95% of the adiabatic-wall temperature is approximately 436°R (242 K), which is the value you should use. Use your editor to modify **heater.dat** as required, noting that the values of arc length at which you specify wall conditions must match the values used for the pressure distribution. As explained on the Heat Transfer sub-menu, this file must consist of the following four lines:

English Units:

```
0.000000E 00  4.360000E 02  0.000000E 00
1.000000E 01  4.360000E 02  0.000000E 00
0.000000E 00  0.000000E 00
0.000000E 00  0.000000E 00
```

SI Units:

```
0.000000E 00  2.420000E 02  0.000000E 00
1.000000E 01  2.420000E 02  0.000000E 00
0.000000E 00  0.000000E 00
0.000000E 00  0.000000E 00
```

The format of the first two lines is (3E14.6), while the last two lines have format (2E14.6). The first column for the first two lines is arc length, the second is wall temperature, and the third is surface heat flux. Note that since you have chosen to specify surface temperature rather than heat flux, any value can be entered for the heat flux; it won't be used in the computation. Similarly, if you choose to specify surface heat flux, the value assigned to surface temperature is arbitrary. The third line gives surface temperature slope at the beginning and end of the interval, while the last line gives surface heat flux slope. Of course, you are not limited to constant properties in the most general case. You may prescribe as many as 50 different values for edge pressure, surface temperature, etc.

At this point, you have prepared all of the freestream conditions, body parameters, and (from an external editor) the two data files **presur.dat** and **heater.dat**. Before reentering **SETEBL**, examine your directory. In addition to **eddybl.dat**, you should find another file **eddybl.bak**. The former is your most recent version of **eddybl.dat**. The latter is the version you created just before taking your lunch break. **SETEBL** always saves your previous work in a file named **eddybl.bak** to provide you with a little extra protection. You no longer need **eddybl.bak**, so delete it if you wish.

### D.5.7 Generating Edge/Wall Conditions

Run **SETEBL** again. When the main menu appears, use a *W*, *ENTER* sequence to execute the Write Data Files option. A message will appear briefly indicating edge conditions are being generated. When all computations are complete, a message appears indicating a data file named **table.dat** has been successfully written. If you receive any other message, there are probably errors in the files you created with your editor in Subsection D.5.6 that you must correct before continuing. What you are doing in this step is executing a subroutine in Program **SETEBL** that accomplishes two ends. First, you generate data file **table.dat** in binary form that is used by Program **EDDYBL**. Second, you compute several parameters appearing in data file **eddybl.dat** that are needed in preparing initial profiles.

### D.5.8 Initial Profiles

In addition to the message that **table.dat** has been successfully written, you also receive the message

Save the profiles in Ascii form? (X=eXit, Y=Yes, ENTER=No)...

Since you have not yet prepared the data needed to generate initial profiles, type an *X*, *ENTER* sequence. Upon returning to the main menu, you are now ready to go to the Initial Profiles sub-menu. Type an *I* followed by pressing the *ENTER* key. The sub-menu that appears has three options, viz., **Integral Parameters**, **Grid Parameters** and **eXit**.

**Integral Parameters.** Go to the **Integral Parameters** sub-menu first by entering another *I*, *ENTER* sequence. Press *ENTER* once to position the arrow next to skin friction. Change the value to 0.0038 in the usual manner. Press *ENTER* again to move the arrow in front of boundary-layer thickness,  $\delta$ . For the conditions specified above, a quick calculation shows that  $\delta$  for your unit Reynolds number is .0144 ft (.004389 m). Change the value of DELTA to 0.0144 (.004389). Now move the arrow to shape factor and change its value to 1.8. Finally, move the arrow one more time to momentum-thickness Reynolds number and change its value to 1500., being careful to remember the decimal point. Inspect your work for possible errors. When you have made all entries correctly, exit this sub-menu.

**Grid Parameters.** Now exercise the *G* option to enter the **Grid Parameters** sub-menu. The first quantity you should change is the initial streamwise stepsize, DS. For this constant pressure case, you can use a stepsize as big as triple the boundary-layer thickness. Hence, change the value of DS to 0.04 ft (0.0122 m). In order to start the computation at a

plate-length Reynolds number of one million, the initial plate length (arc length) must be 0.806 ft (0.246 m), a fact you can deduce by using the freestream unit number of  $1.24 \cdot 10^6 \text{ ft}^{-1}$  ( $4.07 \cdot 10^6 \text{ m}^{-1}$ ) you jotted down earlier. Hence, change SI to 0.806 (0.246). The next parameter is XK, the grading ratio. A somewhat coarser grid can be used for this case than the default grid. Change the value to 1.14 which corresponds to grid increments increasing in a geometric progression at a 14% rate. Finally, change the number of grid points normal to the surface, IEDGE, to 51. Again, inspect your work for possible errors. When your entries are error free, exit this sub-menu. Having returned to the **Initial Profiles** sub-menu, you should now exercise the exit option with the usual *X*, *ENTER* sequence in order to return to the main menu.

**Generating Initial Profiles.** As in Subsection D.5.7, exercise the **Write Data Files** option by entering a *W*, *ENTER* sequence. This will regenerate **table.dat** and you are again presented with the following message.

Save the profiles in Ascii form? (X=eXit, Y=Yes, ENTER=No)...

If you desire a copy of the profiles, in Ascii form, to be sent to a disk file named **setebl.prt** that can be printed and/or examined with an editor after exiting Program **SETEBL**, respond with a *Y*, *ENTER* sequence; otherwise simply press the *ENTER* key. After you have responded to this query, a second query will appear as follows.

Display the profiles on the video? (X=eXit, Y=Yes, ENTER=No)...

If you want to see the profiles on your video display, respond with a *Y*, *ENTER* sequence. Otherwise, press *ENTER*. After you have responded, your screen clears again and a message appears indicating initial profiles are being generated. If you elected to display profiles on your video display, they will now be displayed, a screen at a time. Press *ENTER* to view the next screen. Regardless of the options you have chosen, the precise values of the integral parameters for your computed initial profiles are displayed. Finally, a message appears indicating the binary data file **input.dat** has been successfully written and that you must press *ENTER* in order to continue.

Notice that the value of the conventional sublayer coordinate,  $y^+$ , for the point nearest the surface is printed and its value is 0.175. Subroutine **START** will alert you if this value ever exceeds unity as Program **EDDYBL** requires the value of  $y^+$  nearest the surface to be less than 1 in order to remain numerically stable. If this ever happens, you must either increase XK or IEDGE. When you press *ENTER*, control returns to the main menu.

You will receive a warning if you use the  $k$ - $\epsilon$  model and the value of  $y^+$  for the point nearest the surface is less than 0.1. Values smaller than 0.1 tend to slow the convergence rate for the  $k$ - $\epsilon$  model, and may even cause your run to crash.

### D.5.9 Selecting a Turbulence Model

In order to select the  $k$ - $\omega$  model, go to the **Turbulence Model** sub-menu. Type a  $T$  followed by *ENTER*, and you will find that the fourth quantity listed is a flag called MODEL. Press *ENTER* three times to position the arrow in front of MODEL. Change its value to 0 by typing  $C$  followed by entering a 0 and pressing *ENTER*. Note that the highlighted bar below the menu now indicates you are using the  $k$ - $\omega$  model without viscous correction (low-Reynolds-number) terms. Exit back to the main menu.

For general reference, there are ten turbulence models implemented in **EDDYBL**, and the two input parameters MODEL and NVISC are used to make the selection. The choices are as follows.

MODEL	NVISC	Turbulence Model
-1	-	None (Laminar Flow)
0	0	$k$ - $\omega$ , viscous corrections excluded
0	1	$k$ - $\omega$ , viscous corrections included
1	0	Multiscale, viscous corrections excluded
1	1	Multiscale, viscous corrections included
2	0	$k$ - $\epsilon$ , Jones-Launder (1972)
2	1	$k$ - $\epsilon$ , Launder-Sharma (1974)
2	2	$k$ - $\epsilon$ , Lam-Bremhorst (1981)
2	3	$k$ - $\epsilon$ , Chien (1982)
2	4	$k$ - $\epsilon$ , Yang-Shih (1993)
2	5	$k$ - $\epsilon$ , Fan-Lakshminarayana-Barnett (1993)

### D.5.10 Logical Unit Numbers and Plotting Files

Your final input-data changes will cause printed output to go to your line printer rather than to disk file **eddybl.prt**. You will also verify that two disk files named **profil.dat** and **wall.dat** will be created that can be used as starting conditions for another program or as input to a plotting program. Go to the **Logical Unit Numbers** sub-menu by typing an  $L$ , *ENTER* sequence. The first parameter is IUNIT1 which, by default, is disk file **eddybl.prt**. For Lahey, Microsoft or SVS Fortran versions, change its value to 6. For all other versions, use your normal operating system procedure to

direct the contents of **eddybl.prt** to a line printer. Verify that the value for the parameter **IUPLOT** is some value other than 0. If it is 0, change its value to 10 (or any other convenient value excluding unit 15 and any previously assigned unit number).

Disk file **wall.dat** is written as an unformatted file, each record of which can be read by another FORTRAN program according to the following program fragment.

```

      i=1
10    read(iunit) s(i),res(i),cfe(i),rethet(i),
      *           h(i),che(i),anue(i),pe(i),tw(i)
      if(s(i).ne.-999.) then
        i=i+1
        go to 10
      endif

```

The various quantities saved in disk file **wall.dat** are:

Quantity	Description	Dimensions
s	$s$ , arc length along surface	ft (m)
res	$Re_s$ , Reynolds number based on $s$	None
cfe	$c_{fe} = 2\tau_w / \bar{\rho}_e \tilde{u}_e^2$ , skin friction	None
rethet	$Re_\theta$ , Reynolds number based on $\theta$	None
h	$H$ , shape factor	None
che	$\dot{h} / \bar{\rho}_e \tilde{u}_e C_p$ , Stanton number	None
anue	$Pr_L s \dot{h} / \mu_e C_p$ , Nusselt number	None
pe	$P_e$ , edge pressure	lb/ft <sup>2</sup> (N/m <sup>2</sup> )
tw	$T_w$ , wall temperature	°R (K)

The first line of the file **profil.dat** generated by Program **EDDYBL** contains the streamwise step number,  $M$ , and the number of mesh points normal to the surface, **IEDGE**. The format for this line is (2I6). The remainder of the file consists of **IEDGE** lines of data, format (12E11.4), containing the following boundary-layer profile data, with quantities written on each line in the order listed. Note that for the  $k$ - $\epsilon$  model, the specific dissipation rate,  $\omega$ , is defined by

$$\omega = \frac{\epsilon}{C_\mu k} \quad (\text{D.1})$$

Also, the tensor  $T_{ij}$  is specific to the multiscale model and is given by (see Subsection D.11.2):

$$\bar{\rho} T_{ij} = \tau_{ij} + \frac{2}{3} \bar{\rho} k \delta_{ij} - \frac{2}{3} \bar{\rho} (k - e) \delta_{ij} \quad (\text{D.2})$$

Quantity	Description	Dimensions
$y$	Distance normal to surface	ft (m)
$\tilde{u}$	Horizontal velocity	ft/sec (m/sec)
$\tilde{T}$	Temperature	$^{\circ}\text{R}$ (K)
$\bar{\rho}$	Density	slug/ft <sup>3</sup> (kg/m <sup>3</sup> )
$k$	Turbulence kinetic energy	ft <sup>2</sup> /sec <sup>2</sup> (m <sup>2</sup> /sec <sup>2</sup> )
$\omega$	Specific dissipation rate	sec <sup>-1</sup> (sec <sup>-1</sup> )
$k - e$	Large eddy energy	ft <sup>2</sup> /sec <sup>2</sup> (m <sup>2</sup> /sec <sup>2</sup> )
$T_{xx}$	Large eddy xx-normal stress	ft <sup>2</sup> /sec <sup>2</sup> (m <sup>2</sup> /sec <sup>2</sup> )
$T_{xy}$	Large eddy shear stress	ft <sup>2</sup> /sec <sup>2</sup> (m <sup>2</sup> /sec <sup>2</sup> )
$T_{yy}$	Large eddy yy-normal stress	ft <sup>2</sup> /sec <sup>2</sup> (m <sup>2</sup> /sec <sup>2</sup> )
$y^+$	Compressible sublayer-scaled distance	None
$u^+$	Compressible sublayer-scaled velocity	None

You may now exit back to the main menu. All of your input data are prepared and you are ready to run **EDDYBL**. Exit Program **SETEBL** with a final *X*, *ENTER* sequence.

### D.5.11 Running the Boundary-Layer Program

Run Program **EDDYBL**. Examination of program output reveals that your run didn't go far enough to determine the point where momentum-thickness Reynolds number reaches 6000. After the 30 steps you specified as the upper limit (the default value for IEND1 - **Main Parameters/Grid Parameters** sub-menu),  $Re_{\theta}$  is only 5200. The plate length at the final station is only 2.69 ft (0.82 m), so you allowed a large enough value, i.e., 4.03 ft (1.23 m) for SSTOP.

### D.5.12 Restart Run

You could go back to **SETEBL**, increase IEND1 to, say, 35, and simply rerun **EDDYBL**. On an IBM PC/AT without an 80287, that's another 8 or 9 minutes. Since you might not really want to take another coffee break while your job runs, you might prefer a less time-consuming solution. Program **SETEBL** provides such a possibility through its **Restart** option.

Examine your directory and verify that Program **EDDYBL** has created a new file named **output.dat**. This file contains sufficient information to restart your program. Now, run Program **SETEBL** again. From the main menu, go to the Restart Run sub-menu by typing an *R* followed by pressing *ENTER*. This menu will permit you to change IEND1, the maximum streamwise step number, and SSTOP, the maximum value of arc (plate)

length. Since your value for SSTOP is clearly large enough, you need only change IEND1. With the usual procedure, change IEND1 from 30 to 35. Now type *X* followed by pressing *ENTER* in order to return to the main menu. Before returning, you will receive a message in reverse video as follows:

**"Do you wish to copy OUTPUT.DAT to INPUT.DAT? (Y/N)..."**

Respond Yes by typing *Y* followed by pressing *ENTER*. At this point, for all but the VAX version, **SETEBL** will inform you that it first copies **input.dat** to a new file named **input.bak**. For all versions, **SETEBL** then copies **output.dat** to **input.dat**. The point is, the final output of your original run becomes input for the restart run. Additionally, your original **input.dat** has effectively been renamed as **input.bak** (VAX/VMS creates its own backup file so this file is unnecessary). Upon completion of the copy operation, control returns to the main menu (for the VAX version, you are instructed to press *ENTER* to continue). Exit Program **SETEBL**.

At this point, data files **eddybl.dat** and **input.dat** have been modified as needed to continue your run from where you left off. The file **table.dat** requires no modification as SSTOP remains smaller than the top end of the interval for which you have defined edge and surface properties. Had we made SSTOP larger than 10, you would have to make appropriate changes to **presur.dat** and **heater.dat** to make sure edge and surface conditions are defined at least up to the new value of SSTOP. You would then have to regenerate **table.dat** via the Write Data Files option (Subsection D.5.7).

Now, run Program **EDDYBL** again. If you have made no errors, inspection of the printout combined with a little interpolation shows that  $Re_\theta$  is 6000 at a plate length of approximately 3.15 ft (0.96 m).

### D.5.13 Gas Properties and Profile Printing

At this point, you have seen virtually all of Program **SETEBL**'s menus and options. There are two sub-menus we didn't use in this exercise, viz., **Gas Properties** and **Profile Printing**. Both menus are self explanatory and operate in the same manner as the menus you've already explored.

The **Gas Properties** menu allows you to modify thermodynamic properties such as specific heat ratio, universal gas constant, and viscosity-law coefficients. The default values are set up for air with the Sutherland viscosity law. You can implement a **power-law** viscosity relationship by setting  $SU = 0$ . Note that if you have a viscosity law of the form  $\mu = \mu_{ref} \tilde{T}^n$  then you must set  $VISCON = \mu_{ref}$  and  $VISPOW = n + 1$ .

The **Profile Printing** sub-menu permits you to print velocity, temperature, turbulent energy, etc. profiles at specified streamwise stations. Pro-



gram **EDDYBL** always prints profiles at the final station. Also, whenever **EDDYBL** prints profiles, disk file **output.dat** is automatically written.

### D.5.14 Selecting Laminar, Transitional or Turbulent Flow

Program **EDDYBL** can run in three different modes corresponding to (1) pure laminar flow, (2) transition from laminar to turbulent flow, and (3) pure turbulent flow. The two test cases exercise **EDDYBL** in its pure turbulent mode in which integral parameters are specified and **IBOUND** is set to 1.

To run in the transitional mode, simply select **IBOUND** = 0 in the **Initial Profiles/Integral Parameters** menu. As a result, exact laminar velocity and temperature profiles will be generated in conjunction with approximate laminar profiles for the various turbulence-model parameters. The actual transition point is determined automatically by the model equations and depends strongly upon the freestream values of  $k$  and  $\omega$  that are specified in the **Main Parameters/Freestream Conditions** menu in terms of **ZIOTAE** and **ZIOTAL**. To obtain physically realistic transition Reynolds numbers you must include low-Reynolds-number corrections in the  $k$ - $\omega$  and multiscale models by setting **NVISC** = 1 in the **Turbulence Model** sub-menu. Although the  $k$ - $\epsilon$  models are capable of predicting transition, extremely small streamwise steps are needed with **EDDYBL**, and stable computation is very difficult to achieve.

Even if you are not interested in transition, this mode is nevertheless useful as it provides an alternate method for generating turbulent starting profiles, e.g., by starting laminar and running up to a desired value of  $Re_\theta$ .

Finally, to run **EDDYBL** as a pure laminar boundary-layer program, the turbulence model can be suppressed by setting **MODEL** to -1 in the **Turbulence Model** sub-menu. When this is done, turbulence model computations are bypassed and no transition to turbulence occurs.

## D.6 Applicability and Limitations

Program **EDDYBL** applies to attached, compressible, two-dimensional and axisymmetric boundary layers. The program computes properties of turbulent boundary layers using the Wilcox (1988a)  $k$ - $\omega$  model or the Wilcox (1988b) multiscale model, including effects of surface roughness, surface mass transfer, surface curvature, and low-Reynolds-number corrections. The program also includes several low-Reynolds-number versions of the  $k$ - $\epsilon$  model.

Computations can be initiated either from turbulent starting profiles that are generated from specified integral properties, or from laminar profiles that are automatically generated.

The  $k$ - $\omega$  and multiscale models are very robust and can be integrated through transition from laminar to turbulent flow with and without low-Reynolds-number corrections. By contrast, the  $k$ - $\epsilon$  model requires smaller streamwise steps than the  $k$ - $\omega$  and multiscale models, and, in general, cannot be integrated through transition unless extremely small steps are taken.

If integral properties are unknown and a  $k$ - $\epsilon$  solution is desired, the optimum procedure is to start laminar with the  $k$ - $\omega$  model and integrate through transition. Then, select the desired  $k$ - $\epsilon$  model and use the **Restart** option to continue the run.

Finally, if numerical difficulties are encountered with the  $k$ - $\epsilon$  model, try changing the value of input parameter *PSIEPS* in the Turbulence Model menu. Table 7.2 lists the default value of this parameter ( $\psi_\epsilon$ ); its purpose is explained in Section 7.3.

## D.7 EDDYBL Output Parameters

The following *dimensionless* quantities are printed in the profiles portion of Program **EDDYBL** output.

Name	Symbol/Equation	Definition
i	$i$	Mesh point number
y/delta	$y/\delta$	Dimensionless normal distance
u/Ue	$\tilde{u}/U_e$	Dimensionless velocity
yplus	$y^+ = u_\tau y/\nu_w$	Compressible sublayer-scaled velocity
uplus	$u^+ = u^*/u_\tau$	Compressible sublayer-scaled velocity
k/Ue**2	$k/U_e^2$	Dimensionless turbulence energy
omega	$\nu_e \omega/U_e^2$	Dimensionless dissipation rate
eps/mu	$\mu_T/\mu$	Dimensionless eddy viscosity
L/delta	$\sqrt{k/\beta^*/(\omega\delta)}$	Dimensionless turbulence length scale
uv/tauw	$\tau_{xy}/\tau_w$	Dimensionless Reynolds shear stress
T/Te	$\tilde{T}/T_e$	Temperature ratio

The following quantities are printed in the integral-parameter portion of Program **EDDYBL** output.

Symbol	Meaning	English Units	SI Units
F	Force	pounds (lb)	Newtons (N)
L	Length	feet (ft)	meters (m)
M	Mass	slugs (sl)	kilograms (kg)
Q	Heat flux	Btu/second (Btu/sec)	Watts (W)
T	Time	seconds (sec)	seconds (sec)
$\Theta$	Temperature	$^{\circ}$ Rankine	Kelvins

Name	Symbol/Equation	Definition	Dimensions
beta	$\beta = (2\xi/U_e)dU_e/d\xi$	Pressure gradient parameter	None
Cfe	$c_{fe} = 2\tau_w/\bar{\rho}_e U_e^2$	Skin friction based on $\bar{\rho}_e$	None
Cfw	$c_{fw} = 2\tau_w/\bar{\rho}_w U_e^2$	Skin friction based on $\bar{\rho}_w$	None
delta	$\delta$	Boundary-layer thickness	L
delta*	$\delta^*$	Displacement thickness	L
dPe/ds	$d(P_e/\bar{\rho}_\infty U_\infty^2)/d\bar{s}$	Dimensionless pressure gradient	None
dTe/ds	$d(T_e/T_{ref})/d\bar{s}$	Dimensionless temperature grad.	None
dUe/ds	$d(U_e/U_\infty)/d\bar{s}$	Dimensionless velocity gradient	None
H	$H = \delta^*/\theta$	Shape factor	None
hdot	$\dot{h} = q_w/(T_w - T_{aw})$	Heat transfer coefficient	$QL^{-2}\Theta^{-1}$
Iedge	$N$	Total no. of mesh points in B.L.	None
Itro		Number of iterations	None
kmax	$\sqrt{\beta^*(\bar{\rho}k)_{max}}/\tau_w$	Maximum turbulence energy	None
M	$m$	Streamwise step number	None
Me	$M_e$	Edge Mach number	None
Mue	$\mu_e$	Edge molecular viscosity	$ML^{-1}T^{-1}$
Ne	$N_e$	Mesh point number at B.L. edge	None
Negtiv		Number of points where $k, \omega, \epsilon < 0$	None
Nerror		Number of points not converged	None
Nskip		No. of points below $u^+ = USTOP$	None
Nste	$\dot{h}/\bar{\rho}_e U_e C_p$	Stanton number based on $\bar{\rho}_e$	None
Nstw	$\dot{h}/\bar{\rho}_w U_e C_p$	Stanton number based on $\bar{\rho}_w$	None
Nue	$Pr_L s \dot{h}/\mu_e C_p$	Nusselt number based on $\mu_e$	None
Nuw	$Pr_L s \dot{h}/\mu_w C_p$	Nusselt number based on $\mu_w$	None
Pe	$P_e$	Edge pressure	$FL^{-2}$
qw	$q_w$	Surface heat flux	$QL^{-2}$
radius	$r_o$	Body radius	L
Recov	$r$	Recovery factor	None
Redel*	$Re_{\delta^*} = \bar{\rho}_e U_e \delta^*/\mu_e$	Reynolds number based on $\delta^*$	None
Res	$Re_s = \bar{\rho}_e U_e s/\mu_e$	Reynolds number based on $s$	None
Rethet	$Re_\theta = \bar{\rho}_e U_e \theta/\mu_e$	Reynolds number based on $\theta$	None
Rhoe	$\bar{\rho}_e$	Edge density	$ML^{-3}$
rho*vw	$\bar{\rho}_w \tilde{v}_w$	Surface mass flux	$ML^{-2}T^{-1}$
s	$s$	Arc length	L
tauw	$\tau_w$	Surface shear stress	$FL^{-2}$
Te	$T_e$	Edge temperature	$\Theta$
theta	$\theta$	Momentum thickness	L
Ue	$U_e$	Edge velocity	$LT^{-1}$
utau	$u_\tau$	Friction velocity	$LT^{-1}$
xi	$\xi = \int_0^s \bar{\rho}_e U_e \mu_e r_o^{2j} ds$	Transformed streamwise coord.	L
yplus	$y_2^+$	Value of $y^+$ nearest the surface	None
z	$z$	Axial distance	L

## D.8 Program PLOTEB: Plotting Utility

Program **PLOTEB** creates video and hardcopy plots of skin friction,  $c_f$ , or Stanton number,  $St$ , versus arc length,  $s$ , and a  $u^+$  versus  $y^+$  velocity profile computed with Program **EDDYBL** on IBM PC's and compatibles.

### Input-parameter description:

Program **PLOTEB** reads the following sixteen input parameters from disk file **ploteb.dat** in the order listed below. Integer quantities must be formatted according to (7x,i6) while floating-point quantities must be formatted as (7x,f6.2).

- mon* Monitor type (see Appendix E)
- ifore* Foreground color (see Appendix E)
- iback* Background color (see Appendix E)
- nprin* Printer type (see Appendix E)
- mode* Graphics-mode flag for printers; number of pens for plotters (see Appendix E)
- metric* Input arc length units flag
  - 1 Input arc length is in meters
  - 0 Input arc length is in feet
  - 1 Convert from feet to meters
- ideccf* Number of decimal places for  $c_f/St$  scale
- idecrr* Number of decimal places for arc length scale
- idecup* Number of decimal places for  $u^+$  scale
- isymb* Symbol type for experimental data points
  - 0 Circle
  - 1 Triangle
  - 2 Square
  - 3 Diamond
- jstart* Number of  $c_f/St$  points to skip over at beginning of computation; this is sometimes useful in order to skip over transient behavior at the beginning of a computation. The sign also determines what is plotted.
  - > 0 Plot  $c_f$  versus  $s$
  - < 0 Plot  $St$  versus  $s$
- kcyccf* Increment between points to be plotted for  $c_f/St$  versus  $s$
- kcykup* Increment between points to be plotted for  $u^+$  versus  $y^+$
- kfilt* 0 to suppress data filtering; otherwise use filtering. The filtering algorithm generates a smoothed curve.
- ksize* Plot scaling factor. Using 100 yields a full-size hardcopy plot. Smaller values yield a hardcopy plot reduced by *ksize* per cent.

Thus,  $ksize = 50$  yields a half-size plot.

*symsiz* Size of experimental data symbols, in inches

Next, Program **PLOTEB** reads a single, free-formatted, line to indicate where hardcopy print is directed. This line comes immediately after the specified value for *symsiz* and defines the following five additional parameters.

*devic* Device name of type character\*4; valid devices are LPT1, LPT2, LPT3, COM1, COM2, COM3, COM4

*nbaud* Baud rate for a serial port; valid baud rates are 110, 150, 300, 600, 1200, 2400, 4800, 9600

*parity* Parity of type character\*3 or character\*4 for a serial port; valid parity settings are 'even', 'odd' and 'none'

*nstop* Number of stop bits for a serial port; either 1 or 2

*lword* Word length for a serial port; either 7 or 8

In addition to disk file **ploteb.dat**, an optional disk file named **exper.dat** containing measured skin-friction and velocity-profile data can be included. The first line of the disk file must contain the number of input data pairs with format (i6). If no  $c_f$  or  $St$  data are available, place a zero on this line. If  $c_f$  or  $St$  data are available, this line is followed by  $s-c_f$  (or  $s-St$ ) data pairs with format (2e11.4). Next, enter the data source; as many as twenty characters can be used. The final  $c_f/St$  entry is the location of the box citing the data source. Enter a 1 for upper left, 2 for upper right, 3 for lower right, and 4 for lower left (see Figure D.2). The format is (7x,i6). A similar sequence of input parameters follows for velocity-profile data. The order of the data pairs is  $y^+$  first and  $u^+$  last. For example, the bench-mark case is an incompressible flat-plate boundary layer. Experimental data for this flow are given by Coles and Hirst (1969). The sample **exper.dat** included on the distribution diskette is as follows.

```

      5
      1.5978e 00 3.4500e-03
      2.0899e 00 3.3700e-03
      2.5820e 00 3.1700e-03
      3.0741e 00 3.1700e-03
      3.5663e 00 3.0800e-03
WIEGHARDT
iposcf=      2
      12
      4.2400e 01 1.4570e 01
      8.4800e 01 1.6090e 01

```

```

1.6950e 02 1.7610e 01
3.3910e 02 1.9080e 01
5.0860e 02 2.0470e 01
6.7822e 02 2.1660e 01
8.4779e 02 2.2510e 01
1.0173e 03 2.3540e 01
1.2716e 03 2.4540e 01
1.5259e 03 2.5290e 01
1.6954e 03 2.5630e 01
2.1193e 03 2.5780e 01
WEIGHARDT
iposup=      1

```

**Program Output:** A video plot with two graphs (see Figure D.2) is created on the screen. When the plot is complete, the following message appears:

**Hardcopy output (y/n)?**

Enter a *y* or a *Y* to create a hardcopy plot. Pressing any other key terminates the run without creating a hardcopy plot.

**Comments:**

- The following is a sample input-data file, **ploteb.dat**, for a machine with a standard VGA monitor and an HP DeskJet connected to serial port COM1:.

```

mon    =    18          (Standard VGA monitor)
ifore  =    15          (Bright-white foreground)
iback  =     1          (Blue background)
nprin  =     2          (HP DeskJet)
mode   =     3          (300 dots per inch resolution)
metric=     1          (Convert feet to meters)
ideccf=     1          (One decimal place on Cf scale)
idecs  =     1          (One decimal place on s scale)
idecup=    -1          (Integers on u+ scale)
isymb  =     0          (Circles for experimental data)
jstart=     1          (Skip no points)
kcyccf=     3          (Plot every third Cf point)
kcycup=     1          (Plot every u+ point)
kfilt  =     1          (Use filtering)
ksize  =    100         (Full size plot)

```

```
symsiz= .080          (.08" experimental data symbols)
'com1' , 9600 , 'none' , 1 , 8
```

The last line indicates the printer is connected to serial port COM1: and the port is set at 9600 baud, no parity, 1 stop bit and 8 data bits.

If disk file **ploteb.dat** is not available, Program **PLOTEB** uses the following set of default values :

```
mon = 18, ifore = 15, iback = 1, nprin = 24, mode = 39, ksize = 100,
symsiz = .08, devid = 'LPT1'
```

Note that *nbaud*, *parity*, *nstop* and *lword* are not used for parallel ports.

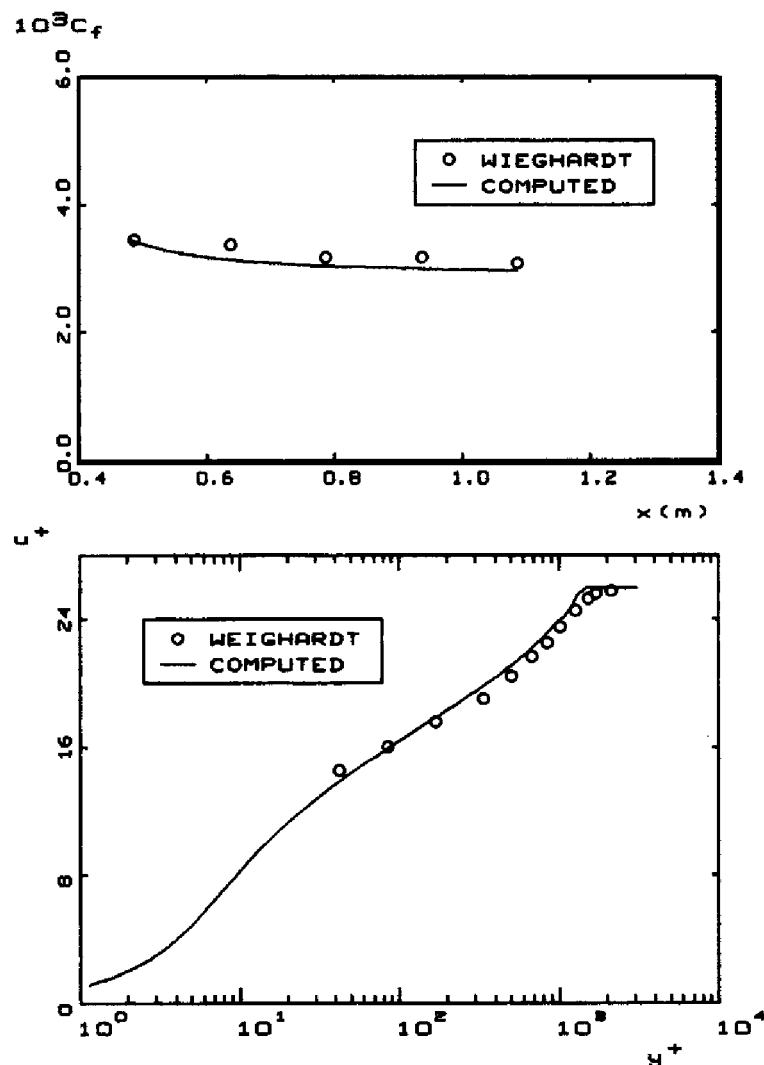


Figure D.2: Sample plot created by Program PLOTEB.

## D.9 Adapting to Other Compilers/Systems

If you change computers or compilers, the appropriate modifications may already be included in the source code provided. If your Fortran compiler is an ANSI-77 Standard compiler and supports most of the standard VAX extensions, only three categories of changes are needed.

1. You must determine the correct syntax for the **include** command. Then, note that the source code provided uses the VAX syntax. Make the appropriate change throughout the source code for your compiler. Examples of VAX and other syntax are:

Fortran Compiler	Include Syntax
VAX, SVS, Lahey, Microsoft	<b>include</b> 'filename'
Cray (UNICOS), SUN	<b>include</b> 'filename'
Microsoft (older versions)	<b>\$include:</b> 'filename'
SVS (older versions)	<b>\$include</b> filename
Cray (COS)	<b>*CALL</b> FILENAME
	↑
	Column 1

2. Change the value of *icpu* defined in the include file named **cpuid**. The values currently assigned are:

<i>icpu</i> = 0	SVS Fortran (680x0, 80386, 80486)
<i>icpu</i> = 1	Lahey/Microsoft Fortran (8088, 80x86)
<i>icpu</i> = 2	VAX/VMS
<i>icpu</i> = 3	SUN Fortran (68020, SPARC)
<i>icpu</i> = 4	Cray (UNICOS)
<i>icpu</i> = 5	Silicon Graphics Iris

3. The only other compiler-specific syntax differences are located in a subroutine called **NAMSYS** that appears in **eddybl.for**. This subroutine opens disk files depending upon the value of *icpu*. Make any changes required for your system.
4. Search the **EDDYBL** and **SETEBL** source code for occurrences of *icpu* to see if the correct action is taken for your compiler and/or operating system. Make any changes required for your system.
5. Modify Program **INSTL** as required for your video display and/or compiler-specific requirements.



## D.10 Compile and Link Commands

This section describes the commands required to compile and link Programs **SETEBL**, **INSTL** and **EDDYBL** for the various Fortran compilers supported. Be sure that you have selected the appropriate value for *icpu* in the include file **cpuid**.

### ICPU = 0: SVS Fortran-386 ... Phar Lap and C<sup>3</sup>

**Special Comments:** For the Phar Lap version, add the **+w1167** option to compile for a Weitek math coprocessor. Linker options for either **fastlink** or **386link** can be specified in an environment variable by including the following in your **autoexec.bat** file ...

```
80387 version
set 386link=-l libf28 libp28 -pack -maxr fffh -s 40000
Weitek version
set 386link=-l libf28w libp28w -pack -maxr fffh -s 40000
```

#### Compile and Link:

```
svs instl.for
svs eddybl.for
svs seteb1.for edge.for grafic.for initil.for ioebl.for main0.for misc.for
```

### ICPU = 0: SVS Fortran-020

**Special Comments:** Use **pload** in place of **load** for Definicon PM-020 and PM-030 boards.

#### Compile and Link:

```
load fc instl -lk
load fc eddybl -lk
load fc seteb1 edge grafic initil ioebl main0 misc -lk
```

### ICPU = 1: Lahey Fortran ... LF90

**Special Comments:** None.

#### Compile and Link:

```
lf90 instl
lf90 eddybl
lf90 seteb1 edge grafic initil ioebl main0 misc
```

**ICPU = 1: Lahey Fortran ... F77L-EM/32****Special Comments:** None.**Compile and Link:**

```

f77l3 instl
386link instl
f77l3 eddybl
386link eddybl
f77l3 seteb1
f77l3 edge
f77l3 grafic
f77l3 initil
f77l3 ioeb1
f77l3 main0
f77l3 misc
386link seteb1 edge grafic initil ioeb1 main0 misc

```

**ICPU = 1: Lahey Fortran ... F77L****Special Comments:** None.**Compile and Link:**

```

f77l instl
optlink instl;
f77l eddybl
optlink eddybl;
f77l seteb1
f77l edge
f77l grafic
f77l initil
f77l ioeb1
f77l main0
f77l misc
optlink seteb1+edge+grafic+initil+ioeb1+main0+misc;

```

**ICPU = 1: Microsoft Fortran****Special Comments:** Using the /e option reduces executable file size.**Compile and Link:**

```

fl instl.for
fl eddybl.for
fl /c seteb1.for edge.for grafic.for initil.for ioeb1.for main0.for misc.for
link seteb1 edge grafic initil ioeb1 main0 misc,,nul, /e;

```

**ICPU = 2: VAX Fortran**

**Special Comments:** None.

**Compile and Link:**

```
for instl
link instl
for eddybl
link eddybl
for setebf
for edge
for grafic
for initil
for ioebf
for main0
for misc
link setebf,edge,grafic,initil,ioebf,main0,misc
```

**ICPU = 3: SUN Fortran ... SUN/OS or MS-DOS/SP-1**

**Special Comments:** Using the **-O3** option yields the maximum degree of optimization.

**Compile and Link:**

```
f77 instl.f -O3 -o instl
f77 eddybl.f -O3 -o eddybl
f77 setebf.f edge.f grafic.f initil.f ioebf.f main0.f misc.f -O3 -o setebf
```

**ICPU = 4: Cray Fortran ... UNICOS**

**Special Comments:** None.

**Compile and Link:**

```
cf77 -o instl instl.f
cf77 -o eddybl eddybl.f
cf77 -o setebf setebf.f edge.f grafic.f initil.f ioebf.f main0.f misc.f
```

**ICPU = 5: Silicon Graphics Iris**

**Special Comments:** None.

**Compile and Link:**

```
f77 -o instl instl.f
f77 -o eddybl eddybl.f
f77 -o setebf setebf.f edge.f grafic.f initil.f ioebf.f main0.f misc.f
```

## D.11 Additional Technical Information

The program uses the conventional Levy-Lees variables [see Hayes and Probstein (1959)] and much of the program notation follows that of Harris and Blanchard (1982). The numerical procedure is the Blottner (1974) variable grid method augmented with an algorithm devised by Wilcox (1981b) to permit large streamwise steps. Section 7.3 of the main text provides an in-depth discussion of the algorithm. This section first presents the governing equations for mean-flow properties and all turbulence-model equations implemented in the program. Then, the transformed, nondimensional form of the equations is presented for the  $k$ - $\omega$  and  $k$ - $\epsilon$  models.

### D.11.1 Mean-Flow Equations

The equations governing conservation of mass, momentum and mean energy for all models are the same. For compressible two-dimensional ( $j = 0$ ) and axisymmetric ( $j = 1$ ) boundary layers, the program uses body-oriented coordinates ( $s, n$ ), where  $s$  is arc length and  $n$  is distance normal to the surface. The equations are as follows.

$$\frac{\partial}{\partial s}(\bar{\rho}\tilde{u}) + \frac{1}{r^j} \frac{\partial}{\partial n}(r^j \bar{\rho}\tilde{v}) = 0 \quad (\text{D.3})$$

$$\bar{\rho}\tilde{u} \frac{\partial \tilde{u}}{\partial s} + \bar{\rho}\tilde{v} \frac{\partial \tilde{u}}{\partial n} = -\frac{dP}{ds} + \frac{1}{r^j} \frac{\partial}{\partial n} \left[ r^j \left( \mu \frac{\partial \tilde{u}}{\partial n} + \bar{\rho}\tau \right) \right] \quad (\text{D.4})$$

$$\bar{\rho}\tilde{u} \frac{\partial \tilde{h}}{\partial s} + \bar{\rho}\tilde{v} \frac{\partial \tilde{h}}{\partial n} = \tilde{u} \frac{dP}{ds} + \mu \left( \frac{\partial \tilde{u}}{\partial n} \right)^2 + \bar{\rho}\epsilon + \frac{1}{r^j} \frac{\partial}{\partial n} \left[ r^j \left( \frac{\mu}{Pr_L} + \frac{\mu_T}{Pr_T} \right) \frac{\partial \tilde{h}}{\partial n} \right] \quad (\text{D.5})$$

The perfect gas law is used as the equation of state and the fluid is assumed calorically perfect so that

$$P = \bar{\rho}R\tilde{T} \quad \text{and} \quad \tilde{h} = C_p\tilde{T} \quad (\text{D.6})$$

In Equations (D.3) through (D.6):  $\tilde{u}$  and  $\tilde{v}$  are streamwise and normal mass-averaged velocity components;  $\bar{\rho}$ ,  $P$  and  $\tilde{h}$  are fluid density, pressure and enthalpy;  $\mu$  and  $\mu_T$  are molecular and eddy viscosity;  $\tau$  is specific Reynolds shear stress;  $\epsilon$  is turbulence dissipation rate;  $Pr_L$  and  $Pr_T$  are laminar and turbulent Prandtl numbers;  $\tilde{T}$  is mass-averaged temperature;  $R$  is the perfect gas constant; and  $C_p$  is specific heat at constant pressure.

### D.11.2 $k$ - $\omega$ and Multiscale Model Equations

For both the  $k$ - $\omega$  and multiscale models the dissipation,  $\epsilon$ , is given by

$$\epsilon = \beta^* \omega k \quad (\text{D.7})$$

where  $k$  is turbulence kinetic energy and  $\omega$  is specific dissipation rate. The equations for  $k$  and  $\omega$  applicable to compressible boundary layers are as follows.

$$\bar{\rho} \tilde{u} \frac{\partial k}{\partial s} + \bar{\rho} \tilde{v} \frac{\partial k}{\partial n} = \bar{\rho} \tau \frac{\partial \tilde{u}}{\partial n} - \beta^* \bar{\rho} \omega k + \frac{1}{r^j} \frac{\partial}{\partial n} \left[ r^j (\mu + \sigma^* \mu_T) \frac{\partial k}{\partial n} \right] \quad (\text{D.8})$$

$$\bar{\rho} \tilde{u} \frac{\partial \omega}{\partial s} + \bar{\rho} \tilde{v} \frac{\partial \omega}{\partial n} = \alpha \frac{\omega}{k} \bar{\rho} \tau \frac{\partial \tilde{u}}{\partial n} - \beta \bar{\rho} \omega \left[ \omega + \hat{\xi} \frac{\partial \tilde{u}}{\partial n} \right] + \frac{1}{r^j} \frac{\partial}{\partial n} \left[ r^j (\mu + \sigma \mu_T) \frac{\partial \omega}{\partial n} \right] \quad (\text{D.9})$$

For the  $k$ - $\omega$  model, the Reynolds shear stress is given by

$$\bar{\rho} \tau = \alpha^* \mu_T \frac{\partial \tilde{u}}{\partial n} \quad (\text{D.10})$$

For the multiscale model, the Reynolds stresses are computed from the following equations:

$$\bar{\rho} \tilde{u} \frac{\partial \tau}{\partial s} + \bar{\rho} \tilde{v} \frac{\partial \tau}{\partial n} = \left[ (1 - \hat{\alpha}) \sigma_y - \hat{\beta} \sigma_x + \frac{2}{3} (1 - \hat{\alpha} - \hat{\beta} + \frac{3}{4} \hat{\gamma}) k \right] \bar{\rho} \frac{\partial \tilde{u}}{\partial n} - C_1 \beta^* \bar{\rho} \omega \tau \quad (\text{D.11})$$

$$\bar{\rho} \tilde{u} \frac{\partial \sigma_x}{\partial s} + \bar{\rho} \tilde{v} \frac{\partial \sigma_x}{\partial n} = \frac{2}{3} \left[ 2(1 - \hat{\alpha}) + \hat{\beta} \right] \bar{\rho} \tau \frac{\partial \tilde{u}}{\partial n} - C_1 \beta^* \bar{\rho} \omega \sigma_x \quad (\text{D.12})$$

$$\bar{\rho} \tilde{u} \frac{\partial \sigma_y}{\partial s} + \bar{\rho} \tilde{v} \frac{\partial \sigma_y}{\partial n} = -\frac{2}{3} \left[ (1 - \hat{\alpha}) + 2\hat{\beta} \right] \bar{\rho} \tau \frac{\partial \tilde{u}}{\partial n} - C_1 \beta^* \bar{\rho} \omega \sigma_y \quad (\text{D.13})$$

where  $C_1$  is defined in terms of the ratio of large eddy energy ( $k - e$ ) to turbulence kinetic energy according to

$$C_1 = 1 + 4 \left( \frac{k - e}{k} \right)^{3/2} \quad (\text{D.14})$$

and  $(k - e)$  satisfies the following equation.

$$\bar{\rho} \tilde{u} \frac{\partial}{\partial s} (k - e) + \bar{\rho} \tilde{v} \frac{\partial}{\partial n} (k - e) = \left( 1 - \hat{\alpha} - \hat{\beta} \right) \bar{\rho} \tau \frac{\partial \tilde{u}}{\partial n} - \beta^* \bar{\rho} \omega k \left( \frac{k - e}{k} \right)^{3/2} \quad (\text{D.15})$$

The quantities  $\sigma_x$  and  $\sigma_y$  are the stress deviator components given in terms of the normal Reynolds stress by

$$\sigma_x = \frac{\overline{\rho u'^2}}{\bar{\rho}} - \frac{2}{3}k \quad \text{and} \quad \sigma_y = \frac{\overline{\rho v'^2}}{\bar{\rho}} - \frac{2}{3}k \quad (\text{D.16})$$

The various closure coefficients, viz.,  $\alpha$ ,  $\beta$ ,  $\beta^*$ ,  $\sigma$ ,  $\sigma^*$ ,  $\hat{\alpha}$ ,  $\hat{\beta}$ ,  $\hat{\gamma}$  and  $\hat{\xi}$  are given by the following. First, we define the fully turbulent (subscript  $\infty$ ), incompressible (subscript  $i$ ) values by

$$\beta_i = 3/40, \quad \beta_\infty^* = 9/100, \quad \sigma = 1/2, \quad \sigma^* = 1/2 \quad (\text{D.17})$$

$$\hat{\alpha} = 42/55, \quad \hat{\beta} = 6/55, \quad \hat{\gamma}_\infty = 1/4, \quad \hat{\xi} = 0 \text{ or } 1 \quad (\text{D.18})$$

$$\alpha_\infty = \frac{\beta_i \left(1 + \hat{\xi} \sqrt{\beta_\infty^*}\right) - \sigma \sqrt{\beta_\infty^*} \kappa^2}{\beta_\infty^*}, \quad \alpha_\infty^* = 1 \quad (\text{D.19})$$

If low-Reynolds-number corrections are excluded, we simply use:

$$\alpha^* = \alpha_\infty^*, \quad \alpha = \alpha_\infty, \quad \beta_i^* = \beta_\infty^*, \quad \hat{\gamma} = \hat{\gamma}_\infty \quad (\text{D.20})$$

If low-Reynolds-number corrections are included, we use the following:

$$\left. \begin{aligned} \alpha^* &= \alpha_\infty^* \frac{\alpha_o^* + Re_T/R_k}{1 + Re_T/R_k} \\ \alpha &= \alpha_\infty \cdot \frac{\alpha_o + Re_T/R_\omega}{1 + Re_T/R_\omega} \cdot (\alpha^*)^{-m} \\ \beta_i^* &= \beta_\infty^* \cdot \frac{5/18 + (Re_T/R_\beta)^4}{1 + (Re_T/R_\beta)^4} \\ \hat{\gamma} &= \hat{\gamma}_\infty \cdot \frac{\hat{\gamma}_o + Re_T/R_k}{1 + Re_T/R_k} \end{aligned} \right\} \quad (\text{D.21})$$

where  $m = 1$  for the  $k$ - $\omega$  model,  $m = 0$  for the multiscale model, and

$$\alpha_o^* = \beta/3, \quad \alpha_o = 1/10, \quad \hat{\gamma}_o = 2\beta_\infty^* \alpha_o^* / \hat{\gamma}_\infty, \quad R_\beta = 8, \quad R_k = 6 \quad (\text{D.22})$$

$$R_\omega = \begin{cases} 27/10, & k\text{-}\omega \text{ model} \\ 3/4, & \text{Multiscale model} \end{cases} \quad (\text{D.23})$$

The quantity  $Re_T$  is turbulence Reynolds number defined by

$$Re_T = \frac{k}{\omega \nu} \quad (\text{D.24})$$

Finally, the compressible values of  $\beta$  and  $\beta^*$  are

$$\beta = \beta_i \left[ 1 - \frac{\beta_i^*}{\beta_i} \xi^* F(M_t) \right], \quad \beta^* = \beta_i^* [1 + \xi^* F(M_t)], \quad \xi^* = 3/2 \quad (\text{D.25})$$

The compressibility function  $F(M_t)$  is given by

$$F(M_t) = \begin{cases} 0, & M_t \leq M_{to} \\ M_t^2 - M_{to}^2, & M_t > M_{to} \end{cases} \quad (D.26)$$

where  $M_t^2 \equiv 2k/a^2$ ,  $a$  is the speed of sound, and  $M_{to}$  is given by

$$M_{to} = 1/4 \quad (D.27)$$

### D.11.3 $k$ - $\epsilon$ Model Equations

For the  $k$ - $\epsilon$  model the equations for  $k$  and  $\epsilon$  are:

$$\bar{\rho}\tilde{u}\frac{\partial k}{\partial s} + \bar{\rho}\tilde{v}\frac{\partial k}{\partial n} = \bar{\rho}\tau\frac{\partial \tilde{u}}{\partial n} - \bar{\rho}\epsilon + \frac{1}{r^j}\frac{\partial}{\partial n} \left[ r^j (\mu + \mu_T/\sigma_k) \frac{\partial k}{\partial n} \right] \quad (D.28)$$

$$\bar{\rho}\tilde{u}\frac{\partial \tilde{\epsilon}}{\partial s} + \bar{\rho}\tilde{v}\frac{\partial \tilde{\epsilon}}{\partial n} = f_1 C_{\epsilon 1} \frac{\tilde{\epsilon}}{k} \bar{\rho}\tau\frac{\partial \tilde{u}}{\partial n} - f_2 C_{\epsilon 2} \bar{\rho} \frac{\tilde{\epsilon}^2}{k} + \bar{\rho}E + \frac{1}{r^j}\frac{\partial}{\partial n} \left[ r^j (\mu + \mu_T/\sigma_\epsilon) \frac{\partial \tilde{\epsilon}}{\partial n} \right] \quad (D.29)$$

where

$$\epsilon = \tilde{\epsilon} + \epsilon_o \quad (D.30)$$

and the eddy viscosity is

$$\mu_T = C_\mu f_\mu \rho k^2 / \tilde{\epsilon} \quad (D.31)$$

Program **EDDYBL** includes six low-Reynolds-number versions of the  $k$ - $\epsilon$  model. The models differ in the form of the damping functions  $f_\mu$ ,  $f_1$ ,  $f_2$ ,  $\epsilon_o$ ,  $E$ , in the values of the closure coefficients, and in the surface boundary condition imposed on  $\tilde{\epsilon}$ . The damping functions depend upon one or more of the following three dimensionless parameters.

$$Re_T = \frac{k^2}{\tilde{\epsilon}\nu}, \quad Re_y = \frac{k^{1/2}n}{\nu}, \quad y^+ = \frac{u_\tau n}{\nu} \quad (D.32)$$

The damping functions, closure coefficients and surface boundary condition on  $\tilde{\epsilon}$  for the six models are as follows.

**Jones-Launder Model**

$$\left. \begin{aligned}
 f_\mu &= e^{-2.5/(1+Re_T/50)} \\
 f_1 &= 1 \\
 f_2 &= 1 - 0.3e^{-Re_T^2} \\
 \epsilon_o &= 2\nu \left( \frac{\partial \sqrt{k}}{\partial n} \right)^2 \\
 E &= 2\nu\nu_T \left( \frac{\partial^2 \tilde{u}}{\partial n^2} \right)^2 \\
 C_{\epsilon 1} &= 1.45, \quad C_{\epsilon 2} = 2.00, \quad C_\mu = 0.09, \quad \sigma_k = 1.0, \quad \sigma_\epsilon = 1.3 \\
 \tilde{\epsilon} &= 0 \quad \text{at} \quad n = 0
 \end{aligned} \right\} \quad (D.33)$$

**Launder-Sharma Model**

$$\left. \begin{aligned}
 f_\mu &= e^{-3.4/(1+Re_T/50)^2} \\
 f_1 &= 1 \\
 f_2 &= 1 - 0.3e^{-Re_T^2} \\
 \epsilon_o &= 2\nu \left( \frac{\partial \sqrt{k}}{\partial n} \right)^2 \\
 E &= 2\nu\nu_T \left( \frac{\partial^2 \tilde{u}}{\partial n^2} \right)^2 \\
 C_{\epsilon 1} &= 1.44, \quad C_{\epsilon 2} = 1.92, \quad C_\mu = 0.09, \quad \sigma_k = 1.0, \quad \sigma_\epsilon = 1.3 \\
 \tilde{\epsilon} &= 0 \quad \text{at} \quad n = 0
 \end{aligned} \right\} \quad (D.34)$$

**Lam-Bremhorst Model**

$$\left. \begin{aligned}
 f_\mu &= (1 - e^{-0.0165Re_y})^2 (1 + 20.5/Re_T) \\
 f_1 &= 1 + (0.05/f_\mu)^3 \\
 f_2 &= 1 - e^{-Re_T^2} \\
 \epsilon_o &= 0 \\
 E &= 0 \\
 C_{\epsilon 1} &= 1.44, \quad C_{\epsilon 2} = 1.92, \quad C_\mu = 0.09, \quad \sigma_k = 1.0, \quad \sigma_\epsilon = 1.3 \\
 \tilde{\epsilon} &= \nu \frac{\partial^2 k}{\partial n^2} \quad \text{at} \quad n = 0
 \end{aligned} \right\} \quad (D.35)$$



**Chien Model**

$$\left. \begin{aligned}
 f_\mu &= 1 - e^{-0.0115y^+} \\
 f_1 &= 1 \\
 f_2 &= 1 - 0.22e^{-(Re_T/6)^2} \\
 \epsilon_o &= 2\nu \frac{k}{n^2} \\
 E &= -2\nu \frac{\tilde{\epsilon}}{n^2} e^{-y^+/2} \\
 C_{\epsilon 1} &= 1.35, \quad C_{\epsilon 2} = 1.80, \quad C_\mu = 0.09, \quad \sigma_k = 1.0, \quad \sigma_\epsilon = 1.3 \\
 \tilde{\epsilon} &= 0 \quad \text{at} \quad n = 0
 \end{aligned} \right\} \quad (D.36)$$

**Yang-Shih Model**

$$\left. \begin{aligned}
 f_\mu &= \frac{[1 - \exp(-1.5 \cdot 10^{-4} R_y - 5 \cdot 10^{-7} R_y^3 - 10^{-10} R_y^5)]^{1/2}}{(1 + 1/\sqrt{Re_T})} \\
 f_1 &= \sqrt{Re_T} / \left(1 + \sqrt{Re_T}\right) \\
 f_2 &= \sqrt{Re_T} / \left(1 + \sqrt{Re_T}\right) \\
 \epsilon_o &= 0 \\
 E &= \nu \nu_T \left(\frac{\partial^2 \tilde{u}}{\partial n^2}\right)^2 \\
 C_{\epsilon 1} &= 1.44, \quad C_{\epsilon 2} = 1.92, \quad C_\mu = 0.09, \quad \sigma_k = 1.0, \quad \sigma_\epsilon = 1.3 \\
 \tilde{\epsilon} &= 2\nu \left(\frac{\partial \sqrt{k}}{\partial n}\right)^2 \quad \text{at} \quad n = 0
 \end{aligned} \right\} \quad (D.37)$$

**Fan-Lakshminarayana-Barnett Model**

$$\left. \begin{aligned}
 f_\mu &= 0.4 \frac{f_w}{\sqrt{Re_T}} + \left(1 - 0.4 \frac{f_w}{\sqrt{Re_T}}\right) \left(1 - e^{-R_y/42.63}\right)^3 \\
 f_1 &= 1 \\
 f_2 &= \left[1 - 0.22e^{-(Re_T/6)^2}\right] f_w^2 \\
 f_w &= 1 - \exp\left[-\frac{\sqrt{R_y}}{2.30} + \left(\frac{\sqrt{R_y}}{2.30} - \frac{R_y}{8.89}\right) \left(1 - e^{-R_y/20}\right)^3\right] \\
 \epsilon_o &= 0 \\
 E &= 0 \\
 C_{\epsilon 1} &= 1.39, \quad C_{\epsilon 2} = 1.80, \quad C_\mu = 0.09, \quad \sigma_k = 1.0, \quad \sigma_\epsilon = 1.3 \\
 \frac{\partial \tilde{\epsilon}}{\partial n} &= 0 \quad \text{at} \quad n = 0
 \end{aligned} \right\} \quad (D.38)$$

### D.11.4 Transformed Equations

The boundary-layer equations are singular at the leading edge of a body. As noted above, the program uses conventional Levy-Lees variables  $(\xi, \eta)$  to remove this singularity. Body oriented physical coordinates  $(s, n)$  are related to transformed coordinates  $(\xi, \eta)$  according to

$$d\xi = \bar{\rho}_e \tilde{u}_e \mu_e r_o^{2j} ds \quad \text{and} \quad d\eta = \frac{\bar{\rho}_e \tilde{u}_e (r_o + n)^j dn}{\sqrt{2\xi}} \quad (\text{D.39})$$

where  $r_o$  is body radius and subscript  $e$  denotes boundary-layer edge. Equivalently, we can write

$$\xi(s) = \int_0^s \bar{\rho}_e \tilde{u}_e \mu_e r_o^{2j} ds \quad \text{and} \quad \eta(s, n) = \frac{\bar{\rho}_e \tilde{u}_e r_o^j}{\sqrt{2\xi}} \int_0^n \left( \frac{\bar{\rho}}{\bar{\rho}_e} \right) t^j dn \quad (\text{D.40})$$

where  $t$  is the transverse curvature defined by

$$t = \frac{r}{r_o} \quad (\text{D.41})$$

The relations between derivatives in the physical  $(s, n)$  and transformed  $(\xi, \eta)$  coordinate system are as follows:

$$\left( \frac{\partial}{\partial s} \right)_n = \bar{\rho}_e \tilde{u}_e \mu_e r_o^{2j} \left( \frac{\partial}{\partial \xi} \right)_\eta + \left( \frac{\partial \eta}{\partial s} \right)_n \left( \frac{\partial}{\partial \eta} \right)_\xi \quad (\text{D.42})$$

$$\left( \frac{\partial}{\partial n} \right)_s = \frac{\bar{\rho}_e \tilde{u}_e r_o^j t^j}{\sqrt{2\xi}} \left( \frac{\bar{\rho}}{\bar{\rho}_e} \right) \left( \frac{\partial}{\partial \eta} \right)_\xi \quad (\text{D.43})$$

The dependent variables are also transformed according to:

$$\left. \begin{aligned} F(\xi, \eta) &= \frac{\tilde{u}}{\tilde{u}_e}, & \Theta(\xi, \eta) &= \frac{\tilde{T} - \tilde{T}_e}{\tilde{T}_e} \\ V(\xi, \eta) &= \frac{2\xi}{\bar{\rho}_e \tilde{u}_e \mu_e r_o^{2j}} \left[ F \left( \frac{\partial \eta}{\partial s} \right) + \frac{\bar{\rho} \tilde{u} r_o^j t^j}{\sqrt{2\xi}} \right] \\ K(\xi, \eta) &= \frac{k}{\tilde{u}_e^2} & \hat{W}(\xi, \eta) &= \frac{2\xi \omega}{\tilde{u}_e^2}, & \hat{\epsilon}(\xi, \eta) &= \frac{2\xi \tilde{\epsilon}}{\tilde{u}_e^4} \end{aligned} \right\} \quad (\text{D.44})$$

The transformed equations for the  $k$ - $\omega$  and  $k$ - $\epsilon$  models can then be expressed as follows.

$$2\xi \frac{\partial F}{\partial \xi} + \frac{\partial V}{\partial \eta} + F = 0 \quad (\text{D.45})$$

$$2\bar{\xi}F\frac{\partial F}{\partial \bar{\xi}} + V\frac{\partial F}{\partial \eta} - \frac{\partial}{\partial \eta} \left[ t^{2j}L(1 + \bar{\mu}_T) \frac{\partial F}{\partial \eta} \right] + \bar{\beta}(F^2 - \Theta - 1) = 0 \quad (\text{D.46})$$

$$\begin{aligned} 2\bar{\xi}F\frac{\partial \Theta}{\partial \bar{\xi}} + V\frac{\partial \Theta}{\partial \eta} - \frac{\partial}{\partial \eta} \left[ t^{2j}L \left( \frac{1}{Pr_L} + \frac{\bar{\mu}_T}{Pr_T} \right) \frac{\partial \Theta}{\partial \eta} \right] \\ - \bar{\alpha}t^{2j}L \left( \frac{\partial F}{\partial \eta} \right)^2 - \frac{\bar{\alpha}}{\hat{\rho}_e \hat{\mu}_e \hat{r}_o^{2j}} (\mathcal{E} + \mathcal{E}_o) = 0 \end{aligned} \quad (\text{D.47})$$

***k*- $\omega$  Model:**

$$\begin{aligned} 2\bar{\xi}F\frac{\partial K}{\partial \bar{\xi}} + V\frac{\partial K}{\partial \eta} - \frac{\partial}{\partial \eta} \left[ t^{2j}L(1 + \sigma^* \bar{\mu}_T) \frac{\partial K}{\partial \eta} \right] \\ + 2\bar{\beta}FK - t^{2j}L\bar{\mu}_T \left( \frac{\partial F}{\partial \eta} \right)^2 + \frac{\beta^*}{\hat{\rho}_e \hat{\mu}_e \hat{r}_o^{2j}} WK = 0 \end{aligned} \quad (\text{D.48})$$

$$\begin{aligned} 2\bar{\xi}F\frac{\partial W}{\partial \bar{\xi}} + V\frac{\partial W}{\partial \eta} - \frac{\partial}{\partial \eta} \left[ t^{2j}L(1 + \sigma \bar{\mu}_T) \frac{\partial W}{\partial \eta} \right] \\ + 2(\bar{\beta} - 1)FW - \alpha \frac{W}{K} t^{2j}L\bar{\mu}_T \left( \frac{\partial F}{\partial \eta} \right)^2 \\ + \frac{\beta}{\hat{\rho}_e \hat{\mu}_e \hat{r}_o^{2j}} \left[ W + \hat{\xi} \frac{\hat{\rho}_e \hat{r}_o^j \sqrt{2\bar{\xi}}}{\hat{\epsilon}} \frac{t^j}{(1 + \Theta)} \frac{\partial F}{\partial \eta} \right] W = 0 \end{aligned} \quad (\text{D.49})$$

$$\bar{\mu}_T = \frac{2\bar{\xi}\hat{\rho}_e}{\hat{\mu}_e \hat{\epsilon}^2} \frac{K}{L(1 + \Theta)^2 W}, \quad \mathcal{E} = \beta^* KW, \quad \mathcal{E}_o = 0, \quad (\text{D.50})$$

***k*- $\epsilon$  Model:**

$$\begin{aligned} 2\bar{\xi}F\frac{\partial K}{\partial \bar{\xi}} + V\frac{\partial K}{\partial \eta} - \frac{\partial}{\partial \eta} \left[ t^{2j}L \left( 1 + \frac{\bar{\mu}_T}{\sigma_k} \right) \frac{\partial K}{\partial \eta} \right] \\ + 2\bar{\beta}FK - t^{2j}L\bar{\mu}_T \left( \frac{\partial F}{\partial \eta} \right)^2 + \frac{1}{\hat{\rho}_e \hat{\mu}_e \hat{r}_o^{2j}} (\mathcal{E} + \mathcal{E}_o) = 0 \end{aligned} \quad (\text{D.51})$$

$$\begin{aligned}
& 2\bar{\xi}F\frac{\partial\mathcal{E}}{\partial\xi} + V\frac{\partial\mathcal{E}}{\partial\eta} - \frac{\partial}{\partial\eta} \left[ t^{2j}L \left( 1 + \frac{\bar{\mu}_T}{\sigma_\epsilon} \right) \frac{\partial\mathcal{E}}{\partial\eta} \right] \\
& + 2(2\bar{\beta} - 1)F\mathcal{E} - C_{\epsilon 1}f_1\frac{\mathcal{E}}{K}t^{2j}L\bar{\mu}_T \left( \frac{\partial F}{\partial\eta} \right)^2 \\
& + \frac{C_{\epsilon 2}f_2}{\hat{\rho}_e\hat{\mu}_e\hat{r}_o^{2j}}\frac{\mathcal{E}^2}{K} - \Sigma = 0
\end{aligned} \tag{D.52}$$

$$\bar{\mu}_T = C_\mu f_\mu \frac{2\bar{\xi}\hat{\rho}_e}{\hat{\mu}_e\hat{\epsilon}^2} \frac{K^2}{L(1+\Theta)^2\mathcal{E}}, \quad \mathcal{E}_o = \frac{A}{U_\infty^3} \frac{2\bar{\xi}}{\hat{u}_e^4} \epsilon_o, \quad \Sigma = \frac{A^2}{U_\infty^4} \frac{(2\bar{\xi})^2}{\hat{\rho}_e\hat{u}_e^6\hat{\mu}_e\hat{r}_o^{2j}} E \tag{D.53}$$

The quantities  $\bar{\alpha}$ ,  $\bar{\beta}$  and  $L$  are defined by

$$\bar{\alpha} \equiv \frac{\tilde{u}_e^2}{C_p\tilde{T}_e}, \quad \bar{\beta} \equiv \frac{2\bar{\xi}}{\tilde{u}_e} \frac{d\tilde{u}_e}{d\xi}, \quad L \equiv \frac{\bar{\rho}}{\bar{\rho}_e} \frac{\mu}{\mu_e} \tag{D.54}$$

and the following dimensionless quantities have been introduced:

$$\left. \begin{aligned}
\bar{\xi} &= \frac{\xi}{\rho_\infty U_\infty \mu_r A^{2j+1}}, & \hat{r}_o &= \frac{r_o}{A}, & \hat{u}_e &= \frac{\tilde{u}_e}{U_\infty} \\
\hat{\rho}_e &= \frac{\bar{\rho}_e}{\rho_\infty}, & \hat{T}_e &= \frac{\tilde{T}_e}{T_r}, & \hat{\mu}_e &= \frac{\mu_e}{\mu_r} \\
\hat{\epsilon} &= \sqrt{\frac{\mu_r}{\rho_\infty U_\infty A}}, & W &= \frac{\hat{W}}{\rho_\infty \mu_r A^{2j}}, & \mathcal{E} &= \frac{\hat{\mathcal{E}}}{\rho_\infty \mu_r A^{2j}}
\end{aligned} \right\} \tag{D.55}$$

Finally, note that subscript  $\infty$  denotes freestream flow condition,  $A$  is a reference length,  $T_r$  is the reference temperature defined as

$$T_r = U_\infty^2 / C_p \tag{D.56}$$

and  $\mu_r$  is the value of  $\mu$  for  $T = T_r$ .

## D.12 Software Package Modules

### Boundary-Layer Program Source:

<b>eddybl.for</b>	Source code for Program <b>EDDYBL</b>
<b>common</b>	Include file for Program <b>EDDYBL</b>
<b>cpuid</b>	Include file specifying CPU type

### Data-Preparation Utility Source:

<b>setebl.for</b>	Source code for the main program
<b>edge.for</b>	Source code for edge condition menus
<b>grafic.for</b>	Source code for reading graphics data
<b>initl.for</b>	Source code for initial profile menus
<b>ioebl.for</b>	Source code for I/O subroutines
<b>main0.for</b>	Source code for main input parameter menus
<b>misc.for</b>	Source code for miscellaneous menus
<b>chars</b>	Include file for Program <b>SETEBL</b>
<b>comeb1</b>	Include file for Program <b>SETEBL</b>
<b>comeb2</b>	Include file for Program <b>SETEBL</b>

### Installation Program Source:

<b>instl.for</b>	Source code for Program <b>INSTL</b>
------------------	--------------------------------------

### Bench-Mark Case Input Data:

<b>blocrv.dat</b>	Mass-transfer, body-curvature data file
<b>heater.dat</b>	Heat-transfer, surface-temperature data file
<b>presur.dat</b>	Pressure-distribution data file

### Plotting Files:

<b>exper.dat</b>	Experimental data file for plotting program
<b>ploteb.dat</b>	Primary plotting-program data file

### Bench-Mark Case Output:

<b>eddybl.prt</b>	Output from bench-mark test case
-------------------	----------------------------------

### Executable Files for IBM PC and Compatible Microcomputers:

<b>eddybl.exe</b>	Program <b>EDDYBL</b>
<b>instl.exe</b>	Program <b>INSTL</b>
<b>ploteb.exe</b>	Program <b>PLOTEB</b>
<b>setebl.exe</b>	Program <b>SETEBL</b>

## Appendix E

# Plotting Program Details

The various plotting programs described in Appendices C and D, viz., **PLOTEB**, **PLOTD**, **PLOTF**, **PLOTP** and **PLOTS**, run on IBM PC and compatible microcomputers with 640k of memory. They create both video and hardcopy plots for many of the standard display devices currently available. The information in this appendix pertains to all five of the plotting programs, the executable versions of which are provided on the distribution diskette accompanying this book. Read the file **read.me** in the root directory of the distribution diskette to determine the location of the executable and input-data files for the plotting programs.

### E.1 Font Files

With the exception of **PLOTEB**, all of the plotting programs reference a font file named **sppfnt.002**, that contains a scientific character font. Copy this file from the distribution diskette to any convenient directory. The plotting programs that use this file include an input parameter called *path* that corresponds to the directory in which **sppfnt.002** is located. Be sure to include the path name in your input data file.

### E.2 Video Devices

Input parameter *mon* selects monitor type and resolution; valid devices are listed on the following page. Note that enhanced VGA modes, i.e., modes with resolution finer than 640 columns by 480 rows, are specific to each manufacturer's video card.

<i>mon</i>	Description	Columns	Rows
4	CGA 4-Color	320	200
5	CGA Black & White	320	200
6	CGA Black & White	640	200
13	EGA 16-Color	320	200
14	EGA 16-Color	640	200
15	EGA Monochrome	640	350
16	EGA 16-Color	640	350
17	MCGA & VGA 2-Color	640	480
18	VGA 16-Color	640	480
19	MCGA & VGA 256-Color	320	200
37	Genoa VGA 16-Color	640	480
39	Genoa VGA 16-Color	720	512
40	Hercules Monochrome	720	348
41	Genoa/Orchid VGA 16-Color	800	600
45	Genoa EGA 256-Color	640	350
46	Genoa/Orchid VGA 256-Color	640	480
47	Genoa VGA 256-Color	720	512
55	Genoa/Orchid VGA 16-Color	1024	768
56	Orchid VGA 256-Color	1024	768
72	AT&T 6300 Monochrome	640	400
84	ATI VGA 16-Color	800	600
89	Genoa VGA 16-Color	720	512
91	Genoa EGA 256-Color	640	350
92	Genoa VGA 256-Color	640	480
93	Genoa VGA 256-Color	720	512
95	Genoa VGA 16-Color	1024	768
99	ATI VGA 256-Color	800	600
100	ATI VGA 256-Color	1024	768
103	ATI VGA 4-Color	1024	768
115	Genoa VGA 16-color	640	480
121	Genoa VGA 16-color	800	600
124	Genoa VGA 16-color	512	512
125	Genoa VGA 256-color	512	512
200	Everex VGA 16-Color	640	480
201	Everex VGA 16-Color	752	410
202	Everex VGA 16-Color	800	600
217	Everex EGA 4-Color	1280	350
219	Everex EGA 256-Color	640	350
220	Everex VGA 256-Color	640	400
221	Everex VGA 256-Color	512	480
296	Video-7 VGA 16-Color	752	410
297	Video-7 VGA 16-Color	720	540
298	Video-7 VGA 16-Color	800	600
299	Video-7 VGA 2-Color	1024	768
300	Video-7 VGA 4-Color	1024	768
301	Video-7 VGA 16-Color	1024	768
302	Video-7 VGA 256-Color	640	400
303	Video-7 VGA 256-Color	640	480
304	Video-7 VGA 256-Color	720	540
305	Video-7 VGA 256-Color	800	600
700	Wyse-700 Monochrome	1280	800

## E.3 Plotting Colors

Input parameters *ifore* and *iback* set foreground and background plotting colors, respectively. The standard MS-DOS color coding scheme is used to set these colors. The MS-DOS color code is summarized below, where *icolor* is the color number and 'color' is the corresponding color.

<i>icolor</i>	color	<i>icolor</i>	color
0	Black	8	Dark Gray
1	Blue	9	Light Blue
2	Green	10	Light Green
3	Cyan	11	Light Cyan
4	Red	12	Light Red
5	Magenta	13	Light Magenta
6	Brown or Yellow	14	Yellow or Light Yellow
7	White	15	Bright White

## E.4 Hardcopy Devices

Two input parameters are required for hardcopy plots, *nprin* and *mode*. The parameter *nprin* specifies the printer or plotter type. For a printer, *mode* specifies the resolution. For a plotter *mode* is the number of pens. Valid devices are as follows.

<i>nprin</i>	Printer type
0	Hewlett-Packard LaserJet Series I
1	Hewlett-Packard LaserJet Series II
2	Hewlett-Packard DeskJet
8	Epson with 8-pin printer head (older models)
24	Epson with 8-pin and 24-pin printer heads
25	Epson color dot-matrix printer
80	HPGL plotter without built-in circle drawing
90	HPGL plotter with built-in circle drawing
115	CGP-115 4-pen color plotter

Resolution for each printer and mode is given below as horizontal by vertical numbers of dots per inch.

***nprin* = 0,1,2 ... Hewlett-Packard**

<i>mode</i>	dots/in	<i>mode</i>	dots/in
0	75 x 75	2	50 x 150
1	100 x 100	3	300 x 300



**nprin = 8 ... Epson 8-pin**

<i>mode</i>	dots/in	<i>mode</i>	dots/in
0	60 x 72	4	80 x 72
1	120 x 72	5	72 x 72
2	120 x 72	6	90 x 72
3	240 x 72		

**nprin = 24,25 ... Epson 24-pin**

<i>mode</i>	dots/in	<i>mode</i>	dots/in
0	60 x 60	32	60 x 180
1	120 x 60	33	120 x 180
2	120 x 60	38	90 x 180
3	240 x 60	39	180 x 180
4	80 x 60	40	360 x 180
6	90 x 60		

# Bibliography

Abid, R. and Speziale, C. G. (1992), "Predicting Equilibrium States with Reynolds Stress Closures in Channel Flow and Homogeneous Shear Flow," ICASE Report 92-28, Univ. Space Research Assoc., Hampton, VA.

Abramowitz, M. and Stegun, I. A. (1965), *Handbook of Mathematical Functions*, Dover Publications, Inc., New York.

Ahmed, S. R., Ramm, G. and Faltin, G. (1984), "Some Salient Features of the Time-Averaged Ground Vehicle Wake," SAE Paper 840300, Society of Automotive Engineers, Warrendale, PA.

Andersen, P. S., Kays, W. M. and Moffat, R. J. (1972), "The Turbulent Boundary Layer on a Porous Plate: An Experimental Study of the Fluid Mechanics for Adverse Free-Stream Pressure Gradients," Report No. HMT-15, Dept. Mech. Eng., Stanford University, CA.

Anderson, D. A., Tannehill, J. C. and Pletcher, R. H. (1984), *Computational Fluid Dynamics and Heat Transfer*, Hemisphere Publishing, Washington.

Baldwin, B. S. and Lomax, H. (1978), "Thin-Layer Approximation and Algebraic Model for Separated Turbulent Flows," AIAA Paper 78-257, Huntsville, AL.

Baldwin, B. S. and Barth, T. J. (1990), "A One-Equation Turbulence Transport Model for High Reynolds Number Wall-Bounded Flows," NASA TM-102847.

Bardina, J., Ferziger, J. H. and Reynolds, W. C. (1983), "Improved Turbulence Models Based on Large Eddy Simulation of Homogeneous, Incompressible, Turbulent Flows," Report No. TF-19, Dept. Mech. Eng., Stanford University, CA.

Barnwell, R. W. (1992), "Nonadiabatic and Three-Dimensional Effects in Compressible Turbulent Boundary Layers," *AIAA Journal*, Vol. 30, No. 4, pp. 897-904.

Beam, R. M. and Warming, R. F. (1976), "An Implicit Finite-Difference Algorithm for Hyperbolic Systems in Conservation Law Form," *Journal of Computational Physics*, Vol. 22, pp. 87-110.

Bender, C. M. and Orszag, S. A. (1978), *Advanced Mathematical Methods for Scientists and Engineers*, McGraw-Hill, New York.

Bergé, P., Pomeau, Y. and Vidal, C. (1984), *Order within Chaos: Towards a Deterministic Approach to Turbulence*, John Wiley & Sons, New York.

Blottner, F. G. (1974), "Variable Grid Scheme Applied to Turbulent Boundary Layers," *Comput. Meth. Appl. Mech. & Eng.*, Vol. 4, No. 2, pp. 179-194.

Boussinesq, J. (1877), "Théorie de l'Écoulement Tourbillant," *Mem. Présentés par Divers Savants Acad. Sci. Inst. Fr.*, Vol. 23, pp. 46-50.

Bradbury, L. J. S. (1965), "The Structure of a Self-Preserving Turbulent Plane Jet," *Journal of Fluid Mechanics*, Vol. 23, pp. 31-64.

Bradshaw, P., Ferriss, D. H. and Atwell, N. P. (1967), "Calculation of Boundary Layer Development Using the Turbulent Energy Equation," *Journal of Fluid Mechanics*, Vol. 28, Pt. 3, pp. 593-616.

Bradshaw, P. (1969), "The Response of a Constant-Pressure Turbulent Boundary Layer to the Sudden Application of an Adverse Pressure Gradient," R. & M. Number 3575, British Aeronautical Research Council.

Bradshaw, P. (1972), "The Understanding and Prediction of Turbulent Flow," *The Aeronautical Journal*, Vol. 76, No. 739, pp. 403-418.

Bradshaw, P. (1973a), "Effects of Streamline Curvature on Turbulent Flow," AGARD-AG-169.

Bradshaw, P. (1973b), "The Strategy of Calculation Methods for Complex Turbulent Flows," Imperial College Aero. Report No. 73-05.

Bradshaw, P. (1992), "Turbulence: The Chief Outstanding Difficulty of Our Subject," Fifth Symposium on Numerical and Physical Aspects of Aerodynamic Flows, 13-15 January 1992, California State University, Long Beach, CA.

Brown, J. D. (1986), "Two Component LDV Investigation of Shock Related Turbulent Boundary Layer Separation with Increasing Three Dimensionality," PhD Thesis, U. C. Berkeley, Berkeley, CA.

Bush, W. B. and Fendell, F. E. (1972), "Asymptotic Analysis of Turbulent Channel and Boundary-Layer Flow," *Journal of Fluid Mechanics*, Vol. 56, Pt. 4, pp. 657-681.

Castro, I. P. and Bradshaw, P. (1976), "The Turbulence Structure of a Highly Curved Mixing Layer," *Journal of Fluid Mechanics*, Vol. 73, p. 265.

Cazalbou, J. B., Spalart, P. R. and Bradshaw, P. (1994), "On the Behavior of Two-Equation Models at the Edge of a Turbulent Region," *Physics of Fluids*, Vol. 6, No. 5, pp. 1797-1804.

Cebeci, T. and Smith, A. M. O. (1974), *Analysis of Turbulent Boundary Layers*, Ser. in Appl. Math. & Mech., Vol. XV, Academic Press.

Chambers, T. L. and Wilcox, D. C. (1977), "Critical Examination of Two-Equation Turbulence Closure Models for Boundary Layers," *AIAA Journal*, Vol. 15, No. 6, pp. 821-828.

Champagne, F. H., Harris, V. G. and Corrsin, S. (1970), "Experiments on Nearly Homogeneous Turbulent Shear Flow," *Journal of Fluid Mechanics*, Vol. 41, Pt. 1, pp. 81-139.

Champney, J. (1989), "Modeling of Turbulence for Compression Corner Flows and Internal Flows," AIAA Paper 89-2344, Monterey, CA.

Chapra, S. C. and Canale, R. P. (1985), *Numerical Methods for Engineers: With Personal Computer Applications*, McGraw-Hill, New York.

Chien, K.-Y. (1982), "Predictions of Channel and Boundary-Layer Flows with a Low-Reynolds-Number Turbulence Model," *AIAA Journal*, Vol. 20, No. 1, pp. 33-38.

Choi, K. S. and Lumley, J. L. (1984), "Return to Isotropy of Homogeneous Turbulence Revisited," *Turbulence and Chaotic Phenomena in Fluids*, ed. T. Tatsumi, New York: North-Holland, pp. 267-272.

Chou, P. Y. (1945), "On the Velocity Correlations and the Solution of the Equations of Turbulent Fluctuation," *Quart. Appl. Math.*, Vol. 3, p. 38.

Clark, J. A. (1968), "A Study of Incompressible Turbulent Boundary Layers in Channel Flows," Transactions of the ASME, Paper 68-FE-26.

Clark, R. A., Ferziger, J. H. and Reynolds, W. C. (1979), "Evaluation of Subgrid-Scale Models Using an Accurately Simulated Turbulent Flow," *Journal of Fluid Mechanics*, Vol. 91, pp. 1-16.

Clauser, F. H. (1956), "The Turbulent Boundary Layer", *Advances in Applied Mechanics*, Vol. IV, Academic Press, New York, pp. 1-51.

Coakley, T. J. (1983), "Turbulence Modeling Methods for the Compressible Navier-Stokes Equations," AIAA Paper 83-1693, Danvers, MA.

Coleman, G. N. and Mansour, N. N. (1991), "Simulation and Modeling of Homogeneous Compressible Turbulence under Isotropic Mean Compression," Eighth Symposium on Turbulent Shear Flows, Munich, Germany.

Coles, D. E. and Hirst, E. A. (1969), *Computation of Turbulent Boundary Layers-1968 AFOSR-IFP-Stanford Conference*, Vol. II, Stanford University, CA.

Comte-Bellot, G. (1963), "Contribution a l'Étude de la Turbulence de Conduite," PhD Thesis, University of Grenoble, France.

Comte-Bellot, G. (1965), "Ecoulement Turbulent entre Deux Parois Parallèles," Publ. Sci. Tech. Ministère de l'Air, No. 419.

Comte-Bellot, G. and Corrsin, S. (1971), "Simple Eulerian Time Correlation of Full- and Narrow-Band Velocity Signals in Grid Generated Isotropic Turbulence," *Journal of Fluid Mechanics*, Vol. 48, pp. 273-337.

Cooley, W. W. and Tukey, J. W. (1965), "An Algorithm for the Machine Calculation of Complex Fourier Series," *Math. Comp.*, Vol. 19, No. 90, pp. 297-301.

Corrsin, S. and Kistler, A. L. (1954), "The Free-Stream Boundaries of Turbulent Flows," NACA TN 3133.

Courant, R. and Hilbert, D. (1966), *Methods of Mathematical Physics*, Vol. II, Interscience Publishers, John Wiley & Sons, New York.

Courant, R., Friedrichs, K. and Lewy, H. (1967), "On the Partial Difference Equations of Mathematical Physics," *IBM Journal*, pp. 215-234.

Craft, T. J., Fu, S., Launder, B. E. and Tselepidakis, D. P. (1989), "Developments in Modeling the Turbulent Second-Moment Pressure Correlations," Report No. TFD/89/1, Mech. Eng. Dept., Manchester Institute of Science and Technology, England.

Craft, T. J. and Launder, B. E. (1992), "New Wall-Reflection Model Applied to the Turbulent Impinging Jet," *AIAA Journal*, Vol. 30, No. 12, pp. 2970-2972.

Crank, J. and Nicolson, P. (1947), "A Practical Method for Numerical Evaluation of Solutions of Partial Differential Equations of the Heat-Conduction Type," *Proceedings of the Cambridge Philosophical Society*, Vol. 43, No. 50, pp. 50-67.

Crow, S. C. (1968), "Viscoelastic Properties of Fine-Grained Incompressible Turbulence," *Journal of Fluid Mechanics*, Vol. 33, Pt. 1, pp. 1-20.

Daly, B. J. and Harlow, F. H. (1970), "Transport Equations in Turbulence," *Physics of Fluids*, Vol. 13, pp. 2634-2649.

Davidov, B. I. (1961), "On the Statistical Dynamics of an Incompressible Fluid," *Doklady AN. SSSR*, Vol. 136, p. 47.

Deardorff, J. W. (1970), "A Numerical Study of Three-Dimensional Turbulent Channel Flow at Large Reynolds Numbers," *Journal of Fluid Mechanics*, Vol. 41, Pt. 2, pp. 453-480.

Deardorff, J. W. (1973), "The Use of Subgrid Transport Equations in a Three-Dimensional Model of Atmospheric Turbulence," *ASME, Journal of Fluids Engineering*, Vol. 95, pp. 429-438.

Deissler, R. G. (1989), "On the Nature of Navier-Stokes Turbulence," NASA TM-109183.

Demuren, A. O. (1991), "Calculation of Turbulence-Driven Secondary Motion in Ducts with Arbitrary Cross Section," *AIAA Journal*, Vol. 29, No. 4, pp. 531-537.

Dhawan, S. and Narasimha, R. (1958), "Some Properties of Boundary Layer Flow During the Transition from Laminar to Turbulent Motion," *Journal of Fluid Mechanics*, Vol. 3, pp. 418-436.

Donaldson, C. duP. and Rosenbaum, H. (1968), "Calculation of the Turbulent Shear Flows Through Closure of the Reynolds Equations by Invariant Modeling," ARAP Report No. 127, Aeronautical Research Associates of Princeton, Princeton, NJ.

Donaldson, C. duP. (1972), "Construction of a Dynamic Model of the Production of Atmospheric Turbulence and the Dispersal of Atmospheric Pollutants," ARAP Report No. 175, Aeronautical Research Associates of Princeton, Princeton, NJ.

Driver, D. M. and Seegmiller, H. L. (1985), "Features of a Reattaching Turbulent Shear Layer in Divergent Channel Flow," *AIAA Journal*, Vol. 23, No. 1, pp. 163-171.

Driver, D. M. (1991), "Reynolds Shear Stress Measurements in a Separated Boundary Layer," AIAA Paper 91-1787, Honolulu, HI.

Dryden, H. L. (1959), *Aerodynamics and Jet Propulsion*, Vol. V, University Press, Princeton, NJ.

DuFort, E. C. and Frankel, S. P. (1953), "Stability Conditions in the Numerical Treatment of Parabolic Differential Equations," *Math. Tables and Other Aids to Computation*, Vol. 7, pp. 135-152.

Dutoya, D. and Michard, P. (1981), "A Program for Calculating Boundary Layers Along Compressor and Turbine Blades," *Numerical Methods in Heat Transfer*, edited by R. W. Lewis, Morgan and O. C. Zienkiewicz, John Wiley & Sons, New York.

Eaton, J. K. and Johnston, J. P. (1980), "Turbulent Flow Reattachment: An Experimental Study of the Flow and Structure Behind a Backward-Facing Step," Report No. MD-39, Dept. Mech. Eng., Stanford University, CA.

Emmons, H. W. (1954), "Shear Flow Turbulence," Proceedings of the 2<sup>nd</sup> U. S. Congress of Applied Mechanics, ASME.

Erlebacher, G., Hussaini, M. Y., Speziale, C. G. and Zang, T. A. (1987), "Toward the Large-Eddy Simulations of Compressible Turbulent Flows," ICASE Report 87-20, Univ. Space Research Assoc., Hampton, VA.

Escudier, M. P. (1966), "The Distribution of Mixing-Length in Turbulent Flows Near Walls," Imperial College, Heat Transfer Section Report TWF/TN/12.

Fage, A. and Falkner, V. M. (1932), "Note on Experiments on the Temperature and Velocity in the Wake of a Heated Cylindrical Obstacle," *Proc. Roy. Soc., Lond.*, Vol. A135, pp. 702-705.

Fan, S., Lakshminarayana, B. and Barnett, M. (1993), "A Low-Reynolds Number  $k$ - $\epsilon$  Model for Unsteady Turbulent Boundary Layer Flows," *AIAA Journal*, Vol. 31, No. 10, pp. 1777-1784.

Favre, A. (1965), "Equations des Gaz Turbulents Compressibles," *Journal de Mecanique*, Vol. 4, No. 3, pp. 361-390.

Fendell, F. E. (1972), "Singular Perturbation and Turbulent Shear Flow Near Walls," *Journal of the Astronautical Sciences*, Vol. XX, No. 3, pp. 129-165.

Fernholz, H. H. and Finlay, P. J. (1981), "A Further Compilation of Compressible Boundary Layer Data with a Survey of Turbulence Data," AGARDograph 263.

Ferziger, J. H. (1976), "Large Eddy Numerical Simulations of Turbulent Flows," AIAA Paper 76-347, San Diego, CA.

Ferziger, J. H. (1989), "Estimation and Reduction of Numerical Error," Forum on Methods of Estimating Uncertainty Limits in Fluid Flow Computations, ASME Winter Annual Meeting, San Francisco, CA.

Fisher, D. F. and Dougherty, N. S. (1982), "Transition Measurements on a  $10^\circ$  Cone at Mach Numbers from 0.5 to 2.0," NASA TP-1971.

Fu, S., Launder, B. E. and Tselepidakis, D. P. (1987), "Accommodating the Effects of High Strain Rates in Modelling the Pressure-Strain Correlation," Report No. TFD/87/5, Mech. Eng. Dept., Manchester Institute of Science and Technology, England.

Gatski, T. B. and Speziale, C. G. (1992), "On Explicit Algebraic Stress Models for Complex Turbulent Flows," ICASE Report No. 92-58, Univ. Space Research Assoc., Hampton, VA.

Germano, M., Piomelli, U., Moin, P. and Cabot, W. (1990), "A Dynamic Subgrid-Scale Eddy Viscosity Model," *Proceedings of the 1990 Summer Program*, Center for Turbulence Research, Stanford, CA.

Ghosal, S., Lund, T. S. and Moin, P. (1992), "A Dynamic Localization Method for Large Eddy Simulation of Turbulent Flows," NASA Ames, Stanford Center for Turbulence Research, Manuscript 139.

Gibson, M. M. and Launder, B. E. (1978), "Ground Effects on Pressure Fluctuations in the Atmospheric Boundary Layer," *Journal of Fluid Mechanics*, Vol. 86, Pt. 3, pp. 491-511.

Gibson, M. M. and Younis, B. A. (1986), "Calculation of Swirling Jets with a Reynolds Stress Closure," *Physics of Fluids*, Vol. 29, pp. 38-48.

Gleick, J. (1988), *Chaos: Making a New Science*, Penguin Books, New York.

Glushko, G. (1965), "Turbulent Boundary Layer on a Flat Plate in an Incompressible Fluid," *Izvestia Academy Nauk. SSSR Mekh.*, No. 4, p. 13.

Goddard, F. E. Jr. (1959), "Effect of Uniformly Distributed Roughness on Turbulent Skin-Friction Drag at Supersonic Speeds," *J. Aero/Space Sciences*, Vol. 26, No. 1, pp. 1-15, 24.

Godunov, S. K. (1959), "Finite Difference Method for Numerical Computation of Discontinuous Solutions of the Equations of Fluid Dynamics," *Matematicheskii Sbornik*, Vol. 47, No. 3, pp. 271-306.

Goldberg, U. C. (1991), "Derivation and Testing of a One-Equation Model Based on Two Time Scales," *AIAA Journal*, Vol. 29, No. 8, pp. 1337-1340.

Goldstein, S. (1938), *Modern Developments in Fluid Dynamics*, Vol. 2, p. 331, Oxford University Press, NY.

Gottlieb, D. and Orszag, S. A. (1977), "Numerical Analysis of Spectral Methods: Theory and Application," *CBMS-NSF Reg. Conf. Ser. Appl. Math.*, Vol. 26, Philadelphia: SIAM.

Grotzbach, G. (1979), "Numerical Investigation of Radial Mixing Capabilities in Strongly Buoyancy-Influenced Vertical, Turbulent Channel Flows," *Nucl. Eng. Des.*, Vol. 54, pp. 49-66.

Halleen, R. M. and Johnston, J. P. (1967), "The Influence of Rotation on Flow in a Long Rectangular Channel - An Experimental Study," Report No. MD-18, Dept. Mech. Eng., Stanford University, CA.

Han, T. (1989), "Computational Analysis of Three-Dimensional Turbulent Flow Around a Bluff Body in Ground Proximity," *AIAA Journal*, Vol. 27, No. 9, pp. 1213-1219.

Hanjalić, K. (1970), "Two-Dimensional Flow in an Axisymmetric Channel," PhD Thesis, University of London.

Hanjalić, K. and Launder, B. E. (1976), "Contribution Towards a Reynolds-Stress Closure for Low-Reynolds-Number Turbulence," *Journal of Fluid Mechanics*, Vol. 74, Pt. 4, pp. 593-610.

Hanjalić, K. and Launder, B. E. (1980), "Sensitizing the Dissipation Equation to Irrotational Strains," *ASME, Journal of Fluids Engineering*, Vol. 102, pp. 34-40.

Harlow, F. H. and Nakayama, P. I. (1968), "Transport of Turbulence Energy Decay Rate," Los Alamos Sci. Lab., University of California Report LA-3854.

Harris, V. G., Graham, J. A. H. and Corrsin, S. (1977), "Further Experiments in Nearly Homogeneous Turbulent Shear Flow," *Journal of Fluid Mechanics*, Vol. 81, p. 657.

Harris, J. E. and Blanchard, D. K. (1982), "Computer Program for Solving Laminar, Transitional, or Turbulent Compressible Boundary-Layer Equations for Two-Dimensional and Axisymmetric Flow," NASA TM-83207.

Hassid, S. and Poreh, M. (1978), "A Turbulent Energy Dissipation Model for Flows with Drag Reduction," *ASME, Journal of Fluids Engineering*, Vol. 100, pp. 107-112.

Haworth, D. C. and Pope, S. B. (1986), "A Generalized Langevin Model for Turbulent Flows," *Physics of Fluids*, Vol. 29, pp. 387-405.

Hayes, W. D. and Probstein, R. F. (1959), *Hypersonic Flow Theory*, Academic Press, p. 290.



Higuchi, H. and Rubesin, M. W. (1978), "Behavior of a Turbulent Boundary Layer Subjected to Sudden Transverse Strain," AIAA Paper 78-201, Huntsville, AL.

Hildebrand, F. B. (1976), *Advanced Calculus for Applications*, Second Edition, Prentice-Hall, Englewood Cliffs, NJ.

Hinze, J. O. (1975), *Turbulence*, Second Ed., McGraw-Hill, New York.

Hoffmann, G. H. (1975), "Improved Form of the Low-Reynolds-Number  $k$ - $\epsilon$  Turbulence Model," *Physics of Fluids*, Vol. 18, pp. 309-312.

Hopkins, E. J. and Inouye, M. (1971), "An Evaluation of Theories for Predicting Turbulent Skin Friction and Heat Transfer on Flat Plates at Supersonic and Hypersonic Mach Numbers," *AIAA Journal*, Vol. 9, No. 6, pp. 993-1003.

Horstman, C. C. (1992), "Hypersonic Shock-Wave/Turbulent-Boundary-Layer Interaction Flows," *AIAA Journal*, Vol. 30, No. 6, pp. 1480-1481.

Huang, P. G., Bradshaw, P. and Coakley, T. J. (1992), "Assessment of Closure Coefficients for Compressible-Flow Turbulence Models," NASA TM-103882.

Huang, P. G. and Coakley, T. J. (1992), "An Implicit Navier-Stokes Code for Turbulent Flow Modeling," AIAA Paper 92-547, Reno, NV.

Hung, C. M. (1976), "Development of Relaxation Turbulence Models," NASA CR-2783.

Ibbetson, A. and Tritton, D. J. (1975), "Experiments on Turbulence in Rotating Fluid," *Journal of Fluid Mechanics*, Vol. 68, Pt. 4, pp. 639-672.

Inger, G. (1986), "Incipient Separation and Similitude Properties of Swept Shock/Turbulent Boundary Layer Interactions," AIAA Paper 86-345, Reno, NV.

Jayaraman, R., Parikh, P. and Reynolds, W. C. (1982), "An Experimental Study of the Dynamics of an Unsteady Turbulent Boundary Layer," Report No. TF-18, Dept. Mech. Eng., Stanford University, CA.

Jeans, J. (1962), *An Introduction to the Kinetic Theory of Gases*, Cambridge University Press, London.

Johnson, D. A. and King, L. S. (1985), "A Mathematically Simple Turbulence Closure Model for Attached and Separated Turbulent Boundary Layers," *AIAA Journal*, Vol. 23, No. 11, pp. 1684-1692.

Johnson, D. A. (1987), "Transonic Separated Flow Predictions with an Eddy-Viscosity/Reynolds-Stress Closure Model," *AIAA Journal*, Vol. 25, No. 2, pp. 252-259.

Johnson, D. A. and Coakley, T. J. (1990), "Improvements to a Nonequilibrium Algebraic Turbulence Model," *AIAA Journal*, Vol. 28, No. 11, pp. 2000-2003.

Johnston, J. P., Halleen, R. M. and Lezius, D. K. (1972), "Effects of a Spanwise Rotation on the Structure of Two-Dimensional Fully-Developed Turbulent Channel Flow," *Journal of Fluid Mechanics*, Vol. 56, pp. 533-557.

Jones, W. P. and Launder, B. E. (1972), "The Prediction of Laminarization with a Two-Equation Model of Turbulence," *International Journal of Heat and Mass Transfer*, Vol. 15, pp. 301-314.

Keefe, L. (1990), "Connecting Coherent Structures and Strange Attractors," in *Near-Wall Turbulence - 1988 Zaric Memorial Conference*, S. J. Kline and N. H. Afgan, eds., Hemisphere, Washington.

Kevorkian, J. and Cole, J. D. (1981), *Perturbation Methods in Applied Mathematics*, Springer-Verlag, New York.

Kim, J., Kline, S. J. and Johnston, J. P. (1980), "Investigation of a Reattaching Turbulent Shear Layer: Flow Over a Backward-Facing Step," *ASME, Journal of Fluids Engineering*, Vol. 102, pp. 302-308.

Kim, J., Moin, P. and Moser, R. (1987), "Turbulence Statistics in Fully Developed Channel Flow at Low Reynolds Number," *Journal of Fluid Mechanics*, Vol. 177, pp. 133-166.

Klebanoff, P. S. (1956), "Characteristics of Turbulence in a Boundary Layer with Zero Pressure Gradient," NACA TN 3178.

Kline, S. J., Morkovin, M. V., Sovran, G. and Cockrell, D. J. (1969), *Computation of Turbulent Boundary Layers-1968 AFOSR-IFP-Stanford Conference*, Vol. I, Stanford University, CA.

Kline, S. J., Cantwell, B. J. and Lilley, G. M. (1981), *1980-81 AFOSR-HTTM-Stanford Conference on Complex Turbulent Flows*, Stanford University, CA.

Knight, D. D., Horstman, C. C., Shapey, B and Bogdanoff, S. (1987), "Structure of Supersonic Flow Past a Sharp Fin," *AIAA Journal*, Vol. 25, No. 10, pp. 1331-1337.

Knight, D. D. (1993), "Numerical Simulation of 3-D Shock Wave Turbulent Boundary-Layer Interactions," AGARD/FDP Short Course on Shock Wave/Boundary Layer Interactions in Supersonic and Hypersonic Flows, von Kármán Institute for Fluid Dynamics, Brussels, Belgium, (May 24-28, 1993).

Kolmogorov, A. N. (1941), "Local Structure of Turbulence in Incompressible Viscous Fluid for Very Large Reynolds Number," *Doklady AN. SSSR*, Vol. 30, pp. 299-303.

Kolmogorov, A. N. (1942), "Equations of Turbulent Motion of an Incompressible Fluid," *Izvestia Academy of Sciences, USSR; Physics*, Vol. 6, Nos. 1 and 2, pp. 56-58.

Lai, Y. G., So, R. M. C., Anwer, M. and Hwang, B. C. (1991), "Calculations of a Curved-Pipe Flow Using Reynolds Stress Closure," *Journal of Mechanical Engineering Science*, Vol. 205, Part C, pp. 231-244.

Lakshminarayana, B. (1986), "Turbulence Modeling for Complex Shear Flows," *AIAA Journal*, Vol. 24, No. 12, pp. 1900-1917.

Lam, C. K. G. and Bremhorst, K. A. (1981), "Modified Form of  $k$ - $\epsilon$  Model for Predicting Wall Turbulence," *ASME, Journal of Fluids Engineering*, Vol. 103, pp. 456-460.

Landahl, M. T. and Mollo-Christensen, E. (1992), *Turbulence and Random Processes in Fluid Mechanics*, Second Ed., Cambridge University Press, New York.

Laufer, J. (1950), "Some Recent Measurements in a Two-Dimensional Turbulent Channel," *Journal of the Aeronautical Sciences*, Vol. 17, pp. 277-287.

Laufer, J. (1951), "Investigation of Turbulent Flow in a Two Dimensional Channel," NACA 1053.

Laufer, J. (1952), "The Structure of Turbulence in Fully Developed Pipe Flow," NACA 1174.

Launder, B. E. and Spalding, D. B. (1972), *Mathematical Models of Turbulence*, Academic Press, London.

Launder, B. E. and Sharma, B. I. (1974), "Application of the Energy Dissipation Model of Turbulence to the Calculation of Flow Near a Spinning Disc," *Letters in Heat and Mass Transfer*, Vol. 1, No. 2, pp. 131-138.

Launder, B. E., Reece, G. J. and Rodi, W. (1975), "Progress in the Development of a Reynolds-Stress Turbulence Closure," *Journal of Fluid Mechanics*, Vol. 68, Pt. 3, pp. 537-566.

Launder, B. E., Priddin, C. H. and Sharma, B. I. (1977), "The Calculation of Turbulent Boundary Layers on Spinning and Curved Surfaces," *ASME, Journal of Fluids Engineering*, Vol. 99, p. 231.

Launder, B. E. and Morse, A. (1979), "Numerical Prediction of Axisymmetric Free Shear Flows with a Second-Order Reynolds Stress Closure," *Turbulent Shear Flows I*, edited by F. Durst, B. E. Launder, F. W. Schmidt and J. Whitelaw, Springer-Verlag, Berlin.

Launder, B. E. (Ed.) (1992), *Fifth Biennial Colloquium on Computational Fluid Dynamics*, Manchester Institute of Science and Technology, England.

Lax, P. D. and Wendroff, B. (1960), "Systems of Conservation Laws," *Communications on Pure and Applied Mathematics*, Vol. 13, pp. 217-237.

Leonard, A. (1974), "Energy Cascade in Large-Eddy Simulations of Turbulent Fluid Flows," *Advances in Geophysics*, Vol. 18A, pp. 237-248.

Liepmann, H. W. and Laufer, J. (1947), "Investigations of Free Turbulent Mixing," NACA TN 1257.

Lilly, D. K. (1965), "On the Computational Stability of Numerical Solutions of Time-Dependent Non-Linear Geophysical Fluid Dynamics Problems," *Monthly Weather Review*, U. S. Weather Bureau, Vol. 93, No. 1, pp. 11-26.

Lilly, D. K. (1966), "On the Application of the Eddy Viscosity Concept in the Inertial Subrange of Turbulence," NCAR Manuscript 123.

Lumley, J. L. (1970), "Toward a Turbulent Constitutive Equation," *Journal of Fluid Mechanics*, Vol. 41, pp. 413-434.

Lumley, J. L. (1972), "A Model for Computation of Stratified Turbulent Flows," Int. Symposium on Stratified Flow, Novosibirsk.

Lumley, J. L. (1978), "Computational Modeling of Turbulent Flows," *Adv. Appl. Mech.*, Vol. 18, pp. 123-176.

MacCormack, R. W. (1969), "The Effect of Viscosity in Hypervelocity Impact Cratering," AIAA Paper 69-354, Cincinnati, OH.

MacCormack, R. W. (1985), "Current Status of Numerical Solutions of the Navier-Stokes Equations," AIAA Paper 85-32, Reno, NV.

Maise, G. and McDonald, H. (1967), "Mixing Length and Kinematic Eddy Viscosity in a Compressible Boundary Layer," AIAA Paper 67-199, New York, NY.

Mansour, N. N., Kim, J. and Moin, P. (1988), "Reynolds Stress and Dissipation Rate Budgets in Turbulent Channel Flow," *Journal of Fluid Mechanics*, Vol. 194, pp. 15-44.

Marshall, T. A. and Dolling, D. S. (1992), "Computation of Turbulent, Separated, Unswept Compression Ramp Interactions," *AIAA Journal*, Vol. 30, No. 8, pp. 2056-2065.

Mellor, G. L. and Herring, H. J. (1973), "A Survey of Mean Turbulent Field Closure Models," *AIAA Journal*, Vol. 11, No. 5, pp. 590-599.

Menter, F. R. (1992a), "Influence of Freestream Values on  $k-\omega$  Turbulence Model Predictions," *AIAA Journal*, Vol. 30, No. 6, pp. 1657-1659.

Menter, F. R. (1992b), "Performance of Popular Turbulence Models for Attached and Separated Adverse Pressure Gradient Flows," *AIAA Journal*, Vol. 30, No. 8, pp. 2066-2072.

Menter, F. R. (1992c), "Improved Two-Equation  $k-\omega$  Turbulence Models for Aerodynamic Flows," NASA TM-103975.

Meroney, R. N. and Bradshaw, P. (1975), "Turbulent Boundary-Layer Growth Over a Longitudinally Curved Surface," *AIAA Journal*, Vol. 13, No. 11, pp. 1448-1453.

Minkowycz, W. J., Sparrow, E. M., Schneider, G. E. and Pletcher, R. H. (1988), *Handbook of Numerical Heat Transfer*, Wiley, New York.

Morkovin, M. V. (1962), "Effects of Compressibility on Turbulent Flow," *The Mechanics of Turbulence*, A. Favre, Ed., Gordon and Breach, p. 367.

- Morris, P. J. (1984), "Modeling the Pressure Redistribution Terms," *Physics of Fluids*, Vol. 27, No. 7, pp. 1620-1623.
- Moser, R. D. and Moin, P. (1984), "Direct Numerical Simulation of Curved Turbulent Channel Flow," NASA TM-85974.
- Myong, H. K. and Kasagi, N. (1990), "A New Approach to the Improvement of  $k$ - $\epsilon$  Turbulence Model for Wall-Bounded Shear Flows," *JSME International Journal*, Vol. 33, pp. 63-72.
- Narayanswami, N., Horstman, C. C. and Knight, D. D. (1993), "Computation of Crossing Shock/Turbulent Boundary Layer Interaction at Mach 8.3," *AIAA Journal*, Vol. 31, No. 8, pp. 1369-1376.
- Nee, V. W. and Kovasznay, L. S. G. (1968), "The Calculation of the Incompressible Turbulent Boundary Layer by a Simple Theory," *Physics of Fluids*, Vol. 12, p. 473.
- Ng, K. H. and Spalding, D. B. (1972), "Some Applications of a Model of Turbulence to Boundary Layers Near Walls," *Physics of Fluids*, Vol. 15, No. 1, pp. 20-30.
- Oh, Y. H. (1974), "Analysis of Two-Dimensional Free Turbulent Mixing," AIAA Paper 74-594, Palo Alto, CA.
- Orszag, S. A. (1972), "Comparison of Pseudo-Spectral and Spectral Approximation," *Stud. Appl. Math.*, Vol. 51, pp. 253-259.
- Papamoschou, D. and Roshko, A. (1988), "The Compressible Turbulent Shear Layer - An Experimental Study," *Journal of Fluid Mechanics*, Vol. 197, p. 453.
- Patel, V. C., Rodi, W. and Scheuerer, G. (1985), "Turbulence Models for Near-Wall and Low Reynolds Number Flows: A Review," *AIAA Journal*, Vol. 23, No. 9, pp. 1308-1319.
- Patterson, G. S. and Orszag, S. A. (1971), "Spectral Calculations of Isotropic Turbulence: Efficient Removal of Aliasing Interactions," *Physics of Fluids*, Vol. 14, pp. 2538-2541.
- Peaceman, D. W. and Rachford, H. H., Jr. (1955), "The Numerical Solution of Parabolic and Elliptic Differential Equations," *J. Soc. Indust. Applied Mathematics*, Vol. 3, No. 1, pp. 28-41.
- Peyret, R. and Taylor, T. D. (1983), *Computational Methods for Fluid Flow*, Springer-Verlag, New York.
- Pope, S. B. (1978), "An Explanation of the Turbulent Round-Jet/Plane-Jet Anomaly," *AIAA Journal*, Vol. 16, No. 3, pp. 279-281.
- Prandtl, L. (1925), "Über die ausgebildete Turbulenz," *ZAMM*, Vol. 5, pp. 136-139.
- Prandtl, L. (1945), "Über ein neues Formelsystem für die ausgebildete Turbulenz," *Nachr. Akad. Wiss. Göttingen, Math-Phys. Kl.* 1945, pp. 6-19.

Press, W. H., Flannery, B. P., Teukolsky, S. A. and Vetterling, W. T. (1987), *Numerical Recipes: The Art of Scientific Computing*, Cambridge University Press, Cambridge.

Price, J. M. and Harris, J. E. (1972), "Computer Program for Solving Compressible Nonsimilar-Boundary-Layer Equations for Laminar, Transitional or Turbulent Flows of a Perfect Gas," NASA TM X-2458.

Rastogi, A. K. and Rodi, W. (1978), "Calculation of General Three-Dimensional Turbulent Boundary Layers," *AIAA Journal*, Vol. 16, No. 2, pp. 151-159.

Reda, D. C., Ketter, F. C. Jr. and Fan, C. (1974), "Compressible Turbulent Skin Friction on Rough and Rough/Wavy Walls in Adiabatic Flow," AIAA Paper 74-574, Palo Alto, CA.

Reynolds, O. (1874), "On the Extent and Action of the Heating Surface for Steam Boilers," *Proc. Manchester Lit. Phil. Soc.*, Vol. 14, pp. 7-12.

Reynolds, O. (1895), "On the Dynamical Theory of Incompressible Viscous Fluids and the Determination of the Criterion," *Philosophical Transactions of the Royal Society of London, Series A*, Vol. 186, p. 123.

Reynolds, W. C. (1970), "Computation of Turbulent Flows-State of the Art," Report No. MD-27, Dept. Mech. Eng., Stanford University, CA.

Reynolds, W. C. (1976), "Computation of Turbulent Flows," *Annual Review of Fluid Mechanics*, Vol. 8, pp. 183-208.

Reynolds, W. C. (1987), "Fundamentals of Turbulence for Turbulence Modeling and Simulation," In Lecture Notes for von Kármán Institute, AGARD Lecture Series No. 86, pp. 1-66, New York: NATO.

Roache, P. J. (1976), *Computational Fluid Dynamics*, Hermosa Publishers, Albuquerque, NM.

Roache, P. J. (1990), "Need for Control of Numerical Accuracy," *Journal of Spacecraft and Rockets*, Vol. 27, No. 2, pp. 98-102.

Roache, P. J. and Salari, K. (1990), "Weakly Compressible Navier-Stokes Solutions with an Implicit Approximate Factorization Code," AIAA Paper 90-235, Reno, NV.

Rodi, W. and Spalding, D. B. (1970), "A Two-Parameter Model of Turbulence and its Application to Free Jets," *Wärme und Stoffübertragung*, Vol. 3, p. 85.

Rodi, W. (1976), "A New Algebraic Relation for Calculating Reynolds Stresses," *ZAMM*, Vol. 56, p. 219.

Rodi, W. (1981), "Progress in Turbulence Modeling for Incompressible Flows," AIAA Paper 81-45, St. Louis, MO.

Rodi, W. and Scheuerer, G. (1986), "Scrutinizing the  $k-\epsilon$  Turbulence Model Under Adverse Pressure Gradient Conditions," *ASME, Journal of Fluids Engineering*, Vol. 108, pp. 174-179.

Rodi, W. (1991), "Experience with Two-Layer Models Combining the  $k$ - $\epsilon$  Model with a One-Equation Model Near the Wall," AIAA Paper 91-216, Reno, NV.

Roe, P. L. (1981), "Approximate Riemann Solvers, Parameter Vectors, and Difference Schemes," *Journal of Computational Physics*, Vol. 43, pp. 357-372.

Rogallo, R. S. and Moin, P. (1984), "Numerical Simulation of Turbulent Flows," *Annual Review of Fluid Mechanics*, Vol. 16, pp. 99-137.

Rotta, J. C. (1951), "Statistische Theorie nichthomogener Turbulenz," *Zeitschrift für Physik*, Vol. 129, pp. 547-572.

Rotta, J. C. (1962), "Turbulent Boundary Layers in Incompressible Flow," *Progress in Aerospace Sciences*, Vol. 2, p. 1.

Rotta, J. C. (1968), "Über eine Methode zur Berechnung turbulenter Scherströmungen," Aerodynamische Versuchsanstalt Göttingen, Rep. 69 A 14.

Rubel, A. and Melnik, R. E. (1984), "Jet, Wake and Wall Jet Solutions Using a  $k$ - $\epsilon$  Turbulence Model," AIAA Paper 84-1523, Snowmass, CO.

Rubel, A. (1985), "On the Vortex Stretching Modification of the  $k$ - $\epsilon$  Turbulence Model: Radial Jets," *AIAA Journal*, Vol. 23, No. 7, pp. 1129-1130.

Rubesin, M. W. (1989), "Turbulence Modeling for Aerodynamic Flows," AIAA Paper 89-606, Reno, NV.

Rubesin, M. W. (1990), "Extra Compressibility Terms for Favre Averaged Two-Equation Models of Inhomogeneous Turbulent Flows," NASA CR-177556.

Saffman, P. G. (1970), "A Model for Inhomogeneous Turbulent Flow," *Proc. Roy. Soc., Lond.*, Vol. A317, pp. 417-433.

Saffman, P. G. and Wilcox, D. C. (1974), "Turbulence-Model Predictions for Turbulent Boundary Layers," *AIAA Journal*, Vol. 12, No. 4, pp. 541-546.

Saffman, P. G. (1976), "Development of a Complete Model for the Calculation of Turbulent Shear Flows," April 1976 Symposium on Turbulence and Dynamical Systems, Duke Univ., Durham, NC.

Sandham, N. D. and Kleiser, L. (1992), "The Late Stages of Transition to Turbulence in Channel Flow," *Journal of Fluid Mechanics*, Vol. 245, p. 319.

Sarkar, S., Erlebacher, G., Hussaini, M. Y. and Kreiss, H. O. (1989), "The Analysis and Modeling of Dilatational Terms in Compressible Turbulence," ICASE Report 89-79, Univ. Space Research Assoc., Hampton, VA.

Sarkar, S. and Speziale, C. G. (1990), "A Simple Nonlinear Model for the Return to Isotropy in Turbulence," *Physics of Fluids A*, Vol. 2, pp. 84-93.

Sarkar, S., Erlebacher, G. and Hussaini, M. Y. (1991), "Compressible and Homogeneous Shear — Simulation and Modeling," 8<sup>th</sup> Symposium on Turbulent Shear Flows, Munich, Paper No./ 21-2.

Schlichting, H. (1979), *Boundary Layer Theory*, Seventh Ed., McGraw-Hill, New York.

Schubauer, G. B. and Skramstad, H. K. (1948), "Laminar-Boundary-Layer Oscillations and Transition on a Flat Plate," NACA 909.

Schumann, U. (1975), "Subgrid Scale Model for Finite Difference Simulations of Turbulent Flows in Plane Channels and Annuli," *Journal of Computational Physics*, Vol. 18, pp. 376-404.

Settles, G. S., Vas, I. E. and Bogdonoff, S. M. (1976), "Details of a Shock Separated Turbulent Boundary Layer at a Compression Corner," *AIAA Journal*, Vol. 14, No. 12, pp. 1709-1715.

Shaanan, S., Ferziger, J. H. and Reynolds, W. C. (1975), "Numerical Simulation of Turbulence in the Presence of Shear," Report No. TF-6, Dept. Mech. Eng., Stanford University, CA.

Shang, J. S. and Hankey, W. L. (1975), "Numerical Solution of the Navier Stokes Equations for Compression Ramp," AIAA Paper 75-4, Pasadena, CA.

Shih, T. H. and Lumley, J. L. (1985), "Modeling of Pressure Correlation Terms in Reynolds Stress and Scalar Flux Equations," Report No. FDA-85-3, Cornell University, Ithaca, NY.

Shih, T. H., Mansour, N. and Chen, J. Y. (1987), "Reynolds Stress Models of Homogeneous Turbulence," *Studying Turbulence Using Numerical Simulation Databases*, NASA Ames/Stanford CTR-S87, p. 191.

Shih, T. H. and Hsu, A. T. (1991), "An Improved  $k-\epsilon$  Model for Near-Wall Turbulence," AIAA Paper 91-611, Reno, NV.

Simpson, R. L. and Wallace, D. B. (1975), "Laminar-turbulent Boundary Layers: Experiments on Sink Flows," Project SQUID, Tech. Rept. SMU-1-PU.

Smagorinsky, J. (1963), "General Circulation Experiments with the Primitive Equations. I. The Basic Experiment," *Mon. Weather Rev.*, Vol. 91, pp. 99-164.

Smith, A. M. O. and Cebeci, T. (1967), "Numerical Solution of the Turbulent Boundary-Layer Equations," Douglas Aircraft Division Report DAC 33735.

Smith, B. R. (1990), "The  $k-k\ell$  Turbulence and Wall Layer Model for Compressible Flows," AIAA Paper 90-1483, Seattle, WA.



So, R. M. C. and Mellor, G. L. (1972), "An Experimental Investigation of Turbulent Boundary Layers Along Curved Surfaces," NASA CR-1940.

So, R. M. C. and Mellor, G. L. (1978), "Turbulent Boundary Layers with Large Streamline Curvature Effects," *ZAMP*, Vol. 29, pp. 54-74.

So, R. M. C., Lai, Y. G., Hwang, B. C. and Yoo, G. J. (1988), "Low Reynolds Number Modeling of Flows Over a Backward Facing Step," *ZAMP*, Vol. 39, pp. 13-27.

So, R. M. C., Lai, Y. G., Zhang, H. S. and Hwang, B. C. (1991), "Second-Order Near-Wall Turbulence Closures: A Review," *AIAA Journal*, Vol. 29, No. 11, pp. 1819-1835.

Spalart, P. R. (1986), "Numerical Study of Sink-Flow Boundary Layers," *Journal of Fluid Mechanics*, Vol. 172, pp. 307-328.

Spalart, P. R. (1988), "Direct Simulation of a Turbulent Boundary Layer up to  $Re_\theta = 1400$ ," *Journal of Fluid Mechanics*, Vol. 187, pp. 61-98.

Spalart, P. R. (1989), "Direct Numerical Study of Leading-Edge Contamination," AGARD CP 438.

Spalart, P. R. and Allmaras, S. R. (1992), "A One-Equation Turbulence Model for Aerodynamic Flows," AIAA Paper 92-439, Reno, NV.

Speziale, C. G. (1985), "Modeling the Pressure-Gradient-Velocity Correlation of Turbulence," *Physics of Fluids*, Vol. 28, pp. 69-71.

Speziale, C. G. (1987a), "Second-Order Closure Models for Rotating Turbulent Flows," *Q. Appl. Math.*, Vol. 45, pp. 721-733.

Speziale, C. G. (1987b), "On Nonlinear  $k-\ell$  and  $k-\epsilon$  Models of Turbulence," *Journal of Fluid Mechanics*, Vol. 178, pp. 459-475.

Speziale, C. G., Abid, R. and Anderson, E. C. (1990), "A Critical Evaluation of Two-Equation Models for Near Wall Turbulence," AIAA Paper 90-1481, Seattle, WA.

Speziale, C. G. (1991), "Analytical Methods for the Development of Reynolds-Stress Closures in Turbulence," *Annual Review of Fluid Mechanics*, Vol. 23, pp. 107-157.

Speziale, C. G., Sarkar, S. and Gatski, T. B. (1991), "Modeling the Pressure-Strain Correlation of Turbulence," *Journal of Fluid Mechanics*, Vol. 227, pp. 245-272.

Steger, J. and Warming, R. F. (1979), "Flux Vector Splitting of the Inviscid Gasdynamics Equations with Application to Finite Difference Methods," NASA TM-78605.

Stewartson, K. (1981), "Some Recent Studies in Triple-Deck Theory," in *Numerical and Physical Aspects of Aerodynamic Flows*, T. Cebeci, ed., Springer-Verlag, p. 142.

Tanaka, T. and Tanaka, E. (1976), "Experimental Study of a Radial Turbulent Jet," *Bulletin of the JSME*, Vol. 19, pp. 792-799.

Tavoularis, S. and Corrsin, S. (1981), "Experiments in Nearly Homogeneous Turbulent Shear Flow with Uniform Mean Temperature Gradient. Part I," *Journal of Fluid Mechanics*, Vol. 104, pp. 311-347.

Tavoularis, S. and Karnik, U. (1989), "Further Experiments on the Evolution of Turbulent Stresses and Scales in Uniformly Sheared Turbulence," *Journal of Fluid Mechanics*, Vol. 204, p. 457.

Taylor, G. I. (1935), "Statistical Theory of Turbulence," *Proc. Roy. Soc., Lond.*, Vol. A151, p. 421.

Tennekes, H. and Lumley, J. L. (1983), *A First Course in Turbulence*, MIT Press, Cambridge, MA.

Thangam, S. and Speziale, C. G. (1992), "Turbulent Flow Past a Backward Facing Step: A Critical Evaluation of Two-Equation Models," *AIAA Journal*, Vol. 30, No. 5, pp. 1314-1320.

Thomann, H. (1968), "Effect of Streamwise Wall Curvature on Heat Transfer in a Turbulent Boundary Layer," *Journal of Fluid Mechanics*, Vol. 33, pp. 283-292.

Townsend, A. A. (1956), "The Uniform Distortion of Homogeneous Turbulence," *Q. J. Mech. Appl. Math.*, Vol. 7, p. 104.

Townsend, A. A. (1976), *The Structure of Turbulent Shear Flow*, Second Ed., Cambridge University Press, Cambridge.

Tucker, H. J. and Reynolds, A. J. (1968), "The Distortion of Turbulence by Irrotational Plane Strain," *Journal of Fluid Mechanics*, Vol. 32, Pt. 4, pp. 657-673.

Uberoi, M. S. (1956), "Effect of Wind Tunnel Contraction on Free Stream Turbulence," *Journal of the Aeronautical Sciences*, p. 754.

Van Driest, E. R. (1951), "Turbulent Boundary Layer in Compressible Fluids," *Journal of the Aeronautical Sciences*, Vol. 18, pp. 145-160, 216.

Van Driest, E. R. (1956), "On Turbulent Flow Near a Wall," *Journal of the Aeronautical Sciences*, Vol. 23, p. 1007.

Van Dyke, M. D. (1964), *Perturbation Methods in Fluid Mechanics*, Academic Press.

Van Leer, B. (1982), "Flux-Vector Splitting for the Euler Equations," ICASE Report 82-30, Univ. Space Research Assoc., Hampton, VA.

Viegas, J. R. and Horstman, C. C. (1979), "Comparison of Multi-equation Turbulence Models for Several Shock Boundary-Layer Interaction Flows," *AIAA Journal*, Vol. 17, No. 8, pp. 811-820.

Viegas, J. R., Rubesin, M. W. and Horstman, C. C. (1985), "On the Use of Wall Functions as Boundary Conditions for Two-Dimensional Separated Compressible Flows," AIAA Paper 85-180, Reno, NV.

Vollmers, H. and Rotta, J. C. (1977), "Similar Solutions of the Mean Velocity, Turbulent Energy and Length Scale Equation," *AIAA Journal*, Vol. 15, No. 5, pp. 714-720.

von Kármán, T. (1930), "Mechanische Ähnlichkeit und Turbulenz," *Proc. Int. Congr. Appl. Mech.*, 3<sup>rd</sup>, Stockholm, Part 1, pp. 85-105.

von Kármán, T. (1934), "Some Aspects of the Turbulence Problem," *Proc. Int. Congr. Appl. Mech.*, 4<sup>th</sup>, Cambridge, p. 54.

Weinstock, J. (1981), "Theory of the Pressure-Strain Rate Correlation for Reynolds Stress Turbulence Closures," *Journal of Fluid Mechanics*, Vol. 105, pp. 369-396.

Wigeland, R. A. and Nagib, H. M. (1978), "Grid-Generated Turbulence With and Without Rotation About the Streamwise Direction," Fluids and Heat Transfer Report R78-1, Illinois Institute of Technology, Chicago, IL.

Wilcox, D. C. and Alber, I. E. (1972), "A Turbulence Model for High Speed Flows," *Proc. of the 1972 Heat Trans. & Fluid Mech. Inst.*, Stanford Univ. Press, pp. 231-252.

Wilcox, D. C. (1974), "Numerical Study of Separated Turbulent Flows," AIAA Paper 74-584, Palo Alto, CA.

Wilcox, D. C. and Chambers, T. L. (1975), "Further Refinement of the Turbulence-Model Transition-Prediction Technique," DCW Industries Report DCW-R-03-02, La Cañada, CA.

Wilcox, D. C. and Traci, R. M. (1976), "A Complete Model of Turbulence," AIAA Paper 76-351, San Diego, CA.

Wilcox, D. C. and Chambers, T. L. (1977), "Streamline Curvature Effects on Turbulent Boundary Layers," *AIAA Journal*, Vol. 15, No. 4, pp. 574-580.

Wilcox, D. C. (1977), "A Model for Transitional Flows," AIAA Paper 77-126, Los Angeles, CA.

Wilcox, D. C. and Rubesin, M. W. (1980), "Progress in Turbulence Modeling for Complex Flow Fields Including Effects of Compressibility," NASA TP-1517.

Wilcox, D. C. (1981a), "Alternative to the  $e^9$  Procedure for Predicting Boundary-Layer Transition," *AIAA Journal*, Vol. 19, No. 1, pp. 56-64.

Wilcox, D. C. (1981b), "Algorithm for Rapid Integration of Turbulence Model Equations on Parabolic Regions," *AIAA Journal*, Vol. 19, No. 2, pp. 248-251.

Wilcox, D. C. (1988a), "Reassessment of the Scale Determining Equation for Advanced Turbulence Models," *AIAA Journal*, Vol. 26, No. 11, pp. 1299-1310.

Wilcox, D. C. (1988b), "Multiscale Model for Turbulent Flows," *AIAA Journal*, Vol. 26, No. 11, pp. 1311-1320.

Wilcox, D. C. (1989), "Wall Matching, A Rational Alternative to Wall Functions," AIAA Paper 89-611, Reno, NV.

Wilcox, D. C. (1990), "Supersonic Compression-Corner Applications of a Multiscale Model for Turbulent Flows," *AIAA Journal*, Vol. 28, No. 7, pp. 1194-1198.

Wilcox, D. C. (1991), "Progress in Hypersonic Turbulence Modeling," AIAA Paper 91-1785, Honolulu, HI.

Wilcox, D. C. (1992a), "The Remarkable Ability of Turbulence Model Equations to Describe Transition," Fifth Symposium on Numerical and Physical Aspects of Aerodynamic Flows, 13-15 January 1992, California State University, Long Beach, CA.

Wilcox, D. C. (1992b), "Dilatation-Dissipation Corrections for Advanced Turbulence Models," *AIAA Journal*, Vol. 30, No. 11, pp. 2639-2646.

Witze, P. O. and Dwyer, H. A. (1976), "The Turbulent Radial Jet," *Journal of Fluid Mechanics*, Vol. 75, pp. 401-417.

Wolfshtein, M. (1967), "Convection Processes in Turbulent Impinging Jets," Imperial College, Heat Transfer Section Report SF/R/2.

Wynanski, I. and Fiedler, H. E. (1968), "Some Measurements in the Self-Preserving Jet," Boeing Scientific Research Labs, Flight Science Laboratory, Document D1-82-0712.

Yang, K.-S. and Ferziger, J. H. (1993), "Large-Eddy Simulation of Turbulent Flow with a Surface-Mounted Two-Dimensional Obstacle Using a Dynamic Subgrid-Scale Model," AIAA Paper 93-542, Reno, NV.

Yang, Z. and Shih, T.-H. (1993), "A New Time Scale Based  $k$ - $\epsilon$  Model for Near Wall Turbulence," *AIAA Journal*, Vol. 31, No. 7, pp. 1191-1198.

Zeierman, S. and Wolfshtein, M. (1986), "Turbulent Time Scale for Turbulent-Flow Calculations," *AIAA Journal*, Vol. 24, No. 10, pp. 1606-1610.

Zeman, O. (1990), "Dilatational Dissipation: The Concept and Application in Modeling Compressible Mixing Layers," *Physics of Fluids A*, Vol. 2, No. 2, pp. 178-188.

Zeman, O. (1991), "The Role of Pressure-Dilatation Correlation in Rapidly Compressed Turbulence and in Boundary Layers," NASA Ames, Stanford Center for Turbulence Research Annual Research Briefs, p. 105.

Zhang, H. S., So, R. M. C., Speziale, C. G. and Lai, Y. G. (1992), "A Near-Wall Two-Equation Model for Compressible Turbulent Flows," AIAA Paper 92-442, Reno, NV.

# Index

- Algebraic models, 23-64
  - Baldwin-Lomax, 8, 52-53, 53ff., 78, 81, 133, 136, 160, 195, 197, 207, 209, 352, 365, 368
  - Cebeci-Smith, 8, 30, 50-51, 53ff., 78, 133, 136, 195, 197, 212, 256f., 352, 365, 368
  - Prandtl eddy viscosity, 31, 48, 53, 69
  - Prandtl mixing length, 2, 6, 8, 23, 27-44, 47, 77, 95, 100, 352, 354-359
- Algebraic Stress Model, 221-223, 233, 243, 266
- Aliasing, 319
- ASM (*see Algebraic Stress Model*)
- Asymptotic:
  - consistency, 73, 133, 138-146, 150-153, 247, 259
  - expansion (*defined*), 338
  - sequence (*defined*), 338
- Autocorrelation, 91, 316, 329
- Averaging:
  - ensemble, 11-12
  - Favre, 172-174
  - phase, 14, 20
  - Reynolds, 11-14
  - spatial, 11-12
  - time, 11
- Backscatter, 327
- Backward-facing step, 161-163, 221, 261-263, 266, 321, 328
- Boundary-layer applications:
  - compressible:
    - flat-plate, 81, 195-198
    - nonadiabatic, 201-202, 255-256
    - rough-wall, 201-203
    - separated, 203-209, 263-266
    - variable-pressure, 198-201
- Boundary-layer applications:
  - incompressible:
    - curved-wall, 215-217, 253-255
    - flat-plate, 59, 81, 133-136, 142, 253
    - mass transfer, 131-132, 136-138
    - rough-wall, 128-130
    - separated, 61-64, 66-68, 81-82, 160
    - spinning-cylinder, 256-257
    - transitional, 155-159
    - unsteady, 256-261
    - variable-pressure, 59-61, 66-67, 78, 81-82, 136, 142-146, 253
- Boussinesq approximation (*defined*), 23
- Butterfly effect, 329
- Cascading, 4-5, 314, 316, 320, 327
- CFL condition (*defined*), 293
- CFL number (*defined*), 293
- Channel flow, 53-59, 94, 132-134, 154-156, 248-250, 364-370
  - rotating, 249
  - skin friction formula, 56
- Clauser defect law, 48, 105, 111
- Common part, 106, 345
- Complete model, 7, 73, 83, 99, 163
- Completely-rough surface, 129-130
- Convective Mach number, 186
- Convergence:
  - grid, 304-305
  - iteration, 303-304
- Correlation (*defined*), 15
  - auto, (*see Autocorrelation*)
  - single-point, 90, 227
  - two-point, 90, 227
- Cross-term stress, 325
- Curved-wall flow:
  - (*see Boundary-layer applications*)
- Defect layer, 44-46, 48, 110-121, 127, 142, 375

- Delta formulation, 298
- Displacement thickness (*defined*), 197
- Dissipating eddies, 4, 85, 89, 146, 233, 314, 318, 320, 323
- Dissipation (*defined*), 75
  - dilatation, 184
  - Favre-averaged, 179
  - incompressible, 74
  - solenoidal, 184
  - tensor, 224
- Distinguished limit, 343
- Drastic surgery, 75, 89, 90, 231, 233
- Dynamic SGS model, 327
- Dynamical system, 328-330
  
- Echo effect (*see Pressure-echo effect*)
- Eddy shock, 183, 185
- Eddy turnover time, 315, 320
- Energy-bearing eddies, 86, 89, 233, 238, 314, 316
- Energy spectral density, 316
- Enstrophy, 86
- Entrainment, 100, 281, 284
- Equilibrium parameter (*defined*), 107
- Equilibrium turbulence, 29-30, 63, 77
- Ergodic hypothesis, 12
- Escudier defect law, 48
  
- Far wake, 32-38, 95ff., 242, 279, 355-356
  - spreading rate (*defined*), 99
- Fast Fourier Transform (FFT), 320
- Filter, 323-325
  - function, 324
  - Gaussian, 324
  - volume-average box, 323
  - width, 323
- Flux Jacobian matrix, 298
- Fourier's law, 175
- Friction velocity (*defined*), 46, 190
  
- Gradient-diffusion approximation, 76
- Grid insensitivity:
  - (*see Convergence, grid*)
  
- Half-equation models, 65-67
  - Hung, 64, 66
  - Johnson-King, 65-67, 78, 160
  - Shang-Hankey, 63
- Heat-flux vector:
  - laminar, (*see Fourier's law*)
  - turbulent, 181
- Heat transfer, 63-64, 158, 172, 182, 195, 197-198, 200-201, 204-205, 207-210, 215, 321-322, 328
- Homogeneous turbulence, 12, 184, 218, 235-242
  - anisotropic, 236
  - isotropic, 93, 235, 326
  - rotating, 218, 234, 242
  - sheared, 235, 240
  - strained, 235, 240, 321
- Hypothesis of local isotropy, 224, 233, 314
  
- Incomplete model, 6, 23, 37, 67, 68, 73, 163
- Inertial subrange, 316
- Inhomogeneous turbulence, 12, 184, 227
- Inner expansion (*defined*), 342
- Integral scale:
  - length, 90, 314
  - time, 91
- Intermittency, 49
- Invariant modeling, 224
  
- Jet:
  - plane, 41-44, 95ff., 242, 359-360
  - radial, 103, 359-360
  - round, 41-44, 95ff., 242, 359-360
  - spreading rate (*defined*), 99
  
- Kármán's constant (*defined*), 47
- Klebanoff intermittency function, 49-52
- Knudsen number (*defined*), 27
- Kolmogorov -5/3 law, 316
- Kolmogorov scales (*defined*), 314
- Kurtosis, 186
  
- Law of the wake, 117
- Law of the wall (*defined*):
  - classical, 47
  - compressible, 189-195
  - curved-wall, 217
  - with suction, 71
- Leonard stress, 325
- Levy-Lees variables, 429
- Locally homogeneous, 227
- Log layer, 44-46, 48, 51, 93-94, 105-110, 122, 171, 189, 195, 197, 217, 235, 244, 322

- Mass transfer  
     (*see Boundary-layer applications*)
- Matching (*defined*), 344
- Mean free path, 23, 25, 27
- Mixing layer, 38-41, 95ff., 242, 321, 357-358  
     compressible, 172, 183-189, 195  
     curved, 242-243  
     spreading rate (*defined*), 99
- Mixing-length hypothesis, 6, 23, 27-30
- Momentum-integral equation, 113
- Morkovin's hypothesis, 172
- Navier-Stokes equation:  
     Favre-averaged, 176  
     filtered, 325  
     Reynolds-averaged, 16
- Navier-Stokes operator, 17, 88, 166
- Nonstationary turbulence, 14
- Oldroyd derivative, 219-220
- One-equation models, 77-83  
     Baldwin-Barth, 8, 79, 81-82, 160, 197  
     Bradshaw-Ferriss-Atwell, 8, 78-79, 94  
     Goldberg, 8, 78, 81  
     Nee-Kovaszny, 78  
     Prandtl-Emmons-Glushko, 6, 74-79, 327  
     Spalart-Allmaras, 8, 79-81, 281
- Outer expansion (*defined*), 341
- Overlap region (*defined*), 344
- Perfect-gas law, 175, 423
- Permutation tensor (*defined*), 334
- Phase-space portrait, 239
- Pipe flow, 4, 53-59, 132-135, 154-157, 248-251, 364-370  
     skin friction formula, 56
- Pope's modification, 102, 104, 359
- Prandtl number:  
     laminar, 175, 328, 423  
     turbulent, 182, 357, 423
- Pressure diffusion, 75-76, 182-183
- Pressure dilatation, 179, 182-183
- Pressure-echo effect, 229-230, 235, 248-249
- Pressure-strain correlation, 222, 224, 226-231, 233, 235, 243  
     rapid (*defined*), 226  
     slow (*defined*), 226
- Pressure-strain redistribution:  
     (*see Pressure-strain correlation*)
- Pressure work, 179, 183
- Production (*defined*), 75
- Pseudo-spectral method, 320, 323
- Rapid pressure strain:  
     (*see Pressure-strain correlation*)
- Rapid pressure-strain models:  
     Launder-Reece-Rodi, 229  
     Lumley, 230  
     Speziale-Sarkar-Gatski, 230
- Realizability, 220, 224, 229
- Realization, 321
- Resolvable scale, 324-325
- Return to isotropy, 214, 220, 222, 228, 239
- Reynolds' analogy, 181
- Reynolds-stress (*defined*), 16  
     anisotropy tensor, 225  
     equation, 19, 179  
     tensor invariants, 230
- Richardson extrapolation, 304-305
- Richardson number, 217
- Rodi's ASM approximation, 221
- Rossby number, 252
- Rotating channel flow:  
     (*see Channel flow, rotating*)
- Rotation tensor (*defined*), 218
- Round-jet/plane-jet anomaly, 102, 104, 242-243
- Rubel-Melnik transformation, 277, 281-282, 286, 351, 353, 371-372
- Second-moment closure models:  
     (*see Second-order closure models*)
- Second-order closure models, 223-235  
     Daly-Harlow, 9, 228  
     Donaldson, 9, 224-225, 228  
     Fu-Launder-Tselepidakis, 231, 241  
     Gibson-Launder, 229, 252  
     Gibson-Younis, 261-262  
     Hanjalić-Launder, 253-254  
     Launder-Reece-Rodi, 9, 226, 231-232, 235ff.  
     Mellor-Herring, 225  
     Shih-Lumley, 231, 241  
     Wilcox multiscale, 232-235, 235ff., 277, 352, 364-365, 368, 371, 373, 391, 408-409, 412, 424  
     Wilcox-Rubesin, 225, 232, 238, 256-257

- Second viscosity:  
   eddy, 181  
   molecular, 175
- Secondary motion, 165, 214, 218, 220-223, 255, 266
- Self preserving (*defined*), 30
- Self similar (*see Self preserving*)
- SGS Reynolds stress, 325
- Similarity-solution method, 33-36  
   existence conditions, 35
- Single-point correlation, 90, 227
- Singular perturbation problem:  
   (*defined*), 339
- Slightly-rough surface, 278, 364, 371
- Slow pressure strain:  
   (*see Pressure-strain correlation*)
- Smagorinsky model, 326-327
- Specific dissipation (*defined*), 85-87
- Spectral method, 319, 320, 323, 324
- Spinning, segmented cylinder, 256-257
- Spreading rate (*defined*):  
   far wake, 99  
   jet, 99  
   mixing layer, 99
- Stability:  
   analysis, 293-297  
   conditional, 294  
   unconditional, 290, 291, 294
- Stanford Olympics:  
   First, 60  
   Second, 60
- Stationary turbulence, 11, 12, 14
- Stiffness, 273-275, 303
- Strain-rate tensor (*defined*), 218
- Strange attractor, 328-329
- Stratification, 214, 218, 224, 266
- Streamline curvature, 7, 50, 110, 214, 215-217, 222-223, 243, 253-255, 412
- Subgrid scale (SGS), 323-324, 326-327
- Surface mass transfer:  
   (*see Boundary-layer applications*)
- Surface roughness:  
   (*see Boundary-layer applications*)
- Taylor microscale, 315
- Term-by-term modeling:  
   (*see Drastic surgery*)
- Thermal conductivity, 175
- Transcendentally small (*defined*), 338
- Turbulence Mach number (*defined*), 184
- Turbulence Reynolds number (*defined*), 139, 152
- Turbulent/nonturbulent interface, 38, 40, 94, 98, 118, 279-286, 305, 320, 354
- Turbulent transport, 76, 182, 225-226
- Two-equation models, 83-92  
    $k$ - $\epsilon$ :  
     Chien, 139-145, 154, 194, 196, 198-200, 261-262, 278, 291, 408, 428  
     Fan-Lakshminarayana-Barnett 139, 291, 408, 428  
     Dutoya-Michard, 139, 142-143  
     Hassid-Poreh, 139, 142-143  
     Hoffmann, 139, 142-143  
     Jones-Launder, 87, 139-142, 144-145, 154, 198, 205, 287, 291, 408, 427  
     Lam-Bremhorst, 139-145, 154, 278, 291, 408, 427  
     Launder-Sharma, 87-89, 92ff., 198, 204, 232, 242-243, 252, 291, 352, 355, 357, 359, 375, 408, 427  
     Myong-Kasagi, 139  
     Reynolds, 139  
     Rodi, 205, 207, 209  
     Shih-Hsu, 139  
     Speziale-Abid-Anderson, 139  
     Standard (*Launder-Sharma*)  
     Yang-Shih, 139, 291, 408, 428  
     Zhang-So-Speziale-Lai, 139, 198, 201-202  
    $k$ - $\omega$ :  
     Kolmogorov, 7-8, 83-88, 92, 123  
     Speziale-Abid-Anderson, 85  
     Standard (*Wilcox*)  
     Wilcox, 9, 84-87, 92ff., 194, 196, 198, 216, 223, 260, 265, 277, 352, 355, 357, 359, 364-365, 368, 371, 373, 375, 391, 408, 412, 424  
    $k$ - $\omega^2$ :  
     Saffman, 8, 84, 88, 94, 123, 281, 284  
     Spalding, 85-86, 124  
     Wilcox-Alber, 9, 85-86, 183  
     Saffman-Wilcox, 9, 85, 190, 203  
     Wilcox-Traci, 9, 85  
     Wilcox-Rubesin, 9, 85-86, 110, 114, 123, 142-144, 151, 214, 219, 238, 256-257, 289



Two-equation models (*Continued*): $k^{1/2}$ - $\omega$ :

Coakley, 85

 $k$ - $k\ell$ :

Ng-Spalding, 91

Rodi-Spalding, 91

Rotta, 83, 90

Smith, 91

Vollmers-Rotta, 281

 $k$ - $\ell$ :

Rotta, 83

 $k$ - $\tau$ :Speziale-Abid-Anderson, 92,  
123-124 $k$ - $k\tau$ :

Zeierman-Wolfshtein, 91, 94

Two-point correlation, 90, 227

Universal equilibrium theory, 314, 316

Unsteady flow, 14, 256-261, 292, 296

Van Driest damping function (*defined*),  
47Velocity thickness (*defined*), 50

Viscous-interface layer, 284-286, 308

Viscous sublayer, 44-46, 48, 122-125,  
128, 130-132, 142, 152, 244-  
247, 261, 277, 305, 322, 373-  
374

von Neumann stability analysis:

(*see Stability, analysis*)

Vortex stretching, 3, 4, 94, 103

Wake (*see Far wake*)

Wake-strength parameter, 117-120, 375

Wall functions, 126-128, 133, 142, 161f.,  
195, 204f., 244f., 248, 255,  
261ff., 275f., 305

Wall-reflection effect:

(*see Pressure-echo effect*)

Weak solution, 279-284

WKB method, 192, 211

Zero-equation models:

(*see Algebraic models*)